PAST RECONSTRUCTION OF THE PHYSICAL AND BIOGEOCHEMICAL OCEAN STATE

EDITED BY: Simona Masina, François Counillon, Marilaure Gregoire, Andrea Storto and Hiroyuki Tsujino

PUBLISHED IN: Frontiers in Earth Science, Frontiers in Marine Science and Frontiers in Environmental Science

frontiers Research Topics

ISSN 1664-8714
ISBN 978-2-88976-710-6
DOI 10.3389/978-2-88976-710-6

About Frontiers

Frontiers is more than just an open-access publisher of scholarly articles: it is a pioneering approach to the world of academia, radically improving the way scholarly research is managed. The grand vision of Frontiers is a world where all people have an equal opportunity to seek, share and generate knowledge. Frontiers provides immediate and permanent online open access to all its publications, but this alone is not enough to realize our grand goals.

Frontiers Journal Series

The Frontiers Journal Series is a multi-tier and interdisciplinary set of open-access, online journals, promising a paradigm shift from the current review, selection and dissemination processes in academic publishing. All Frontiers journals are driven by researchers for researchers; therefore, they constitute a service to the scholarly community. At the same time, the Frontiers Journal Series operates on a revolutionary invention, the tiered publishing system, initially addressing specific communities of scholars, and gradually climbing up to broader public understanding, thus serving the interests of the lay society, too.

Dedication to Quality

Each Frontiers article is a landmark of the highest quality, thanks to genuinely collaborative interactions between authors and review editors, who include some of the world's best academicians. Research must be certified by peers before entering a stream of knowledge that may eventually reach the public - and shape society; therefore, Frontiers only applies the most rigorous and unbiased reviews.
Frontiers revolutionizes research publishing by freely delivering the most outstanding research, evaluated with no bias from both the academic and social point of view. By applying the most advanced information technologies, Frontiers is catapulting scholarly publishing into a new generation.

What are Frontiers Research Topics?

Frontiers Research Topics are very popular trademarks of the Frontiers Journals Series: they are collections of at least ten articles, all centered on a particular subject. With their unique mix of varied contributions from Original Research to Review Articles, Frontiers Research Topics unify the most influential researchers, the latest key findings and historical advances in a hot research area! Find out more on how to host your own Frontiers Research Topic or contribute to one as an author by contacting the Frontiers Editorial Office: frontiersin.org/about/contact

PAST RECONSTRUCTION OF THE PHYSICAL AND BIOGEOCHEMICAL OCEAN STATE

Topic Editors:
Simona Masina, Euro-Mediterranean Center on Climate Change, Bologna, Italy
François Counillon, Nansen Environmental and Remote Sensing Center, Norway
Marilaure Gregoire, University of Liège, Belgium
Andrea Storto, Institute of Marine Science, Department of Earth System Sciences and Technologies for the Environment, National Research Council (CNR), Italy
Hiroyuki Tsujino, Meteorological Research Institute, Japan Meteorological Agency, Japan

Citation: Masina, S., Counillon, F., Gregoire, M., Storto, A., Tsujino, H., eds. (2022). Past Reconstruction of the Physical and Biogeochemical Ocean State. Lausanne: Frontiers Media SA. doi: 10.3389/978-2-88976-710-6

Table of Contents

frontiers | Frontiers in Earth Science

EDITORIAL
published: 31 May 2022
doi: 10.3389/feart.2022.890370

Editorial: Past Reconstruction of the Physical and Biogeochemical Ocean State

Simona Masina[1]*, *François Counillon*[2], *Marilaure Gregoire*[3], *Andrea Storto*[4] and *Hiroyuki Tsujino*[5]

[1]Ocean Modelling and Data Assimilation Division, Fondazione Centro Euro-Mediterraneo Sui Cambiamenti Climatici, Bologna, Italy, [2]Nansen Environmental and Remote Sensing Center and Bjerknes Centre for Climate Research, Bergen, Norway, [3]MAST-FOCUS, Department of Astrophysics, Geophysics and Oceanography, University of Liège, Liège, Belgium, [4]Institute of Marine Sciences, National Research Council (CNR), Roma, Italy, [5]Meteorological Research Institute, Japan Meteorological Agency, Tsukuba, Japan

Keywords: climate reconstructions, reanalyses, observation-based products, ocean cryosphere and biosphere in the Earth system, downstream applications

Editorial on the Research Topic

Past Reconstruction of the Physical and Biogeochemical Ocean State

OPEN ACCESS

Edited by:
Katja Fennel,
Dalhousie University, Canada

Reviewed by:
Matthew Mazloff,
University of California, San Diego, United States
David Ford,
Met Office, United Kingdom
Jann Paul Mattern,
University of California, Santa Cruz, United States

***Correspondence:**
Simona Masina
simona.masina@cmcc.it

Specialty section:
This article was submitted to Interdisciplinary Climate Studies, a section of the journal Frontiers in Earth Science

Received: *05 March 2022*
Accepted: *17 May 2022*
Published: *31 May 2022*

Citation:
Masina S, Counillon F, Gregoire M, Storto A and Tsujino H (2022) Editorial: Past Reconstruction of the Physical and Biogeochemical Ocean State. Front. Earth Sci. 10:890370. doi: 10.3389/feart.2022.890370

INTRODUCTION

Knowledge of the ocean's physical, biogeochemical and ecosystem state and variability is crucial for understanding the evolution of our climate system and better predicting its future. However, the sparseness and inhomogeneous distribution of observations hinder the creation of sound 4-dimensional reconstructions of the past (for an overview of ocean observing systems see the Research Topic Oceanobs'19: An Ocean of Opportunity). Instead, we must rely on a combination of ocean modeling and data analysis to infer past changes. Over the last decade the quality of ocean reanalyses has improved mainly thanks to advances in data assimilation methods and more quality-controlled observation data sets. Reanalyses provide the best-possible state estimate by assimilating observations into a dynamical model (Balmaseda et al., 2015; Masina and Storto, 2017; Storto et al., 2019). In addition, advanced statistical mapping methods (e.g., objective or variational analysis) provide observation-based gridded fields whose resolution depends on the amount of available data (among many Cheng et al., 2017, Ishii et al., 2017; Boyer et al., 2018). For many variables, particularly biogeochemical, the lack of observations more strongly limits the spatial and temporal resolution of these gridded products (Fennel et al., 2019).

The Research Topic gathers contributions aiming at reconstructing the past physical, sea ice and biogeochemical state of the ocean using models in combination with data. Ocean reanalyses and observation-mapping are proposed to further our knowledge, to demonstrate their use in supporting various applications, and to increase confidence in these reconstructions within the scientific community. The products and applications described in this topic provide a foundation for their use in ecosystem-based management, policy advice to support mitigation and adaptation strategies, and in the identification of pathways towards a sustainable ocean.

CONTRIBUTIONS

Reanalyses

Ocean reanalyses are today an important tool for science-based studies and climate investigations. They are also used to initialize prediction systems from sub-seasonal to decadal time scales and to

support observational network monitoring. In the framework of the Copernicus Marine Environment Monitoring Service (CMEMS), validated global and European regional eddy-resolving physical and biogeochemical reanalyses are produced for several purposes. In this Research Topic we present four new products which all serve the scientific purpose for providing reliable and accurate estimates of the interannual variability and trends of the global ocean and sea-ice state (Jean-Michel et al.), the Mediterranean physical (Escudier et al.) and biogeochemical (Cossarini et al.) state and the Black Sea physics (Lima et al.). These products represent a step forward towards our understanding of the mechanism of uptake and redistribution of natural and anthropogenic carbon dioxide and heat by the ocean, as well as the quantification of the induced changes in its physical (e.g. reduced ventilation, increased stratification, etc.) and biogechemical (e.g. acidification, deoxygenation) state. The increasingly higher resolution of ocean reanalyses combined with improved data assimilation methods and observation abundance make them well-suited to represent also the mesoscale variability of surface dynamics. In addition, the reanalyses have strong assets which may serve regional or sub-basin applications and downstream services in support of the blue economy of coastal countries.

Climatologies and Observations-Based Products

In addition to the model-based reanalysis products, two categories of observation-based products include climatologies (mean state and seasonal cycle) and monthly (or higher frequency) gridded fields covering many years. Global (Shahzadi et al.) and high resolution regional (Lee et al.) temperature and salinity climatologies derived from irregularly distributed historical observations by means of traditional or more advanced objective analysis techniques are essential and valuable products. The new climatologies benefit from the increased availability of temperature and salinity profiles derived from the Argo program in the 21st century and provide regional ocean products able to represent mesoscale variability similar to altimetry-derived surface current products. Temperature and salinity climatologies serve different purposes, such as initializing and validating numerical ocean models and understanding climate anomalies.

A limitation of observation-based products is that one needs to formulate a statistical relationship to extrapolate the information contained in the observations in space and to other variables (e.g. using an EOF analysis). In Oke et al., such relationships are computed from a static model covariance matrix, using the ensemble optimal interpolation (EnOI) data assimilation technique. The EnOI is implemented using an ensemble that includes anomalies for multiple space- and time-scales: mesoscale, intraseasonal, seasonal, and interannual. However, unlike in reanalysis, the model is not run in between the assimilation step (offline assimilation).

In the work by Alvera-Azcarate et al. combining at least three satellites has been shown to improve the representation of ocean color variability at 1 km resolution over the Greater North Sea during the period 1998–2020. The multidecadal product allows an analysis of interannual variability and the indication of an earlier spring bloom tendency in the North Sea.

Applications

Using reanalyses and observation-based gridded fields at high spatial resolution is necessary to resolve the mesoscale variability and its contribution to the ocean dynamics and thermodynamics. By means of an eddy detection technique, Bonaduce et al. show that mesoscale eddies represented in a Mediterranean reanalysis represent a significant contribution of the ocean dynamics in the Mediterranean Sea as they account for a large portion of the sea-surface height variability at temporal scales longer than 1 month and for the kinetic energy both at the surface and at depth. Furthermore, temperature anomalies driven by long-lived eddies can affect up to 15–25% of the monthly variability of the upper ocean heat content in the Mediterranean basin.

Yang et al. investigated the contribution of mesoscale ocean eddies to the Atlantic meridional heat transport (MHT) variability, which in turn drives the decadal climate changes recently observed in the North Atlantic and found that the increase of eddy population due to the increase of horizontal resolution in an eddy-resolving global reanalysis (Jean-Michel et al.) does not affect the MHT anomalies significantly.

An alternative to the deterministic production of eddy-resolving reanalyses and observation-based products is the generation of coarser resolution ensemble of reanalyses which allows for uncertainty estimation and optimization of poorly-constrained model parameters. The ensemble approach is particularly valuable for example in data-sparse region such as the Antarctica, where Iovino et al. showed that an eddy-permitting ensemble of reanalyses is capable to reproduce the observed regional spatial and temporal variability of different sea-ice classes (marginal and pack ice).

In another contribution, Singh et al. demonstrated the ability of ensemble data assimilation methods (dual one step ahead smoother) to provide high-quality and improved biogeochemical (BGC) parameters that strongly reduce model bias within an Earth system model by assimilating salinity and temperature profiles and surface biogeochemical (Phytoplankton, Nitrate, Phosphate, Silicate, and Oxygen) observations.

PERSPECTIVES

Model-based and observation-based past reconstructions of the ocean state are complex products which will benefit from the information of the integrated observing system, and the arrival of new datasets from satellites (e.g., Surface Water and Ocean Topography mission) and *in situ* observations (e.g., Deep Argo and BGC Argo). Questions of how to mitigate discontinuities in the observation spectrum will be central to better integrate all the components of the observing system and make the best use of ocean observations also improving quality control procedure.

A key activity for ocean or coupled reanalyses is their use by the climate community to estimate the past and present energy, water and carbon budgets (among many Abraham et al., 2013,

von Schuckmann et al., 2018; Meyssignac et al., 2019), and to provide uncertainty of these estimates. It is thus important to further investigate their ability to provide accurate and reliable estimates of the interannual variability and trends of essential climate variables through continuous evaluation and development of refined data assimilation techniques and multi-model ensemble approaches. The novelty of the methods used for the products presented in this Research Topic includes: combining objective analysis with model based covariance, multiscale optimisation approach, eddy-resolving reanalyses, the verification of eddy characteristics and phytoplankton from remote sensing data, and the estimation of model parameters to reduce model biases.

The challenges that this community is facing span from the need to progress in the context of coupled earth system reconstructions (Baatz et al., 2021), which also require to improve assimilation methods to include the non-Gaussian distributions of biogeochemical and sea-ice observations, to the need of dealing with data-sparse regions and periods to respond to the demand for longer time series and backward in time extensions. These kinds of products are now expected to inform on past and near-present oceanic conditions to supply ocean monitoring indicators with a reliable accuracy, be used to track the health signs of the ocean and changes in line with climate change, and serve policy-makers to implement and adapt environmental strategies. The demand by end-users for products with higher spatial and temporal resolution, especially in coastal regions experiencing increasing threats, adds new challenges involving the difficulties of taking into account the multivariate assimilations of physical and biogeochemical variables, to account for tides, waves, accurate bathymetry, and in general a more realistic representation of coastal hydrological processes.

AUTHOR CONTRIBUTIONS

SM wrote the first draft of the manuscript taking into account all the papers published in the Research Topic. All co-editors made inputs to the initial draft, contributed to the manuscript revision, and read and approved the submitted version of the manuscript.

REFERENCES

Abraham, J. P., Baringer, M., Bindoff, N. L., Boyer, T., Cheng, L. J., Church, J. A., et al. (2013). A Review of Global Ocean Temperature Observations: Implications for Ocean Heat Content Estimates and Climate Change. *Rev. Geophys.* 51, 450–483. doi:10.1002/rog.20022

Baatz, R., Hendricks Franssen, H. J., Euskirchen, E., Sihi, D., Dietze, M., Ciavatta, S., et al. (2021). Reanalysis in Earth System Science: Toward Terrestrial Ecosystem Reanalysis. *Rev. Geophys.* 59, e2020RG000715. doi:10.1029/2020rg000715

Balmaseda, M. A., Hernandez, F., Storto, A., Palmer, M. D., Alves, O., Shi, L., et al. (2015). The Ocean Reanalyses Intercomparison Project (ORA-IP). *J. Operational Oceanogr.* 8 (Suppl. 1), s80–s97. doi:10.1080/1755876X.2015.1022329

Boyer, T. P., García, H. E., Locarnini, R. A., Zweng, M. A., Mishonov, A. V., Reagan, J. R., et al. (2018). World Ocean Atlas 2018. NOAA National Centers for Environmental Information. Dataset. Available online at: https://www.ncei.noaa.gov/archive/accession/NCEIWOA18 (Accessed 22 May 2022).

Cheng, L., Trenberth, K. E., Fasullo, J., Boyer, T., Abraham, J., and Zhu, J. (2017). Improved Estimates of Ocean Heat Content from 1960 to 2015. *Sci. Adv.* 3, e1601545. doi:10.1126/sciadv.1601545

Fennel, K., Gehlen, M., Brasseur, P., Brown, C. W., Ciavatta, S., Cossarini, G., et al. (2019). Perruche C and the GODAE OceanView Marine Ecosystem Analysis and Prediction Task TeamAdvancing Marine Biogeochemical and Ecosystem Reanalyses and Forecasts as Tools for Monitoring and Managing Ecosystem Health. *Front. Mar. Sci.* 6, 89. doi:10.3389/fmars.2019.00089

Ishii, M., Fukuda, Y., Hirahara, S., Yasui, S., Suzuki, T., and Sato, K. (2017). Accuracy of Global Upper Ocean Heat Content Estimation Expected from Present Observational Data Sets. *Sola* 13, 163–167. doi:10.2151/sola.2017-030

Masina, S., and Storto, A. (2017). Reconstructing the Recent Past Ocean Variability: Status and Perspective. *J. Mar. Res.* 75 (6), 727–764. doi:10.1357/002224017823523973

Meyssignac, B., Boyer, T., Zhao, Z., Hakuba, M. Z., Landerer, F. W., Stammer, D., et al. (2019). Measuring Global Ocean Heat Content to Estimate the Earth Energy Imbalance. *Front. Mar. Sci.* 6, 432. doi:10.3389/fmars.2019.00432

Storto, A., Alvera-Azcárate, A., Balmaseda, M. A., Barth, A., Chevallier, M., Counillon, F., et al. (2019). Ocean Reanalyses: Recent Advances and Unsolved Challenges. *Front. Mar. Sci.* 6, 418. doi:10.3389/fmars.2019.00418

von Schuckmann, K., Pierre-Yves, L. T., Neville, S., Ananda, P., Pierre, B., Katja, F., et al. (2018). Copernicus Marine Service Ocean State Report. *J. Oper. Oceanogr.* 11 (Suppl. 1), S1–S142. doi:10.1080/1755876X.2018.1489208

Conflict of Interest: The authors declare that the research was conducted in the absence of any commercial or financial relationships that could be construed as a potential conflict of interest.

frontiers in Earth Science

ORIGINAL RESEARCH
published: 17 June 2021
doi: 10.3389/feart.2021.696985

Combining Argo and Satellite Data Using Model-Derived Covariances: Blue Maps

Peter R. Oke[1], Matthew A. Chamberlain[1], Russell A. S. Fiedler[1], Hugo Bastos de Oliveira[2], Helen M. Beggs[3] and Gary B. Brassington[3]*

[1]CSIRO Oceans and Atmosphere, Hobart, TAS, Australia, [2]Integrated Marine Observing System, University of Tasmania, Hobart, TAS, Australia, [3]Bureau of Meteorology, Melbourne, VIC, Australia

Blue Maps aims to exploit the versatility of an ensemble data assimilation system to deliver gridded estimates of ocean temperature, salinity, and sea-level with the accuracy of an observation-based product. Weekly maps of ocean properties are produced on a 1/10°, near-global grid by combining Argo profiles and satellite observations using ensemble optimal interpolation (EnOI). EnOI is traditionally applied to ocean models for ocean forecasting or reanalysis, and usually uses an ensemble comprised of anomalies for only one spatiotemporal scale (e.g., mesoscale). Here, we implement EnOI using an ensemble that includes anomalies for multiple space- and time-scales: mesoscale, intraseasonal, seasonal, and interannual. The system produces high-quality analyses that produce mis-fits to observations that compare well to other observation-based products and ocean reanalyses. The accuracy of Blue Maps analyses is assessed by comparing background fields and analyses to observations, before and after each analysis is calculated. Blue Maps produces analyses of sea-level with accuracy of about 4 cm; and analyses of upper-ocean (deep) temperature and salinity with accuracy of about 0.45 (0.15) degrees and 0.1 (0.015) practical salinity units, respectively. We show that the system benefits from a diversity of ensemble members with multiple scales, with different types of ensemble members weighted accordingly in different dynamical regions.

Keywords: ocean observations, Argo, satellite observations, ensemble data assimilation, ocean properties, ocean reanalysis

OPEN ACCESS

Edited by:
François Counillon, Nansen Environmental and Remote Sensing Center, Norway

Reviewed by:
Jiang Zhu, Institute of Atmospheric Physics (CAS), China
Mark Buehner, Environment and Climate Change, Canada

****Correspondence:***
Peter R. Oke
peter.oke@csiro.au

Specialty section:
This article was submitted to Interdisciplinary Climate Studies, a section of the journal Frontiers in Earth Science

Received: *18 April 2021*
Accepted: *02 June 2021*
Published: *17 June 2021*

Citation:
Oke PR, Chamberlain MA, Fiedler RAS, Bastos de Oliveira H, Beggs HM and Brassington GB (2021) Combining Argo and Satellite Data Using Model-Derived Covariances: Blue Maps. Front. Earth Sci. 9:696985. doi: 10.3389/feart.2021.696985

1 INTRODUCTION

There are many gridded products that use Argo and other data to produce global estimates of temperature and salinity at different depths[1]. These products can be grouped under two broad categories: observation-based and model-based. Most observation-based products are coarse-resolution (e.g., Ridgway et al., 2002; Roemmich and Gilson, 2009; Guinehut et al., 2012; Locarnini et al., 2013; Schmidtko et al., 2013; Zweng et al., 2013, with horizontal grid spacing of 0.5–1°). Model-based products, here restricted to ocean reanalyses that assimilate observations into an ocean general circulation model, include systems with coarse-resolution (e.g., Kohl and Stammer, 2007; Yin et al., 2011; Balmaseda et al., 2012; Köhl, 2015), some that are eddy-permitting (e.g., Carton

[1]argo.ucsd.edu/data/argo-data-products/.

and Giese, 2006; Carton and Giese, 2008; Ferry et al., 2007), and others that can be regarded as eddy-resolving (e.g., Oke et al., 2005; Oke et al., 2013c; Artana et al., 2019).

An important difference between all of the observation-based products is their assumptions about the background error covariance. All systems use some variant of objective analysis, and they all represent the influence of topography and land on the background error covariance in different ways. Some observation-based products are climatologies, including a mean state and seasonal cycle (e.g., Ridgway et al., 2002; Locarnini et al., 2013; Zweng et al., 2013), and others include monthly (or weekly) fields and span many years (e.g., Roemmich and Gilson, 2009; Guinehut et al., 2012; Good et al., 2013; Schmidtko et al., 2013; Ishii et al., 2017). Most observation-based products perform calculations on pressure surfaces (e.g., Roemmich and Gilson, 2009), but a few operate on isopycnal surfaces (e.g., Schmidtko et al., 2013). Most observation-based products use only Argo data (e.g., Roemmich and Gilson, 2009), or Argo data plus other *in situ* data (e.g., Ridgway et al., 2002). Systems that use both *in situ* and satellite data are less common—Guinehut et al. (2012) is a notable exception. A compelling feature of observation-based products is that they usually "fit" observations quite well. But a possible limitation of this group of products is that most are coarse-resolution, and most don't exploit all of the available observations (most don't use satellite data; though again Guinehut et al. (2012), is an exception).

Like observation-based products, perhaps the most important difference between the model-based products is also how each system estimates the background error covariance. Some systems use objective analysis (e.g., Carton and Giese, 2008), some use variational data assimilation (e.g., Kohl and Stammer, 2007; Köhl, 2015), and some use ensemble data assimilation (e.g., Oke et al., 2013c; Artana et al., 2019). A compelling feature of model-based products is that virtually all systems combine Argo data with other *in situ* data and satellite data, and all produce gridded estimates of all variables—even variables that are not systematically observed, such as velocity. Moreover, model-based products yield estimates that are somewhat dynamically-consistent, including the influence of topography, land, surface forcing, and ocean dynamics. Most systems are not precisely dynamically-consistent, since most do not conserve properties during the assimilation step, when the model fields are adjusted to better match observations. However, on the down-side, model-based products often "fit" observations relatively poorly (Oke et al., 2012; Balmaseda et al., 2015; Ryan et al., 2015; Shi et al., 2017), and many systems are hampered by model-bias (e.g., Oke et al., 2013c).

Blue Maps version 1.0, presented here, is intended to exploit the strengths of both groups of systems, delivering a product with the accuracy of an observation-based product, with the comprehensive ocean representation of a model-based system. We show here that Blue Maps produces gridded estimates with greater accuracy than model-based products, and with more versatility than observation-based products.

This paper is organised with details of the analysis system presented in **Section 2**, results in **Section 3**, an analysis and discussion in **Section 4**, and conclusions in **Section 5**.

2 ANALYSIS SYSTEM

The name, Blue Maps, is intended to acknowledge the origin of the data assimilation system used here—developed under the Bluelink Partnership (Schiller et al., 2020); acknowledge the statistical category for the method—a Best Linear Unbiased Estimate (BLUE); and acknowledge that the tool is intended for deep-water applications (Blue water). The method used to produce analyses for Blue Maps is Ensemble Optimal Interpolation (EnOI; Oke, 2002; Evensen, 2003), and the code-base is EnKF-C (Sakov, 2014), implemented with the EnOI option. Variants of EnOI are widely used to perform ocean reanalyses and forecasts on global scales (e.g., Oke et al., 2005; Brassington et al., 2007; Oke et al., 2013c; Lellouche et al., 2013; Lellouche et al., 2018; Artana et al., 2019) and regional scales (e.g., Counillon and Bertino, 2009; Xie and Zhu, 2010; Oke et al., 2013a; Sakov and Sandery, 2015). Arguably the most important elements of any configuration of EnOI, or an Ensemble Kalman Filter (the "optimal," but more expensive, "parent" of EnOI) are the ensemble construction, the ensemble size, and the localisation length-scales. To understand this, consider the simplified analysis equation:

$$\mathbf{w}^a = \mathbf{w}^b + \mathbf{w}^{inc} \tag{1}$$

$$= \mathbf{w}^b + \sum_{i=1}^{n} \mathbf{c}_i(x,y).\mathbf{A}_i(x,y,z), \tag{2}$$

where **w** is the state vector (here, this is temperature, salinity, and sea-level on a 1/10° grid), **A** is the ensemble of model anomalies, **c** is the weights of the ensemble members, superscripts *a*, *b*, and *inc* denote analysis, background, and increment fields; subscripts *i* denote the *ith* ensemble member; *n* is the ensemble size; and *x*, *y*, and *z* are dimensions in space (*z* is the vertical dimension).

To understand the importance of the ensemble construction, recognise that the increments of the state $\mathbf{w}^{inc}$, are constructed by projecting the background innovations (the differences between the observations and the background field) onto the ensemble. Projections are made for each horizontal grid point, using only observations that fall within the localisation radius. These projections yield two-dimensional maps of ensemble weights **c**, for each ensemble member (note that these are two-dimensional because the system uses horizontal localisation, and not vertical localisation). From **Eq. 2** it is clear that the ensemble is important—determining the features that can be represented in the increment field. If some feature is absent in the ensemble—say, for example, there are no ensemble members with anomalies associated with an eddy in some particular region, increments resembling anomalies associated with an eddy cannot be sensibly constructed with a linear combination of those members for that region. The ensemble should include anomalies that reflect the adjustments needed to bring the

background field into closer agreement with the assimilated observations.

To understand the importance of the localisation radius, note again that for the projections at each horizontal grid point, only observations that fall within the localisation radius are used, and that the influence of an observation on that projection is reduced with distance from that grid point. If the localisation radius is too short—perhaps shorter than the typical distance between observations—then there may be insufficient observations to reliably perform the projection for a given grid point. This can result in increments with spatial scales that are not resolved by the observing system, effectively introducing noise to the analyses. Conversely, if the localisation length-scale is too long, then there may be too few degrees of freedom (depending on ensemble size—see below) for each projection to "fit" the observations (e.g., Oke et al., 2007). For ensemble-based applications, the localisation function is effectively an upper-bound on the assumed background error covariance. The effective length-scales in the ensemble-based covariance can be shorter, but not longer, than the localisation function.

To further understand the importance of the ensemble size, considering **Eq. 2**. If the ensemble is too small to "fit" the background innovations, then the quality of the analyses will be poor, yielding analysis innovations (differences between the observations and analysis fields) that are large. The assimilation process is somewhat analogous to the deconstruction of a time-series into Fourier components; or the approximation of some field by projecting onto a set of basis functions, using a least-square fit. Extending the analogy of the Fourier transformation, if the full spectrum is permitted, then all the details of an unbiased time-series can be represented. But if only a few Fourier components are permitted, then the deconstruction will deliver an approximation. If the Fourier components are chosen unwisely, excluding some dominant frequencies for example, then the deconstructed signal may be a very poor approximation of the original time-series. In the same way, to allow for an accurate assimilation, the ensemble must have a sufficient number and diversity of anomaly fields to permit an accurate projection of the background innovations.

Guided by the understanding outlined above, for any application, it is preferable to use the largest possible ensemble size. This is usually limited by available computational resources (e.g., Keppenne and Rienecker, 2003). If the ensemble is too small, then a shorter localisation radius is needed, to eliminate the impacts of spurious ensemble-based covariances that will degrade the analyses (e.g., Oke et al., 2007). If the localisation radius is too large, then there may be insufficient degrees of freedom for each projection, and the analyses will not "fit" the observations with "appropriate accuracy." By "appropriate accuracy," we mean that analyses "fit" the observations according to their assumed errors (i.e., not a perfect fit, but a fit that is consistent with the assumed observation and background field errors—the target for any Best Linear Unbiased Estimate; e.g., Henderson, 1975). These factors require a trade-off, and some tuning.

What's the status-quo for the ocean data assimilation community? It's typical for EnOI- or EnKF-applications for ocean reanalyses or forecasts to use an ensemble size of 100–200 (e.g., Xie and Zhu, 2010; Fu et al., 2011; Sakov et al., 2012; Oke et al., 2013c; Sakov and Sandery, 2015). By some reports, an ensemble of greater than 100 is regarded as a large ensemble (e.g., Ngodock et al., 2006, 2020). Moreover, such applications typically use localisation length-scales of 100–300 km (e.g., Fu et al., 2011; Sakov et al., 2012; Oke et al., 2013c; Sakov and Sandery, 2015; Lellouche et al., 2018; Artana et al., 2019). Importantly, most of the quoted-localisation length-scales use a quasi-Gaussian function with compact support (Gaspari and Cohn, 1999). This function reduces to zero over the quoted length-scale; and so the *e*-folding scale for these applications is typically about one third of the stated length-scale. These systems all assimilate *in situ* data and satellite data. *In situ* data are dominated by Argo, with nominally 300 km between profiles, and satellite data includes along-track altimeter data, with typically 100 km between tracks. For most cases, the *e*-folding length-scale of the localisation length-scales—and hence the background error covariance—is shorter than the nominal resolution of these key components of the global ocean observing system. This seems to be a feature of ocean reanalysis and forecasts systems that has long been over-looked by the ocean data assimilation community.

For contrast to the typical configuration for ocean reanalyses, summarised above, consider the key elements of a widely-used observation-based product. Roemmich and Gilson (2009) describe an analysis system that maps Argo data to construct gridded temperature and salinity on a 1°-resolution grid. They perform objective analysis on different pressure levels independently, and estimate the background error covariance using a correlation function that is the sum of two Gaussian functions—one with an *e*-folding length-scale of 140 km, and one with an *e*-folding scale of 1,111 km. Furthermore, Roemmich and Gilson (2009) elongate the zonal length-scales at low latitudes. Their choice of background error correlation was reportedly guided by characteristics of altimetric measurements (Zang and Wunsch, 2001). This set-up uses much longer length-scales than most model-based products, and projects observations onto a coarser grid.

For Blue Maps, we calculate weekly analyses of temperature, salinity, and sea-level anomaly (SLA) by assimilating observations into a background field that is updated using damped persistence. The horizontal grid is 1/10°-resolution, and the vertical grid increases with depth, from 5 m spacing at the surface to 150 m at 1,500 m depth. Starting with climatology, using the 2013 version of the World Ocean Atlas (WOA13; Zweng et al., 2013; Locarnini et al., 2013), consecutive analyses are calculated:

$$\mathbf{w}_j^a = \mathbf{w}_j^b + \mathbf{K}\left(\mathbf{y} - \mathbf{H}\mathbf{w}_j^b\right), \tag{3}$$

where

$$\mathbf{w}_j^b = 0.8\mathbf{w}_{j-1}^a + 0.2\mathbf{w}_j^c, \tag{4}$$

where **K** is the gain; **y** is a vector of observations; **H** is an operator that interpolates from state-space to observation-space; the superscript *c* denotes climatology (for time of year), and the subscript *j* denotes the time index. The gain matrix **K** depends on

the assumed ensemble-based background error covariance and the assumed observation error covariance (here assumed to be diagonal, with diagonal elements given the values of assumed observation error variance). EnKF-C calculates analyses using a localisation method called local analysis (Evensen, 2003; Sakov and Bertino, 2011; Sakov, 2014), using a localisation function that is quasi-Gaussian (Gaspari and Cohn, 1999). The weighted sum of the analysis field and climatology, in **Eq. 4**, is equivalent to damped persistence, with an *e*-folding timescale of approximately 14 days.

Observations assimilated into Blue Maps include profiles of temperature and salinity, satellite Sea-Surface Temperature (SST), and along-track SLA. The only *in situ* data used here is Argo data (Roemmich et al., 2019), sourced from the Argo Global Data Acquisition Centres, and include only data with Quality Control flags of one and two (meaning data are good, or probably good; Wong et al., 2020). The assumed standard deviation of the observation error for Argo data is 0.05°C for temperature and 0.05 practical salinity units (psu) for salinity. The instrument error of Argo temperature data is 0.002°C and for salinity is 0.01°psu (Wong et al., 2020), so the larger errors assumed here include a modest estimate for the representation error (e.g., Oke and Sakov, 2008). SLA data are sourced from the Radar Altimeter Database System (RADS Ver. 2, Scharroo et al., 2013), and include corrections for astronomical tides and inverse barometer effects. The assumed standard deviation of the observation error for SLA is 3 cm for Jason-2 and Jason-3, 4 cm for Saral, 5 cm for Cryosat2, and 10 cm for Sentinal-3A. SST data includes only 9 km AVHRR data (May et al., 1998), sourced from the Australian Bureau of Meteorology (Dataset accessed 2015-01-01 to 2018-12-31 from: Naval Oceanographic Office, 2014a; Naval Oceanographic Office, 2014b; Naval Oceanographic Office, 2014c; Naval Oceanographic Office, 2014d). The assumed standard deviation of the observation error for AVHRR SST is 0.37–0.47°C (Cayula et al., 2004). These observation error estimates are used to construct the diagonal elements of the observation error covariance matrix, used in **Eq. 3** to construct the gain matrix.

For any given application of EnOI, it is not always clear how to best construct the ensemble. But given the importance of this element of the data assimilation system, careful thought is warranted. If it is obvious that the errors of the background field will most likely align with a certain spatial- and temporal-scale, then this is likely to be a good starting point. For example, for an eddy-resolving ocean reanalysis, we might expect the errors of the background field to be mostly associated with eddies—and specifically the formation, evolution, properties, and locations of eddies. These elements of an eddy-resolving ocean model are mostly chaotic, and so particular events are not well predicted by a model without data assimilation. For an ocean reanalysis, we might also expect that the model is likely to realistically reproduce variability on longer time-scales, without requiring much constrain from observations. For example, the seasonal cycle in a free-running model is usually realistic, as are anomalies associated with interannual variability (e.g., Oke et al., 2013b; Kiss et al., 2019). Perhaps anomalies on these scales needn't be included in an ensemble for an ocean reanalysis. For the series of Bluelink ReANalysis (BRAN) experiments, we were guided by this principle, and used an ensemble that represented anomalies associated with the mesoscale (e.g., Oke et al., 2008; Oke et al., 2013c). In the most recent version of BRAN, Chamberlain et al. (2021a; 2021b) demonstrated significant improvements using a two-step, multiscale assimilation approach. They found that by using an ensemble of interannual anomalies, they eliminated the model bias that plagued early versions of BRAN (e.g., Oke et al., 2013c). Chamberlain et al. (2021a; 2021b) also showed the benefits of using longer localisation length-scales and a larger ensemble. The configuration of EnOI for Blue Maps has benefitted from lessons learned by Chamberlain et al. (2021a; 2021b).

Unlike an ocean reanalysis, for Blue Maps, there is no underpinning model to represent a seasonal cycle, or interannual variability in response to surface forcing. In this case, there are only two ways that a seasonal cycle can be reproduced in the analyses: by the damping to climatology (**Eq. 4**), or by the assimilation of observations (**Eqs. 1–3**). Similarly for intraseasonal and interannual variability, these signals can only be introduced into the analyses by the assimilation of observations. We have therefore taken a different approach to the ensemble for Blue Maps (compared to BRAN), and we explore the performance of the system with several different ensembles. Specifically, we compare the performance of Blue Maps for six different configurations (**Table 1**). Each ensemble is constructed from a 35 years run (1979–2014) of the version three of the Ocean Forecasting Australian Model (OFAM3, Oke et al., 2013b) forced with surface fluxes from ERA-Interim (Dee and Uppala, 2009). One configuration is similar to early versions of BRAN (e.g., Oke et al., 2008; Oke et al., 2013c; Oke et al., 2018), using a 120-member ensemble that includes anomalies that reflect high-frequency and short-scale (i.e., the short mesoscale) anomalies—hereafter experiment HFSS (High Frequency, Short Scale). Three configurations use a 120-member ensemble, with anomalies that include High-Frequency Long-Scales (HFLS; including the large mesoscale, intraseasonal, and seasonal scales), Low-Frequency Short-Scales (LFSS; including the large mesoscale and interannual scales), and Low-Frequency Long-Scales (LFLS; including large mesoscale, seasonal, and interannual scales) anomalies. Members in each ensemble are constructed by calculating anomalies for different spatiotemporal scales. The specific details are summarised in **Table 1**. Ensemble members for HFLS, for example, are calculated by differencing 3 month averages from 13-month averages (**Table 1**), with four members generated from each year for the last 30 years of a 35-year free model run, with no data assimilation. One configuration that combines all three ensembles with the longer time- and space-scales (LFSS, HFLS, LFLS—child ensembles)—yielding a 360-member multi-scale ensemble, hereafter MS360 (parent ensemble). To help determine the relative impacts of ensemble size (360 *vs* 120) and multi-scales, we also include an experiment with 40 members from the HFLS, LFSS, and LFLS ensembles—yielding a 120-member multi-scale ensemble (MS120). This approach of including multiple space- and time-scales for an EnOI system is similar to the configuration

TABLE 1 | Summary of experiments, including the name of each experiment/ensemble, descriptors of the dominant spatiotemporal scales represented, details of the ensemble construction, ensemble size (*n*)m and localosation radius (LOCRAD, in km). Under ensemble construction, d, m, and y refer to days, months, and years; and Seas is seasonal climatology; and describe how ensemble members are constructed. For example, 1 d–2 m, means 1-day minus 2 month centered-averages; 3–13 m, means 3 month centered-average minus a 13-month centered-average. For each 120-member ensemble, four members are calculated for each year, using fields from 30 years of a 35-year model run. For MS120, 40 members from each of the child ensembles (HFLS, LFSS, and LFLS) are used. The localisation radius refers to the distance over which the localising function reaches zero.

Experiment/Ensemble	Dominant Scales	Ensemble construction	*n*	Locrad (km)
HFSS	Short mesoscale	1 d–2 m	120	300
LFSS	Mesoscale + interannual	1 m–seas	120	900
HFLS	Mesoscale + intraseasonal + seasonal	3–13 m	120	900
LFLS	Mesoscale + interannual + seasonal	3 m–25 y	120	900
MS120	Multi-scale	[HFLS40 LFSS40 LFLS40]	120	900
MS360	Multi-scale	[HFLS LFSS LFLS]	360	900

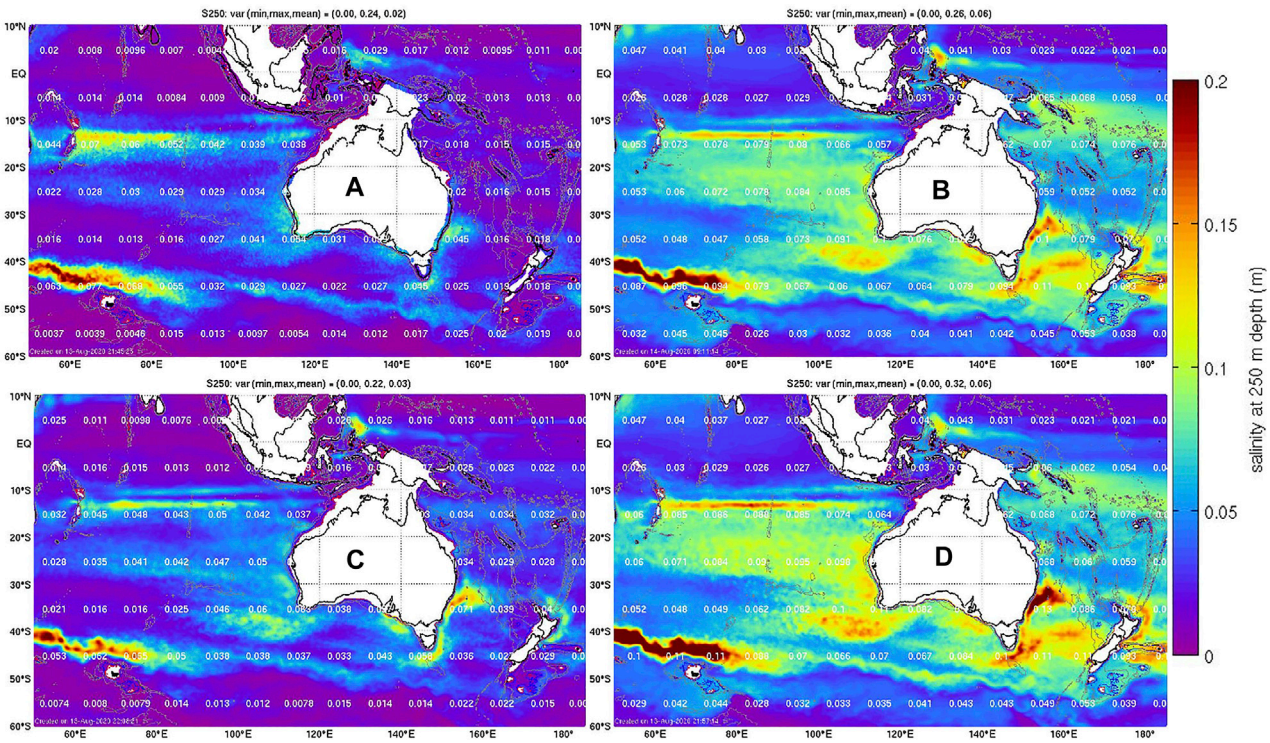

FIGURE 1 | Standard deviation of the anomalies (ensemble spread) of salinity at 250 m depth for the **(A)** HFSS, **(B)** LFSS, **(C)** HFLS, and **(D)** LFLS ensemble. The white numbers overlaying the coloured fields report the 10 × 10° average for the standard deviation for each area.

described by Yu et al. (2019), and is similar to the multi-model EnOI approach described by Cheng and Zhu (2016), Cheng et al. (2017). We consider some characteristics of these ensembles below.

The standard deviation of the salinity anomalies at 250 m depth are shown for each 120-member ensemble in **Figure 1**. This field quantifies the assumed background field error for the EnOI system. The most salient aspect of this comparison is the difference in amplitude of the standard deviations, with much larger values for LFSS and LFLS, compared to HFSS and HFLS. Both HFSS and HFLS also include vast regions of very small values. In those regions of very small assumed background field errors, the assimilation of salinity observations may have only a small impact. In the limit that we assume the background field error is zero—assimilation of data will have no impact at all (because we assume the background field is perfect). The average value for the HFSS, LFSS, HFLS, and LFLS ensemble for salinity at 250 m depth is 0.02, 0.06, 0.03, and 0.06 psu respectively. Because LFSS and LFLS assume a larger background field error, using the same observation error estimates, the experiments with these ensembles should (in theory) "fit" the observations more closely than the experiments using the HFSS and HFLS ensemble. In practice, as discussed above, this also depends on whether the anomalies

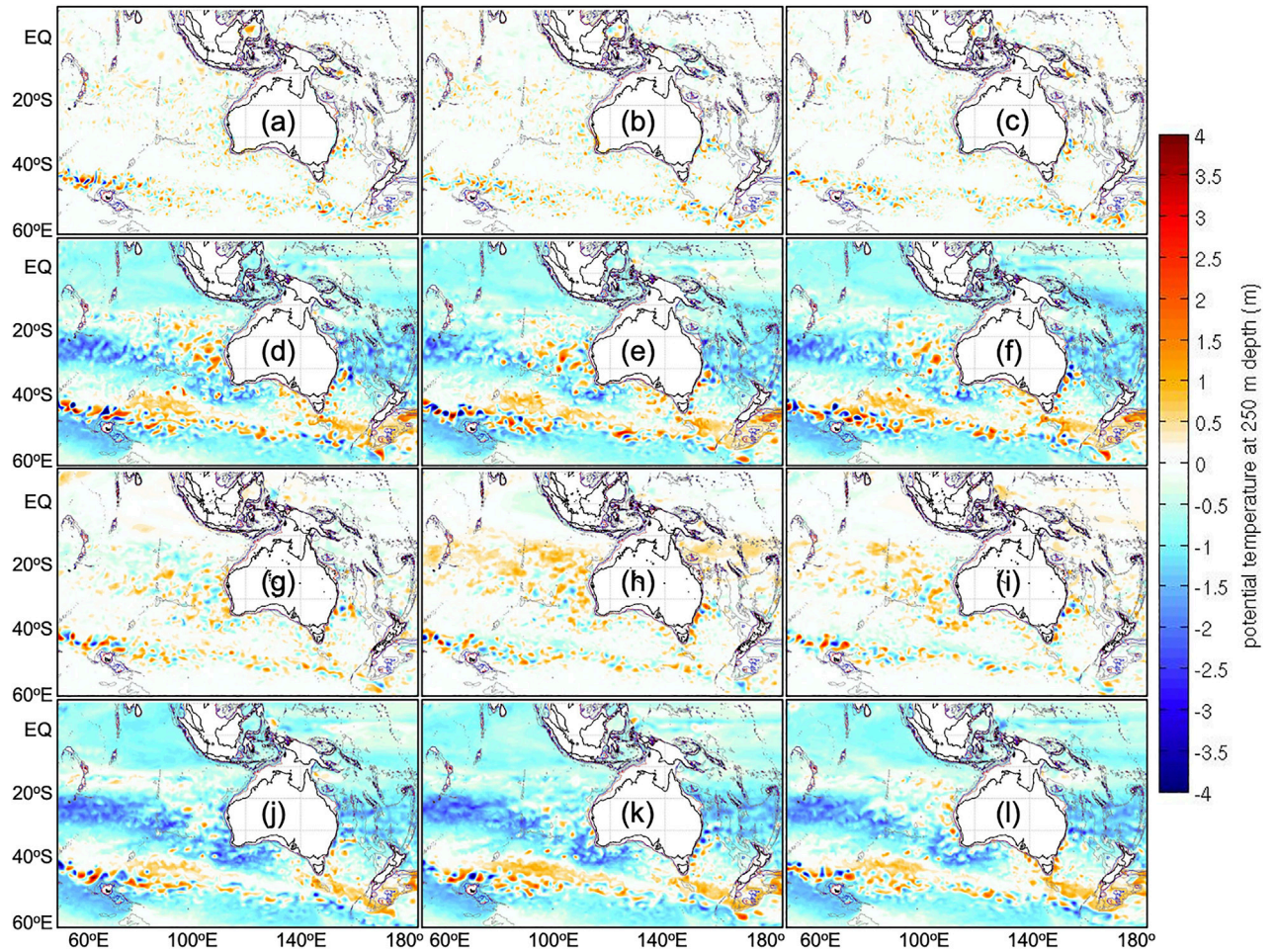

FIGURE 2 | Examples of anomalies from the first three ensemble members for the **(A–C)** HFSS ensemble, **(D–F)** LFSS ensemble, **(G–I)** HFLS ensemble, and the **(J–L)** LFLS ensemble.

in each ensemble are well-suited to "fit" the background innovations (from **Eq. 2**).

Examples of the anomalies for temperature at 250 m depth, showing the first three ensemble members for each ensemble, are presented in **Figure 2**. Several differences between the ensembles are immediately evident. Like the standard deviations for salinity at 250 m depth, the amplitudes of anomalies for temperature at 250 m depth are much smaller in the HFSS and HFLS ensembles compared to the LFSS and LFLS ensembles. This is because the HFSS and HFLS do not include anomalies associated with interannual variability. All of the ensembles include anomalies that we might associate with eddies—showing many positive and negative anomalies on eddy-scales in eddy-rich regions. Close inspection shows that the mesoscale features are smallest in the HFSS ensemble, compared to the other ensembles. The LFSS and LFLS ensembles include zonal bands of significant anomalies, between 20–30°S and 40–50°S, and broad regions of non-zero anomalies at low latitudes. We associate these bands of anomalies with interannual variability. The HFLS ensemble includes some zonal bands of anomalies, with smaller amplitude, between about 40 and 10°S, that we interpret as seasonal anomalies.

Based on the salient characteristics evident in **Figures 1**, **2**, we might expect quite different results using HFSS compared to LFSS, HFLS, and LFLS; and we equally might expect many differences between LFSS compared to HFLS and LFLS.

The length-scales evident in the ensemble fields are also used to guide the localisation length-scales (**Table 1**). For HFSS, the length-scales are short, and so we only test the system using a length-scale of 300 km (with an effective *e*-folding length-scale of about 100 km). For LFSS, HFLS, LFLS, M120, and MS360, the anomalies in the ensemble include broader-scale features. These ensembles may warrant length-scales exceeding 1,000 or even 2000 kms. Here, we're constrained by computational resource, and we settle for experiments with a localisation length-scale of 900 km (with an effective *e*-folding length-scale of about 300 km). Additionally, **Figure 2** also shows that the length-scales in HFLS and significantly shorter than LFSS and LFSS. This suggests that there may be some benefit in using different length-scales for different ensemble members in the MS120 and MS360 experiments. Unfortunately, this is option is not available

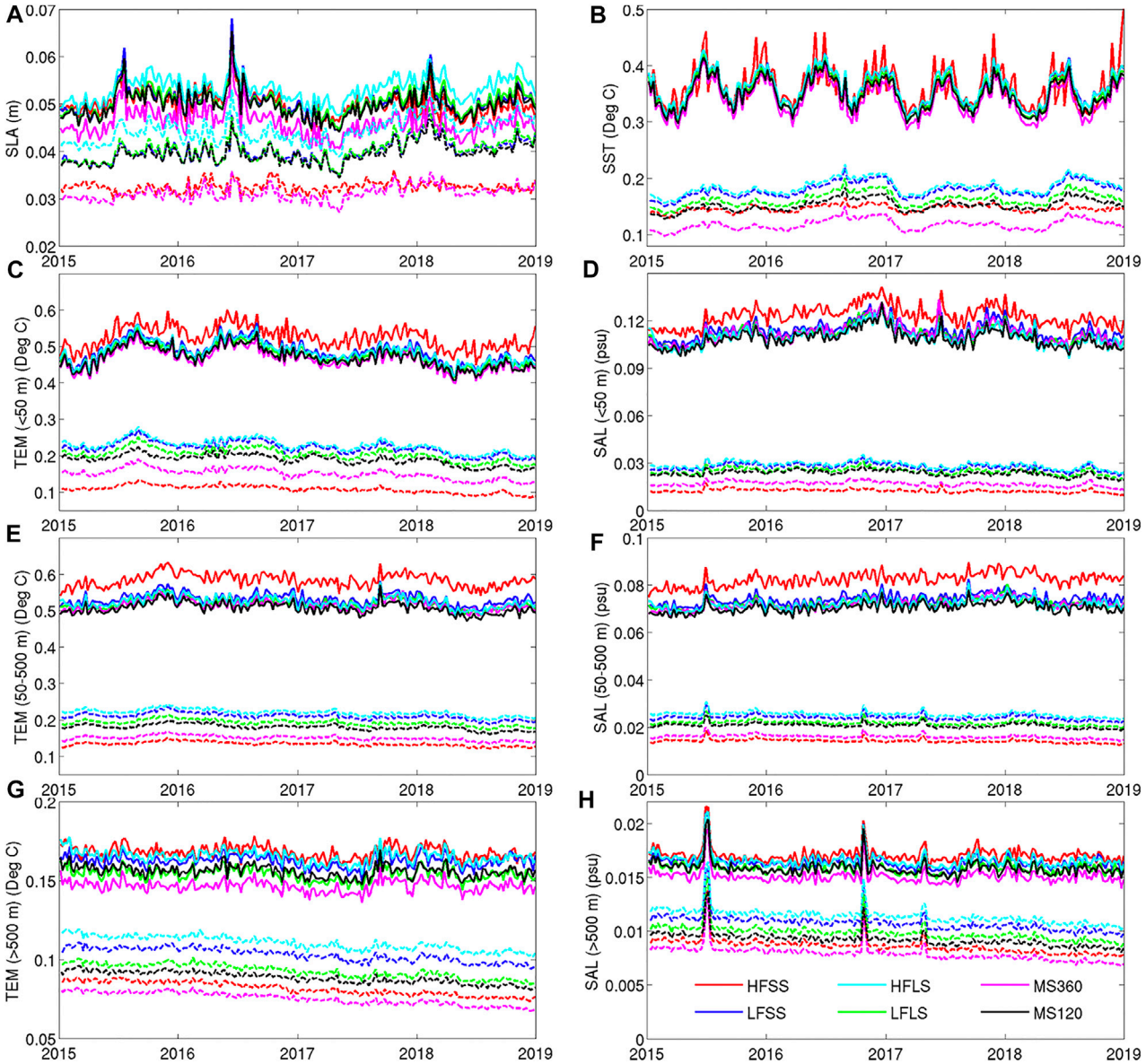

FIGURE 3 | Time-series of MAD between observations and analyses (dashed lines) and background fields (solid lines) for different experiments, for observations within 3 days of each analysis. Results are shown for **(A)** SLA, **(B)** SST, and **(C, E, G)** temperature and **(D, F, H)** salinity for different depth ranges, as labeled on the vertical axes. The legend for different experiments is shown in panel **(H)**.

in EnKF-C (Sakov, 2014), but we note that scale-dependent localisation has been used in the context of four-dimensional ensemble-variational data assimilation for Numerical Weather Prediction (e.g., Buehner and Shlyaeva, 2015; Caron and Buehner, 2018).

3 RESULTS

3.1 Comparisons with Assimilated Data

Blue Maps has been run for six different experiments (**Table 1**) to produce weekly analyses over a 4-year period (1/2015–12/2018). Time series of the mean absolute difference (MAD) between observations and analyses (analysis innovations) and observations and background fields (background innovations) for each experiment are presented in **Figure 3**. This shows the global average for each variable using data within 3 days of each analysis. The averages in both time and space are shown in **Table 2** for background and analysis innovations.

The results in **Figure 3** show that the system's performance for all experiments is relatively stable. There are a few points in time with unusually large innovations. For SLA, there appears to be one of two times when there is large background innovations (e.g., mid-2015, and mid-2016); and for salinity below 500 m

TABLE 2 | Time-average of the global MAD between observations and background fields (top group; titled background innovations)) and between observations and analysis fields (bottom group, titled analysis innovations), for observations within 3 days of each analysis (a 6 days time-window) for SLA (m), SST (°C), temperature (T, °C) and salinity (S, psu). Metrics for T and S are shown for all depths shallower than 2000 m, for 0–50 m, 50–500 m, and 500–2000 m.

Background innovations						
	HFSS	**HFLS**	**LFSS**	**LFLS**	**MS360**	**MS120**
SLA	0.050	0.053	0.050	0.051	0.046	0.050
SST	0.361	0.361	0.360	0.353	0.340	0.349
T (<2,000 m)	0.461	0.407	0.424	0.414	0.407	0.406
T (<50 m)	0.525	0.484	0.487	0.478	0.465	0.470
T (50–500 m)	0.583	0.524	0.532	0.520	0.515	0.507
T (>500 m)	0.168	0.165	0.163	0.154	0.147	0.156
S (<2,000 m)	0.0719	0.0637	0.0656	0.0639	0.0637	0.0625
S (<50 m)	0.123	0.110	0.114	0.111	0.112	0.109
S (50–500 m)	0.0825	0.0722	0.0741	0.0723	0.0721	0.0705
S (>500 m)	0.017	0.016	0.017	0.016	0.015	0.016
Analysis innovations						
	HFSS	**HFLS**	**LFSS**	**LFLS**	**MS360**	**MS120**
SLA	0.032	0.045	0.040	0.040	0.031	0.040
SST	0.146	0.185	0.179	0.163	0.118	0.152
T (<2,000 m)	0.115	0.130	0.183	0.168	0.130	0.157
T (<50 m)	0.108	0.228	0.221	0.203	0.150	0.189
T (50–500 m)	0.134	0.220	0.210	0.192	0.150	0.180
T (>500 m)	0.082	0.111	0.103	0.093	0.076	0.089
S (<2000 m)	0.012	0.014	0.021	0.019	0.014	0.018
S (<50 m)	0.012	0.029	0.027	0.025	0.017	0.023
S (50–500 m)	0.014	0.025	0.024	0.022	0.016	0.021
S (>500 m)	0.009	0.011	0.011	0.010	0.008	0.009

depth, there are three times when the innovations spike (mid-2015, late-2016, and early-2017). We expect that these anomalies are caused by assimilation of bad data.

For SLA and upper-ocean fields, **Figure 3** shows that there is a seasonal cycle in the performance, with analysis and background innovations slightly larger in austral winter. For deep temperature and salinity, the innovations also show a small, quasi-linear reduction in time.

For SLA, smallest analysis innovations are found in HFSS and MS360, indicating that analyses fit the observed SLA equally well for both experiments. But the background innovations are notably larger for HFSS compared to MS360. This indicates that although the analyses in HFSS fit the observations with similar accuracy to MS360, it seems that HFSS includes some unrealistic features that result in larger differences with the next background field. We interpret this as a case of over-fitting in HFSS, and attribute this to the small length-scales in the HFSS ensemble (**Figure 2**) and the short localisation length-scale used for the HFSS experiment (**Table 1**). This result for SLA, is similar to other variables, where HFSS analysis innovations are most similar to MS360 of all the experiments, but with HFSS consistently producing the largest background innovations. This is most clear for temperature and salinity in the depth ranges of 0–50 m and 50–500 m (**Figure 3**). For these metrics, the HFSS analysis innovations are the smallest of all experiments - providing analyses with the best fit to observations—but the HFSS background fields are the largest of all experiments—providing analyses with the worst fit to observation of the experiments presented here. These metrics

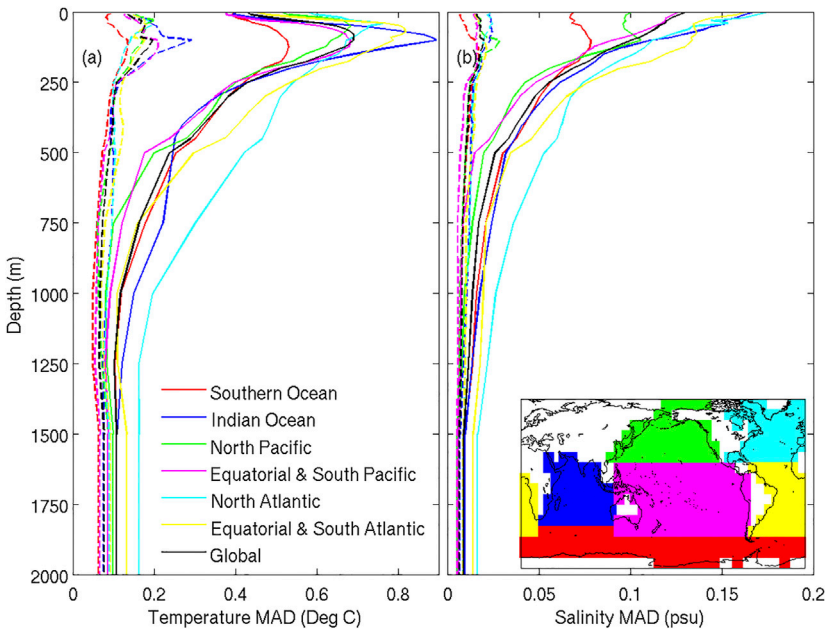

FIGURE 4 | Profiles of MAD between observations and analyses (dashed lines) and observations and background fields (solid lines) for **(A)** temperature and **(B)** salinity. Profiles are shown for different regions (coloured lines) and for the global average (black). The inset in panel **(B)** shows the regional partitioning. Results are for the MS360 experiment. Only observations made within 2 days of each analysis time are included in these calculations.

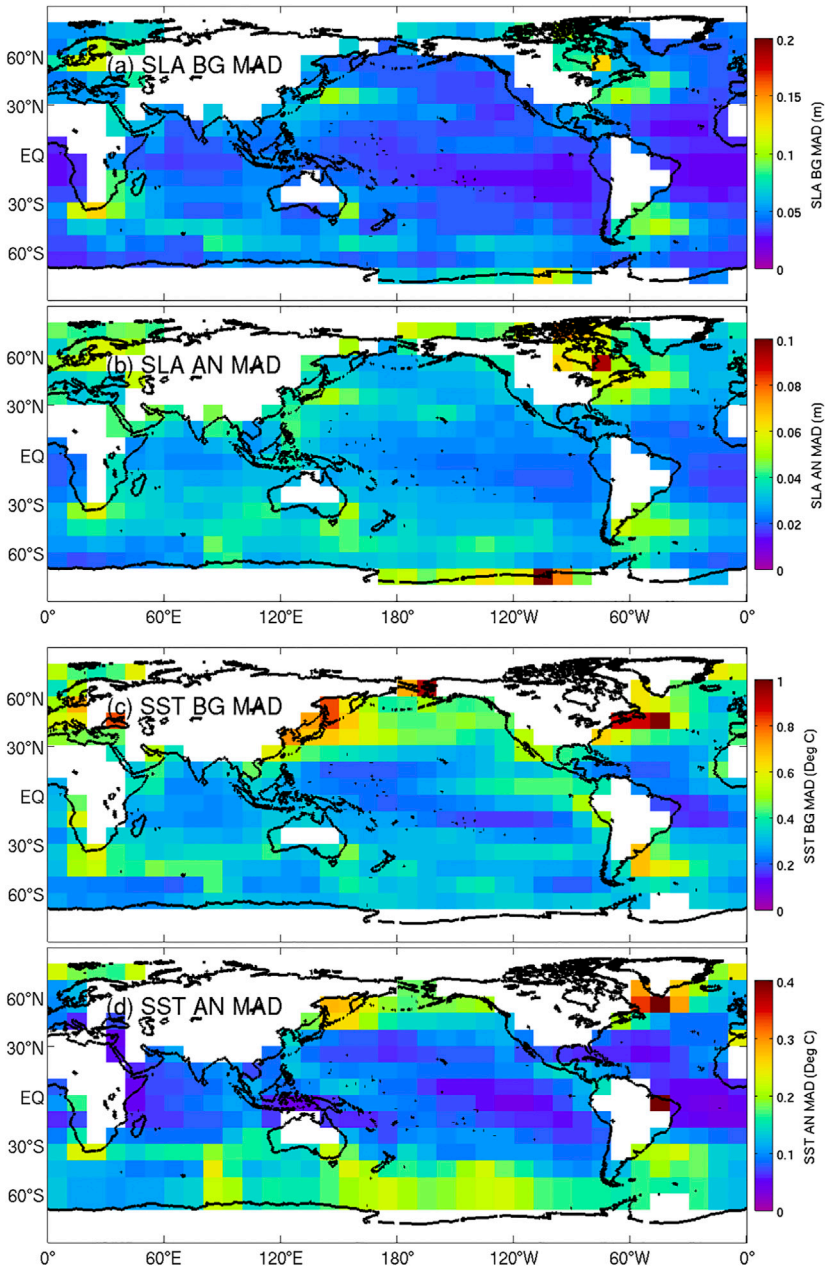

FIGURE 5 | Map of the MAD between **(A,C)** observations and background fields (BG; 7 days after each analysis), and between **(B,D)** observations and analyses (AN) for **(A,B)** SLA and **(C,D)** SST. Results are for the MS360 experiment. Only observations made within 2 days of each analysis time are included in these calculations.

are quantified in **Table 2**, where the HFSS analyses show the smallest analysis innovations, but the largest background innovations for most variables.

Weighing up both the analysis and background innovations reported in **Figure 3** and in **Table 2**, we conclude that the best performing experiment is clearly MS360. It's interesting that MS360 outperforms the child ensembles of LFSS, HFLS, and LFLS for every metric. It is also worth noting that for most metrics, MS120 outperformed LFSS, HFLS, and LFLS, leading us to conclude that the diversity of anomalies in the multi-scale ensemble experiments is beneficial. Furthermore, we find that MS360 outperformed MS120 on all metrics, demonstrating the benefit of increased ensemble size. We will explore why this is the case below, in **Section 4**.

Profiles of MAD for temperature and salinity innovations are presented in **Figure 4**, showing averages over the entire globe, and for each basin for the MS360 experiment only. **Figure 4** includes both profiles for MAD for analysis and background innovations. For both temperature and salinity, the analysis innovations for MS360 are small, showing mis-fits to gridded observations of less

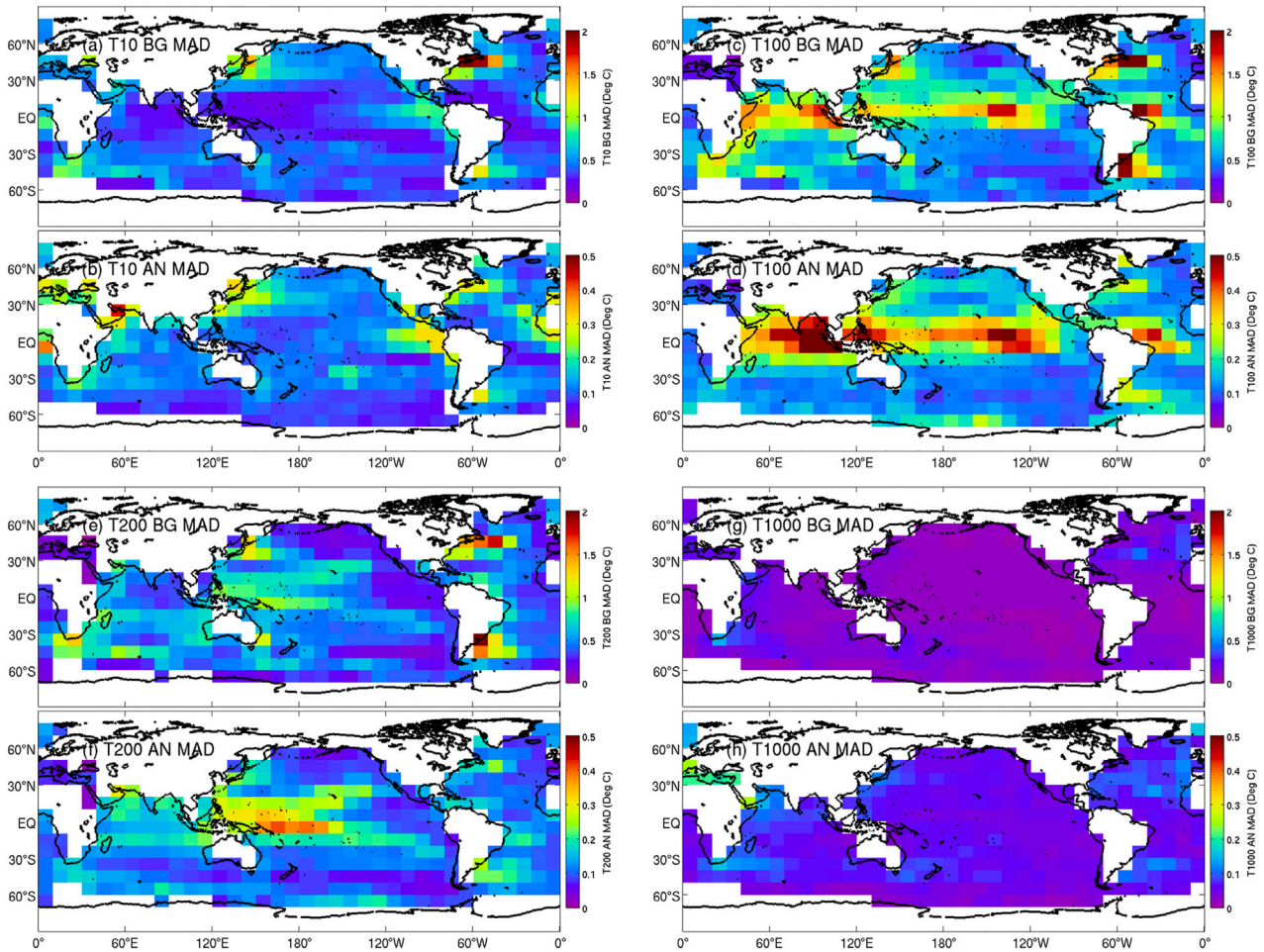

FIGURE 6 | Map of the MAD between **(A,C,E,G)** observations and background fields (7 days after each analysis), and between **(B,D,F,H)** observations and analysis fields, for temperature at **(A,B)** 10 m, T10; **(C,D)** 100 m, T100; **(E,F)** 200 m, T200; and **(G,H)** 1,000 m depth, T1000. Results are for the MS360 experiment. Only observations made within 2 days of each analysis time are included in these calculations.

than 0.1°C for temperature for most depths, and less than 0.01 psu for salinity for most depths. For context, recall that the assumed observation errors for *in situ* temperature and salinity are 0.05°C and 0.05 psu, respectively. For the background innovations for temperature (**Figure 4A**), the MAD is largest at around 100 m depth, the average depth of the thermocline. The largest background innovations in the upper ocean are in the Indian Ocean and the equatorial and South Atlantic Ocean. Below about 200 m depth, the largest background innovations are in the North Atlantic Ocean. For salinity profiles (**Figure 4B**), the MAD is largest at the surface for most regions, with the largest mis-fits in the Atlantic and Indian Oceans. Like temperature, the largest background innovations below about 300 m depth are in the North Atlantic Ocean. The smallest background innovations for salinity are in the upper ocean are in the Southern Ocean.

Maps of the MAD of background and analysis innovations for SLA and SST are presented in **Figure 5** for MS360. As expected, the largest innovations for SLA are in the eddy-rich regions, namely the western boundary current (WBC) extensions and along the path of the Antarctic Circumpolar Current (ACC). SLA innovations are also larger off Antarctica, where there are fewer SLA observations. For SST, there are also local maxima of innovations in each WBC region; and there are larger values north of about 30°S, with the largest values at the northern-most latitudes of the grid.

Maps of the MAD of background and analysis innovations for temperature and salinity at depths of 10, 100, 200, and 1,000 m depth are presented in **Figures 6** and **7**, respectively for MS360. The maps for temperature and salinity at corresponding depths show similar structures, with local maxima and minima in approximately the same regions. At 10 m depth, the largest innovations are in the WBC regions and in the eastern Tropical Pacific. At 100 m depth, in addition to larger values in WBCs, there are also larger values for all longitudes in the tropical bands for each basin. This is where the pycnocline has the strongest vertical gradient, and so any mis-placement of analysed isopycnal depths has a large penalty for MAD of temperature and salinity. At 200 m depth, there is evidence of a band of higher

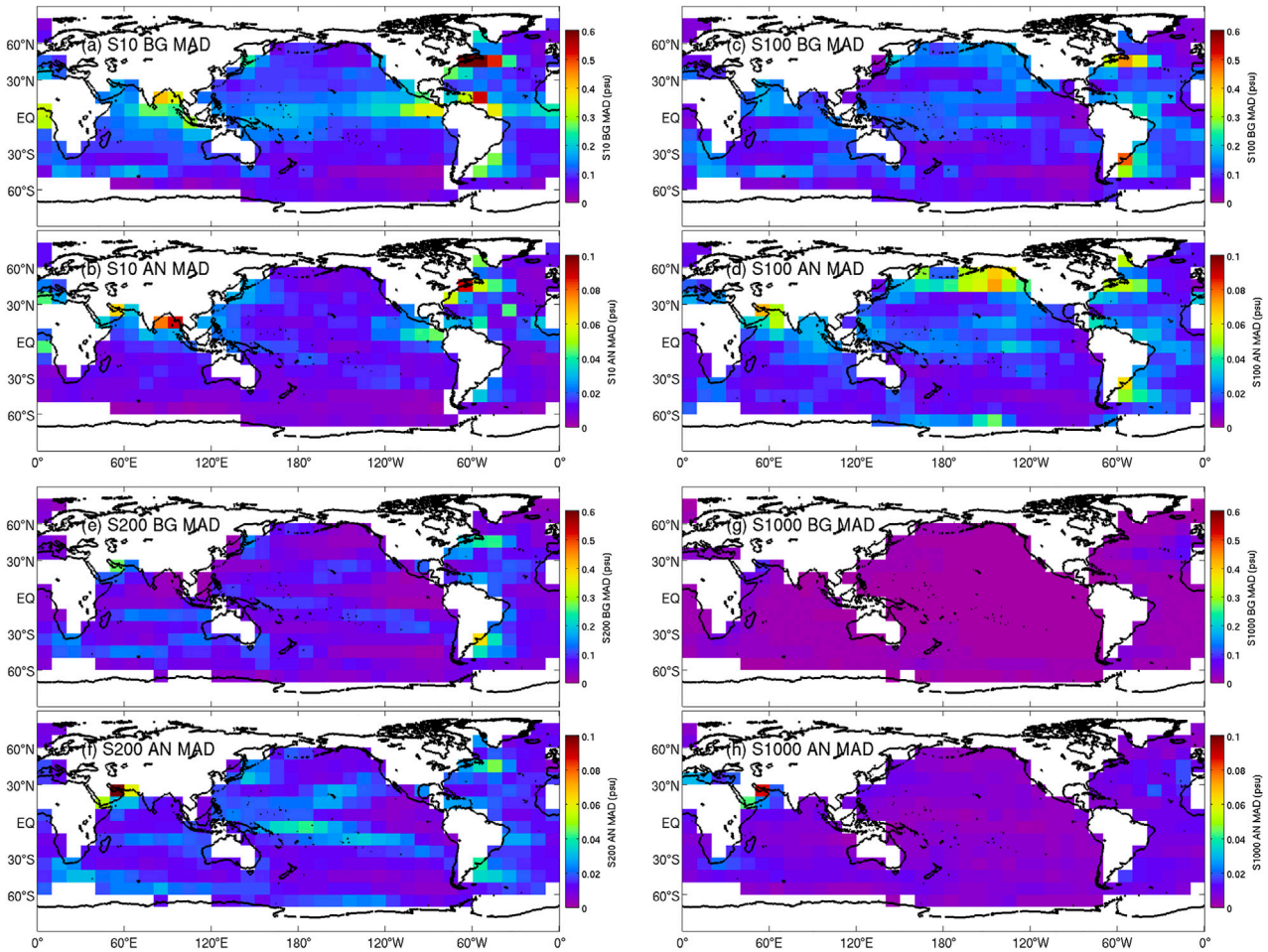

FIGURE 7 | As for **Figure 6**, except for salinity.

innovations nearer the center of each ocean basin at mid-latitudes. For the South Pacific, this band of higher innovations may relate to the decadal variability identified by O'Kane et al. (2014). At 1,000 m depth, the innovations are small everywhere, with modest local maxima in WBC regions.

3.2 Comparisons with Independent Data

For the comparisons presented above, the analyses of the background innovations can be considered as independent validation, since this involves comparisons between Blue Maps analyses and observations that have not been used to construct an analysis. However, for the comparisons of *in situ* temperature and salinity, the observations are mostly from Argo floats. Because Argo floats drift slowly, this means that the "independent" comparisons (based on the background innovations) almost always involves comparisons between background fields with observations in locations where data was recently assimilated. As a result, we might suspect that these comparisons provide an optimistic assessment of the accuracy of the analysis system. We therefore seek an additional, truly independent assessment here.

For an independent assessment, we compare analyses of temperature and salinity with non-Argo data from eXpendable BathyThermographs (XBTs; temperature only), Conductivity-Temperature-Depth (CTD) measurements from ship-borne surveys, moorings (mostly the tropical mooring arrays), and from sensors mounted on marine mammals (mostly in the Southern Ocean, near the Kerguelen Plateau). We source these data from the Coriolis Ocean Dataset for ReAnalysis CORA (CORA, versions 5.0 and 5.1; Cabanes et al., 2013). The global-averaged profiles of the MAD for 1/2015–12/2017 (CORA data are not currently available post-2017) are presented in **Figure 8**. For temperature, this mostly includes data from sensors mounted on marine mammals in the Indian Ocean section of the Southern Ocean, the tropical mooring arrays, and a small number of XBT transects and CTD surveys (**Figure 8A**). For salinity, this is mostly marine mammals and the tropical moorings. The coverage of non-Argo data for this comparison is not truly global, with vast amounts of the ocean without any non-Argo data available. Despite the poor coverage, this comparison provides some assessment against truly independent observations. This

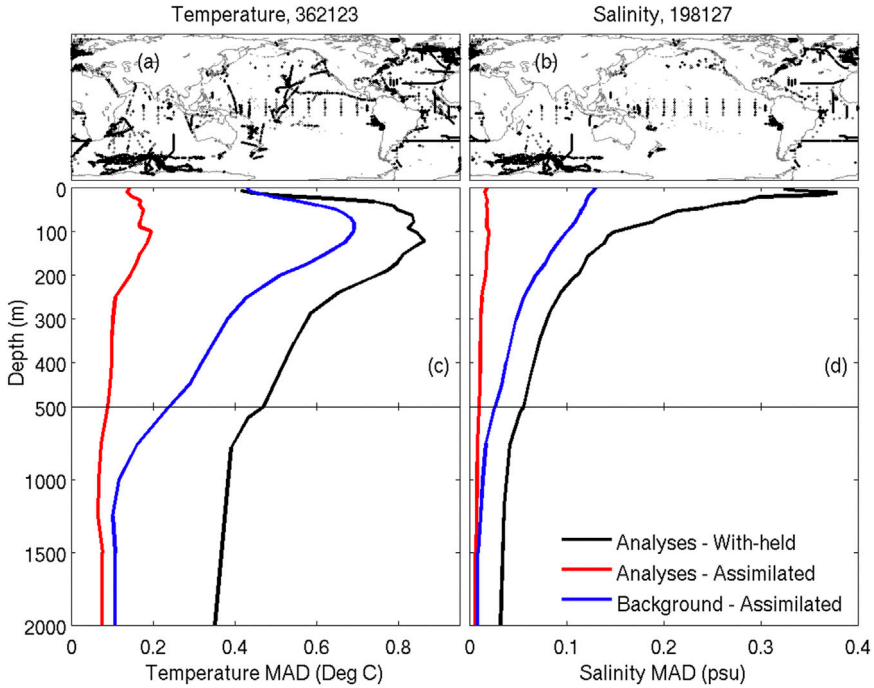

FIGURE 8 | Profiles of global-averaged MAD between analyses (from MS360) and non-Argo with-held observations (black), analyses and assimilated observations (red), and background fields and assimilated observations (blue), for **(C)** temperature and **(D)** salinity, from 1/2015–12/2017. The top panels show the locations of non-Argo **(A)** temperature and **(B)** salinity observations; and the numbers in the title are the number of respective observations. The non-Argo data includes XBT (temperature only) and CTD; plus sensors on marine mammals (MAM) and moorings (MOR).

comparison indicates that the differences between Blue Maps analyses and non-Argo (independent) observations are about the same amplitude as the background innovations, presented in **Figure 4**—slightly higher for salinity. This indicates that misfits with independent data for temperature are largest at about 100 m depth, with values of about 0.8°C; and for salinity are largest at the surface, with value of about 0.3 psu.

Considering the analysis innovations reported in **Table 2** and presented in **Figures 3–8**, we conclude that the gridded estimates of ocean temperature, salinity, and sea-level in Blue Maps have comparable accuracy to observation-based products. Here, we summarise the estimated errors and data-misfits reported elsewhere in the literature for a widely-used gridded SLA product (Pujol et al., 2016), SST product (Good et al., 2020), and temperature and salinity product (Roemmich and Gilson, 2009). For SLA, Pujol et al. (2016) report that the standard deviation of error of a 1/3°-resolution gridded SLA product (DUACS DT2014) ranges from 2.2 cm in low-variability regions, to 5.7 cm in high-variability regions (their **Table 2**). For SST, Good et al. (2020) show that the misfits between gridded SST and Argo match-ups to range from about 0.3 and 0.5°C between 2015–2018 (their Figure 11). For sub-surface temperature, Li et al. (2017) report that misfits between gridded temperature (for Roemmich and Gilson, 2009) and independent *in situ* data from tropical moorings average about 0.5°C, with largest misfits of about 0.8°C at 100 m depth (the surface) and about 0.2°C at 500 m depth (their Figure 9). For salinity, Li et al. (2017) report that misfits between gridded salinity (for Roemmich and Gilson, 2009) and independent *in situ* data from tropical moorings average about 0.1 psu, with largest misfits of about 0.2 psu at the surface and about 0.02 psu at 500 m depth (their **Figure 10**). For each gridded variable, the reported accuracy of these observational products are comparable to the accuracy of Blue Maps analysis fields. We therefore maintain that the accuracy of Blue Maps analyses is comparable to other widely-used observation-based products.

3.3 Example Analyses

To demonstrate the scales represented by Blue Maps analyses, we show some examples of anomalies of sea-level, temperature, and salinity in **Figures 9**, **10**. These examples demonstrate the abundance and amplitude of mesoscale variability in the maps. Anomalies that are obviously associated with eddies are evident in the SLA fields (**Figures 9A**, **10A**) throughout most of the regions displayed. Signals of these eddies are also clearly evident in the anomalies at 250 m depth, and in some regions (e.g., along the path of the ACC—particularly near the Kerguelen Plateau, **Figures 9D,E**; and in the eddy-rich parts of the Tasman Sea, **Figures 10D,E**). Regions of broad-scale anomalies are also evident, including high sea-level, and cold and fresh anomalies in the western, equatorial Pacific (**Figures 9A–C**). The maps also show deep salinity anomalies at 1,000 m depth between 20 and 30°S in the Indian Ocean, and along the path of the ACC (**Figure 9**). Of course, the anomalies displayed here are on depth levels, and so the relative contributions from heaving of

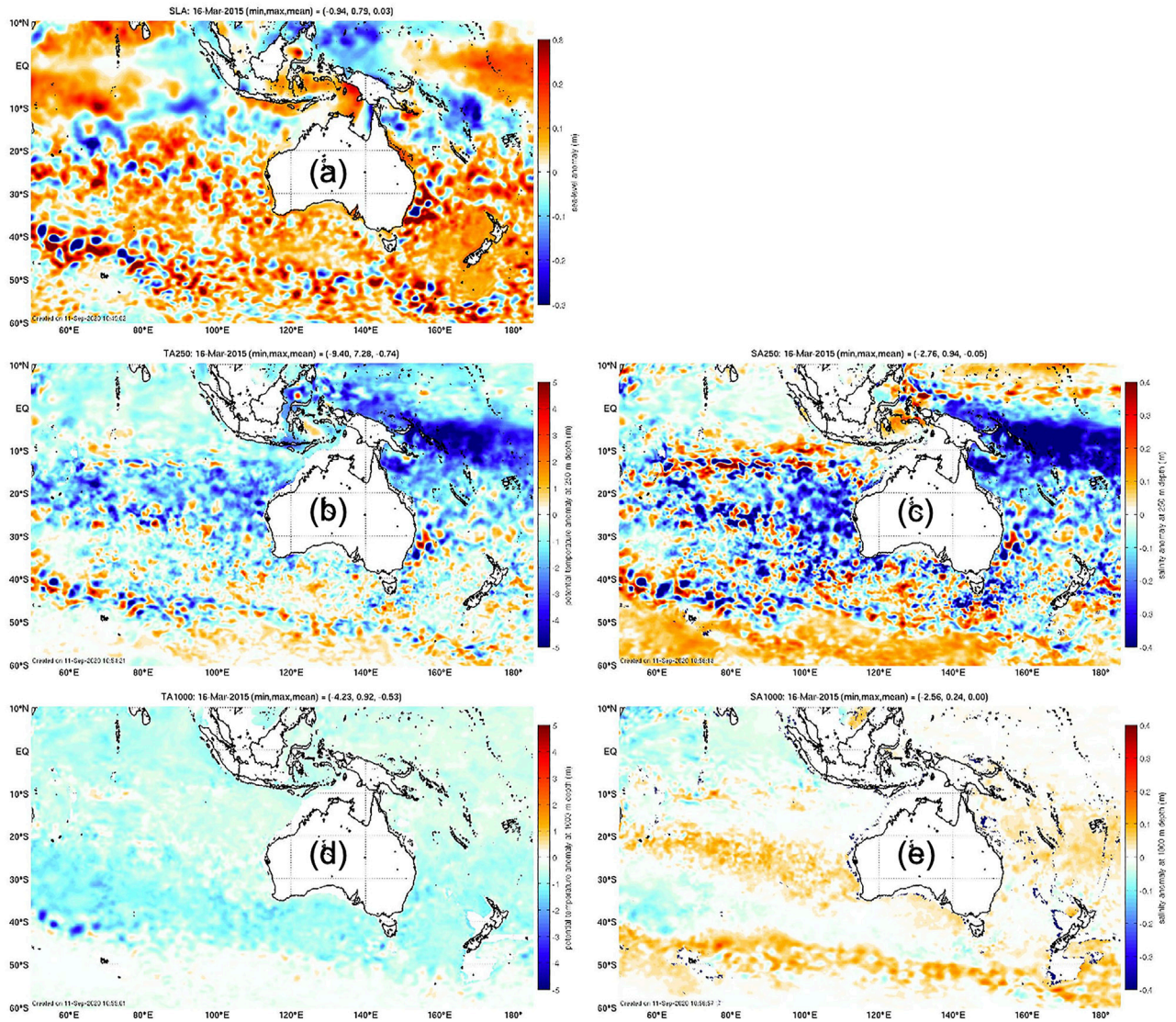

FIGURE 9 | Examples of gridded fields from MS360, showing anomalies of **(A)** sea-level, **(B)** temperature at 250 m depth, **(C)** salinity at 250 m depth, **(D)** temperature at 1,000 m depth, and **(E)** salinity at 1,000 m depth. Fields are shown for March 16, 2015. The title of each panel reports the minimum, maximum, and mean of the field displayed. Anomalies are with respect to seasonal climatology from WOA13 (Locarnini et al., 2013; Zweng et al., 2013) and the mean sea-level field from OFAM3 (Oke et al., 2013b).

the water column and changes in ocean properties from climatology are unclear. Assessment of this aspect of the analyses is important and interesting, but is not addressed in this study.

4 ANALYSIS AND DISCUSSION

4.1 Understanding the Performance of the MS360 Ensemble

An exciting and intriguing result reported in **Section 3** is the superior performance of MS360 compared to LFSS, HFLS, and LFLS—the child ensembles. In this case, the performance of the larger parent ensemble (MS360) is not just marginally better than each of the child ensembles—the difference is quite significant—particularly for the analysis innovations. For many metrics, the MAD for the analysis innovations are up to 30–35% smaller in MS360, the child ensemble experiments (22–36% smaller for salinity at 50–500 m depth, for example, **Table 2**). Here, we seek to understand why the experiment with the MS360 ensemble performs so much better. Based on comparisons between the innovations reported in **Figure 3** and in **Table 2**, we suggested above that both the ensemble size and the diversity of anomalies in the multi-scale analyses are important. We aim to explore this further below.

To understand how the MS360 experiment uses ensemble members from each of the child ensembles, we analyse the ensemble weights (from **Eq. 2**) for 52 analyses—one for each

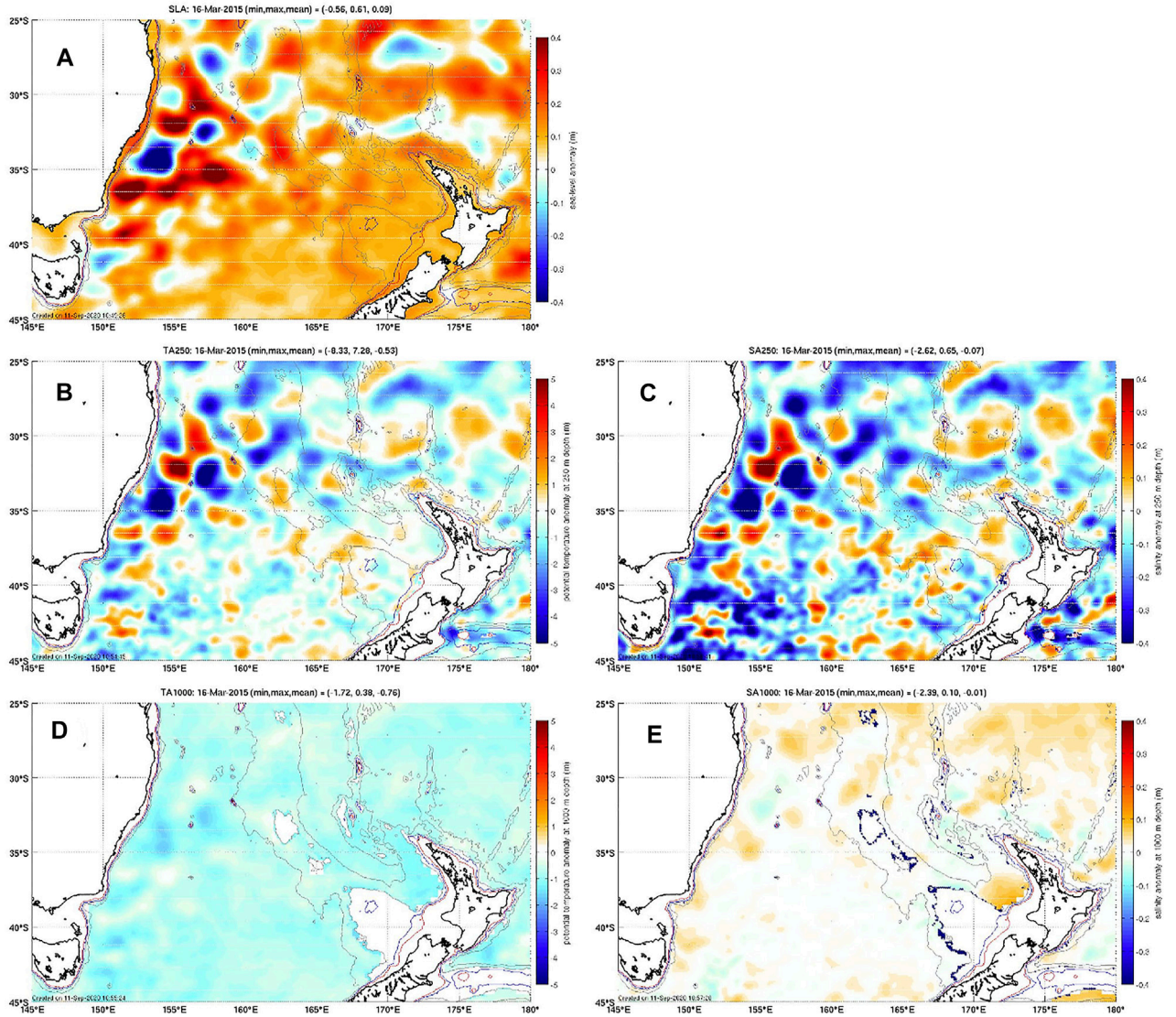

FIGURE 10 | As for **Figure 9**, except for the tasman sea.

week—during 2015. We then calculate the fraction of the increment that can be attributed to each child ensemble by calculating a partial sum of the weighted ensemble members (from **Eq. 2**), using only the members for each child ensemble. We show a map of the average fraction of increment explained by each child ensemble for temperature at 250 m depth, and also present the zonally-averaged profiles, in **Figure 11**. The results show that in different regions, each child ensemble is given a different relative weight. For all examples in **Figure 11**, anomalies in LFLS are combined to produce the largest fraction (about 60%) of the increments for almost all latitudes. We show that anomalies from LFSS are dominant in each WBC region, where there is correspondingly low weight assigned to anomalies from LFLS. This provides a clear indication that different types of ensembles are warranted in different dynamical regimes. Another example of this is in the South Pacific, where there is a band of high values for LFLS extending from the southern tip of South America and extending towards central eastern Australia. Although not perfectly aligned, this is reminiscent of the path of quasi-decadal anomalies identified by O'Kane et al. (2014). There are also different bands where HFLS has relatively higher weight—particularly at low latitudes in the Pacific and Atlantic Oceans, and along the path of the ACC south of Australia. This analysis provides a detailed and complex picture of the relative weights assigned by the EnOI system to each child ensemble. The key message we take away from this analysis, is that different types of anomalies are assigned different weights in different regions.

The analysis of the relative fraction of increment explained by each child ensemble in MS360 (**Figure 11**), confirms that the relative weights of the anomalies in the different child ensembles varies for different dynamical regimes. This result has a number

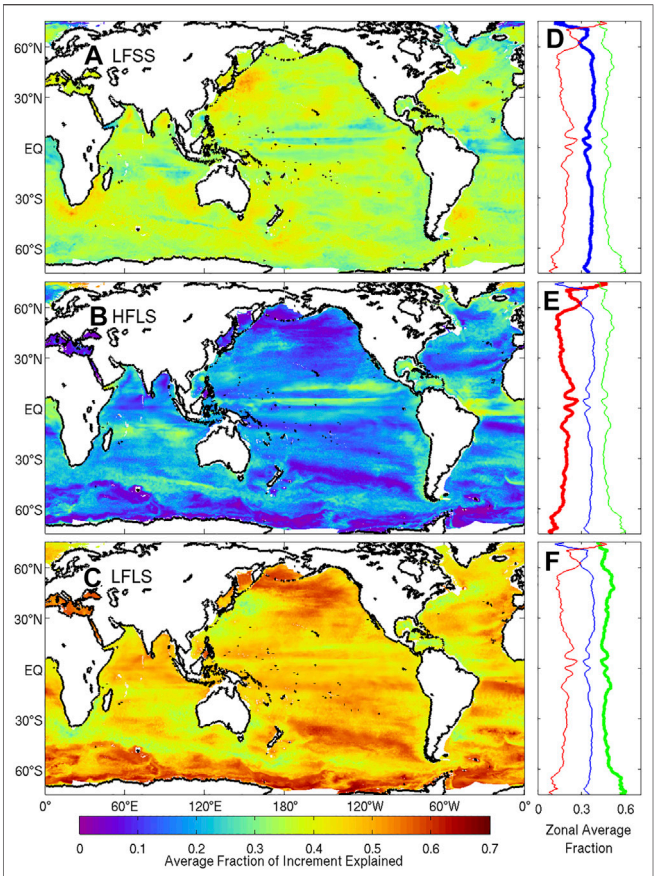

FIGURE 11 | Average fraction of increment explained for temperature at 250 m depth, for each child ensemble, including **(A)** LFSS, **(B)** HFLS, and **(C)** LFLS, in the MS360 experiment. The zonal averages for LFSS (blue), HFLS (red), and LFLS (green) are shown in panels **(D–F)**. Averages are calculated from 52 analyses during 2015.

of implications. Recall that EnOI requires an explicit assumption about the background field errors. Specifically, the construction of the stationary ensemble for EnOI requires the ensemble to be generated by constructing anomalies for some space- and time-scales—here summarised in **Table 1** (column three therein). Almost all applications of EnOI in the literature invoke a single assumption about the background error covariance to construct the ensemble. The only exceptions that we are aware of are presented by Cheng and Zhu (2016), Cheng et al. (2017), and Yu et al. (2019). Here, we show that we achieve a much better result when several different assumptions are made together, and a diversity of ensemble members are combined to construct analyses. Moreover, the results presented here indicate that a different assumption about the background field errors is warranted for different regions.

Another element of Blue Maps that differs from most other applications of EnOI is the use of longer localisation length-scales. For five of the experiments presented here, a 900 km localisation length-scale is used (**Table 1**). To demonstrate the impact of this aspect of the configuration, we present examples of ensemble-based correlations between temperature at a reference location and nearby temperature, in **Figure 12**. To understand the impact of localisation, consider the profiles in **Figure 12A**, for example. For this case, the un-localised ensemble-based correlation (red) closely matches the localised ensemble-based correlation profile using a 900 km localisation function (green), but is significantly different from the localised ensemble-based correlation profile using a 250 km localisation function (blue). If the localisation function with the shorter length-scale is used, then the ensemble-based correlations are heavily modified. By contrast, if a localisation function with the longer length-scale is used, then the ensemble-based correlations are virtually un-modified within several hundred kilometres of the reference location. As a result, using the longer length-scales permits more of the structures—such as the anisotropy—of the ensemble-based correlations to be used for the data assimilation. Whereas, using the short length-scale localisation function, more of the details are eliminated, and the correlation used degrades towards a quasi-Gaussian function (like most objective analysis systems). In this way, some of the benefits of EnOI are lost when a shorter length-scale is used. The other examples presented in **Figure 12** demonstrate the same relationships. We have looked at equivalent fields to these for many other regions. The results in **Figure 12** are similar to many regions poleward of about 15°N and S. In the equatorial region, the unlocalised correlations are much longer (several thousand kilometres in some cases). For those tropical regions, a longer localisation length-scale is warranted—but we cannot afford to implement this computationally, due to memory requirements, to assess the performance.

4.2 Development Experiments

The development of Blue Maps has involved a large number of trial experiments that produced mixed results. Not all of the results from this series of experiments can be reported here in detail. But some of the findings from those experiments will be summarised here, since they may be of interest to the community. The first configuration of Blue Maps used the same configuration as the 2016 version of BRAN (Oke et al., 2018). This was similar to the HFSS experiment reported here. However the HFSS experiment includes a few modifications. Early results used persistence for the background field—not damped persistence (**Eq. 4**). The quality of the analyses degraded in time, with noisy fields emerging and growing in amplitude. It appears that there are insufficient observations to constrain a series of analyses without damped persistence and without an under-pinning model. Damped persistence was adopted thereafter. Many experiments were performed with damping to climatology using an *e*-folding time-scale in the range of 7–90 days. The best overall performance—based on the analysis and background innovations—was found using damping with an *e*-folding time-scale of 14-days. This time-scale is used in all experiments described in this paper. Damped persistence is commonly used for SST analyses. For example, the Operational Sea Surface Temperature and Sea Ice Analysis (OSTIA), produced by the UKMet Office, uses damped persistence with an *e*-folding timescale of 30 days for ice-free regions (Donlon et al., 2012;

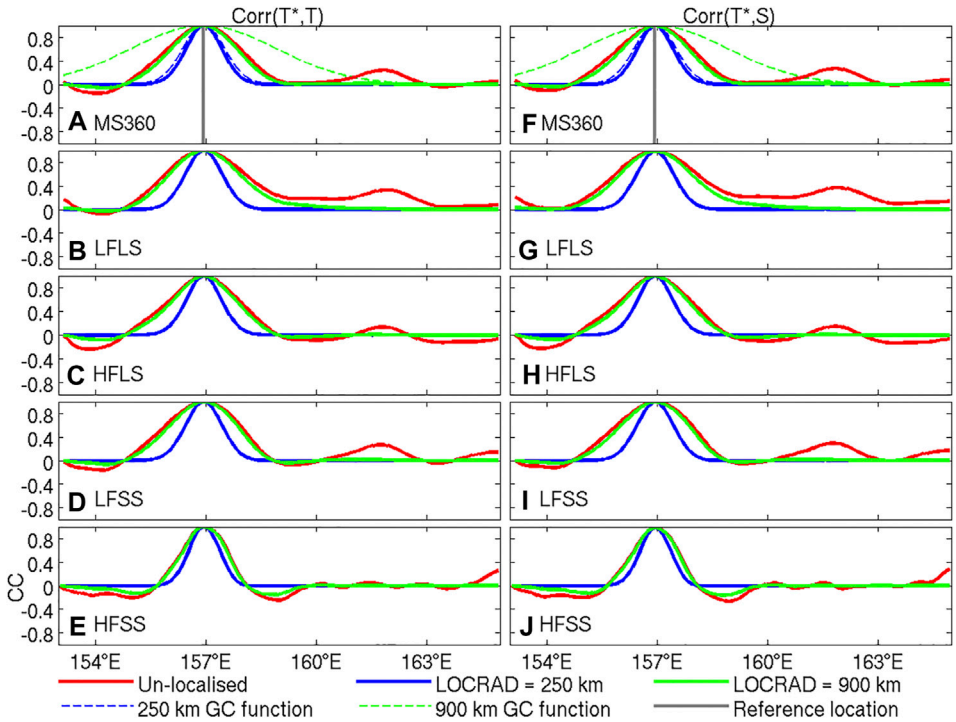

FIGURE 12 | Ensemble-based correlations between temperature at 250 m depth at 32°S and 157°E in the Tasman Sea, and temperature and salinity at the same depth and longitude, but at nearby longitudes using different ensembles: **(A,F)** MS360, **(B,G)** LFLS, **(C,H)** HFLS, **(D,I)** LFSS, and **(E,J)** HFSS. Each panel includes the un-localised ensemble-based correlation (in red), the localised ensemble-based correlation, multiplied by the 250 km localisation function (blue) and multiplied by the 900 km localisation function (green). Also shown in panels **(A)** and **(F)** are the correlations functions with a 250 km (blue-dashed) and 900 km (green-dashed) using the formulation used here and defined by Gaspari and Cohn (1999). The location of the reference point is also shown in panels **(A)** and **(F)** with a vertical grey line.

Fiedler et al., 2019; Good et al., 2020). Similarly, the operational SST analysis produced by the Canadian Meteorological Centre (CMC) uses damped persistence with an *e*-folding timescale of 58 days (Brasnett, 2008; Brasnett and Colan, 2016).

Even using damped persistence, small-scale noise still appeared in analyses in some regions. Close examination of the ensemble fields showed that there were noisy fields in most ensemble members. As a consequence, these noisy features appear in the analyses, according to **Eq. 2**. We eliminated these small-scale features by spatially smoothing of the ensemble fields. This was implemented here (for all ensembles) using a simple horizontal diffusion operator (that applies a spatial smoothing with a footprint of 1x1°). We now understand that a similar approach to smooth the ensemble has long be used for the French ocean reanalysis, as reported by Artana et al. (2019), for GLORYS (the GLobal Ocean ReanalYses and Simulations).

Other experiments explored the sensitivity to localisation length-scale. The results with longer length-scales generally performed better, with fewer fictitious features that are not resolved by the observations. Computational limitations prohibited us from testing the system with longer length-scales.

Some of the lessons learnt during the development of Blue Maps may be of interest to the ocean data assimilation community. Apparently many of the features identified in the early experiments during this development are present in BRAN experiments (e.g., small-scale noise in analyses). But it appears that when fields with these artefacts are initialised in a model, the model efficiently disperses many of the artificial features, and they are not clearly evident in the resulting reanalysis fields (which are often daily-means). Surely, inclusion of these fictitious features - albeit small in amplitude—will degrade the quality of ocean reanalyses. For Blue Maps, these features were easily identified, because there is no model to "cover" over the unwanted features. We plan to apply the learnings from the development described here, to future versions of BRAN.

5 CONCLUSION

A new observation-based product that adapts a data assimilation system that has traditionally been used for ocean forecasting and ocean reanalysis is presented here. The new product is called Blue maps. Blue Maps is tested here by producing weekly analysis over a 4-year period (1/2015–12/2018). We compare the performance of Blue Maps for six different configurations, using different ensembles. The best performance is achieved using a 360-member multi-scale ensemble (MS360) that includes anomalies from several different spatiotemporal scales. For that configuration, analyses of sea-level that are within about 4 cm of observations; and analyses of upper-ocean (deep) temperature and salinity that are within about 0.45 (0.15) degrees and 0.1 (0.015) psu respectively. These misfits are comparable

to ocean reanalysis systems that are underpinned by an ocean model. For example, the 2020 version of the Bluelink ReANalysis (BRAN 2020, Chamberlain et al., 2021a), fits data to within about 0.17–0.45°C and 0.036–0.082 psu (smallest values are for misfits of observations and analysis; largest values are misfits of observations and 3 days "forecasts"). GLORYS12V1 (Lellouche et al., 2019, see their Figure 5B), version 2020, fits the data to within about 0.41°C and 0.061 psu. For equivalent metrics, Blue Maps fits data to within 0.17–0.41°C and 0.014–0.064 psu (smallest values are for misfits of observations and analysis; largest values are misfits of observations and 7 days "damped persistence"). Compared to observation-based products, Blue Maps also compares well. Li et al. (2017) present results from a 1°-resolution product and includes an inter-comparison with other observation-based products. They show that their system performs comparably to analyses produced by Roemmich and Gilson (2009), and a number of other coarse-resolution products. The profiles of analysis-observation misfits in **Figure 4**, for Blue Maps, show much smaller mis-fits than observational products presented by (Li et al., 2017, e.g., their Figure 4).

We show that the superior performance of the Blue Maps configuration using the ensemble with multiple spatiotemporal scales is because of the larger ensemble size (120 compared to 3,670), longer length-scales (compared to most other EnOI applications), and the diversity of ensemble anomalies. We conclude that different assumptions about the system's background error covariance are warranted for different regions. We recognise that the ensemble with 360 members—although larger than most other global applications of EnOI—is still not large. Indeed, the most extreme demonstration of the benefits of a truly large ensemble is presented by Miyoshi et al. (2015), who presented some very impressive results using a 10,240-member ensemble for numerical weather prediction. We suspect further improvements may be achieved if a larger, more diverse ensemble is used. This suggestion will be explored in future experiments with Blue Maps and with BRAN. Future developments of Blue Maps will also likely include explicit analyses of mixed layer depths, biogeochemical parameters (e.g., backscatter), and will include a calculation of weekly fields for a longer period (probably from 2000 to present).

DATA AVAILABILITY STATEMENT

The datasets presented in this study can be found in online repositories. The names of the repository/repositories and accession number(s) can be found below: https://dapds00.nci.org.au/thredds/catalog/gb6/BRAN/Blue_Maps/MAPS-v1p0/catalog.html.

AUTHOR CONTRIBUTIONS

PO conceived and designed the study, performed the calculations, the analysis, and wrote the first draft of the manuscript. MC contributed to the design of the study, development of scripts for producing the analysis system, and organised the observational database. RF prepared some of the ensembles and contributed to the development of scripts for producing the analysis system. HuB developed the first version of system analysis here. HuB developed the first version of the analysis system described here. GB provided important input to the design of the study. All authors contributed to manuscript revision, read, and approved the submitted version.

FUNDING

Funding for this research has been received from IMOS and Bluelink, including funding from CSIRO, BoM, and the Australian Department of Defence.

ACKNOWLEDGMENTS

The authors gratefully acknowledge support from IMOS: a national collaborative research infrastructure, supported by the Australian Government; the Bluelink Partnership: a collaboration between the Australian DoD, BoM and CSIRO; and the National Computational Infrastructure (NCI). Argo data were collected and made freely available by the International Argo Program: part of the Global Ocean Observing System. The AVHRR SST data was sourced from the Naval Oceanographic Office and made available under Multi-sensor Improved Sea Surface Temperature project, with support from the Office of Naval Research. NOAA and TU Delft are also gratefully acknowledged for the provision of RADS data. This study benefited from several constructive discussions with P. Sakov and S. Wijffels. The corresponding author also wishes to acknowledge the Edinburgh Gin Distillery for provision of Gin Liqueur that aided the writing of this paper.

REFERENCES

Artana, C., Ferrari, R., Bricaud, C., Lellouche, J.-M., Garric, G., Sennéchael, N., et al. (2019). Twenty-five Years of Mercator Ocean Reanalysis GLORYS12 at Drake Passage: Velocity Assessment and Total Volume Transport. *Adv. Space Res.* doi:10.1016/j.asr.2019.11.033

Balmaseda, M. A., Mogensen, K., and Weaver, A. T. (2012). Evaluation of the ECMWF Ocean Reanalysis System ORAS4. *Q.J.R. Meteorol. Soc.* 139, 1132–1161. doi:10.1002/qj.2063

Balmaseda, M. A., Hernandez, F., Storto, A., Palmer, M. D., Alves, O., Shi, L., et al. (2015). The Ocean Reanalyses Intercomparison Project (ORA-IP). *J. Oper. Oceanogr.* 8, s80–s97. doi:10.1080/1755876x.2015.1022329

Brasnett, B., and Colan, D. S. (2016). Assimilating Retrievals of Sea Surface Temperature from VIIRS and AMSR2. *J. Atmos. Oceanic Technol.* 33, 361–375. doi:10.1175/jtech-d-15-0093.1

Brasnett, B. (2008). The Impact of Satellite Retrievals in a Global Sea-Surface-Temperature Analysis. *Q.J.R. Meteorol. Soc.* 134, 1745–1760. doi:10.1002/qj.319

Brassington, G. B., Pugh, T. F., Spillman, C., Schulz, E., Beggs, H., Schiller, A., et al. (2007). Bluelink Development of Operational Oceanography and Servicing in Australia. *J. Res. Pract Inf Tech* 39, 151–164.

Buehner, M., and Shlyaeva, A. (2015). Scale-dependent Background-Error Covariance Localisation. *Tellus A: Dynamic Meteorology and Oceanography* 67, 28027. doi:10.3402/tellusa.v67.28027

Cabanes, C., Grouazel, A., von Schuckmann, K., Hamon, M., Turpin, V., Coatanoan, C., et al. (2013). The CORA Dataset: Validation and Diagnostics

of *In-Situ* Ocean Temperature and Salinity Measurements. *Ocean Sci.* 9, 1–18. doi:10.5194/os-9-1-2013

Caron, J.-F., and Buehner, M. (2018). Scale-dependent Background Error Covariance Localization: Evaluation in a Global Deterministic Weather Forecasting System. *Monthly Weather Rev.* 146, 1367–1381. doi:10.1175/mwr-d-17-0369.1

Carton, J. A., and Giese, B. S. (2008). A Reanalysis of Ocean Climate Using Simple Ocean Data Assimilation (SODA). *Monthly Weather Rev.* 136, 2999–3017. doi:10.1175/2007mwr1978.1

Cayula, J. F., May, D., McKenzie, B., Olszewski, D., and Willis, K. (2004). A Method to Add Real-Time Reliability Estimates to Operationally Produced Satellite-Derived Sea Surface Temperature Retrievals. *Sea Technol.* 67–73.

Chamberlain, M. A., Oke, P. R., Fiedler, R. A. S., Beggs, H., Brassington, G. B., and Divakaran, P. (2021a). Next Generation of Bluelink Ocean Reanalysis with Multiscale Data Assimilation: BRAN2020. *Earth Syst. Sci. Data*, submitted

Chamberlain, M. A., Oke, P. R., Brassington, G. B., Sandery, P., Divakaran, P., and Fiedler, R. A. S. (2021b). Multiscale data assimilation in the Bluelink ocean reanalysis (BRAN). Ocean Modelling, submitted.

Cheng, L., and Zhu, J. (2016). Benefits of Cmip5 Multimodel Ensemble in Reconstructing Historical Ocean Subsurface Temperature Variations. *J. Clim.* 29, 5393–5416. doi:10.1175/jcli-d-15-0730.1

Cheng, L., Trenberth, K. E., Fasullo, J., Boyer, T., Abraham, J., and Zhu, J. (2017). Improved Estimates of Ocean Heat Content from 1960 to 2015. *Sci. Adv.* 3, e1601545. doi:10.1126/sciadv.1601545

Counillon, F., and Bertino, L. (2009). Ensemble Optimal Interpolation: Multivariate Properties in the Gulf of Mexico. *Tellus A: Dynamic Meteorol. Oceanogr.* 61, 296–308. doi:10.1111/j.1600-0870.2008.00383.x

Dee, D. P., and Uppala, S. (2009). Variational Bias Correction of Satellite Radiance Data in the ERA-Interim Reanalysis. *Q.J.R. Meteorol. Soc.* 135, 1830–1841. doi:10.1002/qj.493

Donlon, C. J., Martin, M., Stark, J., Roberts-Jones, J., Fiedler, E., and Wimmer, W. (2012). The Operational Sea Surface Temperature and Sea Ice Analysis (OSTIA) System. *Remote Sens. Environ.* 116, 140–158. doi:10.1016/j.rse.2010.10.017

Evensen, G. (2003). The Ensemble Kalman Filter: Theoretical Formulation and Practical Implementation. *Ocean Dyn.* 53, 343–367. doi:10.1007/s10236-003-0036-9

Ferry, N., Rémy, E., Brasseur, P., and Maes, C. (2007). The Mercator Global Ocean Operational Analysis System: Assessment and Validation of an 11-year Reanalysis. *J. Mar. Syst.* 65, 540–560. doi:10.1016/j.jmarsys.2005.08.004

Fiedler, E. K., Mao, C., Good, S. A., Waters, J., and Martin, M. J. (2019). Improvements to Feature Resolution in the OSTIA Sea Surface Temperature Analysis Using the Nemovar Assimilation Scheme. *Q.J.R. Meteorol. Soc.* 145, 3609–3625. doi:10.1002/qj.3644

Fu, W., She, J., and Zhuang, S. (2011). Application of an Ensemble Optimal Interpolation in a North/Baltic Sea Model: Assimilating Temperature and Salinity Profiles. *Ocean Model.* 40, 227–245. doi:10.1016/j.ocemod.2011.09.004

Gaspari, G., and Cohn, S. E. (1999). Construction of Correlation Functions in Two and Three Dimensions. *Q.J R. Met. Soc.* 125, 723–757. doi:10.1002/qj.49712555417

Good, S. A., Martin, M. J., and Rayner, N. A. (2013). En4: Quality Controlled Ocean Temperature and Salinity Profiles and Monthly Objective Analyses with Uncertainty Estimates. *J. Geophys. Res. Oceans* 118, 6704–6716. doi:10.1002/2013jc009067

Good, S., Fiedler, E., Mao, C., Martin, M. J., Maycock, A., Reid, R., et al. (2020). The Current Configuration of the OSTIA System for Operational Production of Foundation Sea Surface Temperature and Ice Concentration Analyses. *Remote Sens.* 12, 720. doi:10.3390/rs12040720

Guinehut, S., Dhomps, A.-L., Larnicol, G., and Le Traon, P.-Y. (2012). High Resolution 3-d Temperature and Salinity fields Derived from *In Situ* and Satellite Observations. *Ocean Sci.* 8, 845–857. doi:10.5194/os-8-845-2012

Henderson, C. R. (1975). Best Linear Unbiased Estimation and Prediction under a Selection Model. *Biometrics* 31, 423–447. doi:10.2307/2529430

Ishii, M., Fukuda, Y., Hirahara, S., Yasui, S., Suzuki, T., and Sato, K. (2017). Accuracy of Global Upper Ocean Heat Content Estimation Expected from Present Observational Data Sets. *Sola* 13, 163–167. doi:10.2151/sola.2017-030

Keppenne, C. L., and Rienecker, M. M. (2003). Assimilation of Temperature into an Isopycnal Ocean General Circulation Model Using a Parallel Ensemble Kalman Filter. *J. Mar. Syst.* 40-41, 363–380. doi:10.1016/s0924-7963(03)00025-3

Kiss, A. E., Hogg, A. M., Hannah, N., Boeira Dias, F., Brassington, G. B., Chamberlain, M. A., et al. (2019). ACCESS-OM2: A Global Ocean-Sea Ice Model at Three Resolutions. *Geosci. Model. Dev. Discuss.* 2019, 1–58. doi:10.5194/gmd-2019-106

Köhl, A., Stammer, D., and Cornuelle, B. (2007). Interannual to Decadal Changes in the ECCO Global Synthesis. *J. Phys. Oceanogr.* 37, 313–337. doi:10.1175/jpo3014.1

Köhl, A. (2015). Evaluation of the GECCO2 Ocean Synthesis: Transports of Volume, Heat and Freshwater in the Atlantic. *Q.J.R. Meteorol. Soc.* 141, 166–181. doi:10.1002/qj.2347

Lellouche, J.-M., Le Galloudec, O., Drévillon, M., Régnier, C., Greiner, E., Garric, G., et al. (2013). Evaluation of Global Monitoring and Forecasting Systems at Mercator Océan. *Ocean Sci.* 9, 57–81. doi:10.5194/os-9-57-2013

Lellouche, J.-M., Greiner, E., Le Galloudec, O., Garric, G., Regnier, C., Drevillon, M., et al. (2018). Recent Updates to the Copernicus Marine Service Global Ocean Monitoring and Forecasting Real-Time 1/12° High-Resolution System. *Ocean Sci.* 14, 1093–1126. doi:10.5194/os-14-1093-2018

Lellouche, J., Legalloudec, O., Regnier, C., Levier, B., Greiner, E., and Drevillon, M. (2019). "Quality Information Document," in Copernicus Marine Environmental Monitoring Service *(CMEMS)* (Toulouse, France: EU Copernicus Marine Service), 2 (1), pp81.

Li, H., Xu, F., Zhou, W., Wang, D., Wright, J. S., Liu, Z., et al. (2017). Development of a Global Gridded Argo Data Set with Barnes Successive Corrections. *J. Geophys. Res. Oceans* 122, 866–889. doi:10.1002/2016jc012285

Locarnini, R., Mishonov, A., Antonov, J., Boyer, T., Garcia, H., Baranova, O., et al. (2013). "World Ocean Atlas 2013, Volume 1: Temperature," in *NOAA Atlas NESDIS 74*. Editors S. Levitus and A. Mishonov (Washington, D.C.: U.S. Government Printing Office), 40.

May, D. A., Parmeter, M. M., Olszewski, D. S., and McKenzie, B. D. (1998). Operational Processing of Satellite Sea Surface Temperature Retrievals at the Naval Oceanographic Office. *Bull. Amer. Meteorol. Soc.* 79, 397–407. doi:10.1175/1520-0477(1998)079<0397:oposss>2.0.co;2

Miyoshi, T., Kondo, K., and Terasaki, K. (2015). Big Ensemble Data Assimilation in Numerical Weather Prediction. *Computer* 48, 15–21. doi:10.1109/mc.2015.332

Naval Oceanographic Office (2014a). *METOP-A AVHRR GAC L2P Swath SST Data Set*. Ver. 1.0. *PO.DAAC, CA, USA* „ Dataset Accessed 2017–01–01 to 2020–01–01 at. doi:10.5067/GHMTG–2PN02

Naval Oceanographic Office (2014b). *METOP-B AVHRR GAC L2P Swath SST Data Set*. Ver. 1.0. *PO.DAAC, CA, USA* , Dataset Accessed 2017–01–01 to 2020–01–01 at. doi:10.5067/GHMTB–2PN02

Naval Oceanographic Office (2014c). *N-18 AVHRR GAC L2P Swath SST Data Set.*Ver. 1.0. *PO.DAAC, CA, USA* , Dataset Accessed 2017–01–01 to 2020–01–01 at. doi:10.5067/GH18G–2PN02

Naval Oceanographic Office (2014d). *N-19 AVHRR GAC L2P Swath SST Data Set*. Ver. 1.0. *PO.DAAC, CA, USA* , Dataset Accessed 2017–01–01 to 2020–01–01 at. doi:10.5067/GH19G–2PN02

Ngodock, H. E., Jacobs, G. A., and Chen, M. (2006). The Representer Method, the Ensemble Kalman Filter and the Ensemble Kalman Smoother: A Comparison Study Using a Nonlinear Reduced Gravity Ocean Model. *Ocean Model.* 12, 378–400. doi:10.1016/j.ocemod.2005.08.001

Ngodock, H., Souopgui, I., Carrier, M., Smith, S., Osborne, J., and D'Addezio, J. (2020). An Ensemble of Perturbed Analyses to Approximate the Analysis Error Covariance in 4dvar. *Tellus A: Dynamic Meteorol. Oceanogr.* 72, 1–12. doi:10.1080/16000870.2020.1771069

O'Kane, T. J., Matear, R. J., Chamberlain, M. A., and Oke, P. R. (2014). ENSO Regimes and the Late 1970's Climate Shift: The Role of Synoptic Weather and South Pacific Ocean Spiciness. *J. Comput. Phys.* 271, 19–38. doi:10.1016/j.jcp.2013.10.058

Oke, P. R., and Sakov, P. (2008). Representation Error of Oceanic Observations for Data Assimilation. *J. Atmos. Oceanic Technol.* 25, 1004–1017. doi:10.1175/2007JTECHO558.1

Oke, P. R., Schiller, A., Griffin, D. A., and Brassington, G. B. (2005). Ensemble Data Assimilation for an Eddy-Resolving Ocean Model of the Australian Region. *Q. J. R. Meteorol. Soc.* 131, 3301–3311. doi:10.1256/qj.05.95

Oke, P. R., Sakov, P., and Corney, S. P. (2007). Impacts of Localisation in the EnKF and EnOI: Experiments with a Small Model. *Ocean Dyn.* 57, 32–45. doi:10.1007/s10236-006-0088-8

Oke, P. R., Brassington, G. B., Griffin, D. A., and Schiller, A. (2008). The Bluelink Ocean Data Assimilation System (BODAS). *Ocean Model.* 21, 46–70. doi:10.1016/j.ocemod.2007.11.002

Oke, P. R., Brassington, G. B., Cummings, J., Martin, M., and Hernandez, F. (2012). GODAE Inter-comparisons in the Tasman and Coral Seas. *J. Oper. Oceanogr.* 5, 11–24. doi:10.1080/1755876x.2012.11020135

Oke, P. R., Cahill, M. L., Griffin, D. A., and Herzfeld, M. (2013a). Constraining a Regional Ocean Model with Climatology and Observations: Application to the Hawaiian Islands. *CAWCR Res. Lett.* 20, 20–26.

Oke, P. R., Griffin, D. A., Schiller, A., Matear, R. J., Fiedler, R., Mansbridge, J., et al. (2013b). Evaluation of a Near-Global Eddy-Resolving Ocean Model. *Geosci. Model. Dev.* 6, 591–615. doi:10.5194/gmd-6-591-2013

Oke, P. R., Sakov, P., Cahill, M. L., Dunn, J. R., Fiedler, R., Griffin, D. A., et al. (2013c). Towards a Dynamically Balanced Eddy-Resolving Ocean Reanalysis: BRAN3. *Ocean Model.* 67, 52–70. doi:10.1016/j.ocemod.2013.03.008

Oke, P. R., Griffin, D. A., Rykova, T., and de Oliveira, H. B. (2018). Ocean Circulation in the Great Australian Bight in an Eddy-Resolving Ocean Reanalysis: The Eddy Field, Seasonal and Interannual Variability. *Deep Sea Res. Part Topical Stud. Oceanography* 157-158, 11–26. doi:10.1016/j.dsr2.2018.09.012

Oke, P. R. (2002). Assimilation of Surface Velocity Data into a Primitive Equation Coastal Ocean Model. *J. Geophys. Res.* 107, 1–25. doi:10.1029/2000JC000511

Pujol, M.-I., Faugère, Y., Taburet, G., Dupuy, S., Pelloquin, C., Ablain, M., et al. (2016). Duacs Dt2014: the New Multi-mission Altimeter Data Set Reprocessed over 20 Years. *Ocean Sci.* 12, 1067–1090. doi:10.5194/os-12-1067-2016

Ridgway, K. R., Dunn, J. R., and Wilkin, J. L. (2002). Ocean Interpolation by Four-Dimensional Weighted Least Squares-Application to the Waters Around Australasia. *J. Atmos. Oceanic Technol.* 19, 1357–1375. doi:10.1175/1520-0426(2002)019<1357:oibfdw>2.0.co;2

Roemmich, D., and Gilson, J. (2009). The 2004-2008 Mean and Annual Cycle of Temperature, Salinity, and Steric Height in the Global Ocean from the Argo Program. *Prog. Oceanogr.* 82, 81–100. doi:10.1016/j.pocean.2009.03.004

Roemmich, D., Alford, M. H., Claustre, H., Johnson, K., King, B., Moum, J., et al. (2019). On the Future of Argo: A Global, Full-Depth, Multi-Disciplinary Array. *Front. Mar. Sci.* 6, 439. doi:10.3389/fmars.2019.00439

Ryan, A. G., Regnier, C., Divakaran, P., Spindler, T., Mehra, A., Smith, G. C., et al. (2015). GODAE OceanView Class 4 Forecast Verification Framework: Global Ocean Inter-comparison. *J. Oper. Oceanogr.* 8, s98–s111. doi:10.1080/1755876x.2015.1022330

Sakov, P., and Bertino, L. (2011). Relation between Two Common Localisation Methods for the EnKF. *Comput. Geosci.* 15, 225–237. doi:10.1007/s10596-010-9202-6

Sakov, P., and Sandery, P. A. (2015). Comparison of EnOI and EnKF Regional Ocean Reanalysis Systems. *Ocean Model.* 89, 45–60. doi:10.1016/j.ocemod.2015.02.003

Sakov, P., Counillon, F., Bertino, L., Lisæter, K. A., Oke, P. R., and Korablev, A. (2012). TOPAZ4: an Ocean-Sea Ice Data Assimilation System for the North Atlantic and Arctic. *Ocean Sci.* 8, 633–656. doi:10.5194/os-8-633-2012

Sakov, P. (2014). *EnKF-C User Guide. arXiv preprint arXiv:1410.1233* (New York, NY: Cornell University), 0–46

Scharroo, R., Leuliette, E., Lillibridge, J., Byrne, D., Naeije, M., and Mitchum, G. (2013). "RADS: Consistent Multi-Mission Products,". *20 Years of Progress in Radar Altimatry*. Editor L. Ouwehand (Paris, France: of ESA Special Publication), Vol. 710, 69.

Schiller, A., Brassington, G. B., Oke, P., Cahill, M., Divakaran, P., Entel, M., et al. (2020). Bluelink Ocean Forecasting australia: 15 Years of Operational Ocean Service Delivery with Societal, Economic and Environmental Benefits. *J. Oper. Oceanogr.* 13, 1–18. doi:10.1080/1755876X.2019.1685834

Schmidtko, S., Johnson, G. C., and Lyman, J. M. (2013). MIMOC: A Global Monthly Isopycnal Upper-Ocean Climatology with Mixed Layers. *J. Geophys. Res. Oceans* 118, 1658–1672. doi:10.1002/jgrc.20122

Shi, L., Alves, O., Wedd, R., Balmaseda, M. A., Chang, Y., Chepurin, G., et al. (2017). An Assessment of Upper Ocean Salinity Content from the Ocean Reanalyses Inter-comparison Project (ORA-IP). *Clim. Dyn.* 49, 1009–1029. doi:10.1007/s00382-015-2868-7

Wong, A. P., Wijffels, S. E., Riser, S. C., Pouliquen, S., Hosoda, S., Roemmich, D., et al. (2020). Argo Data 1999–2019: Two Million Temperature-Salinity Profiles and Subsurface Velocity Observations from a Global Array of Profiling Floats. *Front. Mar. Sci.* 7, 700. doi:10.3389/fmars.2020.00700

Xie, J., and Zhu, J. (2010). Ensemble Optimal Interpolation Schemes for Assimilating Argo Profiles into a Hybrid Coordinate Ocean Model. *Ocean Model.* 33, 283–298. doi:10.1016/j.ocemod.2010.03.002

Yin, Y., Alves, O., and Oke, P. R. (2011). An Ensemble Ocean Data Assimilation System for Seasonal Prediction. *Monthly Weather Rev.* 139, 786–808. doi:10.1175/2010mwr3419.1

Yu, X., Zhang, S., Li, J., Lu, L., Liu, Z., Li, M., et al. (2019). A Multi-Timescale EnOI-like High-Efficiency Approximate Filter for Coupled Model Data Assimilation. *J. Adv. Model. Earth Syst.* 11, 45–63. doi:10.1029/2018ms001504

Zang, X., and Wunsch, C. (2001). Spectral Description of Low-Frequency Oceanic Variability. *J. Phys. Oceanogr.* 31, 3073–3095. doi:10.1175/1520-0485(2001)031<3073:sdolfo>2.0.co;2

Zweng, M. M., Reagan, J. R., Antonov, J. I., Locarnini, R. A., Mishonov, A. V., Boyer, T. P., et al. (2013). "World Ocean Atlas 2013, Volume 2: Salinity," in *NOAA Atlas NESDIS 74*. Editors S. Levitus and A. Mishonov (Washington, D.C.: U.S. Government Printing Office), 39.

Conflict of Interest: The authors declare that the research was conducted in the absence of any commercial or financial relationships that could be construed as a potential conflict of interest.

frontiers in Earth Science

ORIGINAL RESEARCH
published: 02 July 2021
doi: 10.3389/feart.2021.680881

Development of High-Resolution Regional Climatology in the East/Japan Sea With a Primary Focus on Meridional Temperature Gradient Correction

*Jae-Ho Lee and You-Soon Chang**

Department of Earth Science Education, Kongju National University, Kongju, South Korea

In this study, we developed a new high-resolution regional climatology (0.1° by 0.1° by 19 levels) in the East/Japan Sea. National Centers for Environmental Information and Korea Oceanic Data Center already released the regional climatology of East Asian seas including the East/Japan Sea with 0.1° by 0.1° resolution. It provides a reliable temperature and salinity structure compared to previous 1° or 0.25° climatologies. However, this study found an abnormal meridional temperature gradient problem when calculating geostrophic currents based on this new climatology. Geostrophic currents show a strong repetitive eastward flow along the 1° latitudinal band especially in the East/Japan Sea, which corresponds with abnormal meridional temperature gradients at the same areas. This problem could be related to the objective analysis procedure generating the high-resolution climatology. Here, we reproduced a high-resolution climatology without the abnormal meridional temperature gradient problem by using the optimal interpolation method. Results show that the meridional gradient problem can partly be attributed to both the use of the World Ocean Atlas background field on the 1° grid, and the spatial distribution of World Ocean database observation data; however, these are not the primary causes. We corrected the abnormal temperature gradient by increasing the meridional decorrelation length scale without losing the meso-scale feature in the East/Japan Sea, as shown by the wavelet analysis. Improvement of the new gridded field is also validated by using serial hydrographic data and the altimetry-derived surface current product.

Keywords: regional climatology, East/Japan Sea, horizontal temperature gradient, objective analysis, optimal interpolation, geostrophic current

OPEN ACCESS

Edited by:
Andrea Storto,
Institute of Marine Science (CNR), Italy

Reviewed by:
Viktor Gouretski,
Chinese Academy of Sciences, China
Gilles Reverdin,
Center National de la Recherche Scientifique, France

****Correspondence:***
You-Soon Chang
yschang@kongju.ac.kr

Specialty section:
This article was submitted to Hydrosphere, a section of the journal Frontiers in Earth Science

Received: *15 March 2021*
Accepted: *16 June 2021*
Published: *02 July 2021*

Citation:
Lee J-H and Chang Y-S (2021) Development of High-Resolution Regional Climatology in the East/Japan Sea With a Primary Focus on Meridional Temperature Gradient Correction. Front. Earth Sci. 9:680881. doi: 10.3389/feart.2021.680881

INTRODUCTION

The World Ocean Atlas (WOA) has been developed by the National Centers for Environmental Information (NCEI) to describe the three-dimensional temperature and salinity structures of the world ocean. It has served as initial and boundary conditions of ocean circulation models and validated ocean remote sensing data. The original WOA produced in 1982 (Levitus, 1982) was continuously updated through 1994 (NOAA, 1994), 1998 (NOAA, 1998), 2001 (Levitus, 2002; hereafter WOA01), 2005 (Levitus, 2006; hereafter WOA05), 2009 (Levitus, 2009; hereafter WOA09),

2013 (Levitus, 2013; hereafter WOA13), and 2018 (Boyer et al., 2018; hereafter WOA18) as the latest observations became available [https://www.ncei.noaa.gov/products/world-ocean-atlas]. However, WOAs except for recent versions (WOA13 and WOA18) have been produced with a spatial resolution of 1° × 1° on 33 vertical standard depth levels, hence they depict only the general temperature and salinity structure of large-scale in the global ocean.

Boyer and Levitus (1997) first improved the spatial resolution of ocean climatology with 0.25°; however, noise problems associated with spare data coverage were identified by a later study (Chang and Chao, 2000). By employing an additional smoothing scale, Boyer et al. (2005) developed a reliable 0.25° climatology; NCEI climatology is frequently updated and continues to be widely used. Gridded data from a Generalized Digital Environmental Model (GDEM) maintained by the U.S Navy has also been used as the other climatology with the same 0.25° intermediate-resolutions (Carnes, 2009; Carnes et al., 2010). Recent WOAs (WOA13 and WOA18) have 102 standard depth levels and are presented on 1° and 0.25° grids due to the increasing observing system in the 21st century. World Ocean Experiment-Argo Global Hydrographic Climatology (WAGHC), a new global ocean hydrographic climatology version with 0.25° grids, has also been generated on isobaric and isopycnal surface (Gouretski, 2018, 2019).

However, these climatologies with 0.25° intermediate resolutions are still inadequate for detailed regional-scale studies. Chang and Shin (2012) developed a high-resolution 0.1° grid climatology, however their study area was confined to the southwestern coastal area of the East/Japan Sea. Therefore, it is necessary to improve the spatial resolution of oceanic climatology ensuring preservation of data quality and wider regional-scale analysis of target regions.

In the 21st century, on account of the successful international Argo project [http://www.argo.net], available temperature and salinity profiles rapidly increased, enabling NCEI to develop and release high-resolution regional climatologies. The new regional climatologies include nine major regions; the Southwest North Atlantic, Northwest Atlantic, GIN Seas, Northern North Pacific, Northeast Pacific, Nordic Sea, Arctic Ocean, Gulf of Mexico, and East Asian seas [https://www.ncei.noaa.gov/regional-ocean-climatologies].

In particular, the East Asian Seas Regional Climatology (EASRC) was developed from the collaboration between the NCEI and Korea Oceanic Data Center (KODC). The study area extends from 115 to 143°E and 24 to 52°N including the East China Sea, Yellow Sea, Bohai Sea, East/Japan Sea, northern Philippine Sea, and the adjacent Northwest Pacific Ocean (Johnson and Boyer, 2015). It has various versions for annual, seasonal, and monthly mean periods on 1, 0.25, and 0.1° latitude-longitude grids.

Since these regional climatologies were newly developed, it is imperative that detailed assessments are provided. Chang and Shin (2014) reported the vertical gradient problem of the EASRC, which was showing an anomalous density inverse in coastal regions, related to the weakness of most isobarically-averaged climatologies (Gouretski, 2008; Gouretski,2 019). In this study, we also found another problem related to an abnormal meridional temperature gradient, particularly in the East/Japan Sea. The East/Japan Sea is a semi-enclosed marginal sea, considered a miniature ocean because of various oceanographic processes such as subpolar fronts, meso-scale eddies, and coastal upwelling (Kim et al., 2001). Therefore, it is important that we present a detailed hydrological structure of this area.

Figure 1A shows the altimetry-derived surface current field around the East/Japan Sea in February, provided by AVISO (Pascual et al., 2006). AVISO-Archiving, Validation and Interpretation of Stellite Oceanographic data provided by the Center National d'Etudes Spatiales (CNES) is an objective analysis product based on satellite altimeters. It provides surface current data derived from absolute dynamic topography with 0.25° by 0.25° resolution. **Figure 1B** presents geostrophic current derived from temperature and salinity gridded fields of the EASRC. Both products offer an accurate depiction of the general current patterns such as the strong nearshore branch of the Tsushima current and the Ulleung eddy system. However, the EASRC failed to present an appropriate position of the cold eddy near the Wonsan Bay as compared to AVISO data. Another difference is that the EASRC presents strong, recurring zonal current flows along the 38, 39, and 40°N latitudinal bands. The vector correlation coefficient between the two data from 37 to 41°N was appeared 0.52. With regards to horizontal temperature distribution, the EASRC illustrates both the large and small-scale features in the East/Japan Sea (**Figure 2A**). However, when calculating temperature difference in the meridional direction at 0.1° latitude interval (dT/dy), a strong meridional temperature gradient was observed between 38 and 41°N at almost each latitudinal interval of 1° (**Figure 2B**). The averaged meridional temperature gradient is −0.35, −0.39, −0.65, and −0.33°C/km at 38, 39, 40, and 41°N, respectively, which corresponds to the abnormally repetitive zonal current in this area as shown in **Figure 1B**.

Therefore, this study reproduced and evaluated the same high-resolution field without this meridional gradient problem by using the optimal interpolation (OI) method. This problem has been observed in all seasons, but henceforth, this study will present the spatial distribution in February, when this problem is most evident.

The following section provides the data used, and details about the OI method implemented in this study. *Results* presents the meridional gradient patterns generated from several different OI versions. *Summary and Discussion* discusses the results and provides an overall summary.

DATA AND METHODS

Data

This study used *in situ* World Ocean Database 2013 (hereafter WOD13) and gridded WOA13 data, which is the same as the recent version of the EASRC. All data are collected from NCEI as well. In the WOD13, we used the following datasets: Ocean Station Data (OSD), Mechanical Bathythermographs (MBT), Expendable Bathythermograph Data (XBT), High resolution Conductivity-Temperature-Depth (CTD), Drifting Buoy Data

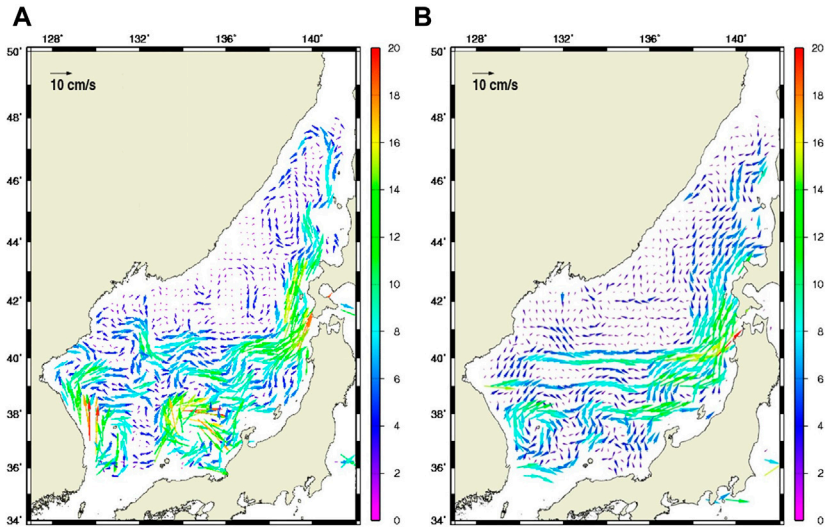

FIGURE 1 | (A) Altimetry-derived surface current from AVISO and **(B)** geostrophic currents from EASRC in February.

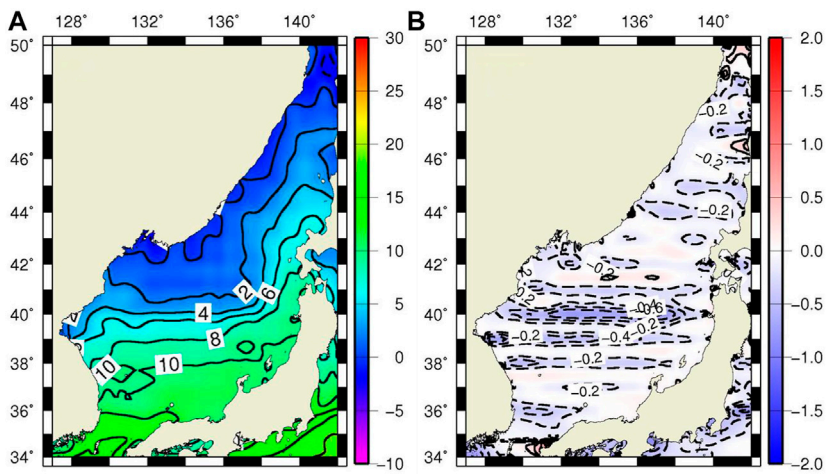

FIGURE 2 | (A) Horizontal temperature distribution and **(B)** meridional temperature gradient at the surface of EASRC in February.

(DRB), Moored Buoy Data (MRB), Profiling Floats Data (PFL), Undulating Ocean Recorder Data (UOR), and Glider Data (GLD), https://www.ncei.noaa.gov/products/world-ocean-database) subject to the Quality Control (QC) procedure based on the NCEI technical report (Boyer and Levitus, 1994) and previous research (Chang et al., 2009).

First, the QC flag check of WOD13 data was performed and only good data were used in this study. Duplication and range checks for position, date, and pressure levels were carried out in the next step. Data that deviated from the standard range of temperature and salinity were eliminated and the density inversion check was also performed. WOD13 data includes observed level data and interpolated to a set of 102 standard levels. This study used standard level data observed from 1955 to 2012. We used a total of 1,443,820 profiles and 27,278 profiles have been rejected through the QC process. We also used the monthly mean of the WOA13 with a spatial resolution of 1° × 1° on 24 vertical levels from the surface to a depth of 1,500 m as background data to interpolate it even in areas where observations were scarce. It is to be noted that WOA was used similar to datasets on every 1° × 1° grid of the entire study area, eliminating the possibility of spatial imbalance in the final product. In this study, an objective analysis field for 19 vertical levels was generated using WOA13 with a 1° resolution and WOD13 observation data.

Method

In order to generate gridded temperature and salinity field at each depth, we employed the OI method as follows. The objective estimate $(T(S)^{obj})$ of the temperature (salinity) at each grid point of standard depths is given by

$$T(S)^{obj} = \langle d \rangle + \omega \cdot (d - \langle d \rangle) \quad (1)$$

where $d = [d_1, \ldots, d_n]$; it denotes the set of historical observed WOD13 and gridded WOA13 temperature (salinity) profiles on the grid point being interpolated and $\langle d \rangle$ denotes the mean value of the set d within the influence radius. This term is a simple arithmetic mean with no weight applied.

Each historical WOD13 data (d) can be separated into a true signal (s) and some random noise (η), and the signal and noise variance of the data can be approximated from the relationship $d = s + \eta$ (Fukumori and Wunsch, 1991). The signal variance is approximated by $s = (1/N)\sum_i (d_i - \langle d \rangle)^2$, where N is the number of data points; The noise variance is estimated from the data difference of neighboring stations; it is calculated as $\eta = (1/2N)\sum_i (d_i - d_j)^2$, where d_j is the data point that has the shortest distance from d_i; further ω is the weighting matrix, expressed as $\omega = Cdg \cdot [Cdd + I \cdot \langle \eta^2 \rangle]^{-1}$ (McIntosh, 1990), where I denotes the identity matrix, Cdg denotes the data-grid covariance matrix, and Cdd denotes the data-data covariance matrix which are expressed as:

$$Cdg_i(x, y) = \langle s^2 \rangle \cdot \exp\left\{ - \left[Dx_{i,g}^2 / Lx^2 + Dy_{i,g}^2 / Ly^2 \right] \right\} \quad (2)$$

$$Cdd_{i,j}(x, y) = \langle s^2 \rangle \cdot \exp\left\{ - \left[Dx_{i,j}^2 / Lx^2 + Dy_{i,j}^2 / Ly^2 \right] \right\} \quad (3)$$

The covariance used in this study is a function of the spatial length scale (Lx, Ly), where Dx and Dy are the spatial distances between the observed data (subscripted with i) and the grid point (subscripted with g) in zonal and meridional directions, respectively. If the number of data (N) is small, there will be a higher weight toward <d> rather than weighting matrix.

RESULTS

Reproduction of Meridional Gradient Problem

In order to investigate the possible cause of the meridional temperature gradient problem shown in the EASRC, similar meridional temperature gradient patterns must initially be reproduced.

The EASRC employed search passes within three circles of different radii (211, 155, and 111 km) to obtain a better representation of the objective analysis (OA) fields in this area, utilizing the response function of Barnes (1964). This study applied the same influence radius as the EASRC, but failed to represent any similar meridional temperature gradient problems, which may be related to differences in the OA method and datasets used after the QC procedure. Alternately, through multiple sensitivity experiments, an influence radius as 211 km in the longitudinal and 111 km in the latitudinal direction was set to reproduce the meridional temperature gradient problem. Several previous studies using the OI method applied a horizontal anisotropy scale, with Lx being greater than Ly, to reflect the predominant zonal currents in the ocean interior (Bohme and Send, 2005; Chang and Shin, 2012).

Figure 3 shows the OI result with a 0.1° grid resolution using both WOA13 and WOD13. The spatial distribution of temperature is very similar to that of the EASRC (**Figure 2A**), particularly with respect to the shape of the isothermal line and polar front position (**Figure 3A**). As for the meridional temperature gradient (dT/dy) shown in **Figure 3B**, strong negative values less than −0.2°C/km appeared at every 1° grid interval, from latitudes 38 to 41°N, with a minimum of about −0.6°C/km at 40°N. The average meridional temperature gradient by latitude was −0.32°C/km at 38°N, −0.37°C/km at 39°N, −0.77°C/km at 40°N, and −0.30°C/km at 41°N, which is similar to the mean temperature gradient of the EASRC (**Figure 2B**). This result indicates that the OI field generated by this study suitably reproduces the problem in the EASRC as shown in **Figure 2B**. We will further investigate the possible cause of the meridional temperature gradient problem, and provides the optimal OI fields without the same problem.

Effect of WOA13

We hypothesized that this abnormal meridional repetitive pattern was connected to the 1° by 1° grid WOA13 background data. Therefore, we generated a new OI field with the same influence radius using only WOA13 data (**Figure 4**). The spatial temperature distribution (**Figure 4A**) is smoother than in **Figure 3A**. Repetitive meridional gradient values less than −0.2°C/km can clearly be observed from latitudinal bands 38 to 41°N in **Figure 4B**. This anomalous pattern could be caused by the increased weight of WOA13 data at every 1° grid during the OI process for the generation of 0.1° high-resolution data.

To rectify this, the WOA13 background data was reproduced on a regular 0.1° by 0.1° grid by using the linear interpolation method, and then OI was applied again (**Figures 4C,D**). Consequently, the temperature distribution was similar to the result using the 1° grid WOA13 data as previously shown in **Figure 4A**. However, the abnormal repetitive patterns of the meridional temperature gradient at 1° intervals clearly disappeared (**Figure 4D**). This implies that the abnormal meridional gradient problem can be corrected by using a relatively high-resolution climatology, such as WOA with a 0.25° resolution, GDEM, or WAGHC, rather than a 1° grid background field.

When the irregular *in situ* WOD13 data was supplemented for the OI process, it complicated the temperature distribution (**Figure 4E**). Interestingly, the abnormal meridional temperature gradient appeared again with a 1° grid meridional interval (**Figure 4F**).

Effect of WOD13

Based on the results depicted in **Figure 4**, we concluded that the repetitive temperature gradient pattern at 1° interval is affected not only by WOA13 data with a regular 1° grid but also by randomly distributed WOD13 data. In **Figure 5**, we regenerated OI fields just from WOD13 data and investigated its spatial distributions.

Figures 5A,B show data distribution and the latitudinal change of the amount of data within the influence radius. A total 949 profiles were estimated within the influence radius of

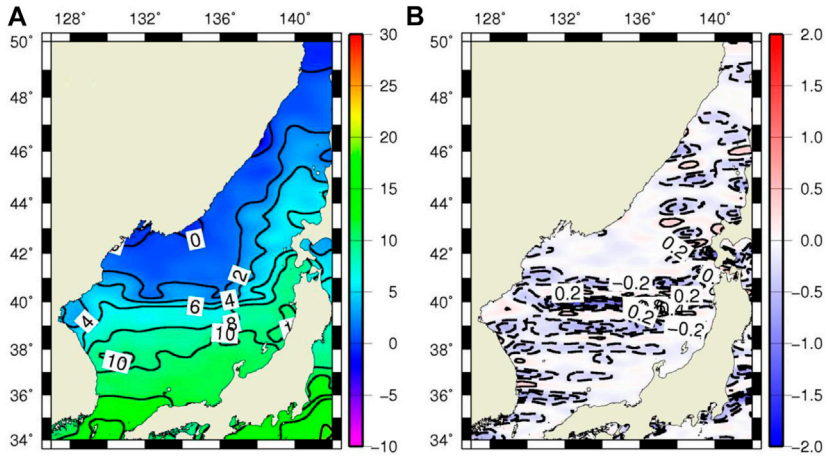

FIGURE 3 | (A) Horizontal temperature distribution and **(B)** meridional temperature gradient at surface in February. This is a new optimal interpolation product with 0.1° resolution using both 1° gridded WOA13 and irregular WOD13. Influence radius applied was 211 km (zonal) and 111 km (meridional).

136° E, 40° N. This position was selected because the largest meridional gradient value was noted at this latitude. **Figures 5C,D** show the spatial distribution of temperature and the meridional temperature gradient, respectively. The temperature distribution is similar to **Figure 3A** and the abnormal repetitive temperature gradient pattern at a 1° interval is also similar to that of **Figure 3B**. At the central latitude of 40° N, a total of 141 profiles were estimated within the zonal influence radius of 211 km. The number of data repeatedly increased at 1° intervals (see red bars in **Figure 5B**). Most ship observations were performed along the designated observation line, which ran predominantly along either latitudinal or longitudinal line. Consequently, the trend of number of observations along latitudinal lines being abundant remains consistent (see **Figure 9**). Thus, it is expected that the repetitive meridional temperature gradient pattern with 1° interval is closely related to the weighting of repetitive data numbers located at 1° grid intervals.

By randomly extracting WOD13 data of up to 20 profiles along 0.1° latitudinal intervals within the influence radius shown in **Figures 5E,F**, we produced another OI field. **Figures 5G,H** represent the temperature distribution and meridional gradient, respectively. Although data numbers constantly provided within the influence radius of every latitudinal band, results show that temperature distribution is similar to the previous version and that the repetitive gradient pattern still exists, but with decreased magnitude.

To confirm the weak relationship between spatial distributions of WOD13 data and the meridional gradient problem, this study generated another OI field using WOA13 data projected to a WOD13 position (**Figure 6**). Consequently, the temperature distribution is similar to the result obtained using WOA13 data with a regular 0.1° grid as previously shown in **Figure 4C**. In addition, the repetitive meridional gradient pattern at 1° grid intervals disappeared, which is consistent with the results shown in **Figure 4D**. We thereby confirmed that the cause of the meridional gradient problem is not closely related to the spatial distribution of WOD13 data.

Effect of Influence Radius

Since this abnormal meridional gradient was reproduced accurately when we applied a horizontal anisotropy scale, we performed a sensitivity experiment with several influence radii having the same value in the zonal and meridional directions. **Figures 7A,B** depict the results of the new OI with an influence radius of 111 km in both zonal and meridional direction, based on the same two data (1° gridded WOA13 and irregular WOD13). Compared to **Figure 3** which uses the same data except for a longer influence radius in the zonal direction, temperature distribution is more complicated especially along the 10°C isothermal line. However, the repetitive gradient pattern still exists, and is related to the same meridional influence radius of **Figure 3**.

When we used the same 211 km influence radius in the zonal and meridional directions as shown in **Figures 7C,D**, the spatial distribution was similar to that of the existing OI results shown in **Figure 3**. In this case, repetitive patterns with a 1° interval in the meridional directions were significantly reduced. The same tendency was exhibited in the OI result using a 311 km radius circle (**Figure 7F**), but showed a smoother temperature distribution (**Figure 7E**).

One of the advantages of high-resolution climatology is its capacity to reproduce various meso-scale features. However, the smoothing effect due to the increased influence radius can lead to their disappearance. Therefore, we performed a wavelet analysis to determine the spatial variability of meso-scale features from the EASRC and various OI results, with the exception of the case using 111 km influence radius (**Figure 7**). Wavelet is a method of analyzing spectral characteristics over a period of time; however, in this study, we used it to analyze the characteristics of space by applying

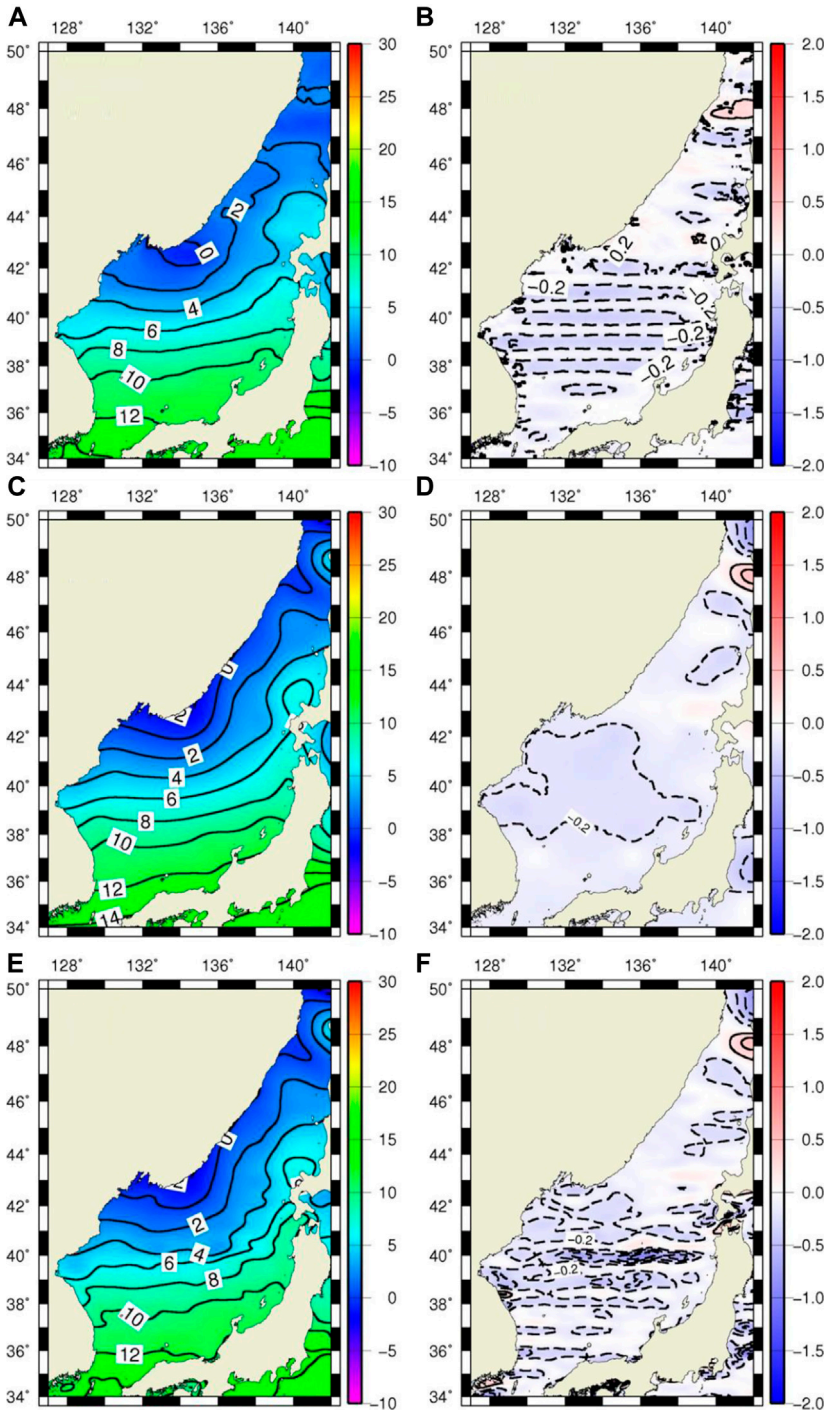

FIGURE 4 | The same as **Figure 3** except for **(A, B)** only 1° gridded WOA13, **(C, D)** only linear interpolated 0.1° WOA13, and **(E, F)** both 0.1° gridded WOA13 and irregular WOD13.

distance instead of time. The southwestern (northeastern) part of the East/Japan Sea was defined as the first (last) data position and the number of data position was increased in the meridional direction. In order to focus on the meso-scale features, we extracted the sea surface temperature anomaly (SSTA) by 230 km high-pass filtering.

Figure 8A shows the spectral density function of the SSTA in the EASRC. **Figure 8B** indicates the spatial-averaged spectral density function with a 95% confidence level. In the spatial-averaged spectral density function, a peak is appeared at a diameter of approximately 160 km which satisfies a 95% confidence level.

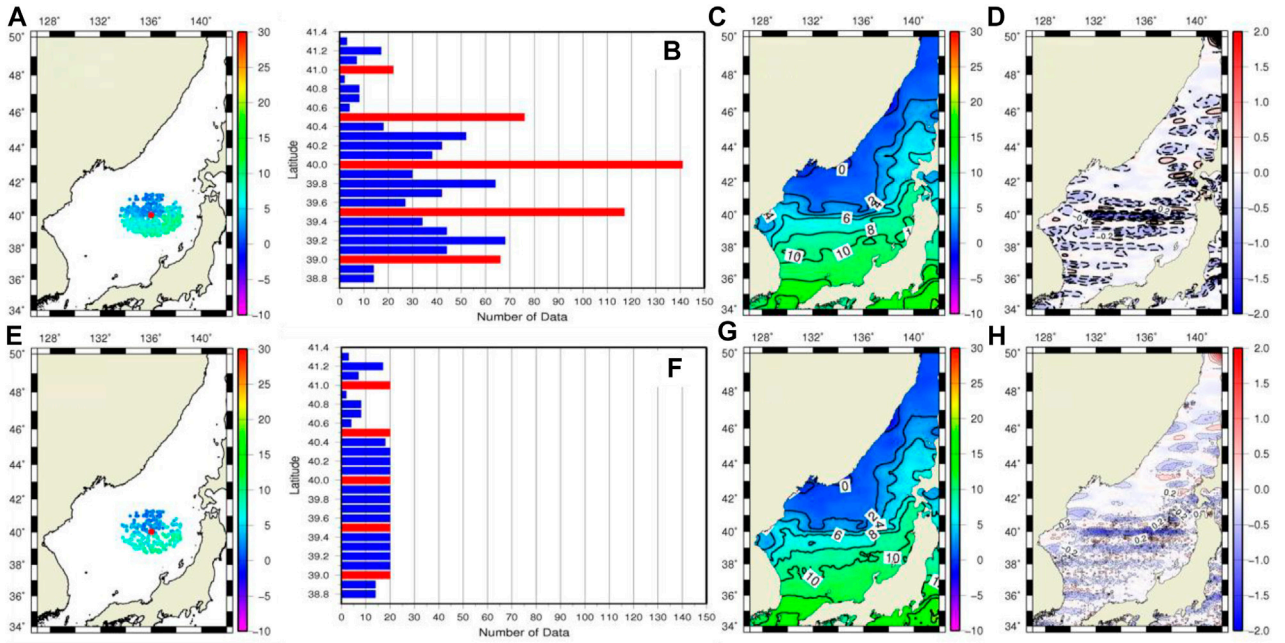

FIGURE 5 | (A) Data position and **(B)** latitudinal change of the number of data within the influence radius of 136°E, 40°N, **(C)** horizontal temperature distribution, and **(D)** meridional temperature gradient by using only the irregular WOD13. Bottom panels provide the same information as the upper panels except for reduced WOD13 data that was randomly extracted for up to 20 profiles along 0.1° each latitudinal band within the influence radius.

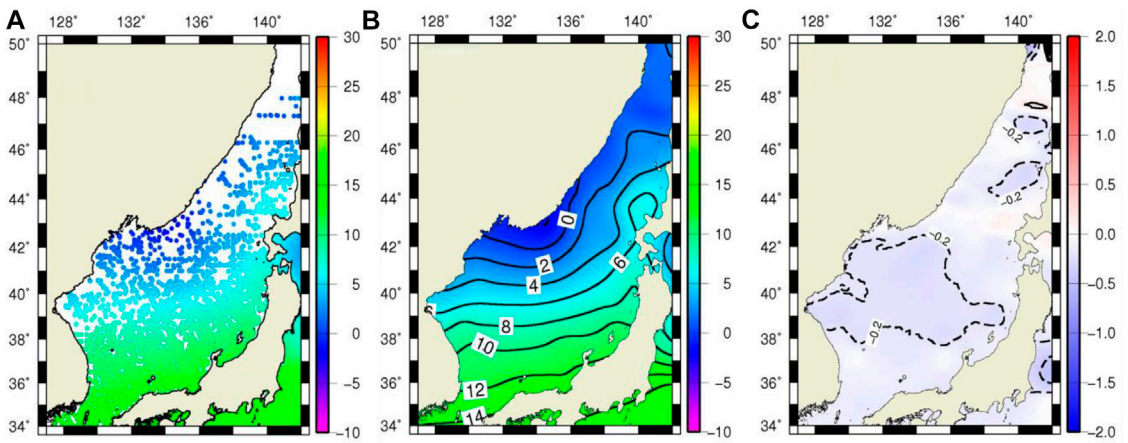

FIGURE 6 | (A) Data position, **(B)** horizontal temperature distribution, and **(C)** meridional temperature gradient at the surface in February by using 0.1° WOA13 that was projected to a WOD13 position.

For the new OI data, with an increased influence radius of 211 km in a meridional direction (**Figure 7C**), we performed the same analysis; the results are presented in **Figures 8C,D**. This, in contrast with the original EASRC in **Figures 8A,B**, shows similar results indicating the most significant peak on the meso-scale with a diameter of about 160 km within the 95% significant confidence level. Interestingly, the magnitude of the spatial-averaged spectral density function (0.58) is stronger than that of EASRC (0.55) in the 95% confidence level. In the original EASRC, various meso-scale features were not simulated due to the meridional temperature gradient problem. However, the new OI data with the influence radius of a circle of 211 km simulated various meso-scale features and solved the meridional temperature gradient problem.

As expected, another OI field using 311 km influence radius did not exhibit a peak in the spatial averaged spectral density

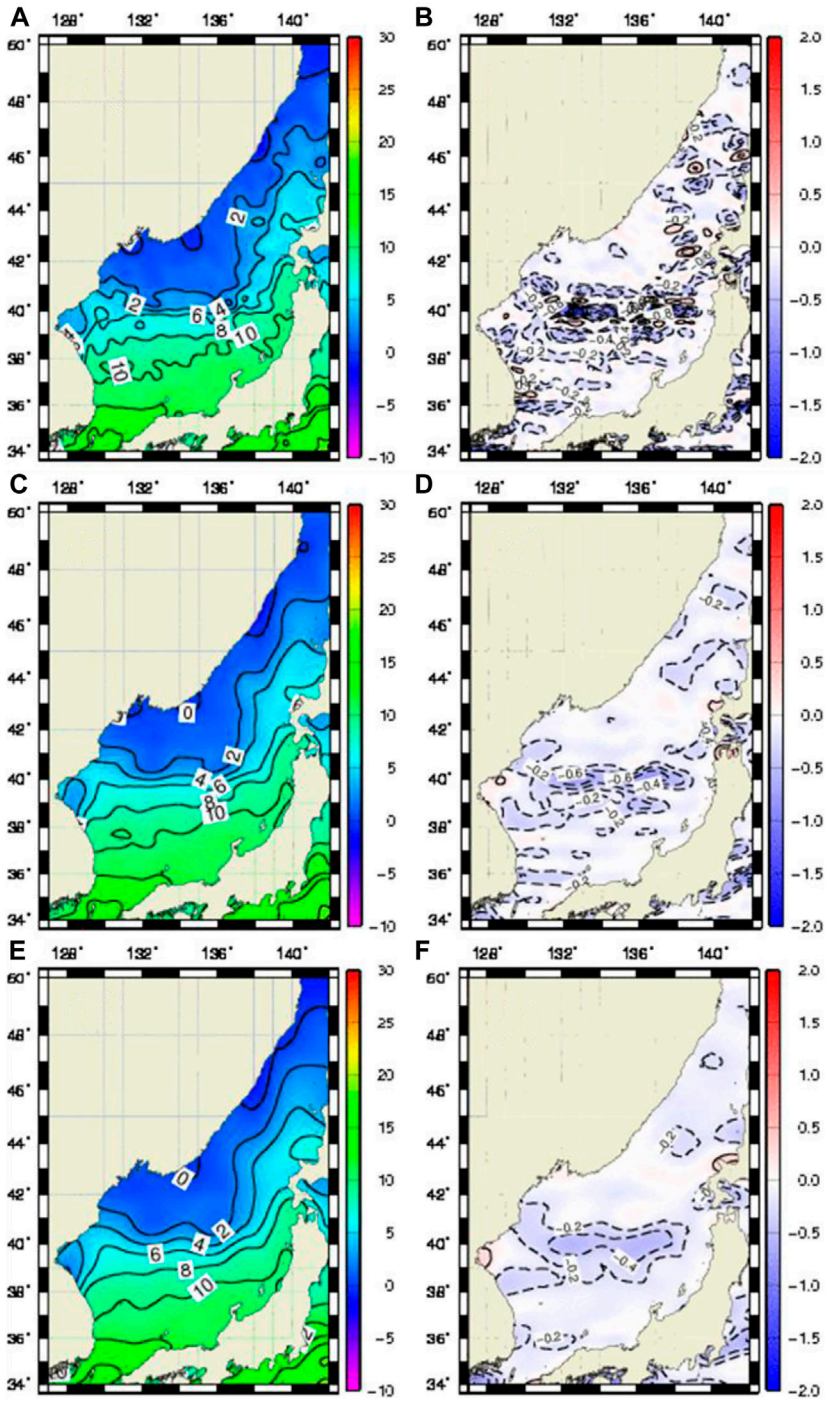

FIGURE 7 | The same as **Figure 3** except for three different influence radii. **(A, B)** The influence radius applied were 111 km, **(C, D)** 211 km, and **(E, F)** 311 km, respectively.

function around 160 km within the 95% confidence level, and its amplitude was significantly reduced due to the smoothing effect (**Figures 8E,F**).

Therefore, OI results obtained by applying a circle of 211 km influence radius (hereafter "new OI") in **Figures 7C,D, 8C,D** showed that the abnormal temperature gradient problem has been resolved, and that the spatial variability in the meso-scale was well simulated. This result cannot prove that the new OI exhibits a real resolution of 0.1° that is a finer than meso-scale. We generated additional OI field using shorter period data for recent

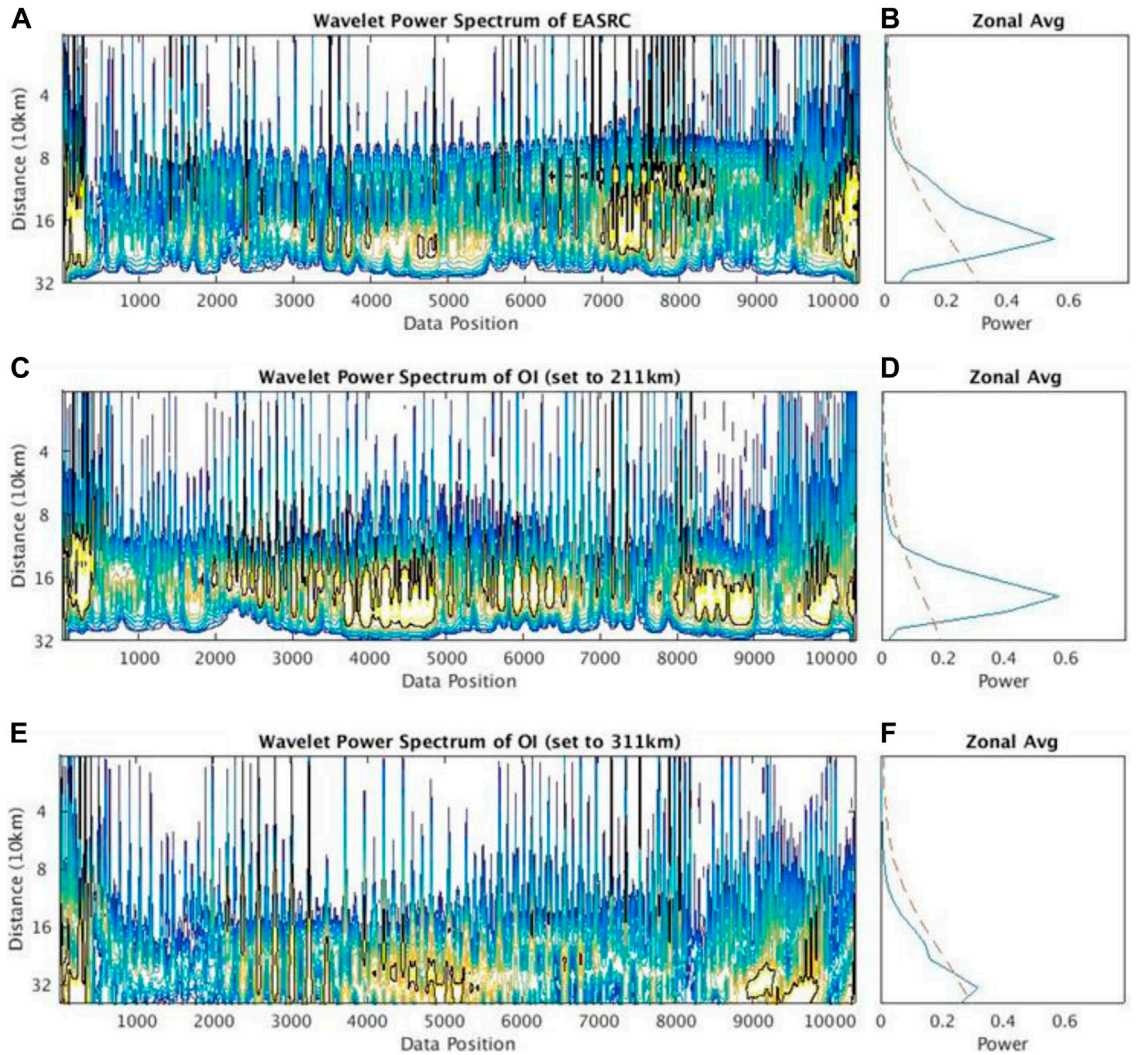

FIGURE 8 | (A) Wavelet spectrum for sea surface temperature anomaly using Morlet wavelet with 95% significant confidence level (black line) in February of the EASRC and **(B)** spatial-averaged wavelet power spectrum with 95% significant confidence level (dotted line). The same information except for OI results are set to **(C, D)** 211 km and **(E, F)** 311 km.

20 years and investigated the spatial variability, but it also revealed the maximum spectral density around 160 km (not shown). It is inferred that the resolution of spatial variability will be more affected by the average period (less than monthly mean) rather than duration of data used. Therefore, it may be impossible to produce the monthly mean climatology simulating a fine scale about 0.1° in this area, which will be investigated in the further separate study.

Validation

We verified the EASRC and new OI field based on serial hydrographic lines that have been observed at the same position for a long time. One of the serial observation datasets was obtained from the 102, 103, 104, 105, 106, and 107 lines provided by the National Institute of Fisheries Science's Korea Oceanographic Data Center (NIFS/KODC) (the six lines of southwestern East/Japan Sea shown in **Figure 9**). The others represent the PM and G line data provided by the Japan Metrological Agency (JMA) (two lines of eastern East/Japan Sea shown in **Figure 9**). They have been simply averaged at each station from 1983 to 2010 for NIFS/KODC data and 1997 to 2010 for JMA data, respectively.

Figure 9 shows the spatial distribution of temperature in February, along the observational lines at 10 m depth obtained from long-term mean serial hydrographic data (**Figure 9A**), the EASRC (**Figure 9B**), and new OI fields with no meridional gradient problem generated by this study (**Figure 9C**). Since the surface data was relatively insufficient compared to the 10 m data shown in **Figure 9A**, verification was performed at 10 m instead of at the surface.

Both the EASRC (−0.61°C) and new OI (−0.44°C) show cold bias compared to the observation, which might be associated with

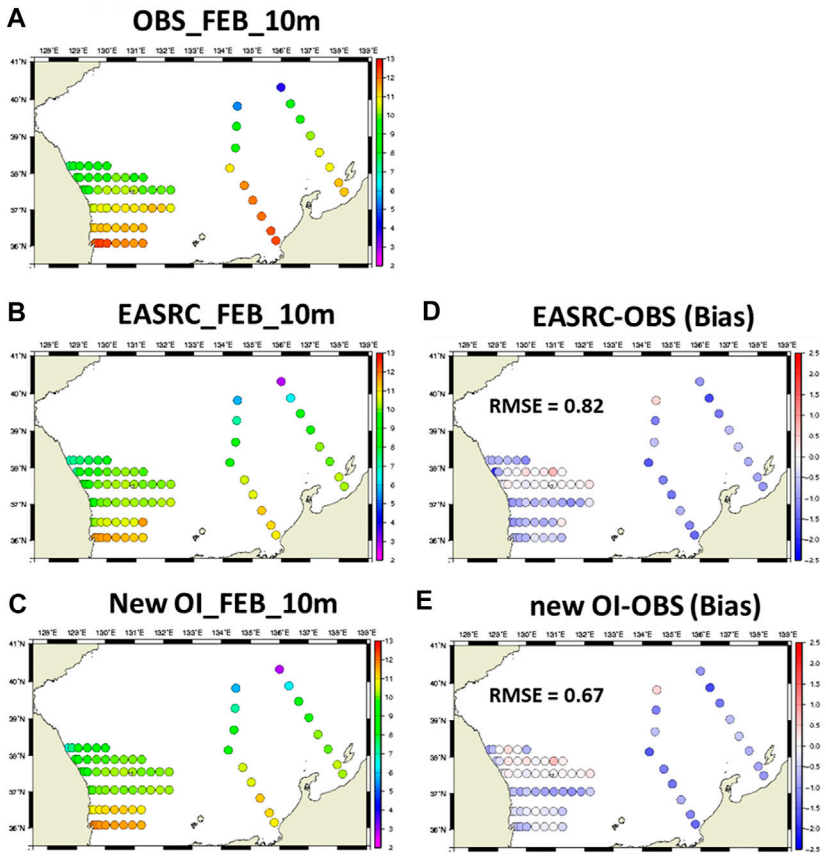

FIGURE 9 | Spatial distribution of temperature and the bias with respect to serial observation at 10 m depth in February. [**(A)** Observation, **(B)** EASRC, **(C)** new OI, **(D)** EASRC-OBS, **(E)** new OI-OBS].

an averaged period (**Figures 9D,E**). Both our climatologies contained many observations made before 1983 and 1997 based on WOD13 since 1955, therefore they reflect fewer of the recent sea warming signals in the East/Japan Sea. The root mean square error (RMSE) of the EASRC was 0.82°C, and the RMSE of the new OI was calculated to be 0.67°C. Thus, it was shown that the new OI was relatively similar to the observed data than the EASRC. This improvement is generally observed in different seasons (August) and depths (100 m depth) (see **Supplementary Figures S1–S3**). The objective of this study is to resolve the meridional temperature gradient problem as shown in the EASRC, rather than provide a synthetic assessment for the climatology, hence further detailed analysis is beyond the scope of this paper.

We also computed the geostrophic flow by using the new OI temperature and salinity profiles (**Figure 10**). The strong abnormal zonal flow that appeared in the original EASRC field has been significantly reduced. The East Korea Warm Current and the cold eddy near the Wonsan Bay were also resolved, and are now comparable to the AVISO data, as previously shown in **Figure 1**. The vector correlation coefficient between AVISO and the new OI was 0.54, showing a higher correlation than with the EASRC (0.52).

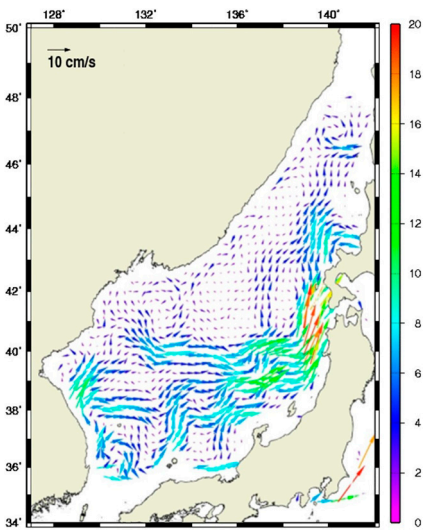

FIGURE 10 | Spatial distribution of geostrophic currents from the new OI in February.

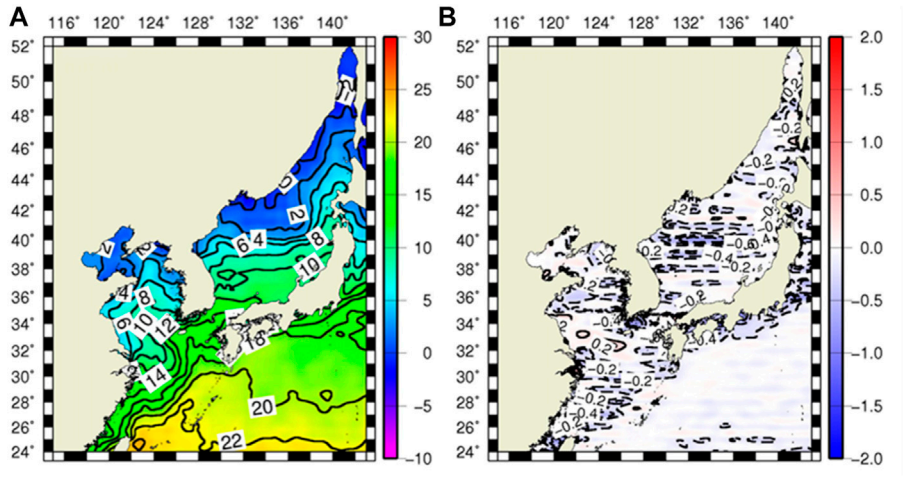

FIGURE 11 | The same as **Figure 2** except for the entire East Asian marginal seas.

SUMMARY AND DISCUSSION

This study found abnormal meridional temperature gradients from the East Asian Seas regional high-resolution climatology developed by NCEI and KODC and reproduced a similar high-resolution field by using the OI method. We used both WOD and WOA data to consider areas where observation data were insufficient.

In the results obtained using the OI method, the abnormal temperature gradient problem was partly related to the use of the WOA background field at the 1° grid. This problem was alleviated by employing a relatively high-resolution climatology background field less than 1° grid. In addition, it was significantly influenced by WOD data. When we examined the distribution of WOD data, we found that the number of data repeatedly increases along the 1° interval latitude band; however, this was not the main cause for the meridional temperature gradient problem. This problem was eliminated by increasing the influence radius in the meridional direction with respect to the existing influence radius. However, the EASRC data showing meridional temperature gradient problem also used similar circles with radii of 211, 155, and 111 km. Hence, it was inferred that changing the influence radius could not be a major solution for other OA products using different methods.

When we calculated the geostrophic current with the new OI field with the circle of 211 km influence radius, we found that strong zonal flows of 1° intervals are significantly reduced and they are similar to altimetry-derived surface current products. Moreover, spectral analysis using wavelet transform confirmed that despite the increased radius of influence in the zonal direction, the new OI maintains meso-scale variability suitably well compared to the original EASRC.

The latitudinal bands showing the strong repetitive meridional gradient pattern generally correspond to the movement of the polar front in the East/Japan Sea. Therefore, it is necessary to consider the interannual variability of the polar front when generating the monthly mean climatological fields. An improved climatological mean field can be produced when the effect of bottom topography reflecting potential vorticity change, and vertical gradient correction are considered (Chang and Shin, 2012; Chang and Shin, 2014). Moreover, this study including all NOAA climatologies produced the climatology mean field based on isobaric interpolation. Gouretski (2018), Gouretski, (2019) emphasized that the isobaric interpolation method produces "artificial water masses" in high-gradient regions. Since mixing processes in the actual oceanic environment occur along an isopycnal surfaces, if the isopycnal interpolation method is used instead of the isobaric interpolation method, an improved climatology mean field can be produced. More detail analyses are expected in this regard, via subsequent research.

In this study, this problem was solved by a different OA method from the EASRC. Therefore, we could not find a fundamental solution to the problem that emerges in the EASRC. **Figure 11** shows spatial temperature distribution and the meridional gradient for the all the East Asian seas in the EASRC. Repetitive meridional gradient patterns are also found in the Yellow Sea and the East China Sea, but not in the southern part of Japan including the Northwestern Pacific. Therefore, to accurately complete the high-resolution climatology of the East Asian seas, it is necessary to analyze the features of each area (the East/Japan Sea, the Yellow Sea, the East China Sea, and the Northwestern Pacific) by applying different OA methods, including different radii of influence, and employing additional quantitative estimations.

DATA AVAILABILITY STATEMENT

The original contributions presented in the study are included in the article/**Supplementary Material**, further inquiries can be directed to the corresponding author.

AUTHOR CONTRIBUTIONS

Y-SC designed the study and J-HL carried out OI experiments. All authors contributed to the manuscript writing through discussion on the manuscript.

FUNDING

This research was supported by the National Research Foundation of Korea (2019R1A2C1008490) and Chungcheong Sea Grant Program founded by Korean Ministry of Oceans and Fisheries.

ACKNOWLEDGMENTS

We appreciate reviewers for insightful reviews of this paper.

SUPPLEMENTARY MATERIAL

The Supplementary Material for this article can be found online at: https://www.frontiersin.org/articles/10.3389/feart.2021.680881/full#supplementary-material

Supplementary Figure 1 | Spatial distribution of temperature and the bias with respect to serial observation at 100 m depth in February. [**(A)** Observation, **(B)** EASRC, **(C)** new OI, **(D)** EASRC-OBS, **(E)** new OI-OBS].

Supplementary Figure 2 | The same as **Supplementary Figure S1** except serial observation is at 10 m depth for August.

Supplementary Figure 3 | The same as **Supplementary Figure S1** except serial observation is at 100 m depth for August.

REFERENCES

Barnes, S. L. (1964). A Technique for Maximizing Details in Numerical Weather Map Analysis. *J. Appl. Meteorol.* 3, 396–409. doi:10.1175/1520-0450(1964)003<0396:atfmdi>2.0.co;2

Böhme, L., and Send, U. (2005). Objective Analyses of Hydrographic Data for Referencing Profiling Float Salinities in Highly Variable Environments. *Deep Sea Res. Part Topical Stud. Oceanography* 52, 651–664. doi:10.1016/j.dsr2.2004.12.014

Boyer, T., Levitus, S., Garcia, H. E., Garcia, H., Locarnini, R. A., Stephens, C., et al. (2005). Objective Analyses of Annual, Seasonal, and Monthly Temperature and Salinity for the World Ocean on a 0.25° Grid. *Int. J. Climatol.* 25, 931–945. doi:10.1002/joc.1173

Boyer, T. P., Garcia, H. E., Locarnini, R. A., Zweng, M. M., Mishonov, A. V., Reagan, J. R., et al. (2018). World Ocean Atlas 2018. [indicate Subset Used]. NOAA National Centers for Environmental Information. Available at https://accession.nodc.noaa.gov/NCEI-WOA18.

Boyer, T. P., and Levitus, S. (1997). *Objective Analyses of Temperature and Salinity for the World Ocean on a 0.25° Grid*, 11. Washington, D.C: NOAA Atlas NESDISU.S. Gov. Print. Off.

Boyer, T. P., and Levitus, S. (1994). "Quality Control and Processing of Historical Temperature, Salinity and Oxygen Data," in *NOAA Technical Report No. 81* (Washington, D.C: U.S. Department of Commerce), 65.

Carnes, M. R. (2009). *Description and Evaluation of GDEM-V3.0, NRL Memo. 7330-09-9165, 21*. Mississippi: Naval Research Laboratory, Stennis Space Center, Miss. doi:10.2172/966897

Carnes, M. R., Helber, R. W., Barron, C. N., and Dastugue, J. M. (2010). *Validation Test Report for GDEM4, Rep. NRL/MR/7330-10-9271*. Arlington, Va: Space and Nav. Warfare Syst. Command. doi:10.21236/ADA530343

Chang, C.-W. J., and Chao, Y. (2000). A Comparison between the World Ocean Atlas and Hydrobase Climatology. *Geophys. Res. Lett.* 27, 1191–1194. doi:10.1029/1999GL002379

Chang, Y.-S., Rosati, A. J., Zhang, S., and Harrison, M. J. (2009). Objective Analysis of Monthly Temperature and Salinity for the World Ocean in the 21st century: Comparison with World Ocean Atlas and Application to Assimilation Validation. *J. Geophys. RES.* 114, C02014. doi:10.1029/2008JC004970

Chang, Y.-S., and Shin, H.-R. (2012). Objective Analysis of Monthly Temperature and Salinity Around the Southwestern East Sea (Japan Sea) on a 0.1° Grid. *Continental Shelf Res.* 45, 54–64. doi:10.1016/j.csr.2012.06.001

Chang, Y.-S., and Shin, H.-R. (2014). Vertical Gradient Correction for the Oceanographic Atlas of the East Asian Seas. *J. Geophys. Res. Oceans* 119, 5546–5554. doi:10.1002/2014JC009845

Fukumori, I., and Wunsch, C. (1991). Efficient Representation of the North Atlantic Hydrographic and Chemical Distributions. *Prog. Oceanography* 27, 111–195. doi:10.1016/0079-6611(91)90015-E

Gouretski, V. (2019). A New Global Ocean Hydrographic Climatology. *Atmos. Oceanic Sci. Lett.* 12, 226–229. doi:10.1080/16742834.2019.1588066

Gouretski, V. (2018). World Ocean Circulation Experiment - Argo Global Hydrographic Climatology. *Ocean Sci.* 14, 1127–1146. doi:10.5194/os-14-1127-2018

Johnson, D. R., and Boyer, T. P. (2015). *Regional Climatology of the East Asian Seas: An Introduction*, Vol. 79 Silver Spring, MD: NOAA Atlas NESDIS, 37.

Kim, K., Kim, K.-R., Min, D.-H., Volkov, Y., Yoon, J.-H., and Takematsu, M. (2001). Warming and Structural Changes in the East (Japan) Sea: A Clue to Future Changes in Global Oceans?. *Geophys. Res. Lett.* 28 (17), 3293–3296. doi:10.1029/2001GL013078

Levitus, S. (1982). "Climatological Atlas of the World Ocean," in *NOAA Professional Paper 13* (Washington, DC: U.S. Government Printing Office).

McIntosh, P. C. (1990). Oceanographic Data Interpolation: Objective Analysis and Splines. *J. Geophys. Res.* 95, 13529–13541. doi:10.1029/JC095iC08p13529

NOAA (1994). "World Ocean Atlas 1994, Vol. 1–5," in *NOAA Atlas NESDIS, Vol. 1–5* (Silver Spring, MD: NOAA).

NOAA (1998). "World Ocean Atlas 1998, Vol. 1 –12," in *NOAA Atlas NESDIS, Vol. 27– 38* (Silver Spring, MD: NOAA).

Pascual, A., Faugère, Y., Larnicol, G., and Le Traon, P.-Y. (2006). Improved Description of the Ocean Mesoscale Variability by Combining Four Satellite Altimeters. *Geophys. Res. Lett.* 33, L02611. doi:10.1029/2005GL024633

S. Levitus (2002). "World Ocean Atlas 2001, Vol. 1–6," in *NOAA Atlas NESDIS, Vol. 49-54* (Silver Spring, MD: NOAA).

S. Levitus (2006). "World Ocean Atlas 2005, Vol. 1–4," in *NOAA Atlas NESDIS, Vol. 61-64* (Silver Spring, MD: NOAA).

S. Levitus (2009). "World Ocean Atlas 2009, Vol. 1–4," in *NOAA Atlas NESDIS, Vol. 68-71* (Silver Spring, MD: NOAA).

S. Levitus (2013). "World Ocean Atlas 2013, Vol. 1–4," in *NOAA Atlas NESDIS, Vol. 73-76* (Silver Spring, MD: NOAA).

Conflict of Interest: The authors declare that the research was conducted in the absence of any commercial or financial relationships that could be construed as a potential conflict of interest.

frontiers in Earth Science

ORIGINAL RESEARCH
published: 21 July 2021
doi: 10.3389/feart.2021.698876

The Copernicus Global 1/12° Oceanic and Sea Ice GLORYS12 Reanalysis

Lellouche Jean-Michel[1]*, *Greiner Eric*[2], *Bourdallé-Badie Romain*[1], *Garric Gilles*[1], *Melet Angélique*[1], *Drévillon Marie*[1], *Bricaud Clément*[1], *Hamon Mathieu*[1], *Le Galloudec Olivier*[1], *Regnier Charly*[1], *Candela Tony*[1], *Testut Charles-Emmanuel*[1], *Gasparin Florent*[1], *Ruggiero Giovanni*[1], *Benkiran Mounir*[1], *Drillet Yann*[1] and *Le Traon Pierre-Yves*[1,3]

[1]*Mercator Ocean International, Ramonville Saint Agne, France,* [2]*Collecte Localisation Satellites, Ramonville Saint Agne, France,* [3]*Ifremer, Plouzané, France*

GLORYS12 is a global eddy-resolving physical ocean and sea ice reanalysis at 1/12° horizontal resolution covering the 1993-present altimetry period, designed and implemented in the framework of the Copernicus Marine Environment Monitoring Service (CMEMS). The model component is the NEMO platform driven at the surface by atmospheric conditions from the ECMWF ERA-Interim reanalysis. Ocean observations are assimilated by means of a reduced-order Kalman filter. Along track altimeter sea level anomaly, satellite sea surface temperature and sea ice concentration, as well as *in situ* temperature and salinity vertical profiles are jointly assimilated. A 3D-VAR scheme provides an additional correction for the slowly-evolving large-scale biases in temperature and salinity. The performance of the reanalysis shows a clear dependency on the time-dependent *in situ* observation system. The general assessment of GLORYS12 highlights a level of performance at the state-of-the-art and the capacity of the system to capture the main expected climatic interannual variability signals for ocean and sea ice, the general circulation and the inter-basins exchanges. In terms of trends, GLORYS12 shows a higher than observed warming trend together with a slightly lower than observed global mean sea level rise. Comparisons made with an experiment carried out on the same platform without assimilation show the benefit of data assimilation in controlling water mass properties and sea ice cover and their low frequency variability. Moreover, GLORYS12 represents particularly well the small-scale variability of surface dynamics and compares well with independent (non-assimilated) data. Comparisons made with a twin experiment carried out at 1/4° resolution allows characterizing and quantifying the strengthened contribution of the 1/12° resolution onto the downscaled dynamics. GLORYS12 provides a reliable physical ocean state for climate variability and supports applications such as seasonal forecasts. In addition, this reanalysis has strong assets to serve regional applications and provide relevant physical conditions for applications such as marine biogeochemistry. In the near future, GLORYS12 will be maintained to be as close as possible to real time and could therefore provide relevant and continuous reference past ocean states for many operational applications.

Keywords: ocean and sea ice reanalysis, data assimilation, high-resolution model, ocean variability, operational oceanography, Copernicus marine service

OPEN ACCESS

Edited by:
Andrea Storto,
National Research Council (CNR), Italy

Reviewed by:
Armin Koehl,
University of Hamburg, Germany
Daniel James Lea,
Met Office, United Kingdom

***Correspondence:**
Lellouche Jean-Michel
jlellouche@mercator-ocean.fr

Specialty section:
This article was submitted to Interdisciplinary Climate Studies, a section of the journal Frontiers in Earth Science

Received: *22 April 2021*
Accepted: *29 June 2021*
Published: *21 July 2021*

Citation:
Jean-Michel L, Eric G, Romain Bé-B, Gilles G, Angélique M, Marie D, Clément B, Mathieu H, Olivier LG, Charly R, Tony C, Charles-Emmanuel T, Florent G, Giovanni R, Mounir B, Yann D and Pierre-Yves LT (2021) The Copernicus Global 1/12° Oceanic and Sea Ice GLORYS12 Reanalysis. Front. Earth Sci. 9:698876. doi: 10.3389/feart.2021.698876

INTRODUCTION

The Copernicus Marine Environment Monitoring Service (http://marine.copernicus.eu, hereafter referred to as Copernicus Marine Service or CMEMS) provides regular and systematic reference information on the physical state, variability and dynamics of the ocean, sea ice and marine ecosystems, for the global ocean and the European regional seas. This capacity encompasses the provision of consistent retrospective data records for recent years (reprocessing and reanalysis) (Le Traon et al., 2019). There is a growing need to assess the state and health of the ocean to support climate and marine environment policies. CMEMS Ocean State Reports and related Ocean Monitoring Indicators have been developed to answer these needs (von Schuckmann et al., 2020). They rely on continuous and high quality time series from reanalyses and reprocessed observations, which go up to real time. CMEMS users also regularly ask for long time series of data that can be used to provide a statistical and qualitative reference framework for their applications.

Ocean reanalyses aim at providing the most accurate past state of the ocean in its four dimensions. Several research fields are involved: processing of observations from satellites and *in situ* instruments, numerical modeling and data assimilation. Assimilating observations into an ocean model is not a recent issue. The use of historical data quickly found pragmatic solutions of good quality (Carton and Hackert, 1989). The models of the time were not very sophisticated, without ice and even without taking into account salinity or high latitudes. The first revolution came with the development of satellite altimetry, allowing observing the mesoscale globally. It already appeared that it would be necessary to have models with sufficient spatial resolution to resolve inter-basin exchanges; the problem of the altimetric reference height needed to assimilate the altimeter data was also raised (Greiner and Perigaud, 1994). The next revolution came more gradually with the rise in power of supercomputers. It became possible to have an ocean model resolution that solved the first Rossby radius, and to introduce more physics (Barnier et al., 2006). As atmospheric forcing progressed in parallel, the significant biases of the first models became less troublesome. The third revolution came with the deployment of the Argo global array of profiling floats and the capability to observe the three-dimensional ocean in near real time. This opened the door to the development of global operational oceanography (Dombrowsky et al., 2009; Le Traon, 2013).

In the meantime, climatic coupled simulations were produced to predict the evolution of the earth climate due to global warming. They had to be validated over the observed period (Coupled Model Intercomparison Project: Meehl et al., 2000). Ocean reanalyses thus came into play to provide a reliable reference state of the recent period characterized by a rapid sea level rise of about 3 mm/yr compared to the centennial trend of 1 mm/yr (Carton et al., 2005). As coupled ocean-atmosphere-ice simulations progressed, the capability to produce meaningful seasonal forecasts was demonstrated. It then became important to have a comprehensive global physical ocean state, including sea ice, to initialize seasonal forecasts (MacLachlan et al., 2015), to provide boundary conditions for regional models having higher resolution and smaller-scale physical processes (Tranchant et al., 2016), and to force biogeochemical models (Gutknecht et al., 2016).

While it was obvious that a minimum spatial resolution was essential to resolve inter-basin exchanges (Indonesian Throughflow, Gibraltar and Fram Straits), it was soon acknowledged that high horizontal resolution was necessary to properly represent western boundary currents (Hewitt et al., 2016) and intense jets such as the Gulf Stream (Chassignet and Xu, 2017). Resolution is also important for resolving fine structures at high latitudes and thus linking mid-latitudes to the polar oceans. Hewitt et al. (2020) show that the explicitly represented or parameterized ocean mesoscale affects not only the mean state of the ocean but also climate variability and future climate response, particularly in terms of the Atlantic Meridional Overturning Circulation. The study of the melting of the polar ice caps will undoubtedly benefit from the contribution of high resolution circulation. The resolution of mesoscale eddies and the western boundary currents has reduced sea surface temperature biases, improved ocean heat transport, created deeper and stronger overturning circulation and enhanced the Antarctic Circumpolar Current (Hewitt et al., 2016). Thoppil et al. (2011) also show that increased resolution reduces the deficit of turbulent kinetic energy in the upper and abyssal ocean relative to surface drifting buoys and deep current meters.

An increase in the resolution results in a corresponding increase in turbulence. This causes the appearance of small vortices or filaments that are observed but not necessarily well placed. This leads to uncertainty in the simulations and this is how the ensemble approach recently appears in the world of ocean reanalysis (Zuo et al., 2019). The ensemble does not help to correctly position the vortices but gives uncertainties on the positions and also on unobserved variables. A set of four global ocean reanalyses based on NEMO has first been used by Masina et al. (2017) to assess interannual variability and trends in surface temperature or sea level, as well as other variables that are difficult to observe directly (transport, kinetic energy). Since 2016, the Copernicus Marine Service has been producing and disseminating the ensemble mean and standard deviation of those four global ocean reanalysis produced at eddy-permitting resolution for the period from 1993 to present, called GREP (Global ocean Reanalysis Ensemble Product) (Storto et al., 2019a). This dataset offers the possibility to investigate the potential benefits of a multi-system approach and, in particular, the added value of the information on the ensemble spread, implicitly contained in the GREP ensemble, for temperature, salinity, and steric sea level studies. This approach is essential to identify robust features of reanalyses, but also the shortcomings of observation or assimilation systems (Balmaseda et al., 2015). Uncertainty information is crucial for ocean climate monitoring at both global and regional levels. For example, this uncertainty is important for downscaling or regional climate projection studies. Fortunately, Storto et al. (2019a) show that the error of GREP is consistent with that of high resolution products. In other words, a high-resolution reanalysis is well complemented by an uncertainty estimate obtained using a lower-resolution ensemble.

It is also becoming increasingly urgent to close the ocean's mass and heat balances. But high resolution favors local assimilation methods, and this makes it difficult to impose global constraints (Storto et al., 2017). This is all the more difficult as the oceanic and atmospheric observation networks vary over time. When we start integrating the model, we may see waves being triggered or potential energy being converted into kinetic energy if we start from rest. Transient signals resulting from the imbalance between initial conditions, model dynamics and forcing may appear and last for several years. The reaction of the system when the first altimeter observations are assimilated (late 1992) is referred to as the altimeter shock. Hamon et al. (2019) show that a large part of this problem comes from errors in the reference height or mean dynamic topography (MDT) that must be added to the sea level anomalies in order to compare them with the absolute height simulated by the model. This introduces an error that is not compensated for by a large number of *in situ* observations. On the contrary, there is a regular decrease in the amount of XBTs profiles which reaches a minimum around 1997. This favors the development of a bias over several years, initiated by the altimeter shock and superimposed to the bias of the model without assimilation. On the other hand, altimetry data assimilation can correct some T/S biases in regions where the MDT is unbiased (e.g., Antarctic Circumpolar Current). The development of the Argo network from 2003 onwards allows a significant improvement in the observation of the ocean above 2,000 m, which makes it possible to correct the biases that may exist in the system. But the onset of the Argo network can also introduce spurious variability or trends in the system, which need to be characterized and distinguished from real climate variability or trends.

In recent years, Mercator Ocean has steadily improved its physical reanalysis of the global ocean by refining the ocean model, the assimilation scheme and the assimilated data sets. The last upgrade concerned a 1/4° eddy-permitting reanalysis covering the altimetry era 1992 onwards (Garric et al., 2018) called GLORYS2V4 (hereafter, G2V4) and which is one member of GREP. In order to propose a global eddy-resolving physical reanalysis in the framework of CMEMS, activities have been carried out at Mercator Ocean to develop the GLORYS12 reanalysis, covering the same period and based on the current real-time global forecasting high-resolution CMEMS system. To keep a homogeneous quality over the entire period, GLORYS12 is restricted to the altimetry era since the observational network before the altimeters' arrival is not informative on mesoscale. Several scientific studies have already investigated thoroughly local ocean processes by comparing the GLORYS12 reanalysis with independent observations campaigns (e.g., Artana et al., 2018; Artana et al., 2019a; Poli et al., 2020; Chenillat et al., 2021; Verezemskaya et al., 2021). The objective of this paper is to provide some hindsight about the global behavior of the reanalysis compared to assimilated or independent observations, with a review of the strengths and weaknesses. Based on comparisons with extra experiments (lower horizontal resolution, same horizontal resolution but without data assimilation) and sometimes with GREP, this work aims at informing on the scientific value of the global high-resolution ocean reanalysis GLORYS12.

The paper is organized as follows. The main characteristics of the GLORYS12 reanalysis are described in *Description of GLORYS12*. Results of the scientific and statistical evaluation, including comparisons with assimilated and independent observations, are given in *General Assessment*. The behavior of the reanalysis in terms of interannual variability and long-term trends is analyzed respectively in *Eddy Kinetic Energy Time Evolution* and *Trends and Evolutions of Temperature, Salinity and Sea Level*. Lastly, *Summary and Conclusion* contains a summary of the scientific assessment, as well as a discussion of the improvements planned for a future version of the global high-resolution Mercator Ocean reanalysis.

DESCRIPTION OF GLORYS12

The ingredients of the GLORYS12 reanalysis are largely those of the current real-time global CMEMS high-resolution forecasting system PSY4V3 (Lellouche et al., 2018). However, compared to the forecasting system, GLORYS12 starts in December 1991 (October 2006 for PSY4V3) using temperature and salinity fields from the EN4.2.0 monthly gridded climatology (Good et al., 2013), benefits from the use of reanalyzed atmospheric forcing instead of analyses and forecasts and higher-quality reprocessed observations, and includes refined data assimilation procedures (e.g., three-dimensional T/S *in situ* seasonal observations errors computed from PSY4V3).

The ocean and sea ice general circulation model is based on the NEMO platform (Madec and The NEMO Team, 2008). The horizontal grid is quasi-isotropic with a resolution of 1/12° (9.25 km at the equator and around 4.5 km at subpolar latitudes) and 50 vertical levels, with the spacing increasing with depth (22 levels are within the first 100 m leading to a vertical resolution of 1 m in the upper levels and 450 m at 5,000 m depth). The ocean model is driven at the surface by the European Centre for Medium-Range Weather Forecasts (ECMWF) ERA-Interim atmospheric reanalysis (Dee et al., 2011). A 3 h sampling of atmospheric quantities is used to reproduce the diurnal cycle. Momentum and heat turbulent surface fluxes are computed from the Large and Yeager (2009) bulk formulae. Moreover, due to large known biases in precipitations and radiative fluxes at the surface, a satellite-based large-scale correction is applied to the ERA-Interim precipitations and radiative fluxes. Corrections are made towards the Passive Microwave Water Cycle (PMWC) satellite product (Hilburn, 2009) for precipitations and towards the NASA/GEWEX Surface Radiation Budget 3.0/3.1 product (Stackhouse et al., 2011) for shortwave and longwave fluxes, except poleward of 65°N and 60°S due to the poor reliability of such satellite-based estimates at high latitudes.

As the Boussinesq approximation is applied to the model equations, conserving the ocean volume and varying its mass, the simulations do not properly directly represent the global mean steric effect on the sea level. For improved consistency with assimilated satellite observations of sea level anomalies, which are unfiltered from the global mean steric component, a globally diagnosed mean steric sea level trend is added at each time step to the modeled dynamic sea level. Lastly, in order to avoid mean sea-surface-height drift due to the large uncertainties in the water budget closure, the following two corrections to the freshwater forcing fields were applied: 1) the surface freshwater global budget

was set to an imposed seasonal cycle (Chen et al., 2005), with only spatial departures from the mean global budget being kept from the forcing, and 2) a trend was imposed to the surface mass budget to represent the freshwater input into the ocean (from glaciers, land water storage changes, Greenland and Antarctica ice sheets mass loss). Note that two different values over two different time periods were used to estimate the acceleration of melting over the last two decades, 1.31 mm/yr for the period 1993–2001 and 2.2 mm/yr for the period 2002-present. These values were the latest estimates made available by the IPCC-AR13 (Church et al., 2013) at the time the reanalysis was set up. This term is implemented as a surface freshwater flux in the open ocean areas populated with observed icebergs.

Different types of observations are assimilated using a reduced-order Kalman filter derived from a singular evolutive extended Kalman (SEEK) filter (Brasseur and Verron, 2006) with a three-dimensional multivariate background error covariance matrix and a 7 day assimilation cycle (Lellouche et al., 2013). Reprocessed along-track satellite altimeter missions sea level anomalies (SLA) from CMEMS (Pujol et al., 2016), satellite AVHRR sea surface temperature (SST) from NOAA, Ifremer/CERSAT sea ice concentration (Ezraty et al., 2007), and *in situ* temperature and salinity (T/S) vertical profiles from CMEMS quality controlled CORA database (Cabanes et al., 2013; Szekely et al., 2019) are jointly assimilated. In addition to the Argo data, the CORA database includes temperature and salinity vertical profiles from the sea mammal database (Roquet et al., 2011) which is a precious source of observations at high latitudes, where *in situ* observations are scarce. A "hybrid" MDT was also used as a reference for altimeter data assimilation. This hybrid MDT is based on the CNES-CLS13 MDT (Rio et al., 2014) with some adjustments (Hamon et al., 2019) made using high-resolution analyses, updates to the GOCE geoid made since the CNES-CLS13 MDT was produced, and an improved post-glacial rebound model (also called a glacial isostatic adjustment).

A separate monovariate-monodata SEEK analysis is carried out for the assimilation of the sea ice concentration, in parallel to the multivariate-multidata analysis for the ocean. The two analyses are completely independent. Sea ice concentration observation errors were imposed at 25% for concentrations close to zero and 5% for concentrations of the order of 100%. These errors associated with sea ice concentration retrievals follow the findings from Ivanova et al. (2015). For all values within this interval, the observation error is estimated using a simple linear interpolation between the two extreme values. For the update of sea ice thickness in the model, the proportional mean thickness analysis update from Tietsche et al. (2013) with a similar proportionality constant of 2 m is adopted in order to control somewhat the sea ice volume. In other words, for a sea ice concentration update (analysis increment) of 1%, the mean sea ice thickness is changed by 2 cm.

In addition to the multivariate reduced-order Kalman SEEK filter, GLORYS12 employs a 3D-VAR scheme, which takes into account cumulative three-dimensional T/S innovations over the last or the past few months in order to estimate large-scale T/S biases when enough T/S vertical profiles are available. The aim of the bias correction is to correct the large scale, slowly-evolving error of the model whereas the SEEK assimilation scheme is used to correct the smaller scales of the model forecast error. Temperature and salinity are treated separately because temperature and salinity biases are not necessarily correlated. The bias correction is fully effective under the thermocline, away from density gradients. Lastly, these bias corrections are applied as tendencies in the model prognostic equations, with a one-month or a few months timescale. From January 2004, as Argo observations become available, a steep increase of the number of T/S vertical profiles can be diagnosed. This is why the 3D-VAR bias correction is performed on a 3 month window until the end of 2003, and starting in 2004, it is reduced to a 1 month window with many more observations covering all oceans, giving access to reliable information on the monthly variability of the subsurface ocean.

From a technical point of view, GLORYS12 was run on 54 nodes (1,296 processors) of Meteo France BULL machine from December 1991 to December 2019. A 7 day simulation takes about 4 h of elapsed computer time, including SEEK and 3D-VAR analyses. Note that this requires 14 days of model run because of the additional model integration over the 7 day assimilation window due to the use of incremental analysis update to inject corrections into the model compared to a more "classical" model correction where increment would be applied on one time step (see Figure 4 in Lellouche et al., 2013). This means that a total of about 8 months of computer time was necessary to perform the GLORYS12 reanalysis simulation. This illustrates that the development of a global high-resolution ocean reanalysis in a timely manner is currently a challenge and remains dependent on computing resources.

Moreover, in the development phase of GLORYS12, two other twin numerical simulations were performed starting from the same initial condition as GLORYS12 and run until the end of 2016. The first one is a free simulation (without any data assimilation, hereafter F12) maintaining the same ocean model tunings, and the second one (hereafter G4) only differs from GLORYS12 by the spatial resolution (from 1/12° to 1/4°). Inter-comparisons between the three simulations were then carried out on the common period (1993–2016) in order to better analyze and try to quantify on the one hand, the impact of data assimilation, and on the other hand the added value of high resolution.

GENERAL ASSESSMENT

This section gives a quality assessment of the different simulations, including comparisons with the assimilated observations as well as with independent (i.e. not assimilated) observations. There, one can find some statistics using observation minus background model first trajectory (called "innovation") and observation minus "best" second model trajectory or analysis (called "residual").

Comparison With Temperature and Salinity Vertical Profiles

The existence of global biases or drifts in temperature and salinity is first checked using assimilation diagnostics (mean innovations

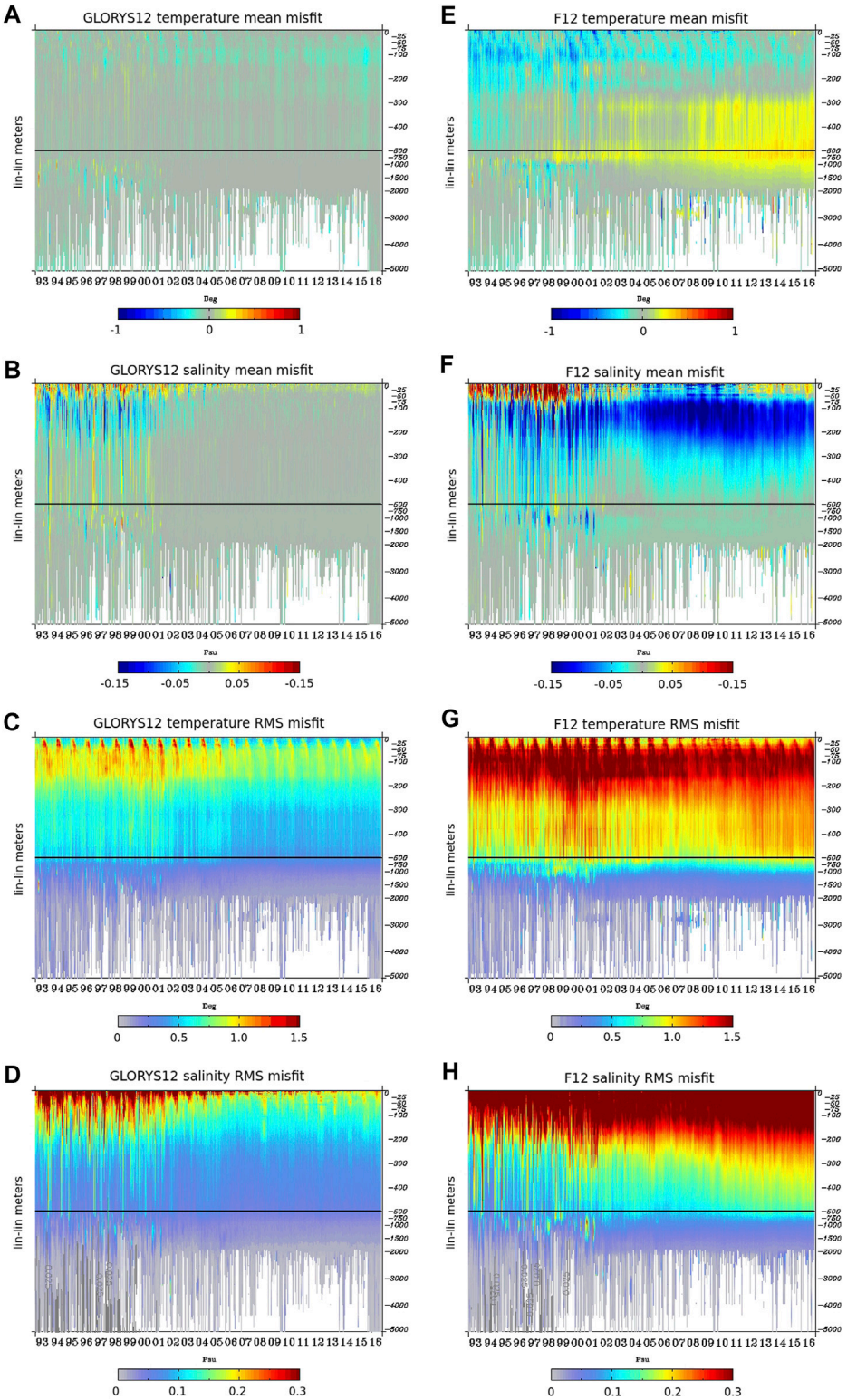

FIGURE 1 | Assimilation diagnostics with respect to the vertical temperature and salinity profiles over the 1993–2016 period. Mean misfits (observation minus background model first trajectory) for temperature **(A,E)** and for salinity **(B,F)** and RMS misfits for temperature **(C,G)** and for salinity **(D,H)**. Left panels (respectively right panels) concern GLORYS12 (respectively F12). These scores are averaged overall seven days of the data assimilation window, with a mean lead time equal to 3.5 days. Units are °C for temperature and psu for salinity.

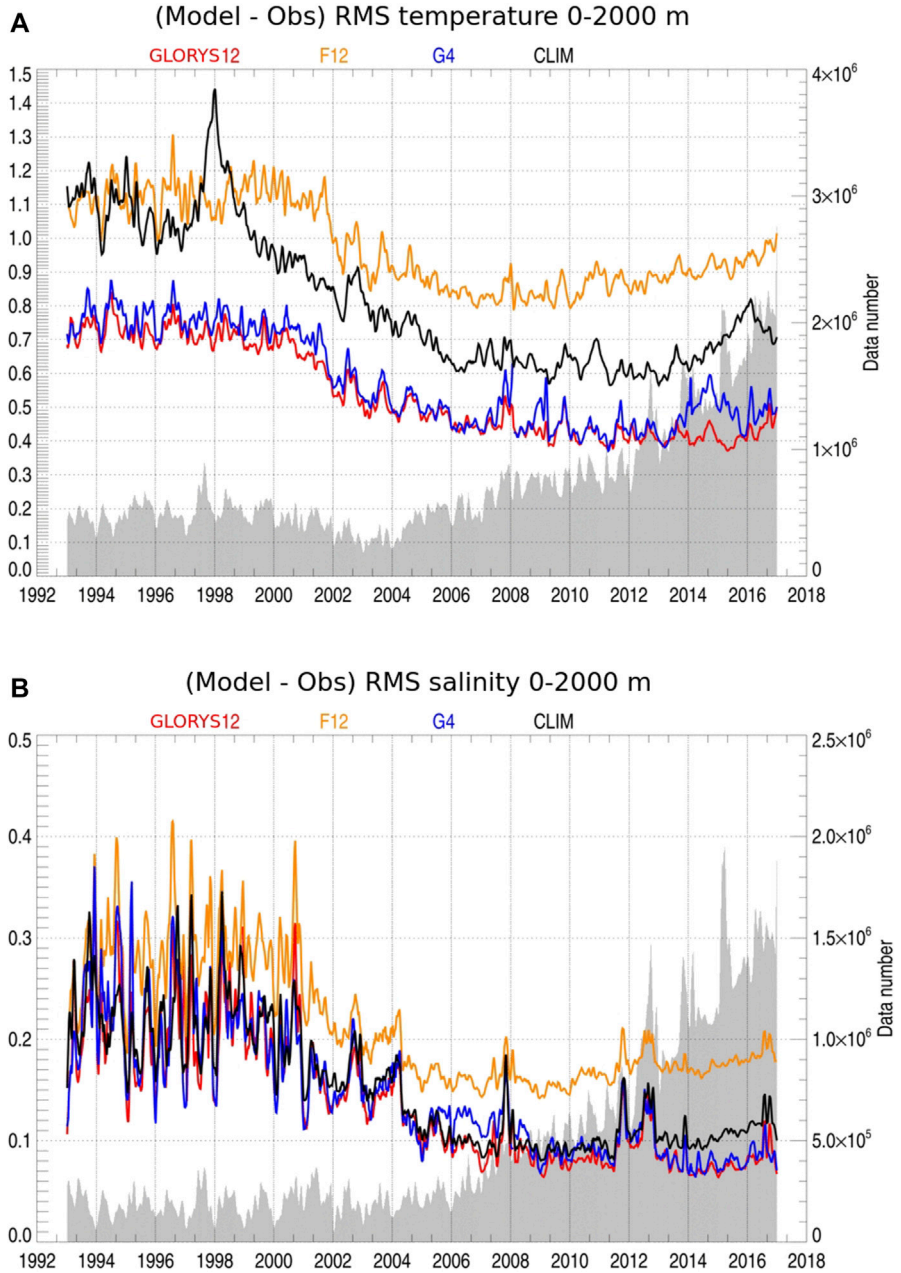

FIGURE 2 | Time series over the 1993–2016 period of the 0–2,000 m RMS difference between the model analysis (best model trajectory) and the *in situ* T/S observations from the CORA database for GLORYS12 (in red), F12 (in orange), G4 (in blue) and Levitus WOA13 climatology (in black): **(A)** Temperature (units in °C), **(B)** salinity (units in psu). Time series of the number of available observations appear in grey.

and root mean square (RMS) of innovations) as a function of time and depth (**Figure 1**). These departures from the assimilated observations are computed before the observations are assimilated, and thus before the SEEK correction is applied. They are shown here on global average, in order to assess the global behavior of the system. The comparison between the left (GLORYS12) and right (F12) panels highlights the beneficial impact of the data assimilation performed in GLORYS12. The biases (mean misfit) and the errors (RMS misfits) are considerably reduced for temperature and salinity from F12 to GLORYS12. The system F12 without data assimilation exhibits a warm bias in the first 200 m over the 1993–2016 period and a cold bias in the 300–1,000 m layer appearing from around 1998. For the salinity, a fresh bias is present at the surface which is stronger in the 1990s, while a very strong salty bias appears in the first 500 m and increases in time (**Figures 1E,F**). These biases are reduced in GLORYS12, but they slightly remain in the form of a seasonal bias in temperature, showing a potential error in the

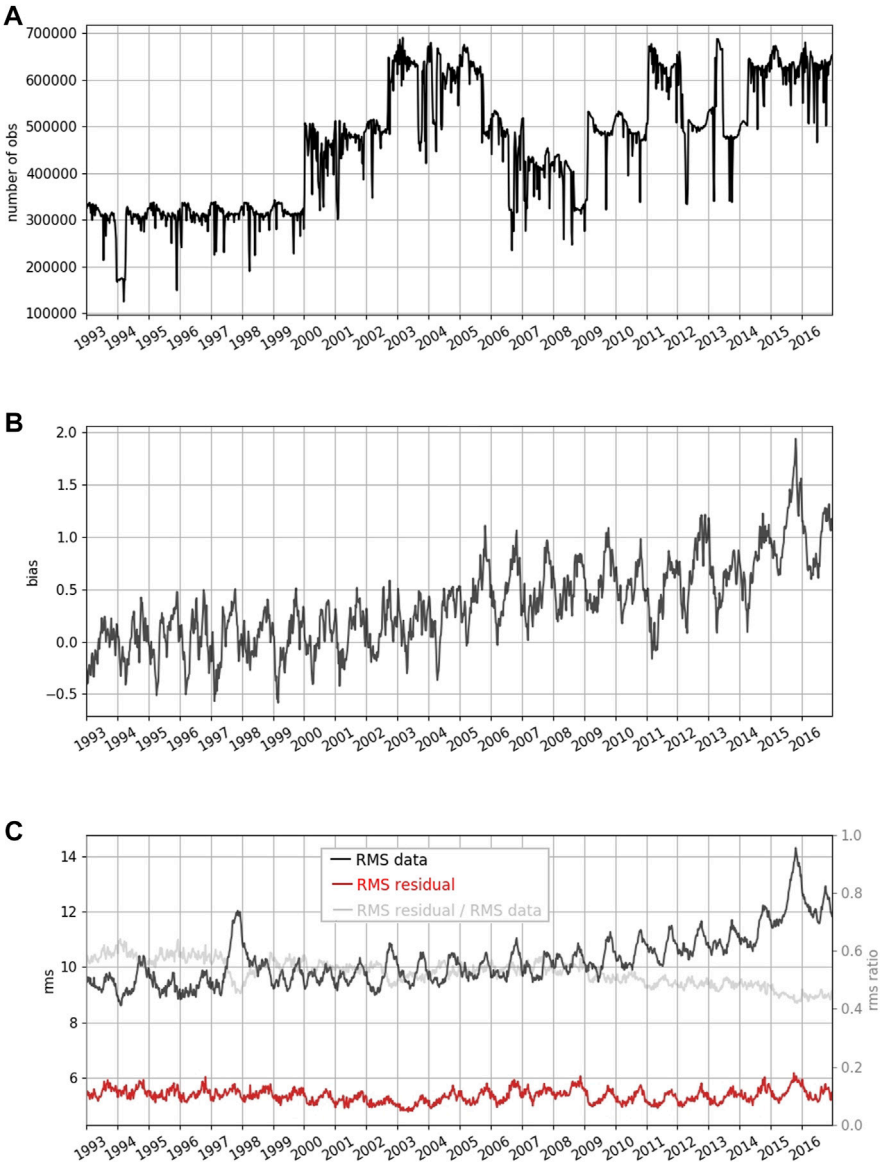

FIGURE 3 | Time evolution of SLA data assimilation statistics averaged over the whole domain: **(A)** data number, **(B)** mean innovations, **(C)** RMS of the SLA data (in black), RMS of residuals (in red), RMS of residuals divided by RMS of SLA observations (in light grey, with the scale on the right). The scores are averaged over all seven days of the data assimilation window, with a lead time equal to 3.5 days. Units are cm.

stratification above 100 m (**Figures 1A,C**). The temporal evolution of the GLORYS12 salinity bias is given in **Figure 1B** and shows a clear dependency of the data assimilation system on the *in situ* observations availability, with a strong reduction of the error in the second half of the period, after 2004 and the onset of the Argo network.

From a more integrated point of view, **Figure 2** shows the ability of the different systems GLORYS12, F12 and G4 in reproducing observed temperature and salinity in the 0–2,000 m layer. For that, we checked time series of the RMS difference between the model and the observations for temperature and salinity where observations are available in the water column. We compare also the observations to the Levitus WOA13 monthly temperature (Locarnini et al., 2013) and salinity (Zweng et al., 2013) climatology. We first note that the vertically integrated accuracy of GLORYS12 is very similar to that of G4, even if GLORYS12 slightly outperforms G4 throughout the 1993–2016 period. Between 1993 and 2002, departures from *in situ* observations are around 0.75°C for temperature and 0.2 psu for salinity. The average accuracy reaches 0.45°C in temperature and 0.1 psu in salinity during the Argo period, thanks to the increase of the number of observations assimilated in G4 and GLORYS12. For salinity, the statistics are very noisy before 2004 due to very sparse data that are not representative of the global state of the oceans. The departure between climatology and observations is an indicator of the minimum performance that

the system must achieve. G4 and GLORYS12 temperatures are both significantly more accurate than the climatological temperature throughout the period. For salinity, the reanalysis clearly outperforms the climatology only after 2013, when the number of observations has doubled since the beginning of the Argo era. The free simulation F12 nearly always exhibits far lower scores than the climatology. The only exception takes place when F12 captures the very strong El Niño-Southern Oscillation (ENSO) signal in temperature in 1997/1998, and thus F12 is closer to *in situ* observations than the climatology can be during these two years, even on global average. The F12 RMS differences reach in 2016, 1°C for temperature and 0.2 psu for salinity, twice the RMS departures obtained with GLORYS12. Worse, we can observe a tendency for these errors to increase between 2008 and 2016, showing the drift of the system without data assimilation.

Comparison With Satellite Sea Level Anomaly

The assimilation of sea level anomalies together with the MDT is crucial for the realism of the reanalysis's ocean circulation. The statistics in **Figure 3** use innovations and residuals coming from the sea level anomalies data assimilation. Residuals include the analysis correction injected into the model using incremental analysis update. The scores are averaged over all 7 days of the data assimilation window, which means the results are indicative of the average performance of GLORYS12 over the 7 days, with a mean lead time equal to 3.5 days.

The number of assimilated SLA observations (**Figure 3A**) varies with the number of altimeters in-flight throughout the period 1993–2016. This 24 year period involves eleven different altimeters. Following TOPEX-Poseidon in September 1992, the constellation has grown from one to six satellites flying simultaneously, even if we can notice a temporary decrease between 2005 and 2010.

The biases are weak in the 1990s, as the mean innovations vary around zero (**Figure 3B**). However, from 2004, a bias is diagnosed, which tends to increase and reaches 1 cm at the end of the period, with peaks varying from 1 cm or even 2 cm at times. This means that GLORYS12 tends to become too low in comparison with altimetry by about 0.25 mm per year. This bias is predominantly associated with the orbit standard used in the assimilated sea level anomalies (Taburet et al., 2019, their Figure 8B). Despite this bias, the reanalysis is close to altimetric observations with a residual RMS difference of the order of 5.5 cm on global average (**Figure 3C**, red curve). This RMS difference is consistent with the a priori prescribed observation error, which is equal to the sum (in variance) of the SLA instrumental error (about 2 cm on average) plus the MDT error (about 5 cm on average, with the largest values being located on shelves, along the coast and mesoscale activity or sharp front areas). This good performance is partly due to the use of the "Desroziers" method (Desroziers et al., 2005) to adapt the observation errors online, which yields more information from the observations being used (see Lellouche et al. (2018) for more details). Moreover, the model is able to explain the observed signal **Figure 3C**, black curve) as shown by the ratio of RMS residual to RMS data (**Figure 3C**, light grey curve), which decreases with time and converges towards a value much less than one. The performance of GLORYS12 remains stable and even improves while the variance of observations increases.

Comparison With Satellite Sea Ice Observations: Mean State and Low Frequency Variability

This section focuses on the ability of GLORYS12 to reproduce the mean state, expressed in terms of the mean seasonal cycle, interannual variability and trends over the 1993–2016 period, of spatially integrated quantities such as sea ice extent and volume and amount of open waters within the sea ice pack. The sea ice extent is usually defined as the area of ocean with a sea ice concentration of 15% or more. Sea ice area is the total area covered only by sea ice and is always less than the extent. The difference gives the amount of open water in the ice pack. The latter quantity then represents both the presence of leads within the sea ice pack and the marginal ice zone (MIZ) close to the ice edge. This quantity is collectively referred to as "leads" in the subsequent text.

To assess the overall consistency with observations we compare modelled sea ice extent and leads to the observational product CERSAT assimilated in GLORYS12, and to the mean of the ensemble of three observational products (CERSAT, NOAA/NSIDC, and OSI-SAF) which provides an estimate of the observational error. The NOAA/NSIDC passive microwave sea ice concentration climate data record (CDR) is an estimate of sea ice concentration that is produced by combining concentration estimates from two algorithms developed at the NASA Goddard Space Flight Center: the NASA Team algorithm (Cavalieri et al., 1997) and the Bootstrap algorithm (Comiso, 2000). The final CDR value is the highest between concentrations estimated by Bootstrap and NASA Team. OSI-SAF (Ocean Sea Ice Satellite Application Facilities), produced by EUMETSAT and distributed by CMEMS, is currently assimilated by the Arctic and in the PSY4V3 monitoring and forecasting systems of CMEMS. These two latter observational products are the datasets most widely used by the sea ice community. Other sea ice concentration algorithms exist and the subsample of products used in this paper is not sufficient to fully assess the uncertainty of the observations (e.g., Ivanova et al., 2015).

Arctic Ocean

In the Arctic Ocean, compared to the assimilated CERSAT data, GLORYS12 has a larger sea ice extent during winter time and a similar extent during summer time (**Figure 4A**). GLORYS12 sea ice extent largely remains in the spread of the observation based products, an ensemble in which CERSAT represents the member having the least sea ice extent. GLORYS12 constantly stays in the lower bound of the GREP product which shows a constant overestimation with a large spread during summer time. GLORYS12 favorably reduces the amplitude of the sea ice extent seasonal cycle simulated by F12. Similar conclusions are found with the sea ice concentration variable (not shown). The increase of resolution (GLORYS12 versus G4) has no visible

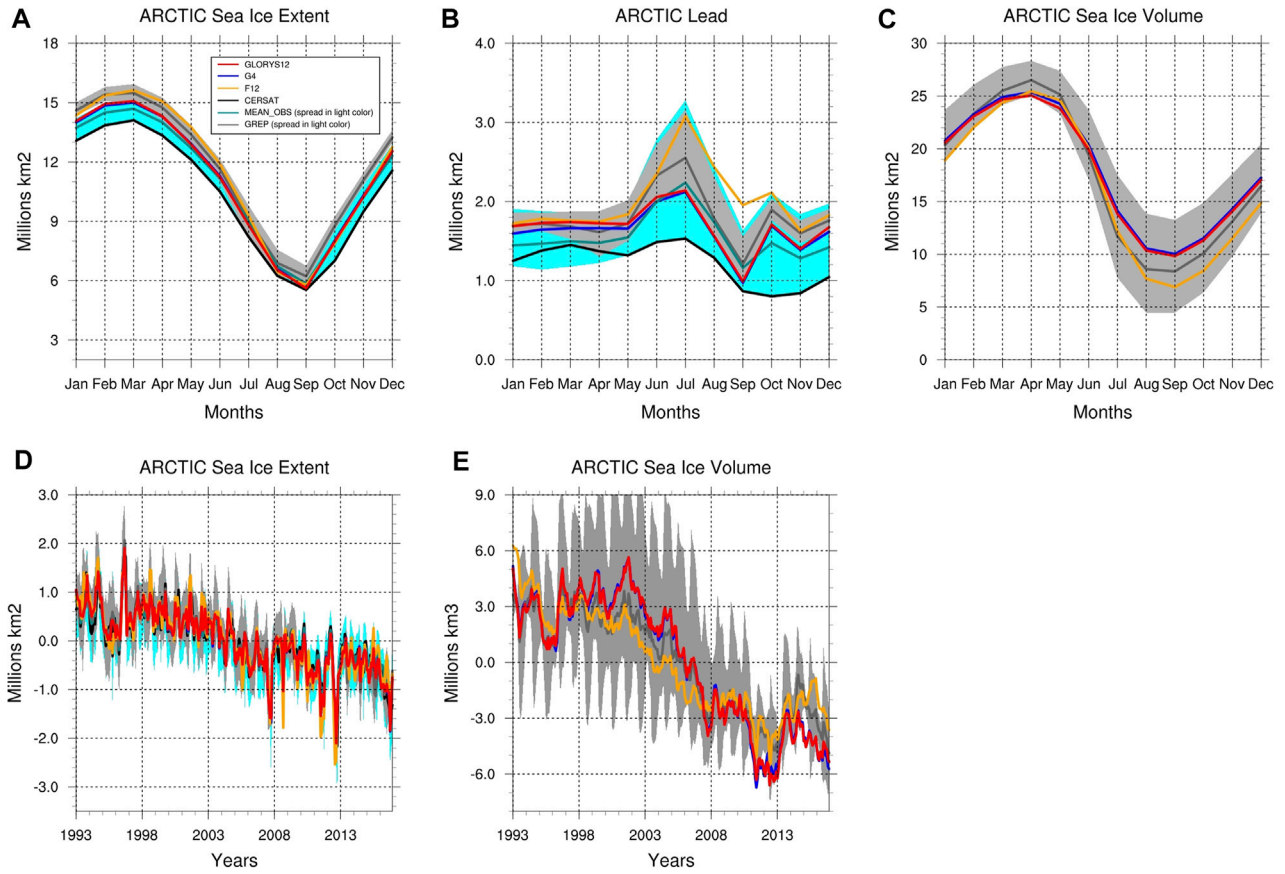

FIGURE 4 | Arctic Ocean–Mean seasonal cycle (1993–2016) of **(A)** Sea ice extent, **(B)** Sea ice leads, and **(C)** Volume. Interannual monthly variability of **(D)** Sea ice extent and **(E)** Sea ice volume. Units are in million km^2 for sea ice extent and leads and in million km^3 for sea ice volume. GLORYS12 (red), F12 (orange), G4 (blue), GREP (dark grey with the spread in light grey), mean observations (dark cyan with the spread in cyan) among CERSAT (black), NOAA/NSIDC (not shown) and OSI-SAF (not shown).

impact on the mean state (seasonal cycle), the interannual variability and the trend of sea ice extent, leads and volume (**Figure 4**).

The presence of open waters within the GLORYS12 sea ice pack is much larger than in the assimilated CERSAT data (**Figure 4B**). This is particularly true during the melting season (June-August), period of the maximum of the surface covered by the MIZ, where GLORYS12 shows an excess of half a million km^2 during July. However, the large spread of the observation based products all along the year indicates large uncertainties in sea ice concentration algorithms retrievals. This is particularly true during summertime where this spread represents nearly the same amount of MIZ estimated by CERSAT. CERSAT data represents the lower bound of the large spread of the observations and GLORYS12 matches particularly well the ensemble mean of the observations. The spread shown around the GREP mean ensemble (**Figure 4B**) highlights how different physical parameterizations and/or assimilation methods within the four members of GREP can impact the representation of open waters within the Arctic sea ice pack.

F12 simulates a larger surface covered by leads and MIZ all through the year compared to GLORYS12. The assimilation of sea ice concentration therefore tends to reduce the presence of open water within the sea ice pack. The methodology for the mean analysis update of sea ice thickness adopted in GLORYS12 results in a general thicker sea ice cover compared to F12. Comparisons with *in situ* data in the Western Basin (**Figure 5B**) and in the Central Basin (**Figure 5C**) confirm a general thicker ice in GLORYS12. The unrealistic piling up of sea ice thickness in the Beaufort Gyre present in all GLORYS reanalysis (Chevallier et al., 2017; Uotila et al., 2019) is also present in GLORYS12. Comparisons with Cryosat-2 in January 2014 (**Figure 5A**) show an overestimation of the order of almost 1 m in the area. This overestimation is confirmed by comparisons with *in situ* data from the BGEP campaign (**Figure 5B**). This ice build-up prevents efficient melting and ends up with generally thicker sea ice conditions in summertime. This phenomenon occurs as soon as the assimilation of sea ice concentration data is activated, e.g. during summer 1993. Comparisons with Cryosat-2 also show that this unrealistic ice accretion in the Western Basin is accompanied, however, by thinner sea ice conditions in Central and Eurasian basins (**Figure 5A**). Comparisons with *in situ* data from the NPEO campaign confirm the presence of thinner ice in GLORYS12 in the Central Arctic Basin (**Figure 5C**).

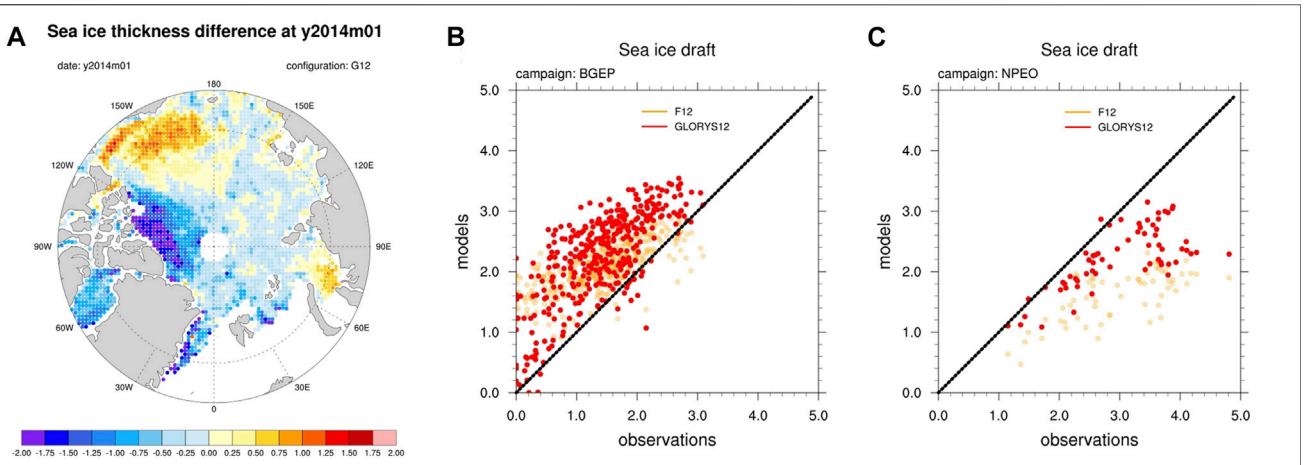

FIGURE 5 | (A) Differences of sea ice thickness between GLORYS12 and Cryosat-2 data (Ricker et al., 2014). Model versus observations plots of sea ice drafts on a linear scale with GLORYS12 (red) and F12 (orange) and *in situ* observations from **(B)** BGEP (Beaufort Gyre Exploration Project, (Krishfield et al., 2014)) campaign, **(C)** NPEO (North Pole Environment Observatory, (Drucker et al., 2003)) campaign.

Nevertheless, GLORYS12 improves the too thin sea ice cover found in F12 in the Central Arctic Basin, e.g. in areas of multi-year ice types. The resulting total sea ice volume is improved compared to the previous Mercator Ocean reanalysis system G2V4 (Chevallier et al., 2017; Uotila et al., 2019) and compares better with PIOMAS data (Schweiger et al., 2011). Over the same period (1993–2016), the seasonal cycles of GLORYS12, F12, G2V4 and PIOMAS have respective minimums and maximums of 9.8 and 25 million km^3, 6.9 and 25.5 million km^3, 13.2 and 28.3 million km^3, and 9.4 and 25.7 million km^3.

The large spread in the sea ice volume present in the GREP multi-model product again reflects the impact of the disparity in assimilation methods and parameterizations applied in these reanalyses (**Figure 4C**).

CERSAT data show a significant (95%-level confidence) and negative trend in sea ice extent at a rate of −79 900 km^2/yr and observation based products at a rate of −77 300 km^2/yr. The simulation without assimilation F12 already reproduces this negative linear trend with a somewhat overstated rate of −86 850 km^2/yr. Both reanalyses (GLORYS12 and G4) with respectively −85 320 and −84 000 km^2/yr trends, favorably reduce this strong loss of surface covered by sea ice in the Arctic Ocean. With −89 400 km^2/yr, the GREP ensemble mean has a stronger trend compared to GLORYS12. The spread among GREP members narrowed somewhat after 2010, a period marked by a succession of historic summer lows. These latter results are similar to those presented in the GREP-based Ocean Monitoring Indicators (OMI) sea ice extent (https://marine.copernicus.eu/access-data/ocean-monitoring-indicators/northern-hemisphere-sea-ice-extent-multi-model-ensembles).
The weak interannual trends of the surface covered by leads and MIZ found either with the reanalysis or with the observations are not significant and are therefore not discussed.

The most important differences between GLORYS12 and F12 are in the reproduction of interannual variability and trend in sea ice volume. The strong accumulation of ice that became thick in the late 1990s and early 2000s shown in GLORYS12 is not in F12 (**Figure 4E**). The resulting trend is consecutively more pronounced in GLORYS12 than in F12, respectively −465 900 and −380 800 km^3/yr. These trends can be compared with that of PIOMAS from about −427 100 km^3/yr over the same period (1993–2016). Once again, the spread present in GREP product at this lower frequency variability highlights the large uncertainty in the representation of Arctic sea ice volume by the different reanalysis products (Chevallier et al., 2017).

Antarctica

As for the Arctic Ocean, GLORYS12 and G4 reanalyses have very similar results in Antarctica. F12 faces a consistent bias found in many models (Roach et al., 2018) and simulates a sea ice cover with too low sea ice concentrations throughout the year (not shown). As a result, and under unknown triggering effects, a first window through the sea ice occurred in winter of 1997 in eastern part of the Weddell Sea and started to transfer energy during winter between the ocean and the atmosphere. This energy exchange broke the stratification present at the surface, e.g. warm and salty waters overlaid by fresh surface waters, and started to homogenize the water column by vertical motions. The unusual presence of these relatively warmer waters on the surface prevented the formation and presence of ice locally. This phenomenon has persisted from one year to the next and spread to wider areas. The ice cover could never return to its normal extent, especially in winter (**Figure 6A**). Thanks to the assimilation of sea ice concentration, GLORYS12 avoids this behavior and keeps a seasonal cycle very comparable to observations (**Figure 6A**). GLORYS12 exhibits a sea ice extent very close to the observations with, however, and as in the Arctic, a tendency to have a slightly higher extent, particularly in winter. Further, GLORYS12 sea ice extent is within the spread of the GREP ensemble.

As in the Arctic, the CERSAT data (extent and leads), are the lowest estimates of all observations. The lead observations spread

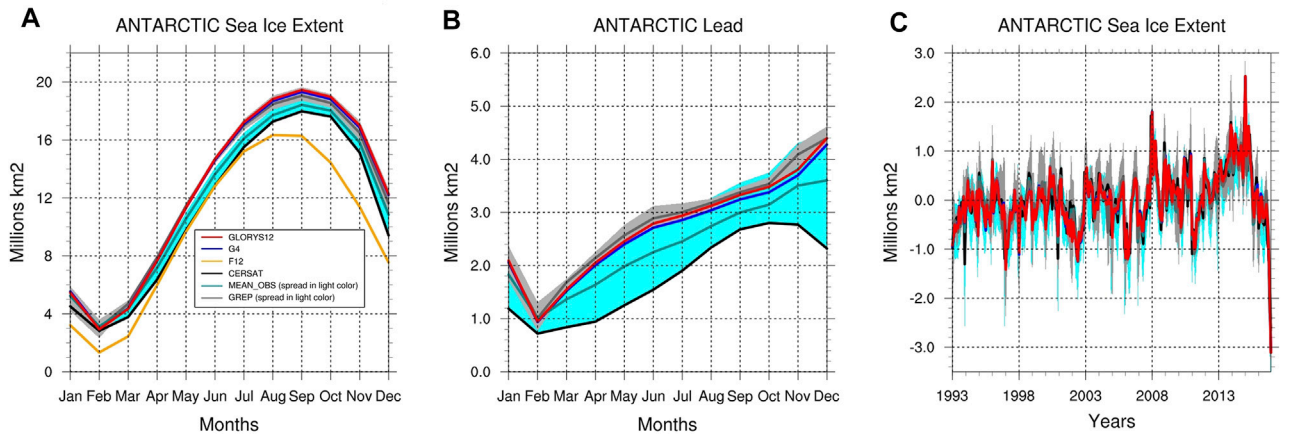

FIGURE 6 | Antarctica - Same as **Figure 4** for mean seasonal cycle (1993–2016) of **(A)** Sea ice extent, **(B)** Leads, and **(C)** interannual monthly variability of sea ice extent. The simulation F12 is not shown in panels **(B,C)**.

is much larger than that of GREP and even reaches 2 million km^2 in the spring, the equivalent of the total lead area estimated by CERSAT. GLORYS12 sea ice extent and surface of leads are within the spread of the GREP ensemble. The Antarctic sea ice extent in spring 2016 attained a record minimum (Turner et al., 2017) for the 1993–2016 period, presenting an abrupt departure from the slowly but steadily expanding until several monthly record high in 2014. Combined with this high variability, the resulting weak positive trend found in all reanalyses and all observations is not significant (95%-level confidence). This non-significance is in agreement with the study of Yuan et al. (2017).

Large-Scale Dynamics

Meridional Heat Transport and Inter-Basin Volume Exchanges Transports

Large-scale ocean transports play a major role in the Earth Climate. Various estimates of global heat and mass transports at key sections have already been calculated from direct ocean hydrographic sections (Talley et al., 2003), from the World Ocean Circulation Experiment based on the inversion of hydrographic data (e.g., Ganachaud and Wunsch, 2003; Lumpkin and Speer, 2007), and from ocean reanalyses (e.g., Stammer et al., 2004; Haines et al., 2012; Valdivieso et al., 2017). More recently, Bricaud et al. (2018) gave estimations of volume transports through key sections from GREP and of meridional heat transport (MHT) based on the 1/4° reanalysis G2V4 and its associated free run for the three major basins (global, Atlantic and Pacific+Indian). In this section, we provide estimations of GLORYS12, G4 and F12 MHT and volume transports through key sections and compare them to observation-based estimates and to GREP product.

Given large uncertainties linked with the oceanic observations sampling, **Figure 7** shows a good agreement of transport estimates between volume transports through different sections from GREP product and from Lumpkin and Speer (2007) (**Figure 7A**) with a median value of the relative error of 30%, and the same diagnostics for GLORYS12, F12 and G4 (**Figure 7B**).

GLORYS12 reanalysis transport at Drake Passage has been particularly and extensively studied in Artana et al. (2019b). The authors show that GLORYS12 estimates are within recent observation-based estimates (8 Sv larger than Koenig et al. (2014) estimate and well below the estimate of 173.3 ± 10.7 Sv using measurements from the cDrake project (Donohue et al., 2016)) and especially emphasizes that accurately assessing the absolute transport through Drake Passage remains a challenge. However, with respectively 156.9 ± 4.5 and 154.6 ± 4.8 Sv, GLORYS12 and G4 transports at Drake Passage are very close to each other and considerably reduce the transport estimate compared with that from the simulation without assimilation F12. Artana et al. (2019b) have shown that the mean volume transport of GLORYS12 over 1993–2010 (157 ± 3 Sv) is similar to a nine-ensemble mean of 152 ± 19 Sv over the same period from lower resolution global reanalyses (resolution ranging from 1° to 1/4°, five are of European origin using varying versions of the NEMO ocean, three are American and one is Japanese) (Uotila et al., 2019). Antarctic Circumpolar Current (ACC) transports in both GLORYS12 and G4 are in the spread of the GREP NEMO-based ensemble but remain in the upper bound of this set of estimates. It is also larger than Lumpkin's estimates.

Compared to the canonical climatological estimation of 0.8 Sv from Woodgate et al. (2006), the Bering Strait transport is larger in both GLORYS12 and G4 (1.3 Sv). Both GLORYS12 and G4 estimates are closer to the most recent estimates, which show that, over the last decade, volume transport in Bering Strait has been steadily increasing and is now well above 1 Sv (Woodgate,2018). Both GLORYS12 and G4 estimates (1.3 Sv) favorably reduce the too strong F12 transport (1.43 Sv).

As the only deep water passage to the Arctic Ocean, transports through Fram Strait determine to a large extent the exchanges between the North Atlantic and the Arctic Ocean. With respectively, 1.9 ± 0.7, 2.4 ± 0.7, and 2.4 ± 0.7 Sv, GLORYS12, G4 and F12 are close to the canonical observation-based estimates of ~2 Sv from Fahrbach et al. (2001). At Fram Strait and at the

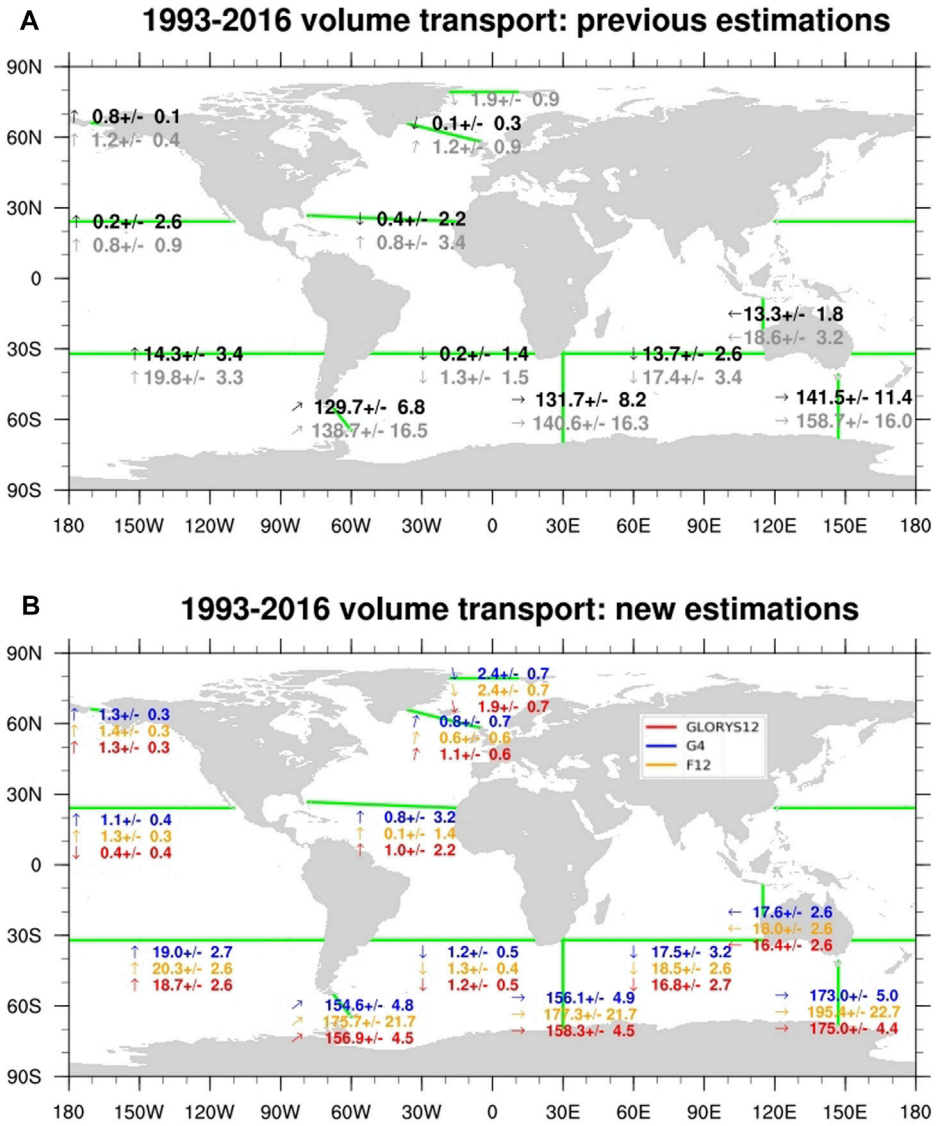

FIGURE 7 | Mean volume transport and its variability for the 1993–2016 period from **(A)** Lumpkin (in black) and GREP 1/4° ensemble product (in grey) and from **(B)** GLORYS12 (in red), F12 (in orange) and G4 (in blue). Units are in Sv.

Greenland-Iceland-Scotland section, GLORYS12 transports are identical to GREP estimations.

Generally, GLORYS12, G4 and all reanalyses included in GREP provide transport estimates that are higher than values deduced from observations, whether at high latitudes, as just mentioned, or at tropical latitudes (Indonesian Throughflow and meridian sections at 30°N and 30°S, **Figure 7A**).

Meridional heat transports for the three major basins (**Figure 8**) are estimated using 5 day mean fields in order to avoid aliasing errors found with monthly mean sampling (Crosnier et al., 2001). MHTs in GLORYS12 and G4 are in general very close to each other. In Global and Pacific-Indian basins, GLORYS12 and G4 differ at the Equator where a strong gradient is present in their respective MHT. For the Global basin, the MHT peak at 5°N is 1.2 PW for GLORYS12 and 1.6 PW for G4. For the Pacific-Indian basin, the MHT peak at 5°N is 0.2 PW for GLORYS12 and 0.7 PW in G4. In the Atlantic basin, they differ at 40°N, where MHT is 1.2 PW for GLORYS12 and 1.4 PW in G4. Compared to G4, GLORYS12 then simulates higher MHT northward poleward transport in regions with strong gradients (equatorial dynamics and Gulf Stream current). Conversely, GLORYS12 displays lower values in the [40°S–60°S] latitude band of the Antarctic Circumpolar Current (ACC) fronts compared to G4 estimates.

GLORYS12 and G4 MHTs greatly differ from F12 in the Southern subtropical gyres with a significant stronger northward heat transport in the [40°S–20°N] latitude band. This results in a weaker poleward heat transport by Southern tropical gyres in reanalyses than in the simulation without assimilation. While this weakening is more consistent with the error bars in the Atlantic, it

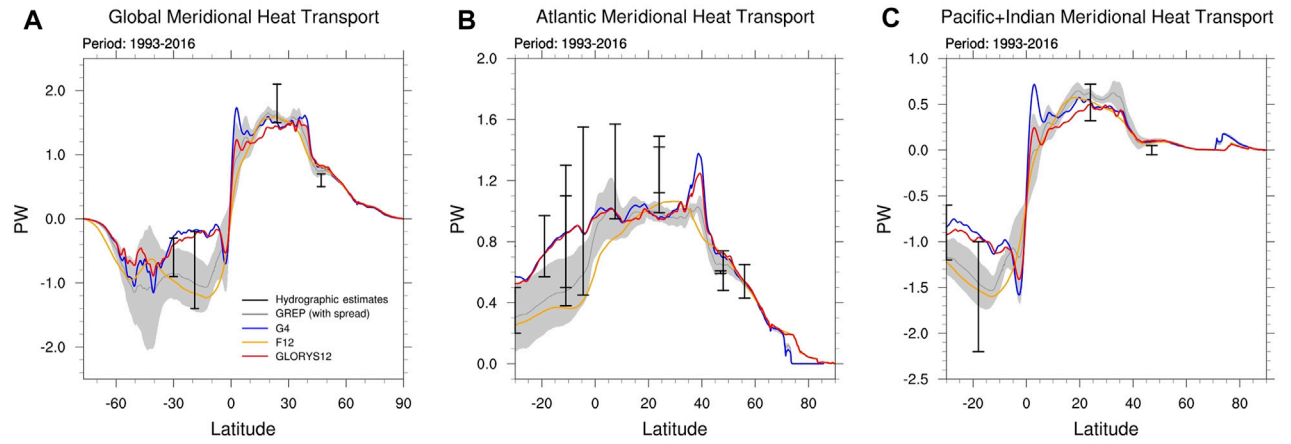

FIGURE 8 | Mean Meridional Heat Transport for the 1993–2016 period for Global Ocean **(A)**, Atlantic Ocean **(B)** and Pacific + Indian Oceans **(C)**. GLORYS12 is plotted in red, F12 in orange, G4 in blue, GREP ensemble product in grey and hydrographic estimates in black. Units are PW.

drives heat transport out of the error bars in the Indo-Pacific. However, the error bars proposed by Ganachaud and Wunsch (2003) or Lumpkin and Speer (2007) are very large, particularly in the tropical band of the Atlantic Basin.

In GLORYS12 and G4, the Global and the Pacific-Indian basins equatorial MHT gradient is stronger than in F12. The current interpretation is that those peaks are overestimated due to spurious velocities induced in particular by the assimilation of SLA (and MDT) in the equatorial region (Gasparin et al., 2021). For the Global basin, F12 MHT is lower than GLORYS12 and G4 MHTs in the [40°S–0°] latitude band and close to lower values of the hydrographic estimates, whereas GLORYS12 and G4 MHTs are close to the upper values of the hydrographic estimates. For the Atlantic basin, F12 MHT is lower than GLORYS12 and G4 MHTs in the [30°S–20°N] latitude band and close to lower values of the hydrographic estimates, whereas GLORYS12 and G4 MHTs are close to the middle values of the hydrographic estimates. For the Pacific-Indian basin, F12 MHT is lower than GLORYS12 and G4 MHT in the [30°S–0°] latitude band and close to middle values of the hydrographic estimates, whereas GLORYS12 and G4 MHTs are close to the upper values of the hydrographic estimates.

Moreover, the time mean state and interannual-decadal variability of the North Atlantic ocean since 1993 have been assessed in Jackson et al. (2019). The authors show that GLORYS12 is able to reproduce the main aspects of the circulation including convection, AMOC and gyre strengths, and transports.

Velocity Validation Against Drifter's Estimation

In this section, we use velocity observations from surface drifters (that are not assimilated) to assess the level of performance of GLORYS12 qualitatively. To avoid contamination by the windage due to a drogue loss (Grodsky et al., 2011), we use the drogued-only 15 m drifter dataset coming from the CMEMS *in situ* Thematic Assembly Centre (Rio and Etienne, 2019). Model counterparts of the drifter's velocities are interpolated at the right time and averaged over the 2003–2016 period. Results at 15 m (**Figures 9A,B**) are very similar to those from the CMEMS real time system (Lellouche et al., 2018). The general circulation with major currents is well represented. The main shortcoming concerns the tropical Pacific South Equatorial Current which is too strong in GLORYS12. It has been shown that this was mainly due to a bias in the reference height for the altimetry (Hamon et al., 2019). It can also be noted that the ACC is slightly too strong near the surface. We now use estimated velocities at 900 m derived from Argo profiling floats when drifting at their parking depth (Lebedev et al., 2007). Comparisons in panels C and D of **Figure 9** show a good general agreement between the observations and GLORYS12. The ACC has the right intensity at this depth. This is consistent with Thoppil et al. (2011) results which show that high-resolution model and data assimilation improve the representation of fine structures at depth at high latitude. The only notable differences concern the striations of the equatorial band (Cravatte et al., 2017) which are slightly underestimated and not reproduced at the right latitude by GLORYS12.

Ocean Variability

Eddy Kinetic Energy

In order to estimate the mesoscale activity present in GLORYS12, comparisons of geostrophic Eddy Kinetic Energy (EKE) deduced from GLORYS12 and from F12, G4 and the L4 CMEMS DUACS gridded product (Taburet et al., 2019) have been performed over the 2007–2016 period. These comparisons are made over the last 10 years of the 1993–2016 period to ensure that the simulations, in particular F12, have reached a state of equilibrium (see *Eddy Kinetic Energy Time Evolution*). Geostrophic EKEs of GLORYS12, F12, and G4 are deduced from daily sea surface height (SSH) from which geostrophic velocities are computed. Geostrophic EKE of the DUACS product is calculated directly from the daily geostrophic velocities included in the product.

Figure 10 shows the geostrophic EKE for GLORYS12 (panel A), and the differences against the three others estimates:

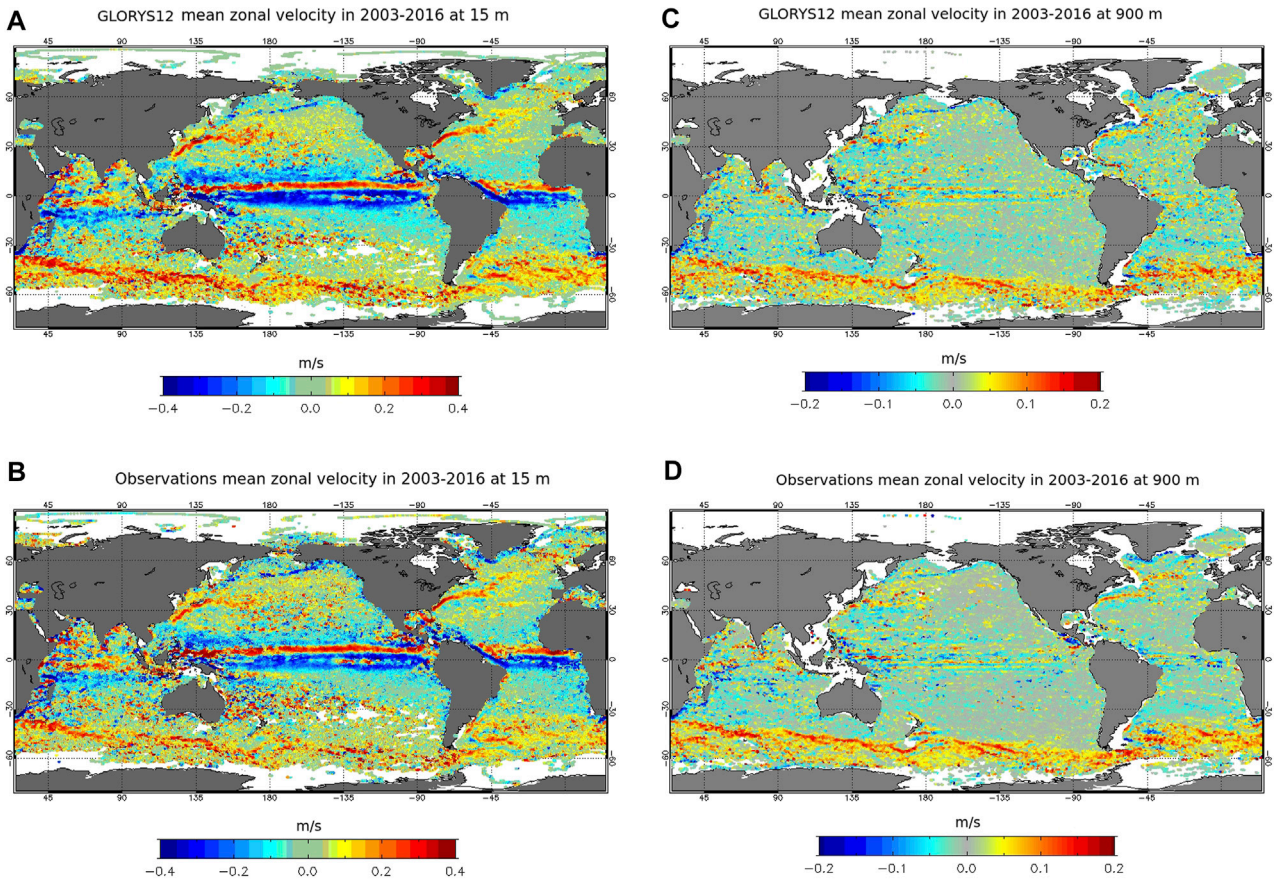

FIGURE 9 | Panels **(A,B)**: mean zonal velocity at 15 m over the 2003–2016 period for GLORYS12 **(A)** and observations **(B)**. Observations come from drogued-only subsurface drifters (Rio and Etienne, 2019). Panels **(C,D)**: mean zonal velocity at 900 m over the 2003–2016 period for GLORYS12 **(C)** and observations **(D)**. Observations come from estimated velocities derived from Argo profiling floats (Lebedev et al., 2007). Units are m/s.

GLORYS12 minus DUACS (panel B), GLORYS12 minus F12 (panel C) and GLORYS12 minus G4 (panel D). We observe very realistic structures in GLORYS12. All the large dynamic systems are very well represented (Western Boundary Currents (WBCs), Agulhas recirculation, Leeuwin Current, ACC). Compared to DUACS, the differences in the major currents are small. However, we observe a higher level of EKE almost everywhere of 25–50 cm^2/s^2. DUACS shows stronger EKE levels at some specific locations, such as the equatorial band (10°S–10°N) and towards Madagascar. These departures from DUACS are consistent with that depicted by Chassignet and Xu (2017) for models at 1/25° and 1/50° resolution without data assimilation. The authors show that using proper temporal and spatial filtering, similar energy levels can be found between different databases. Still, the direct comparison with the EKE derived from the DUACS maps remains complex because DUACS maps do not include the smaller space and time scales that are filtered out through the mapping procedure. In particular, DUACS underestimates the EKE by more than 20% in the mid and high latitudes (Le Traon and Dibarboure, 2002).

Comparing GLORYS12 to F12, one can observe strong differences, especially in the WBCs where the incorrect positioning of the currents in the free simulation creates large dipoles on the difference map. These differences show that data assimilation helps positioning better the main observed currents in GLORYS12. Almost everywhere, except the ACC, the energy level in GLORYS12 is significantly higher than the energy level in F12, with differences varying from 50 to 150 cm^2/s^2. This means data assimilation potentially adds information everywhere in the model dynamics, with a strong signature in EKE. It is important to mention that the EKE level in F12 is of the same order of magnitude than that of other simulations with equivalent resolution and without data assimilation, as presented in Chassignet et al. (2020) (not shown). The increase of EKE in GLORYS12 does not correct a potential underestimation of the energy level by F12. GLORYS12 can add new information such as the breakdown of internal waves, but can also limit the attenuation of mesoscale activity in F12 via the assimilation of the SLA. Nevertheless, in the ACC, F12 is more energetic than GLORYS12. The reason of this difference is still not explained and requires further investigations. The comparison between GLORYS12 and G4 shows a general increase in the EKE level with increasing resolution. This overall increase is approximately 10%. The stronger EKE in GLORYS12 is an expected direct effect

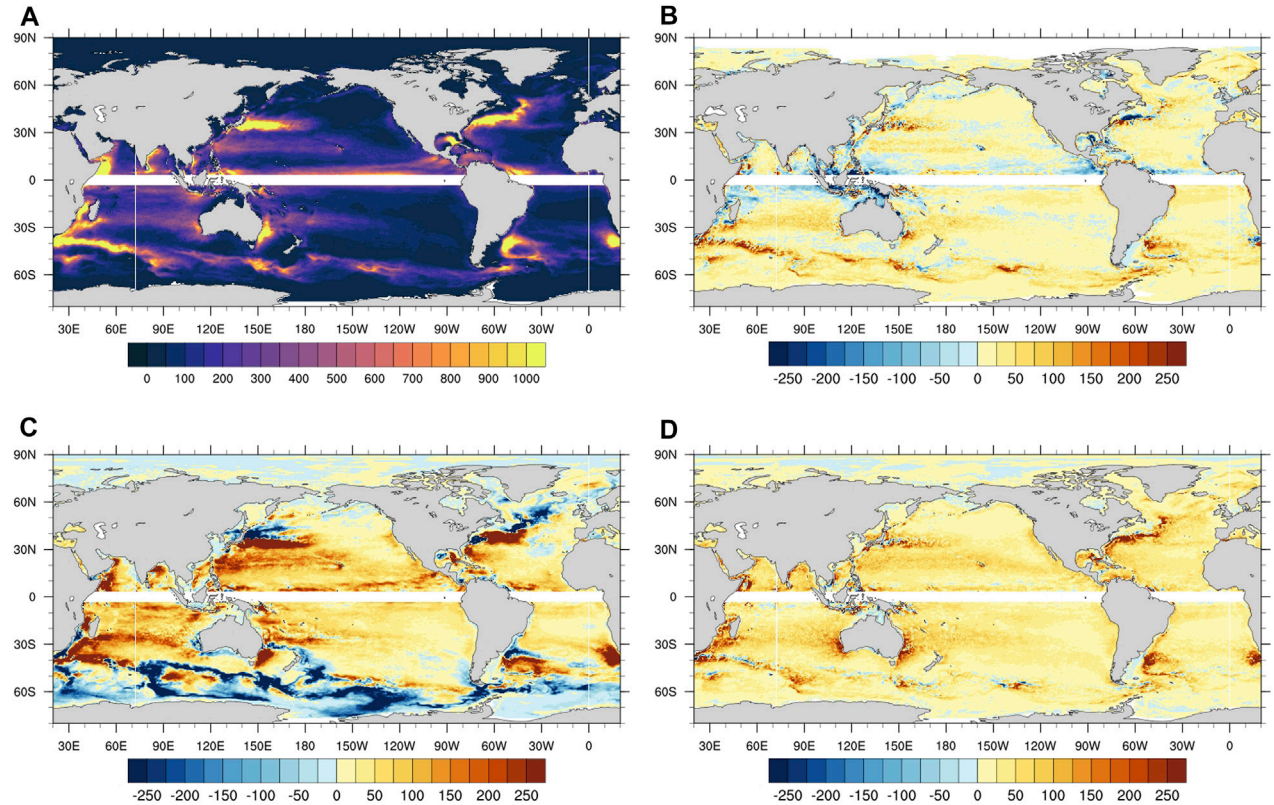

FIGURE 10 | Geostrophic Eddy Kinetic Energy over the 2007–2016 period for GLORYS12 **(A)** and differences against the three others estimates: GLORYS12 minus DUACS product **(B)**, GLORYS12 minus F12 **(C)** and GLORYS12 minus G4 **(D)**. Units are cm^2/s^2.

of the increase of resolution, allowing the representation of small structures.

Quantification of Energy Gain

To go further in the understanding of the energy level in GLORYS12, a spectral analysis is performed in order to quantify the energy gain in GLORYS12 SST analyses (with respect to G4 and F12) at different spatial scales. A local spectral decomposition was made on SST from daily model outputs during the year 2013, which is a neutral year considering the North Atlantic Oscillation and ENSO indices. Moreover, working over a single year has the advantage of avoiding mixing structures placed differently according to climatic indices.

For each point of a regular subsampling of the GLORYS12 model grid (one point in ten), a mean power spectral density (PSD) is obtained by averaging the results over the four main directions S-N, W-E, SW-NE, and NW-SE. In practice, the decomposition is performed using the one-dimensional SST signal over the four 1,000 km synthetic continuous tracks centered on the regular subsampled grid points. In order to avoid sampling issues, G4 outputs have been first interpolated on the same grid as GLORYS12. This methodology is directly derived from that of Dufau et al. (2016), used for spectra calculation along altimetry tracks. As expected, the overall average results confirm that GLORYS12 contains more energy at finer scales (not shown). We also find that G4, F12, and GLORYS12 have roughly the same energy at large scales but the difference between GLORYS12 and the two other configurations tends to increase towards the smaller scales. The difference between GLORYS12 and G4 are less than 20% around 200 km. The difference between GLORYS12 and F12 is about 20% near 55 km.

Focusing on the typical length scale of the mesoscale activity (50–250 km range), **Figure 11** shows that the power gain is evenly distributed over the entire ocean. Panels (A–C) show the local percentage of power in the mesoscale band normalized by the total power (in the 20–980 km band) for G4, GLORYS12 and F12 respectively. The comparison between the maps highlights the local change in the slope of the PSD (not shown). Except for the equatorial area, constrained mainly by large-scale atmospheric phenomena, it appears that the SST in GLORYS12 is the most energetic in the mesoscale part of the spectrum. Given the logarithmic behavior of the energy spectrum, the average difference of one percent between the power fraction of the mesoscale energy of GLORYS12 and G4 remains significant. The data assimilation has also a small effect on the mesoscale power fraction. Thus, GLORYS12 is uniformly more energetic than F12 in the global ocean, except the Northern part of the Atlantic.

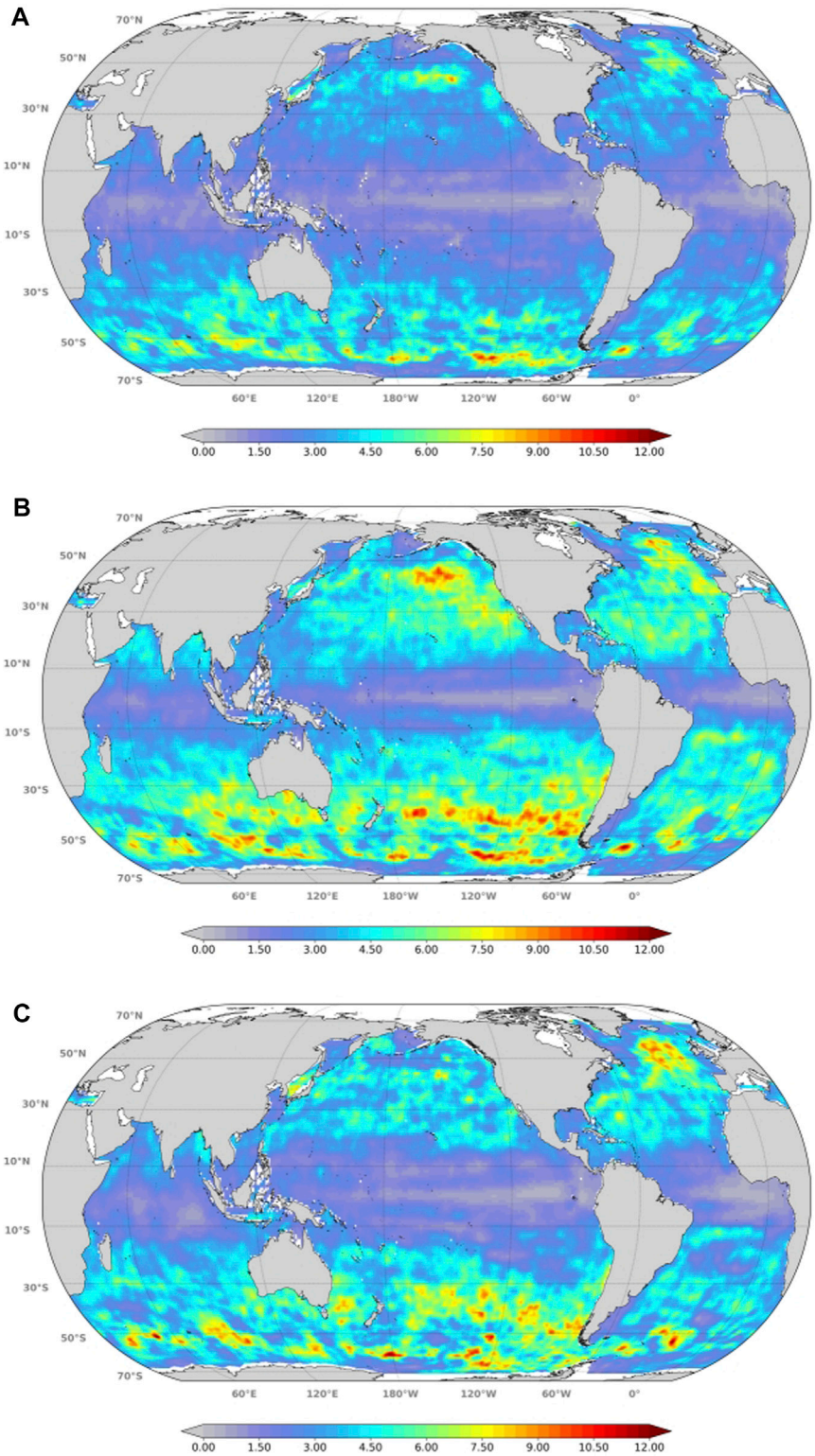

FIGURE 11 | Power fraction in the mesoscale (50–250 km) band normalized by the total power in the 20–980 km band for G4 **(A)**, GLORYS12 **(B)** and F12 **(C)** SST in year 2013. Units are %.

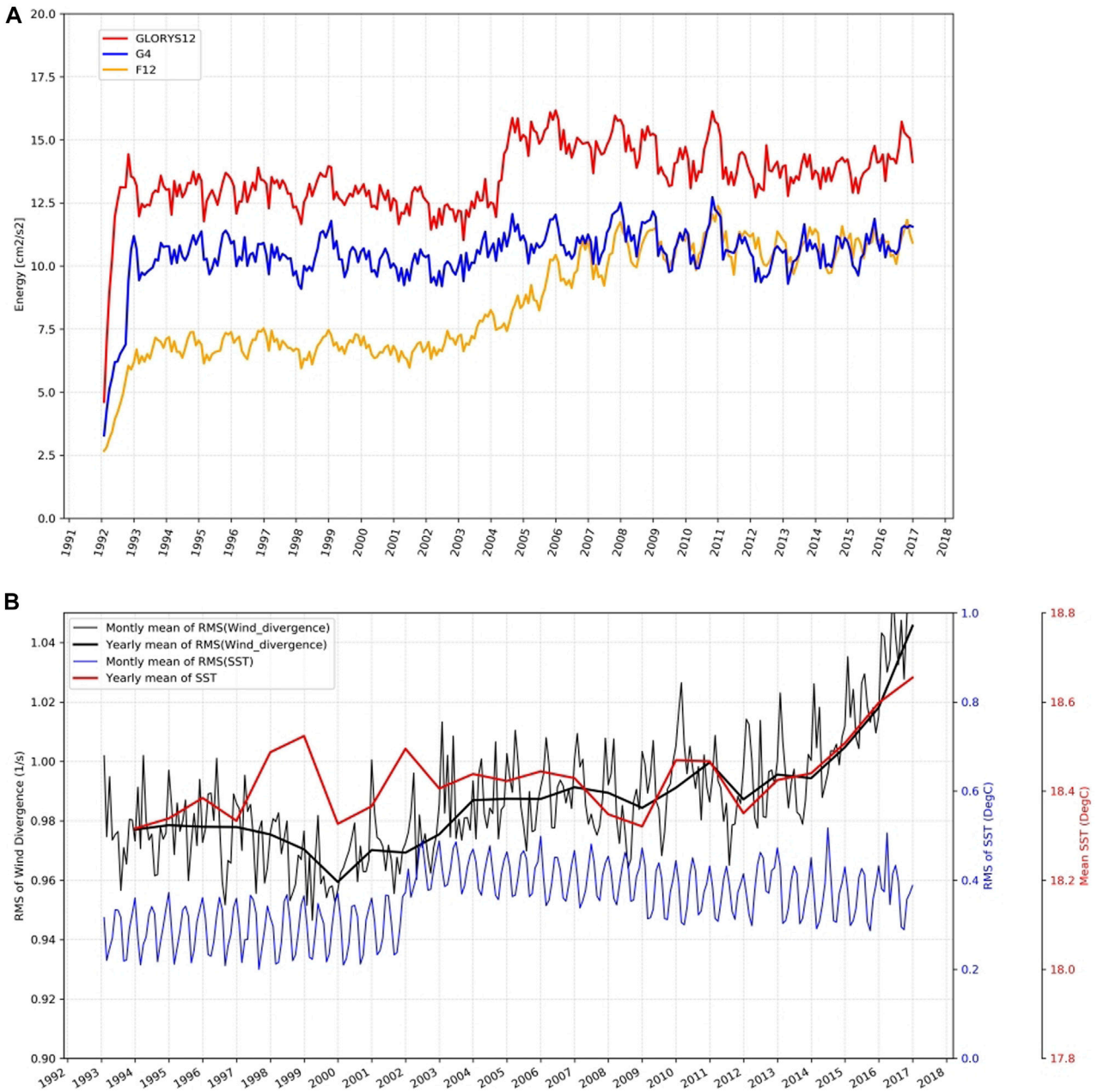

FIGURE 12 | (A) Three-dimensional mean of monthly Eddy Kinetic Energy (in cm^2/s^2) for GLORYS12 (in red), F12 (in orange), G4 (in blue). **(B)** Monthly mean of spatial variance of daily SST (in blue), monthly (thin black) and yearly (thick black) mean of spatial variance of daily wind divergence, and yearly mean of SST (in red).

EDDY KINETIC ENERGY TIME EVOLUTION

Three-dimensional average EKEs can also be assessed from GLORYS12, F12, and G4 daily velocity fields. **Figure 12A** shows the temporal evolution of the three-dimensional mean of monthly EKEs deduced from velocity. No observation comparison is available since a three-dimensional total EKE cannot be deduced from the observations. Consistently with the surface geostrophic component (**Figure 10**), GLORYS12 is more energetic compared to G4 and F12. The average value is equal to 14 cm^2/s^2 for GLORYS12, 10 cm^2/s^2 for F12 and 8.5 cm^2/s^2 for G4. Simulations start from rest and a first stabilization of the energy level occurs after 1 year for the simulations with data assimilation (GLORYS12 and G4) and after 3 years for F12, corresponding to the spin up time needed for model simulations to reach their energetic equilibrium. The seasonal cycle is well marked in all time series and after the first three years, important interannual variations are present, as in 1997–1998 with the strong ENSO event which induced a strong decrease of the global EKE.

However, time series exhibit two main discontinuities. The first one occurs in the three simulations at the beginning of 2002 with an increase of energy until 2007. The strongest signature is observable in F12 with a change of mean state from 7 to 10 cm^2/s^2. From 2002, an increase in the amplitude of the seasonal cycle is also observed in all simulations, where the intra-annual amplitudes change from 1 to 2 cm^2/s^2. As this change of the system mean state is observed in the simulation F12 without data assimilation, it can therefore only come from atmospheric forcing. A deeper study of ERAinterim is needed to understand the behavior of GLORYS12, F12, and G4. ERAinterim is an atmospheric reanalysis derived from an atmospheric general circulation model with data assimilation but having boundary conditions at the interfaces of the atmosphere. In particular, ERAinterim uses a SST estimated from observations. The spatial resolution of SST products used during the production of ERAinterim changed from 1° to 0.5° (Dee et al., 2011) and this change induces modification of atmospheric circulation (Parfitt et al., 2017). **Figure 12B** (blue curve) shows the evolution of the spatial RMS of SST (a monthly mean has been applied to the daily data). The change of SST resolution in January 2002 is well marked with the increase reflecting the increase in variability. This change in the boundary condition of the reanalysis induces a change in the atmospheric fields and a modification of the wind field. Different mechanisms for adjustments of atmosphere to the oceanic small scales are described in many studies (e.g., Lindzen and Nigam, 1987; Hayes et al., 1989; Chelton et al., 2001; Spall, 2007; Minobe et al., 2008; Small et al., 2008; Renault et al., 2017). These local circulations do not appear on large-scale wind fields. It is therefore necessary to consider local circulations. These latter can be obtained by different filtering methods, but energy scales will depend on the filtering. If the divergence or rotational wind is considered, the smallest spatial variations of wind will be highlighted. The black curve in **Figure 12B** shows the spatial variability of the ERAinterim wind divergence. In 2002, the variations of wind divergence exhibit an increase at the same time of RMS SST variation. This demonstrates the atmospheric response to the SST change. After 2014 there is a strong increase which seems related to the increase in global average SST (**Figure 12B**, red curve). The increase in SST leads to more instabilities of the atmospheric column and therefore more divergence. However, this does not entirely translate into the energy transmitted to the ocean model. In summary, the increase in SST resolution in January 2002 results in an increase in small-scale variability in the atmospheric reanalysis winds, and part of this wind variability increase is transmitted to GLORYS12, F12, and G4. The second discontinuity occurs in 2004 where a strong and rapid increase is present in GLORYS12 (2.5 cm^2/s^2 in 6 months) and one to a lesser extent in G4 (1 cm^2/s^2). No sudden increase at this date is observed in F12. This suggests that the source comes from data assimilation. In order to take into account the increase of the number of assimilated *in situ* T/S vertical profiles from January 2004 (see **Figure 2**), the time window in which the 3D-VAR bias correction is performed was reduced from 3 to 1 month in both G4 and GLORYS12. It would therefore seem that this reduction in the time window, combined with the increase in the number of assimilated *in situ* observations, creates an increase in energy and therefore changes the regime state of the system. This increase in energy is much more pronounced in GLORYS12 than in G4, due to the ability of GLORYS12 to create realistic mesoscale features.

TRENDS AND EVOLUTIONS OF TEMPERATURE, SALINITY AND SEA LEVEL

Time Evolution of Temperature and Salinity Anomalies

Figure 13 shows the time evolution of temperature and salinity anomalies over the whole domain for F12, GLORYS12, and G4. An anomaly for a specific date is defined as the difference between the value at this current date and the initial state of the simulation. Note that for this diagnostic, the interannual signal has been removed using a digital time filter. GLORYS12 and G4 reanalyses show a warming in the 0–1,000 m layer (**Figures 13C,E**). It is a little too strong according to the mean misfits shown on **Figure 1A**. The freshening in the first 1,500 m (which occurs notably in the ACC) before Argo is present in G4 and to a lesser extent in GLORYS12 (**Figures 13D,F**). From the beginning of the year 2004, this freshening is strongly reduced in G4 and turns into a saltening in the first 200 m. This can be linked to the change in the time window to compute the T/S bias correction and by the increase in the number of assimilated profiles. Before the arrival of Argo floats in large quantity at the start of 2004, G4 and to a lesser extent GLORYS12 did not seem able to correct the salinity bias that had set in. GLORYS12 has a better behavior in salinity because the fronts are much better resolved in GLORYS12 than in G4, in particular the polar front which is poorly positioned in G4 (not shown). January 2002 seems to be a crucial date for F12 which presents a strong cooling in temperature in the 200–1,000 m layer, spreading at depth afterwards (**Figure 13A**). This behavior can be correlated to the change in the atmospheric fields discussed in *Eddy Kinetic Energy Time Evolution*. Moreover, the F12 simulation without data assimilation shows a strong salinity drift in the first 500 m (**Figure 13B**).

Sea Level Time Evolution

Of particular importance for sea level trends, along-track altimetric observations from various missions are assimilated in GLORYS12 and G4, together with *in situ* temperature and salinity profiles and other observations. Altimetric observations capture sea level trends due to land ice mass loss and land water storage changes, in addition to trends due to sterodynamic sea level changes (e.g., Gregory et al., 2019). As mentioned in the description of the ocean model in *Description of GLORYS12*, a global mean sea level (GMSL) trend is added at each time step to the modeled dynamic sea level. This added GMSL signal is composed of the diagnosed global mean steric sea level change and of a barystatic (land ice related, Gregory et al., 2019) sea level trend of 1.31 mm/yr over 1993–2001 and of 2.20 mm/yr over 2002–2016. The GMSL change is added to all simulations, prior to data assimilation for GLORYS12 and G4. In assimilated

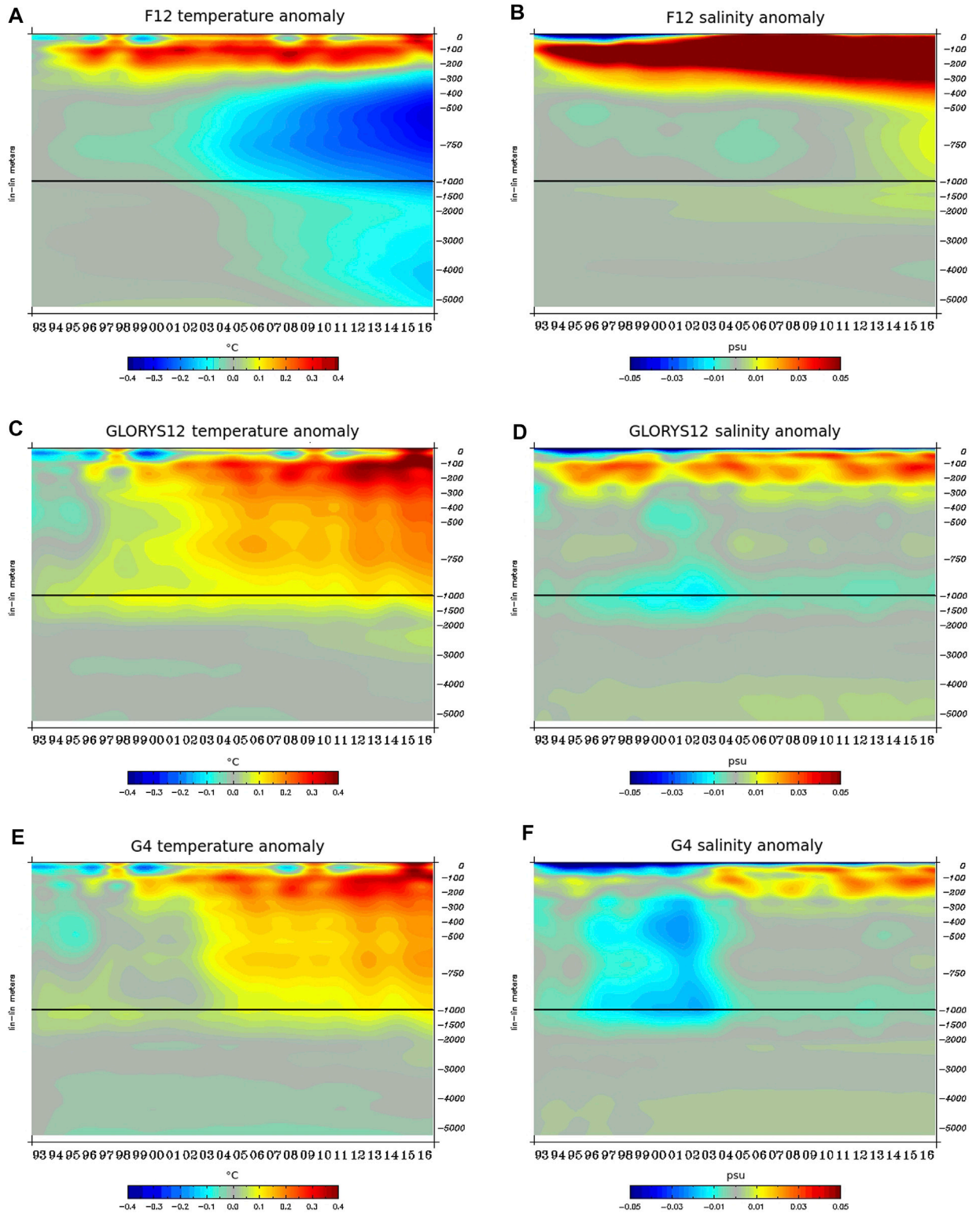

FIGURE 13 | Time evolution of temperature (in °C, left panels) and salinity (in psu, right panels) anomalies over the whole domain for F12 (top panels **A,B**), for GLORYS12 (middle panels **C,D**) and for G4 (low panels **E,F**). An Anomaly for a specific date is defined as the difference between the value at this current date and the value at the initial state. The interannual signal has been removed using a digital time filter.

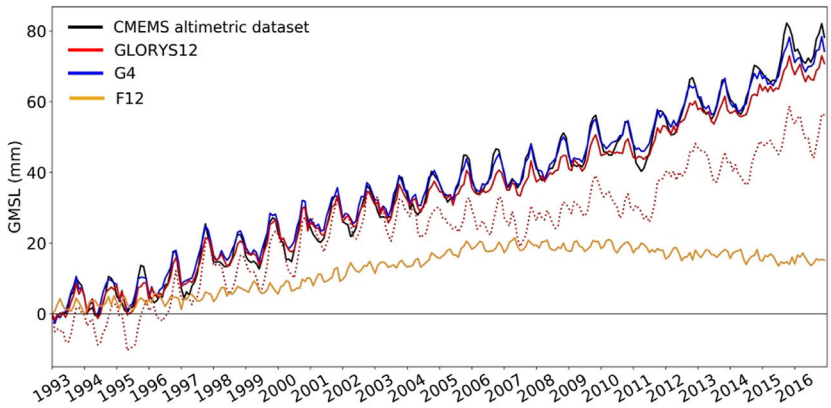

FIGURE 14 | Global mean sea level monthly time series for the CMEMS gridded reprocessed altimetric dataset (007_048, in black), GLORYS12 (in red), F12 (in orange) and G4 (in blue). The global mean steric sea level of GLORYS12 is also shown (dashed red line). The same ocean mask has been used when computing the global mean. Only points with valid monthly means in altimetric sea level data along the whole 1993–2016 period have been used in the global mean.

altimetric sea level observations, no correction has been applied for the drift of T/P-A over 1993–1998 (e.g., Beckley et al., 2017; Legeais et al., 2019), but regional GIA-related trends have been subtracted from the altimetric observations before assimilation (based on Peltier, 2004).

In terms of GMSL rise, G4 and GLORYS12 are in close agreement with altimetry (**Figure 14**). Yet, after 2004, G4 tends to better represent the seasonal cycle of GMSL changes than GLORYS12. The GMSL rise trend is also in closer agreement with altimetric observation (3.00 mm/yr over 1993–2016) in G4 (2.90 mm/yr) than in GLORYS12 (2.77 mm/yr). Although the barystatic sea level trend is added to the modelled sea level in all simulations (see *Description of GLORYS12*), the correct partition between the steric and barystatic components of GMSL changes is not yet ensured in GLORYS12 and G4. According to **Figure 1A**, there is an excess of heat storage around 100 m. As a result, the barystatic sea level trend is not fully retained in the system. Assimilation of altimetric sea level therefore leads to a too large global mean steric sea level rise in both G4 and GLORYS12. In GLORYS12, the global mean thermosteric sea level trend over 2005–2016 is 2.43 mm/yr (averaged over areas sampled by altimetry, **Figure 15A**). Thus, thermal expansion explains 70% of the GMSL trend of 3.20 mm/yr over the same period in GLORYS12, while it should only account for around 40% of the GMSL trend (Oppenheimer et al., 2019). As a result, the actual barystatic sea level trend in GLORYS12 over 2005–2016 is 0.77 mm/yr, instead of the 2.20 mm/yr added to the modelled sea level over 2002–2016. The issue in the separation of the barystatic and steric components of GMSL can be illustrated with the drop of around 5 mm in the altimetry derived GMSL in 2011 (**Figure 14**). This observed drop in GMSL is related to the 2010/11 El Niño event that led to more precipitation over Australia, northern South America and Southeast Asia. The corresponding ocean to land mass transfer increased the land water storage and accordingly decreased GMSL for months as the corresponding water was retained in endorheic basins (e.g., Boening et al., 2012). GLORYS12 and G4 also show a drop in GMSL in 2011. As only a barystatic sea level trend was added to GLORYS12 and G4, assimilation of altimetric data translated this mass signal into a steric signal, with an overall ocean cooling and contraction.

Finally, the free simulation F12, where no GMSL correction is applied, exhibits a very low GMSL rise (0.75 mm/yr over 1993–2016, **Figure 14**), highlighting the benefits from data assimilation to represent GMSL changes. The steric part of GMSL rise in F12 is close to zero in the 1990s and then drops to negative values (cooling (see *Time Evolution of Temperature and Salinity Anomalies* and **Figure 13A**), especially in the Southern Ocean (not shown)), explaining the low GMSL trend in F12.

At regional scales, sea level trends over the 1993–2016 period in GLORYS12 are in close agreement with sea level trends inferred from the CMEMS reprocessed and gridded altimetry product (**Figures 15A,B**). The main patterns of sea level trends observed by altimetry (e.g., Forget and Ponte, 2015; Dangendorf et al., 2019) are captured in the reanalysis, with the largest trends in the western tropical Pacific, northwestern Pacific, northern Southern Ocean, and the lowest trends in the subpolar North Atlantic, off Alaska, in the eastern tropical Pacific and in the southern most parts of the Pacific sector of the Southern Ocean. Regional sea level trend differences between the GLORYS12 reanalysis and the reference altimetric datasets remain small as they do not exceed ±2 mm/yr in the majority of the ocean observed by altimetry (the average local uncertainty in sea level trends over 1993–2019 from altimetry is 0.83 mm/yr, Prandi et al., 2021). Over the global ocean (covered by altimetry), the trend differences between GLORYS12 and altimetry have a median value of −0.26 mm/yr and a standard deviation of 0.60 mm/yr. Two main regional patterns can be distinguished in the regional sea level trend differences in **Figure 15C**. The pattern around Australia could correspond to the rate of change of the geoid (Peltier, 2004) as no regional GIA correction has been applied to altimetric data, while a two-dimensional trend GIA correction has been added to the modelled sea level trend. The pattern in the eastern Pacific

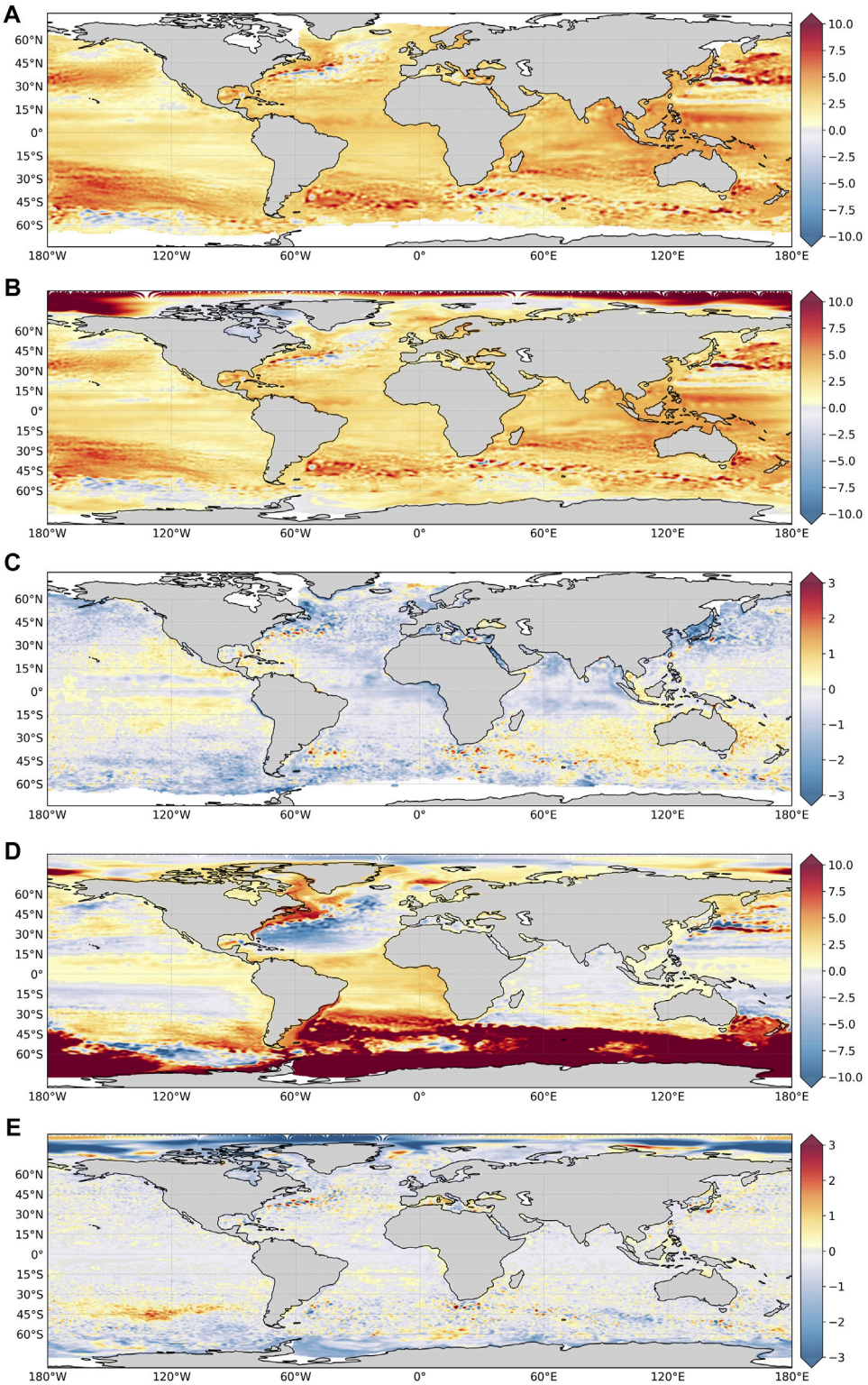

FIGURE 15 | Regional sea level trends over the 1993–2016 period (in mm/yr) for **(A)** the CMEMS gridded reprocessed altimetric dataset (007_048), **(B)** GLORYS12, **(C)** GLORYS12 minus altimetric dataset, **(D)** GLORYS12 minus F12, **(E)** GLORYS12 minus G4. The global mean sea level trend has not been removed. No GIA correction has been applied to altimetric trends in panel **(A)**. Note the different ranges covered by the color bars in panels (**C,E**).

could be related to the Pacific Decadal Oscillation (e.g., Hamlington et al., 2014). In GLORYS12, the largest regional sea level trends are found in the Arctic Ocean, reaching locally more than 25 mm/yr (**Figure 15B**). Averaged over the entire Arctic Basin, excluding the Canadian Archipelago, the mean sea level trend is 3.2 mm/yr (higher than the global mean). However, observed sea level trends from altimetry are not available yet over the whole Arctic Ocean making it difficult to evaluate the GLORYS12 sea level trends in this region. Rose et al. (2019) estimates the sea level trend over the Arctic Ocean to 2.2 mm/yr over 1991–2018. However, their estimate covers the 65°N–81.5°N domain, excluding the northernmost area (with no continuous data) where GLORYS12 reaches the highest sea level trends. A comparison of regional steric sea level trends over the European seas from GLORYS12 and regional reanalyses produced and distributed by CMEMS is provided in Storto et al. (2019b). The comparison pinpoints that differences between GLORYS12 and regional reanalyses mostly stem from the freshwater budget representation.

Data assimilation clearly and strongly improves the representation of regional sea level trends. Differences in sea level trends between GLORYS12 and F12, highlighting the impact of data assimilation in the reanalysis, are shown in **Figure 15D**. Using altimetry as a reference dataset (**Figure 15A**), the spatial standard deviation of sea level trend differences in F12 is 6.9 mm/yr, while it is an order of magnitude lower, 0.6 mm/yr, in GLORYS12. The largest differences are found in the Southern Ocean, reaching more than 10 mm/yr, and in the North Atlantic, with a dipole across the Gulf Stream with differences reaching more than ±5 mm/yr. In the Southern Ocean, the negative sea level trends in F12 are related to the strong cooling and the unrealistic loss of sea ice cover of the region in the free simulation, as described in *Time Evolution of Temperature and Salinity Anomalies*. The significant biases in sea level trends in F12 in the Southern Ocean and in the North Atlantic Ocean have been broadly corrected through data assimilation in GLORYS12.

Increasing the ocean model resolution from 1/4° to 1/12° in the two assimilative systems does not strongly impact regional sea level trends. Differences between GLORYS12 and G4 are shown in **Figure 15E**. Using altimetry as a reference dataset (**Figure 15A**), the spatial standard deviation of sea level trend differences in G4 is 0.62 mm/yr, very close to the 0.60 mm/yr in GLORYS12. The main differences are located in the Arctic Ocean, in regions of high EKE (WBC, Southern Ocean) (**Figure 15E**). The comparison between **Figure 15C** and **Figure 15E** show a zonal band around 45°S of underestimated trends in the Southeastern Pacific in G4.

SUMMARY AND CONCLUSION

A detailed evaluation of the global Mercator Ocean reanalysis GLORYS12 at 1/12° is presented here over the 1993–2016 period, based on comparisons with observations as well as inter-comparisons with sister simulations. In general, GLORYS12 provided a realistic representation of key oceanic quantities such as sea level, water mass properties, mesoscale activity or sea ice extent. This high-resolution reanalysis allows us to document oceanic variability on a large range of scales going from meso to global and from daily to decadal scales over the altimetry period (1993-present). As the first European high-resolution global reanalysis, GLORYS12 outperforms its sister simulations at lower horizontal resolution (1/4°) or at the same resolution but without data assimilation, even though it slightly suffers from the unregular evolution of the *in situ* global ocean observing system despite adapting assimilation procedures. For instance, the representation of temperature and salinity is strongly impacted by the arrival of the global Argo array in 2004 reducing the departures from *in situ* observations by a factor of 2. Note that F12 presents some flaws and improving the configuration shared by the free and the assimilation run could improve the reanalysis.

Comparison with altimetry demonstrates that the SLA variability is well-represented by GLORYS12, with a residual error which is consistent with observation error. Mesoscale activity provided by altimetry is superimposed to the MDT, used as a reference level for altimetry assimilation. The major source of error in sea level comes from the uncertainty of the MDT (Hamon et al., 2019). This mean quantity is fundamental for reanalyses assimilating altimetry, because it constrains the mean circulation of the model. This is especially important to properly represent the mean paths of the Gulf Stream, of the Kuroshio, or of the North Atlantic Current which are mainly constrained by the fronts in the MDT. Uncertainty in the MDT can perturb energy balances (e.g., Vidard et al., 2009; Gasparin et al., 2021), and further investigations are fully required to improve the accuracy of the MDT and make the best use of altimetry data without generating collateral issues.

The energy level in GLORYS12 is broadly consistent with observations as seen in surface currents, although few zonal currents are too strong (ACC, western Pacific South Equatorial Current). A slightly higher magnitude of GLORYS12 compared to DUACS product or to its lower resolution sister simulation is likely due to the coarser horizontal resolution of these latter estimates, which cannot represent the full energy spectrum embedded in GLORYS12. Currents at 900 m depth are realistic except for tropical striations (Cravatte et al., 2017) which are sometimes misplaced. These positive results show that high horizontal resolution is determinant to resolve small-scale structures at high latitudes and thus linking mid-latitudes to the polar oceans (Hewitt et al., 2016). The increased resolution allows better representing finer SST features, especially in the mesoscale range (Thoppil et al., 2011). The assimilation brings energy in this particular range whereas the difference between GLORYS12 and F12 becomes negligible towards the diffusion scales of the model. Note that the energy gains from both the horizontal resolution and the data assimilation are fairly uniform across the global ocean, except in the equatorial area, potentially due to the predominance of the wind-driven dynamics. The time evolution of the monthly EKE clearly highlights two major discontinuities, which result from changes in the ERAinterim atmospheric forcing in 2002 and in the *in situ* observing system in 2004. The issue seen in 2002 should be resolved in the next reanalysis version using 1) the new atmospheric reanalysis ERA5,

which does not seem to include such variations, and 2) an atmospheric boundary layer model to force the oceanic model (Brivoal et al., 2020; Lemarié et al., 2021). However, further investigations are required to overcome the discontinuity in 2004, resulting from the modification of the 3D-VAR bias correction time window to take into account the increase in the number of *in situ* T/S vertical profiles due to the arrival of the Argo array.

As key aspects of the large-scale circulation, inter-basins exchanges of volume in GLORYS12 are larger compared to observation-based estimates and compared to others reanalyses. Note that the impact of the increased horizontal resolution is not dominant since G4 estimates are similar to GLORYS12. Data assimilation improves transports through sections, by favorably reducing excessive volume transports of the twin simulation F12. In terms of heat transport, GLORYS12 estimates compares better than G4 to observation-based estimates. Note that the large volume transport in GLORYS12 (as in G4) induces sharp and strong heat transports on the equatorial region and on the Gulf Stream, which are not seen in the F12 simulation without assimilation and in the GREP product.

Assessing the representation of the deep ocean is quite complex given that long-term and regional deep ocean observations are not available yet. Unexpected behavior in the Tropical Indian and North East Atlantic basins have been identified and might be due to errors and/or strong climatic signals (Southern Oscillation Index and North Atlantic Oscillation) during the first decade of the reanalysis. However, one should remain cautious about the validity of the low frequency of GLORYS12 in deep part of these two regions. There is an unrealistic cooling in F12 south of 60°S which occurs rapidly from 2001 in Weddell and Ross seas, and near Amery Ice Shelf. On the contrary, GLORYS12 presents an unbroken time series, made up of the usual climatic signals of the region (not shown).

GLORYS12 captures well the low frequency variability (interannual and long-term variability) of the sea ice extent both in the Arctic and Antarctic Oceans. The assimilation of sea ice concentration improves the seasonal cycle of the Arctic sea ice extent but, in the same time, weakens the presence of leads and creates thicker ice. The representation of the sea ice cover is also significantly improved in Antarctica, where the model alone has difficulties in stabilizing the coupling between the sea ice and the ocean underneath. Estimates of leads and MIZ are found larger in models than in observations, but note that MIZ remains a zone of larger error and uncertainty in both models and observations. The horizontal resolution has no impact on the mean state, interannual variability and trends of sea ice quantities such as extent and volume. Several improvements are expected in the future with a more advanced sea ice model towards the SI^3/LIM platform with the possibility to represent the ice in different categories (Rousset et al., 2015), and the assimilation of sea ice thickness with the aim of improving and better controlling the sea ice volume.

The evolution of GMSL in GLORYS12 and G4 is in agreement with that from altimetric data. However, decomposing the steric and mass components of GMSL rise shows that the reanalyses have a too large steric component. The dominant source of error in sea level comes from the uncertainty in the MDT (Hamon et al., 2019). The issue of correctly adding and retaining the barystatic sea level rise in the reanalysis (Storto et al., 2017) with a correct mass/steric separation during data assimilation will be addressed in the next reanalysis to be produced by Mercator Ocean (with the inclusion of monthly corrections of GMSL instead of a trend). The reanalyses clearly outperform the free simulation which shows a modest sea level rise mostly due to a large cooling of the Southern Ocean. Regional sea level trends are correctly represented in GLORYS12 and G4. Data assimilation clearly and strongly improves the representation of regional sea level trends. This is especially true in the Southern Ocean, where the large negative sea level trends in F12 caused by a strong cooling and unrealistic loss of sea ice cover have been corrected through data assimilation in GLORYS12.

Several key developments on the reanalysis system should significantly improve the performance of the next version of GLORYS12. First, the latest versions of NEMO (Madec et al., 2019) will allow to have access to a more coherent Bulk formulation (Brodeau et al., 2017) compared to that used in atmospheric reanalyses, and to the latest wind-current coupling parameterization of Renault et al. (2020) and/or to a boundary layer model (Brivoal et al., 2020; Lemarié et al., 2021) dedicated to high resolution ocean coupling atmosphere. In addition, the use of a four-dimensional approach with the data assimilation scheme will also allow an improvement in the spatiotemporal continuity of mesoscale structures, particularly when assimilating SST swath data. This should also benefit to the Tropical Instability Waves in the tropics. Another interesting ingredient, which is currently being implemented in the Mercator Ocean assimilation scheme, is to perform the analysis in a smoothing mode (Cosme et al., 2010), allowing taking into account observations outside the time window of the current assimilation cycle. This can be applied for a reanalysis and could be efficient in reducing errors, especially in regions where the observations have very heterogeneous spatial coverage in time. Other evolutions are expected to benefit GLORSYS12, such as the inclusion of waves (Law Chune and Aouf, 2018) improving surface currents with a change in vertical physics or a refined MDT allowing to better represent the equatorial dynamics (Gasparin et al., 2021). GLORYS12 was initialized only 1 year before the assimilation of the altimetry, which seems insufficient for the model to damp all the transients related to the initialization. To further reduce the shock of initialization and the propagation of artificial tropical waves, a 3 year spin-up before assimilating altimetry can be considered. Similar to the flux correction in Magnusson et al. (2013), a systematic correction of the seasonal cycle, estimated over the Argo period and applied for the full reanalysis period, will be introduced to overcome the discontinuity due to the arrival of the Argo array.

The GLORYS12 reanalysis is a complex system resulting from extensive efforts combining information and developments from observations, assimilation and modelling communities. Given the strengths and weaknesses of the reanalysis mentioned in the present work, it is essential to intensify GLORYS12 evaluation for several reasons:

(i) GLORYS12 benefits from the information of the integrated observing system, and its evolution will continue with the arrival of new datasets from satellites (e.g., Surface Water and Ocean Topography mission) and *in situ* observations (e.g., Deep Argo). Questions of how to mitigate discontinuities in the observation spectrum will be central to better integrate all the components of the observing system and make the best use of ocean observations.
(ii) The scientific value of GLORYS12 has been already demonstrated in regional and global studies but also to force regional physical and biogeochemical models. For that reason, any improvements in GLORYS12 should benefit the wider ocean community.
(iii) A key activity for global ocean reanalyses is their use by the climate community to estimate the past and present energy budgets. It is thus important to further investigate the ability of GLORYS12 to provide an accurate estimate of the sea level and heat budgets, through refined data assimilation techniques conserving essential energy balances.
(iv) GLORYS12 is now expected to inform on past and near-present oceanic conditions to supply ocean monitoring indicators, used to track the health signs of the ocean and changes in line with climate change. This information serving policy-makers to implement and adapt environmental strategies will be routinely available (monthly scale). Careful data analyses are needed to ensure that each element of the value chain will allow high quality information at such high frequency delivery.

We plan to continue developing modelling and assimilation techniques to provide the best estimate of global oceanic stratification and circulation at high resolution, to refine the description of key quantities, and to evaluate them by comparing with assimilated and independent datasets.

DATA AVAILABILITY STATEMENT

The raw data supporting the conclusion of this article will be made available by the authors, without undue reservation.

AUTHOR CONTRIBUTIONS

LJ-M, GE, B-BR, GG, MA, BC, HM, CT and RC contributed to the text by proposing some paragraphs, points of discussion and references. LJ-M designed and performed the two numerical simulations with data assimilation at 1/4° and 1/12°, coordinated the individual contributions and compiled them into the manuscript. LO performed the free simulation at 1/12°. TC-E, RG, and BM helped for the tuning of the assimilation system. DM, GF, DY, and LP-Y did a first review of the preliminary version of the manuscript.

ACKNOWLEDGMENTS

This study has been conducted using E.U. Copernicus Marine Service Information. All the essential ocean physical variables from the GLORYS12 reanalysis are available with free access through the CMEMS data portal. The authors thank the two reviewers DJL and AK for their careful reading and for providing very constructive comments that improved the paper. This manuscript is an expanded version of the paper submitted at European Geophysical Union 2021 conference referenced as Lellouche et al. (2021) The Copernicus global 1/12° oceanic and sea ice reanalysis, EGU General Assembly 2021, online, 19–30 Apr 2021, EGU21-14961, https://doi.org/10.5194/egusphere-egu21-14961.

REFERENCES

Artana, C., Ferrari, R., Bricaud, C., Lellouche, J.-M., Garric, G., Sennéchael, N., et al. (2021b). Twenty-Five Years of Mercator Ocean Reanalysis GLORYS12 at Drake Passage: Velocity Assessment and Total Volume Transport. *Adv. Space Res.* 68, 447–466. doi:10.1016/j.asr.2019.11.033

Artana, C., Lellouche, J.-M., Sennéchael, N., and Provost, C. (2018). The Open-Ocean Side of the Malvinas Current in Argo Floats and 24 Years of Mercator Ocean High-Resolution (1/12) Physical Reanalysis. *J. Geophys. Res. Oceans* 123, 8489–8507. doi:10.1029/2018JC014528

Artana, C., Provost, C., Lellouche, J. M., Rio, M. H., Ferrari, R., and Sennéchael, N. (2019a). The Malvinas Current at the Confluence with the Brazil Current: Inferences from 25 Years of Mercator Ocean Reanalysis. *J. Geophys. Res. Oceans* 124, 7178–7200. doi:10.1029/2019JC015289

Balmaseda, M. A., Hernandez, F., Storto, A., Palmer, M. D., Alves, O., Shi, L., et al. (2015). The Ocean Reanalyses Intercomparison Project (ORA-IP). *J. Oper. Oceanogr.* 8, s80–s97. doi:10.1080/1755876X.2015.1022329

Barnier, B., Madec, G., Penduff, T., Molines, J., Treguier, A.-M., Le Sommer, J., et al. (2006). Impact of Partial Steps and Momentum Advection Schemes in a Global Ocean Circulation Model at Eddy-Permitting Resolution. *Ocean Dyn.* 56 (5–6), 543–567. doi:10.1007/s10236-006-0082-1

Beckley, B. D., Callahan, P. S., Hancock, D. W., Mitchum, G. T., and Ray, R. D. (2017). On the "Cal-Mode" Correction to TOPEX Satellite Altimetry and its Effect on the Global Mean Sea Level Time Series. *J. Geophys. Res. Oceans* 122, 8371–8384. doi:10.1002/2017JC013090

Boening, C., Willis, J. K., Landerer, F. W., Nerem, R. S., and Fasullo, J. (2012). The 2011 La Niña: So strong, the Oceans Fell. *Geophys. Res. Lett.* 39, a–n. doi:10.1029/2012GL053055

Brasseur, P., and Verron, J. (2006). The SEEK Filter Method for Data Assimilation in Oceanography: A Synthesis. *Ocean Dyn.* 56, 650–661. doi:10.1007/s10236-006-0080-3

Bricaud, C., Drillet, Y., and Garric, G. (2018). Ocean Mass and Heat Transport. In Copernicus Marine Service Ocean State Report. *J. Oper. Oceanogr.* 11, s1–s142. doi:10.1080/1755876X.2018.1489208

Brivoal, T., Samson, G., Giordani, H., Bourdallé-Badie, R., Lemarié, F., and Madec, G. (2020). Impact of the Current Feedback on Kinetic Energy Over the North-East Atlantic from a Coupled Ocean/atmospheric Boundary Layer Model. *Ocean Sci. Discuss.* 1–27. doi:10.5194/os-2020-78

Brodeau, L., Barnier, B., Gulev, S. K., and Woods, C. (2017). Climatologically Significant Effects of Some Approximations in the Bulk Parameterizations of Turbulent Air-Sea Fluxes. *J. Phys. Oceanogr.* 47, 5–28. doi:10.1175/JPO-D-16-0169.1

Cabanes, C., Grouazel, A., von Schuckmann, K., Hamon, M., Turpin, V., Coatanoan, C., et al. (2013). The CORA Dataset: Validation and Diagnostics of *In-Situ* Ocean Temperature and Salinity Measurements. *Ocean Sci.* 9, 1–18. doi:10.5194/os-9-1-2013

Carton, J. A., Giese, B. S., and Grodsky, S. A. (2005). Sea Level Rise and the Warming of the Oceans in the Simple Ocean Data Assimilation (SODA) Ocean Reanalysis. *J. Geophys. Res.* 110. doi:10.1029/2004JC002817

Carton, J. A., and Hackert, E. C. (1989). Application of Multi-Variate Statistical Objective Analysis to the Circulation in the Tropical Atlantic Ocean. *Dyn. Atmospheres Oceans* 13, 491–515. doi:10.1016/0377-0265(89)90051-1

Cavalieri, D. J., Parkinson, C. L., Gloersen, P., and Zwally, H. J. (1997). *Arctic and Antarctic Sea Ice Concentrations from Multichannel Passive-Microwave Satellite Data Sets: October 1978-September 1995 - User's Guide. NASA Technical Memorandum 104647*. Greenbelt, MD: Goddard Space Flight Center.

Chassignet, E. P., and Xu, X. (2017). Impact of Horizontal Resolution (1/12° to 1/50°) on Gulf Stream Separation, Penetration, and Variability. *J. Phys. Oceanogr.* 47, 1999–2021. doi:10.1175/JPO-D-17-0031.1

Chassignet, E. P., Yeager, S. G., Fox-Kemper, B., Bozec, A., Castruccio, F., Danabasoglu, G., et al. (2020). Impact of Horizontal Resolution on Global Ocean-Sea Ice Model Simulations Based on the Experimental Protocols of the Ocean Model Intercomparison Project Phase 2 (OMIP-2). *Geosci. Model. Dev.* 13, 4595–4637. doi:10.5194/gmd-13-4595-2020

Chelton, D. B., Esbensen, S. K., Schlax, M. G., Thum, N., Freilich, M. H., Wentz, F. J., et al. (2001). Observations of Coupling between Surface Wind Stress and Sea Surface Temperature in the Eastern Tropical Pacific. *J. Clim.* 14, 1479–1498. doi:10.1175/1520-0442(2001)014<1479:oocbsw>2.0.co;2

Chen, J. L., Wilson, C. R., Tapley, B. D., Famiglietti, J. S., and Rodell, M. (2005). Seasonal Global Mean Sea Level Change from Satellite Altimeter, GRACE, and Geophysical Models. *J. Geodesy* 79, 532–539. doi:10.1007/s00190-005-0005-9

Chenillat, F., Huck, T., Maes, C., Grima, N., and Blanke, B. (2021). Fate of Floating Plastic Debris Released along the Coasts in a Global Ocean Model. *Mar. Pollut. Bull.* 165, 112116. doi:10.1016/j.marpolbul.2021.112116

Chevallier, M., Smith, G. C., Dupont, F., Lemieux, J.-F., Forget, G., Fujii, Y., et al. (2017). Intercomparison of the Arctic Sea Ice Cover in Global Ocean-Sea Ice Reanalyses from the ORA-IP Project. *Clim. Dyn.* 49, 1107–1136. doi:10.1007/s00382-016-2985-y

Church, J. A., Clark, P. U., Cazenave, A., Gregory, J. M., Jevrejeva, S., Levermann, A., et al. (2013). "Sea Level Change," in *Climate Change 2013: The Physical Science Basis. Contribution of Working Group I to the Fifth Assessment Report of the Intergovernmental Panel on Climate Change*. Editors T. F. Stocker, D. Qin, and G.-K. Plattner (Cambridge, NY: Cambridge University Press), 1137–1216.

Comiso, J. J. (2000). *Bootstrap Sea Ice Concentrations from Nimbus-7 SMMR and DMSP SSM/I-SSMIS, Version 2* (Boulder, Colorado: NASA National Snow and Ice Data Center Distributed Active Archive Center).

Cosme, E., Brankart, J.-M., Verron, J., Brasseur, P., and Krysta, M. (2010). Implementation of a Reduced Rank Square-Root Smoother for High Resolution Ocean Data Assimilation. *Ocean Model.* 33, 87–100. doi:10.1016/j.ocemod.2009.12.004

Cravatte, S., Kestenare, E., Marin, F., Dutrieux, P., and Firing, E. (2017). Subthermocline and Intermediate Zonal Currents in the Tropical Pacific Ocean: Paths and Vertical Structure. *J. Phys. Oceanography* 47 (9), 2305–2324. doi:10.1175/jpo-d-17-0043.1

Crosnier, L., Barnier, B., and Treguier, A. M. (2001). Aliasing Inertial Oscillations in a 1/6° Atlantic Circulation Model: Impact on the Mean Meridional Heat Transport. *Ocean Model.* 3, 21–31. doi:10.1016/S1463-5003(00)00015-9

Dangendorf, S., Hay, C., Calafat, F. M., Marcos, M., Piecuch, C. G., Berk, K., et al. (2019). Persistent Acceleration in Global Sea-Level Rise since the 1960s. *Nat. Clim. Chang.* 9, 705–710. doi:10.1038/s41558-019-0531-8

Dee, D. P., Uppala, S. M., Simmons, A. J., Berrisford, P., Poli, P., Kobayashi, S., et al. (2011). The ERA-Interim Reanalysis: Configuration and Performance of the Data Assimilation System. *Q.J.R. Meteorol. Soc.* 137, 553–597. doi:10.1002/qj.828

Desroziers, G., Berre, L., Chapnik, B., and Poli, P. (2005). Diagnosis of Observation, Background and Analysis-Error Statistics in Observation Space. *Q. J. R. Meteorol. Soc.* 131, 3385–3396. doi:10.1256/qj.05.108

Dombrowsky, E., Bertino, L., Brassington, G., Chassignet, E., Davidson, F., Hurlburt, H., et al. (2009). GODAE Systems in Operation. *Oceanog.* 22, 80–95. doi:10.5670/oceanog.2009.68

Donohue, K. A., Tracey, K. L., Watts, D. R., Chidichimo, M. P., and Chereskin, T. K. (2016). Mean Antarctic Circumpolar Current Transport Measured in Drake Passage. *Geophys. Res. Lett.* 43 (11), 760–767. doi:10.1002/2016GL070319

Drucker, R., Martin, S., and Moritz, R. (2003). Observations of Ice Thickness and Frazil Ice in the St. Lawrence Island Polynya from Satellite Imagery, Upward Looking Sonar, and Salinity/Temperature Moorings. *J. Geophys. Res.* 108 (C5), 3149. doi:10.1029/2001JC001213

Dufau, C., Orsztynowicz, M., Dibarboure, G., Morrow, R., and Le Traon, P. Y. (2016). Mesoscale Resolution Capability of Altimetry: Present and Future. *J. Geophys. Res. Oceans* 121, 4910–4927. doi:10.1002/2015JC010904

Ezraty, R., Girard-Ardhuin, F., Piolle, J. F., Kaleschke, L., and Heygster, G. (2007). *Arctic and Antarctic Sea Ice Concentration and Arc-Tic Sea Ice Drift Estimated from Special Sensor Microwave Data*. 2.1 Edn. (Brest, France and University of Bremen, Germany: Department d'Oceanographie Physique et Spatiale, IFREMER).

Fahrbach, E., Meincke, J., Østerhus, S., Rohardt, G., Schauer, U., Tverberg, V., et al. (2001). Direct Measurements of Volume Transports through Fram Strait. *Polar Res.* 20, 217–224. doi:10.3402/polar.v20i2.6520

Forget, G., and Ponte, R. M. (2015). The Partition of Regional Sea Level Variability. *Prog. Oceanogr.* 137, 173–195. doi:10.1016/j.pocean.2015.06.002

Ganachaud, A., and Wunsch, C. (2003). Large-Scale Ocean Heat and Freshwater Transports During the World Ocean Circulation Experiment. *J. Clim.* 16, 696–705. doi:10.1175/1520-0442(2003)016<0696:lsohaf>2.0.co;2

Garric, G., Parent, L., Greiner, E., Drévillon, M., Hamon, M., Lellouche, J. M., et al. (2018). "Performance and Quality Assessment of the Global Ocean Eddy-Permitting Physical Reanalysis GLORYS2V4 Operational Oceanography Serving Sustainable Marine Development," in Proceedings of the 8th EuroGOOS International Conference. Bergen, Norway, October 3–5, 2017. Editors E. Buch, V. Fernandez, G. Nolan, and D. Eparkhina (Brussels, Belgium: EuroGOOS), 516.

Gasparin, F., Cravatte, S., Greiner, E., Perruche, C., Hamon, M., Van Gennip, S., et al. (2021). Excessive Productivity and Heat Content in Tropical Pacific Analyses: Disentangling the Effects of *In Situ* and Altimetry Assimilation. *Ocean Model.* 160, 101768. doi:10.1016/j.ocemod.2021.101768

Good, S. A., Martin, M. J., and Rayner, N. A. (2013). EN4: Quality Controlled Ocean Temperature and Salinity Profiles and Monthly Objective Analyses with Uncertainty Estimates. *J. Geophys. Res. Oceans* 118, 6704–6716. doi:10.1002/2013JC009067

Gregory, J. M., Griffies, S. M., Hughes, C. W., Lowe, J. A., Church, J. A., Fukimori, I., et al. (2019). Concepts and Terminology for Sea Level: Mean, Variability and Change, Both Local and Global. *Surv. Geophys.* 40, 1251–1289. doi:10.1007/s10712-019-09525-z

Greiner, E., and Perigaud, C. (1994). Assimilation of Geosat Altimetric Data in a Nonlinear Reduced-Gravity Model of the Indian Ocean. Part 1: Adjoint Approach and Model-Data Consistency. *J. Phys. Oceanogr.* 24, 1783–1804. doi:10.1175/1520-0485(1994)024<1783:aogadi>2.0.co;2

Greiner, E., Garric, G., Melet, A., and Bricaud, C. (2021). The Copernicus Global 1/12° Oceanic and Sea Ice Reanalysis, EGU General Assembly 2021, online, April 19–30, 2021, . EGU21-14961.

Grodsky, S. A., Lumpkin, R., and Carton, J. A. (2011). Spurious Trends in Global Surface Drifter Currents. *Geophys. Res. Lett.* 38, L10606. doi:10.1029/2011GL047393

Gutknecht, E., Reffray, G., Gehlen, M., Triyulianti, I., Berlianty, D., and Gaspar, P. (2016). Evaluation of an Operational Ocean Model Configuration at 1/12° Spatial Resolution for the Indonesian Seas (NEMO2.3/INDO12) - Part 2: Biogeochemistry. *Geosci. Model. Dev.* 9, 1523–1543. doi:10.5194/gmd-9-1523-2016

Haines, K., Valdivieso, M., Zuo, H., and Stepanov, V. N. (2012). Transports and Budgets in a 1/4° Global Ocean Reanalysis 1989-2010. *Ocean Sci.* 8, 333–344. doi:10.5194/os-8-333-2012

Hamlington, B. D., Strassburg, M. W., Leben, R. R., Han, W., Nerem, R. S., and Kim, K.-Y. (2014). Uncovering an Anthropogenic Sea-Level Rise Signal in the Pacific Ocean. *Nat. Clim Change* 4, 782–785. doi:10.1038/nclimate2307

Hamon, M., Greiner, E., Le Traon, P.-Y., and Remy, E. (2019). Impact of Multiple Altimeter Data and Mean Dynamic Topography in a Global Analysis and Forecasting System. *J. Atmos. Oceanic Technology* 36, 1255–1266. doi:10.1175/JTECH-D-18-0236.1

Hayes, S. P., McPhaden, M. J., and Wallace, J. M. (1989). The Influence of Sea-Surface Temperature on Surface Wind in the Eastern Equatorial Pacific: Weekly to Monthly Variability. *J. Clim.* 2, 1500–1506. doi:10.1175/1520-0442(1989)002<1500:tiosst>2.0.co;2

Hewitt, H. T., Roberts, M. J., Hyder, P., Graham, T., Rae, J., Belcher, S. E., et al. (2016). The Impact of Resolving the Rossby Radius at Mid-latitudes in the Ocean: Results from a High-Resolution Version of the Met Office GC2 Coupled Model. *Geosci. Model. Dev.* 9, 3655–3670. doi:10.5194/gmd-9-3655-2016

Hewitt, H. T., Roberts, M., Mathiot, P., Biastoch, A., Blockley, E., Chassignet, E. P., et al. (2020). Resolving and Parameterising the Ocean Mesoscale in Earth System Models. *Curr. Clim. Change Rep.* 6, 137–152. doi:10.1007/s40641-020-00164-w

Hilburn, K. A. (2009). The Passive Microwave Water Cycle Product. Report Number 072409. Santa Rosa, CA: Remote Sensing System, 30.

Ivanova, N., Pedersen, L. T., Tonboe, R. T., Kern, S., Heygster, G., Lavergne, T., et al. (2015). Inter-Comparison and Evaluation of Sea Ice Algorithms: towards Further Identification of Challenges and Optimal Approach Using Passive Microwave Observations. *Cryosphere* 9, 1797–1817. doi:10.5194/tc-9-1797-2015

Jackson, L. C., Dubois, C., Forget, G., Haines, K., Harrison, M., Iovino, D., et al. (2019). The Mean State and Variability of the North Atlantic Circulation: A Perspective from Ocean Reanalyses. *J. Geophys. Res. Oceans* 124, 9141–9170. doi:10.1029/2019JC015210

Koenig, Z., Provost, C., Ferrari, R., Sennéchael, N., and Rio, M.-H. (2014). Volume Transport of the Antarctic Circumpolar Current: Production and Validation of a 20 Year Long Time Series Obtained from *In Situ* and Satellite Observations. *J. Geophys. Res. Oceans* 119, 5407–5433. doi:10.1002/2014JC009966

Krishfield, R. A., Proshutinsky, A., Tateyama, K., Williams, W. J., Carmack, E. C., McLaughlin, F. A., et al. (2014). Deterioration of Perennial Sea Ice in the Beaufort Gyre from 2003 to 2012 and its Impact on the Oceanic Freshwater Cycle. *J. Geophys. Res. Oceans* 119 (2), 1271–1305. doi:10.1002/2013JC008999

Large, W. G., and Yeager, S. G. (2009). The Global Climatology of an Interannually Varying Air-Sea Flux Data Set. *Clim. Dyn.* 33, 341–364. doi:10.1007/s00382-008-0441-3

Law Chune, S., and Aouf, L. (2018). Wave Effects in Global Ocean Modeling: Parametrizations vs. Forcing from a Wave Model. *Ocean Dyn.* 68, 1739–1758. doi:10.1007/s10236-018-1220-2

Le Traon, P. Y. (2013). From Satellite Altimetry to Argo and Operational Oceanography: Three Revolutions in Oceanography. *Ocean Sci.* 9, 901–915. doi:10.5194/os-9-901-2013

Le Traon, P. Y., Reppucci, A., Alvarez Fanjul, E., Aouf, L., Behrens, A., Belmonte, M., et al. (2019). From Observation to Information and Users: The Copernicus Marine Service Perspective. *Front. Mar. Sci.* 6, 234. doi:10.3389/fmars.2019.00234

Lebedev, K. V., Yoshinari, H., Maximenko, N. A., and Hacker, P. W. (2007). YoMaHa'07: Velocity Data Assessed from Trajectories of Argo Floats at Parking Level and at the Sea Surface IPRC Technical Note No. 4, Honolulu, Hawaii. doi:10.13140/RG.2.2.12820.71041

Legeais, J. F., Llovel, W., Melet, A., and Meyssignac, B. (2019). Copernicus Marine Service Ocean State Report, Issue 3. *J. Oper. Oceanogr.* 12, s77–s82. doi:10.1080/1755876X.2020.1785097

Lellouche, J.-M., Greiner, E., Le Galloudec, O., Garric, G., Regnier, C., Drevillon, M., et al. (2018). Recent Updates to the Copernicus Marine Service Global Ocean Monitoring and Forecasting Real-Time 1/12° High-Resolution System. *Ocean Sci.* 14, 1093–1126. doi:10.5194/os-14-1093-2018

Lellouche, J.-M., Le Galloudec, O., Drévillon, M., Régnier, C., Greiner, E., Garric, G., et al. (2013). Evaluation of Global Monitoring and Forecasting Systems at Mercator Océan. *Ocean Sci.* 9, 57–81. doi:10.5194/os-9-57-2013

Lemarié, F., Samson, G., Redelsperger, J.-L., Giordani, H., Brivoal, T., and Madec, G. (2021). A Simplified Atmospheric Boundary Layer Model for an Improved Representation of Air-Sea Interactions in Eddying Oceanic Models: Implementation and First Evaluation in NEMO (4.0). *Geosci. Model. Dev.* 14, 543–572. doi:10.5194/gmd-14-543-2021

Lindzen, R. S., and Nigam, S. (1987). On the Role of Sea Surface Temperature Gradients in Forcing Low-Level Winds and Convergence in the Tropics. *J. Atmos. Sci.* 44, 2418–2436. doi:10.1175/1520-0469(1987)044<2418:otross>2.0.co;2

Locarnini, R. A., Mishonov, A. V., Antonov, J. I., Boyer, T. P., Garcia, H. E., Baranova, O. K., et al. (2013). in "World Ocean Atlas 2013," in *Volume 1: Temperature*. Editors S. Levitus and A. Mishonov (Silver Spring, Maryland: NOAA Atlas NESDIS 73), 40.

Lumpkin, R., and Speer, K. (2007). Global Ocean Meridional Overturning. *J. Phys. Oceanogr.* 37, 2550–2562. doi:10.1175/JPO3130.1

MacLachlan, C., Arribas, A., Peterson, K. A., Maidens, A., Fereday, D., Scaife, A. A., et al. (2015). Global Seasonal Forecast System Version 5 (GloSea5): A High-Resolution Seasonal Forecast System. *Q.J.R. Meteorol. Soc.* 141, 1072–1084. doi:10.1002/qj.2396

Madec, G., Bourdallé-Badie, R., Chanut, J., Clementi, E., Coward, A., Ethé, C., et al. (2019). *NEMO Ocean Engine*. Paris: Notes Du Pôle De Modéisation De L'institut Pierre-Simon Laplace (IPSL).

Madec, G.The NEMO Team (2008). *NEMO Ocean Engine, Note du Pôle de modélisation*. France: Institut Pierre-Simon Laplace (IPSL), 1288–1619.

Magnusson, L., Alonso-Balmaseda, M., Corti, S., Molteni, F., and Stockdale, T. (2013). Evaluation of Forecast Strategies for Seasonal and Decadal Forecasts in Presence of Systematic Model Errors. *Clim. Dyn.* 41, 2393–2409. doi:10.1007/s00382-012-1599-2

Masina, S., Storto, A., Ferry, N., Valdivieso, M., Haines, K., Balmaseda, M., et al. (2017). An Ensemble of Eddy-Permitting Global Ocean Reanalyses from the MyOcean Project. *Clim. Dyn.* 49, 813–841. doi:10.1007/s00382-015-2728-5

Meehl, G. A., Boer, G. J., Covey, C., Latif, M., and Stouffer, R. J. (2000). The Coupled Model Intercomparison Project (CMIP). *Bull. Amer. Meteorol. Soc.* 81, 313–318. doi:10.1175/1520-0477(2000)081<0313:TCMIPC>2.3

Minobe, S., Kuwano-Yoshida, A., Komori, N., Xie, S.-P., and Small, R. J. (2008). Influence of the Gulf Stream on the Troposphere. *Nature* 452, 206–209. doi:10.1038/nature06690

Oppenheimer, M., Glavovic, B. C., Hinkel, J., van de Wal, R., Magnan, A. K., Abd-Elgawad, A., et al. (2019). "Sea Level Rise and Implications for Low Lying Islands, Coasts and Communities," in *IPCC Special Report on the Ocean and Cryosphere in a Changing Climate*. Editor H. O. Pörtner, 169. Available at: https://report.ipcc.ch/srocc/pdf/SROCC_FinalDraft_Chapter4.pdf.

Parfitt, R., Czaja, A., and Kwon, Y.-O. (2017). The Impact of SST Resolution Change in the ERA-Interim Reanalysis on Wintertime Gulf Stream Frontal Air-Sea Interaction. *Geophys. Res. Lett.* 44, 3246–3254. doi:10.1002/2017GL073028

Peltier, W. R. (2004). Global Glacial Isostasy and the Surface of the Ice-Age Earth: The ICE-5G (VM2) Model and GRACE. *Annu. Rev. Earth Planet. Sci.* 32, 111–149. doi:10.1146/annurev.earth.32.082503.144359

Poli, L., Artana, C., Provost, C., Sirven, J., Sennéchael, N., Cuypers, Y., et al. (2020). Anatomy of Subinertial Waves along the Patagonian Shelf Break in a 1/12° Global Operational Model. *J. Geophys. Res. Oceans* 125. doi:10.1029/2020JC016549

Prandi, P., Meyssignac, B., Ablain, M., Spada, G., Ribes, A., and Benveniste, J. (2021). Local Sea Level Trends, Accelerations and Uncertainties Over 1993-2019. *Sci. Data* 8, 1. doi:10.1038/s41597-020-00786-7

Pujol, M.-I., Faugère, Y., Taburet, G., Dupuy, S., Pelloquin, C., Ablain, M., et al. (2016). DUACS DT2014: the New Multi-mission Altimeter Data Set Reprocessed over 20 Years. *Ocean Sci.* 12, 1067–1090. doi:10.5194/os-12-1067-2016

Renault, L., Masson, S., Arsouze, T., Madec, G., and McWilliams, J. C. (2020). Recipes for How to Force Oceanic Model Dynamics. *J. Adv. Model. Earth Syst.* 12, e2019MS001715. doi:10.1029/2019MS001715

Renault, L., McWilliams, J. C., and Masson, S. (2017). Satellite Observations of Imprint of Oceanic Current on Wind Stress by Air-Sea Coupling. *Sci. Rep.* 7, 17747. doi:10.1038/s41598-017-17939-1

Ricker, R., Hendricks, S., Helm, V., Skourup, H., and Davidson, M. (2014). Sensitivity of CryoSat-2 Arctic Sea-Ice Freeboard and Thickness on Radar-Waveform Interpretation. *The Cryosphere* 8, 1607–1622. doi:10.5194/tc-8-1607-2014

Rio, M.-H., and Etienne, H. (2019). *Global Ocean Delayed Mode* In-Situ *Observations of Ocean Surface Currents* SEANOE.

Rio, M.-H., Pascual, A., Poulain, P.-M., Menna, M., Barceló, B., and Tintoré, J. (2014). Computation of a New Mean Dynamic Topography for the Mediterranean Sea from Model Outputs, Altimeter Measurements and Oceanographic *In Situ* Data. *Ocean Sci.* 10, 731–744. doi:10.5194/os-10-731-2014

Roach, L. A., Dean, S. M., and Renwick, J. A. (2018). Consistent Biases in Antarctic Sea Ice Concentration Simulated by Climate Models. *Cryosphere* 12, 365–383. doi:10.5194/tc-12-365-2018

Roquet, F., Charrassin, J.-B., Marchand, S., Boehme, L., Fedak, M., Reverdin, G., et al. (2011). Delayed-Mode Calibration of Hydrographic Data Obtained from Animal-Borne Satellite Relay Data Loggers. *J. Atmos. Ocean. Technol.* 28, 787–801. doi:10.1175/2010JTECHO801.1

Rose, S. K., Andersen, O. B., Passaro, M., Ludwigsen, C. A., and Schwatke, C. (2019). Arctic Ocean Sea Level Record from the Complete Radar Altimetry Era: 1991-2018. *Remote Sens.* 11, 1672. doi:10.3390/rs11141672

Rousset, C., Vancoppenolle, M., Madec, G., Fichefet, T., Flavoni, S., Barthélemy, A., et al. (2015). The Louvain-La-Neuve Sea Ice Model LIM3.6: Global and Regional Capabilities. *Geosci. Model. Dev.* 8, 2991–3005. doi:10.5194/gmd-8-2991-2015

Schweiger, A., Lindsay, R., Zhang, J., Steele, M., Stern, H., and Kwok, R. (2011). Uncertainty in Modeled Arctic Sea Ice Volume. *J. Geophys. Res.* 116. doi:10.1029/2011JC007084

Small, R. J., deSzoeke, S. P., Xie, S. P., O'Neill, L., Seo, H., Song, Q., et al. (2008). Air-sea Interaction over Ocean Fronts and Eddies. *Dyn. Atmos. Oceans* 45, 274–319. doi:10.1016/j.dynatmoce.2008.01.001

Spall, M. A. (2007). Midlatitude Wind Stress-Sea Surface Temperature Coupling in the Vicinity of Oceanic Fronts. *J. Clim.* 20, 3785–3801. doi:10.1175/JCLI4234.1

Stackhouse, P. W., Zhang, T., Colleen Mikovitz, J., and Hinkelman, L. M. (2011). The NASA/GEWEX Surface Radiation Budget Release 3.0: 24.5-Year Dataset. *GEWEX News* 21 (1), 10–12.

Stammer, D., Ueyoshi, K., Köhl, A., Large, W. G., Josey, S. A., and Wunsch, C. (2004). Estimating Air-Sea Fluxes of Heat, Freshwater, and Momentum Through Global Ocean Data Assimilation. *J. Geophys. Res.* 109, C05023. doi:10.1029/2003JC002082

Storto, A., Alvera-Azcárate, A., Balmaseda, M. A., Barth, A., Chevallier, M., Counillon, F., et al. (2019b). Ocean Reanalyses: Recent Advances and Unsolved Challenges. *Front. Mar. Sci.* 6. doi:10.3389/fmars.2019.00418

Storto, A., Masina, S., Simoncelli, S., Iovino, D., Cipollone, A., Drevillon, M., et al. (2019a). The Added Value of the Multi-System Spread Information for Ocean Heat Content and Steric Sea Level Investigations in the CMEMS GREP Ensemble Reanalysis Product. *Clim. Dyn.* 53, 287–312. doi:10.1007/s00382-018-4585-5

Storto, A., Yang, C., and Masina, S. (2017). Constraining the Global Ocean Heat Content through Assimilation of CERES-Derived TOA Energy Imbalance Estimates. *Geophys. Res. Lett.* 44 (10), 520–529. doi:10.1002/2017GL075396

Szekely, T., Gourrion, J., Pouliquen, S., and Reverdin, G. (2019). CORA, Coriolis Ocean Dataset for Reanalysis. *SEANOE*. doi:10.17882/46219

Taburet, G., Sanchez-Roman, A., Ballarotta, M., Pujol, M.-I., Legeais, J.-F., Fournier, F., et al. (2019). DUACS DT2018: 25 Years of Reprocessed Sea Level Altimetry Products. *Ocean Sci.* 15, 1207–1224. doi:10.5194/os-15-1207-2019

Talley, L. D., Reid, J. L., and Robbins, P. E. (2003). Data-Based Meridional Overturning Streamfunctions for the Global Ocean. *J. Clim.* 16, 3213–3226. doi:10.1175/1520-0442(2003)016<3213:DMOSFT>2.0.CO;2

Thoppil, P. G., Richman, J. G., and Hogan, P. J. (2011). Energetics of a Global Ocean Circulation Model Compared to Observations. *Geophys. Res. Lett.* 38. doi:10.1029/2011GL048347

Tietsche, S., Notz, D., Jungclaus, J. H., and Marotzke, J. (2013). Assimilation of Sea-Ice Concentration in a Global Climate Model - Physical and Statistical Aspects. *Ocean Sci.* 9, 19–36. doi:10.5194/os-9-19-2013

Tranchant, B., Reffray, G., Greiner, E., Nugroho, D., Koch-Larrouy, A., and Gaspar, P. (2016). Evaluation of an Operational Ocean Model Configuration at 1/12° Spatial Resolution for the Indonesian Seas (NEMO2.3/INDO12) - Part 1: Ocean Physics. *Geosci. Model. Dev.* 9, 1037–1064. doi:10.5194/gmd-9-1037-2016

Traon, P. Y. L., and Dibarboure, G. (2002). Velocity Mapping Capabilities of Present and Future Altimeter Missions: The Role of High-Frequency Signals. *J. Atmos. Ocean. Technol.* 19, 2077–2087. doi:10.1175/1520-0426(2002)019<2077:vmcopa>2.0.co;2

Turner, J., Phillips, T., Marshall, G. J., Hosking, J. S., Pope, J. O., Bracegirdle, T. J., et al. (2017). Unprecedented Springtime Retreat of Antarctic Sea Ice in 2016. *Geophys. Res. Lett.* 44, 6868–6875. doi:10.1002/2017GL073656

Uotila, P., Goosse, H., Haines, K., Chevallier, M., Barthélemy, A., Bricaud, C., et al. (2019). An Assessment of Ten Ocean Reanalyses in the Polar Regions. *Clim. Dyn.* 52, 1613–1650. doi:10.1007/s00382-018-4242-z

Valdivieso, M., Haines, K., Balmaseda, M., Chang, Y.-S., Drevillon, M., Ferry, N., et al. (2017). An Assessment of Air-Sea Heat Fluxes from Ocean and Coupled Reanalyses. *Clim. Dyn.* 49, 983–1008. doi:10.1007/s00382-015-2843-3

Verezemskaya, P., Barnier, B., Gulev, S. K., Gladyshev, S., Molines, J. M., Gladyshev, V., et al. (2021). Assessing Eddying (1/12°) Ocean Reanalysis GLORYS12 Using the 14-yr Instrumental Record from 59.5°N Section in the Atlantic. *J. Geophys. Res. Oceans* 126. doi:10.1029/2020JC016317

Vidard, A., Balmaseda, M., and Anderson, D. (2009). Assimilation of Altimeter Data in the ECMWF Ocean Analysis System 3. *Monthly Weather Rev.* 137, 1393–1408. doi:10.1175/2008MWR2668.1

von Schuckmann, K., Le Traon, P.-Y., Smith, N., Pascual, A., Djavidnia, S., Gattuso, J.-P., et al. (2020). Copernicus Marine Service Ocean State Report, Issue 4. *J. Oper. Oceanogr.* 13, S1–S172. doi:10.1080/1755876X.2020.1785097

Woodgate, R. A., Aagaard, K., and Weingartner, T. J. (2006). Interannual Changes in the Bering Strait Fluxes of Volume, Heat and Freshwater Between 1991 and 2004. *Geophys. Res. Lett.* 33, L15609. doi:10.1029/2006GL026931

Woodgate, R. A. (2018). Increases in the Pacific Inflow to the Arctic from 1990 to 2015, and Insights into Seasonal Trends and Driving Mechanisms from Year-Round Bering Strait Mooring Data. *Prog. Oceanogr.* 160, 124–154. doi:10.1016/j.pocean.2017.12.007

Yuan, N., Ding, M., Ludescher, J., and Bunde, A. (2017). Increase of the Antarctic Sea Ice Extent Is Highly Significant Only in the Ross Sea. *Sci. Rep.* 7, 41096. doi:10.1038/srep41096

Zuo, H., Balmaseda, M. A., Tietsche, S., Mogensen, K., and Mayer, M. (2019). The ECMWF Operational Ensemble Reanalysis-Analysis System for Ocean and Sea Ice: A Description of the System and Assessment. *Ocean Sci.* 15, 779–808. doi:10.5194/os-15-779-2019

Zweng, M. M., Reagan, J. R., Antonov, J. I., Locarnini, R. A., Mishonov, A. V., Boyer, T. P., et al. (2013). "World Ocean Atlas 2013," in *Volume 2: Salinity*. Editors S. Levitus and A. Mishonov (Silver Spring, Maryland: NOAA Atlas NESDIS 74), 39.

Conflict of Interest: Authors LJ-M, B-BM, GG, MA, DM, BC, HM, LO, RC, CT, TC-E, GF, RG, BM, DY, and LP-Y were employed by the company Mercator Ocean International. Author GE was employed by the company Collecte Localisation Satellites.

frontiers in Environmental Science

ORIGINAL RESEARCH
published: 31 August 2021
doi: 10.3389/fenvs.2021.711363

A New Global Ocean Climatology

Kanwal Shahzadi[1*†], *Nadia Pinardi*[1†], *Alexander Barth*[2†], *Charles Troupin*[2†], *Vladyslav Lyubartsev*[3†] *and Simona Simoncelli*[4†]

[1]Department of Physics and Astronomy, University of Bologna, Bologna, Italy, [2]GeoHydrodynamics and Environment Research, University of Liege, Liege, Belgium, [3]Euro-Mediterranean Center on Climate Change Foundation, Bologna, Italy, [4]Istituto Nazionale di Geofisica e Vulcanologia (INGV), Bologna, Italy

OPEN ACCESS

Edited by:
Hiroyuki Tsujino,
Meteorological Research Institute, Japan

Reviewed by:
Lijing Cheng,
Institute of Atmospheric Physics (CAS), China
Viktor Gouretski,
Chinese Academy of Sciences (CAS), China

***Correspondence:**
Kanwal Shahzadi
kanwal.shahzadi3@unibo.it

†ORCID:
Nadia Pinardi
orcid.org/0000-0003-4765-0775
Kanwal Shahzadi
orcid.org/0000-0001-6208-1844
Alexander Barth
orcid.org/0000-0003-2952-5997
Charles Troupin
orcid.org/0000-0002-0265-1021
Vladyslav Lyubartsev
orcid.org/0000-0001-5596-7823
Simona Simocelli
orcid.org/0000-0003-1283-2798

Specialty section:
This article was submitted to Interdisciplinary Climate Studies, a section of the journal Frontiers in Environmental Science

Received: 18 May 2021
Accepted: 16 August 2021
Published: 31 August 2021

Citation:
Shahzadi K, Pinardi N, Barth A, Troupin C, Lyubartsev V and Simoncelli S (2021) A New Global Ocean Climatology. Front. Environ. Sci. 9:711363. doi: 10.3389/fenvs.2021.711363

A new global ocean temperature and salinity climatology is proposed for two time periods: a long time mean using multiple sensor data for the 1900–2017 period and a shorter time mean using only profiling float data for the 2003–2017 period. We use the historical database of World Ocean Database 2018. The estimation approach is novel as an additional quality control procedure is implemented, along with a new mapping algorithm based on Data Interpolating Variational Analysis. The new procedure, in addition to the traditional quality control approach, resulted in low sensitivity in terms of the first guess field choice. The roughness index and the root mean square of residuals are new indices applied to the selection of the free mapping parameters along with sensitivity experiments. Overall, the new estimates were consistent with previous climatologies, but several differences were found. The cause of these discrepancies is difficult to identify due to several differences in the procedures. To minimise these uncertainties, a multi-model ensemble mean is proposed as the least uncertain estimate of the global ocean temperature and salinity climatology.

Keywords: global ocean climatologies, temperature analysis, salinity analysis, data interpolating variational analysis, quality control, multi-model ensemble

1 INTRODUCTION

Defining the climatological state of the ocean is a formidable task. Climatology can be defined as the study of the statistics of environmental variables that characterise the ocean's physical and biochemical state. The focus of this work is on estimating the monthly mean values of temperature and salinity in the global ocean using data derived from historical observational records. Climatology is an essential input to numerical ocean models in terms of initialization and validation, and is intrinsically useful for understanding climate anomalies.

Standardising historical observations is a major challenge in climatological studies, in terms of metadata and quality control. The observations are collected from numerous sources and contain various errors. Thus, a robust quality control procedure is essential before any kind of analysis is conducted. Interpolating or mapping the observations is also major step in estimating climatologies. As defined by Daley (1993): "Spatial analysis is the estimation by numerical algorithm of state variables on a three-dimensional regular grid from observations available at irregularly distributed locations." These numerical algorithms are based on theoretical and statistical assumptions that have significantly evolved over the past 20 years. Such techniques are referred as interpolation schemes.

Our analysis is based upon the World Ocean Data (WOD) archive of temperature and salinity profiles, which is probably the most comprehensive archive of data collected in the 20th century. The database already contains quality flagged profiles, which are described later in the paper. We applied

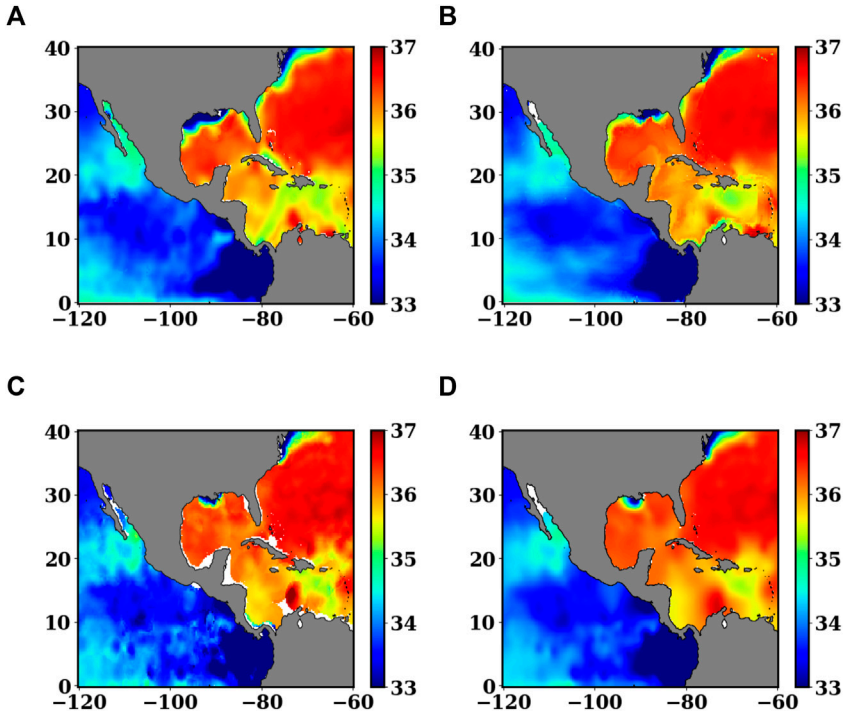

FIGURE 1 | January salinity near the Panama Isthmus. **(A)** WOA18 estimate (correlation length = 214 km, using all data from WOD18), **(B)** WAGHC (correlation length = 333 km, signal to noise ratio = 0.5, using data from WOD13, in particular Ocean Station Data, Conductivity Depth Temperature, Profiling Floats and Autonomous Pinniped, with additional data from the Alfred Wegener Institute, Bremerhaven, and from other institutions in Canada), **(C)** B-OA estimate (correlation length = 300 km and observational error variance = 0.3), and **(D)** DIVAnd estimate (correlation length = 300 km and noise to signal ratio equal to 0.5).

another layer of quality checks to this, which were found to be significant as they eliminate further outliers.

The first global ocean gridded climatology, referred to as the World Ocean Atlas (WOA), was proposed by Levitus (1982) and is the basis for all subsequent estimates. The WOA has been regularly updated every 4 years since 1994. WOA uses the basic interpolation schemes defined by Barnes (1964). We use the latest WOD18 and WOA18 updates (Garcia et al., 2018), and (Locarnini et al., 2019; Zweng et al., 2019). The WOCE (World Ocean Circulation Experiment) Argo Hydrographic Global Ocean Climatology [WAGHC, Gouretski (2019)] is another global ocean climatological estimate and is the first to be produced at isopycnal and isobaric levels. The WAGHC interpolation scheme is based on Objective Analysis (OA) following Gandin (1960). In this study, we propose a new climatology developed within the framework of the SeaDataCloud project (Simoncelli et al., 2021) and computed with the Data Interpolating Variational Analysis [DIVAnd, (Brasseur, 1991), Troupin et al. (2012), and Barth et al. (2014)]. The SeaDataCloud global climatology is available from the SeaDataNet web catalog [1] together with its relative Product Information Document (Shahzadi et al., 2020), (Shahzadi et al., 2020). Hereafter, it will be referred as SDC climatology, and a climatology using the Objective Analysis (OA) interpolation scheme of Bretherton et al. (1976), for the first time adapted to the global ocean by Jia et al. (2016), referred to as B-OA (Bretherton et al., 1976).

An obvious question is why another climatology is required. Climatologies are based on different observational datasets and use different interpolation schemes, so they address uncertainties in different ways. The specific interpolation of observations across land-sea boundaries represents a common uncertainty. Most established interpolating algorithms do not naturally consider objective methods that prohibit the use of observations across land-sea boundaries, which is an important characteristics of our algorithm. To show deviations between climatological interpolating algorithms at the land-ocean interface, we analyzed the differences among climatologies around peninsulas. For example, in the Isthmus of Panama, a narrow land area between the Caribbean Sea and the Pacific Ocean, observations could be misinterpreted, as they span unconnected ocean water masses. **Figure 1** gives a comparison of the four available climatologies, and it is clear that they give very different estimates. In **Figure 1C** the B-OA shows that salinity spreads from the Pacific to the Atlantic along the Columbian coast. By contrast, **Figure 1D** demonstrates that the SDC climatology completely suppresses the contamination of the Caribbean Sea with Pacific Ocean salinities and vice-versa. However, in WAGHC and WOA, despite the use of the separate first guess fields across the Isthmus (Tim Boyer personal communications, and an anonymous reviewer), low salinity anomalies are reported

[1]https://www.nodc.noaa.gov/OC5/WOD/pr_wod.html.

TABLE 1 | Number of profiles and measurements in Dataset1 and Dataset2.

Dataset Name	Temperature profiles	Temperature measurements	Salinity profiles	Salinity measurements
Dataset1	6,012,750	803,362,255	5,265,504	757,320,791
Dataset2	1,658,955	384,430,391	1,557,989	362,928,173

for the Caribbean Sea, which are not present in the other gridded products. As the interpolation scheme and first guess field are computed separately in each basin in these two estimates then salinity variations among these estimates could be due to different observations used or the interpolation scheme. Another difference between climatologies is evident along the Louisiana coasts of the Gulf of Mexico, where the Mississippi river outflow dominates, which could be due to the algorithm, the first guess or the volume of data used in the analyses. Climatologies may therefore differ both qualitatively and quantitatively in general and specific aspects. DIVAnd objectively solves the problem of the interpolation of oceanographic observations across land boundaries, but it is similar to other statistical models as it makes assumptions about the statistical distribution parameters of the ocean variables of interest. Thus, a multi-model ensemble of all available climatologies is likely to provide a more accurate solution, as demonstrated later in this paper.

The main objective of this study is to estimate a global ocean climatology using DIVAnd, after applying proper quality control to the historical dataset. The additional quality control algorithm we use is defined in **section 2.1**. Sensitivity experiments are also conducted for interpolation parameters such as the signal to noise ratio and the field correlation length. Finally, the results are compared with the WOA18 and WAGHC datasets. Those for the B-OA are disregarded because they are similar to the results for the WAGHC.

In **section 2**, the historical datasets used for climatology are reviewed together with the quality control procedure. The interpolation scheme and the implementation domain, together with the choices of the interpolation parameters, are discussed in **section 3**. Monthly mean temperature and salinity fields are compared with those of other climatologies in the **section 4** while the **section 5** concludes the paper.

2 HISTORICAL DATASETS

Two climatology versions were estimated based on two datasets extracted from the World Ocean Database 18 [WOD18, Garcia et al. (2018)]. Dataset1 (see **Table 1**) uses multiple platforms, such as bottle data from Ocean Station Data (OSD) and Conductivity Temperature and Depth (CTD) from ship surveys, Mooring Buoys (MRBs) and Profiling Floats (PFLs). MRB profiles are only distributed across the equatorial and tropical regions, while CTD, OSD and PFL profiles cover the global ocean domain. The data from other available platforms were not used because we considered corresponding measurements of temperature and salinity and an approximately equal number of profiles for the surface and the upper pycnocline. Thus, Expendable Bathythermograph (XBT) and Mechanical Bathythermograph (MBT) data were disregarded because only temperature measurements were available. Drifting Buoy (DRB), and Surface-Only (SUR) data were also not selected because the recordings for these are only taken at the surface, and Autonomous Pinniped Bathythermograph (APB) and gliders (GLD) were not used because they consist of high temporal resolution measurements that are not considered appropriate for climatological estimates. The observations selected for Dataset1 cover 1900 to 2017 and the climatology estimated from this dataset is referred to as SDC_V1.

Dataset2 (see **Table 1**) only contains PFL profiles, which are from autonomous vehicles equipped with several oceanographic sensors. This contains data from manufacturer floats such as PLACE, MARVOR, SOLO and APEX. The Argo program launched in 2000 revolutionised ocean observations, and such floats have since become numerous in all of the world's ocean basins. In Dataset2, only profiling floats from 2003 to 2017 were considered, and the majority of PFLs were APEX floats. PFL measurements before 2003 were not considered because these are affected by problems such as pressure drift (Barker et al., 2011), offsets in the salinity due to biofouling (Wong et al., 2003), (Owens and Wong, 2009) and transmission errors. We therefore only selected consolidated profiles from 2003 to 2017 to avoid erroneous observations. The volume of PFL data from the last 15 years exceeds the data available from all other platforms, as shown in **Figure 2**.

2.1 Additional Quality Control Procedure

WOD implements two types of quality control checks, represented by different quality flags: first an individual value flag (WODf) for each measured point in the vertical for checking systematic errors in the observations; and second a profile flag (WODfp) that denotes a statistical quality check, as explained in Locarnini et al. (2019). In the following text, WODf and WODfp are together referred to as WOD QC. Uncertainties in the ocean historical observations are sum of gross errors and representativeness errors as pointed by Janjić et al. (2018) and Cowley et al. (2021) which defined it as Type A and Type B uncertainty. A more sophisticated automated quality control procedures has been achieved during the last years by the International Quality-Controlled Ocean Database (IQuOD) v0.1. Further IQuoD v0.1 contains only temperature profiles with the uncertainty estimate of gross error (Type A) while quality control of representativeness error (Type B) was out of the scope of the project as mentioned by Cowley et al. (2021). Therefore, we felt there is a need of Additional QC (AQC) to remove the observations containing representativeness error (Type B) and we implemented it as follow:

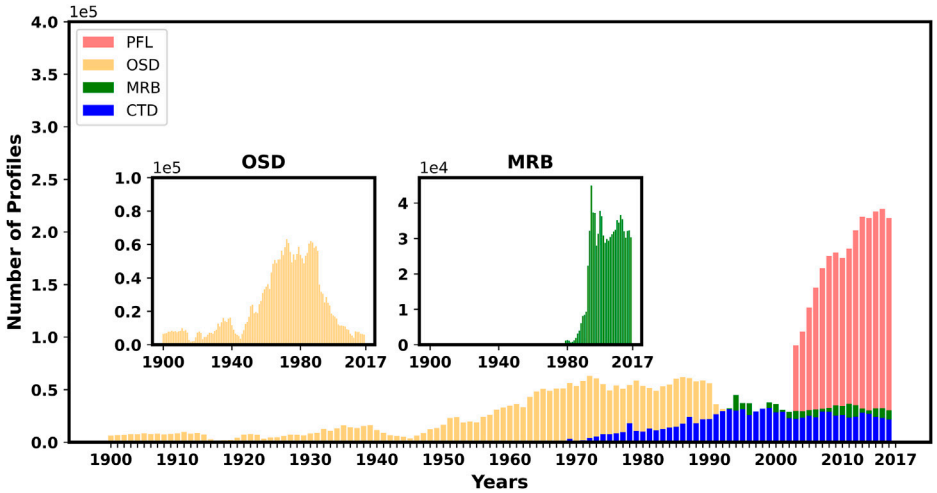

FIGURE 2 | Number of profiles from the four measuring platforms used in this study and extracted from WOD18: Ocean Station Data (OSD); Moored Buoys (MRB); Conductivity Depth Temperature (CTD); and Profiling Floats (PFL).

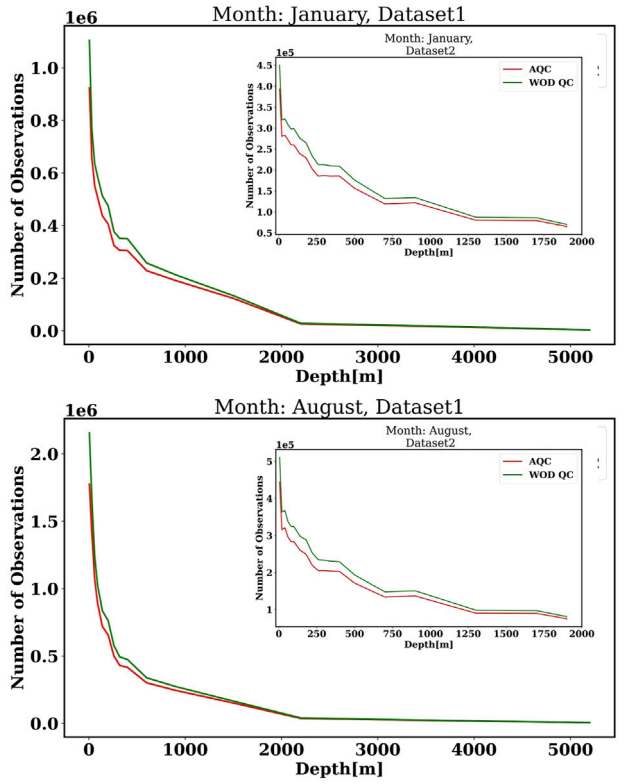

FIGURE 3 | Number of observations (Temperature) using WOD QC and AQC for Dataset1 and Dataset2: January **(top)**; August **(bottom)**.

i) The domain is divided into $5 \times 5^{\circ}$ boxes, where mean and standard deviations (std) are computed and used as thresholds in step (ii).
ii) Data outside 2 std in each box is eliminated and the procedure is repeated until convergence is achieved, which is denoted when no data are greater in value than the std level.

The AQC is iterative, unlike the WOD QC, and it is applied after the WOD QC is considered. The numbers of observations before and after the application of the AQC are given in **Figure 3**. Distribution of salinity observations (January) at surface before and after the application of AQC are shown in **Supplementary Figure S5** in supplementary material. The application of AQC has eliminated the observations with representative error which were still present with WOD18, i.e. (WODf and WODfp) QC. The application of AQC eliminates less than 15% of the total profiles.

3 INTERPOLATION SCHEME

DIVAnd is based on the Variational Inverse Method (VIM) and applied on a curvilinear orthogonal grid using a finite difference scheme (Barth et al., 2014). This method is equivalent to Optimal Interpolation (OI), and the main difference between DIVAnd and OI is in the consideration of land boundaries, as explained in the introduction.

In DIVAnd, the cost function is minimised and contains three terms: the misfit between the observations and the reconstructed Field; the regularity or smoothness constraint; and the advection constraint. This cost function can be written as:

$$J[\phi] = \sum_{i=1}^{N} \mu_i [d_i - \varphi(x_i, y_i)]^2 + \|\varphi - \varphi_b\|^2 + J_c(\varphi), \qquad (1)$$

where d_i are the observations at the location (x_i, y_i), φ is the target field in the regular grid, or the analysis, φ_b is the first guess field or "background" and μ_i are weights derived from specific error estimates (Troupin et al., 2012) and the correlation length L, which are described later. J_c is the advection constraint, in which variable gradients are assumed along the coasts only, thus imposing no normal flux of temperature and salinity across land-sea boundaries. The smoothness constraint is defined as:

TABLE 2 | Depth layers used for SDC climatology: the nominal depth is selected at the middle of each layers. The levels for SDC_V1 extend from 5 m to 6,000 m and for SDC_V2 from 5 to 2000 m.

No	Nominal Depth(m)	Layer	No	Nominal Depth(m)	Layer
1	5	0–10	24	370	365–375
2	10	5–15	25	400	395–405
3	20	15–25	26	450	445–455
4	30	25–35	27	500	495–505
5	40	35–45	28	600	595–605
6	50	45–55	29	700	695–705
7	60	55–65	30	800	795–805
8	70	65–75	31	900	895–905
9	80	75–85	32	1,100	1,095–1,105
10	90	85–95	33	1,300	1,295–1,305
11	100	95–105	34	1,500	1,495–1,505
12	120	115–125	35	1700	1,695–1705
13	140	135–145	36	1900	1895–1905
14	160	155–165	37	2,200	2,195–2,205
15	180	175–185	38	2,700	2,695–2,705
16	200	195–205	39	3,200	3,195–3,205
17	220	215–225	40	3,700	3,695–3,705
18	240	235–245	41	4,200	4,195–4,205
19	260	255–265	42	4,700	4,695–4,705
20	280	275–285	43	5200	5195–5205
21	300	295–305	44	5700	5695–5705
22	320	315–325	45	6,000	5995–6,005
23	340	335–345			

$$\|\varphi - \varphi_b\|^2 = \alpha_2 \int_\Omega (\nabla\nabla\varphi : \nabla\nabla\varphi + \alpha_1 \nabla\varphi.\nabla\varphi + \alpha_0 \varphi^2) d\Omega, \quad (2)$$

The non-dimensional form of the cost function is:

$$\tilde{J}[\phi] = \sum_{i=1}^{N} \mu_i L^2 [d_i - \varphi(x_i, y_i)]^2 + \int_{\tilde{\Omega}} (\tilde{\nabla}\tilde{\nabla}\varphi : \tilde{\nabla}\tilde{\nabla}\varphi + \alpha_1 L^2 \tilde{\nabla}\varphi.\tilde{\nabla}\varphi + \alpha_0 L^4 \varphi^2) d\tilde{\Omega} + J_c(\varphi), \quad (3)$$

: is generalisation of the scalar product of two vectors and is defined as

$$\nabla\nabla\varphi : \nabla\nabla\varphi = \sum_i \sum_j (\partial^2\varphi/\partial x_i \partial x_j)(\partial^2\varphi/\partial x_i \partial x_j). \quad (4)$$

In DIVAnd the following values are assumed:

$$\begin{aligned} \alpha_0 L^4 &= 1 \\ \alpha_1 L^2 &= 2 \\ \alpha_2 &= 1 \\ \mu_i L^2 &= 4\pi \frac{\sigma^2}{\epsilon_i^2} \end{aligned} \quad (5)$$

Equation 5 shows that μ is defined as the ratio of signal variance σ^2, which is considered the background error variance of the observations, ϵ_i^2. For more details of the solution method, see Barth et al. (2014).

The best estimate or analysis depends on the values of two key parameters, the correlation length L and the Noise to Signal ratio (N/S), i.e., $\frac{1}{\mu_i}$ **Eq. 5**. Large values of the correlation length indicate a larger number of weighted average observations in the estimate of the field at each grid point, resulting in a smoother field, while smaller values will allow for smaller-scale feature resolution, resulting in a noisier field.

Large N/S of imply larger analysis field deviations from the observations, or conversely, the analysis field is closer to the background field. However, small values of N/S mean that the analysis field is closer to the observations relative to the first guess field. We denote this parameter to always be less than one so the observations are more important than the background. As discussed in the following sections, the importance of the background is limited in our analysis due to the AQC used.

3.1 Horizontal and Vertical Analysis Domain

The global domain for the analysis extends from 0°E to 360°W and from 80°N to −80°S. The grid spacing is $\frac{1}{4}^\circ$ in latitude and longitude. The bathymetry is specified from the GEBCO 30" data (IOC and IHO, 2003). We consider 45 (surface to 6000m) and 36 (surface to 2000m) non-uniform depth layers in this analysis for SDC_V1 and SDC_V2, respectively, as listed in **Table 2**.

We considered a vertical discretization consisting of 10 m layers around the nominal vertical depth of the analysis, as reported in **Table 2**. This prevents vertical smearing of the vertical temperature and salinity gradients, and unrealistic thermocline and halocline results being obtained. In addition, we avoid the use of data far from the interpolation level as the profiles may have vertical data gaps.

To better resolve the upper thermocline structure, a larger number of layers are defined from the surface to 500 m, and the remaining levels are at distances of 100 m between 500 m and 1900 m depth and of 500 m between 1900 m and 6,000 m. Data are grouped in monthly time steps and all data collected during the month contribute equally to the estimate of the monthly climatology.

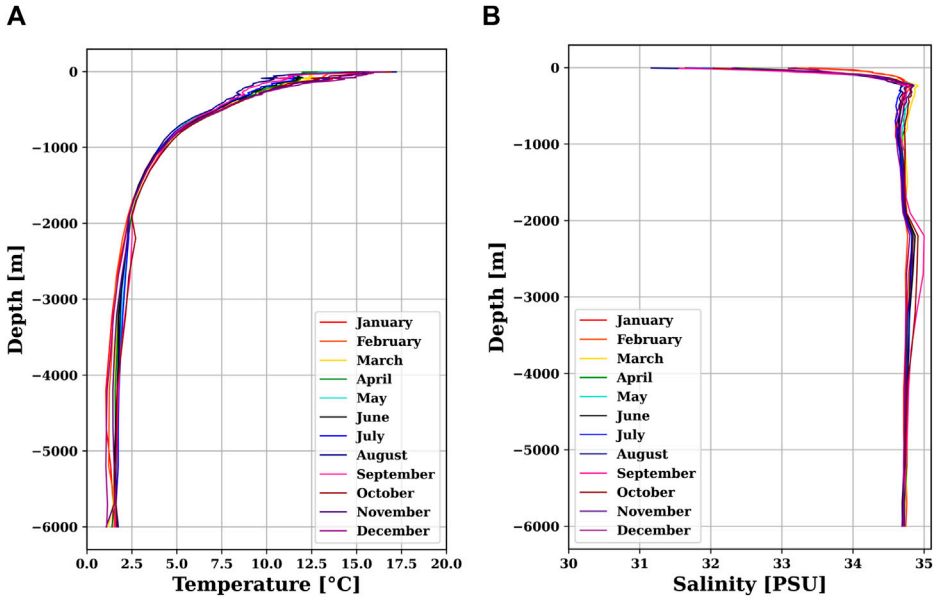

FIGURE 4 | Background1(spatial mean of data at each layer) for SDC_V1 computed from Dataset1: Temperature **(A)**; and Salinity **(B)**.

3.2 Background Fields

The choice of the first guess field or background field may be important when data are irregularly spaced both horizontally and vertically. Two types of backgrounds were tested in this study. The first, Background1, is a vertical profile corresponding to a spatial mean of observations over the entire global ocean (**Figure 4**) for Dataset1. The second, Background2, is estimated by using the DIVAnd obtained from Background1, a correlation length of 1,000 km and a N/S ratio of 0.5. Similarly to Background1 several authors have taken zonal averages of observations and used it as first guess for climatologies (Levitus, 1982). However, averaging water masses across the deep portions of different ocean basins that are completely disconnected on the timescales of 100 years give rise to high standard deviations in deep waters. Notwithstanding these limitations and the simplicity of the first guess, the use of DIVAnd and AQC makes the analysis quite insensitive to the background as shown below. We select the background according to the computed climatology residuals, calculated as:

$$r^i(xo_\alpha, yo_\beta, z_\gamma) = H(\theta^i{}_c(x_k, y_j, z_p)) - y_o(xo_\alpha, yo_\beta, z_\gamma) \quad (6)$$

where (x_k, y_j, z_p) are the m, n, q grid points of the three dimensional interpolating grid, respectively, $y_o(xo_\alpha, yo_\beta, zo_\gamma)$ are the observations at α, β, γ points and θ^i_c is the $i-th$ climatology under consideration. H is the bilinear interpolation or observational operator that interpolates the climatology to the observational point. r^i is clearly an estimate of the error of the climatology at the observational grid points, due to the smoothing carried out by the interpolation scheme and all of the assumptions within the numerical scheme.

Figures 5A,B show the Root Mean Squares(RMS) of residuals of the SDC_V1 analysis conducted using Background1 and the WOD QC. **Figures 5C,D** shows the difference of the residuals between the climatologies computed with Background2 and Background1. The difference is visible and quantitatively significant.

However, when AQC is used, as shown in **Figures 5E,F** the background does not appreciably change the climatological estimate. The AQC eliminates outliers or non-representative data, which reduces the sensitivity of the analysis to the background specification. The quality of the input dataset determines the influence of the background on the estimate: if only the WOD QC input dataset is used, i.e., outliers/non-representative data are left in, the choice of background becomes more important and the difference between residuals using different backgrounds is large, particularly for salinity. Thus, we conduct our analysis for both Dataset1 and Dataset2 with Background1.

3.3 Sensitivity Experiments for DIVAnd Parameter Choices

Selecting the correlation lengths L and N/S for a global ocean domain is challenging. The global ocean contains a multiplicity of scales. Therefore, a single L value could either overly smear the general circulation fronts (such as the western boundary currents) or contaminate the climatology with mesoscale eddies or other higher frequency processes. L has previously been estimated using the data itself, by binning the data and fitting analytical curves (Nittis et al., 1993). However, in the global ocean the data is so non-uniformly spaced that the L estimation quality of different ocean areas will be very different. Thus, we take a new view of the traditional approach and use equal L values for every location, as in WOA18 (Locarnini et al., 2019).

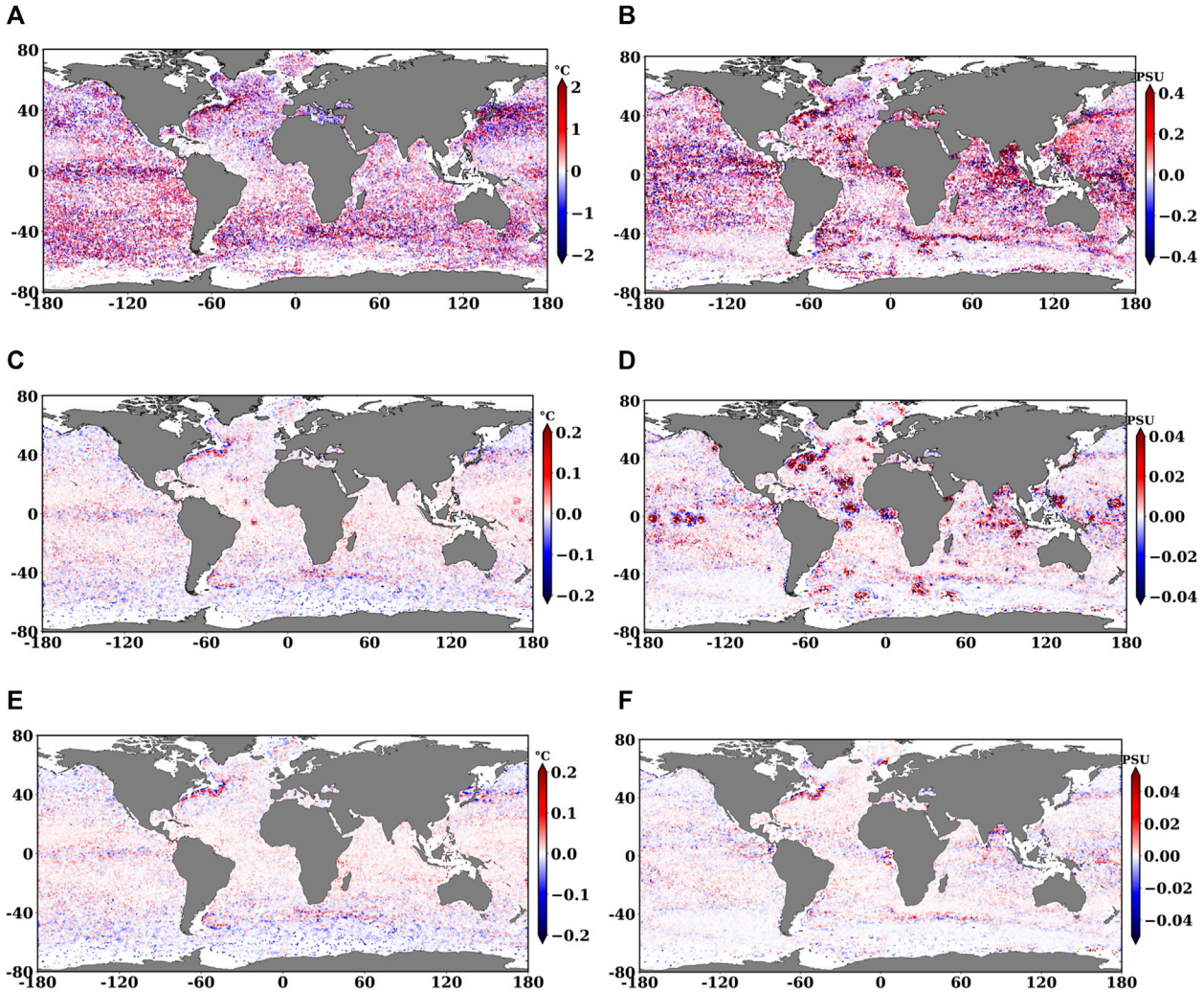

FIGURE 5 | Residual and residuals difference for Temperature **(A,C, E)** and Salinity **(B,D,F)** at 5 m using WOD QC with choice of Background1. RMS of residuals in **(A)** 0.69°*C*, and **(B)** 0.94*PSU*. Difference of residuals with Background2 and Background1 using WOD QC, RMS of residuals in **(C)** 0.02°*C*, and **(D)** 0.03*PSU*. Difference of residuals of Background2 and Background1 using AQC, RMS of residuals in **(E)** 0.02°*C*, and **(F)** 0.01*PSU*.

We conducted several sensitivity experiments to select reasonable values using L values ranging from 100 to 1,000 km and N/S values from 0.1 to 50.

A roughness index is defined as the mean of the derivative of field in the two directions as:

$$RI = \frac{1}{N} \sum_{i,j=1}^{n,m} \sqrt{(\Delta_{x_i} f)^2 + (\Delta_{y_j} f)^2} \tag{7}$$

where Δ is the finite difference derivative in the latitudinal and longitudinal directions, x_i is the grid spacing in the longitudinal direction and y_j in the latitudinal direction, and $N = n * m$ is the total number of the interpolating grid points.

RI gives a measure of the spatial scale of the field. For example, a field with mesoscale features will have high RI values while a smoother field with large-scale features will have low values. We do not find that using the Rossby radius of deformation and/or its corresponding wavelength can correctly define the correlation length for a climatology. The correlation length is the result of many propagating waves in the ocean, which combine to form a mean field that is necessarily smooth. Thus, a roughness index or its inverse, a smoothness index, is a better choice for establishing the correlation length of the interpolating algorithm in terms of the wavelength of the primary process that creates the climatology. Many climate indices are in fact "smoothed" to extract basic long-term signals.

As expected, for large L values the analysis gives a small RI value, as shown in **Figure 6**. We also establish that the RI should not exceed the standard deviation (std) of the data itself, as shown by the dotted blue line in **Figure 6**. The criteria of accepting a value of RI less than the field STD evidently only eliminates L at 100 km, varying slightly with depth. The "elbow" of all of the curves lies between 0.4 and 0.6 for the N/S ratio, and thus we select 0.5. When selecting this N/S value and taking an RI equal to

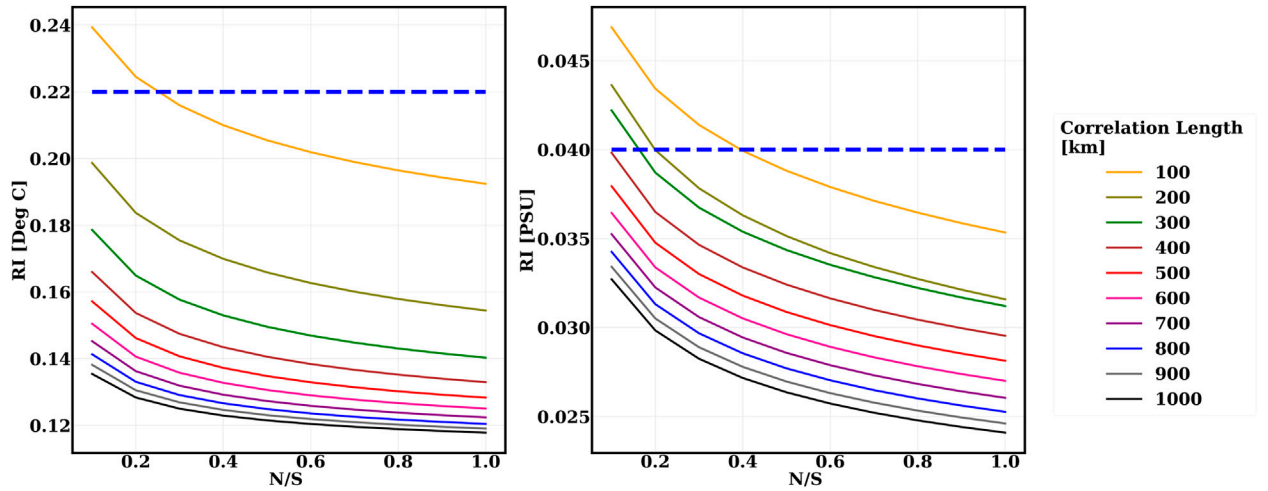

FIGURE 6 | Roughness Index of SDC_V1: Temperature **(left)** and Salinity **(right)** for January at *5m* for different CL and N/S (dotted blue line represents the standard deviation of *in-situ* observations).

approximately half of the field STD, we obtain a value for L of 300 km.

4 DISCUSSION

We conducted temperature and salinity mapping with a correlation length of 300 km and an N/S of 0.5 for Dataset1 and Dataset2 for all depths and months. **Figure 7** shows the mapped temperature and salinity fields for Dataset1 for January at different depth levels. The fields are masked if the analysis errors are greater than 30% (relative to the field standard deviation). We find that the Pacific area still suffers from a scarcity of data, in addition to the deep ocean.

SDC_V1 is a longer-term average while SDC_V2 is an estimate of the last 15 years. The difference between these two estimates is shown in **Figure 8**. SDC_V2 is warmer and more saline than SDC_V1, and the root mean square (RMS) difference varies from 0.4° to 0.5 °C and 0.7 to 0.6 PSU for temperature and salinity, respectively. To better quantify the sign of the differences we computed the global mean bias of salinity and temperature in **Figure 9**. The negative mean bias at the surface indicates that SDC_V2 is less saline than SDC_V1. This might be due to the last 15 years (2003–2017) increase of freshening of surface waters with respect to the (1900–2017) time period. However such freshening does not go subsurface due to buoyancy effects. In the subsurface at the contrary, SDC_V2 is more saline than SDC_V1 and we argue that this is allowed by compensating effects between high tempratures and high salt in the equation of state, as described by Chen et al. (2019).

4.1 Validation Using Other Climatologies

Validating the analysis is an essential step, as it indicates the reliability of the results. We validate our results using the WOA18 and WAGHC (isobarically averaged version) climatological estimates because they have similar interpolating grids at 1/4° resolution. Other climatologies might exist but at lower space and time resolution. The main source of data in WAGHC is from WOD13, and in particular OSD, CTD, PFL and APB. Additional data were obtained from the Alfred Wegener Institute, Bremerhaven, and from various institutions in Canada for the period between 1900 and 2016 (Gouretski, 2018). The data considered in WOA18 are profiles from OSD, CTD, PFL, MRB, Mechanical Bathythermographs, Digital Bathythermographs, Expendable Bathythermographs, moored and drifting buoys, gliders, undulating oceanographic recorders (UOR), pinniped mounted CTD sensors and surface-only data (Locarnini et al., 2019) and (Zweng et al., 2019). WOA18 monthly climatology is computed from surface to 1500 m on 22 depth levels at a spatial resolution of 0.25 over the 6 decades of 1955–1964, 1965–1974, 1975–1984, 1985–1994, 1995–2004 and 2005–2012. While seasonal fields are computed for deeper depth from surface to 6000 m on 57 depth levels. We understand the climatologies are done for different periods but we argue that a comparison is a first step to check consistency between them.

To compute the differences between the climatologies, we interpolated the WOA18 time average fields over the 6 decades on the DIVAnd analysis grid using linear interpolation, and similarly for WAGHC. **Supplementary Figures S1–S4** in the supplementary material show that differences are localised and are maximum in dynamically active regions such as along the Gulf Stream, the South equatorial current, the Gulf of Guinea, the Bay of Bengal, etc. Moreover, largest differences are found in the Arctic region that might be mainly due to different observational data sets used. We have also added several **Supplementary Tables S1–S14** in the supplementary material evaluating the BIAS and the RMSD of salinity and temperature computed as the spatial average of the differences between the climatologies in different layers for the equatorial regions (-10°S to 10°N), north and south Atlantic, Pacific (11°N

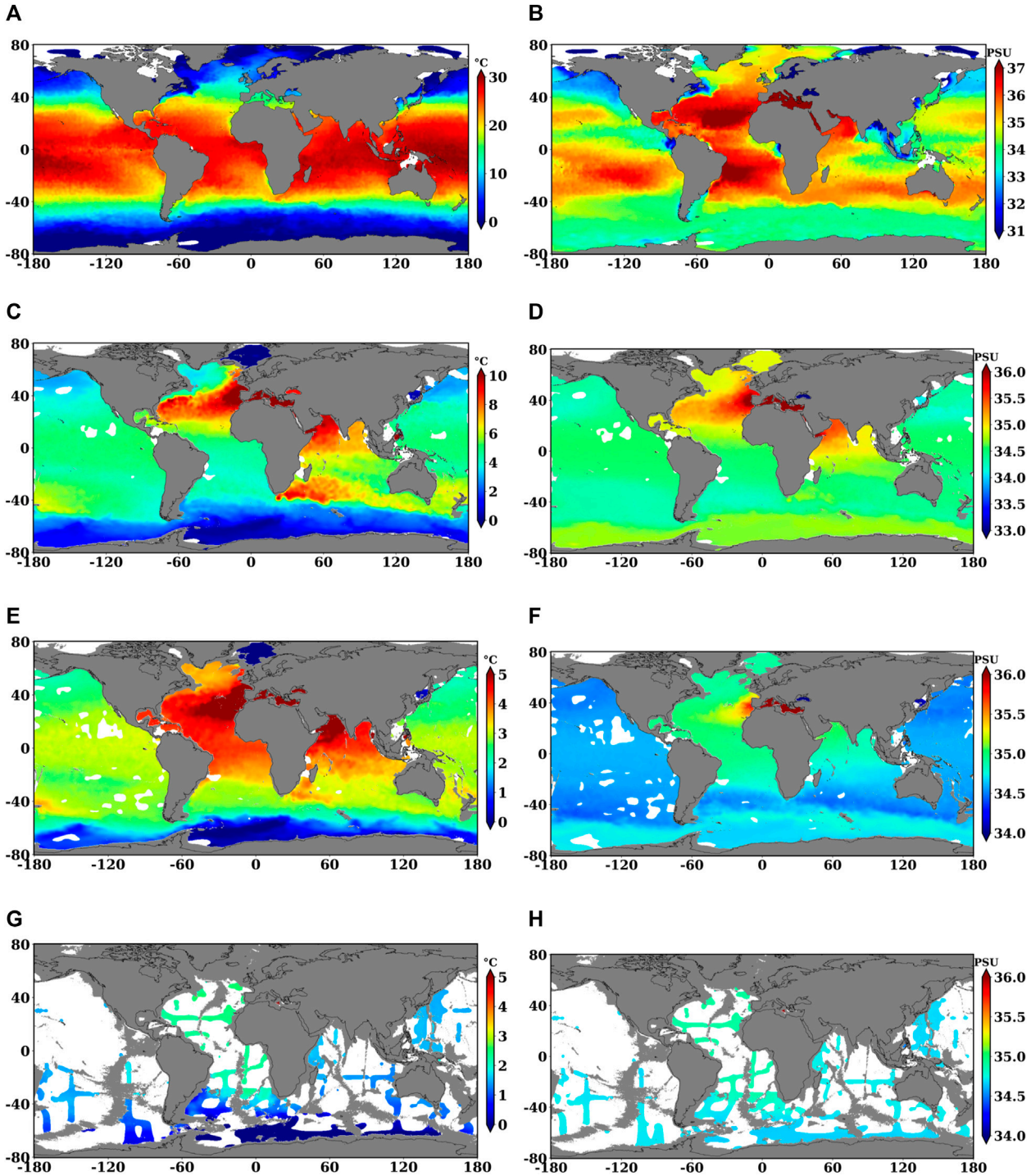

FIGURE 7 | Temperature **(A,C,E,G)** and Salinity **(B,D,F,H)** climatology for January at 5*m*, 900*m*, 1050*m* and 3700*m*, respectively, from SDC_V1.

to 80 °N) and (-80°S to -9°S), respectively, and Indian Ocean (20°N to -40°S). SDC_V1 has a positive bias with respect to WOA and a negative bias for WAGHC for both temperature and salinity at all the depths in all regions. Maximum differences are found at surface and thermocline depths. Further, larger temperature differences are noticed in the north and south Atlantic, and Indian ocean for WOA, while WAGHC has maximum differences in the north Atlantic region. Maximum temperature differences are found in equatorial Atlantic and Pacific for WOA while for WAGHC maximum RMSD is found in Atlantic ocean. Overall, the comparison of RMSD values shows larger differences for both temperature and salinity with WOA as

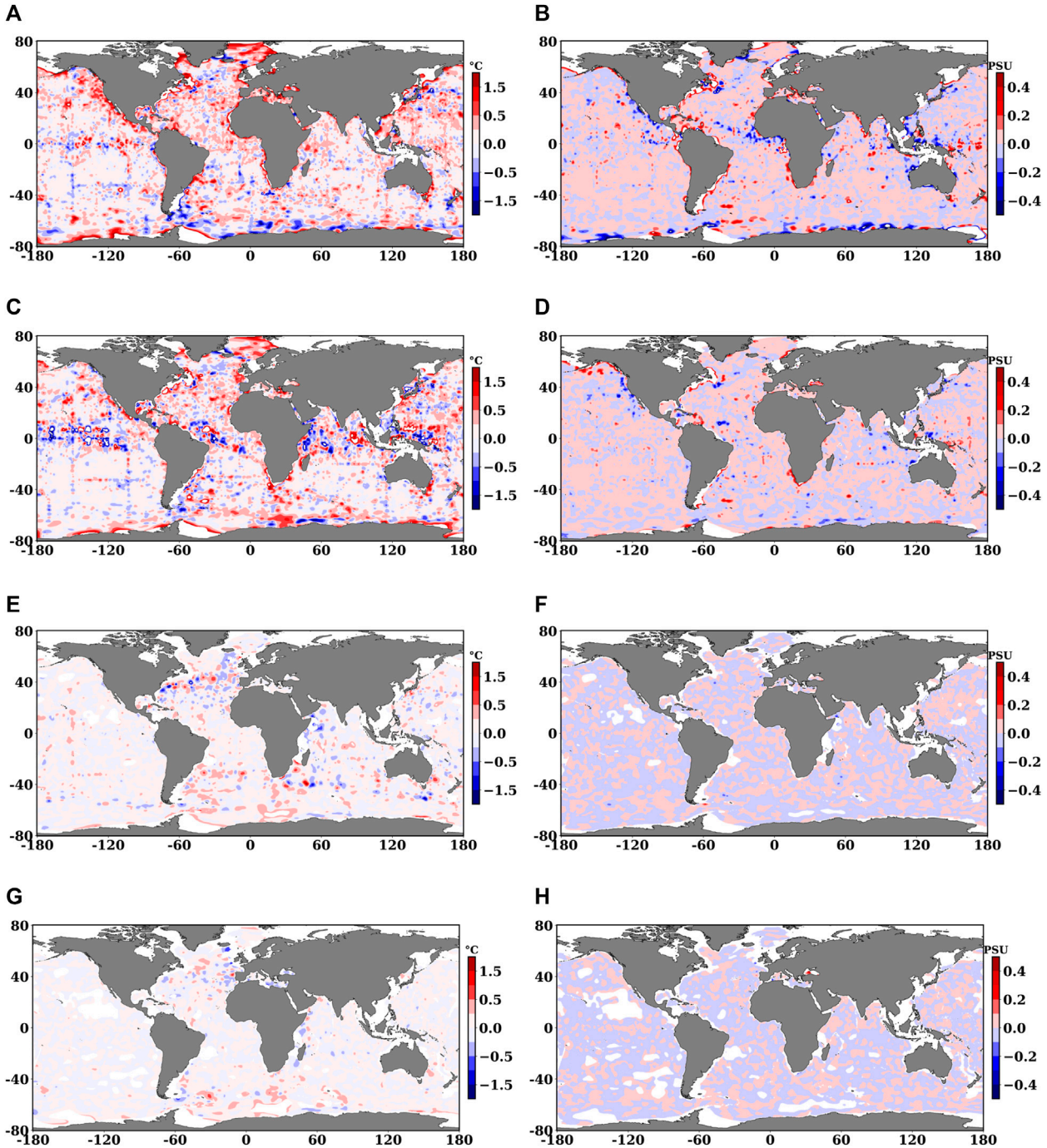

FIGURE 8 | January mapping differences between SDC_V2 and SDC_V1 for Temperature with RMSD **(A)** 0.4°*C*, **(C)** 0.39°*C*, **(E)** 0.08 °*C*, **(G)** 0.04 °*C*, and Salinity with RMSD **(B)** 0.66*PSU*, **(D)** 0.05*PSU*, **(F)** 0.01*PSU*, and **(H)** 0.01*PSU* at 5*m*, 100*m*, 900*m* and 1500*m*, respectively.

compared to WAGHC that is probably due to the fact the interpolation scheme SDC and WAGHC are similar.

Moreover, Hovmoller diagram was constructed for the horizontal spatial average of the RMS differences between WOA18 and WAGHC. **Figure 10** shows that the largest RMS temperature differences are found with SDC_V1 at the thermocline depth for both WOA18 and WAGHC, but the differences are more prominent with WOA18. We argue that this difference at the thermocline is due to the different interpolations of the observational profiles at the levels, which create potential anomalies or simply different data being used. The differences in salinity are greater in the surface layer and for the summer months, probably due to the different number of profiles used.

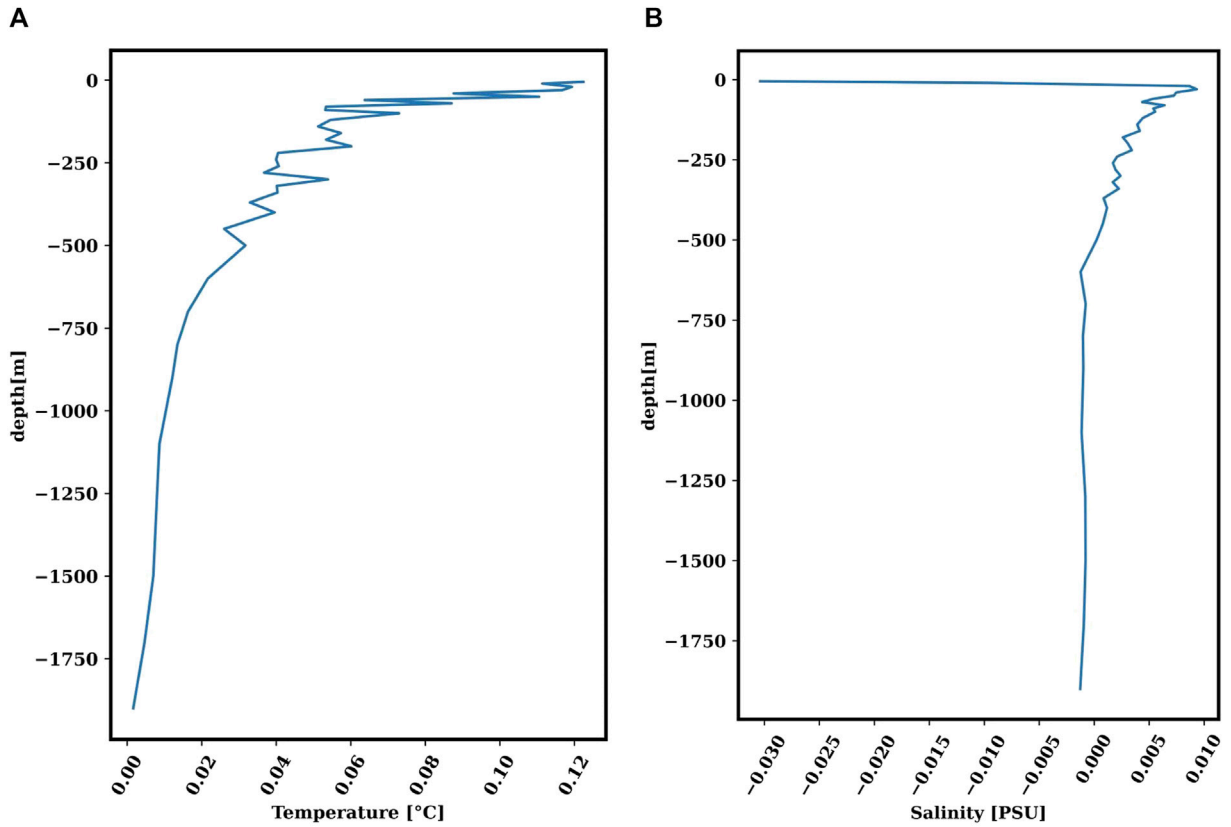

FIGURE 9 | Global mean bias profile (difference between SDC_V2 and SDC_V1) for **(A)** Temperature and **(B)** Salinity during January.

4.2 Ensemble Mean Climatology

In the previous section we reveal some of the differences between the four climatological estimates. Such uncertainties are due to the characteristics of the selected input dataset, the specific background and statistical interpolation algorithms, and the type of quality control applied. As for numerical models, a multi-model statistical estimate can reduce the errors of specific quality assessment indices. Thus, a diverse combination of climatological estimating methods can provide the best estimate of the climatological state of the ocean. Ensemble methodologies have been proposed in the past for the reconstruction of atmospheric temperatures (Krishnamurti et al., 1999) and for climatologies of global ocean salinities (Liu et al., 2020). Furthermore it is well knwon that ensemble mean is a commonly used post-processing methodology for reanalyses (Frankcombe et al., 2018) and climate projections (Solomon et al., 2007). In these works, it is shown that the ensemble mean is a statistically better estimate of the truth, so we have applied this to the different global ocean climatologies. The multi-model ensemble mean will reduce the uncertainties associated with the statistical ensemble mean estimate. Our multi-model ensemble climatology is the ensemble mean of four climatologies WOA, WAGHC, and SDC_V1 and SDC_V2. Each member of the ensemble is considered to be a different climatology derived from a different statistical interpolating model, and the ensemble mean of these models should be superior to that of any of the single models within a particular evaluation score (Krishnamurti et al., 1999). The evaluation score applied is derived from the comparison between the ensemble mean residual and each single climatology residual.

The climatology multi-model ensemble mean, $\theta_c^E(x,y,z)$ is defined as:

$$\theta_c^E(x,y,z) = \sum_{i=1}^{N} \frac{\theta^i{}_c(x,y,z)}{N}, \tag{8}$$

The residual defined in **Eq. 6** contains various sources of errors in addition to the difference between the climatology and the observations. We assume first that the climatological estimate is the sum of true climatological value and the interpolation errors, so-called ϵ_H:

$$H(\theta^i{}_c(x_k,y_j,z_p)) = H(\theta^i{}_c(x_k,y_j,z_p))^T + \epsilon_H. \tag{9}$$

Moreover, the observations itself are sum of true observational values and errors, ϵ_o:

$$y_o(xo_\alpha, yo_\beta, z_\gamma) = y_o(xo_\alpha, yo_\beta, z_\gamma)^T + \epsilon_o, \tag{10}$$

Finally, the residuals in the **Eq. 6** can now be decomposed as follows:

$$r^i(xo_\alpha, yo_\beta, z_\gamma) = H(\theta^i{}_c(x_k,y_j,z_p))^T + \epsilon_H - y_o(xo_\alpha, yo_\beta, z_\gamma)^T - \epsilon_o \tag{11}$$

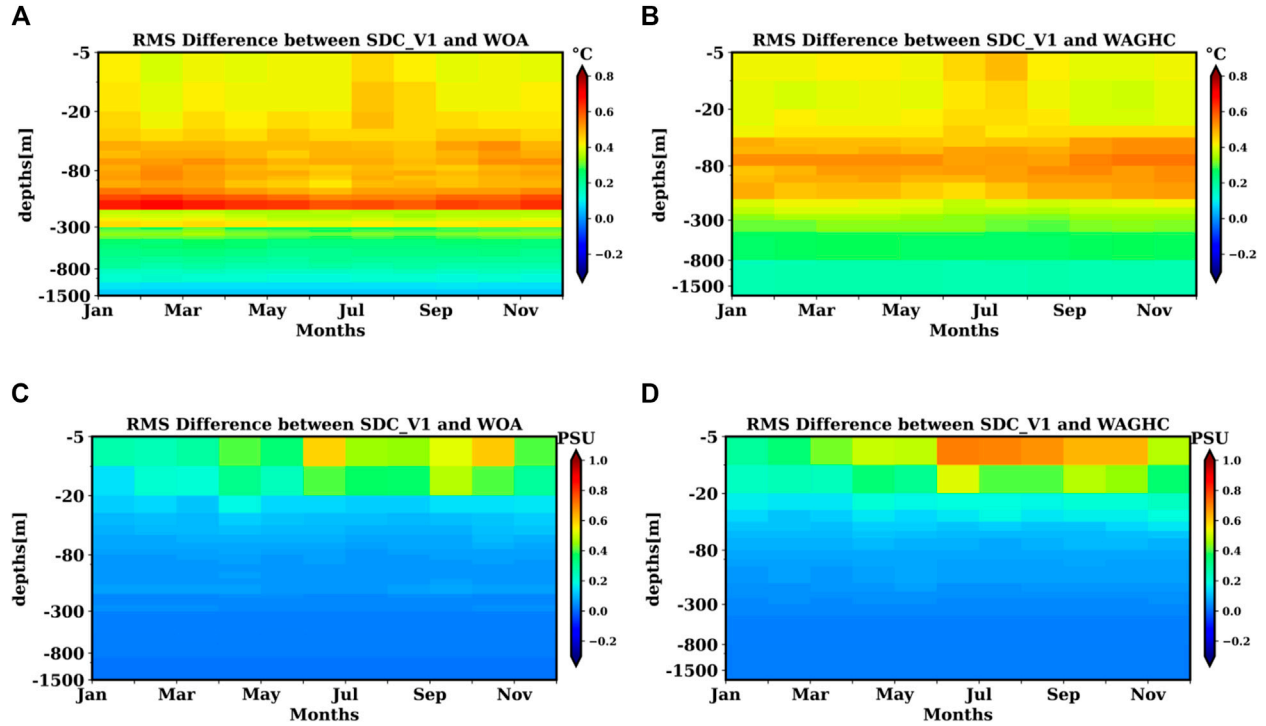

FIGURE 10 | Hovmoller diagram of the root mean square difference between SDC_V1 and WOA for **(A,C)** and SDC_V1 and WAGHC for **(B,D)**. Left panels give temperature and right panels salinity.

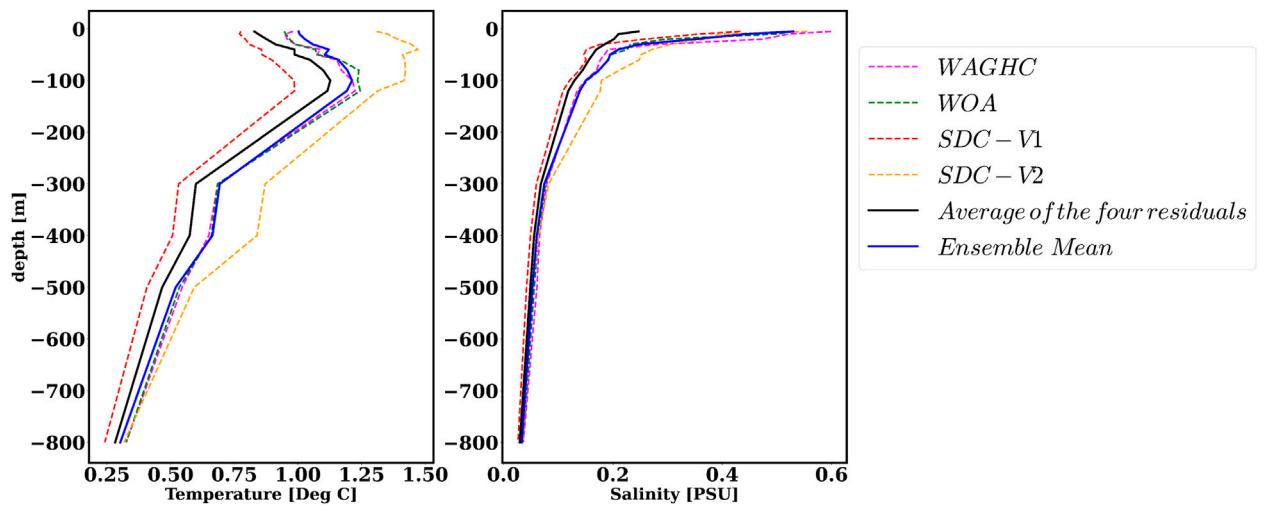

FIGURE 11 | Standard deviation of anomaly residuals $\tilde{r}^i$ for available climatological estimates ($\theta^i{}_c$) (dashed lines), average of the four residuals (continuous blue line) and standard deviation of ensemble mean climatology residuals (black continuous line).

Thus the residuals are the sum of the differences between the true climatology and the true observational values plus the two different types of errors. We call this synthetically residual errors. A lower residual error is not a necessary condition for a high quality climatology but we argue that it is a sufficient criteria. A climatological estimate with lower residual will be considered as a better estimate.

The resulting vertical profile is denoted by $\tilde{r}(z)$ and is defined as:

$$\tilde{r}^{i}(z_{\gamma}) = \sqrt{\sum_{\alpha,\beta=1}^{M,L} \frac{(r^{i}(xo_{\alpha}, yo_{\beta}, z_{\gamma}) - \bar{r}^{i}(z_{l}))^{2}}{M * L}}. \quad (12)$$

where $M * L$ is the number of horizontal observational grid points.

Figure 11 shows the $\tilde{r}^{i}$. The ensemble residual STD is the second lowest, confirming that the multi-model ensemble mean is a good estimate of the climatology. The lowest values are achieved by SDC_V1, but we argue that this is due to the fact that we computed the residuals directly from the dataset used to generate the SDC_V1 climatology.

5 SUMMARY AND FUTURE WORK

Two versions of a global ocean climatology for temperature and salinity were estimated using a new interpolation scheme, DIVAnd, which enables a better assessment of coastal constraints. We demonstrated that an additional quality control is required to produce a good quality climatology. Two backgrounds were analyzed: a spatial mean of observations in the horizontal and an analysis conducted with a very large correlation length of 1000 *km* and N/S of 0.5. The results show that if pre-processing is carried out using the AQC procedure, the resulting analysis field is less dependent on the choice of the background field (see **Figure 5**).

In addition, ours is the first study in which the selection of DIVAnd parameters is deduced from a new roughness index (RI), which quantifies the degree of smoothness of the analysis as a function of the correlation length and N/S values.

When comparing the SDC_V1 climatology with WOA and WAGHC we find reasonable agreement, but also significant differences in terms of the thermocline and surface layers. The SDC_V1 climatology is closer to WAGHC than WOA18 in terms of both temperature and salinity. One reason could be connected to the fact that the OA parameters used and the technique itself are similar to DIVAnd. Currently available historical datasets enable an almost complete reconstruction of the global ocean fields. However, data gaps still exist, and differences among interpolation schemes and input dataset quality control lead to significant uncertainties in the climatological estimates. For the first time, we have demonstrated that a multi-model ensemble of different climatologies can produce low residual error compared to each single climatological estimate.

Future work can consider the application of the improved quality control procedure developed in Shahzadi et al. (2021) using a regime-oriented division instead of regular 5° square rectangles in a global domain. An optimised choice of DIVAnd parameters that are different for each level may improve the results. A validation with independent datasets such as satellite observations or a randomly subsampled input dataset will enable an assessment of whether the analysis under- or over-fits the observations. Further as pointed by Lozier et al. (1994), an isopycnal climatology using DIVAnd is required to avoid the artificial mixing water masses.

DATA AVAILABILITY STATEMENT

The datasets presented in this study can be found in online repositories. The names of the repository/repositories and accession number(s) can be found below: https://doi.org/10.12770/98d22ac0-5398-4889-8f8e-8f28273b548b.

AUTHOR CONTRIBUTIONS

KS wrote the text and created the figures in the paper. NP corrected and wrote parts of the sections, and in particular contributed to the conceptual framing of the work. VL helped assess the structure of the WOD dataset in the early stages of the quality control algorithm, and AB and CT help with the application of the DIVAnd interpolation scheme. SS assisted in revising the content of the PhD thesis that served as the basic material for this article.

FUNDING

The study was fully funded by the European project Horizon2020 SeaDataCloud - Further developing the pan-European infrastructure for marine and ocean data management Grant Agreement Number: 730960 and is part of the PhD thesis of KS at the University of Bologna. NP was additionally funded by the University of Bologna.

ACKNOWLEDGMENTS

We thank Dr. Tim Boyer, NOAA (United States) reviewer of the PhD thesis, who suggested important improvements.

SUPPLEMENTARY MATERIAL

The Supplementary Material for this article can be found online at: https://www.frontiersin.org/articles/10.3389/fenvs.2021.711363/full#supplementary-material

REFERENCES

Barker, P. M., Dunn, J. R., Domingues, C. M., and Wijffels, S. E. (2011). Pressure Sensor Drifts in Argo and Their Impacts. *J. Atmos. Oceanic Technology* 28, 1036–1049. doi:10.1175/2011jtecho831.1

Barnes, S. L. (1964). A Technique for Maximizing Details in Numerical Weather Map Analysis. *J. Appl. Meteorol.* 3, 396–409. doi:10.1175/1520-0450(1964)003<0396:atfmdi>2.0.co;2

Barth, A., Beckers, J.-M., Troupin, C., Alvera-Azcárate, A., and Vandenbulcke, L. (2014). divand-1.0: N-Dimensional Variational Data Analysis for Ocean Observations. *Geosci. Model. Dev.* 7, 225–241. doi:10.5194/gmd-7-225-2014

Brasseur, P. P. (1991). A Variational Inverse Method for the Reconstruction of General Circulation fields in the Northern Bering Sea. *J. Geophys. Res.* 96, 4891–4907. doi:10.1029/90jc02387

Bretherton, F. P., Davis, R. E., and Fandry, C. B. (1976). A Technique for Objective Analysis and Design of Oceanographic Experiments Applied to Mode-73. *Deep Sea Research and Oceanographic Abstracts*, 23. Elsevier, 559–582. doi:10.1016/0011-7471(76)90001-2

Chen, L., Huang, J. G., Ma, Q., Hänninen, H., Tremblay, F., and Bergeron, Y. (2019). Long-term Changes in the Impacts of Global Warming on Leaf Phenology of Four Temperate Tree Species. *Glob. Change Biol.* 25, 997–1004. doi:10.1111/gcb.14496

Cowley, R., Killick, R., Boyer, T., Gouretski, V., Reseghetti, F., Kizu, S., et al. (2021). International Quality-Controlled Ocean Database (Iquod) V0. 1: the Temperature Uncertainty Specification. *Front. Mar. Sci.* 8, 607. doi:10.3389/fmars.2021.689695

Daley, R. (1993). *Atmospheric Data Analysis*, 2. Cambridge University Press.

Frankcombe, L. M., England, M. H., Kajtar, J. B., Mann, M. E., and Steinman, B. A. (2018). On the Choice of Ensemble Mean for Estimating the Forced Signal in the Presence of Internal Variability. *J. Clim.* 31, 5681–5693. doi:10.1175/jcli-d-17-0662.1

Gandin, L. (1960). On Optimal Interpolation and Extrapolation of Meteorological fields. *Trudy GGO* 114, 75–89.

Garcia, H., Boyer, T., Locarnini, R., Baranova, O., and Zweng, M. (2018). *World Ocean Database 2018: Users Manual (Prerelease). NOAA Atlas NESDIS81.*

Gouretski, V. (2019). A New Global Ocean Hydrographic Climatology. *Atmos. Oceanic Sci. Lett.* 12, 226–229. doi:10.1080/16742834.2019.1588066

Gouretski, V. (2018). World Ocean Circulation Experiment - Argo Global Hydrographic Climatology. *Ocean Sci.* 14, 1127–1146. doi:10.5194/os-14-1127-2018

IOC and IHO (2003). *Bodc: Centenary Edition of the Gebco Digital Atlas, Published on Cd-Rom on Behalf of the Intergovernmental Oceanographic Commission and the International Hydrographic Organization as Part of the General Bathymetric Chart of the Oceans*. Liverpool, UK: British Oceanographic Data Centre.

Janjić, T., Bormann, N., Bocquet, M., Carton, J., Cohn, S., Dance, S., et al. (2018). On the Representation Error in Data Assimilation. *Quart. J. R. Meteorol. Soc.*, 144. doi:10.1002/qj.3130

Jia, W., Wang, D., Pinardi, N., Simoncelli, S., Storto, A., and Masina, S. (2016). A Quality Control Procedure for Climatological Studies Using Argo Data in the north pacific Western Boundary Current Region. *J. Atmos. Oceanic Technology* 33, 2717–2733. doi:10.1175/jtech-d-15-0140.1

Krishnamurti, T. N., Kishtawal, C. M., LaRow, T. E., Bachiochi, D. R., Zhang, Z., Williford, C. E., et al. (1999). Improved Weather and Seasonal Climate Forecasts from Multimodel Superensemble. *Science* 285, 1548–1550. doi:10.1126/science.285.5433.1548

Levitus, S. (1982). *Climatological Atlas of the World Ocean, NOAA Professional Paper No. 13*. US Department of Commerce.

Liu, C., Liang, X., Chambers, D. P., and Ponte, R. M. (2020). Global Patterns of Spatial and Temporal Variability in Salinity from Multiple Gridded Argo Products. *J. Clim.* 33, 8751–8766. doi:10.1175/jcli-d-20-0053.1

Locarnini, M., Mishonov, A., Baranova, O., Boyer, T., Zweng, M., Garcia, H., et al. (2019). Temperature, World Ocean Atlas 2018. NOAA Atlas NESDIS81. Available online at https://accession.nodc.noaa.gov/NCEI-WOA18

Lozier, M. S., McCartney, M. S., and Owens, W. B. (1994). Anomalous Anomalies in Averaged Hydrographic Data. *J. Phys. Oceanogr.* 24, 2624–2638. doi:10.1175/1520-0485(1994)024<2624:aaiahd>2.0.co;2

Nittis, K., Pinardi, N., and Lascaratos, A. (1993). Characteristics of the Summer 1987 Flow Field in the Ionian Sea. *J. Geophys. Res.* 98, 10171–10184. doi:10.1029/93jc00451

Owens, W. B., and Wong, A. P. S. (2009). An Improved Calibration Method for the Drift of the Conductivity Sensor on Autonomous CTD Profiling Floats by θ-S Climatology. *Deep Sea Res. Oceanographic Res. Pap.* 56, 450–457. doi:10.1016/j.dsr.2008.09.008

Solomon, S., Manning, M., Marquis, M., and Qin, D. (2007). *Climate Change 2007-the Physical Science Basis: Working Group I Contribution to the Fourth Assessment Report of the IPCC (Vol. 4)*. Cambridge University Press.

Shahzadi, K., Pinardi, N., and Lyubartsev, V. (2021). A Non-linear Quality Control Procedure for Representativeness Errors in Ocean Historical Datasets. *Bollettino di Geofisica* 12, 99.

Shahzadi, K., Pinardi, N., Lyubartsev, V., Zavatarelli, M., and Simoncelli, S. (2020). *SeaDataCloud Temperature and Salinity Climatologies for the Global Ocean V2)*. ITALY. Report (scientific report). doi:10.13155/77512

Simoncelli, S., Coatanoan, C., Myroshnychenko, V., Bäck, Ö., Sagen, H., Scory, S., et al. (2021). Seadatacloud Data Products for the European Marginal Seas and the Global Ocean. Available online at: http://hdl.handle.net/2268/259074 .

Troupin, C., Barth, A., Sirjacobs, D., Ouberdous, M., Brankart, J.-M., Brasseur, P., et al. (2012). Generation of Analysis and Consistent Error fields Using the Data Interpolating Variational Analysis (Diva). *Ocean Model.* 52-53, 90–101. doi:10.1016/j.ocemod.2012.05.002

Wong, A. P. S., Johnson, G. C., and Owens, W. B. (2003). Delayed-Mode Calibration of Autonomous CTD Profiling Float Salinity Data Byθ-SClimatology*. *J. Atmos. Oceanic Technol.* 20, 308–318. doi:10.1175/1520-0426(2003)020<0308:dmcoac>2.0.co;2

Zweng, M., Seidov, D., Boyer, T., Locarnini, M., Garcia, H., Mishonov, A., et al. (2019). Salinity, World Ocean Atlas 2018. NOAA Atlas NESDIS81. Available online at: https://accession.nodc.noaa.gov/NCEI-WOA18

Conflict of Interest: The authors declare that the research was conducted in the absence of any commercial or financial relationships that could be construed as a potential conflict of interest.

Publisher's Note: All claims expressed in this article are solely those of the authors and do not necessarily represent those of their affiliated organizations, or those of the publisher, the editors and the reviewers. Any product that may be evaluated in this article, or claim that may be made by its manufacturer, is not guaranteed or endorsed by the publisher.

frontiers in Marine Science

ORIGINAL RESEARCH
published: 07 September 2021
doi: 10.3389/fmars.2021.710973

Climate Signals in the Black Sea From a Multidecadal Eddy-Resolving Reanalysis

Leonardo Lima[1], Stefania Angela Ciliberti[2], Ali Aydoğdu[1], Simona Masina[1], Romain Escudier[1], Andrea Cipollone[1], Diana Azevedo[2], Salvatore Causio[2], Elisaveta Peneva[3], Rita Lecci[2], Emanuela Clementi[1], Eric Jansen[2], Mehmet Ilicak[4], Sergio Creti[2], Laura Stefanizzi[2], Francesco Palermo[2] and Giovanni Coppini[2]*

[1] Ocean Modeling and Data Assimilation Division, Centro Euro-Mediterraneo sui Cambiamenti Climatici, Lecce, Italy, [2] Ocean Predictions and Applications Division, Centro Euro-Mediterraneo sui Cambiamenti Climatici, Lecce, Italy, [3] Department of Meteorology and Geophysics, Faculty of Physics, Sofia University "St. Kliment Ohridski", Sofia, Bulgaria, [4] Eurasia Institute of Earth Sciences, Istanbul Technical University, Istanbul, Turkey

OPEN ACCESS

Edited by:
Pengfei Lin, Institute of Atmospheric Physics, Chinese Academy of Sciences (CAS), China

Reviewed by:
Jing Ma, Nanjing University of Information Science and Technology, China
Yeqiang Shu, Key Laboratory of Marginal Sea Geology, South China Sea Institute of Oceanology, Chinese Academy of Sciences (CAS), China
Chuanyu Liu, Institute of Oceanology, Chinese Academy of Sciences (CAS), China

***Correspondence:**
Leonardo Lima
leonardo.lima@cmcc.it

Specialty section:
This article was submitted to Global Change and the Future Ocean, a section of the journal Frontiers in Marine Science

Received: *17 May 2021*
Accepted: *05 August 2021*
Published: *07 September 2021*

Citation:
Lima L, Ciliberti SA, Aydoğdu A, Masina S, Escudier R, Cipollone A, Azevedo D, Causio S, Peneva E, Lecci R, Clementi E, Jansen E, Ilicak M, Cretì S, Stefanizzi L, Palermo F and Coppini G (2021) Climate Signals in the Black Sea From a Multidecadal Eddy-Resolving Reanalysis. Front. Mar. Sci. 8:710973. doi: 10.3389/fmars.2021.710973

Ocean reanalyses are becoming increasingly important to reconstruct and provide an overview of the ocean state from the past to the present-day. In this article, we present a Black Sea reanalysis covering the whole satellite altimetry era. In the scope of the Copernicus Marine Environment Monitoring Service, the Black Sea reanalysis system is produced using an advanced variational data assimilation method to combine the best available observations with a state-of-the-art ocean general circulation model. The hydrodynamical model is based on Nucleus for European Modeling of the Ocean, implemented for the Black Sea domain with a horizontal resolution of 1/27° × 1/36°, and 31 unevenly distributed vertical levels. The model is forced by the ECMWF ERA5 atmospheric reanalysis and climatological precipitation, whereas the sea surface temperature is relaxed to daily objective analysis fields. The model is online coupled to OceanVar, a 3D-Var ocean data assimilation scheme, to assimilate sea level anomaly along-track observations and *in situ* vertical profiles of temperature and salinity. Temperature fields present a continuous warming in the layer between 25 and 150 m, where the Black Sea Cold Intermediate Layer resides. This is an important signal of the Black Sea response to climate change. Sea surface temperature shows a basin-wide positive bias and the root mean square difference can reach 0.75°C along the Turkish coast in summer. The overall surface dynamic topography is well reproduced as well as the reanalysis can represent the main Black Sea circulation such as the Rim Current and the quasi-permanent anticyclonic Sevastopol and Batumi eddies. The system produces very accurate estimates of temperature, salinity and sea level which makes it suitable for understanding the Black Sea physical state in the last decades. Nevertheless, in order to improve the quality of the Black Sea reanalysis, new developments in ocean modeling and data assimilation are still important, and sustaining the Black Sea ocean observing system is crucial.

Keywords: variational data assimilation, past reconstruction, eddy-resolving reanalysis, climate change, ocean monitoring indicators

INTRODUCTION

The Black Sea is the largest land-locked basin in the world with an area of 4.2×10^5 km^2, a volume of 5.3×10^5 km^3 and a maximum depth of 2200 m (Özsoy and Ünlüata, 1997). It is connected to the Marmara Sea and Azov Sea through the straits of Bosphorus and Kerch, respectively. It is an estuarine basin, characterized by a positive net freshwater balance, mainly due to the outflow of some of the largest European rivers such as the Danube and Dniepr, and a high-rate of precipitation which in total exceeds the total evaporation most of the time over the basin (Kara et al., 2008; Volkov and Landerer, 2015). The resulting salinity of about 18 psu in the upper layer forms a strong stratification all over the basin where a saltier water of Mediterranean origin, crossing the Marmara Sea and the Bosphorus Strait, becomes the major source of ventilation for the anoxic lower layer (Ünlülata et al., 1990; Stanev and Beckers, 1999; Stanev et al., 2001). Another main characteristic of the Black Sea is the Cold Intermediate Layer (CIL) formed at the depth of the winter convection (Özsoy and Ünlüata, 1997). The upper layer circulation of the Black Sea is dominated by the Rim Current, a quasi-permanent cyclonic jet following the bottom topography which interacts with several anti-cyclonic eddies (e.g., Batumi and Sevastopol) along its pathway in the basin (Oguz et al., 1993; Korotaev et al., 2003).

The evolution of remote sensing has been crucial to understand some of the above-mentioned Black Sea processes, since it provides high temporal and spatial resolution observations (Korotaev et al., 2001). Kubryakov and Stanichny (2015) investigated the seasonal and interannual variability of the Black Sea eddies and found a relationship between the eddy properties and the intensity of the Rim Current using altimeter observations. In addition, sea surface temperature observations have helped to detect recent warming in the Black Sea as a response of climate change (Ginzburg et al., 2004; Shapiro et al., 2010; Mulet et al., 2018). However, the major challenge for studying the ocean dynamics in the Black Sea is the historical scarcity of sub-surface observations. Although this situation has been improved in the recent years with the first deployment of Argo floats after 2002 (Grayek et al., 2015), the number of in-situ observations significantly increased only after 2010. For instance, profiling floats contributed to the detection of a recent warming in the Black Sea and the reduction of the cold-water content in the CIL (Akpinar et al., 2017; Stanev et al., 2019).

Numerical ocean models represent a powerful complementary tool to investigate the three-dimensional state of the Black Sea circulation in time in absence of dense observations. Kara et al. (2005) used an eddy-resolving model to investigate the effects of ocean turbidity on upper-ocean circulation features including sea surface height and mixed layer depth. From a 56-year model simulation, Miladinova et al. (2017) revealed that temperature has a seasonal cycle at the surface, decreasing with depth down to the CIL. Next, the same simulation was used to investigate the formation and changes of the CIL and revealed that the cooling capacity of the CIL is highly variable and decreased drastically in the last decade of the simulation (Miladinova et al., 2018). Gunduz et al. (2020) related the reduced events of CIL formation in recent years to the amplified response to climate change of the Black Sea. Although current ocean models are highly sophisticated, including improvements in parameterization of physical processes of unresolved scale and incorporating numerical techniques that are optimal for ocean regions dynamically different, they still have some limitations and incorporate uncertainties from several sources (Lima et al., 2019). Therefore, they are not completely appropriate for providing accurate ocean monitoring indicators when used alone, nor to fully study the oceanic dynamics in the Black Sea.

Ocean reanalyses reconstruct the ocean state with a long integration of an ocean model constrained by atmospheric surface forcing and observations via data assimilation (Haines, 2018; Storto et al., 2019a). They provide a four-dimensional time series of the ocean state to study ocean dynamics and unravel sources and impacts of ocean variability. Ocean reanalyses can also provide initial and boundary conditions to other models as in downscaling simulations (de Souza et al., 2020) and uncoupled seasonal forecast initializations (Balmaseda, 2017). In the Black Sea, Knysh et al. (2011) conducted a pioneering investigation utilizing an ocean reanalysis. They applied a simple data assimilation scheme to ingest available in-situ observations from 1971 to 1993.

In this work we present a Black Sea reanalysis (BS-REA) that covers the altimeter era starting from 1993 until 2018. This reanalysis system has been continuously developed in the scope of the Copernicus Marine Environment Monitoring Service (CMEMS, Le Traon et al., 2019) since 2016 (Lima et al., 2020b). It is based on an eddy-resolving ocean model coupled with an advanced data assimilation scheme, which is very innovative for the Black Sea region. Here, we present a recently upgraded version in both model and data assimilation components, which we believe will help the community for a better understanding of the physical properties and dynamics of the Black Sea. Our objective is to ensure the best representation of the sea circulation and its thermohaline structure, as well as to provide more accurate ocean monitoring indicators that can help to understand the Black Sea response to climate change.

This article was organized as follows: in section 2 we outline the BS-REA configuration in detail; in section 3 we present the main characteristics of the BS-REA and discuss the results, and finally in section 4 the conclusions are drawn.

BS-REA CONFIGURATION

Ocean Model

The present BS-REA hydrodynamic model is configured for the Black Sea region (the Azov Sea is not included) and it is based on NEMO v3.6 implicit free-surface implementation (Madec and The Nemo team, 2016), with a horizontal resolution of 1/27° in the zonal direction and 1/36° in the meridional direction, and 31 unevenly spaced vertical z-levels. This horizontal spatial resolution is chosen in order to have the same cartesian resolution in latitudinal and longitudinal directions, around 3 km at the model domain latitudes, which is conformed to an eddy-resolving

scale; the Rossby radius of deformation in the Black Sea is approximately 20 km (Hallberg, 2013). The BS-REA horizontal spatial domain is shown in **Figure 1**.

The model is forced by the ECMWF ERA-5 atmospheric reanalysis (Hersbach et al., 2020) at the surface with a 0.25° of spatial resolution and 1-hour time frequency. The atmospheric forcing variables are: the zonal and meridional components of 10 m wind (in m s^{-1}), total cloud cover (in %), 2 m air temperature (in K), 2 m dew point temperature (in K) and mean sea level pressure (in Pa). Precipitation (in kg/m^2 s) over the basin is obtained from GPCP rainfall monthly database (Adler et al., 2003; Huffman et al., 2009), from which monthly climatological means are estimated considering the period 1979–2019. The momentum, heat and water fluxes are computed at the air-sea interface based on the bulk formulae originally developed for the Mediterranean Sea (Castellari et al., 1998; Pettenuzzo et al., 2010) and applied as in the Black Sea forecasting system (Ciliberti et al., 2020).

The model bathymetry is based on the GEBCO gridded dataset at 30" resolution[1] in the Black Sea basin. The bathymetry is improved around the Bosphorus Strait with a high-resolution dataset, extensively described in Gürses (2016). Once acquired the high-resolution dataset, an optimal barycentric interpolation method is used to interpolate scattered bathymetric data on the regular spatial grid. The coastline is revised to account for and properly represents the coastal peculiarities and structures in the basin by using the NOAA shoreline dataset[2]. The river locations are remapped considering the new bathymetry.

For the river runoff, we use a monthly climatological mean estimate for the period 1960–1984 and provided by the SESAME project (Ludwig et al., 2009). The total number of rivers is 72, including the major ones such as Danube, Dnieper, Rioni, Dniester, Sakarya and Kizilirmak. The Danube runoff is distributed over five grid points to better represent its major branches, i.e., Chilia, Sulina, St. George. This special treatment accounts that the Chilia is the greatest one with three sub-branches. One is located in the south, in the Romanian territory, while the other two are in Ukraine. Sulina and St. George are located in the larger Danube floodplain, which occupies around 3500 km^2. Thus, the distribution of the Danube discharge over its three main branches follows Panin et al. (2016); the Chilia spread 52% of the total discharge, while the remaining 48% is distributed in the Sulina (20%) and St. George (28%) branches, respectively. The salinity of the river waters is assumed to be zero.

Since the current model configuration of the BS-REA has closed lateral boundaries, the Bosphorus Strait net transport is parameterised as a river by means of surface boundary conditions while temperature and salinity are relaxed to a previous estimate. The net transport is computed iteratively from a simulation and a series of assimilation runs. A first iteration, which is a simulation, adopts a monthly climatology (Kara et al., 2008) and integrates for the whole reanalysis period. Then, every following iteration imposes the net outflow corrected by E-P-R estimates from the previous one in order to balance the water budget; evaporation (E) is model-derived and depends on each integration whereas precipitation (P) and river runoff (R) are monthly climatology as described above. In the BS-REA, a final correction, estimated from the CMEMS SSALTO/DUACS Delayed-Time Level-4 sea level anomalies measured by multi-satellite altimetry observations (Taburet et al., 2019), is applied to the freshwater balance at a single grid point adjacent to the Bosphorus Strait in order to impose

[1]https://www.gebco.net/

[2]https://www.ngs.noaa.gov/CUSP

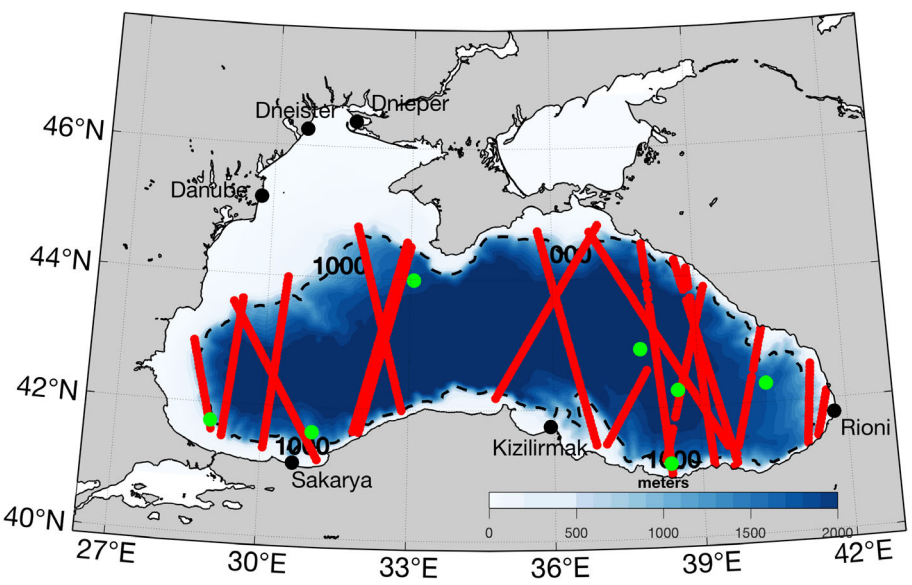

FIGURE 1 | Black Sea spatial domain and bathymetry. The red lines indicate the sea level anomaly along-track and green dots indicate the T and S *in situ* profiles available for data assimilation within the 4-day observation window on 18 October 2018.

the observed trend and variability in the mean sea surface height. T and S are relaxed toward a monthly climatological profile computed from a high-resolution multi-year simulation (Aydoğdu et al., 2018), to properly represent the water mass properties exchanged between the Mediterranean and Black Seas via the Bosphorus Strait. This relaxation is applied at five grid points surrounding the location of the Bosphorus Strait with a time frequency of 1 hour.

Finally, we restore the SST over the basin to the gridded CMEMS SST product (Buongiorno Nardelli et al., 2013). The restoring is done by added a damping term to the surface heat flux with a constant coefficient of dQ/dT = −200 W/m^2/K.

Observations

The BS-REA assimilates sea level anomaly (SLA), temperature and salinity observations. The specific products assimilated are: (i) in-situ T/S profiles from both SeaDataNet[3] (Pecci et al., 2020) and CMEMS NRT in-situ product (von Schuckmann et al., 2016) and (ii) along-track sea level anomaly from all available missions, pre-processed and distributed by the CMEMS Sea Level TAC (Taburet et al., 2019). For SLA assimilation, the choice of the mean dynamic topography (MDT) is a key point and can impact the quality of results (Yan et al., 2015). In BS-REA, a model-based MDT is computed using a 20-year (1993–2012) mean of sea surface height derived from a model integration with the assimilation of T and S profiles only.

The in-situ instrumental errors assume different values for T and S and vary in the vertical dimension based on statistics derived from Ingleby and Huddleston (2007), whereas the in-situ representation errors vary horizontally on the model grid according to previous model statistics with respect to observations and adopt same values for T and S. Both components of *in situ* errors are constant over time. For SLA observations, the instrumental error is set to 4 cm, and the representation errors monthly and spatially vary following Oke and Sakov (2008).

Data Assimilation Scheme

The data assimilation scheme is the OceanVar (Dobricic and Pinardi, 2008; Storto et al., 2011), a three-dimensional variational (3D-Var) assimilation algorithm. The 3D-Var scheme aims to iteratively find an optimal analysis field, x_a, that minimizes a cost function (Eq. 1).

$$J = \frac{1}{2}\delta x^T B^{-1}\delta x + \frac{1}{2}\left(H\delta x - d\right)^T R^{-1}\left(H\delta x - d\right) \quad (1)$$

$\delta x = x - x_b$, where x is the unknown ocean state, equal to the analysis x_a at the minimum of J, x_b is the background state, $d = y - H(x_b)$ is the misfit between an observation y and its modeled correspondent (in the observation space) where H, the observation operator, maps the model fields at the observation location. The method accounts for the background and observation uncertainties through the error covariance matrices B and R, respectively. The observational error covariance matrix R is diagonal in the observation space and includes the sum of instrumental and representation errors and an error component according to the time of each observation with respect to the analysis time, i.e., the observation error is multiplied by a weight depending on the absolute temporal distance between observation and analysis.

OceanVar was originally developed for the Mediterranean Sea (Dobricic and Pinardi, 2008) and later extended to global ocean applications (Storto et al., 2011, 2014). In OceanVar, in order to avoid the inversion of the B matrix and to precondition the minimization of the cost function, the B matrix is defined as $B = VV^T$, in which V is decomposed in a sequence of linear operators: $V = V_\eta V_h V_v$. Hence the V operator is used to model the background error covariance matrix and includes correlations among variables and each of its linear operators are described below. In addition, a new control variable v is used for the minimization step by considering the transformation $v = V^+\delta x$ and thereby $\delta x = Vv$; the superscript "+" indicates a generalized inverse. The inclusion of the control variable in Eq. 1 results in a rearranged cost function, as follows:

$$J = \frac{1}{2}v^t v + \frac{1}{2}\left(HVv - d\right)^T R^{-1}\left(HVv - d\right) \quad (2)$$

Thus, the variational cost function is solved with the incremental formulation (Courtier, 1997) and the pre-conditioning of the cost function minimization is achieved through a change-of-variable transformation from the physical (Eq. 1) to the control space (Eq. 2).

OceanVar is a multivariate scheme, i.e., the state vector, x, can contain the following model state variables: T, S, SLA u and v. However, only the first three variables are employed in the present BS-REA implementation; each control vector element is a linear combination of SLA, T, S. The assimilation of *in situ* profiles includes a background quality-check according to Eq. 3,

$$\frac{d^2}{\sigma_b^2 + \sigma_o^2} > \alpha \quad (3)$$

which rejects observations in the case the square departure from the background (d^2) exceeds the sum of the background (σ_b^2) and observation (σ_o^2) error variances by a threshold value (α). This threshold is currently set to 11 for both S and T.

For the minimization of J, the balance of the two terms in Eq. 2 defines the shape and magnitude of the analysis increments. The V_v operator consists of background-error T and S vertical covariances that are extracted empirically from a model integration with the assimilation of T and S profiles using the full model resolution; the same above-mentioned integration that is used to compute the model-based MDT. The daily temperature and salinity anomalies with respect to the monthly mean are calculated to generate a set of monthly EOFs (Empirical Orthogonal Functions, only the first 15 modes are retained). V_h represents horizontal correlations that are modeled through a first-order recursive filter (Farina et al., 2015), with a fixed correlation length-scale of 20 km. Determined by V_η, the SLA is covaried with T and S through a balance model (dynamic height) that imposes local hydrostatic and geostrophic balance among

[3]http://www.seadatanet.org

T, S, and SLA increments (Storto et al., 2011), according to the equation:

$$\rho_0 g\delta\eta \; + \; \int_{-h_b}^{0} g\delta\rho\,(T,S)dz \; = \; \delta p_b \tag{4}$$

where $\delta\eta$ and $\delta\rho$ are, respectively, the sea level anomaly and density increments, so that $\delta\rho$ is integrated in the vertical from the bottom depth h_b to the surface. The $\rho(T,\ S)$ relation is calculated with the 1980 United Nations Educational, Scientific and Cultural Organization (UNESCO) International Equation of State (IES 80; Fofonoff and Millard, 1985). We assume a "level of no motion" at 1000 m, which corresponds to the depth h^* where horizontal velocities are considered practically zero. This implies, through geostrophy, that the corresponding pressure increment δp_h^* vanishes too, which results in the equation:

$$H\,(x - x_b) \; = \; -\frac{1}{\rho_0}\int_{-h^*}^{0} \delta\rho\,(x - x_b)dz \tag{5}$$

Once the analysis increments are computed with OceanVar, the method of incremental analysis update (IAU) is used to spread the analysis increments in the first time-steps during the model initialization (Bloom et al., 1996). As a further reading on the data assimilation scheme, we refer to Dobricic and Pinardi (2008) and Storto et al. (2011).

Bias Correction

All data assimilation systems are affected by biases due to imperfect numerical models, inaccurate observations and limitations in the assimilation scheme itself (Dee, 2005). From a previous experiment with the assimilation of T, S, and SLA, we detected the evolution of systematic biases in T and S over time periods with very sparse *in situ* observations. For example, we have noticed drifts in temperature below 300 m starting in 1996 when the number of *in situ* profiles drastically reduces while altimeter observations are available. Since such drift was not present in another experiment with the assimilation of only *in situ* profiles, we conclude that it was generated by the SLA assimilation conducted alone.

In order to prevent those drifts, BS-REA employs a large-scale bias correction (LSBC) below 300 m throughout integration. The LSBC is formulated as:

$$\frac{dx}{dt} \; = \; M\,(x) - L\,(b) \tag{6}$$

We define the estimated bias $b \; = \; x - x_{clim}$ as the difference between the instantaneous temperature and salinity fields with respect to T and S climatologies, which is computed for the period 1993–2018 from the above mentioned experiment that assimilates only *in situ* profiles; $\frac{dx}{dt}$ denotes the T and S tendencies, whereas $M\,(x)$ represents all dynamical and thermodynamical processes and boundary conditions involving T and S during the NEMO integration. The operator L is the estimator of the model bias. It consists of a low-pass spatial filter, configured to filter out spatial scales shorter than 20 km, and is formulated as a first-order Shapiro filter (Shapiro, 1970) that uses 250 iterations. The final bias is subtracted from the tendency, as in the incremental algorithm (Bloom et al., 1996) with a relaxation coefficient of 1200 days in order to not deplete the seasonal variability.

Numerical Experiments: Strategy and Setup

Following a spin-up of 5 years (1988–1992) with T and S assimilation, the BS-REA starts from 1993, as soon as the altimeter observations are available, with an assimilation cycle of 2-days. That is, if the model initializes at time t, the next analysis is performed at time $t \; + \; 2$. The observation window is 4 days centered at the analysis time, i.e., each cycle includes observations from 2 days before and after the analysis time. **Table 1** summarizes the main aspects of the BS-REA configuration, which are also described in Lima et al. (2020a). For comparison, we also present a control experiment, covering the same period of BS-REA, with exactly the same set up for air-sea interaction, such as the same atmospheric forcing and heat flux correction using the analyzed SST, but without data assimilation and LSBC.

RESULTS AND DISCUSSION

In this section we present the assessment of the BS-REA. Estimated Accuracy Numbers (EAN), which include bias and root mean square difference (RMSD), are computed using the daily outputs of the reanalysis and compared to observations using a quasi-independent approach since the validation is done by comparing the daily-averaged BS-REA fields with respect to both assimilated and rejected observations. Moreover, we provide ocean monitoring indicators such as the temperature, salinity, and ocean

TABLE 1 | BS-REA main configurations.

Model resolution	$1/36^o \times 1/27^o$
Vertical coordinates	31 Z levels
Temporal coverage	1993–2018
Spin up	1988–1992 with T/S data assimilation
Atmospheric forcing	ERA5 (1 h; 0.25 degree)
DA frequency	2 days
Observation window	4-day centered at the analysis time
SST relaxation	CNR-CMEMS SST L4 REP
in situ TS assimilation	SeaDataNet and CMEMS NRT *in situ* TAC
SLA assimilation	CMEMS sea level along-track REP product for the European seas
Mean Dynamic Topography	Model-based Time-averaged SSH (1993–2012) from an integration with the assimilation of only *in situ* T and S
SLA instrumental errors	4 cm
SLA representation errors	Monthly 2-D fields Oke and Sakov (2008)
In situ instrumental errors	Ingleby and Huddleston (2007)
In situ representation errors	Static 2-D field
Initialization	Incremental analysis update (IAU)
Recursive filter	Correlation length-scale of 20 km
Large Scale Bias Correction	Below 300 m

heat content anomalies for the Black Sea. Finally, we describe the sea level and upper circulation based on the BS-REA results.

BS-REA Evaluation

In **Figure 2**, the seasonal maps of the SST bias and RMSD are shown. There is a predominance of positive SST bias all over the basin while a negative bias manifests in limited zones such as the western Anatolian coast in summer and autumn, in river influenced areas in the northwestern shelf during the whole year and in the vicinity of the Azov Sea except in spring. The BS-REA exhibits the lowest RMSD in spring, whereas the highest RMSDs are reached in summer and autumn. For instance, the RMSD exceeds 0.75°C along the upwelling region centered at 33°E (Sur et al., 1994; Özsoy and Ünlüata, 1997) in the Turkish coast, where we believe that overestimated surface winds from

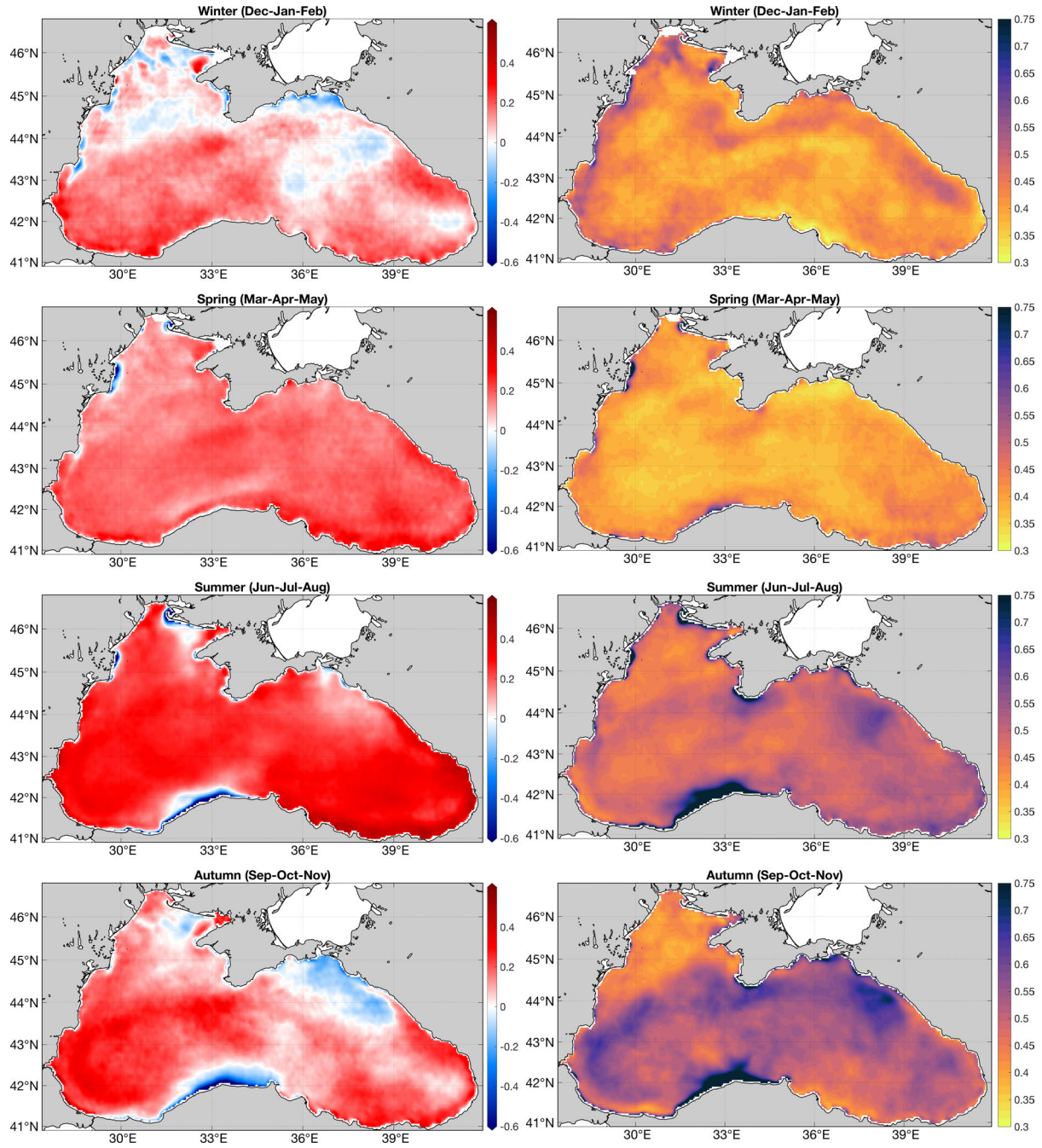

FIGURE 2 | Seasonal maps of the mean bias (left) and RMSD (right) of the SST (°C) with respect to the satellite SST-L4 products over the period between 1993 and 2018. From top to bottom: winter, spring, summer, and autumn.

TABLE 2 | EAN estimations for BS-REA and the control experiment without data assimilation.

	RMSD		BIAS	
	Control	BS_REA	Control	BS-REA
SST °C	0.32	0.33	0.08	0.08
T °C (0–10 m)	0.97	0.59	−0.25	0.01
T °C (10–100 m)	1.50	0.63	0.51	−0.03
T °C (100–500 m)	0.35	0.07	0.23	0.001
T °C (500–1500 m)	0.09	0.07	0.08	0.05
S PSU (0–10 m)	0.66	0.41	0.20	−0.02
S PSU (10–100 m)	0.77	0.16	0.54	0.001
S PSU (100–500 m)	0.28	0.09	−0.07	0.01
S PSU (500–1500 m)	0.02	0.01	0.001	−0.002
SLA m	3.67	2.25	0.00	

Note that the comparison between model and observation SLA includes a bias removal in such a way the bias should always be 0.

the atmospheric dataset may intensify the upwelling events in summer and autumn.

In general, BS-REA performs better than the control experiment in terms of bias and RMSD (**Table 2**). The only variable where it is similar or even slightly lower is the SST which is strongly controlled by the atmospheric forcing and the SST relaxation, both of which are the same in the two experiments. For temperature, the highest RMSDs for the layer 10–100 m are 0.63°C and 1.50°C for BS-REA and the control, respectively. While the control experiment has a negative bias of −0.25°C in the upper layers, BS-REA retains a quite reduced positive bias of 0.01°C.

In **Figure 3**, we show the vertical temperature error and bias profiles for different subregions in the Black Sea. The RMSD is relatively higher in the northwestern region (dark blue) that is under the influence of the Danube River where a maximum RMSD close to 2.25°C arises around the thermocline. The other two regions with relatively large errors are the northeastern (light blue) and southwestern ones (green), which, respectively, may be related to the absences of the Azov Sea and an open Bosphorus Strait in the BS-REA configuration. Bias profiles manifest the largest discrepancies with the observations above 40 m where there is a predominance of a negative bias (above −0.5°C), except in the northwestern region affected by a positive bias. The Hovmöller diagrams of the temperature bias and RMSD (**Figure 4**, upper panels) reveal a clear seasonal pattern such that the values are low (high) in winter (summer). The highest errors are in the thermocline, where the prevalence of negative biases is evident each summer from 10 m down to 60 m. There is an evident lack of in-situ observations between 1997 and 2003 in the Black Sea which limits the reanalysis system to be constrained only by altimeter observations for a long time period.

BS-REA shows significant improved skills also for salinity with respect to the control experiment (**Table 2**). The RMSD is reduced in the entire water column from 0.66 PSU to 0.41 PSU (0.77 PSU to 0.16 PSU) in 0–10 m (10–100 m). The bias is also decreased from surface down to 500 m, mainly in the layer

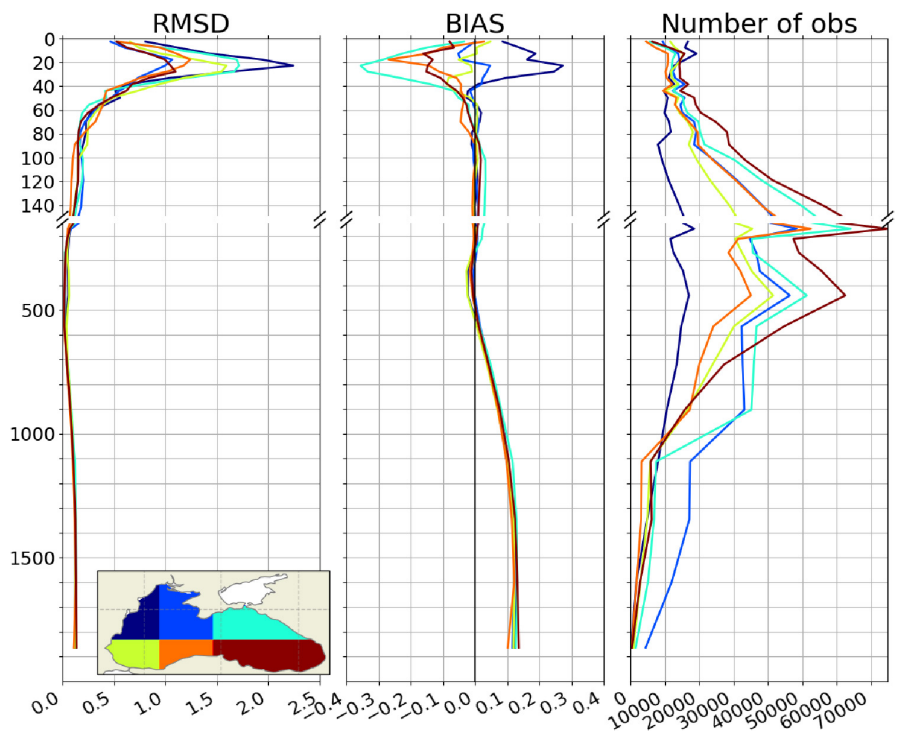

FIGURE 3 | Vertical profiles of the root mean square deviation (left panel), bias (middle panel), and number of observations (right panel) for temperature (°C) for different subdomains in the Black Sea, by comparing the BS-REA results against *in situ* profilers in the Black Sea domain from 1 January 1993 to 31 December 2018.

10–100 m where the BS-REA bias is 0.001 PSU. BS-REA presents a slightly negative bias of −0.02 PSU in 0–10 m.

The vertical error profiles for different regions show that BS-REA represents with less quality the salinity above 20 m, in particular in the northwestern region (**Figure 5**). In this region, the RMSD overcomes 1.2 PSU at surface and the bias reaches −0.2 PSU at around 10 m depth. This is probably due to the limitation of imposing monthly climatological runoff such as

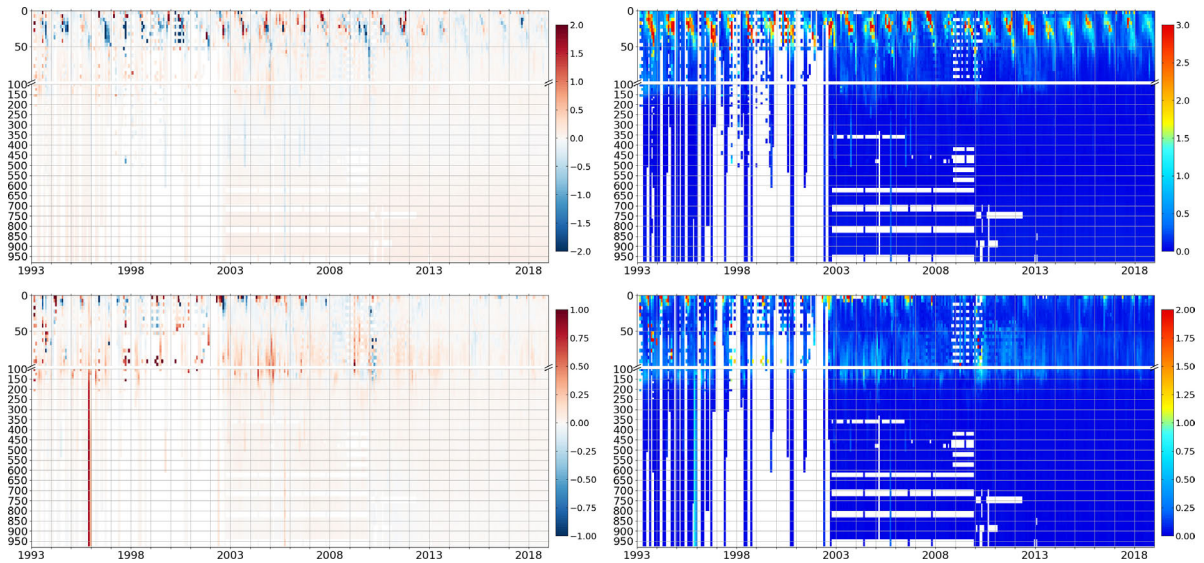

FIGURE 4 | Monthly Hovmöller diagrams of bias (left) and root mean square difference (right) computed against observations of temperature in °C (top) and salinity in PSU (bottom) available in the Black Sea domain from 1 January 1993 to 31 December 2018.

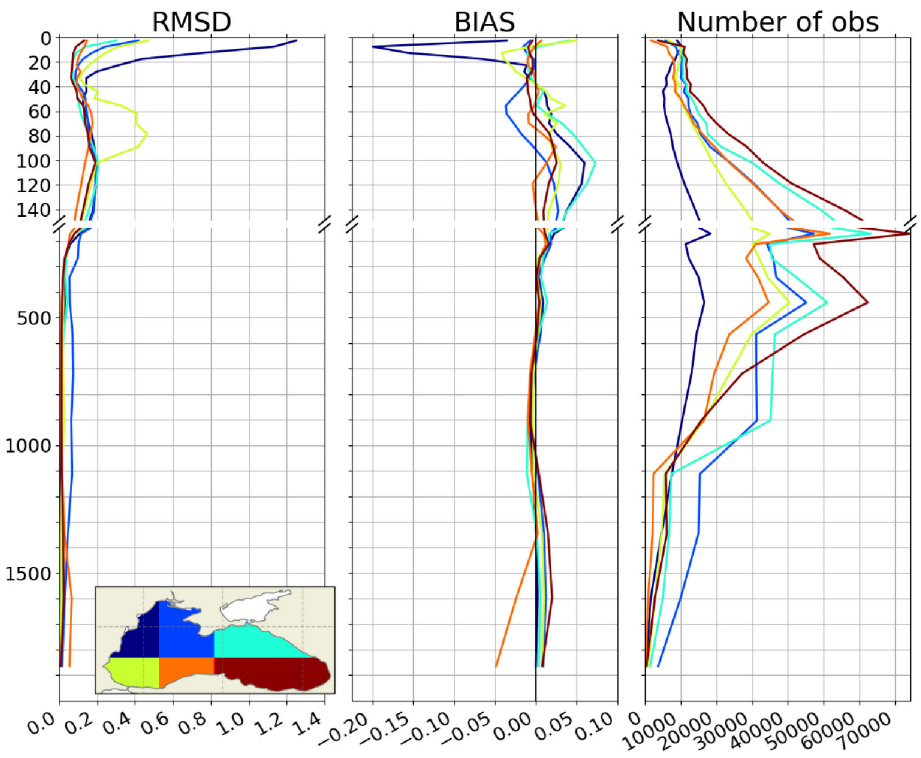

FIGURE 5 | Vertical profiles of the root mean square deviation (left panel), bias (middle panel) and number of observations (right panel) for salinity (PSU) for different sub-domains in the Black Sea, by comparing the BS-REA results against *in situ* profilers in the Black Sea domain from 1 January 1993 to 31 December 2018.

for the Danube River, which may cause a poor representation of salinity close to the river mouth. Unfortunately, we do not have a long and uninterrupted time series of river discharges for the Black Sea to be used for a more accurate parameterization. In deeper levels, the salinity RMSD is relatively higher only in the southwestern region in the layer 60–100 m where the RMSD exceeds 0.4 PSU. This may be due to the parameterization of the Bosphorus Strait in the current model configuration in which we relax the model towards a climatology from a model simulation. Nevertheless, bias is low in the southwestern Black Sea and comparable to other regions. Hovmöller diagrams show that both salinity bias and RMSD remain low over time (**Figure 4**, bottom panels). However, we note large RMSD that may exceed 1.5 PSU near the surface, mainly during some temporal intervals before 2008.

The mean RMSD of sea level anomaly is 2.25 cm for BS-REA which corresponds to a reduction of ∼39% with respect to the control (**Table 2**). Time series of SLA RMSD present a continuous reduction of the values during the first years of BS-REA integration. Error values fluctuate around 2 cm since 2005, whereas the control error ranges between 3 and 4 cm, sometimes exceeding 4 cm (**Figure 6**). Horizontal maps of RMSD reveal minor seasonal differences with the largest values close to the shelf areas (not shown), where there is a dominance of the mesoscale activities along the Rim Current. For example, relatively high errors can be found in the Crimean Peninsula, where there is a regular activity of the Sevastopol eddy, and in the southeastern region, which is related to the presence of the Batumi eddy. These eddies are quasi-stationary anticyclonic features that have been examined in the Black Sea (Kubryakov and Stanichny, 2015; Kubryakov et al., 2018).

Temperature and Salinity Trends

This section examines the time variability of temperature and salinity as well as their trends for the whole BS-REA period (1993–2018) and its latest 14 years (2005–2018).

Initially, the basin-averaged temperature time series shown in **Figure 7** demonstrate a high seasonal variability in 0–25 m, with values above (below) 20°C (7.5°C) in most of the summers (winters). The seasonal signal weakens between 25 and 150 m and disappears below 150 m. The temperature trends are estimated in two different periods (1993–2018 and 2005–2018) and indicate an overall warming of the basin especially in the period 2005–2018 with a decreasing trend in deeper layers. The values are 0.083°C year^{-1} (0.12°C year^{-1}) in 0–25 m and reduce to 0.0041°C year^{-1} (0.0092°C year^{-1}) in 150–300 m for the period 1993–2018 (2005–2018). For comparison, Ginzburg et al. (2004) used satellite measurements to reveal a positive trend of 0.09°C year^{-1} in sea surface temperature over the years 1982–2000. Miladinova et al. (2017) did not detect a significant trend in the SST from model simulations considering the period 1960–2015, whereas the temperature at 200 m indicated a positive trend of 0.005°C year^{-1}. BS-REA warming is more noticeable starting from 2005, especially in the 150–300 m layer, where instead a negative trend between 1993 and 2001 is reproduced by the reanalysis. BS-REA also presents a continuous warming in the layer 25–150 m, where the Black Sea CIL resides. In response, the CIL almost disappeared in recent years as is discussed in the next paragraph. Stanev et al. (2019) reached a similar result using observations.

Figure 8 (top left panel) shows the time evolution of basin mean temperature and the 8°C isotherm is chosen to track the Black Sea CIL over time. The CIL formation is related to the water cooling during the winter season and its presence is evident continuously until 2008. From 1993 to 2000, the CIL resides from surface down to ∼100 m. There is a weakening of the CIL in 2001 when the temperature exceeds 8°C in most of the water column. The CIL forms again in 2002 but not as strong as in the previous years so that the 8°C isotherm occupies depths above 75 m. The pattern completely changes after 2008, when the temperatures clearly increase in such a way that the CIL disappears most of the time. Between 25 and 150 m the temperature increase (shown in **Figure 7**) reflects a trend value of 0.045°C year^{-1} for the period 2005–2018, by revealing a faster warming of the Black Sea over recent years. Degtyarev (2000) also noted a positive temperature trend of 0.016°C years^{-1} in a less thick layer (50–100 m) from 1985 to 1997. After 2008, the formation and presence of the CIL is observed only in 2012 and, to a lesser extent, in 2017. **Figure 8** (bottom left panel) shows the basin mean temperature anomaly with respect to a reference climatology evaluated from the same

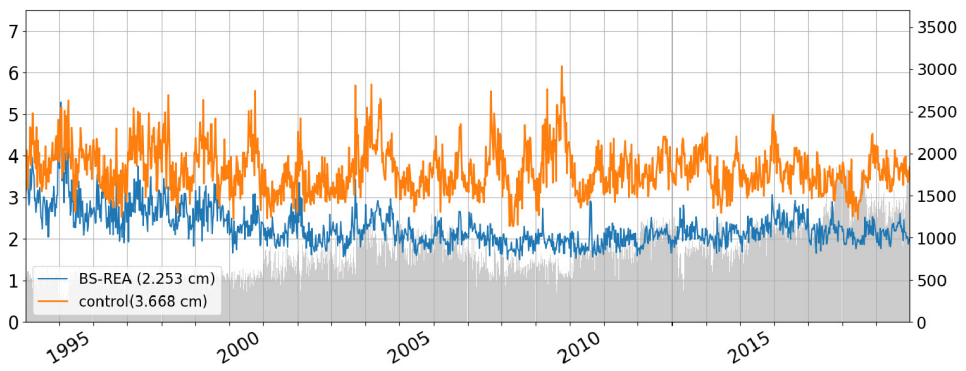

FIGURE 6 | Time series of sea level anomaly RMSD by considering the results of BS-REA (blue) and control experiment (orange) against sea level anomaly along-track observations in the Black Sea domain. The shaded area and the right axis correspond to the number of observations.

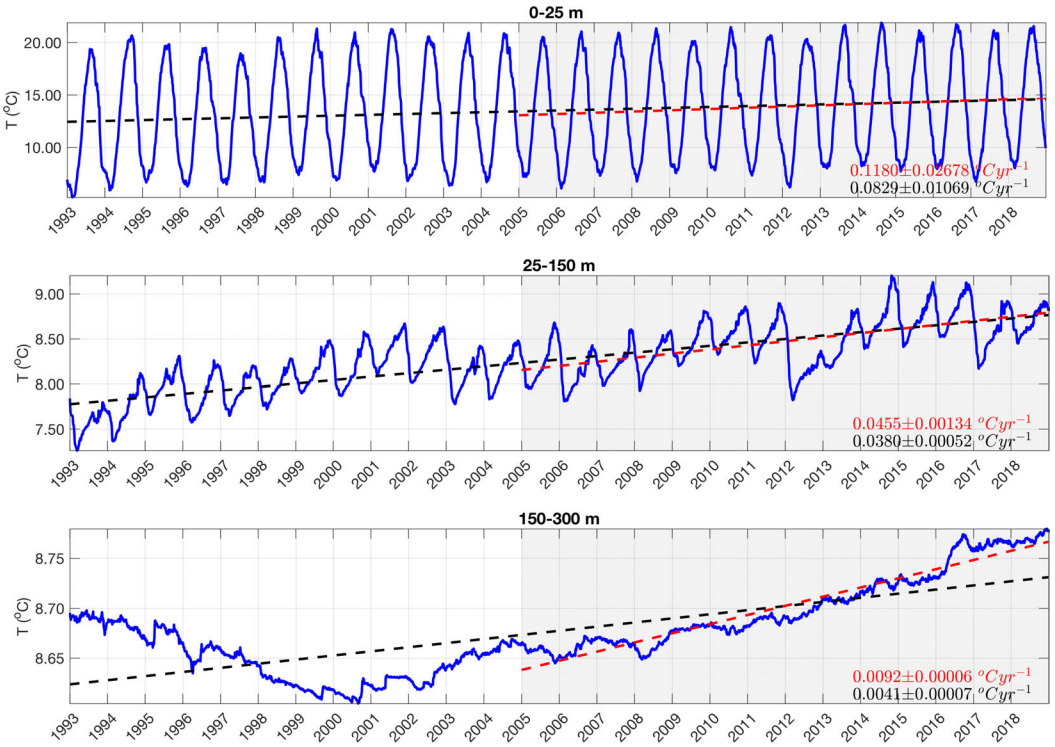

FIGURE 7 | Time evolution of the basin-averaged temperature in °C computed from BS-REA in different layers: 0—25 m (top), 25–150 m (central), and 150–300 m (bottom). The dashed lines are the linear trends for the period 1993–2018 (black) and 2005–2018 (red), mean trend values are also reported in the figures (bottom right corner).

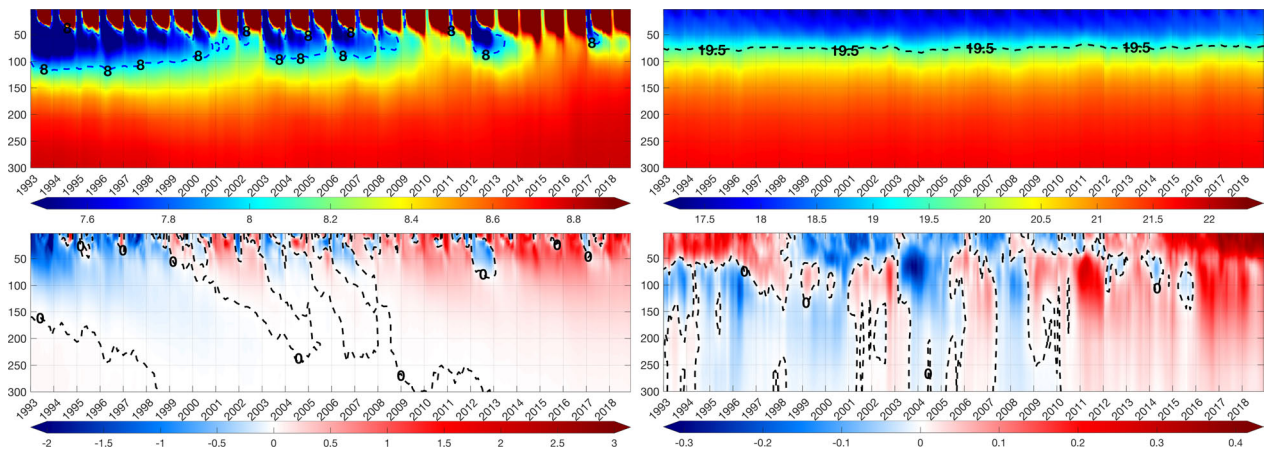

FIGURE 8 | Time versus depth diagrams of the monthly basin-averaged temperature in °C (top left), anomaly of temperature in °C (bottom left), monthly basin-averaged salinity in PSU (top right), and anomaly of salinity in PSU (bottom right). The monthly anomaly estimates considered the climatological period 1993–2014 of each corresponding month. The blue dashed line indicates the mean position of the 8°C isotherm (top left), whereas the dashed black line represents the isoline of 19.5 PSU (top right) and null anomaly (bottom panels).

reanalysis in the period 1993–2014. The temperature anomaly is mostly negative before 1999, while during the period 1999–2008, it shows a clear annual variability in the upper 250 m, fluctuating between negative and positive values around the reference baseline. Since 2009, there is a predominance of positive anomalies so that values exceed 1.5 °C at upper layers, which again supports the Black Sea warming and disappearance of the CIL during recent years. Reports based on previous versions of BS-REA also found a surface warming and an increase in the ocean heat content of the Black Sea in the past few years (Mulet et al., 2018; Lima et al., 2020c) which will be discussed in section 3.3.

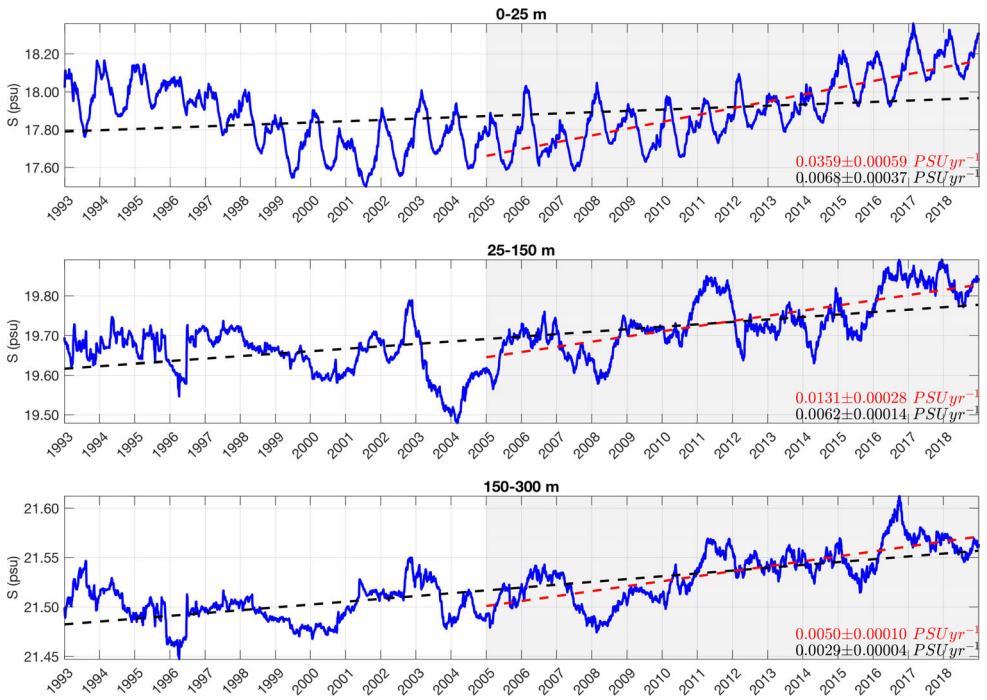

FIGURE 9 | Time evolution of the basin-averaged salinity in PSU computed from BS-REA in different layers: 0–25 m (top), 25–150 m (central), and 150–300 m (bottom). The dashed lines are the linear trends for the period 1993–2018 (black) and 2005–2018 (red), mean trend values are also reported in the figures (bottom right corner).

In **Figure 9**, similar analyses for salinity reveal that salinity trends reduce in depth and are higher during the most recent period (2005–2018) especially in surface layers. Trends are 0.0068 PSU year^{-1} (0.0359 PSU year^{-1}) in 0–25 m, decrease to 0.0062 PSU year^{-1} (0.0131 PSU year^{-1}) in 25–100 m and finally to 0.0029 PSU year^{-1} (0.005 PSU year^{-1}) in 150–300 m during the period 1993–2018 (2005–2018). For comparison, Miladinova et al. (2017) identified different salinity trends at the surface (negative), upper (weaker negative) and main halocline (positive) for the period 1960–2015. The time evolution of salinity shows well-defined layers, such that mean values are less than 18.5 PSU above 50 m, reach 20–20.5 PSU at 100 m and exceed 21.5 PSU in deeper waters down to 300 m (**Figure 8**; top right panel). Above 50 m, salinity anomalies, evaluated with respect to a reference climatology from the same reanalysis in the period 1993–2014 exhibit periods that alternates with the predominance of positive and negative anomalies: anomalies are positive until the beginning of 1998, mostly negative from 1998 to 2011, and again positive starting from 2012 (**Figure 8**; bottom right panel). A notable characteristic is the presence of larger positive anomalies from 2016, which indicates a recent salinization in the sea. In 50–100 m, large negative anomalies are present in 2004–2005, whereas maximum positive anomalies are seen in 2011. After 2016, salinity anomalies are only positive.

Ocean Heat Content

The investigation of the Black Sea ocean heat content follows Lima et al. (2020c), who defined the ocean heat content like anomalies with respect to the reference period of 2005–2014, following the equation below:

$$OHC = \int_{z_1}^{z_2} \rho_0 c_p \, (T_m - T_{clim}) dz \qquad (7)$$

with ρ_0 equal to 1020 kg m^{-3} and c_p equal to 4181.3 J kg^{-1}°C $^{-1}$ are, respectively, the density and specific heat capacity; and dz indicate the a certain ocean layer limited by the depths z_1 and z_2; T_m corresponds to the monthly average temperature and T_{clim} is the climatological temperature of the corresponding month.

In this study the ocean heat content is estimated as the deviation from the reference period of 1993–2014. A clear positive trend of 0.11 W m^{-2} characterizes the 0–10 m layer (**Figure 10**). Above this trend, warm peaks appear in the second half of the year 1994, less intense in 1996 and increased again in 2010 and 2012. The highest positive peak occurs in the 2018 autumn. As thicker layers are considered, the trends increase, whereas time series present a lower variability over time; for the period 1993–2018, trends are 0.45 W m^{-2}, 0.81 W m^{-2} and 0.83 W m^{-2}, respectively, in 0–50, 0–200, and 0–1000 m. For comparison, trends are also estimated for the period 2005–2018 and reveal higher values down to 200 m as compared to Lima et al. (2020c) (**Table 3**), which may be related to the different period (2005–2014) that they used to estimate the reference climatology. Considering thicker layers, it becomes clear that an increase in ocean heat content weakens the CIL like in 2001, whereas its decreasing favors the CIL restoration like in the years 2012 and 2017, as is viewed in **Figure 8** (top left panel). In 2012, times

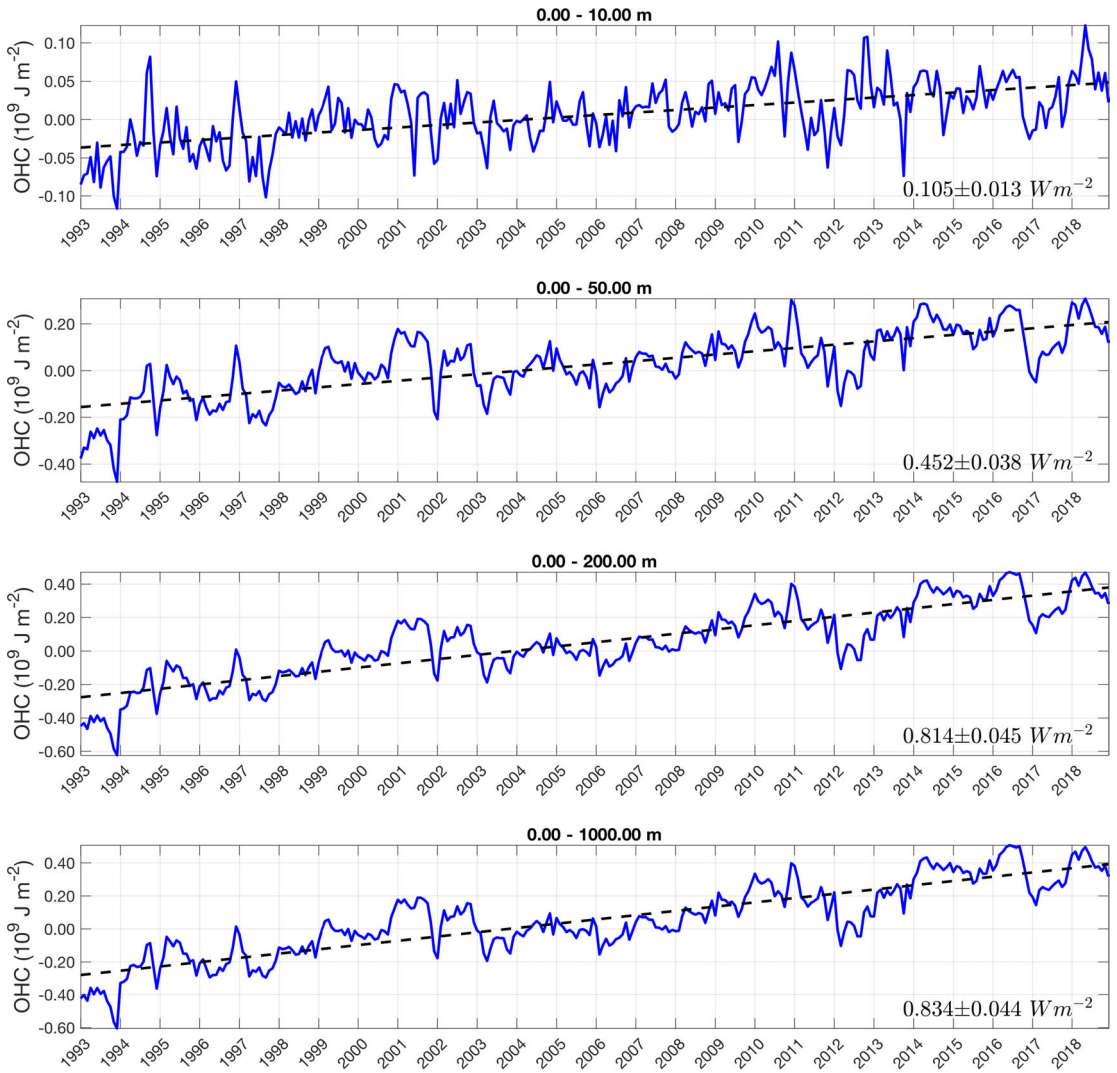

FIGURE 10 | Monthly basin-averaged of the ocean heat content anomalies (in 10^9 J m^{-2}) estimated for the BS-REA. The monthly ocean heat content anomalies are defined as the deviation from the climatological ocean heat content mean (1993–2014) of each corresponding month. Mean trend values are also reported in the figures (bottom right corner).

series for 0–10 m exhibits colder waters already in 2011 that appear in 2012 only when layers as thick as 50 m are considered, which indicates that colder waters moved from surface in 2011 to generate the CIL in 2012 (**Figure 10**). A migration of colder and saltier water from surface to deeper layers also produced a signature in the temperature and salinity anomalies (**Figure 8**; bottom panels). A less intense CIL formation occurred in 2017 and again a water cooling in the 0–10 m layer is evident in the previous year, 2016.

Spatial maps of yearly depth-integrated ocean heat content anomalies (0–200 m) show a predominance of negative values from 1993 until 1998 (**Figure 11**). Lowest values are found in 1993 at the margins of the basin. In 1999, positive values appear mostly in shallow regions at the basin borders, but also in deeper regions like along the Rim Current pathway near the Crimean Peninsula. In this region, positive values may be associated with the presence of the Sevastopol eddy, a quasi-stationary anticyclonic eddy located close to the Crimean Peninsula. The pattern changes completely in 2001 and 2002, when the ocean

TABLE 3 | Trends estimations together with the 95% confidence interval (in brackets) for the ocean heat content anomaly (W m^{-2}) from BS-REA and Lima et al. (2020c) for the period 1993–2018 and 2005–2018.

	1993–2018	2005–2018	
	BS-REA	BS-REA	Lima et al. (2020c)
0–10 m	0.105 (0.013)	0.089 (0.032)	0.063 (0.038)
0–50 m	0.452 (0.038)	0.482 (0.087)	0.447 (0.131)
0–200 m	0.814 (0.045)	0.922 (0.103)	0.880 (0.181)
0–1000 m	0.834 (0.044)	1.049 (0.102)	1.082 (0.175)

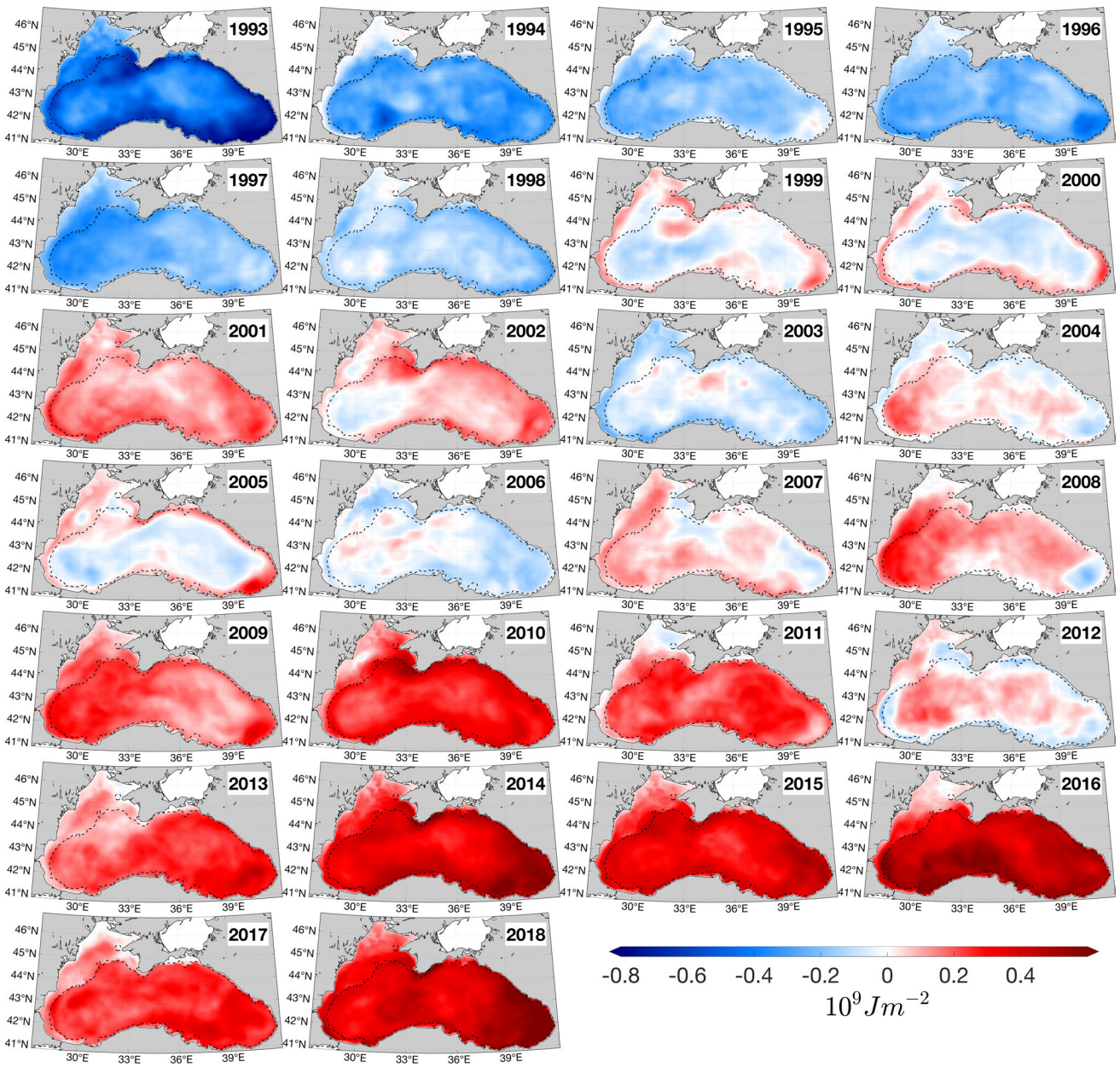

FIGURE 11 | Yearly depth-integrated (0-200 m) ocean heat content anomalies (in 10^9 J m^{-2}) estimated for the BS-REA and defined as the deviation from the reference period of 1993–2014. Black isoline indicates the 200 m isobath.

heat anomaly assumes positive values in a large part of the basin, which brings a weakening of the Black Sea CIL in these years (see also **Figure 8**; top left panel). In the period from 2003 to 2006, there is again a predominance of negative values, except in 2004, when a prevalence of positive values is viewed in the central region. Since 2007, the warming signal is very clear in such a way that the ocean heat content anomalies achieve the highest positive values near the Crimean Peninsula in 2010, near the Bulgarian and Turkish coasts in 2016 and in the southeastern region in 2013, 2015 and 2018. However, this continuous warming is interrupted in 2012 and less explicitly in 2017, years in which a replenishment of the CIL is verified, as is also shown in **Figure 8**.

Surface Topography and Upper Layer Circulation

Figure 12 shows annual and seasonal mean sea surface height (SSH) fields overlaid by the upper 100 m depth-averaged velocity. The mean SSH varies spatially, i.e., low values dominate the inner basin while the shelf and coastal zones have high values. Similar formation persists when the signal is decomposed into

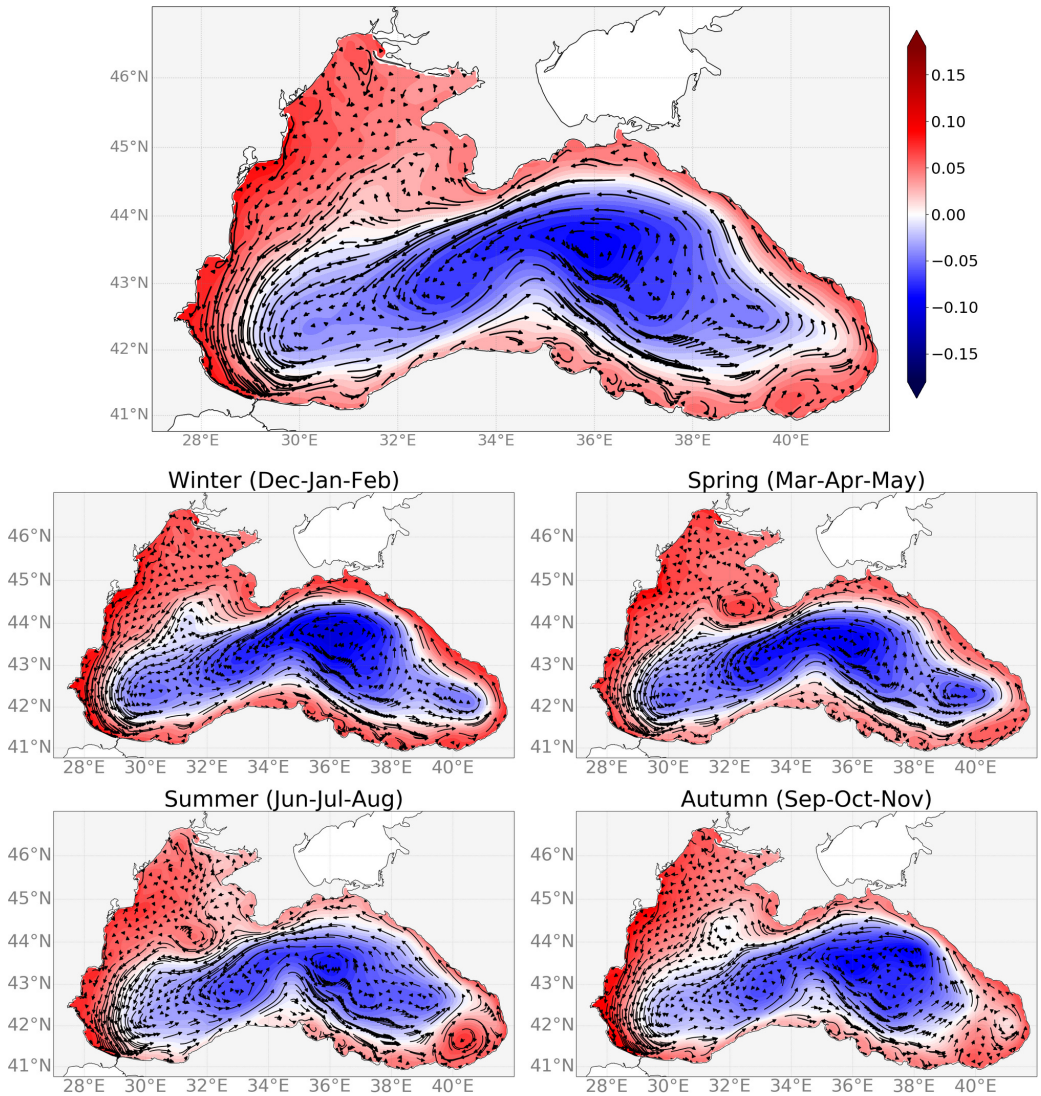

FIGURE 12 | Mean sea surface height and 100 m depth average velocity derived from the BS-REA evaluated for the whole period 1993-2018 (top panel) and each season considering the climatological period 1993–2018.

its seasonal components. In winter and spring, the negative values of SSH extend to the easternmost coast. In summer and autumn, the western basin presents similar SSH properties while, in the eastern basin, the negative values are more restricted to the inner basin.

The upper layer Black Sea circulation structures are consistent with the SSH gradients showing a seasonal variability with the only exception of the permanent Rim Current encircling the entire basin and forming a large-scale cyclonic gyre. The mean upper layer circulation develops around the Rim current together with the Batumi gyre in the easternmost basin and smaller scale eddies along the Anatolian coast. The Rim current bifurcates into two branches after the Crimean Peninsula with a smaller one recirculating in the northwestern shelf and merges back to the main branch around 30.5°E. The Rim current accelerates along the Turkish coast around 32°E, then detaches from the shelf and penetrates into the deep basin before going again close to the coast around 35.5°E. In winter, the eastern and western gyres are less defined. Following the Rim Current, the Batumi anticyclonic eddy is well defined in summer, seems to be more confined near the Georgia coast in autumn, but it is less apparent in winter and spring. Next, the presence of Sevastopol anticyclonic eddy is very clear near the southwest of the Crimean Peninsula in spring and summer, whereas it is less distinguishable in winter and autumn. All these circulation patterns are consistent with the previous estimates described in Oguz et al. (1993); Özsoy and Ünlüata (1997), Korotaev et al. (2003) and Gunduz et al. (2020).

CONCLUSION

The BS-REA system shows very satisfactory skills compared to the model simulation, which highlights the importance of using data assimilation to improve the model representation. BS-REA

also has the ability to represent the main Black Sea circulation, the Rim Current, as well as the mesoscale features in the Black Sea, such as the quasi-stationary anticyclones Sevastopol and Batumi eddies, respectively, near the Crimean Peninsula and southeastern region. Notwithstanding, the BS-REA has shown a reduced ability to represent the impact of Danube waters on the sea, which is possibly due to the current model configuration such as the application of monthly climatological runoff. Furthermore, the absence of the Bosphorus and Kerch straits negatively impacts the BS-REA representation in regions adjacent to the Azov and Marmara Seas.

The system is very suitable for understanding the physical state of the Black Sea in recent years and allows to obtain more accurate ocean monitoring indicators for the sea, which are important to understand its response to climate change. The temperature analyses have indicated a recent faster warming of the Black Sea that has impacted its CIL formation. Since 2009, the disappearance of CIL is evident, although some weaker CIL sporadic events are detected in 2012 and 2017. Additional investigations show a relative reduction in the ocean heat content in these years, which coincides with the reemergence of the CIL.

Trends in temperature, salinity and ocean heat content reveal a warming and salinification of the Black Sea, especially in the past few years. However, since trends based on short records are very sensitive to the beginning and end values of the time series and cannot in general reflect long-term climate trends, longer time series are needed to confirm these tendencies. This requires a continuous improvement of the BS-REA system through new developments in ocean modeling and data assimilation together with the maintenance of the Black Sea ocean observation system. In addition, for future work, we consider comparing our results with global models such as those from the Ocean Model Intercomparison Project (Lin et al., 2020; Chassignet et al., 2020) and global ocean reanalyses (Storto et al., 2019a,b), which can also allow us to quantify uncertainties through an ensemble of model results in the Black Sea.

In order to further improve the reanalysis, the next generation of the Black Sea systems will include a revision of the hydrodynamical core and new capacities from the data assimilation scheme. Regarding the core model, the new version will use higher resolution in vertical (e.g., from 31 to 121 z-levels with partial steps) and upgrade to NEMO v4.0. The Bosphorus Strait is going to be represented as an open boundary thanks to the inclusion of the Marmara Sea box in the numerical grid: it will ingest the high-resolution model solutions provided by the Unstructured Turkish Straits System (U-TSS, Ilicak et al., 2021) - T, S, SSH, U, V - with the scope to optimally interface the Black Sea with the Mediterranean Sea. Such new developments, together with the revision of the land forcing and data assimilation scheme to account for high resolution EOF, will be part of the new Black Sea forecasting system (Ciliberti et al., 2021) that entered in service in May 2021 and will be uptaken by the BS-REA in the near future.

DATA AVAILABILITY STATEMENT

The datasets presented in this study can be found in online repositories. The names of the repository/repositories and accession number(s) can be found below: https://doi.org/10.25423/CMCC/BLKSEA_MULTIYEAR_PHY_007_004.

AUTHOR CONTRIBUTIONS

LL led the work, developed the reanalysis system, and contributed to the elaboration of this work at all levels. SCi led the hydrodynamical model development and provided a valuable scientific contribution to improve this work at different levels. DA, SCa, and MI contributed to the hydrodynamical model development. SM contributed to the scientific scope, providing important insights to improve this work at different levels. AA contributed to improving the model setup, particularly for the correction of the model freshwater budget and provided a valuable scientific contribution to improve this work at different levels. RE contributed to define the validation strategy. AC contributed to set up the bias correction scheme. AA, RE, AC, and EJ contributed to define the data assimilation strategies. RL provided the access to all available observational dataset. SCr, LS, and FP contributed to set up the operational procedures and interfaces. EP, GC, and EC provided useful comments that helped to guide this work. All authors contributed to the article and approved the submitted version.

FUNDING

This research was funded by the Copernicus Marine Environment and Monitoring Service for the Black Sea Monitoring and Forecasting Centre (Contract No. 72-CMEMS-MFC-BS).

REFERENCES

Adler, R. F., Huffman, G. J., Chang, A., Ferraro, R., Xie, P. P., Janowiak, J., et al. (2003). The version-2 global precipitation climatology project (GPCP) monthly precipitation analysis (1979-present). *J. Hydrometeor.* 4, 1147–1167. doi: 10.1175/1525-7541(2003)004<1147:tvgpcp>2.0.co;2

Akpinar, A., Fach, B. A., and Oguz, T. (2017). Observing the subsurface thermal signature of the Black Sea cold intermediate layer with Argo profiling floats. *Deep Sea Res. I Oceanogr. Res. Papers* 124, 140–152. doi: 10.1016/j.dsr.2017.04.002

Aydoğdu, A., Pinardi, N., Özsoy, E., Danabasoglu, G., Gürses, Ö., and Karspeck, A. (2018). Circulation of the Turkish straits system under interannual atmospheric forcing. *Ocean Sci.* 14, 999–1019. doi: 10.5194/os-14-999-2018

Balmaseda, M. A. (2017). Data assimilation for initialization of seasonal forecasts. *J. Mar. Res.* 75, 331–359. doi: 10.1357/002224017821836806

Bloom, S. C., Takacs, L. L., Silva, A. M. D., and Ledvina, D. (1996). Data assimilation using incremental analysis updates. *Mon. Wea. Rev.* 124, 1256–1271. doi: 10.1175/1520-0493(1996)124<1256:dauiau>2.0.co;2

Buongiorno Nardelli, B., Tronconi, C., Pisano, A., and Santoleri, R. (2013). High and ultra-high resolution processing of satellite sea surface temperature data

over Southern European seas in the framework of MyOcean project. *Rem. Sens. Environ.* 129, 1–16. doi: 10.1016/j.rse.2012.10.012

Castellari, S., Pinardi, N., and Leaman, K. (1998). A model study of air-sea interactions in the Mediterranean Sea. *J. Mar. Sys.* 18, 89–114. doi: 10.1016/s0924-7963(98)90007-0

Chassignet, E. P., Yeager, S. G., Fox-Kemper, B., Bozec, A., Castruccio, F., Danabasoglu, G., et al. (2020). Impact of horizontal resolution on global ocean–sea ice model simulations based on the experimental protocols of the Ocean Model Intercomparison Project phase 2 (OMIP-2). *Geosci. Model Dev.* 13, 4595–4637. doi: 10.5194/gmd-13-4595-2020

Ciliberti, S. A., Jansen, E., Martins, D., Gunduz, M., Ilicak, M., Stefanizzi, L., et al. (2021). *Black Sea Physical Analysis and Forecast (CMEMS BS-Currents, EAS4 system) (Version 1) [Data set]. Copernicus Monitoring Environment Marine Service (CMEMS).* doi: 10.25423/CMCC/BLKSEA_ANALYSISFORECAST_PHY_007_001_EAS4

Ciliberti, S. A., Peneva, E. L., Jansen, E., Martins, D., Cretí, S., Stefanizzi, L., et al. (2020). *Black Sea Analysis and Forecast (CMEMS BS-Currents, EAS3 system) (Version 1) [Data set]. Copernicus Monitoring Environment Marine Service (CMEMS).* doi: 10.25423/CMCC/BLKSEA_ANALYSIS_FORECAST_PHYS_007_001_EAS3

Courtier, P. (1997). Variational methods. *J. Meteor. Soc. Japan* 75, 211–218.

de Souza, J. M. A. C., Couto, P., Soutelino, R., and Roughan, M. (2020). Evaluation of four global ocean reanalysis products for New Zealand waters–A guide for regional ocean modelling. *N. Zeal. J. Mar. Freshw. Res.* 55, 1–24. doi: 10.1080/00288330.2020.1713179

Dee, D. P. (2005). Bias and data assimilation. *Q. J. R. Meteorol. Soc.* 131, 3323–3343. doi: 10.1256/qj.05.137

Degtyarev, A. K. (2000). Estimation of temperature increase of the Black Sea active layer during the period 1985– 1997. *Meteor. Gidrol.* 6, 72–76. (in Russian),

Dobricic, S., and Pinardi, N. (2008). An oceanographic three-dimensional variational data assimilation scheme. *Ocean Model.* 22, 89–105. doi: 10.1016/j.ocemod.2008.01.004

Farina, R., Dobricic, S., Storto, A., Masina, S., and Cuomo, S. (2015). A revised scheme to compute horizontal covariances in an oceanographic 3D-VAR assimilation system. *J. Comput. Phys.* 284, 631–647. doi: 10.1016/j.jcp.2015.01.003

Fofonoff, N. P., and Millard, R. C. Jr. (1985). Algorithms for computation of fundamental properties of seawater. *UNESCO Mar. Sci. Tech. Paper* 44:53.

Ginzburg, A. I., Kostianoy, A. G., and Sheremet, N. A. (2004). Seasonal and interannual variability of the Black Sea surface temperature as revealed from satellite data (1982–2000). *J. Mar. Syst.* 52, 33–50. doi: 10.1016/j.jmarsys.2004.05.002

Grayek, S., Stanev, E. V., and Schulz-Stellenfleth, J. (2015). Assessment of the Black Sea observing system. A focus on 2005-2012 Argo campaigns. *Ocean Dyn.* 65, 1665–1684. doi: 10.1007/s10236-015-0889-8

Gunduz, M., Özsoy, E., and Hordoir, R. (2020). A model of Black Sea circulation with strait exchange (2008–2018). *Geosci. Model Dev.* 13, 121–138. doi: 10.5194/gmd-13-121-2020

Gürses, Ö (2016). *Dynamics of the Turkish Straits System–A Numerical Study with a Finite Element Ocean Model Based on an Unstructured Grid Approach.* Ph D. thesis. Erdemli: Institute of Marine Sciences, METU.

Haines, K. (2018). "Ocean reanalyses," in *New Frontiers in Operational Oceanography*, eds E. Chassignet, A. Pascual, J. Tintoré, and J. Verron (Liguria: GODAE OceanView), 545–562. doi: 10.17125/gov2018.ch19

Hallberg, R. (2013). Using a resolution function to regulate parameterizations of oceanic mesoscale eddy effects. *Ocean Model.* 72, 92–103. doi: 10.1016/j.ocemod.2013.08.007

Hersbach, H., Bell, B., Berrisford, P., Hirahara, S., Horanyi, A., Munoz-Sabater, J., et al. (2020). The ERA5 global reanalysis. *Q. J. R. Meteorol. Soc.* 146, 1999–2049. doi: 10.1002/qj.3803

Huffman, G. J., Adler, R. F., Bolvin, D. T., and Gu, G. (2009). Improving the global precipitation record: GPCP version 2.1. *Geophys. Res. Lett.* 36:L17808.

Ilicak, M., Federico, I., Barletta, I., Mutlu, S., Karan, H., Ciliberti, S. A., et al. (2021). Modeling of the turkish strait system using a high resolution unstructured grid ocean circulation model. *J. Mar. Sci. Eng.* 9:769. doi: 10.3390/jmse9070769

Ingleby, B., and Huddleston, M. (2007). Quality control of ocean temperature and salinity profiles—Historical and real-time data. *J. Mar. Syst.* 65, 158–175. doi: 10.1016/j.jmarsys.2005.11.019

Kara, A. B., Wallcraft, A. J., and Hurlburt, H. E. (2005). How does solar attenuation depth affect the ocean mixed layer? Water turbidity and atmospheric forcing impacts on the simulation of seasonal mixed layer variability in the Turbid Black Sea. *J. Clim.* 18, 389–409. doi: 10.1175/JCLI-3159.1

Kara, A. B., Wallcraft, A. J., Hurlburt, H. E., and Stanev, E. V. (2008). Air–sea fluxes and river discharges in the Black Sea with a focus on the Danube and Bosphorus. *J. Mar. Syst.* 74, 74–95. doi: 10.1016/j.jmarsys.2007.11.010

Knysh, V. V., Korotaev, G. K., Moiseenko, V. A., Kubryakov, A. I., Belokopytov, V. N., and Inyushina, N. V. (2011). Seasonal and interannual variability of Black Sea hydrophysical fields reconstructed from 1971-1993 reanalysis data. *Izv. Atmos. Ocean. Phys.* 47:399. doi: 10.1134/S000143381103008X

Korotaev, G., Oguz, T., Nikiforov, A., and Koblinsky, C. (2003). Seasonal, interannual, and mesoscale variability of the Black Sea upper layer circulation derived from altimeter data. *J. Geophys. Res. Oceans* 108:3122.

Korotaev, G. K., Saenko, O. A., and Koblinsky, C. J. (2001). Satellite altimetry observations of the Black Sea level. *J. Geophys. Res. Oceans* 106, 917–933. doi: 10.1029/2000jc900120

Kubryakov, A. A., Bagaev, A. V., Stanichny, S. V., and Belokopytov, V. N. (2018). Thermohaline structure, transport and evolution of the Black Sea eddies from hydrological and satellite data. *Prog. Oceanogr.* 167, 44–63. doi: 10.1016/j.pocean.2018.07.007

Kubryakov, A. A., and Stanichny, S. V. (2015). Seasonal and interannual variability of the Black Sea eddies and its dependence on characteristics of the large-scale circulation. *Deep Sea Res. I Oceanogr. Res. Papers* 97, 80–91. doi: 10.1016/j.dsr.2014.12.002

Le Traon, P.-Y., Reppucci, A., Alvarez Fanjul, E., Aouf, L., Behrens, A., Belmonte, M., et al. (2019). From observation to information and users: the copernicus marine service perspective. *Front. Mar. Sci.* 6:234. doi: 10.3389/fmars.2019.00234

Lima, L., Ciliberti, S. A., Aydogdu, A., Escudier, R., Masina, S., Azevedo, D., et al. (2020a). *Black Sea Physical Reanalysis (CMEMS BS-Currents) (Version 1) [Data set]. Copernicus Monitoring Environment Marine Service (CMEMS).* doi: 10.25423/CMCC/BLKSEA_MULTIYEAR_PHY_007_004

Lima, L., Masina, S., Ciliberti, S. A., Peneva, E. L., Cretí, S., Stefanizzi, L., et al. (2020b). *Black Sea Physical Reanalysis (CMEMS BS-Currents) (Version 1) [Data set]. Copernicus Monitoring Environment Marine Service (CMEMS).* doi: 10.25423/CMCC/BLKSEA_REANALYSIS_PHYS_007_004

Lima, L., Peneva, E., Ciliberti, S., Masina, S., Lemieux, B., Storto, A., et al. (2020c). Copernicus marine service ocean state report, issue 4. *J. Oper. Oceanogr.* 13(Sup1.), s41–s47. doi: 10.1080/1755876X.2020.1785097

Lima, L. N., Pezzi, L. P., Penny, S. G., and Tanajura, C. A. S. (2019). An investigation of ocean model uncertainties through ensemble forecast experiments in the Southwest Atlantic Ocean. *J. Geophys. Res. Oceans* 124, 432–452. doi: 10.1029/2018JC013919

Lin, P. F., Yu, Z. P., Liu, H., Yu, Y., Li, Y., Jiang, J., et al. (2020). LICOM model datasets for CMIP6 ocean model intercomparison project (OMIP). *Adv. Atmos. Sci.* 37, 6239–6249. doi: 10.1007/s00376-019-9208-5

Ludwig, W., Dumont, E., Meybeck, M., and Heussner, S. (2009). River discharges of water and nutrients to the Mediterranean and Black Sea: major drivers for ecosystem changes during past and future decades? *Prog. Oceanogr.* 80, 199–217. doi: 10.1016/j.pocean.2009.02.001

Madec, G., and The Nemo team (2016). *NEMO Ocean Engine: Version 3.6 Stable. Note du Pole de Modelisation ISSN No 1288-1619 N 27.* Guyancourt: Institut Pierre-Simon Laplace.

Miladinova, S., Stips, A., Garcia-Gorriz, E., and Macias Moy, D. (2017). Black Sea thermohaline properties: long-term trends and variations. *J. Geophys. Res. Oceans* 122, 5624–5644. doi: 10.1002/2016JC012644

Miladinova, S., Stips, A., Garcia-Gorriz, E., and Macias Moy, D. (2018). Formation and changes of the Black Sea cold intermediate layer. *Prog. Oceanogr.* 167, 11–23. doi: 10.1016/j.pocean.2018.07.002

Mulet, S., Buongiorno Nardelli, B., Good, S., Pisano, A., Greiner, E., Monier, M., et al. (2018). Ocean temperature and salinity. In: copernicus marine service ocean state report. *J. Oper. Oceanogr.* 11(suppl. 1), s13–s16. doi: 10.1080/1755876X.2018.1489208

Oguz, T., Latun, V. S., Latif, M. A., Vladimirov, V. V., Sur, H. I., Markov, A. A., et al. (1993). Circulation in the surface and intermediate layers of the Black Sea. *Deep Sea Res. I Oceanogr. Res. Papers* 40, 1597–1612. doi: 10.1016/0967-0637(93)90018-x

Oke, P. R., and Sakov, P. (2008). Representation error of oceanic observations for data assimilation. *J. Atmos. Oceanic Technol.* 25, 1004–1017. doi: 10.1175/2007jtecho558.1

Özsoy, E., and Ünlüata, Ü. (1997). Oceanography of the Black Sea: a review of some recent results. *Earth Sci. Rev.* 42, 231–272. doi: 10.1016/s0012-8252(97)81859-4

Panin, N., Tiron Duțu, L., and Duțu, F. (2016). The Danube Delta, an overview of its holocene evolution. *J. Med. Geogr* 126, 37–54. doi: 10.4000/mediterranee.8186

Pecci, L., Fichaut, M., and Schaap, D. (2020). "SeaDataNet, an enhanced ocean data infrastructure giving services to scientists and society," in *Proceedings of the IOP Conference Series: Earth and Environmental Science 2020*, Vol. 509, Bristol. doi: 10.1088/1755-1315/509/1/012042

Pettenuzzo, D., Large, W. G., and Pinardi, N. (2010). On the correction of ERA-40 surface flux products consistent with the Mediterranean heat and water budgets and the connection between basin surface total heat flux and NAO. *J. Geophys. Res* 115:C06022. doi: 10.1029/2009JC005631

Shapiro, G. I., Aleynik, D. L., and Mee, L. D. (2010). Long term trends in the sea surface temperature of the Black Sea. *Ocean Sci.* 6, 491–501. doi: 10.5194/os-6-491-2010

Shapiro, R. (1970). Smoothing, filtering and boundary effects. *Rev. Geophys.* 8, 359–387. doi: 10.1029/rg008i002p00359

Stanev, E. V., and Beckers, J. M. (1999). Barotropic and baroclinic oscillations in strongly stratified ocean basins: numerical study of the Black Sea. *J. Mar. Syst.* 19, 65–112. doi: 10.1016/S0924-7963(98)00024-4

Stanev, E. V., Peneva, E., and Chtirkova, B. (2019). Climate change and regional ocean water mass disappearance: case of the Black Sea. *J. Geophys. Res. Oceans* 124, 4803–4819. doi: 10.1029/2019JC015076

Stanev, E. V., Simeonov, J. A., and Peneva, E. L. (2001). Ventilation of Black Sea pycnocline by the Mediterranean plume. *J. Mar. Syst.* 31, 77–97. doi: 10.1016/S0924-7963(01)00048-3

Storto, A., Alvera-Azcárate, A., Balmaseda, M. A., Barth, A., Chevallier, M., Counillon, F., et al. (2019a). Ocean reanalyses: recent advances and unsolved challenges. *Front. Mar. Sci.* 6:418. doi: 10.3389/fmars.2019.00418

Storto, A., Dobricic, S., Masina, S., and Di Pietro, P. (2011). Assimilating along-track altimetric observations through local hydrostatic adjustment in a global ocean variational assimilation system. *Mon. Weather Rev.* 139, 738–754. doi: 10.1175/2010mwr3350.1

Storto, A., Masina, S., and Dobricic, S. (2014). Estimation and impact of non-uniform horizontal correlation length-scales for global ocean physical analyses. *J. Atmos. Ocean. Technol.* 31, 2330–2349. doi: 10.1175/JTECH-D-14-00042.1

Storto, A., Masina, S., Simoncelli, S., Iovino, D., Cipollone, A., Drevillon, M., et al. (2019b). The added value of the multi-system spread information for ocean heat content and steric sea level investigations in the CMEMS GREP ensemble reanalysis product. *Clim. Dyn.* 53, 287–312. doi: 10.1007/s00382-018-4585-5

Sur, H. İ., Özsoy, E., and Ünlüata, Ü. (1994). Boundary current instabilities, upwelling, shelf mixing and eutrophication processes in the Black Sea. *Prog. Oceanogr.* 33, 249–302. doi: 10.1016/0079-6611(94)90020-5

Taburet, G., Sanchez-Roman, A., Ballarotta, M., Pujol, M.-I., Legeais, J.-F., Fournier, F., et al. (2019). DUACS DT2018: 25 years of reprocessed sea level altimetry products. *Ocean Sci.* 15, 1207–1224. doi: 10.5194/os-15-1207-2019

Ünlülata, Ü., Oğuz, T., Latif, M. A., and Özsoy, E. (1990). "On the physical oceanography of the Turkish Straits," in *The Physical Oceanography of Sea Straits. NATO ASI Series (Mathematical and Physical Sciences)*, Vol. 318, ed. L. J. Pratt (Dordrecht: Springer), 25–60. doi: 10.1007/978-94-009-0677-8_2

Volkov, D. L., and Landerer, F. W. (2015). Internal and external forcing of sea level variability in the Black Sea. *Clim. Dyn.* 45, 2633–2646. doi: 10.1007/s00382-015-2498-0

von Schuckmann, K., Le Traon, P. Y., Alvarez-Fanjul, E., Axell, L., Balmaseda, M., Breivik, L. A., et al. (2016). The copernicus marine environment monitoring service ocean state report. *J. Oper. Oceanogr.* 9(Suppl. 2), s235–s320. doi: 10.1080/1755876X.2016.1273446

Yan, C., Zhu, J., and Tanajura, C. A. S. (2015). Impacts of mean dynamic topography on a regional ocean assimilation system. *Ocean Sci.* 11, 829–837. doi: 10.5194/os-11-829-2015

Conflict of Interest: The authors declare that the research was conducted in the absence of any commercial or financial relationships that could be construed as a potential conflict of interest.

Publisher's Note: All claims expressed in this article are solely those of the authors and do not necessarily represent those of their affiliated organizations, or those of the publisher, the editors and the reviewers. Any product that may be evaluated in this article, or claim that may be made by its manufacturer, is not guaranteed or endorsed by the publisher.

frontiers in Marine Science

ORIGINAL RESEARCH
published: 13 September 2021
doi: 10.3389/fmars.2021.707632

Analysis of 23 Years of Daily Cloud-Free Chlorophyll and Suspended Particulate Matter in the Greater North Sea

Aida Alvera-Azcárate[1], Dimitry Van der Zande[2], Alexander Barth[1], Charles Troupin[1], Samuel Martin[1] and Jean-Marie Beckers[1]*

[1] AGO-GHER, University of Liège, Liège, Belgium, [2] Operational Directorate Natural Environment, Royal Belgian Institute of Natural Sciences, Brussels, Belgium

Satellite-derived estimates of ocean color variables are available for several decades now and allow performing studies of the long-term changes occurred in an ecosystem. A daily, gap-free analysis of chlorophyll (CHL) and suspended particulate matter (SPM, indicative of light availability in the subsurface) at 1 km resolution over the Greater North Sea during the period 1998–2020 is presented. Interannual changes are described, with maximum average CHL values increasing during the period 1998–2008, a slightly decreasing trend in 2009–2017 and an stagnation in recent years. The typical spring bloom is observed to happen earlier each year, with about 1 month difference between 1998 and 2020. The duration of the bloom (time between onset and offset) appears also to be increasing with time, but the average CHL value during the spring bloom does not show a clear trend. The causes for earlier spring blooms are still unclear, although a rising water temperature can partially explain them through enhanced phytoplankton cell division rates or through increased water column stratification. SPM values during winter months (prior to the development of the spring bloom) do not exhibit a clear trend over the same period, although slightly higher SPM values are observed in recent years. The influence of sea surface temperature in the spring bloom timing appears to be dominant over the influence of SPM concentration, according to our results. The number of satellites available over the years for producing CHL and SPM in this work has an influence in the total amount of available data before interpolation. The amount of missing data has an influence in the total variability that is retained in the final dataset, and our results suggest that at least three satellites would be needed for a good representation of ocean color variability.

Keywords: spring bloom phenology, remote sensing, ocean color, chlorophyll, suspended particle matter, North Sea, DINEOF

KEYPOINTS

- Analysis of 23 years (1998–2020) of daily satellite-based chlorophyll and suspended particulate matter products in the Greater North Sea using DINEOF (Data Interpolating Empirical Orthogonal Functions).
- Description of changes in spring bloom phenology, with earlier blooms observed through time.
- The number of satellites used to obtain the data has an influence on retained variance, with at least 3 satellites needed for a correct representation of variability.

OPEN ACCESS

Edited by:
Simona Masina, Euro-Mediterranean Center on Climate Change, Italy

Reviewed by:
Frank Dehairs, Vrije University Brussel, Belgium
Elisa Capuzzo, Centre for Environment, Fisheries and Aquaculture Science (CEFAS), United Kingdom

****Correspondence:***
Aida Alvera-Azcárate
a.alvera@ulg.ac.be

Specialty section:
This article was submitted to Ocean Observation, a section of the journal Frontiers in Marine Science

Received: *10 May 2021*
Accepted: *17 August 2021*
Published: *13 September 2021*

Citation:
Alvera-Azcárate A, Van der Zande D, Barth A, Troupin C, Martin S and Beckers J-M (2021) Analysis of 23 Years of Daily Cloud-Free Chlorophyll and Suspended Particulate Matter in the Greater North Sea. Front. Mar. Sci. 8:707632. doi: 10.3389/fmars.2021.707632

1. INTRODUCTION

The North Sea is a semi-enclosed shallow shelf sea in northwestern Europe, and it is one of the most productive seas in the world (Ducrotoy et al., 2000). It is surrounded by heavily populated countries with important industrial and agricultural activities, resulting in large quantities of nutrients and pollutants being added to the North Sea through riverine inputs (Ducrotoy et al., 2000). As a result, the North Sea has suffered from eutrophication issues during several decades (e.g., Desmit et al., 2020; Xu et al., 2020; Friedland et al., 2021). Despite de-eutrophication policies implemented since the 1990s, such as the EU Marine Strategy Framework Directive (MSFD) which aims at reaching a Good Environmental Status (GES) in European waters, the North Sea still receives relatively high nutrient inputs (nitrogen and phosphorous, Van der Zande et al., 2019b). This results in intense phytoplankton blooms occurring every year between March and October, with the southern parts of the North Sea, shallower and more affected by industrial and agricultural activities, presenting more intense blooms (Lancelot et al., 2005; Rousseau et al., 2013; Desmit et al., 2015, 2020). Phytoplankton blooms are at the basis of the marine food web, driving biogeochemical cycles, producing oxygen and acting as a carbon pump (Xu et al., 2020). Phytoplankton spatial and temporal dynamics can be influenced by several factors, including the availability of nutrients and light, water temperature, and grazing (Capuzzo et al., 2017; Xu et al., 2020).

Spring bloom onset in the open ocean typically occurs when turbulent mixing decays, causing convection to stop (Ferrari et al., 2015). On well-mixed environments, spring bloom onsets typically when the upper mixed layer is shallower than a given critical depth (Huisman et al., 1999). Some studies point out to a shift in the timing of the spring bloom in the North Sea to earlier dates in recent years (e.g., Desmit et al., 2020). While the causes for this are not completely understood, Hunter-Cevera et al. (2016) point to temperature-induced changes in phytoplankton cell-division rates as a possible cause. Increasing temperature trends observed in the North Sea (Høyer and Karagali, 2016) can therefore contribute to earlier phytoplankton blooms. Chlorophyll concentration (CHL) is used as a proxy for phytoplankton concentration, and Suspended Particulate Matter (SPM) is directly related to the amount of light that is available for primary producers (Capuzzo et al., 2015). Ocean color properties have been routinely measured from satellite for several decades (e.g., Sathyendranath et al., 2019), which allows for long-term studies. In order to assess the changes that have occurred in CHL and SPM in the North Sea, long-time series of daily data must be used (Philippart et al., 2010). Considering different hydrodynamic regions can also help understand how physical properties like currents and stratification influence the distribution of CHL and SPM (Capuzzo et al., 2017).

Interannual changes in CHL and SPM have been studied in the North Sea by several authors (e.g., Fettweis et al., 2007, 2014; Philippart et al., 2010; Capuzzo et al., 2015; Desmit et al., 2020) using *in situ* and/or satellite data. *In situ* data are sparse and long term series are very difficult to maintain. On the other hand, satellite data are affected by the presence of clouds or quality flagging (e.g., low sun angle in higher latitudes) that limit the amount of measurements. Gap-free estimates are needed when assessing long-term changes in the total concentration of CHL and SPM in coastal waters, for example in support of the MSFD in European waters. CHL time series are therefore used as an indicator for eutrophication (Ferreira et al., 2011), and satellite-derived gap-free CHL offer the temporal and spatial coverage necessary for such monitoring activities (Van der Zande et al., 2019b).

DINEOF (Data Interpolating Empirical Orthogonal Functions, Beckers and Rixen, 2003; Alvera-Azcárate et al., 2005) is an EOF-based technique that is used to interpolate missing data (due, for example, to the presence of clouds) in satellite data sets. It has been used in numerous works, with ocean color variables (e.g., Sirjacobs et al., 2011; Alvera-Azcárate et al., 2015), sea surface temperature (Alvera-Azcárate et al., 2005) or sea surface salinity (Alvera-Azcárate et al., 2015) among others and has shown to be reliable even with high amounts of missing data (e.g., Alvera-Azcárate et al., 2005, 2009).

The main objective of this work is to assess the spatial and temporal dynamics of CHL and SPM of the Greater North Sea over a period of 23 years (1998 to 2020) using a gap-free high spatial (1 km) and temporal (daily) satellite dataset. This analysis covers a wide area and the gap-free analysis allows for a better estimation of changes in CHL and SPM both in time and space. The spatial and temporal variability of these reconstructed variables will be assessed, with special attention to the timing of the spring bloom and how it has changed over the period of study. The dataset is composed of a varying number of satellite sensors, providing us with insight on the influence of the number of available satellites in the variability retained in the final product. Section 2 describes the satellite data used, the domain of study, and the reconstruction approach using DINEOF. Section 3 contains a brief description of the reconstruction results and the EOF basis obtained. Section 4 discusses the timing of the spring bloom onset and how it has changed over the considered period. Conclusions are provided in section 5.

2. MATERIALS AND METHODS

2.1. Study Area

The domain of study is shown in **Figure 1**, and covers the North Sea and the easternmost part of the North Atlantic Ocean, from 48°N to 66°N and from 8°W to 12°E. The bathymetry in this region is very varied, from the shallow plains of the southern part of the North Sea, with depths of less than 50 m, to depths of more than 3,000 m north of the Faroe Islands. Within the shallow parts of the North Sea, the Norwegian channel surrounding Norway reaches up to 700 m. In the center of the North Sea, the Dogger bank is a shallow sandbank that extends over several tens of kilometers and is a productive fishing ground (e.g., Kröncke, 2011).

Circulation in the North Sea is mainly cyclonic, under the influence of prevailing westerly winds (Winther and Johannessen, 2006; Sündermann and Pohlmann, 2011). The main water inflow pathways are located at the northern part

of the domain between the British Isles (mainly Shetland) and Norway, and in a lesser degree through the English Channel. Water also flows directly from the Atlantic Ocean toward the Baltic Sea through the Norwegian Channel. Tides are mainly semi-diurnal and follow also a cyclonic path in the North Sea (Sündermann and Pohlmann, 2011; Vindenes et al., 2018). The strong tidal currents result in strong mixing, specially in the shallower parts of the southern North Sea (Sündermann and Pohlmann, 2011).

2.2. Satellite Data

Generating reliable satellite estimates of CHL in optically complex coastal waters is still challenging. Many algorithms exist and give quite different performances for different optical conditions. For this reason, we applied the approach of Lavigne et al. (2021) who defined the limits of applicability of three popular and complementary algorithms: (1) the OC4 blue-green band ratio algorithm (O'Reilly et al., 1998) which was designed for open ocean waters; (2) the OC5 algorithm (Gohin et al., 2002) which is based on look-up tables and corrects OC4 overestimation in moderately turbid waters; and (3) a near infrared-red (NIR-red) band ratio algorithm (Gons et al., 2002) designed for high turbid waters. This approach allows automatic pixel-based switching between the most appropriate algorithms for a certain water type. Additionally, the neural-net approach FUB-WEW (Free University of Berlin Water processor, Fub v4.01, Schroeder et al., 2007) was used for the Kattegat region due to its high color dissolved organic matter concentration. Source products were obtained from publicly accessible archives: the Copernicus Marine Environment Monitoring Service (CMEMS), European Space Agency (i.e., ODESA) and other data providers (i.e., IFREMER). More details can be found in Van der Zande et al. (2019b). The SPM products were generated by applying the approach of Nechad et al. (2010) to the OC-CCI Remote Sensing Reflectance (Rrs) product obtained from CMEMS (OCEANCOLOUR_ATL_OPTICS_L3_REP_OBSERVATIONS_009_066, CMEMS data portal). All daily satellite products were generated with a spatial resolution of approximately 1 km, resulting in a matrix of 1913× 1639 pixels in space for each day. The winter months December and January were excluded from the analysis as no ocean color products were available over a large part of the Greater North Sea due to low sun angle which complicates atmospheric correction procedures.

2.3. DINEOF

The CHL and SPM datasets were reconstructed using DINEOF (Data Interpolating Empirical Orthogonal Functions, Beckers and Rixen, 2003; Alvera-Azcárate et al., 2005). DINEOF calculates the expected value for the missing data based on the spatio-temporal information contained in the dataset, using a series of EOF modes. EOFs provide an efficient way of calculating the main modes of variability of a dataset, in order of increasing explained variance (von Storch and Zwiers, 1999). However, EOFs should not be directly calculated on uncomplete data, and DINEOF provides a way to overcome this and provide an estimate for the missing data at the same time. DINEOF calculates an EOF basis from the initial gappy data, by initiating the missing data to the average value of the matrix as first guess. As the matrix is demeaned to work with anomalies for the EOF decomposition, the initial missing data are in fact initialized with a value of zero. Using this matrix with zero at the missing locations, the first EOF (i.e., the main mode) is calculated. The missing data values are then recalculated using the EOF basis, obtaining an improved guess for those values. The process is iterated until convergence is reached for the missing data values. The number of EOF modes is increased (first one EOF, then the two first EOFs, and so on). Normally there can be as many EOF modes as the temporal size of the matrix being reconstructed (considering time as the smallest dimension, which is typically the case in satellite datasets). However, higher order EOFs contain a very small fraction of the total variability and may contain also noise and other transient errors, so in order to avoid retaining that information in the final product and to keep the computing time reasonable, only a truncated EOF series is used. The optimal number of EOFs that are retained for the final reconstruction of the missing data is determined by cross-validation: about 2-3% of valid data (i.e., not missing) are marked as missing data, and at each step DINEOF calculates the error between the initial data and the expected value provided by the EOF basis. The cross-validation data are taken in the form of clouds (as explained in Beckers et al., 2006) to better represent the nature of missing data in satellite images. DINEOF has been used in many previous works, and can be applied to variables like sea surface temperature and winds (Alvera-Azcárate et al., 2007), sea surface salinity (Alvera-Azcárate et al., 2016), chlorophyll (Huynh et al., 2020), etc.

Images with more than 98% of missing data were removed prior to the DINEOF reconstruction, which effectively removes mostly data from December and January. After removal of these images, there is still a very high amount of missing data, specially at high latitudes. As an example, the percentage of missing data for years 1998 and 2018 is shown in **Figure 2**. The percentage of missing data in 2018 is lower than in 1998 because of the availability of more satellite systems and sensors in recent years, namely MODIS, VIIRS and Sentinel-3 for recent years compared to only SeaWiFS in 1998 to 2002. The temporal distribution of the percentage of missing data (panel a of **Figure 2**) shows lower amounts of missing data during summer months, although on average there is always at least 60% of the domain with no data. Such a high amount of missing data makes it impractical to quantify the inter-annual variability with high confidence, and therefore an interpolation to reconstruct these gaps is necessary.

Given the large size of the domain and the long time series that is being used in this work, each year has been reconstructed separately. Because December and January are not included in the analysis due to their high percentage of missing data, there is no continuity problem between each year. Making a separate analysis for each year also ensures that the EOF basis used for the reconstruction is not dominated by the main seasonal cycle. The data are transformed using a natural logarithm before the DINEOF analysis to ensure a distribution closer to a normal one.

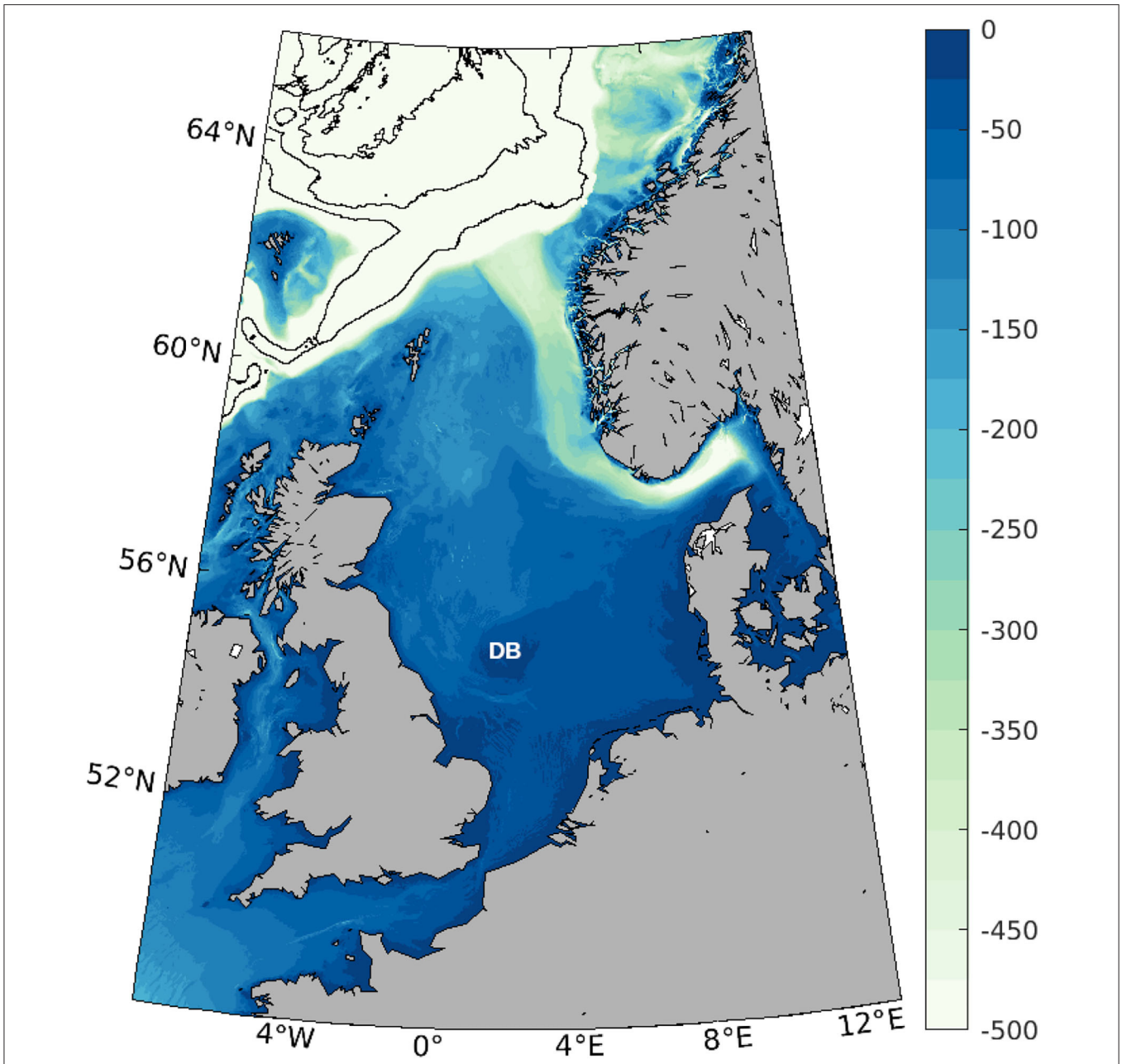

FIGURE 1 | Domain of study with bathymetry (in m). The contours in the northwest part of the domain correspond to the 1,000, 2,000, and 3,000 m depth. DB shows the location of the Dogger Bank.

2.4. Determination of Spring Bloom Onset Date

In order to assess the timing of the spring bloom in the North Sea and if this timing has changed through the years, we have used a threshold method following (Brody et al., 2013). The median of the North Sea CHL concentration is determined for every year and the date on which the concentration of CHL first reaches a value 5% above this median is chosen as the date the spring bloom starts. Other suggested methods in Brody et al. (2013), like the maximum rate of change in CHL growth, reflect the moment in which the bloom is already well underway and not in its starting phase. A 30-day Gaussian filtered time series is used to avoid short-term variations influencing in the calculation of the spring bloom timing.

3. DINEOF RESULTS

In this section the main results obtained with DINEOF are presented. The reconstruction for each year has a different

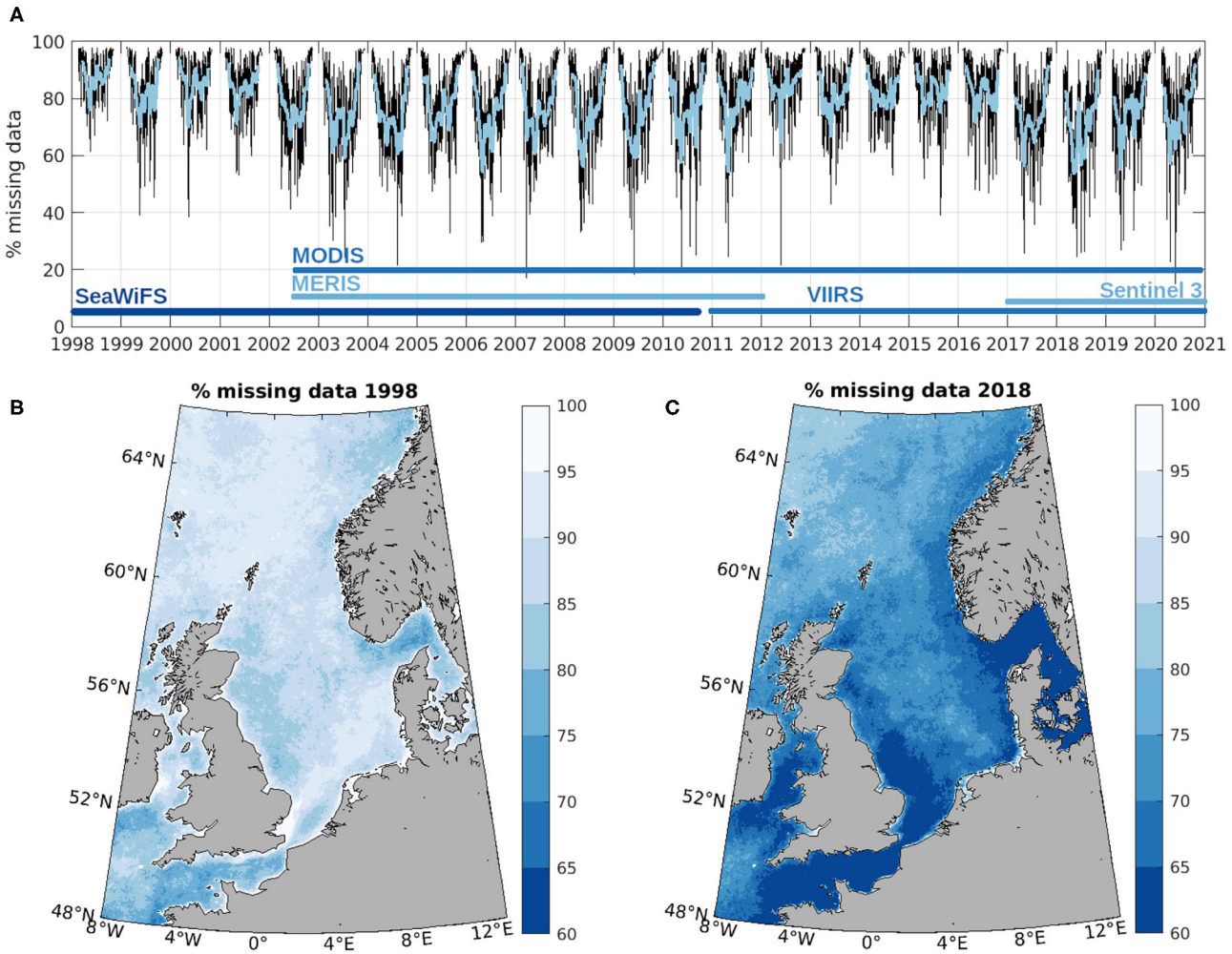

FIGURE 2 | Percentage of missing data in the domain of study. **(A)** Spatially averaged percentage of missing data in the initial time series (black) and with a 30-day Gaussian low-pass filter (blue). **(B)** Temporal average of the percentage of missing data for 1998 (year with the highest average percentage of missing data). **(C)** Temporal average of the percentage of missing data for 2018 (year with the lowest average percentage of missing data).

number of optimal EOFs depending on factors like the available data, the cloud coverage and the structures that are observed in the initial data (i.e., when no clouds or other missing data obscure them). For example, in the reconstruction of the CHL dataset in 1998 (the year with the maximum percentage of missing data), 5 EOFs were found optimal to reconstruct the missing data by DINEOF. For 2004, with a low percentage of missing data, 13 EOFs were found as optimal by DINEOF. For the SPM reconstructions, the minimum number of EOFs retained was 5 (for 2008) and the maximum was 19 (for 2009).

3.1. Validation

The multi-year dataset (both the original cloudy data and the DINEOF reconstruction) have been used in the frame of the EU-funded JMP-EUNOSAT project (Joint Monitoring Programme of the Eutrophication of the North Sea with Satellite data), to assess the use of satellite data to monitor the eutrophication in the North Sea with the help of satellite data, and a thorough validation has been realized in that project (Van der Zande et al., 2019a). The quality of the DINEOF reconstruction has been therefore assessed in the frame of the JMP-EUNOSAT project. The satellite-based CHL observations were compared to *in situ* observations collected in national monitoring programs. Differences between *in situ* and satellite CHL observations were quantified based on direct match ups within the *in situ* data archive. Considering all available data, the uncertainty is estimated with the Mean Absolute Difference (MAD) resulting in a value of 1.89 $\mu g/l$, which corresponds to a Mean Absolute Percentage Difference (MAPD) of 45.26%. The satellite products tend to overestimate CHL values when CHL is less than $1 \mu g/l$ resulting in a slope of 0.64 and a relative high scatter ($r^2 = 0.60$) around the 1:1 line for higher CHL values. Validation of the DINEOF gap-filled products was performed with daily match up study using Dutch monitoring data ranging from clear to very turbid water conditions. Dutch monitoring

data consisted of ship-based water samples collected between 1998 and 2016 in the Dutch coastal zone available at https://waterinfo.rws.nl/. Only surface samples (maximum depth of 3 m) analyzed using the HPLC method were accepted. The match-up analysis between the daily satellite CHL products and available *in-situ* CHL observations was performed following the approach of Bailey and Werdell (2006) allowing a maximum time difference of 2 hours. Applying the DINEOF technique results in a significant increase of available match ups (from 216 to 755) without strongly changing the correlation statistics (MAD original: 2.47 $\mu g/l$, MAD DINEOF: 2.83 $\mu g/l$, **Figure 3**) showing the potential of this approach to improve satellite-based observations for regions where satellite data availability is limited.

3.2. Example of Short-Term and Small-Scale Variability

An example of the reconstructed CHL data is shown in **Figure 4**, with a sequence of 5 days in May 2018 (with 5-day intervals to avoid showing too similar images). This sequence has been chosen because a CHL bloom is happening in the northernmost part of the domain, and the currents have advected the CHL which serves as a tracer for mesoscale eddies. These eddies are partially visible in the initial data, and the reconstruction is able to retain that kind of variability, even in a part of the domain that has a very large amount of missing data. In the central part of the North Sea, between Scotland and Norway, an elongated bloom is seen, which fades with time. This feature is also retained in the DINEOF reconstruction. Only one every 5 days is shown in **Figure 4** for clarity, but intermediate dates also contributed to the final reconstruction and the shaping of the meso- and small-scale variability.

The same dates are also shown for SPM in **Figure 5**. Large SPM concentrations are found in the shallower regions in the southern half of the domain, which seem to decrease with time. The variability in the northern part of the domain is not as clearly observed in the initial SPM but the reconstruction seems to retain these scales as well. A high SPM concentration feature develops south of the Faroe Islands and in general we can appreciate that the concentration of SPM increases in the northern part of the domain during these days. The spatial and temporal variability retained by the DINEOF reconstruction is similar to what is observed in the initial data.

3.3. EOF Modes

The EOF modes that are provided by DINEOF have also been inspected for CHL (**Figure 6**) and SPM (**Figure 7**). In general, the first three modes display the same general patterns for all years, with obviously differences in small-scale patterns and intensity. As an illustration of the patterns represented in these modes, **Figure 6** shows the first 4 EOF spatial and temporal modes in 2008 for CHL. The first EOF mode contains the seasonal variability due mainly to the spring bloom, as indicated by the first temporal mode showing a maximum in spring. The first spatial EOF mode has a larger amplitude along the coastal regions. The second EOF mode still shows a signal at the beginning of the year, indicating the CHL activity linked to the spring bloom, although this time in the center region of the North Sea. The third EOF appears to show the activity linked to blooms at higher latitudes, occurring for example around the Faroe Islands and peaking later in the year in the months of July and August. The fourth EOF is also included to show the smaller spatial and temporal variability included in the higher order modes.

For SPM we only show the first 2 modes, as the higher order ones include small-scale variability and are therefore much more variable from year to year. **Figure 7** shows the SPM spatial and temporal modes for 2008. The first spatial mode shows a larger amplitude in the southern coastal regions, which are shallower and receive large riverine discharges. The plume of the Thames river is also clearly seen, with high SPM values reaching several hundreds of km from its source. Maximum values, as expected, are found during the winter months (**Figure 7**). The second EOF mode highlights the central region of the North Sea, with higher SPM values again in winter. The southern coastal zones and the open sea waters in the north show a similar amplitude which peaks during summer months.

Given the high amount of data being analyzed, the correlation between the different EOF modes for the CHL data were also calculated. The aim was to examine in which years the CHL patterns are more similar to each other and which years the patterns of CHL are more different. **Figure 8** shows the correlation between each year and all other years, for the first CHL EOF mode. The correlation matrix shows a diagonal with a correlation of 1 (correlation of each year CHL to itself), and symmetric values off the diagonal, with higher values for years with stronger correlation between them. The correlation between the first mode among all years is high (always higher than 0.8), as expected, since this mode shows the seasonal cycle as seen for example in **Figure 6**. However, we can also observe that there is a higher correlation among specific periods: the 1998–2001 period, the 2002–2012 period, the 2013–2016 period and the 2017–2020 period. As shown in **Figure 2**, the number of satellites used to compute the CHL data has been different through time, and this has an influence in the amount of missing data. The clusters of correlation shown in **Figure 8** correspond well to changes in the total number of satellites available. **Figure 8** also shows in the bottom panel the percentage of variability explained by the EOFs used in the DINEOF reconstruction, and this also reflects the changes in the number of satellites: analyses in years with one or two satellites have lower retained explained variability than years with three satellites. A similar result was observed in the first SPM EOF (not shown). This result seems to suggest that the availability of at least three ocean color satellites, providing better data coverage, results in improved representation of the variability by interpolation techniques, and sets up a target on the minimal requirements for a correct measurement of the ocean color variability.

3.4. Interannual Variability

A spatial average of the daily CHL and SPM products over the whole domain has been performed to assess interannual

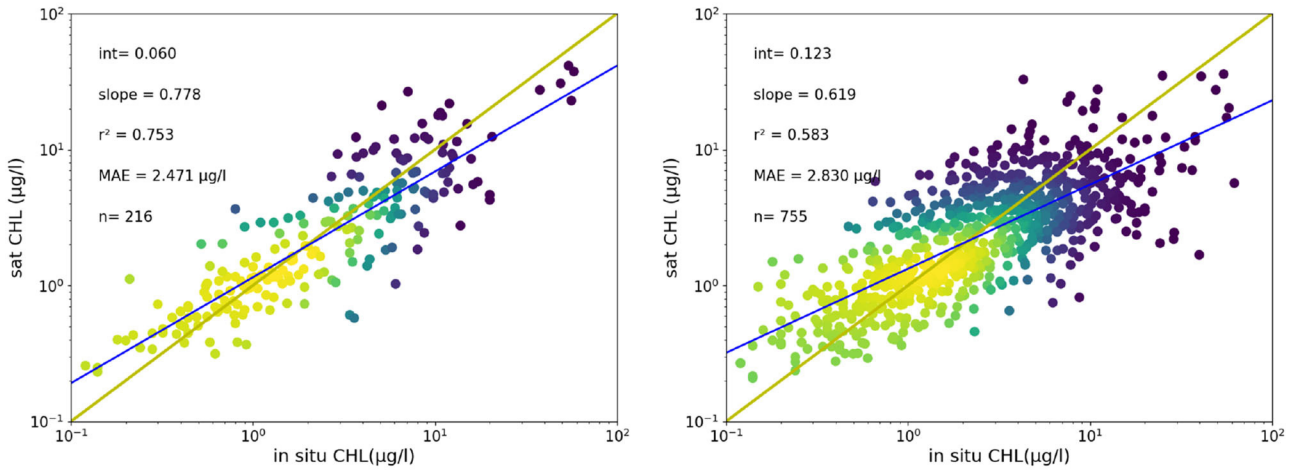

FIGURE 3 | Scatterplots of *in situ* and satellite CHL observations for the Netherlands using the JMP-EUNOSAT CHL archive, without **(left)** and with DINEOF interpolation **(right)**. The relationship between both data sets are described by the Mean Absolute Difference (MAD), Mean Absolute Percentage Error (MAPD). The determination coefficient (r^2) and the slope characterizes the regression (adapted from Van der Zande et al., 2019b).

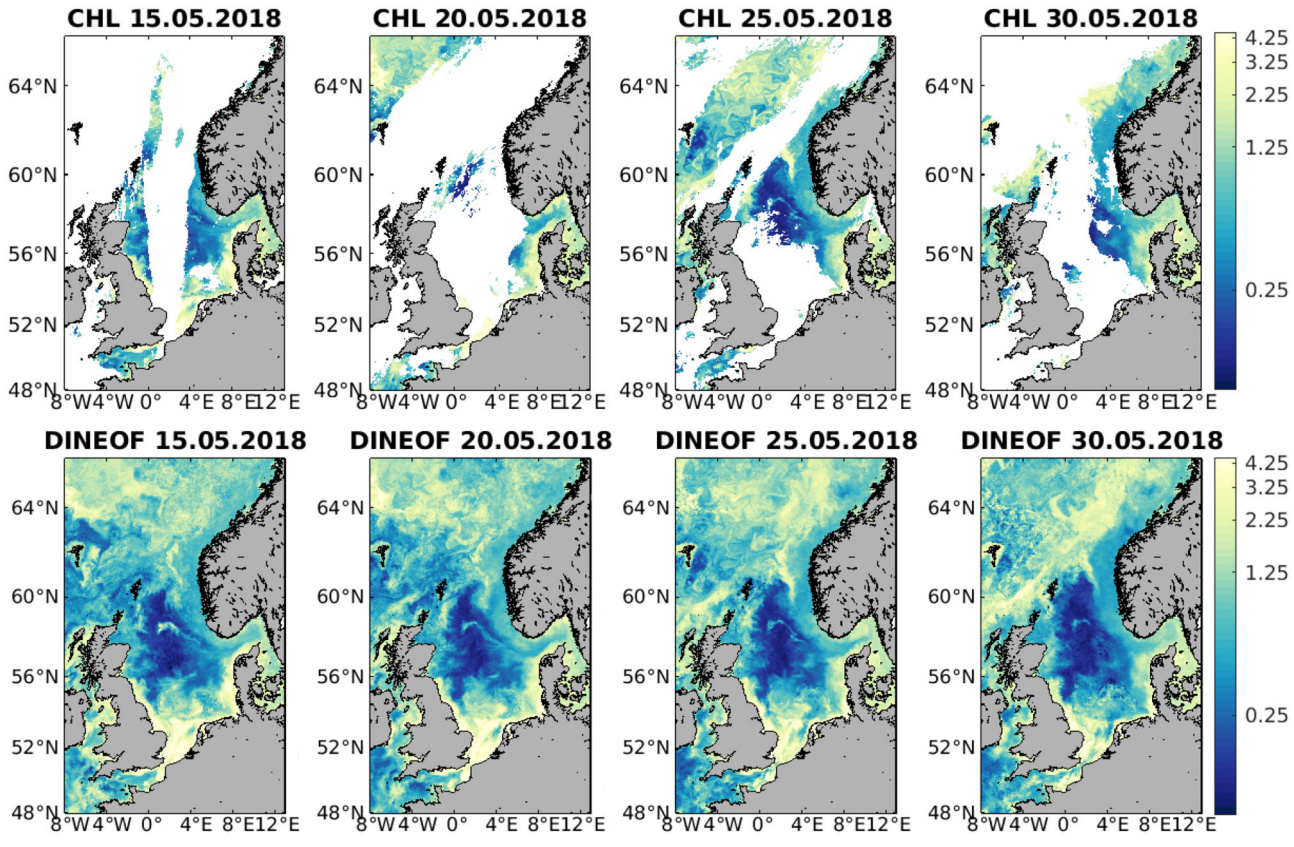

FIGURE 4 | Example of CHL ($\mu g/l$) on 15, 20, 25, and 30 May 2018 for the initial data **(top)** and corresponding DINEOF reconstruction **(bottom)**.

variability, and the time series has been filtered using a 30-day Gaussian low-pass filter (**Figure 9**). A large interannual variability in the average CHL value as well as in the strength of the spring peak can be observed. The reasons for this interannual variability are numerous, including variations in water temperature, water turbidity and nutrient availability

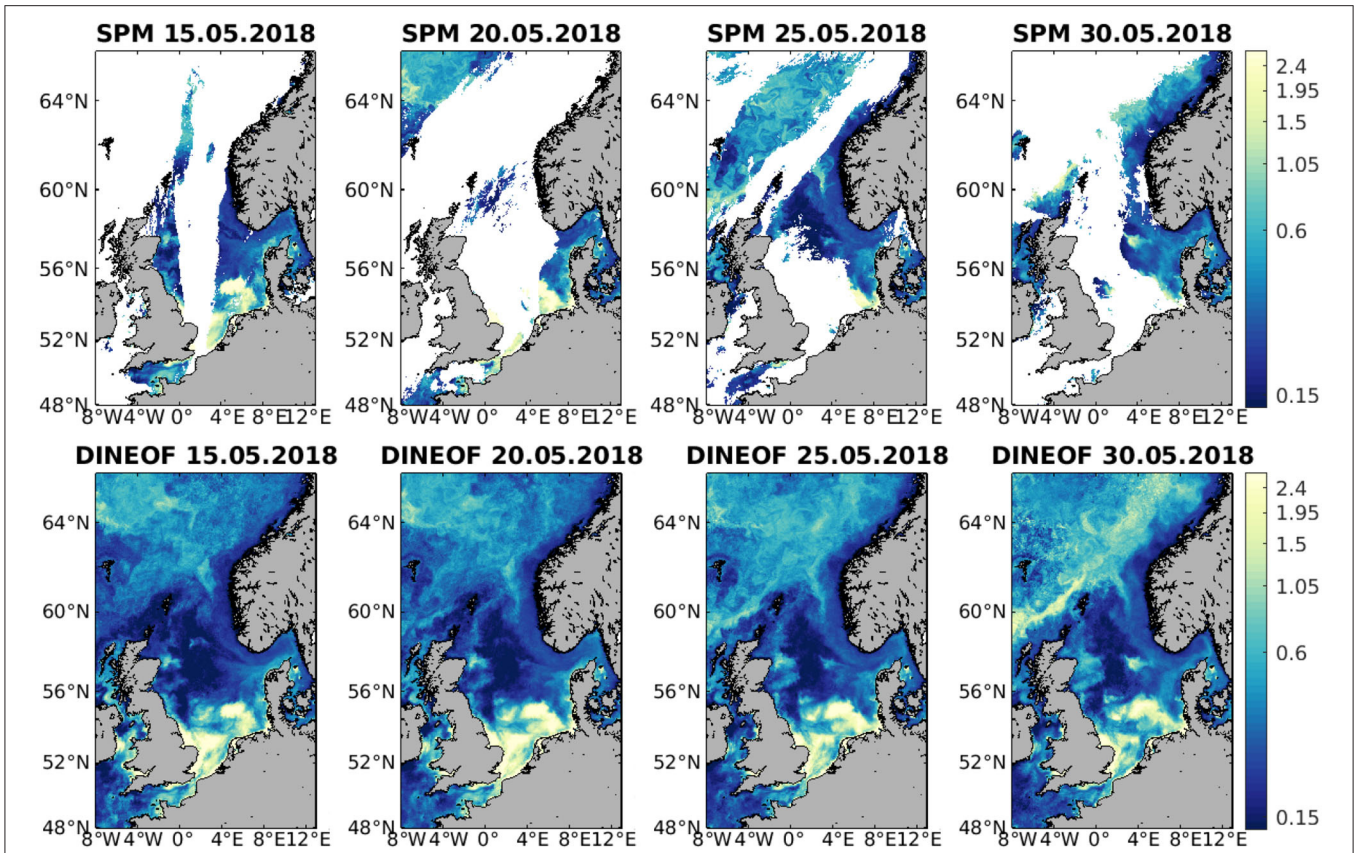

FIGURE 5 | Example of SPM (*mg/l*) on 15, 20, 25, and 30 May 2018 for the initial data **(top)** and corresponding DINEOF reconstruction **(bottom)**.

(Desmit et al., 2020). The European Marine Strategy Framework Directive (MSFD), implemented in 2008, requires the European member states to achieve Good Environmental Status (GES), limiting for example the amount of nutrients that are shed to the rivers by agricultural activities. One of the consequences of this limitation in nutrients would be a decrease in the eutrophication of the North Sea, and in **Figure 9** (top panel) it can indeed be observed that the average CHL concentration has decreased since 2008, with a stagnation, and even a slight increase, in recent years (2017–2020). Friedland et al. (2021) observed a decrease in CHL levels in the North Sea during the 2005–2012 period using an ensemble model simulation, and attributed this to a decrease in nutrient load from rivers into the North Sea. The highest CHL concentration in the average satellite time series of **Figure 9** was reached in the spring bloom of 2008 (with 2.46 $\mu g/l$). The lowest concentration of CHL during the spring bloom in this same figure is observed in 2017 with 1.5 $\mu g/l$.

SPM time series (**Figure 9**, middle panel) shows a large variability in the winter values (with the time series starting in February of each year), when SPM reaches its highest values. Years like 2002, 2008, and 2014 show very high winter SPM concentrations, and in general the winter SPM average values have been higher in the periods 2002–2008 and 2014–2020 than in the rest of the time series. Minimum values are reached during summer months (**Figure 9**), when mixing and resuspension decreases. The interannual variability of the minimum values is not as high as the variability observed in maximum values.

4. SPRING BLOOM ONSET

Following the threshold method described in section 2.4, we have calculated the date on which spring bloom starts each year. The dates of the spring bloom onset are shown in **Figure 10**. Despite interannual variability, there is a clear tendency at sooner spring bloom onset dates in recent years, i.e., the spring bloom appears to start on earlier dates. The trend toward earlier dates is significant with a *p*-value of 4.13e-05. A similar finding was already observed by Desmit et al. (2020) although their study was limited to the southern North Sea and used *in situ* data (i.e., the spatial extension was smaller). The date of the spring bloom onset has decreased 1.5 days per year in average over the studied period. The reasons for a change on the date of spring bloom onset can be varied. In the North Sea, as in the global ocean, water temperature has been increasing over the last decades as a result of climate change. For example, Desmit et al. (2020) reported an increase of the sea surface temperature in the North Sea of $\sim$ $0.035°C\ yr^{-1}$ using *in situ* data from 1971 to 2014, and Høyer and Karagali (2016) found a $0.037°C\ yr^{-1}$ increment for the North Sea from 1982 to 2012 using a reanalysis product. Using CMEMS "European North West Shelf/Iberia Biscay Irish

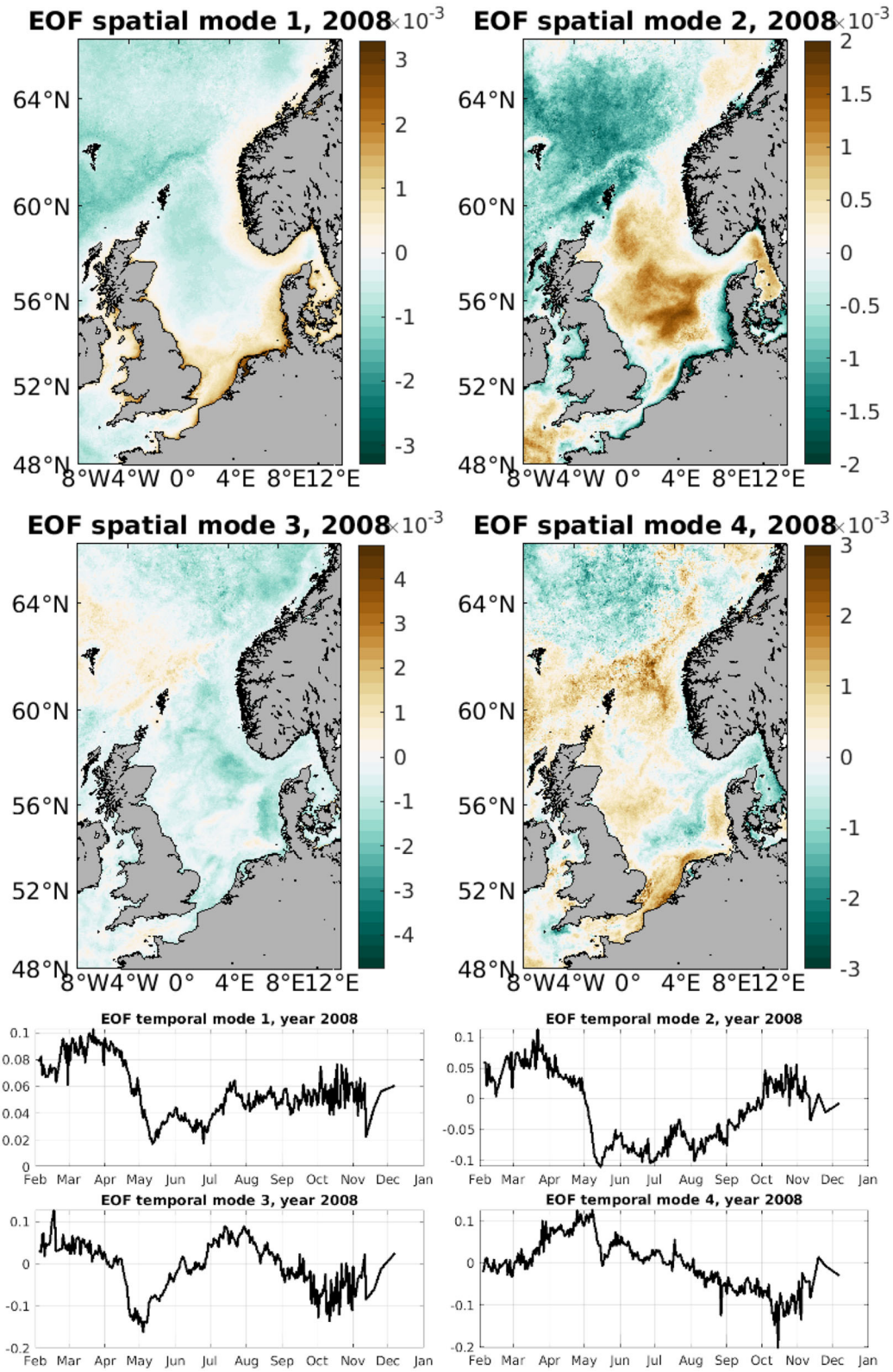

FIGURE 6 | First four spatial CHL EOF modes for 2008 (**top** two rows) and first four temporal CHL EOF modes for 2008 (**bottom** two rows).

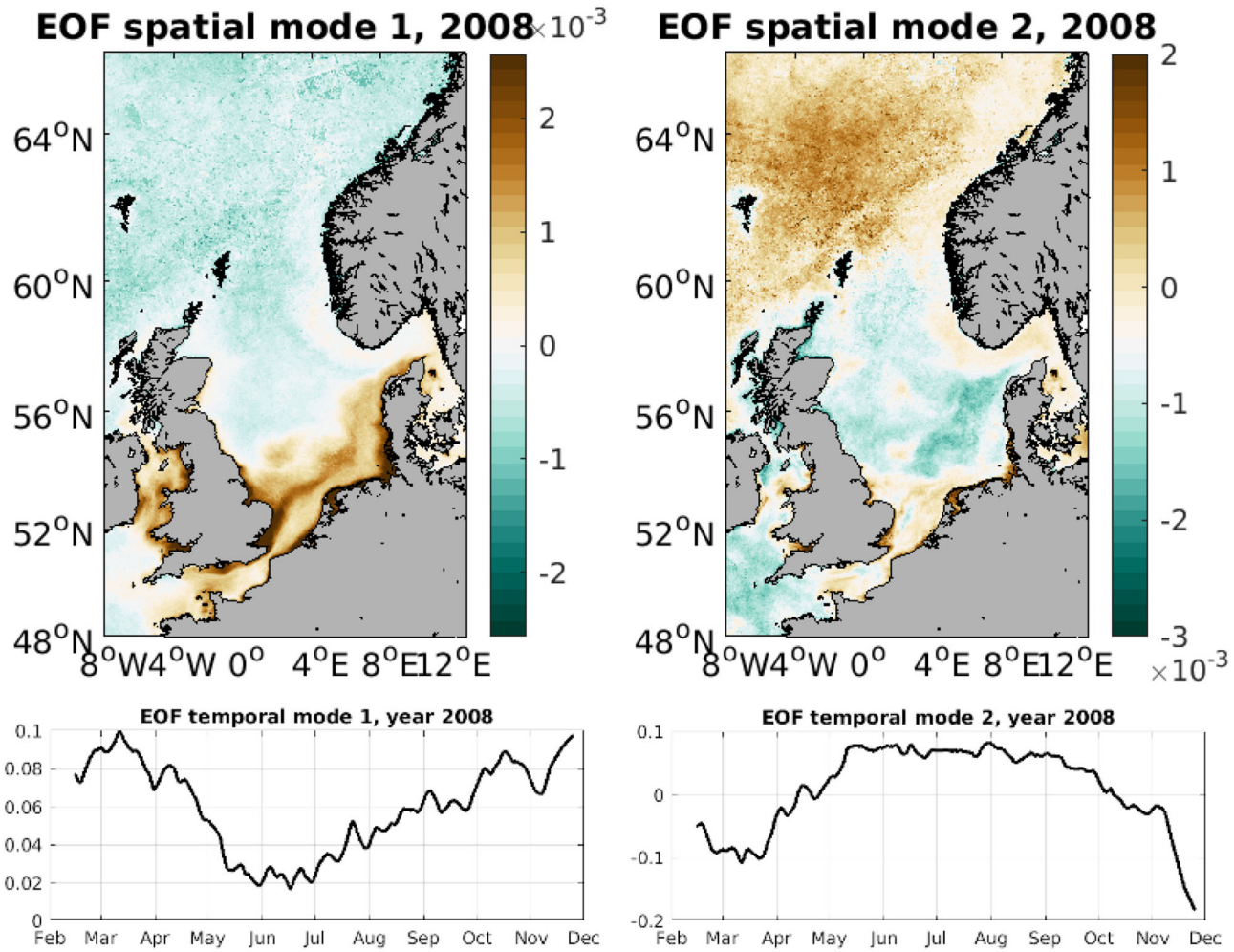

FIGURE 7 | First two spatial SPM EOF modes for 2008 **(top)** and first two temporal SPM EOF modes for 2008 **(bottom)**.

Seas - High Resolution L4 Sea Surface Temperature Reprocessed" Sea Surface Temperature (SST) satellite product, the daily average SST over the domain of study was calculated for the years 1998–2019 (last year available for this product at the moment of access), as shown in **Figure 9**. A warming of $0.31^{\circ}C$ has been calculated from 1998 to 2019, or $0.015^{\circ}C\ yr^{-1}$. This value differs from the others found in the references mentioned, but this difference can be attributed to the different spatial domains, periods considered and products used. All results however point at an increasing water temperature in the North Sea over the last decades. If nutrients are not limited, higher temperatures can accelerate phytoplankton cell division rates (e.g., Edwards et al., 2016; Hunter-Cevera et al., 2016), contributing to earlier blooms. The effect of rising temperature must be accompanied by a stratification of the water column to favor earlier blooms.

The time of the spring bloom ending was also calculated following the opposite criterion as for the onset, i.e., the date on which the concentration of CHL first goes below the yearly median plus 5%. This is used to assess the duration of the spring bloom (time between onset and offset). While there is a high year-to-year variability in the duration of the spring bloom (**Figure 11**), a tendency toward longer blooms can be observed in more recent years, although this trend is not statistically significant. The years with longer bloom periods typically have a slow growing or weaning periods, as in 2013 and 2004, respectively (examples shown in **Figure 11**), causing the bloom period to be longer. Longer spring bloom periods do not mean higher CHL peaks or stronger blooms, and no significant correlation has been found between the strength of the peak (calculated as the difference between the maximum CHL value attained each year and the median value) and the duration of the bloom.

The average CHL concentration between the onset and offset of the bloom (**Figure 12** top panel) shows increasing values during the period 1998–2008 and then a decreasing trend. Values in the 2017–2020 period are similar to what was observed during

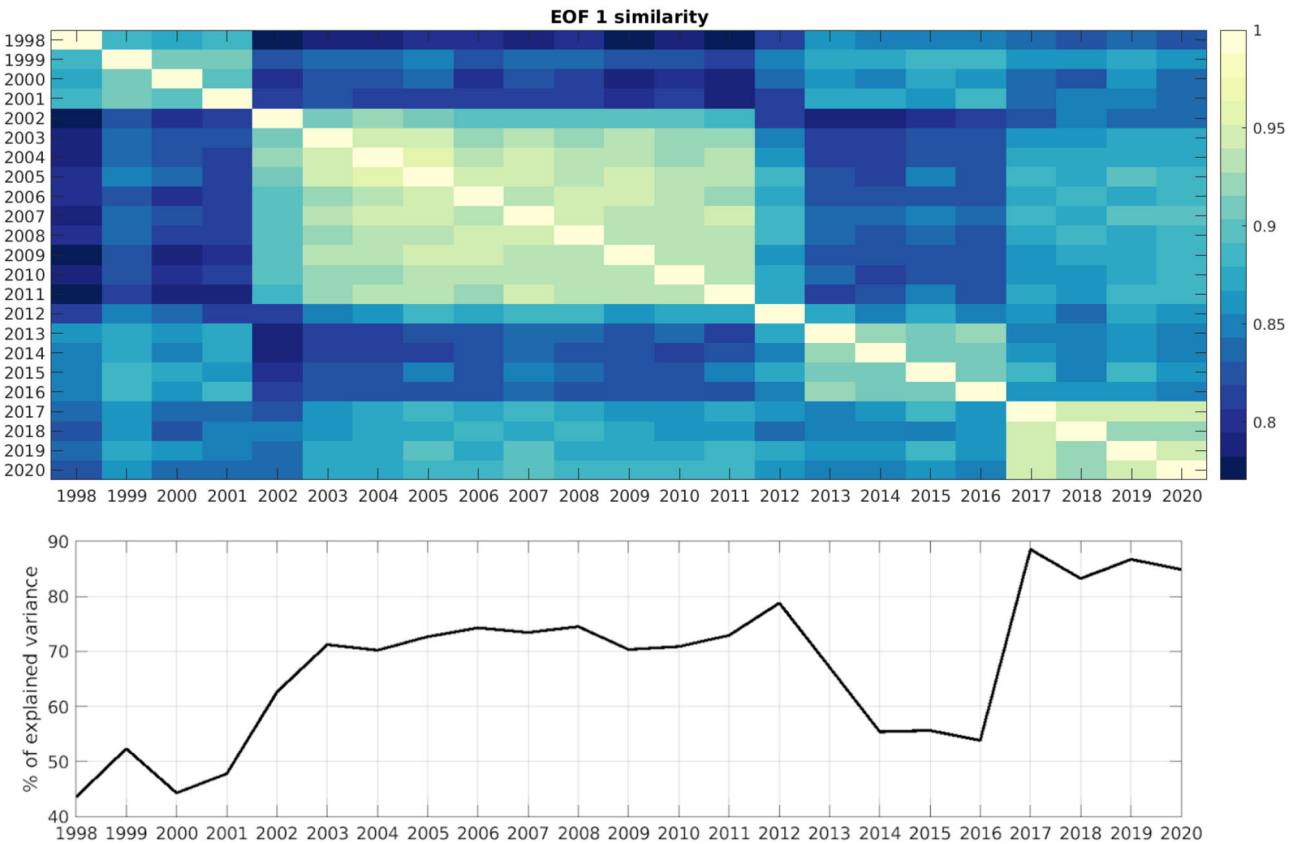

FIGURE 8 | (Top) Correlation between each year first EOF CHL mode and all the other years. **(Bottom)** Percentage of explained variance retained in the DINEOF interpolated dataset.

the early 2000s. Therefore, having spring blooms earlier in the year does not impact the average amount of CHL during the bloom. The amount of SPM during the winter months (February-March, as January is not used in our analysis because of the low availability of data) does not show a significant trend, but values appear in general to be higher during recent years. Studies of the influence of water clarity on phytoplankton growth reveal different results depending on the region. Several works (e.g., Capuzzo et al., 2015; Opdal et al., 2019; Wilson and Heath, 2019) found that light availability for phytoplankton growth has decreased on average in the North Sea during the XXth century through an increment of SPM. Philippart et al. (2013) on the other hand have found no significant increase or decrease of turbidity over four decades in the Wadden Sea (southeastern part of the North Sea). Our results do not show a clear trend in the average SPM concentration over the Greater North Sea over the period of study, so we cannot conclude that light availability has had an influence in the spring bloom onset date.

The time of maximum CHL concentration during each year bloom period has been also calculated (**Figure 12** bottom panel). As the date of spring bloom onset has shifted to earlier dates, we could expect a similar shift in the peak of the bloom. While we can observe a general decrease in **Figure 12** the variability is also high, specially during 2002–2013. The maximum CHL concentration during recent years (2014–2020) is reached 1–2 weeks earlier than what was observed in the early 2000s. While the linear trend over all the years is not significant ($p = 0.07$), it would be worth revisiting this when more data become available, to determine if there is a shift in the date when the spring bloom reaches its maximum.

The data presented show that the spring bloom in the Greater North Sea has shifted to earlier dates during the last 23 years, with the maximum CHL value probably occurring also in earlier dates. Bloom duration shows high variability but appears to have become longer, but the average amount of CHL during the spring bloom period does not show a clear trend over time, indicating that the blooms have not become stronger nor weaker due to the shift in time. From all the analyses shown in **Figures 10–12**, only the date on which the spring bloom starts each year (i.e., **Figure 10**) shows a statistically significant trend. SPM values during winter months show also higher values during more recent years, although there is a lot of variability in these data. Higher SPM would imply lower CHL or later spring bloom onset dates as more turbid waters hinder light availability for primary producers. We therefore suggest that the role of increasing water temperature has had a stronger effect in spring bloom onset date than SPM concentration. However, given the large size of the domain of study, multiple factors are probably

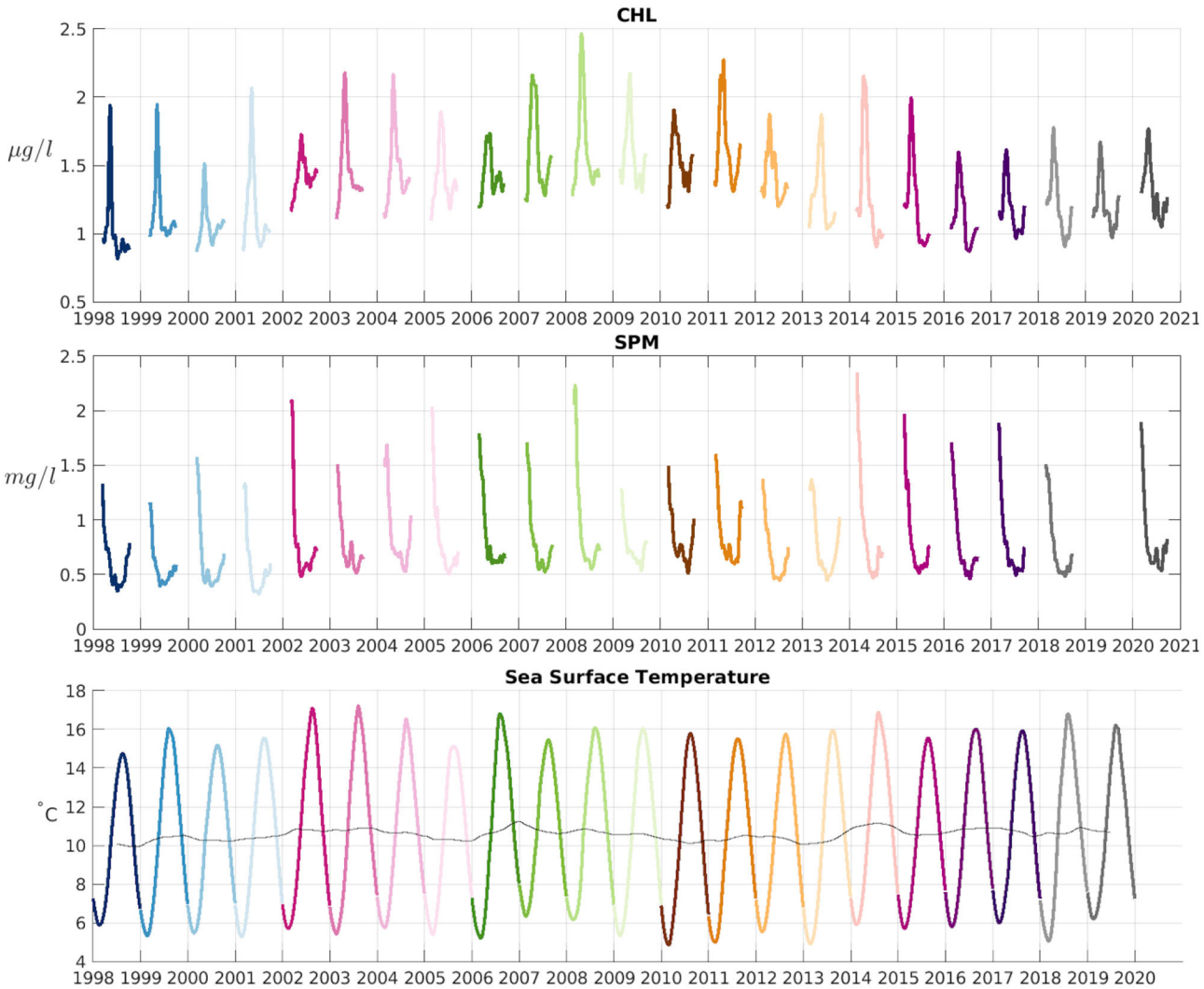

FIGURE 9 | (Top) CHL Spatial average over the whole domain of **Figure 1** during the 23 years of the study. **(Middle)** SPM averaged over the same region. Data from December-January is not plotted. **(Bottom)** SST spatial average over the whole domain. The thin black line shows the 1-yr running mean. Different colors for each year are used to ease comparison between variables for a given year. This color scheme is used in other multi-year figures in this work to ease comparison.

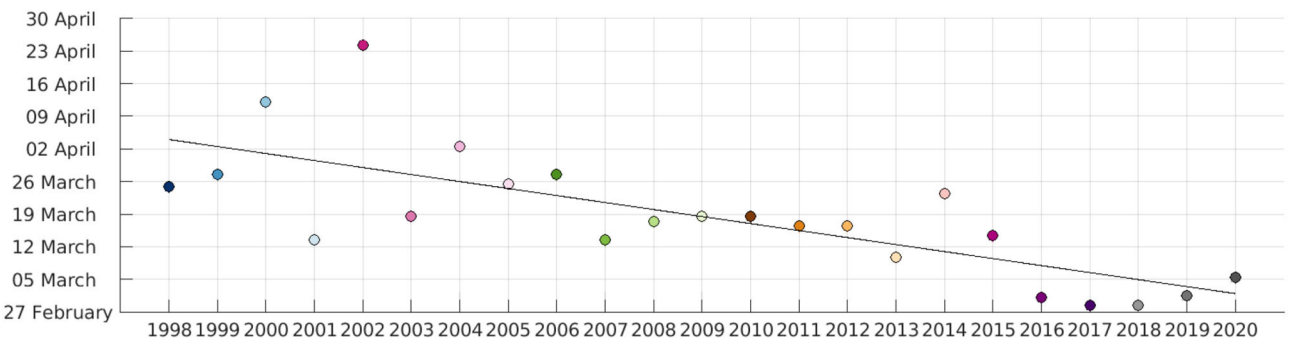

FIGURE 10 | Date on which the CHL concentration reaches the annual median value for the first time each year. The solid black line shows a linear fit to the dates, with $r = 0.75$ and a p-value of 4.1267e-05.

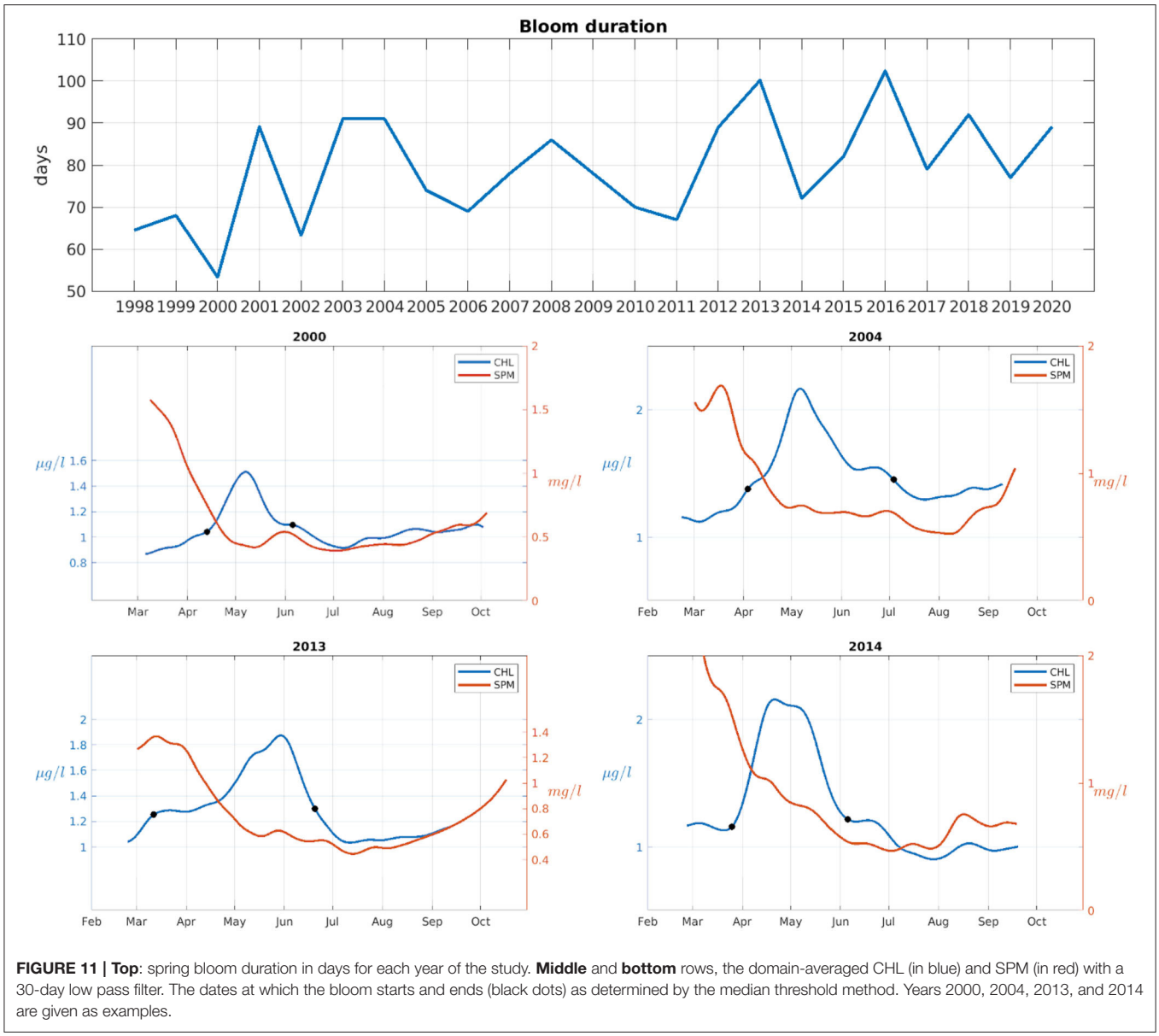

FIGURE 11 | Top: spring bloom duration in days for each year of the study. **Middle** and **bottom** rows, the domain-averaged CHL (in blue) and SPM (in red) with a 30-day low pass filter. The dates at which the bloom starts and ends (black dots) as determined by the median threshold method. Years 2000, 2004, 2013, and 2014 are given as examples.

responsible for the observed change in spring bloom onset date, with the relative influence of each factor probably varying in each region.

5. CONCLUSIONS

We have performed a daily, gap-free reconstruction of chlorophyll (CHL) and suspended particulate matter (SPM) in the Greater North Sea region over the period 1998 to 2020 with a spatial resolution of 1 km. Missing data have been reconstructed using DINEOF (Data Interpolating Empirical Orthogonal Functions). The mesoscale variability observed in the initial, gappy data (eddies, fronts, Thames river plume) are retained in the final datasets, demonstrating the high resolution of the reconstructed data. Both the initial and reconstructed data were validated in Van der Zande et al. (2019b) and showed a correct level of accuracy. The EOF modes used for the reconstruction show that, in general, the southern part of the domain has the largest variability. This is due in part to the shallower depths, and the largely urbanized coasts of this region which result in more nutrients reaching the coastal waters through river run-off.

The interannual variability was observed to be high, with changes in year-to-year CHL and SPM annual cycle, as well as their maximum and minimum values. Maximum CHL values obtained during the spring bloom have increased during the period 1998–2008, and show a decrease during 2008–2017. The maximum CHL appears to be slightly increasing again during the period 2017–2020.

This work has shown that the start date of the spring bloom occurs earlier every year in the North Sea, with starting dates in

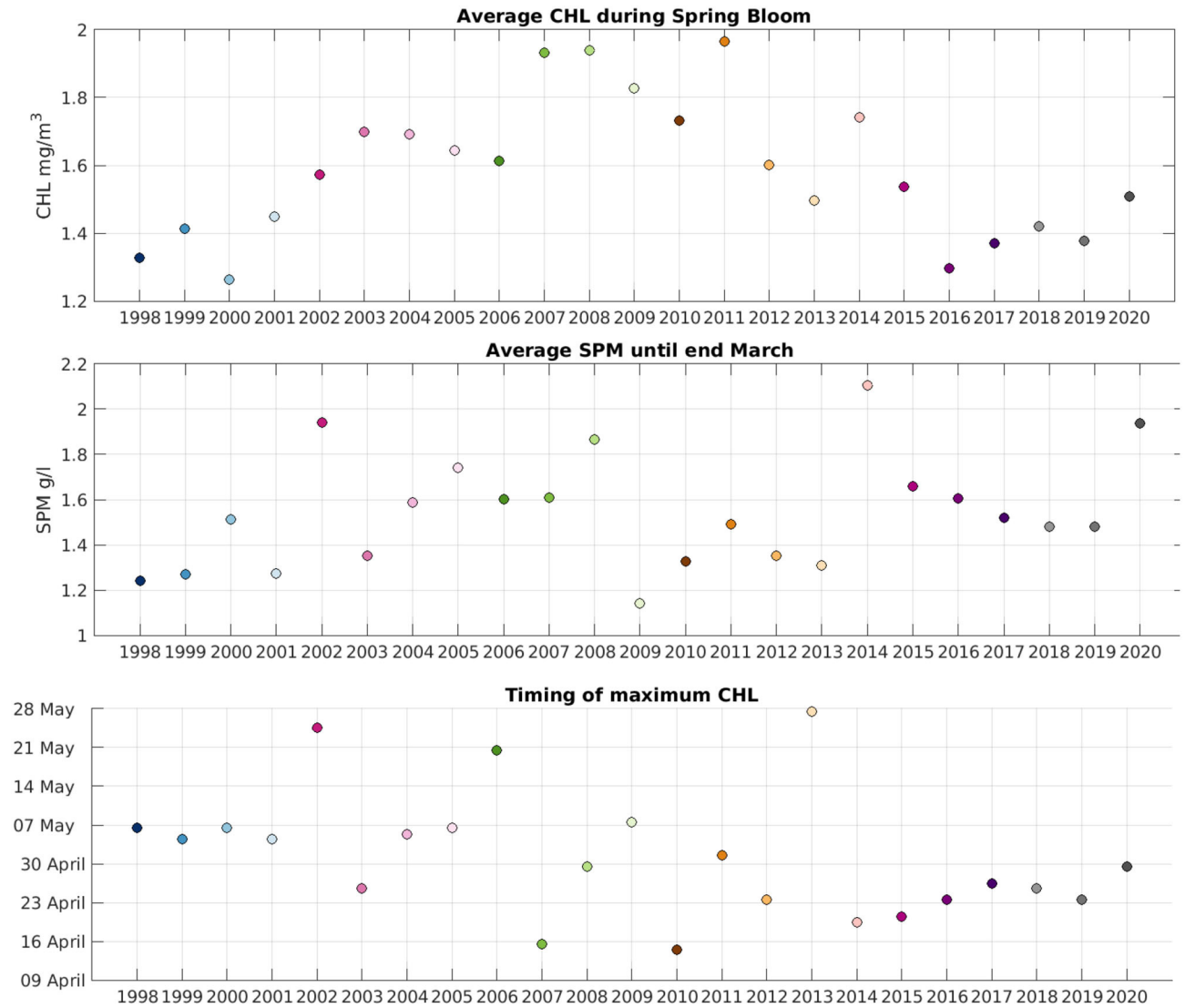

FIGURE 12 | (Top) Average CHL during the spring bloom period each year. **(Middle)** Average SPM during February and March. **(Bottom)** Time at which the maximum CHL concentration is reached each year.

2020 about 1 month earlier than in 1998. Earlier spring bloom dates have been described in the southern part of the North Sea using *in situ* data (Desmit et al., 2020), and our study has shown this trend on a global scale covering the Greater North Sea, using satellite data. Increasing water temperatures can explain at least in part this trend, although it remains unclear what the role of the SPM has been. The SPM average concentration in February-March each year does not show a clear trend that could help explain the earlier dates of the spring bloom.

Another major conclusion of this work is related to the use of a variable number of satellites in long-term ocean color analyses, and the impact of this number in the final product. The number of satellites used to compute CHL and SPM has an impact in the amount of explained variance by the EOF modes used in DINEOF, as more satellites provide also a better spatio-temporal coverage of all scales of variability. In order to retain a large amount of the initial variability, at least three satellites measuring ocean color are required. Periods with only 1 or 2 satellites showed a lower amount of percentage of retained variance in the final, interpolated product. This result sets up a target on the minimal number of satellites that would be needed for a correct measurement of the ocean color variability, specially in zones with a high amount of clouds and other sources of missing data.

Analysis of long time series of CHL and SPM data are necessary to understand the impact of human activities on the ecosystem. Using gap-free satellite data at high spatial resolution is necessary to resolve the small-scale variability that contributes to the net variations of CHL and SPM, and our DINEOF analysis of these variables has been shown to provide enough detail to resolve these structures. Due to the

large size of the domain of study, with shallow waters in the southern, highly populated region, an open connection to the Atlantic Ocean to the North, and the opening to the Baltic sea to the East, the factors influencing spring bloom phenology can be also multiple. Future work should address the changes observed in sub-regions of the North Sea, like the Southern North Sea, the Norwegian channel or the Faroe Islands.

DATA AVAILABILITY STATEMENT

The raw data supporting the conclusions of this article will be made available by the authors, without undue reservation.

AUTHOR CONTRIBUTIONS

AA-A realized the reconstruction analyses, made the figures, and wrote the manuscript. DV prepared the initial data, did the validation and contributed to discussion, and writing of the manuscript. AB contributed to the interpretation of the results, the discussion, and the writing of the manuscript. CT contributed to the discussion and the writing of the manuscript. SM contributed to the discussion and the writing of the manuscript. J-MB contributed to the discussion and the writing of the manuscript. All authors contributed to the article and approved the submitted version.

ACKNOWLEDGMENTS

This research was performed with funding from the Belgian Science Policy Office (BELSPO) STEREO III programme in the framework of the MULTI-SYNC project (contract SR/00/359). Computational resources have been provided by the Consortium des Équipements de Calcul Intensif (CÉCI), funded by the Fonds de la Recherche Scientifique de Belgique (F.R.S.-FNRS) under Grant No. 2.5020.11 and by the Walloon Region.

REFERENCES

Alvera-Azcárate, A., Barth, A., Beckers, J.-M., and Weisberg, R. H. (2007). Multivariate reconstruction of missing data in sea surface temperature, chlorophyll and wind satellite fields. *J. Geophys. Res.* 112:C03008. doi: 10.1029/2006JC003660

Alvera-Azcárate, A., Barth, A., Parard, G., and Beckers, J.-M. (2016). Analysis of SMOS sea surface salinity data using DINEOF. *Remote Sens. Environ.* 180, 137–145. doi: 10.1016/j.rse.2016.02.044

Alvera-Azcárate, A., Barth, A., Rixen, M., and Beckers, J.-M. (2005). Reconstruction of incomplete oceanographic data sets using empirical orthogonal functions. Application to the Adriatic Sea surface temperature. *Ocean Modell.* 9, 325–346, doi: 10.1016/j.ocemod.2004.08.001

Alvera-Azcárate, A., Barth, A., Sirjacobs, D., and Beckers, J.-M. (2009). Enhancing temporal correlations in EOF expansions for the reconstruction of missing data using DINEOF. Ocean Science 5, 475–485. doi: 10.5194/os-5-475-2009

Alvera-Azcárate, A., Vanhellemont, Q., Ruddick, K., Barth, A., and Beckers, J.-M. (2015). Analysis of high frequency geostationary ocean colour data using DINEOF. *Estuar. Coast. Shelf Sci.* 159, 28–36. doi: 10.1016/j.ecss.2015.03.026

Bailey, S., and Werdell, P. (2006). A multi-sensor approach for the on-orbit validation of ocean color satellite data products. *Remote Sens. Environ.* 102, 12–23. doi: 10.1016/j.rse.2006.01.015

Beckers, J.-M., Barth, A., and Alvera-Azcárate, A. (2006). DINEOF reconstruction of clouded images including error maps. Application to the sea surface temperature around Corsican Island. *Ocean Sci.* 2, 183–199. doi: 10.5194/os-2-183-2006

Beckers, J.-M., and Rixen, M. (2003). EOF calculations and data filling from incomplete oceanographic data sets. *J. Atmos. Ocean. Technol.* 20, 1839–1856. doi: 10.1175/1520-0426(2003)020<1839:ECADFF>2.0.CO;2

Brody, S. R., Lozier, M. S., and Dunne, J. P. (2013). A comparison of methods to determine phytoplankton bloom initiation. *J. Geophys. Res. Oceans* 118, 2345–2357. doi: 10.1002/jgrc.20167

Capuzzo, E., Lynam, C. P., Barry, J., Stephens, D., Forster, R. M., Greenwood, N., et al. (2017). A decline in primary production in the north sea over 25 years, associated with reductions in zooplankton abundance and fish stock recruitment. *Glob. Change Biol.* 24, 1–13. doi: 10.1111/gcb.13916

Capuzzo, E., Stephens, D., Silva, T., Barry, J., and Forster, R. M. (2015). Decrease in water clarity of the southern and central North Sea during the 20th century. *Glob. Change Biol.* 21, 2206–2214. doi: 10.1111/gcb.12854

Desmit, X., Nohe, A., Borges, A.-V., Prins, T., De Cauwer, K., Lagring, R., et al. (2020). Changes in chlorophyll concentration and phenology in the North Sea in relation to de-eutrophication and sea surface warming. *Limnol. Oceanogr.* 65, 828–847. doi: 10.1002/lno.11351

Desmit, X., Ruddick, K., and Lacroix, G. (2015). Salinity predicts the distribution of chlorophyll a spring peak in the southern North Sea continental waters. *J. Sea Res.* 103, 59–74. doi: 10.1016/j.seares.2015.02.007

Ducrotoy, J. P., Elliott, M., and Jonge, V. N. (2000). The North Sea. *Mar. Pollut. Bull.* 41, 5–23. doi: 10.1016/S0025-326X(00)00099-0

Edwards, K. F., Thomas, M. K., Klausmeier, C. A., and Litchman, E. (2016). Phytoplankton growth and the interaction of light and temperature: a synthesis at the species and community level. *Limnol. Oceanogr.* 61, 1232–1244. doi: 10.1002/lno.10282

Ferrari, R., Merrifield, S. T., and Taylor, J. R. (2015). Shutdown of convection triggers increase of surface chlorophyll. *J. Mar. Syst.* 147, 116–122. doi: 10.1016/j.jmarsys.2014.02.009

Ferreira, J., Andersen, J., Borja, A., Bricker, S., Camp, J., Cardoso da Silva, M., et al. (2011). Overview of eutrophication indicators to assess environmental status within the European Marine Strategy Framework Directive. *Estuar. Coast. Shelf Sci.* 93, 117–131. doi: 10.1016/j.ecss.2011.03.014

Fettweis, M., Baeye, M., Van der Zande, D., Van den Eynde, D., and Lee, J. (2014). Seasonality of floc strength in the southern North Sea. *J. Geophys. Res. Oceans* 119, 1911–1926. doi: 10.1002/2013JC009750

Fettweis, M., Nechad, B., and den Eynde, D. V. (2007). An estimate of the suspended particulate matter (SPM) transport in the southern North Sea using SeaWiFS images, *in situ* measurements and numerical model results. *Continent. Shelf Res.* 27, 1568–1583. doi: 10.1016/j.csr.2007.01.017

Friedland, R., Macias, D., Cossarini, G., Daewel, U., Estournel, C., Garcia-Gorriz, E., et al. (2021). Effects of nutrient management scenarios on marine eutrophication indicators: a pan-European, multi-model assessment in support of the marine strategy framework directive. *Front. Mar. Sci.* 8:596126. doi: 10.3389/fmars.2021.596126

Gohin, F., Druon, J. N., and Lampert, L. (2002). A five channel chlorophyll concentration algorithm applied to SeaWiFS data processed by SeaDAS in coastal waters. *Int. J. Remote Sens.* 23, 1639–1661. doi: 10.1080/01431160110071879

Gons, H. J., Rijkeboer, M., and Ruddick, K. G. (2002). A chlorophyll-retrieval algorithm for satellite imagery (Medium Resolution Imaging Spectrometer) of inland and coastal waters. *J. Plankton Res.* 24, 947–951. doi: 10.1093/plankt/24.9.947

Høyer, J., and Karagali, I. (2016). Sea surface temperature climate data record for the North Sea and Baltic Sea. *J. Clim.* 29, 2529–2541. doi: 10.1175/JCLI-D-15-0663.1

Huisman, J., van Oostveen, P., and Weissing, F. J. (1999). Critical depth and critical turbulence: Two different mechanisms for the development of phytoplankton blooms. *Limnol. Oceanogr.* 44, 1781–1787.

Hunter-Cevera, K. R., Neubert, M. G., Olson, R. J., Solow, A. R., Shalapyonok, A., Sosik, H. M. (2016). Physiological and ecological drivers of early spring blooms of a coastal phytoplankter. *Science* 354, 326–329. doi: 10.1126/science.aaf8536

Huynh, T. H. N., Alvera-Azcárate, A., and Beckers, J.-M. (2020). Analysis of surface chlorophyll a associated with sea surface temperature and surface wind in the South China Sea. *Ocean Dyn.* 70, 139–161. doi: 10.1007/s10236-019-01308-9

Kröncke, I. (2011). Changes in Dogger Bank macrofauna communities in the 20th century caused by fishing and climate. *Estuar. Coast. Shelf Sci.* 94, 234–245.

Lancelot, C., Spitz, Y., Gypens, N., Ruddick, K., Becquevort, S., Rousseau, V., et al. (2005). Modelling diatom and Phaeocystis blooms and nutrient cycles in the Southern Bight of the North Sea: the MIRO model. *Mar. Ecol. Prog. Ser.* 289, 63–78. doi: 10.3354/meps289063

Lavigne, H., Van der Zande, D., Ruddick, K., Cardoso Dos Santos, J., Gohin, F., Brotas, V., et al. (2021). Quality-control tests for OC4, OC5 and NIR-red satellite chlorophyll-a algorithms applied to coastal waters. *Remote Sens. Environ.* 255:112237. doi: 10.1016/j.rse.2020.112237

Nechad, B., Ruddick, K., and Park, Y. (2010). Calibration and validation of a generic multisensor algorithm for mapping of total suspended matter in turbid waters. *Remote Sens. Environ.* 114, 854–866. doi: 10.1016/j.rse.2009.11.022

Opdal, A. F., Lindemann, C., and Aksnes, D. L. (2019). Centennial decline in north sea water clarity causes strong delay in phytoplankton bloom timing. *Glob. Change Biol.* 25, 3946–3953. doi: 10.1111/gcb.14810

O'Reilly, J. E., Maritorena, S., Mitchell, B., Siegel, D., Carder, K. L., Garver, S. A., et al. (1998). Ocean color chlorophyll algorithms for SeaWiFS. *J. Geophys. Res. Oceans* 103, 24937–24953.

Philippart, C., Salama, M. S., Kromkamp, J. C., van der Woerd, H. J., Zuur, A. F., and Cadee, G. C. (2013). Four decades of variability in turbidity in the western Wadden Sea as derived from corrected Secchi disk readings. *J. Sea Res.* 82, 67–79. doi: 10.1016/j.seares.2012.07.005

Philippart, C., van Iperen, J., Cadee, G., and Zuur, A. (2010). Long-term field observations on seasonality in chlorophyll-a concentrations in a shallow coastal marine ecosystem, the Wadden Sea. *Estuar. Coasts* 33, 286–294. doi: 10.1007/s12237-009-9236-y

Rousseau, V., Lantoine, F., Rodriguez, F., LeGall, F., Chretiennot-Dinet, M.-J., and Lancelot, C. (2013). Characterization of Phaeocystis globosa (Prymnesiophyceae), the blooming species in the Southern North Sea. *J. Sea Res.* 76, 105–113. doi: 10.1016/j.seares.2012.07.011

Sathyendranath, S., Brewin, R., Brockmann, C., Brotas, V., Calton, B., Chuprin, A., et al. (2019). An ocean-colour time series for use in climate studies: the experience of the ocean-colour climate change initiative (OC-CCI). *Sensors* 19:4285. doi: 10.3390/s19194285

Schroeder, T., Schaale, M., and Fischer, J. (2007). Retrieval of atmospheric and oceanic properties from MERIS measurements: a new Case-2 water processor for BEAM. *Int. J. Remote Sens.* 28, 5627–5632. doi: 10.1080/01431160701601774

Sirjacobs, D., Alvera-Azcárate, A., Barth, A., Lacroix, G., Park, Y., Nechad, B., et al. (2011). Cloud filling of ocean color and sea surface temperature remote sensing products over the Southern North Sea by the Data Interpolating Empirical Orthogonal Functions methodology. *J. Sea Res.* 65, 114–130. doi: 10.1016/j.seares.2010.08.002

Sündermann, J., and Pohlmann, T. (2011). A brief analysis of North Sea physics. *Oceanologia* 53, 663–689. doi: 10.5697/oc.53-3.663

Van der Zande, D., Eleveld, M., Lavigne, H., Gohin, F., Pardo, S., Tilstone, G., et al. (2019a). Joint Monitoring Programme of the EUtrophication of the NOrth Sea with SATellite data user case in Copernicus Marine Service Ocean State Report. *J. Operat. Oceanogr.* 12, 1–123. doi: 10.1080/1755876X.2019.1633075

Van der Zande, D., Lavigne, H., Blauw, A., Prins, T., Desmit, X., Eleveld, M., et al. (2019b). *Enhance Coherence in Eutrophication Assessments Based on Chlorophyll, Using Satellite Data as Part of the EU Project–Joint Monitoring Programme of the Eutrophication of the North Sea With Satellite Data (JMP-EUNOSAT)*. Technical report, RBINS. Available online at: https://www.informatiehuismarien.nl/projecten/algaeevaluated/information/results/

Vindenes, H., Orvik, K., Søiland, H., and Wehde, H. (2018). Analysis of tidal currents in the North Sea from shipboard acoustic Doppler current profiler data. *Continent. Shelf Res.* 162, 1–12. doi: 10.1016/j.csr.2018.04.001

von Storch, H., and Zwiers, F. W. (1999). *Statistical Analysis in Climate Research.* Cambridge: Cambridge University Press, 484. doi: 10.1017/CBO9780511612336

Wilson, R. J., and Heath, M. R. (2019). Increasing turbidity in the north sea during the 20th century due to changing wave climate. *Ocean Sci.* 15, 1615–1625. doi: 10.5194/os-15-1615-2019

Winther, N. G., and Johannessen, J. A. (2006). North Sea circulation: Atlantic inflow and its destination. *J. Geophys. Res. Oceans* 111:C12. doi: 10.1029/2005JC003310

Xu, X., Lemmen, C., and Wirtz, K. W. (2020). Less nutrients but more phytoplankton: long-term ecosystem dynamics of the Southern North Sea. *Front. Mar. Sci.* 7:662. doi: 10.3389/fmars.2020.00662

Conflict of Interest: The authors declare that the research was conducted in the absence of any commercial or financial relationships that could be construed as a potential conflict of interest.

Publisher's Note: All claims expressed in this article are solely those of the authors and do not necessarily represent those of their affiliated organizations, or those of the publisher, the editors and the reviewers. Any product that may be evaluated in this article, or claim that may be made by its manufacturer, is not guaranteed or endorsed by the publisher.

frontiers in Earth Science

ORIGINAL RESEARCH
published: 14 September 2021
doi: 10.3389/feart.2021.724879

Ocean Mesoscale Variability: A Case Study on the Mediterranean Sea From a Re-Analysis Perspective

Antonio Bonaduce[1], Andrea Cipollone[2], Johnny A. Johannessen[3], Joanna Staneva[4], Roshin P. Raj[1] and Ali Aydogdu[2]*

[1]Nansen Environmental and Remote Sensing Center and Bjerknes Center for Climate Research, Bergen, Norway, [2]Ocean Modeling and Data Assimilation Division, Centro Euro-Mediterraneo Sui Cambiamenti Climatici, Bologna, Italy, [3]Nansen Environmental and Remote Sensing Center and Geophysical Institute, University of Bergen, Bergen, Norway, [4]Helmholtz Zentrum Hereon, Geesthacht, Germany

OPEN ACCESS

Edited by:
Andrea Storto, National Research Council (CNR), Italy

Reviewed by:
Chunhua Qiu, Sun Yat-sen University, China
Francesco Bignami, National Research Council (CNR), Italy
Xavier Carton, Université de Bretagne Occidentale, France

***Correspondence:**
Antonio Bonaduce
antonio.bonaduce@nersc.no

Specialty section:
This article was submitted to Interdisciplinary Climate Studies, a section of the journal Frontiers in Earth Science

Received: *14 June 2021*
Accepted: *26 August 2021*
Published: *14 September 2021*

Citation:
Bonaduce A, Cipollone A, Johannessen JA, Staneva J, Raj RP and Aydogdu A (2021) Ocean Mesoscale Variability: A Case Study on the Mediterranean Sea From a Re-Analysis Perspective. Front. Earth Sci. 9:724879. doi: 10.3389/feart.2021.724879

The mesoscale variability in the Mediterranean Sea is investigated through eddy detection techniques. The analysis is performed over 24 years (1993–2016) considering the three-dimensional (3D) fields from an ocean re-analysis of the Mediterranean Sea (MED-REA). The objective is to achieve a fit-for-purpose assessment of the 3D mesoscale eddy field. In particular, we focus on the contribution of eddy-driven anomalies to ocean dynamics and thermodynamics. The accuracy of the method used to disclose the 3D eddy contributions is assessed against pointwise *in-situ* measurements and observation-based data sets. Eddy lifetimes ≥ 2 weeks are representative of the 3D mesoscale field in the basin, showing a high probability (> 60%) of occurrence in the areas of the main quasi-stationary mesoscale features. The results show a dependence of the eddy size and thickness on polarity and lifetime: anticyclonic eddies (ACE) are significantly deeper than cyclonic eddies (CE), and their size tends to increase in long-lived structures which also show a seasonal variability. Mesoscale eddies result to be a significant contribution to the ocean dynamics in the Mediterranean Sea, as they account for a large portion of the sea-surface height variability at temporal scales longer than 1 month and for the kinetic energy (50–60%) both at the surface and at depth. Looking at the contributions to ocean thermodynamics, the results exhibit the existence of typical warm (cold) cores associated with ACEs (CEs) with exceptions in the Levantine basin (e.g., Shikmona gyre) where a structure close to a mode-water ACE eddy persists with a positive salinity anomaly. In this area, eddy-induced temperature anomalies can be affected by a strong summer stratification in the surface water, displaying an opposite sign of the anomaly whether looking at the surface or at depth. The results show also that temperature anomalies driven by long-lived eddies (≥ 4 weeks) can affect up to 15–25% of the monthly variability of the upper ocean heat content in the Mediterranean basin.

Keywords: fit-for-purpose assessment, regional ocean re-analysis, Mediterranean Sea, eddy detection and tracking, 3D mesoscale field, eddy-induced anomalies

1 INTRODUCTION

Mesoscale eddies can originate nearly everywhere in the ocean, and typically exhibit different properties (e.g., heat, salt, carbon) with respect to their surroundings, which can be transported as they move around the ocean (Chelton et al., 2007; Chelton et al., 2011b; Zhao et al., 2018). At the surface, mesoscale eddies are identified from satellite altimetry data, where depression (elevation) in the sea level anomaly (SLA) field reveals a cyclonic (anticyclonic) structure (Chelton et al., 2011a). Although only the surface expression of mesoscale eddies is visible in remote sensing measurement of SLA and sea-surface temperature (SST), they are three-dimensional (3D) structures that can reach down into the pycnocline. Temperature and salinity anomalies induced by eddies tend to be opposite depending on the polarity of an eddy: cyclones (CE) versus anticyclones (ACE) (Gaube et al., 2013; Dong et al., 2014; Raj et al., 2016; Raj et al., 2020). Mode-water eddies represent a substantial exception to this general rule (Barceló-Llull et al., 2017; Zhang et al., 2017; Shi et al., 2018). Schütte et al. (2016) show the existence of ACEs with both negative SST and salinity anomaly and positive ones. Pegliasco et al. (2015) observed ACEs with a lens-like structure of isopycnals in the eastern boundary upwelling regions. In this context, eddy-detection systems (e.g., Dong et al., 2012; Petersen et al., 2013; Xu et al., 2014; Faghmous et al., 2015; Frenger et al., 2015; Lin et al., 2015) are an ad-hoc diagnostic tool designed to isolate mesoscale features, track them in time, and exclusively analyze the parcel of water trapped inside. These systems can disentangle the "anomalous" content dragged by eddies, that can differ from the ambient waters, in terms of nutrient concentration, tracers, and energetic component. Combining multiple observing system networks, from *in-situ* and remote-sensing, it is now possible to investigate eddy-induced anomalies in water mass structures, estimate ocean heat, and salt transport by advective trapping (e.g. Gaube et al., 2013; Dong et al., 2014), and hence infer the quasi-3D structure of the non-linear features. Conversely, the representation of ocean mesoscale dynamics is strongly limited by the spatial coverage and temporal sampling of a given satellite mission (e.g., Bonaduce et al., 2018; Chen et al., 2021). Moreover, the temporal and spatial co-location with the available Argo profiling floats in certain areas of the ocean is affected by uneven data coverage and sampling frequency (e.g., Liu et al., 2020), which can represent a shortcoming to investigate the properties of water masses induced by the occurrence of 3D eddies.

These limitations can be overcome by exploiting the synergy between multiple observing systems and ocean model dynamics. Ocean re-analyses combine information from multiple observing networks (e.g., satellite altimetry and Argo profiling floats) with ocean model dynamics and atmospheric forcing through multivariate data assimilation methods (Storto et al., 2019) to obtain optimized 4D estimates of the state of the ocean. These are non-linear, dynamically-reconstructed ocean fields that outperform observation-only reconstructed products in several crucial climate indexes (Wunsch and Heimbach, 2014; Balmaseda et al., 2015), as well as in the representation of the small-scale variability at depth (Cipollone et al., 2017).

The objective of this work is to achieve a fit-for-purpose assessment of the representation of the 3D structure of mesoscale eddies in a regional ocean reanalysis for the Mediterranean Sea.

In this area, eddies have a deep and stable structure, penetrating well below the mixed layer depth down to 400–500 m (e.g., Fusco et al., 2003). Their structures are almost stationary, mainly trapped between the most prominent ocean currents of the basin (e.g., Pinardi et al., 1997; Pinardi and Masetti, 2000; Pinardi et al., 2015), thus behaving like a preferred energetic pathway to transform potential into eddy kinetic energy (EKE) and mixing deep and surface water (e.g., Rubio et al., 2009). A mere look at surface physics only would be a too coarse approximation, and it is therefore crucial to have access to the full 3D eddy structure, for any quantitative estimate of anomalous flow and the impact on ocean circulation and water masses. The features of the ocean circulation in the Mediterranean Sea have been investigated so far from either models or observations. A fundamental contribution to the understanding of ocean general circulation and mesoscale dynamics in the Mediterranean Sea was made by the Physical Oceanography of the Eastern Mediterranean Group, based on innovative observational strategy and pioneering numerical simulations (e.g., Robinson et al., 1992; Robinson and Golnaraghi, 1993; Robinson et al., 2001). Comparing the geostrophic velocities derived from satellite altimetry missions (ERS-1 and TOPEX/Poseidon; Ayoub et al., 1998) and ocean currents from numerical experiments, Pinardi and Masetti (2000) emphasized the influence of the eddy field on large scale circulation. Pinardi et al. (2015), considering ocean currents from model re-analyses over 2 decades, achieved a new schematic of ocean circulation in the Mediterranean Sea, and underlined how cyclonic and anticyclonic gyres in the northern and southern parts of the basin, respectively, characterize the large scale circulation. Observations and model-based activities were carried out by Marullo et al. (2003) to investigate the variability of the mixed layer in the Levantine basin driven by the Rhodes and Ierapetra Gyres. Fernandez et al. (2005) studied the interannual eddy-driven variability and showed that it is persistent and evolves slowly, independently of the annual cycle of the atmospheric forcing. The anomalies in the circulation patterns can happen not only in the top layers but also in deeper layers, which are hardly related to the changes in the atmospheric forcing. Escudier et al. (2016) described the 3D structure of the western Mediterranean basin eddies by using several eddy-resolving model simulations and satellite altimetry. Considering a similar spatial domain, Mason et al. (2019) compared global and regional operational models to obtain new insight into the 3D eddy properties. Mkhinini et al. (2014) studied a long-lived eddy in the eastern part of the basin analyzing 2D altimetry maps. Well-known stationary eddies in the Levantine basin were the subject of specific oceanographic campaigns (Ioannou et al., 2017; Mauri et al., 2019; Velaoras et al., 2019).

In this work, we focus on the Mediterranean basin to investigate the entire 3D mesoscale field that emerges from an eddy-resolving ocean re-analysis. In particular, we look at the surface and 3D signatures of the non-linear eddy structures and their contributions to the kinetic energy in the ocean and the vertical structure of water masses. The consolidated ocean re-analysis considered in this work (Simoncelli et al., 2019) is

implemented in the region at a horizontal resolution of 1/16° (Oddo et al., 2014; Tonani et al., 2015) which provides an excellent playground in terms of resolution and eddy population.

The renalysis dataset explored covers 24 years (1993–2016) of daily averaged fields with a grid spacing of about 6–7 km (the exact spacing varies according to latitude). Although sub-mesoscale processes, not presently included in the circulation model, are known to have an impact on mesoscale fronts and vortexes (Haza et al., 2012; Sasaki et al., 2014), this resolution is sufficient to sustain turbulence generated by the model itself at the first baroclinic wavelength or coming from assimilation procedure increments. In this sense, the Mediterranean region is fully resolved both at spatial (Hallberg, 2013) and temporal scale, i.e., eddies can be followed in time with daily sub-sampling while their typical lifetime ranges between several days and few months.

The paper is organized as follows: **Section 2** describes the ocean re-analysis and eddy detection algorithm considered to characterize the 3D mesoscale structures in the Mediterranean Sea. **Section 3** assesses the accuracy of the methodology by comparing with observations and describes the eddy contributions to ocean dynamics and water masses structure (thermodynamics). **Section 4** summarizes and provides conclusions to this work.

2 MATERIALS AND METHODS

2.1 Mediterranean Re-Analysis

The version of MED-REA used in this work (Simoncelli et al., 2019) relies on a fully eddy-resolving horizontal resolution (6–7 km) ocean general circulation model (OGCM), based on the Nucleus for European Modelling of the Ocean (NEMO; Madec, 2016) and implemented in the Mediterranean region (Oddo et al., 2009; Oddo et al., 2014). The system is extensively validated against *in-situ* and remote-sensing observations and, up to 2020 provided also operational services within the framework of the Copernicus Marine Environment and Monitoring Service (CMEMS). The MED-REA is forced by the 6-h, 0.75° horizontal-resolution Era-Interim atmospheric re-analysis (Dee et al., 2011) from the European Center for Medium-Range Weather Forecast (ECMWF) and global ocean monthly mean climatology fields (Drévillon et al., 2008) are considered as lateral open boundary conditions (Oddo et al., 2009). The assimilative system considers the most updated and best quality flagged observational records of temperature (T), salinity (S), and sea surface height (SSH), retrieved from a variety of observational networks (both from *in-situ* and remote-sensing observations), which are ingested into the system during the numerical integration, through a 3D variational (3D-VAR; Dobricic and Pinardi, 2008) data assimilation scheme, to obtain an ocean synthesis which has the potential to provide more accurate information than observation-only or model-only based ocean estimations (e.g., Heimbach et al., 2019). We explore MED-REA daily outputs of SSH, zonal and meridional currents, ocean temperature, and salinity over a 24-year period (1993–2016) to investigate the mesoscale eddies in the Mediterranean region, through innovative eddy detection and tracking methods.

2.2 Methods

In this Section, we exploit a three-dimensional eddy-detection system (Cipollone et al., 2017) capable of constraining 3D mesoscale structures simultaneously through static and dynamic features (see **Supplementary Appendix SA**). The system has been improved to extract the "anomalous" eddy content in contrast to its non-homogeneous surrounding water. Eddy and background values are extracted at the same time thus removing any potential bias coming from calculations based on climatological fields or spatial smoothing. The accuracy of the method is assessed against *in-situ* observations in one specific region of the Mediterranean Sea (MED) where a number of Argo profiling floats (Good et al., 2013) are present both within and outside of the eddy (~500 floats during the period 2008–2010).

The background to the observed eddy-driven anomalies are defined in the temperature and salinity fields. We consider eddy-specific temporal and spatial scales to define the properties of the surrounding water masses, which are then considered as a reference for estimates of the anomalies induced by the mesoscale 3D features. A detailed description of the eddy detection and tracking algorithm is given in **Supplementary Appendix SA**.

2.2.1 Definition of Spatial Anomaly in Presence of Non-Homogeneous Background

The notion of "anomaly" generally refers to a certain phenomenon or signal that departs from a "standard" background field and brings therefore a non-zero information content (e.g., Wilks, 2011). While the anomalous behaviour is simple to detect by inspection qualitatively, on the other hand, it is not always obvious how to more quantitatively define what should be retained in the background and what should contribute to the anomaly. In oceanography, climatological fields are often used as a proxy for the identification of "standard" behaviours. The time average is therefore used as a spatial smoother and therefore the main stationary, cyclical phenomena are retained in the background term, i.e., the total field Q may be expressed as:

$$Q(t,x,y) = \bar{Q}(\mathrm{mod}(t,\Delta t),x,y)_{\mathrm{clim}} + Q_{\mathrm{anom}}(t,x,y) \quad \text{where}$$

$$\bar{Q}(i,x,y) = \frac{1}{N}\sum_{j=1}^{N} Q(j*\Delta t + i,x,y) \quad \text{with} \quad i \in [1,\Delta t]$$

$$N = \mathrm{int}[dim(t)/\Delta t] \tag{1}$$

where Δt represents the length of the temporal cycle (typically 1 year), $\bar{Q}$ is the background stationary part, and Q_{anom} is the turbulent component containing the anomalous signal to extract. In the context of mesoscale variability, **Eq. 1** can be considered a first-order approximation that suffers the possible presence of trends and strong bias due to the fact that the climatological background can be far from the actual background for a specific year. In Mason et al. (2019) and Gaube et al. (2014) a spatial Gaussian smoother with a half width of 6° is used to remove the mesoscale variability and define the background. In the following, we employ a bias-free method where the anomaly is calculated with respect to the local "surrounding" waters at the eddy perimeter (**Figures 1A–F**). The

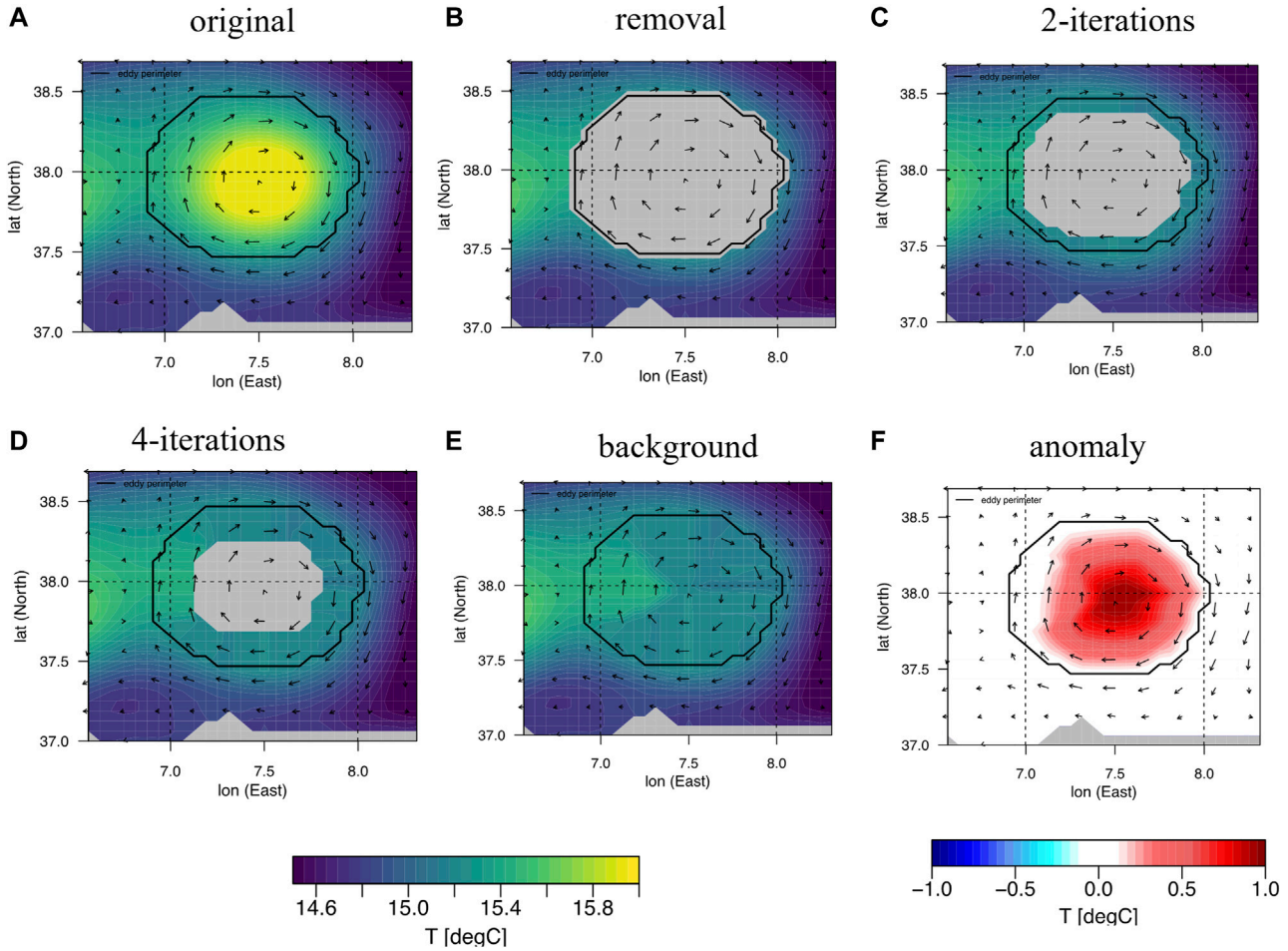

FIGURE 1 | Calculation of the eddy anomaly: **(A)** original temperature field with an eddy detected and delimited by its perimeter (black line). Vectors correspond to ocean currents. **(B)** The parcel of water delimited by the perimeter is masked. **(C)** and **(D)** Temperature values outside the perimeter are extrapolated inside the mask (see **Section 2**) to define the background field **(E)**. 4) The anomaly **(F)** is finally obtained as the difference between the original tracer field and the background.

calculation of anomaly is based on the creation of a background field that mimics a continuous tracer field in the absence of eddy, by replacing it with "surrounding" waters. However, these "surrounding" waters can be not as homogeneous as expected. In an area of strong density gradient or close to the coast, it is not unusual for an eddy to have a heterogeneous perimeter, with opposite sides floating in water that can differ by several degrees. In this case, the choice of the "surrounding" water cannot be a unique value, the use of the mean of the perimetral annulus could generate a background value that is, discontinuous at the eddy border and largely depending on the exact location and extension of the perimeter. Such a perimeter can change during time, extending more in the cold/warm part of the region, thus changing substantially the reference mean. In the current methodology, to avoid any artifacts coming from the definition of "surrounding" waters, each inner point of the eddy is filled with values "extrapolated" from the closest perimetrical points (**Figure 1**). The inner (eddy) annulus closest to the eddy perimeter is filled first, each point is replaced with the mean value of the closest ocean points (up to four points) from the eddy perimeter. When the first inner annulus is filled, the algorithm proceeds with the second inner annulus till the eddy center. The background obtained in this case does not have any discontinuity at the eddy perimeter. The spatial structure of the anomaly is rather robust depending on the local boundary values avoiding possible non-local effects coming from temperature values that differ at the other side of the eddy.

The overall procedure is shown in **Figure 1**: once the eddy is detected (a), the algorithm removes the corresponding area in the tracer field (b), and extrapolates the border values to fill the missing area (c and d) thus generating a possible background field (e). The anomaly (f) is then calculated with respect to such field as follows:

$$Q_{\mathrm{anom}}(t,x,y) = Q(t,x,y) - \langle Q \rangle_{\mathrm{back}}(t,x,y) \qquad (2)$$

where the interpolation starts from the eddy contour using the closest ocean points out of the eddy, and proceeds inside to obtain a background guess $\langle Q \rangle_{\mathrm{back}}(t, x, y)$. The method reduces to a minimum the inclusion of spurious biases coming from a sub-optimal definition of the background field and the impact of seasonal variability. A second benefit is that the overall results are pretty stable as a function of the eddy lifetime. The inclusion of

spurious eddies would lead to an underestimation of the eddy anomaly content, being inner and outer water similar and the spatial anomaly close to zero. Another source of underestimation can come from the fact that the detected perimetral water partially overlaps with the anomaly itself (**Figure 1**). In the following Section, the method is applied in a case study and compared with observations to assess the overall skill.

3 RESULTS

In this Section we first validate the eddy-detection method used to investigate eddy-driven three-dimensional anomalies, looking at a specific case study in the Levantine basin, which is the area of the Mediterranean Sea characterized by prominent mesoscale features of the ocean circulation (e.g., Alhammoud et al., 2005). We then continue describing the 3D mesoscale field that emerges from the analysis of eddy-driven content in Mediterranean re-analysis.

3.1 A Case Study: The Shikmona Gyre Area

The sparsity of profiling data usually prevents an instantaneous and direct measure of the 3D eddy anomaly content. Such a measure requires the sampling of at least two different profiling floats at the same time; one trapped inside the eddy while the other acts as a probe mapping the surroundings. Thanks to the recent deployment of the array of Argo profiling floats an increasing number of such dual observations are becoming freely available. We select an area in the Levantine basin well documented by several different types of observations and for which there can be found some long-lasting measurements of two or more profilers with one profiler effectively trapped by the quasi-stationary structure that usually occurs in that area. These data are taken from the Met Office EN4 dataset that gathers quality-controlled subsurface ocean temperature and salinity profiles (v4.2.1; Good et al., 2013). The area is delimited by the green box shown in **Figure 2A** and corresponds to the area where a quasi-stationary mode-water ACE generally occurs. This eddy has recently been well documented by two cruises in Mauri et al., 2019 that show the peculiar characteristics with saltier and warmer temperature at depth. The measure of the temperature anomaly profile from observations is calculated only when two or more profilers occur within the target area on the same day, with one float trapped within the eddy. The identification of trapped observations usually relies on the analysis of altimetry maps, reconstructed from along-track satellite retrievals (Dong et al., 2014; Zhang et al., 2016), which entails an eddy-detection performed on a two-dimensional SLA field. Floats are considered trapped if they profile inside the SLA-eddy pattern. In our study, on the other hand, a profile is considered trapped if it occurs inside the 3D eddy structure detected from the MED-REA. The use of a 3D ocean re-analysis allows assessment of whether the eddy anomaly estimated in the model ($T_{eddy} - T_{back}$), is also measured by the profilers ($T^{obs}_{eddy} - T^{obs}_{back}$). The density plot in **Figure 2A** shows the number of "trapped" observations inside eddies longer than 14 days, covering the period 2008–2010, while the contours show the probability of an eddy to appear in that region.

Anticyclonic eddies are typically warm-core at depth, however the sharp warming of sea surface water that occurs in the East-Mediterranean sea changes the picture. **Figures 2B,C** show the temperature anomaly calculated using the eddy detection system applied to the MED-REA and *in-situ* ARGO observations, respectively. For each panel, three different temporal averages are displayed: the first panel shows the time-series of monthly anomaly from 2008 to 2011, the second corresponds to the monthly climatology of the anomaly, while the third shows the vertical mean profile of anomaly only in the presence of an eddy. The water trapped by ACE is generally warmer at depth, however starting from August, a dipole-like structure of the anomaly tends to appear both in the MED-REA and in the observations. The water trapped in August is colder at the top and warmer at the bottom. During fall, the cold anomaly tends to drift down reaching about 100 m in winter before disappearing. The same trend can be seen both in the observations and in the re-analysis, but the method tends to underestimate the anomaly in magnitude compared to the observations. Here it is worth keeping in mind that the algorithm evaluates the total anomaly by averaging over the eddy area, while observations are point-wise measurements. Calculating the anomaly using the model temperature at the observation positions, the model-based anomaly profiles closely follow those in the observations, as it can be noticed by comparing black and red lines in **Figure 2C**. Note that although the EN4 dataset is not directly assimilated, Argo profiles are assimilated during the ocean re-analysis integration.

Such a peculiar structure of the anomaly inside the eddy can be visually inspected in the temperature field of August 2008. **Figure 3** shows the zonal sections of the temperature field for the re-analysis and an observation-derived product, called ARMOR3D (Guinehut et al., 2012; Mulet et al., 2012), at the eddy position. ARMOR3D is a statistical three-dimensional reconstruction of several physical variables that employs only observations (T, S, SST) at a resolution of 1/4°. The presence of a cold-core at the top and a warm one at the bottom (300 m) is present in the two datasets. In ARMOR3D the center of the eddy is moved slightly north and is larger compared to the re-analysis, probably due to the dataset's coarser resolution. The same picture can be seen looking at the vertical temperature profiles from *in-situ* observations for the same month (**Figure 3C**). Mauri et al. (2019), analysing the data of two cruises in late 2016 and comparing them with satellite SST data, observe that in August the SST at the core of the eddy is colder than the perimetral water, while at depth the situation reverses. The colder SST signal tends to disappear during fall. The authors suggest that such behavior is probably due to the stiffening of the thermocline in the Eastern Mediterranean Sea in August. The rapid increase of the temperature at the surface leads to an environmental temperature that is, now warmer than the one inside the eddy, where the water parcels tend to be more vertically homogeneous and thermalize slowly. Moreover, despite the anticyclonic behaviour the salinity is higher inside the eddy (Mauri et al., 2019) and reflects its mode-water nature. This is also seen by analyzing the re-analysis with our detection method, as in **Figure 8**, while the other anticyclones typically show fresher water inside.

3.2 Eddy Population

It is very well-known that the number of detected eddies can largely change according to the technical details of the detection system in use, and it is therefore extremely important to quantify the impact of possible spurious (or missed) eddies detected on the

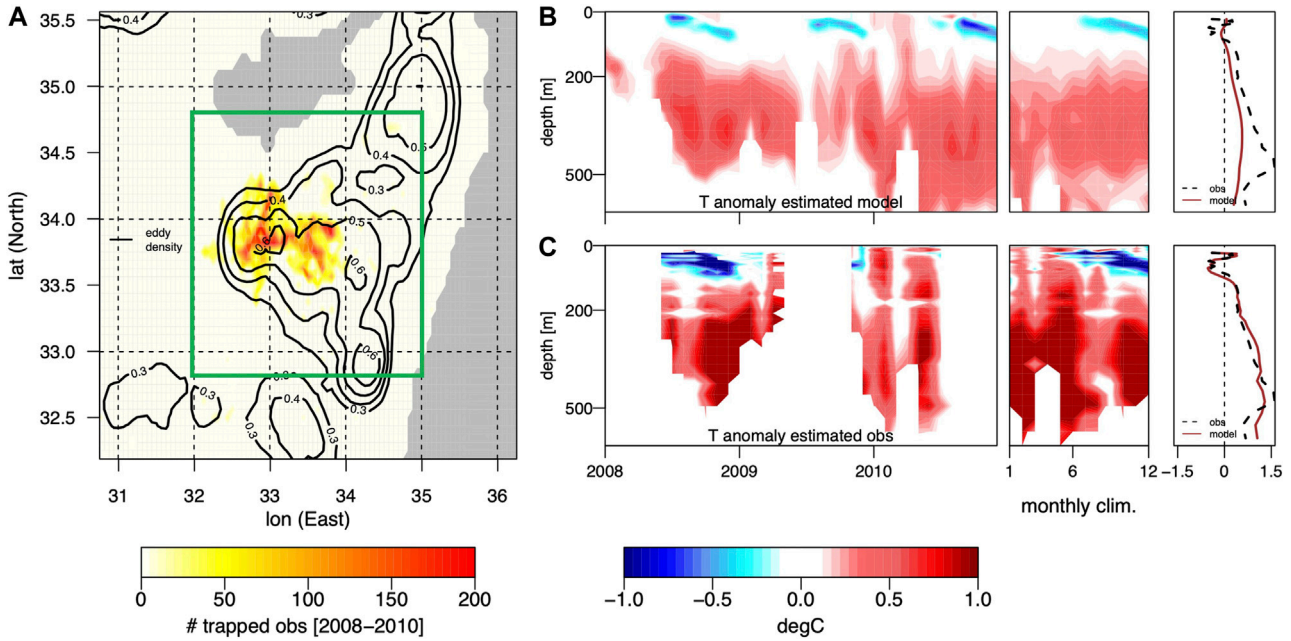

FIGURE 2 | (A) Number of "eddy-trapped" observations over the period 2008–2010 considering eddies with lifetime ≥ 2 weeks occurring in the Shikmona gyre area (green frame). Black contours show the eddy probability density from the MED-REA, i.e., the probability to find an eddy in the specific area. **(B)** Three plots showing respectively: the time-series of eddy temperature anomaly from the MED-REA, its monthly climatology, the overall mean of temperature anomaly profile. **(C)** same as **(B)** for Argo profiling floats. In this panel, the average anomaly from observations (black dotted line) is compared with the average anomaly from MED-REA values, extrapolated at the observation positions (red line).

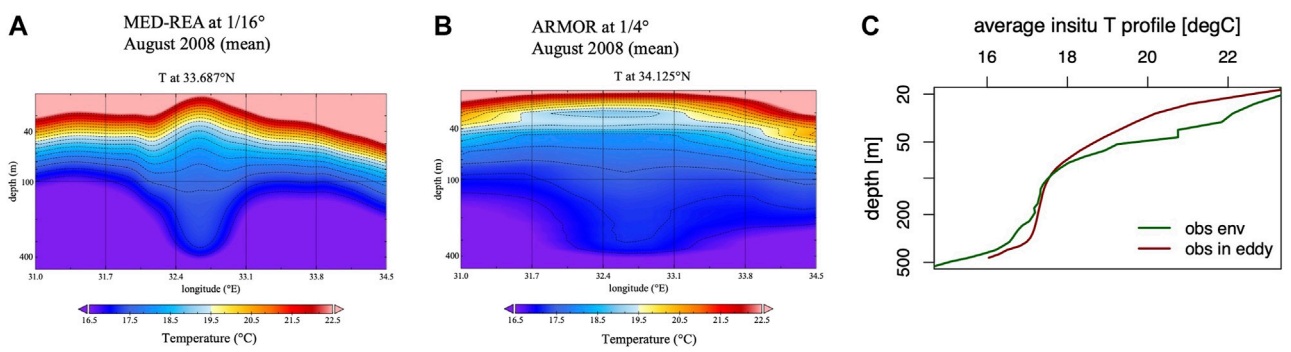

FIGURE 3 | Panels **(A)** and **(B)** show the monthly zonal sections of temperature in the Shikmona gyre area (green-box in **Figure 2**) for August 2008 extracted from two products MED-REA and ARMOR3D respectively. **(C)** Temperature profiles calculated from *in-situ* observations occurring in the region (**Figure 2**) during the same month. *In-situ* profiles are gathered both inside (trapped) and outside the eddy.

final results. An eddy miss would lead to underestimating the eddy-driven anomaly in the region; in **Section 3.1** the vertical temperature anomaly is compared with the one extracted from point-wise Argo observations in the Shikmona area to estimate the accuracy. A second possible misrepresentation comes from the detection of false-positive eddies that could potentially spoil the calculation of the anomaly. To reduce the impact of such events, in addition to the use of stringent conditions on rotation, lifetime, and depth (see **Supplementary Appendix SA**), the anomaly content is here defined with respect to the eddy surrounding environment (see **Section 2.2.1**). The stability of the anomaly signal as a function of the lifetime is also presented to support the results. Therefore the exact numbers in the population should not be taken as an absolute reference but rather as a relative one, comparing results for different lifetimes.

Eddy population is defined in terms both of the occurrence and persistence of non-linear structures in the Mediterranean basin. Different lifetimes are shown to stress the contribution of eddies that preserve their properties while spanning over different temporal scales.

During the 24 years analysed, the number of eddies does not seem to show any global statistically-significant trend. Transient

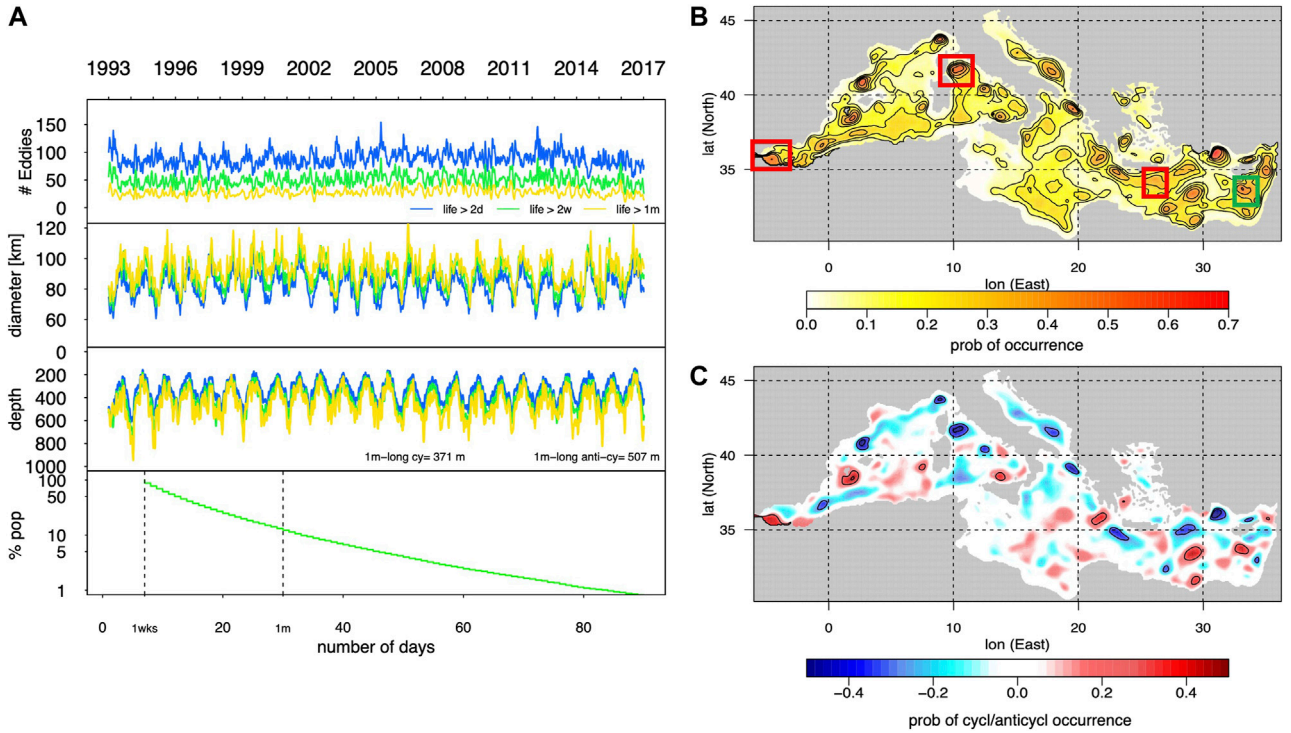

FIGURE 4 | Eddy statistics for the Mediterranean Sea: **(A)** Number of eddies, eddy diameter (*km*) and eddy depth (*m*) as a function of lifetime and years. The eddy depth is also given as function of 1 month long lived cyclonic/anticyclonic structures. Eddy decay (% pop.) as a function of lifetime. Probability of eddy occurrence **(B)** and CE versus ACE **(C)**; frames show the areas of the Alboran, North Tyrrhenian, Ierapetra (red frames), and Shikmona (green frame) gyres.

eddies/patterns, living a few days only, contribute to the high-frequency variability in the statistics where short-living eddies are included. The population of short-living eddies is probably affected by the strength of transient wind and the variability of mixed-layer-depth. Patterns whose vertical extension is not stably deeper than the mixed layer depth contribute to this day-by-day variability. The impact of the variability generated by short-living eddies is out of the scope of the present study that is, mainly focused on the stable signal generated by eddies rather than their variability. Eddies lasting more than 2 weeks are characterized by an average thickness of ~400 m and by a radius of 45 km (**Figure 4**), while anti-cyclonic structures are significantly deeper than cyclonic eddies (**Table 1**). The average eddy diameter and depth tend to increase with the lifetime, reducing the impact of transient eddies that usually are smaller and shallower. The maximum of deepening occurs in winter when the water is less stratified, while eddies are shallower during summertime, following the variability of the mixed layer depth. Atmospheric forcings can also play a role in the year-by-year variability of long-living eddies as well as sporadic events connected to thermohaline circulation changes (Roether et al., 2014). The conservation of angular momentum is likely to play a role in the opposite seasonality of horizontal and vertical extension: smaller, deeper eddies in winter tend to become larger and shallower in summer.

The bottom panel in **Figure 4A** shows the percentage of eddy population as a function of their minimum lifetime (in abscissa) starting from eddies living more than 7 days. The population reduces from 50 to 20% down to 2.5% for structures living longer than 2 weeks, 1 month, 2-months, respectively.

The mean spatial distribution of eddies longer than 14 days, is shown in the upper-right panel (**Figure 4**) as the probability of eddy occurrence (density probability). The areas of the main quasi-stationary eddies are well represented with more than 60–70% probability. The mean spatial distribution of eddy polarity weighted by the eddy density is shown in the lower-left panel (**Figure 4**). We use eddy density as a weight to remove low-density areas that show strong polarity, but that are not statistically reliable: e.g., eddy polarity tends to zero in low-density areas or areas with high-density but weak polarity.

A strong polarity signal is retained by the well-known quasi-stationary eddies. The overall mesoscale polarity field agrees well with the knowledge of Mediterranean surface/subsurface circulation (e.g., Pinardi et al., 1997) and observations of mesoscale variability (Fusco et al., 2003).

Non-linear features with lifetimes ≥ 2 days were considered as a reference to assess the eddy population as a function of the lifetime. In particular, the ratio between the number of eddies detected at the relevant lifetime and those in the reference provides evidence about the portion of the eddy population that tends to dissipate over different temporal scales. **Figure 5** shows the percentage of un-dissipated eddies, obtained considering 3D non-linear features with lifetimes longer than 14 and 28 days, compared to the reference (lifetime ≥

TABLE 1 | Average number of eddies persisting per day, their mean depth and mean diameter as function of lifetime and type (ACE/CE).

Lifetime greater than	Average number per day (ACE/CE)	Average depth (m) (ACE/CE)	Averaged diameter (km) (ACE/CE)
2 days	89 (49/40)	334 (381/275)	82 (80/84)
14 days	50 (28/21)	402 (454/331)	88 (85/93)
1 month	28 (16/12)	450 (507/371)	92 (86/100)
2 months	9 (5/4)	512 (602/412)	98 (88/109)

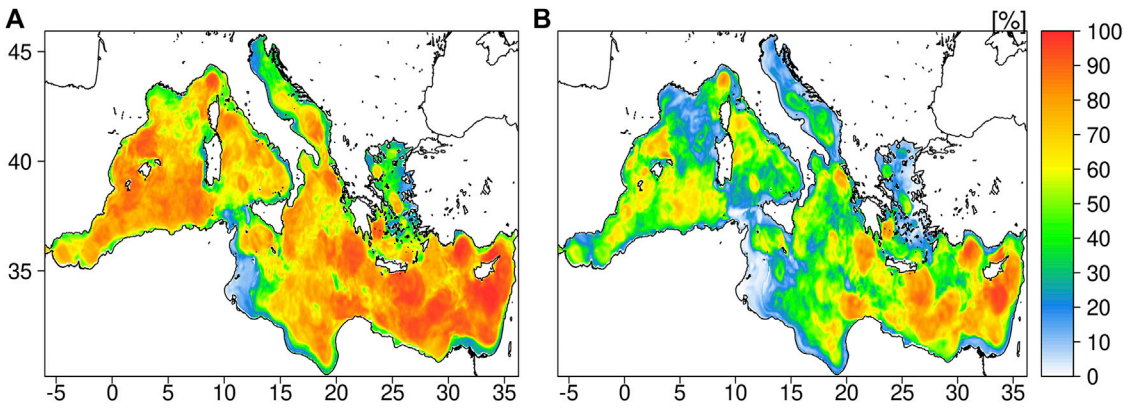

FIGURE 5 | The percentage of un-dissipated eddies, considering non-linear structures with lifetimes of at least 14 days **(A)** and 28 days **(B)**, compared to those with a lifetime of at least 2 days during the 24-year period 1993–2016.

2 days). In the Figure, a value of 50% means that, for a specific lifetime, the eddy population is half of the total number of eddies with lifetimes ≥ 2 days. It is evident that the eddy population in the Mediterranean Sea is well described by eddies lasting at least 14 days, while long-lived (≥ 28 days) features tend to persist in the eastern part of the basin. Starting from those results, mesoscale structures with lifetimes ≥ 14 days were taken into account to look at the 2D expressions and 3D structure of the eddy population in the Mediterranean Sea.

3.3 Dynamic Contributions

In this Section, we investigate the contribution of mesoscale eddies to ocean dynamics by looking at their signature in the SSH variability and EKE. Eddy detection methods rely on the surface expression of mesoscale features. Those can be identified from satellite altimetry maps as elevations (ACE) and depressions (CE) of the sea surface. As such, it is interesting to understand how the SSH variability can be influenced by eddies at temporal and spatial scales which depend on the eddy structures and lifetimes. **Figure 6** shows the percentage of the variance of the SSH variability explained by eddies, over the period 1993–2106. The results were obtained by comparing the initial SSH fields with the background (**Section 2**) and considering eddy lifetimes ≥ 14 and 28 days. The values are expressed as the percentage decrease of the variance in the background with respect to the initial fields. A value of 50% means that the variance of the SSH fields in the background has halved with respect to initial fields. The results clearly show how the signature of mesoscale eddies characterizes the SSH variability. Eddies with a lifetime ≥ 14 days (left panel) explain more than 50% of the variance of the signal both in the western Mediterranean Sea (e.g., Alboran Gyre and the Tyrrhenian Sea) and in the Levantine basin, where the largest values were observed in the occurrence of the Ierapetra, Mersa Matruh and Shikmona gyres. It is interesting to notice that long-lived eddies (≥ 28 days; right panel) show similar values, thus indicating that mesoscale features characterize the SSH variability over temporal scales longer than months.

A 3D eddy detection method allows to depict both the horizontal and vertical structure of the mesoscale features and to quantify their contribution to the ocean dynamics, as long as the EKE vanishes in the water column due to dissipation. To assess how the mesoscale variability observed at the ocean surface projects into the 3D ocean circulation, in this Section we look at the EKE driven by the non-linear eddies. Following the approach proposed by Cipollone et al. (2017), who extended the formulation of relative kinetic energy in Chelton et al. (2011b) to take into account 3D structures, we consider the relative EKE (REKE) to represent the fraction of ocean kinetic energy carried by eddies in space and time (see **Supplementary Appendix SB** for further details). **Figure 7** shows the REKE associated with mesoscale eddy lifetime ≥ 14 days, both considering their surface expression (left panel) and 3D structure. At the surface, the REKE was up to the order of ≥ 50% looking at the dominant mesoscale features in the

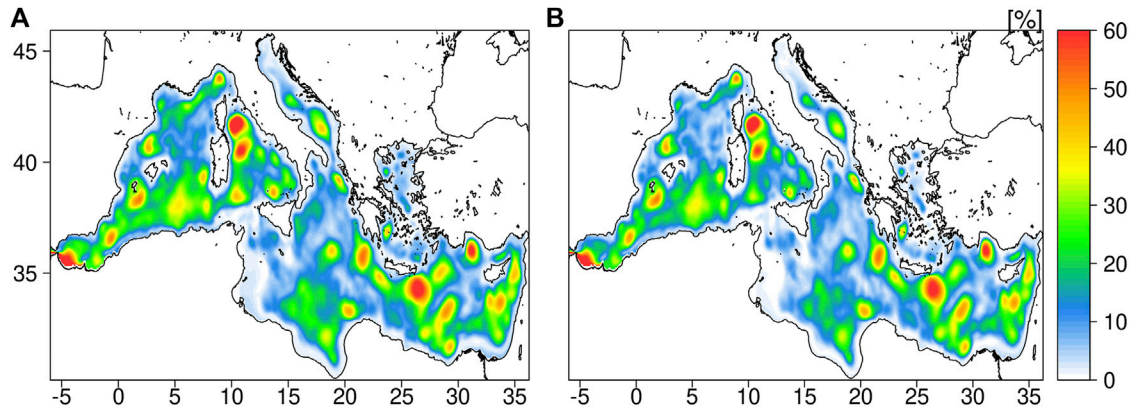

FIGURE 6 | The percentage of variance of sea-surface height variance explained by eddies. The panels show the percentage of variance explained by eddies with a lifetime of 14 **(A)** and 28 days **(B)**, during the 24-year period from 1993 to 2016.

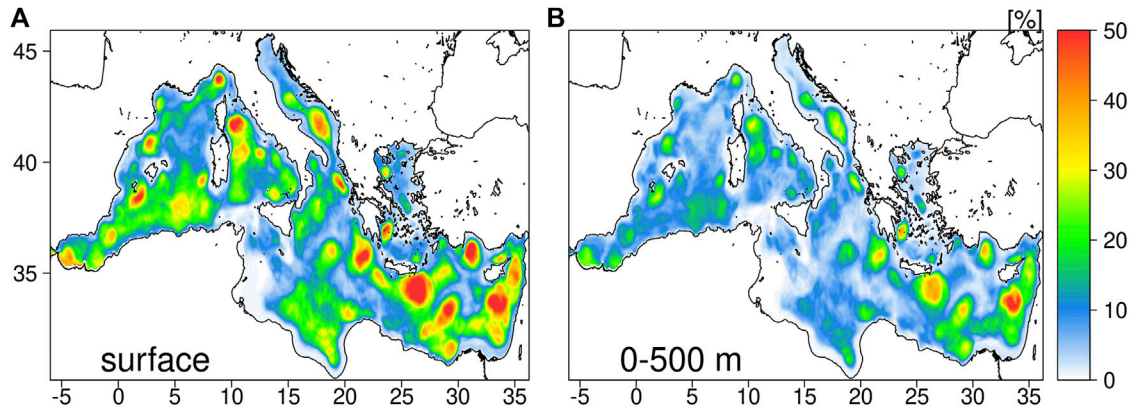

FIGURE 7 | REKE at the surface **(A)** and the 3D structure to 500 m **(B)** expressed in percentage (%). The panels are obtained over a 24-year period, from 1993 to 2016, for eddies with a lifetime *geq* 14 days.

Mediterranean basin. The results in **Section 3.2**, show average eddy depths of 500 m (**Table 1**). The latter was used as a reference depth to consider 3D eddy contributions. Looking at vertically integrated REKE values, it is possible to appreciate the differences between the western and eastern parts of the Mediterranean basin. The largest REKE values were observed in the occurrence of the Pelops (ACE), Ierapetra (ACE), Rhodes (CE), Mersa Mathru (ACE), Shikmona gyres (ACE). Those are well-known quasi-stationary mesoscale features in the Levantine Basin (e.g., Pinardi et al., 2005), reaching hundreds of meters into the water column (e.g., Fusco et al., 2003). The absolute EKE values (cm^2/s^2) driven by eddies occurring in specific areas of the Mediterranean Sea (red and green boxes in **Figure 4**) are shown in **Table 2**. In particular, the largest REKE values (30–40%) at depth were observed in the areas of the Ierapetra and Shikmona gyres. This is in line with the typical characteristic of ACEs, associated with pycnocline depressions, which tend to penetrate deeper in the water column compared to CEs (e.g., Rhines, 2001).

Eddy Driven 3D Anomalies and Thermodynamic Contributions

ACE and CE are typically associated with warm and cold temperature anomalies (e.g., Dong et al., 2014). Cyclonic eddies induce negative anomalies of temperature and/or positive anomalies of salinity and therefore positive anomalies of density. This is because cyclones tend to uplift the pycnocline. The effect is the opposite for anticyclonic eddies which lower the pycnocline. The maximum of the anomalies is also deeper for anticyclones. The lowered pycnocline in anticyclones will create a maximum of the temperature anomaly below the mean depth of the pycnocline whereas an uplifted pycnocline in cyclones will create a minimum above. This behaviour can be reflected in the mesoscale eddies of the western Mediterranean, for example, in the Alboran and Tyrrhenian Seas, while interesting departures can be observed in the eastern part of the basin.

Panels in **Figure 8** show the ACE/CE anomalies for different variables and selected regions: Alboran gyre (ALB), Shikmona area (SHIK), Ierapetra gyre (IERA), and North Tyrrhenian Gyre (NTG), as depicted in **Figure 4**. For each region, we separate

TABLE 2 | Absolute value of EKE trapped by the eddies occurring in different regions of the Mediterranean Sea and averaged over different depths. Eddies with lifetime greater than 2 weeks are used.

Average depth	Alboran ACE/CE cm^2/s^2	IERA ACE/CE cm^2/s^2	Shikmona ACE/CE cm^2/s^2	NTG ACE/CE cm^2/s^2
Surface	1.6/2.3	6.8/1.4	1.6/0.9	1./0.6
0–100 m	1.2/2.1	6.9/1.3	1.9/0.8	1./0.5
0–200 m	1.1/2.1	6.6/1.2	2/0.7	0.9/0.5
0–500 m	1.1/2.0	6.5/1.2	2.2/0.7	0.7/0.4

contributions from ACE and CE eddies and calculate the anomaly in T, S, rotational velocity (v_R) and REKE. The monthly time series of the anomaly is then shown from 1993 to 2016 together with the monthly climatology of the anomaly and the mean anomaly profile inside the eddy. While the monthly climatology includes also months without eddies and provides the mean anomaly for each month, the last mean profile shows different information being calculated only in the case the eddy is present. This can be seen as the typical signature of the eddy in the case of its appearance at a specific depth.

In the western part of the basin, the Alboran gyre, made of at least two semi-permanent structures which tend to be predominant according to the seasons (e.g., Escudier et al., 2016), plays a fundamental role in modulating the entrance of the Atlantic waters into the Mediterranean Sea (Pinardi et al., 2015). Here we focus our attention on the westernmost anticyclonic structure (hereafter referred to as ALBO), which resides in the Alboran Sea irrespective of the season considered (**Figure 4**). As expected looking at ACEs, the ALBO shows specific properties characterized by warmer (fresher) temperature (salinity) anomalies. Looking at the temporal evolution (1993–2016) of the eddy-driven anomalies (left panels) it is also possible to investigate their contributions over different seasons. In **Figure 8**, central panels show the eddy-driven anomalies as a climatology. Salinity anomalies in ALBO were negative from December to April, around 0.2 psu. The Alboran Sea is characterized by fresher Atlantic waters at the surface and denser water at the bottom exiting the Mediterranean Sea. Water masses stratification varies seasonally, due to wind-driven circulation and solar radiation, and it is typically higher during summer in the Mediterranean Sea. The water masses trapped in ALBO showed positive salinity anomalies at the surface and negative at depth down to 200 m from May to September.

In the northern Tyrrhenian gyre, a large quasi-stationary CE eddy is almost continuously present. This eddy induces negative anomalies of temperature and positive anomalies of salinity, uplifting the pycnocline and tending to strengthen in late summer/autumn exceeding the −0.5°C value.

The REKE profile is typical of a bowl-shape eddy while tracer anomalies can reach down to ~150 m that can be interpreted as the eddy "trapping depth," usually defined as the vertical extent of the trapped fluid inside the eddy (e.g., Chaigneau et al., 2011). No relevant ACE are detected in this region. The peculiar eddy-driven temperature anomaly profile of the Shikmona ACE is already discussed in the dedicated Section and compared with the literature results. This ACE is a mode-water eddy that differs from the standard ACE showing a positive anomaly in salinity, as demonstrated by two recent field campaigns (Mauri et al., 2019). The rotational speed that constrains the water masses trapped by the eddy is about 0.2 m/s in all the seasons, being almost uniform down to 300 m. The REKE profiles show that it contributes to the EKE of the regions with more than 30% down to 300 m. In the exact position of the eddy, the percentage can rise to 60–70% as seen in the map of REKE (**Figure 7**).

The sector in the Ierapetra region (**Figure 4**) is characterised by high-mesoscale activity with a strong quasi-stationary ACE, continuously detected in almost all the months. The presence of such ACE has been demonstrated in several oceanographic cruises and analysing satellite altimetry data (Ioannou et al., 2017; Ioannou et al., 2019). It can be inferred that a positive temperature anomaly, higher than 0.5°C, persists in all the seasons at depth. The same mechanism that generates a negative summertime temperature anomaly in the Shikmona ACE, and described in the dedicated Section, seems to be present in this area. In the late summer/autumn season the SST in the Eastern Mediterranean sea is characterized by abrupt heating that stiffens the stratification and leads to an environmental temperature that in a short time becomes higher than water temperature in the ACE. The latter tends to be more uniform acting against the stratification, i.e., the temperature inside ACE is rather homogeneous while the environmental one is strongly stratified and generates the vertical dipole structure in the anomaly content. The standard ACE behavior is recovered in winter and spring. Such dipole is not seen in the salinity, which shows mainly negative and very shallow anomalies compared to the temperature. Looking at the REKE anomaly, it is interesting to notice that the profile differs from the bowl-shape structure typically associated with NTG CE and reaches a trapping depth of 200 m. During 2008 the ACEs were deeper, and also the salinity anomaly at depth tended to change sign. This is in line with the results obtained by Velaoras et al. (2014) who, looking at thermohaline circulation in the Cretan Sea, observed a large outflow of dense waters from the Aegean to the Cretan Sea over the period 2007–2009. The authors argued that this was an Eastern Mediterranean Transient (EMT; Roether et al., 2014; Pinardi et al., 2019) - like event connected to thermohaline circulation changes, instead of being driven by atmospheric forcings or water fluxes. The CE in the same regions shows an opposite behavior of ACE although the anomaly is smaller in magnitude (0.2°C).

Mesoscale eddies can act as gateways for heat absorption and loss in the ocean. It is then interesting to quantify how eddy-driven anomalies affect the ocean heat content (OHC). At a depth range between 0 and 700 m, the OHC in the Mediterranean Sea was in the order of $10^9\,J\,m^{-2}$ (basin integral over the period 1993–2016; not shown), in agreement with the already existing estimates for the Mediterranean basin (von Schuckmann et al.,

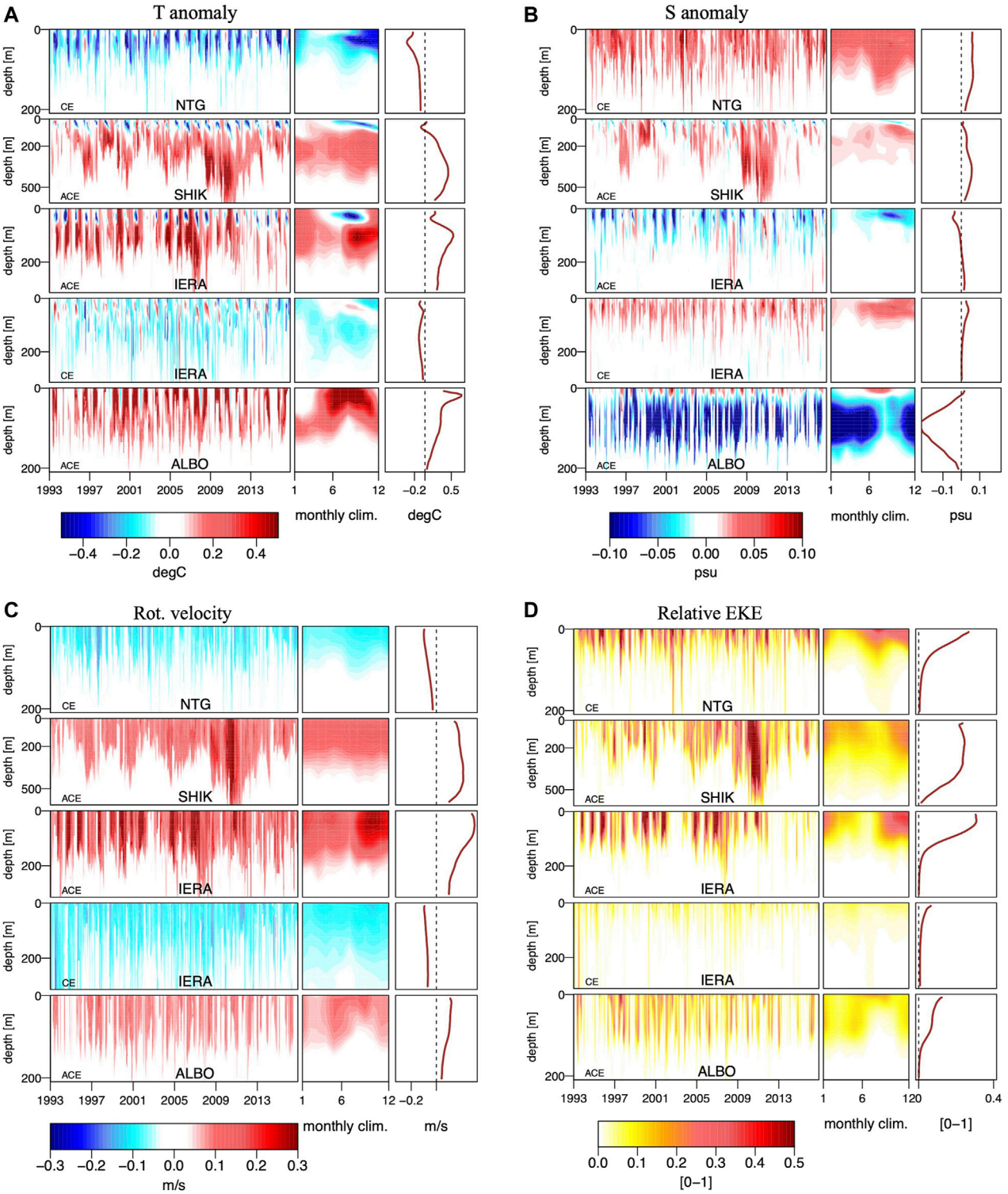

FIGURE 8 | Time series of eddy-driven anomalous profile calculated in different regions (North Tyrrhenian Gyre–NTG, Shikmona area–SHIK, Ierapetra region–IERA, and Alboran Gyre–ALBO) for different variables: **(A)** temperature, **(B)** salinity, **(C)** rotational velocity, and **(D)** REKE. In the IeraPetra region, both ACE and CE contributions are shown. For each time series, the monthly climatology of the anomalous profiles and the mean eddy anomalous profiles are also shown. The latter is not averaged over months without eddies, only trapped waters contribute.

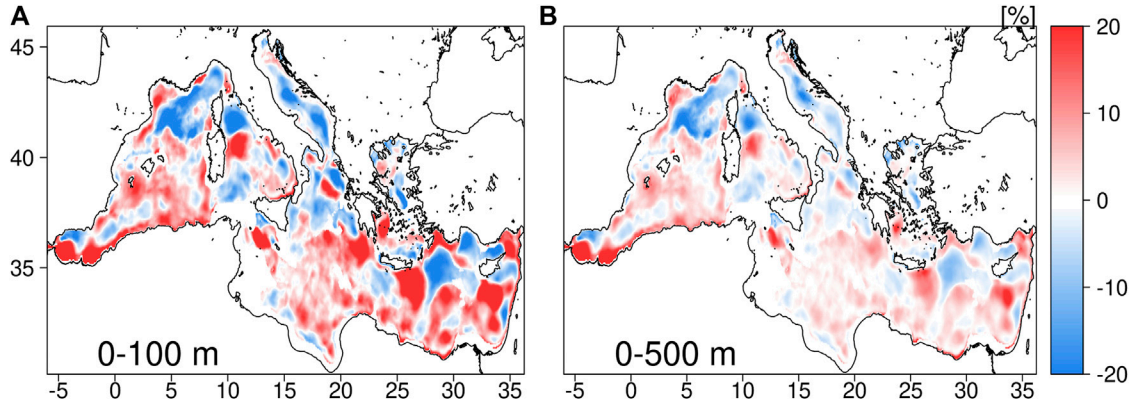

FIGURE 9 | Eddy-driven ocean heat content anomalies versus depth derived from MED-REA temperature fields. The panels show the results obtained over a 24-years (1993–2016) period considering eddies with a lifetime of at least 4 weeks. Values are expressed as a percentage (%) of total ocean heat content monthly standard deviation.

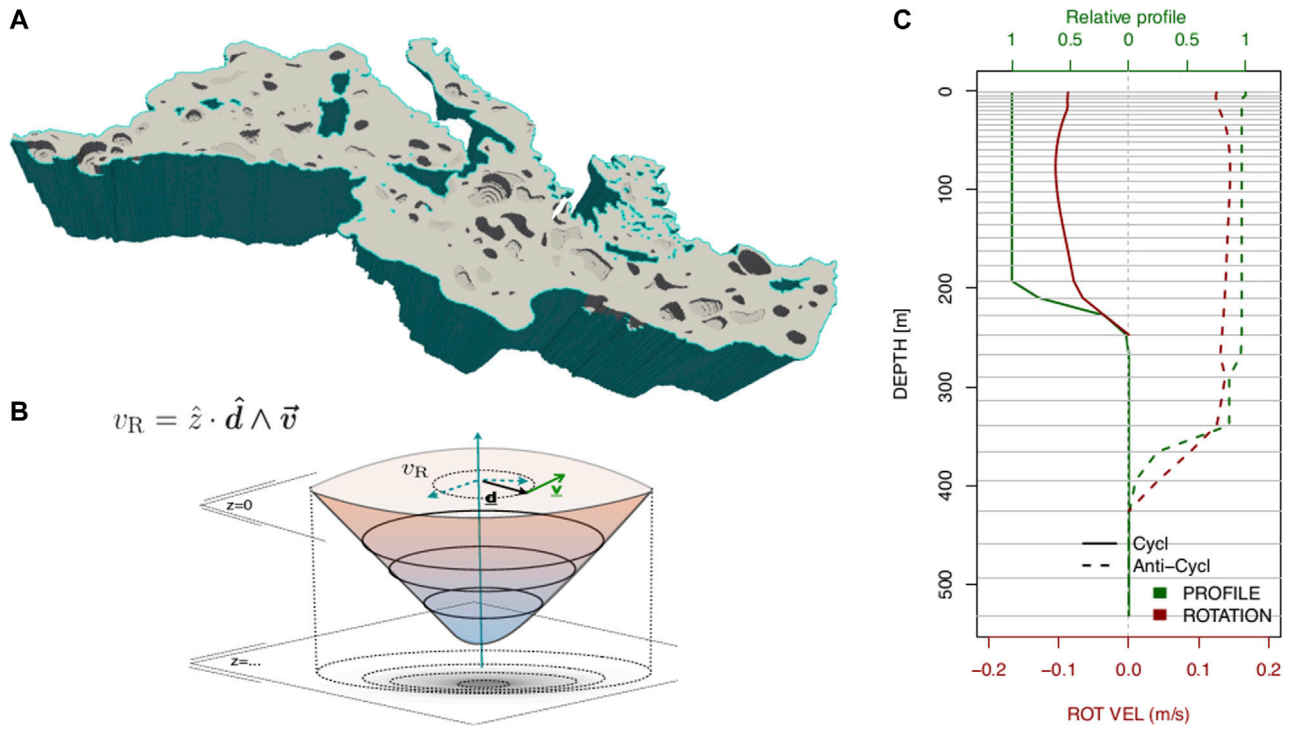

FIGURE 10 | (A) Example of one-week-long eddy population detected in 1 day. **(B)** Schematic illustration of vertical change in orbital velocity. **(C)** Examples of relative vertical profile (green) generated by the rotational velocity v_R (red color) for cyclonic (solid line) and anti-cyclonic (dashed) eddy at each vertical level. The relative vertical profile shows the vertical inner shape of the eddy defined by its area at each vertical level, normalized by the area at the surface. It is therefore always 1 at the surface and 0 at the bottom; the vertical line going from 1 to 0 corresponds to the eddy shape segmented by the detection system.

2016; Iona et al., 2018). Considering those initial estimates as a reference, **Figure 9** shows the OHC anomalies obtained considering long-lived eddies (≥ 4 weeks). In particular, the values are expressed as a percentage (%) of total ocean heat content monthly standard deviation, obtained integrating MED-REA ocean temperature fields over different depth ranges. Considering a depth range between 0 and 100 m, the mesoscale contributions to the OHC in the Mediterranean Sea were in the order of 20%. Positive (negative) contributions reflected the characteristics of ACE (CE) eddies, acting as warm (cold) cores and thus underlying their role in modulating the magnitude OHC in the upper ocean. As already discussed in **Section 3.3**, a maximum depth of 500 m was selected to look at 3D eddy-driven anomalies. At this depth

range, contributions up to 15% were observed in the occurrence of the most prominent mesoscale features.

4 CONCLUDING DISCUSSION

The eddy population in the Mediterranean Sea was investigated by means of eddy detection and tracking algorithms applied to the 3D dimensional ocean fields from MED-REA over a 24-year period (1993–2016). In particular, we focused on the contributions to ocean dynamics and thermodynamics of eddy-induced anomalies. Mesoscale eddies are non-linear features of the circulation showing properties that may differ from the surrounding waters as a function of their spatial and temporal scales.

To remove any bias arising from the use of a climatological background, in this work eddy-driven anomalies were defined with respect to the non-homogeneous surrounding waters.

The accuracy of the method, to disclose the 3D mesoscale contributions, was assessed against Argo profiling floats trapped by eddies as well as from the observation-based data sets (i.e., ARMOR3D).

The eddy population in the Mediterranean Sea was characterized according to the occurrence and persistence of non-linear structures. Tracking the eddies, the results showed that structures living ≥ 2 weeks are representative of the 3D mesoscale field in the basin, showing a high probability (> 60%) of occurrence in the areas of the main quasi-stationary eddies. The emerging mesoscale polarity (ACEs/CEs) field was in line with previous model and observation-based studies (Pinardi et al., 1997; Fusco et al., 2003; Escudier et al., 2016) with an average thickness of ~400 m and a radius of 45 km. The results also showed the dependency of eddies size and thickness to polarity and lifetime. ACEs were significantly deeper than CEs and the average eddy diameter and thickness tended to increase in long-lived structures. Eddy thickness shows also seasonal variability: eddies tend to be shallower in stratified waters during summer and deeper during winter. Looking at eddies as a function of their lifetime, the results showed how the eddy population decreases to 20% considering long-lived structures (e.g., ≥ 1 month). The contribution of mesoscale eddies to the ocean dynamics was assessed by investigating their surface expression and 3D structure. At the surface, the signature of mesoscale features explained most of the variance of the SSH field, showing significant contributions at temporal scales longer than 1 month. Mesoscale eddies drive a large portion of the kinetic energy in the Mediterranean Sea, and REKE values were larger than 50–60% both at the surface and at depth (e.g., in the area of Shikmona gyre).

Vertical profiles of velocity and REKE are shown for several areas and the trapping depth is discussed. Looking at the contributions to the ocean thermodynamics, the results exhibit the existence of typical warm (cold) cores associated with ACEs (CEs), with the relevant exception in the area of the Shikmona gyre that shows a structure which is closer to a mode-water ACE eddy with a positive salinity anomaly. This result seems to be confirmed by several oceanographic cruises (Mauri et al., 2019). The vertical temperature anomalies of eastern Mediterranean eddies are affected by a strong summer stratification in the surface water, showing an opposite sign of the anomaly whether looking at surface or at depth. A dedicated comparison against Argo floats in the Shikmona area has been performed to confirm such behavior together with a comparison with observation-only ocean reconstructions. In late 2008, there is a deepening of the Ierapetra gyre that coincides with a well-known large outflow of dense waters from the Aegean sea (EMT-like event, Velaoras et al., 2014).

Mesoscale contributions to ocean thermodynamics were assessed looking at the OHC. The results show that the temperature anomalies of long-lived eddies (≥ 4 weeks) account for up to the 15–25% of the OHC monthly variability in the upper ocean.

During the development of this work, a new high-resolution (1/24°) realization of the MED-REA was achieved, and it is currently distributed through the CMEMS data portal (Escudier et al., 2020). New approaches, based on machine-learning (ML) methods, to detect and reconstruct mesoscale structures from observations (e.g., Moschos et al., 2020) and models (George et al., 2021) were also developed recently. In this sense, the proposed method can represent the foundation for creating training data sets for ML-based and transfer-learning methods (e.g., Kadow et al., 2020) to reconstruct the 3D mesoscale field in the ocean emerging from the synergy between multi-platform observations and multiple eddy-resolving ocean syntheses.

DATA AVAILABILITY STATEMENT

The raw data supporting the conclusion of this article will be made available by the authors on request.

AUTHOR CONTRIBUTIONS

AB and AC conducted all the analyses and wrote the paper. JJ and JS reviewed the whole manuscript. RR and AA commented on a preliminary draft and contributed to finalizing the manuscript.

FUNDING

This collaborative study was supported through the Bjerknes Center for Climate Research (BCCR) initiative for strategic projects.

ACKNOWLEDGMENTS

We acknowledge the CINECA award under the ISCRA initiative for the availability of high-performance computing resources and support. The analyses were also performed using the highperformance computer at Helmholtz Zentrum Hereon. JS gratefully acknowledges the support by the H2020 Project IMMERSE.

SUPPLEMENTARY MATERIAL

The Supplementary Material for this article can be found online at: https://www.frontiersin.org/articles/10.3389/feart.2021.724879/full#supplementary-material

REFERENCES

Alhammoud, B., Béranger, K., Mortier, L., Crépon, M., and Dekeyser, I. (2005). Surface Circulation of the Levantine Basin: Comparison of Model Results With Observations. *Prog. Oceanography* 66, 299–320. doi:10.1016/j.pocean.2004.07.015

Ashkezari, M. D., Hill, C. N., Follett, C. N., Forget, G., and Follows, M. J. (2016). Oceanic Eddy Detection and Lifetime Forecast Using Machine Learning Methods. *Geophys. Res. Lett.* 43, 234–312. doi:10.1002/2016GL071269

Ayoub, N., Le Traon, P.-Y., and De Mey, P. (1998). A Description of the Mediterranean Surface Variable Circulation From Combined Ers-1 and Topex/poseidon Altimetric Data. *J. Mar. Syst.* 18, 3–40. doi:10.1016/s0924-7963(98)80004-3

Balmaseda, M. A., Hernandez, F., Storto, A., Palmer, M. D., Alves, O., Shi, L., et al. (2015). The Ocean Reanalyses Intercomparison Project (ORA-IP). *J. Oper. Oceanography* 8, s80–s97. doi:10.1080/1755876X.2015.1022329

Barceló-Llull, B., Sangrà, P., Pallàs-Sanz, E., Barton, E. D., Estrada-Allis, S. N., Martínez-Marrero, A., et al. (2017). Anatomy of a Subtropical Intrathermocline Eddy. *Deep Sea Res. Oceanographic Res. Pap.* 124, 126–139. doi:10.1016/j.dsr.2017.03.012

Bonaduce, A., Benkiran, M., Remy, E., Le Traon, P. Y., and Garric, G. (2018). Contribution of Future Wide-Swath Altimetry Missions to Ocean Analysis and Forecasting. *Ocean Sci.* 14, 1405–1421. doi:10.5194/os-14-1405-2018

Chaigneau, A., Le Texier, M., Eldin, G., Grados, C., and Pizarro, O. (2011). Vertical Structure of Mesoscale Eddies in the Eastern South Pacific Ocean: A Composite Analysis from Altimetry and Argo Profiling Floats. *J. Geophys. Res.* 116. doi:10.1029/2011JC007134

Chelton, D. B., Gaube, P., Schlax, M. G., Early, J. J., and Samelson, R. M. (2011a). The Influence of Nonlinear Mesoscale Eddies on Near-Surface Oceanic Chlorophyll. *Science* 334, 328–332. doi:10.1126/science.1208897

Chelton, D. B., Schlax, M. G., and Samelson, R. M. (2011b). Global Observations of Nonlinear Mesoscale Eddies. *Prog. Oceanography* 91, 167–216. doi:10.1016/j.pocean.2011.01.002

Chelton, D. B., Schlax, M. G., Samelson, R. M., and de Szoeke, R. A. (2007). Global Observations of Large Oceanic Eddies. *Geophys. Res. Lett.* 34, L15606. doi:10.1029/2007GL030812

Chen, G., Chen, X., and Huang, B. (2021). Independent Eddy Identification With Profiling Argo as Calibrated by Altimetry. *J. Geophys. Res. Oceans.* 126, e2020JC016729. doi:10.1029/2020JC016729

Cipollone, A., Masina, S., Storto, A., and Iovino, D. (2017). Benchmarking the Mesoscale Variability in Global Ocean Eddy-Permitting Numerical Systems. *Ocean Dyn.* 67, 1313–1333. doi:10.1007/s10236-017-1089-5

Dee, D. P., Uppala, S. M., Simmons, A. J., Berrisford, P., Poli, P., Kobayashi, S., et al. (2011). The ERA-Interim Reanalysis: Configuration and Performance of the Data Assimilation System. *Q.J.R. Meteorol. Soc.* 137, 553–597. doi:10.1002/qj.828

Dobricic, S., and Pinardi, N. (2008). An Oceanographic Three-Dimensional Variational Data Assimilation Scheme. *Ocean Model.* 22, 89–105. doi:10.1016/j.ocemod.2008.01.004

Doglioli, A. M., Blanke, B., Speich, S., and Lapeyre, G. (2007). Tracking Coherent Structures in a Regional Ocean Model With Wavelet Analysis: Application to Cape basin Eddies. *J. Geophys. Res.* 112. doi:10.1029/2006JC003952

Dong, C., Lin, X., Liu, Y., Nencioli, F., Chao, Y., Guan, Y., et al. (2012). Three-dimensional Oceanic Eddy Analysis in the Southern california Bight from a Numerical Product. *J. Geophys. Res.* 117, a–n. doi:10.1029/2011JC007354

Dong, C., McWilliams, J. C., Liu, Y., and Chen, D. (2014). Global Heat and Salt Transports by Eddy Movement. *Nat. Commun.* 5, 3294. doi:10.1038/ncomms4294

Drévillon, M., Bourdallé-Badie, R., Derval, C., Lellouche, J. M., Rémy, E., Tranchant, B., et al. (2008). The GODAE/Mercator-Ocean Global Ocean Forecasting System: Results, Applications and Prospects. *J. Oper. Oceanography* 1, 51–57. doi:10.1080/1755876X.2008.11020095

Duo, Z., Wang, W., and Wang, H. (2019). Oceanic Mesoscale Eddy Detection Method Based on Deep Learning. *Remote Sensing* 11, 1921. doi:10.3390/rs11161921

Escudier, R., Clementi, E., Omar, M., Cipollone, A., Pistoia, J., Aydogdu, A., et al. (2020). Mediterranean Sea Physical Reanalysis (Version 1) [Data Set]. *Copernicus Monit. Environ. Mar. Serv. (Cmems).* doi:10.25423/CMCC/MEDSEA_MULTIYEAR_PHY_006_004_E3R1

Escudier, R., Renault, L., Pascual, A., Brasseur, P., Chelton, D., and Beuvier, J. (2016). Eddy Properties in the Western Mediterranean Sea From Satellite Altimetry and a Numerical Simulation. *J. Geophys. Res. Oceans* 121, 3990–4006. doi:10.1002/2015JC011371

Faghmous, J. H., Frenger, I., Yao, Y., Warmka, R., Lindell, A., and Kumar, V. (2015). A Daily Global Mesoscale Ocean Eddy Dataset from Satellite Altimetry. *Sci. Data.* 2, 150028. doi:10.1038/sdata.2015.28

Fernández, V., Dietrich, D. E., Haney, R. L., and Tintoré, J. (2005). Mesoscale, Seasonal and Interannual Variability in the Mediterranean Sea Using a Numerical Ocean Model. *Prog. Oceanography* 66, 321–340. doi:10.1016/j.pocean.2004.07.010

Frenger, I., Münnich, M., Gruber, N., and Knutti, R. (2015). Southern OCean Eddy Phenomenology. *J. Geophys. Res. Oceans* 120, 7413–7449. doi:10.1002/2015JC011047

Fusco, G., Manzella, G. M. R., Cruzado, A., Gačić, M., Gasparini, G. P., Kovačević, V., et al. (2003). Variability of Mesoscale Features in the Mediterranean Sea from Xbt Data Analysis. *Ann. Geophys.* 21, 21–32. doi:10.5194/angeo-21-21-2003

Gaube, P., Chelton, D. B., Strutton, P. G., and Behrenfeld, M. J. (2013). Satellite Observations of Chlorophyll, Phytoplankton Biomass, and Ekman Pumping in Nonlinear Mesoscale Eddies. *J. Geophys. Res. Oceans* 118, 6349–6370. doi:10.1002/2013jc009027

Gaube, P., McGillicuddy, D. J., Chelton, D. B., Behrenfeld, M. J., and Strutton, P. G. (2014). Regional Variations in the Influence of Mesoscale Eddies on Near-Surface Chlorophyll. *J. Geophys. Res. Oceans* 119, 8195–8220. doi:10.1002/2014jc010111

George, T. M., Manucharyan, G. E., and Thompson, A. F. (2021). Deep Learning to Infer Eddy Heat Fluxes From Sea Surface Height Patterns of Mesoscale Turbulence. *Nat. Commun.* 12, 1–11. doi:10.1038/s41467-020-20779-9

Good, S. A., Martin, M. J., and Rayner, N. A. (2013). EN4: Quality Controlled Ocean Temperature and Salinity Profiles and Monthly Objective Analyses With Uncertainty Estimates. *J. Geophys. Res. Oceans* 118, 6704–6716. doi:10.1002/2013JC009067

Guinehut, S., Dhomps, A.-L., Larnicol, G., and Le Traon, P.-Y. (2012). High Resolution 3-D Temperature and Salinity fields Derived from *In Situ* and Satellite Observations. *Ocean Sci.* 8, 845–857. doi:10.5194/os-8-845-2012

Hallberg, R. (2013). Using a Resolution Function to Regulate Parameterizations of Oceanic Mesoscale Eddy Effects. *Ocean Model.* 72, 92–103. doi:10.1016/j.ocemod.2013.08.007

Haza, A. C., Özgökmen, T. M., Griffa, A., Garraffo, Z. D., and Piterbarg, L. (2012). Parameterization of Particle Transport at Submesoscales in the Gulf Stream Region Using Lagrangian Subgridscale Models. *Ocean Model.* 42, 31–49. doi:10.1016/j.ocemod.2011.11.005

Heimbach, P., Fukumori, I., Hill, C. N., Ponte, R. M., Stammer, D., Wunsch, C., et al. (2019). Putting it All Together: Adding Value to the Global Ocean and Climate Observing Systems With Complete Self-Consistent Ocean State and Parameter Estimates. *Front. Mar. Sci.* 6, 55. doi:10.3389/fmars.2019.00055

Ioannou, A., Stegner, A., Le Vu, B., Taupier-Letage, I., and Speich, S. (2017). Dynamical Evolution of Intense Ierapetra Eddies on a 22 Year Long Period. *J. Geophys. Res. Oceans.* 122, 9276–9298. doi:10.1002/2017jc013158

Ioannou, A., Stegner, A., Tuel, A., LeVu, B., Dumas, F., and Speich, S. (2019). Cyclostrophic Corrections of Aviso/Duacs Surface Velocities and its Application to Mesoscale Eddies in the Mediterranean Sea. *J. Geophys. Res. Oceans.* 124, 8913–8932. doi:10.1029/2019JC015031

Iona, A., Theodorou, A., Sofianos, S., Watelet, S., Troupin, C., and Beckers, J.-M. (2018). Mediterranean Sea Climatic Indices: Monitoring Long-Term Variability and Climate Changes. *Earth Syst. Sci. Data.* 10, 1829–1842. doi:10.5194/essd-10-1829-2018

Kadow, C., Hall, D. M., and Ulbrich, U. (2020). Artificial Intelligence Reconstructs Missing Climate Information. *Nat. Geosci.* 13, 408–413. doi:10.1038/s41561-020-0582-5

Lin, X., Dong, C., Chen, D., Liu, Y., Yang, J., Zou, B., et al. (2015). Three-Dimensional Properties of Mesoscale Eddies in the South china Sea Based on Eddy-Resolving Model Output. *Deep Sea Res. Part Oceanographic Res. Pap.* 99, 46–64. doi:10.1016/j.dsr.2015.01.007

Liu, Z., Liao, G., Hu, X., and Zhou, B. (2020). Aspect Ratio of Eddies Inferred From Argo Floats and Satellite Altimeter Data in the Ocean. *J. Geophys. Res. Oceans.* 125, e2019JC015555. doi:10.1029/2019JC015555

Madec, G. (2016). *NEMO Ocean Engine Publisher*. Institut Pierre-Simon Laplace (IPSL).

Marullo, S., Napolitano, E., Santoleri, R., Manca, B., and Evans, R. (2003). Variability of Rhodes and Ierapetra Gyres During Levantine Intermediate Water Experiment: Observations and Model Results. *J. Geophys. Res.* 108. doi:10.1029/2002JC001393

Mason, E., Ruiz, S., Bourdalle-Badie, R., Reffray, G., García-Sotillo, M., and Pascual, A. (2019). New Insight into 3-d Mesoscale Eddy Properties From Cmems Operational Models in the Western Mediterranean. *Ocean Sci.* 15, 1111–1131. doi:10.5194/os-15-1111-2019

Mauri, E., Sitz, L., Gerin, R., Poulain, P.-M., Hayes, D., and Gildor, H. (2019). On the Variability of the Circulation and Water Mass Properties in the Eastern Levantine Sea Between September 2016-August 2017. *Water.* 11, 1741. doi:10.3390/w11091741

Mkhinini, N., Coimbra, A. L. S., Stegner, A., Arsouze, T., Taupier-Letage, I., and Béranger, K. (2014). Long-Lived Mesoscale Eddies in the Eastern Mediterranean Sea: Analysis of 20 Years of AVISO Geostrophic Velocities. *J. Geophys. Res. Oceans.* 119, 8603–8626. doi:10.1002/2014JC010176

Moschos, E., Schwander, O., Stegner, A., and Gallinari, P. (2020). Deep-SST-Eddies: A Deep Learning Framework to Detect Oceanic Eddies in Sea Surface Temperature Images. In ICASSP 2020 - 2020 IEEE International Conference on Acoustics, Speech and Signal Processing. (ICASSP), 4307–4311. doi:10.1109/icassp40776.2020.9053909

Mulet, S., Rio, M.-H., Mignot, A., Guinehut, S., and Morrow, R. (2012). A New Estimate of the Global 3D Geostrophic Ocean Circulation Based on Satellite Data and *In-Situ* Measurements. *Deep Sea Res. Part Topical Stud. Oceanography* 77-80, 70–81. doi:10.1016/j.dsr2.2012.04.012

Oddo, P., Adani, M., Pinardi, N., Fratianni, C., Tonani, M., and Pettenuzzo, D. (2009). A Nested Atlantic-Mediterranean Sea General Circulation Model for Operational Forecasting. *Ocean Sci.* 5, 461–473. doi:10.5194/os-5-461-2009

Oddo, P., Bonaduce, A., Pinardi, N., and Guarnieri, A. (2014). Sensitivity of the Mediterranean Sea Level to Atmospheric Pressure and Free Surface Elevation Numerical Formulation in NEMO. *Geoscientific Model. Development under Rev.* doi:10.5194/gmd-7-3001-2014

Pegliasco, C., Chaigneau, A., and Morrow, R. (2015). Main Eddy Vertical Structures Observed in the Four Major Eastern Boundary Upwelling Systems. *J. Geophys. Res. Oceans.* 120, 6008–6033. doi:10.1002/2015jc010950

Petersen, M. R., Williams, S. J., Maltrud, M. E., Hecht, M. W., and Hamann, B. (2013). A Three-Dimensional Eddy Census of a High-Resolution Global Ocean Simulation. *J. Geophys. Res. Oceans.* 118, 1759–1774. doi:10.1002/jgrc.20155

Pinardi, N., Cessi, P., Borile, F., and Wolfe, C. L. P. (2019). The Mediterranean Sea Overturning Circulation. *J. Phys. Oceanography* 49, 1699–1721. doi:10.1175/jpo-d-18-0254.1

Pinardi, N., Korres, G., Lascaratos, A., Roussenov, V., and Stanev, E. (1997). Numerical Simulation of the Interannual Variability of the Mediterranean Sea Upper Ocean Circulation. *Geophys. Res. Lett.* 24, 425–428. doi:10.1029/96gl03952

Pinardi, N., and Masetti, E. (2000). Variability of the Large Scale General Circulation of the Mediterranean Sea From Observations and Modelling: a Review. *Palaeogeogr. Palaeoclimatol. Palaeoecol.* 158, 153–173. doi:10.1016/s0031-0182(00)00048-1

Pinardi, N., Zavatarelli, M., Adani, M., Coppini, G., Fratianni, C., Oddo, P., et al. (2015). Mediterranean Sea Large-Scale Low-Frequency Ocean Variability and Water Mass Formation Rates From 1987 to 2007: A Retrospective Analysis. *Prog. Oceanography* 132, 318–332. doi:10.1016/j.pocean.2013.11.003

Pinardi, N., Zavatarelli, M., Crise, A., and Ravioli, M. (2005). "The Physical, Sedimentary and Ecological Structure and Variability of Shelf Areas in the Mediterranean Sea,". *The Sea*. Editors A. R. Robinson and K. H. Brink, Vol. 14.

Raj, R. P., Johannessen, J. A., Eldevik, T., Nilsen, J. E. Ø., and Halo, I. (2016). Quantifying Mesoscale Eddies in the Lofoten basin. *J. Geophys. Res. Oceans.* 121, 4503–4521. doi:10.1002/2016JC011637

Raj, R. P., Halo, I., Chatterjee, S., Belonenko, T., Bakhoday-Paskyabi, M., Bashmachnikov, I., et al. (2020). Interaction Between Mesoscale Eddies and the Gyre Circulation in the Lofoten basin. *J. Geophys. Res. Oceans.* 125, e2020JC016102. doi:10.1029/2020JC016102

Rhines, P. B. (2001). "Mesoscale Eddies," in *Encyclopedia of Ocean Sciences*. Editor J. H. Steele (Oxford: Academic Press), 1717–1730. doi:10.1006/rwos.2001.0143

Robinson, A. R., and Golnaraghi, M. (1993). Circulation and Dynamics of the Eastern Mediterranean Sea; Quasi-Synoptic Data-Driven Simulations. *Deep Sea Res. Part Topical Stud. Oceanography.* 40, 1207–1246. doi:10.1016/0967-0645(93)90068-x

Robinson, A. R., Leslie, W. G., Theocharis, A., and Lascaratos, A. (2001). Mediterranean Sea Circulation. *Encyclopedia ocean Sci.* 3, 1689–1705. doi:10.1006/rwos.2001.0376

Robinson, A. R., Malanotte-Rizzoli, P., Hecht, A., Michelato, A., Roether, W., Theocharis, A., et al. (1992). General Circulation of the Eastern Mediterranean. *Earth-Science Rev.* 32, 285–309. doi:10.1016/0012-8252(92)90002-b

Roether, W., Klein, B., and Hainbucher, D. (2014). The Eastern Mediterranean Transient. *Geophys. Monogr.* 202, 75–83. doi:10.1002/9781118847572.ch6

Rubio, A., Barnier, B., Jord, G., Espino, M., and Marsaleix, P. (2009). Origin and Dynamics of Mesoscale Eddies in the Catalan Sea (Nw Mediterranean): Insight from a Numerical Model Study. *J. Geophys. Res. Oceans.* 114, C06009. doi:10.1029/2007jc004245

Sasaki, H., Klein, P., Qiu, B., and Sasai, Y. (2014). Impact of Oceanic-Scale Interactions on the Seasonal Modulation of Ocean Dynamics by the Atmosphere. *Nat. Commun.* 5, 5636. doi:10.1038/ncomms6636

Schütte, F., Brandt, P., and Karstensen, J. (2016). Occurrence and Characteristics of Mesoscale Eddies in the Tropical Northeastern Atlantic Ocean. *Ocean Sci.* 12, 663–685. doi:10.5194/os-12-663-2016

Shi, F., Luo, Y., and Xu, L. (2018). Volume and Transport of Eddy-Trapped Mode Water South of the Kuroshio Extension. *J. Geophys. Res. Oceans.* 123, 8749–8761. doi:10.1029/2018JC014176

Simoncelli, S., Fratianni, C., Pinardi, N., Grandi, A., Drudi, M., Oddo, P., et al. (2019). *Mediterranean Sea Physical Reanalysis (CMEMS MED-Physics) [Data Set]*. Copernicus: Monitoring Environment Marine Service (CMEMS). doi:10.25423/MEDSEA_REANALYSIS_PHYS_006_004

Storto, A., Alvera-Azcárate, A., Balmaseda, M. A., Barth, A., Chevallier, M., Counillon, F., et al. (2019). Ocean Reanalyses: Recent Advances and Unsolved Challenges. *Front. Mar. Sci.* 6, 418. doi:10.3389/fmars.2019.00418

Tonani, M., Balmaseda, M., Bertino, L., Blockley, E., Brassington, G., Davidson, F., et al. (2015). Status and Future of Global and Regional Ocean Prediction Systems. *J. Oper. Oceanography* 8, s201–s220. doi:10.1080/1755876x.2015.1049892

Velaoras, D., Krokos, G., Nittis, K., and Theocharis, A. (2014). Dense Intermediate Water Outflow From the Cretan Sea: A Salinity Driven, Recurrent Phenomenon, Connected to Thermohaline Circulation Changes. *J. Geophys. Res. Oceans.* 119, 4797–4820. doi:10.1002/2014JC009937

Velaoras, D., Papadopoulos, V. P., Kontoyiannis, H., Cardin, V., and Civitarese, G. (2019). Water Masses and Hydrography During April and June 2016 in the Cretan Sea and Cretan Passage (Eastern Mediterranean Sea). *Deep Sea Res. Part Topical Stud. Oceanography* 164, 25–40. doi:10.1016/j.dsr2.2018.09.005

von Schuckmann, K., Le Traon, P.-Y., Alvarez-Fanjul, E., Axell, L., Balmaseda, M., Breivik, L.-A., et al. (2016). The Copernicus Marine Environment Monitoring Service Ocean State Report. *J. Oper. Oceanography* 9, s235–s320. doi:10.1080/1755876X.2016.1273446

Wilks, D. S. (2011). "Empirical Distributions and Exploratory Data Analysis," in *Statistical Methods in the Atmospheric Sciences of International Geophysics*. Editor D. S. Wilks (Academic Press), Vol. 100, 23–70. doi:10.1016/B978-0-12-385022-5.00003-8

Wunsch, C., and Heimbach, P. (2014). Bidecadal Thermal Changes in the Abyssal Ocean. *J. Phys. Oceanography* 44, 2013–2030. doi:10.1175/jpo-d-13-096.1

Xu, C., Shang, X.-D., and Huang, R. X. (2011). Estimate of Eddy Energy Generation/Dissipation Rate in the World Ocean From Altimetry Data. *Ocean Dyn.* 61, 525–541. doi:10.1007/s10236-011-0377-8

Xu, C., Shang, X.-D., and Huang, R. X. (2014). Horizontal Eddy Energy Flux in the World Oceans Diagnosed From Altimetry Data. *Sci. Rep.* 4, 5316. doi:10.1038/srep05316

Zhang, Z., Tian, J., Qiu, B., Zhao, W., Chang, P., Wu, D., et al. (2016). Observed 3D Structure, Generation, and Dissipation of Oceanic Mesoscale Eddies in the South China Sea. *Sci. Rep.* 6, 24349. doi:10.1038/srep24349

Zhang, Z., Zhang, Y., and Wang, W. (2017). Three-Compartment Structure of Subsurface-Intensified Mesoscale Eddies in the Ocean. *J. Geophys. Res. Oceans.* 122, 1653–1664. doi:10.1002/2016JC012376

Zhao, J., Bower, A., Yang, J., Lin, X., and Penny Holliday, N. (2018). Meridional Heat Transport Variability Induced by Mesoscale Processes in the Subpolar North Atlantic. *Nat. Commun.* 9, 1124. doi:10.1038/s41467-018-03134-x

Conflict of Interest: The authors declare that the research was conducted in the absence of any commercial or financial relationships that could be construed as a potential conflict of interest.

The handling editor declared a past co-authorship with several of the authors AB, AC.

Publisher's Note: All claims expressed in this article are solely those of the authors and do not necessarily represent those of their affiliated organizations, or those of the publisher, the editors and the reviewers. Any product that may be evaluated in this article, or claim that may be made by its manufacturer, is not guaranteed or endorsed by the publisher.

frontiers in Earth Science

ORIGINAL RESEARCH
published: 24 November 2021
doi: 10.3389/feart.2021.702285

A High Resolution Reanalysis for the Mediterranean Sea

Romain Escudier[1]†, Emanuela Clementi[1], Andrea Cipollone[1], Jenny Pistoia[1], Massimiliano Drudi[2], Alessandro Grandi[2], Vladislav Lyubartsev[2], Rita Lecci[2], Ali Aydogdu[1], Damiano Delrosso[3], Mohamed Omar[1‡], Simona Masina[1], Giovanni Coppini[1] and Nadia Pinardi[4]*

[1]Ocean Modeling and Data Assimilation Division, Centro Euro-Mediterraneo Sui Cambiamenti Climatici, Lecce, Italy, [2]Ocean Predictions and Applications Division, Centro Euro-Mediterraneo Sui Cambiamenti Climatici, Lecce, Italy, [3]Istituto Nazionale di Geofisica e Vulcanologia, Sezione di Bologna, Bologna, Italy, [4]Department of Physics and Astronomy, University of Bologna, Bologna, Italy

In order to be able to forecast the weather and estimate future climate changes in the ocean, it is crucial to understand the past and the mechanisms responsible for the ocean variability. This is particularly true in a complex area such as the Mediterranean Sea with diverse dynamics like deep convection and overturning circulation. To this end, effective tools are ocean reanalyses or reconstructions of the past ocean state. Here we present a new physical reanalysis of the Mediterranean Sea at high resolution, developed in the Copernicus Marine Environment Monitoring Service (CMEMS) framework. The hydrodynamic model is based on the Nucleus for European Modelling of the Ocean (NEMO) combined with a variational data assimilation scheme (OceanVar). The model has a horizontal resolution of 1/24° and 141 unevenly distributed vertical z* levels. It provides daily and monthly temperature, salinity, current, sea level and mixed layer depth as well as hourly fields for surface velocities and sea level. ECMWF ERA-5 atmospheric fields force the model and daily boundary conditions in the Atlantic are taken from a global reanalysis. The reanalysis covers the 33 years from 1987 to 2019. Initialized from SeaDataNet climatology in January 1985, it reaches a nominal state after a 2-years spin-up. *In-situ* data from CTD, ARGO floats and XBT are assimilated into the model in combination with satellite altimetry observations. This reanalysis has been validated and assessed through comparison to *in-situ* and satellite observations as well as literature climatologies. The results show an overall improvement of the comparison with observations and a better representation of the main dynamics of the region compared to a previous, lower resolution (1/16°), reanalysis. Temperature and salinity RMSD are decreased by respectively 14 and 18%. The salinity biases at depth of the previous version are corrected. Climate signals show continuous increase of the temperature and salinity, confirming estimates from observations and other reanalysis. The new reanalysis will allow the study of physical processes at multi-scales, from the large scale to the transient small mesoscale structures and the selection of climate indicators for the basin.

Keywords: ocean, mediterranean sea, reanalysis, numerical modelling, observations, data assimilation, multi-scale

OPEN ACCESS

Edited by:
Xander Wang,
University of Prince Edward Island, Canada

Reviewed by:
You-Soon Chang,
Kongju National University, South Korea
Smitha Ratheesh,
Space Applications Centre (ISRO), India
Chunxue Yang,
National Research Council (CNR), Italy

****Correspondence:***
Romain Escudier
romain.escudier@mercator-ocean.fr

†Present address:
Observations pour Les Systèmes D'analyse et de Prévision, Mercator Ocean International, Toulouse, France

‡Deceased

Specialty section:
This article was submitted to Interdisciplinary Climate Studies, a section of the journal Frontiers in Earth Science

Received: *29 April 2021*
Accepted: *22 October 2021*
Published: *24 November 2021*

Citation:
Escudier R, Clementi E, Cipollone A, Pistoia J, Drudi M, Grandi A, Lyubartsev V, Lecci R, Aydogdu A, Delrosso D, Omar M, Masina S, Coppini G and Pinardi N (2021) A High Resolution Reanalysis for the Mediterranean Sea. Front. Earth Sci. 9:702285. doi: 10.3389/feart.2021.702285

1 INTRODUCTION

Reanalysis is a crucial tool to understand the events of the past and help us find the underlying processes that should be represented by the numerical models. Reanalysis products are computed by constraining a numerical model with available observations using data assimilation. They have been used extensively in ocean sciences (Storto et al., 2019) as they provide 4D fields that correspond to the best estimate of the ocean state. Atmospheric models and observations are introduced into the system through the surface forcings, ocean physics through the ocean global circulation model (OGCM) and finally the data assimilation scheme adds the ocean observations.

Ocean reanalyses were initially computed to monitor and understand climate change (e.g., Carton and Santorelli 2008). They also allow to study important signals and processes that cannot be observed completely such as deep water formation (e.g., Somot et al., 2016), subsurface and bottom circulation (Pinardi et al., 2015) or the overturning circulation (Pinardi et al., 2019). In addition, subregional models need the reanalyses as initial conditions and boundary conditions. In the Mediterranean Sea, there are different models that uses the Mediterranean reanalysis for their setup such as the Adriatic Forecasting System (Oddo et al., 2005), the Sicily Channel Regional Model (Olita et al., 2012), the Tyrrhenian Sea Forecasting (Vetrano et al., 2010) or the Western Mediterranean OPerational forecasting system (WMOP, Juza et al., 2016).

The Mediterranean Sea is a challenging area with a strong anthropogenic pressure due to the density of human population living along its coasts (Hulme et al., 1999). It is therefore crucial to study and understand the climate in this region and it has been flagged as a hotspot for climate change (Giorgi, 2006). In this semi-enclosed sea, many fundamental processes that occur in the global ocean happen at a smaller scale, often called a miniature ocean (Bethoux et al., 1999; Tsimplis et al., 2006). Examples of these processes are mesoscale dynamics (Robinson et al., 2001; Mkhinini et al., 2014; Escudier et al., 2016), deep convection (MEDOC Group et al., 1970; Houpert et al., 2016), cascading (Dufau-Julliand et al., 2004) or the overturning circulation in the basin (Pinardi et al., 2019). The increased understanding and upgrade of ocean forecasting products depends on the ability to maintain the observing system and the progressive inclusion of relevant processes in numerical models, especially in view of the climate challenges facing the Mediterranean Sea (Tintoré et al., 2019).

The first effort to compute a reanalysis for the Mediterranean Sea was made by Adani et al. (2011). This reanalysis used the OPA numerical model (Océan PArallélisé, Madec et al., 1997) on a 1/16° regular horizontal grid (Tonani et al., 2008). Evolutions of this reanalysis became a product in Copernicus Marine Environment Monitoring Service (CMEMS), which represents the previous version of the reanalysis presented here (Simoncelli et al., 2016; Simoncelli et al., 2019). It will be hereafter referred as MEDREA16. Another reanalysis (MEDRYS) was created to address mainly the issue of inconsistency in the atmospheric forcing (Hamon et al., 2016). For this product, special attention was given to the atmospheric forcing using consistent and higher resolution data. It showed the importance of the atmospheric forcing to fully resolve the dynamics.

In this paper, we present a new reanalysis of the Mediterranean Sea physical state performed in the framework of CMEMS for the period 1987–2019 (Escudier et al., 2020). CMEMS objective is to provide regular information on the ocean state for the global ocean and European regional seas such as the Mediterranean (Le Traon et al., 2019). In order to fulfill this mission, they offer freely available descriptions of the current ocean state (analysis), predictions of the situation 10 days ahead (forecast), and the provision of consistent retrospective data records (reprocessing and reanalysis). The new reanalysis is part of the latter for the Mediterranean region and is the current available product on the CMEMS website: https://marine.copernicus.eu/. It is a significant upgrade from the previously available product in CMEMS (MEDREA16) and it will address some issues that were encountered such as biases in the deeper layers (Juza et al., 2015). The new reanalysis, computed on a 1/24° horizontal grid, will be hereafter called MEDREA24.

After describing all the elements of the system, we will assess its performance by comparing it to observations, evaluate the climate signals from the reanalyses and finish with a discussion on the results.

2 DESCRIPTION

2.1 Numerical Model

The oceanic equations of motion of the Mediterranean physical system are solved by an Ocean General Circulation Model (OGCM) based on NEMO (Nucleus for European Modelling of the Ocean) version 3.6 (Madec et al., 2017). The code is developed and maintained by the NEMO-consortium.

NEMO has been implemented in the Mediterranean at 1/24° x 1/24° horizontal resolution and 141 unevenly spaced vertical levels (thickness is 2 m in the upper layers and does not exceed 100 m in the deepest layers) with a baroclinic time step of 240 s (the barotropic time step is 2.4 s). This reanalysis benefits from several modeling upgrades that were included during the last years in the CMEMS Mediterranean operational analysis and forecast system described in Clementi et al. (2017). The model covers the whole Mediterranean Sea and also extends into the Atlantic in order to better resolve the exchanges with the Atlantic Ocean at the Strait of Gibraltar (see **Figure 1**). On the other side, the Dardanelles inflow is parameterized as a river and the climatological net inflow rates as well as the salinity values are taken from Kourafalou and Barbopoulos (2003). The topography is created starting from the GEBCO 30arc-second grid (Weatherall et al., 2015), filtered (using a Shapiro filter) and manually modified in critical areas such as: islands along the Eastern Adriatic coasts, Gibraltar and Messina straits, Atlantic box edge.

The NEMO code solves the primitive equations using the time-splitting technique which allows the external gravity waves to be explicitly resolved with non-linear free surface formulation and time-varying vertical z* coordinates. The advection scheme for active tracers, temperature and salinity, is a mixed

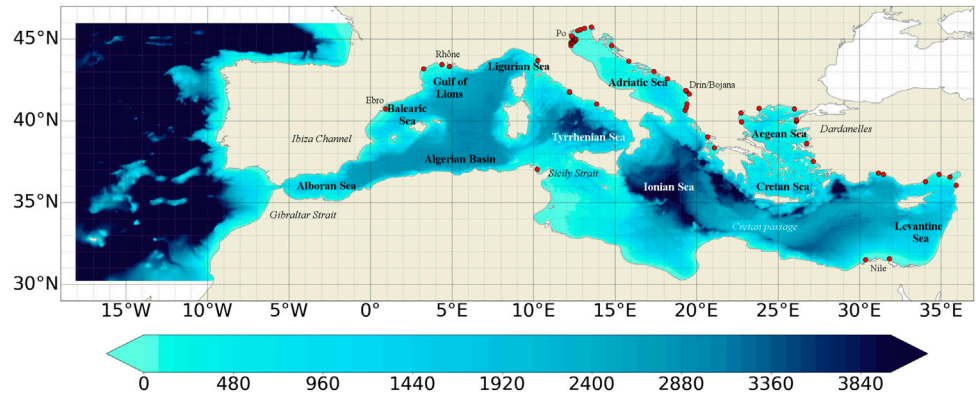

FIGURE 1 | Domain and bathymetry of MEDREA24 (in meters). Position of the river input are in red.

TABLE 1 | Comparison with Previous reanalysis.

		MEDREA16	MEDREA24
model	**Resolution**	1/16° (5–6 km) horizontal 72 vertical levels	1/24° (4.5 km) horizontal 141 vertical levels
	Bathymetry	Modified DBDB1 (1 min)	Modified GEBCO (30arc-sec)
	Physical model	NEMO v3.2 linear free-surface, Z coordinates	NEMO V3.6 non-linear free-surface, Z* coordinates
	River inputs	7 with Q > 100m^3/s (climato)	39 with Q > 50m^3/s (climato)
	Lateral Boundaries	Monthly climatological fields from GLO-MFC 1/4°	Daily mean fields from CGLORS REA 1/4°
	Atmospheric forcing	ERA-INTERIM (0.75°, 6 hrs)	ERA5 (0.25°, 1 h)
assimilation	**System**	Dobricic and Pinardi (2008)	from Storto et al. (2016)
	EOF	20 seasonally and regionally varying from 3 years simulation	50 seasonally and spatially varying from 32 years reanalysis
	Observations	Merged database: SeaDataNet/MyOcean/CMEMS	New merged database: SeaDataNet/CMEMS
	SST nudging	−40 W/m2/K constant	Gaussian around 00:00 (max = -110 W/m2/K)
	Period	1987–2018	1987–2019 (running)
outputs	**Released variables**	T, S, SSH, UV	T, S, SSH, UV, MLD, Tb
	File frequency	Daily, monthly	Daily, monthly, hourly (SSH, SSUV)
	Daily outputs	centered at 00:00 UTC	centered at 12:00 UTC

up-stream/MUSCL (Mono-tonic Upwind Scheme for Conservation Laws; Van Leer 1979), originally implemented by Estubier and Lévy (2000) and modified by Oddo et al. (2009). The vertical diffusion and viscosity terms are a function of the Richardson number as parameterized by Pacanowski and Philander (1981). The model interactively computes air-surface fluxes of momentum, mass, and heat. The bulk formulae implemented are described in Pettenuzzo et al. (2010) and are currently used in the Mediterranean operational system Tonani et al. (2015). A detailed description of other specific features of the model implementation can be found in Oddo et al. (2009, 2014).

The vertical background viscosity and diffusivity values are set to $1.2e^{-6}\ m^2/s$ and $1.0e^{-7}\ m^2/s$ respectively, while the horizontal bilaplacian eddy diffusivity and viscosity are set respectively equal to $-1.2e^8 m^4/s$ and $-2e^8 m^4/s$. A quadratic bottom drag coefficient with a logarithmic formulation has been used according to Maraldi et al. (2013) and the model uses vertical partial cells to fit the bottom depth shape.

The hydrodynamic model is nested in the Atlantic within the global reanalysis C-GLORSv5 (Storto and Masina, 2016). C-GLORSv5 runs at eddy-permitting resolution (1/4° horizontal resolution and 50 vertical levels) and is corrected by a variational data assimilation system (OceanVar) that assimilates *in-situ* observation from United Kingdom Met Office Hadley Centre EN3/EN4 dataset (Good et al., 2013) together with along-track altimetric satellite observations processed by the DUACS multimission altimeter data processing system and also available as CMEMS product (SEALEVEL_GLO_PHY_L3_REP_OBSERVATIONS_008_062). Heat and freshwater fluxes are constrained through nudging schemes towards sea-surface temperature observations supplied by NOAA (Reynolds et al., 2007) and sea surface salinity from OI EN4 dataset (Good et al., 2013). A large-scale bias correction (LSBC) scheme is also included to correct the model tendencies.

The initial conditions for MEDREA24 are taken from a temperature and salinity monthly climatology computed from monthly averages (named SDN_V2aa, Simoncelli et al., 2015) produced within It has been calculated utilizing the extensive historical *in situ* data set from 1900 to 1987. We considered only observations before 1987 to compute the initial condition because we did not want the climatology to be affected by the Eastern

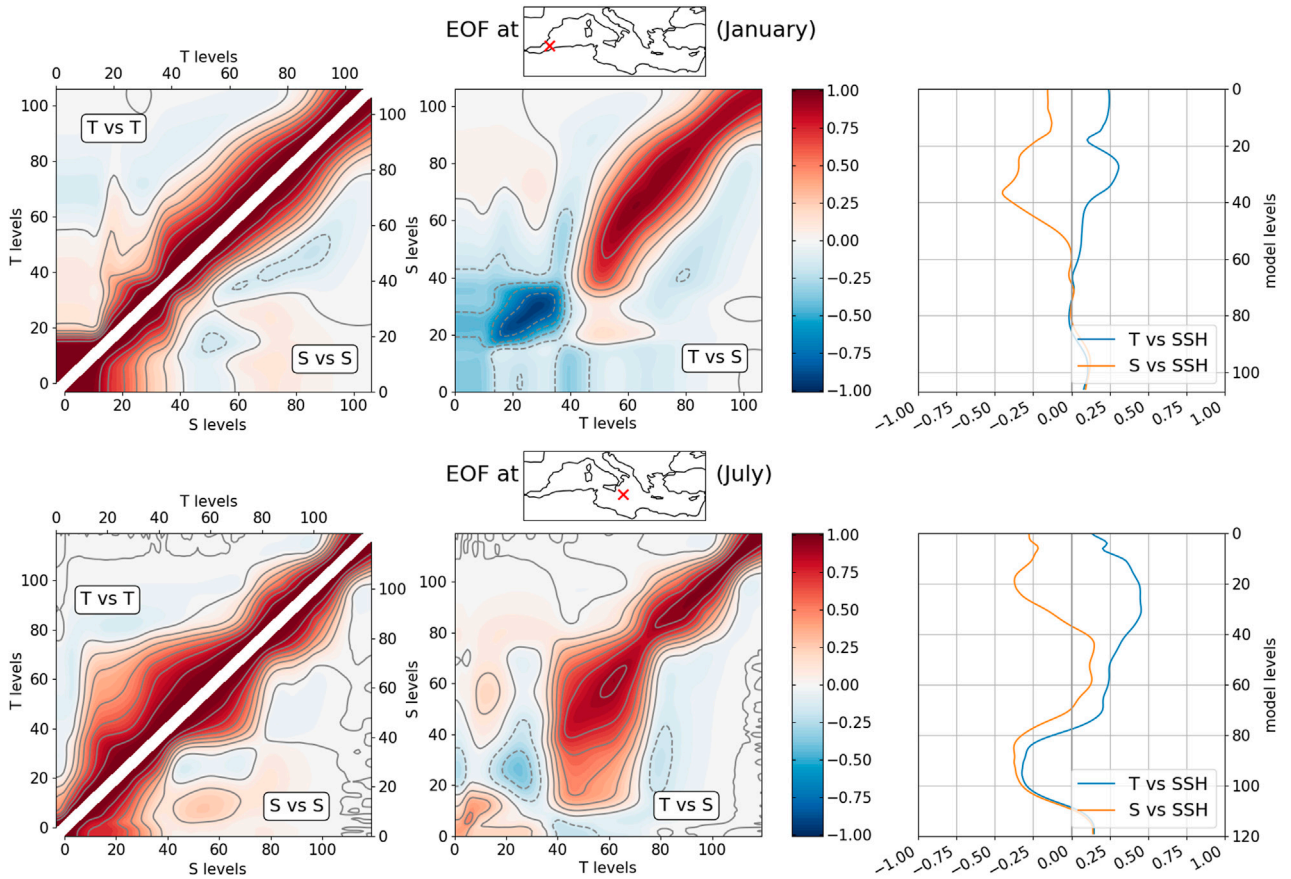

FIGURE 2 | Examples of correlations computed from the EOF on two model grid points for two different months: January on the upper row and July on the lower row. On each row, the left is the correlation obtained between temperatures (and salinities) at different model levels, the center is the correlation between temperature and salinity at different levels and the right is the correlation between SSH and temperature (or salinity).

Mediterranean Transient (EMT, see Malanotte-Rizzoli et al., 1999).

The model is forced by momentum, water and heat fluxes interactively computed by bulk formulae using the ERA5 reanalysis dataset (30 km horizontal resolution and hourly time frequency, Hersbach et al., 2020) and the model surface temperatures (details of the air-sea physics are in Tonani et al., 2008). The water balance is computed as Evaporation minus Precipitation and Runoff. The evaporation is derived from the latent heat flux, the precipitations are provided by ERA5, while the runoff of the 39 rivers implemented is provided by monthly mean climatological datasets. We use the Global Runoff Data Centre dataset (Fekete et al., 1999) for the Po, Ebro, Nile and Rhône rivers; the dataset from Raicich (1996) for: Vjosë and Seman rivers; the UNEP-MAP dataset (Demiraj et al., 1996) for the Buna/Bojana river; and finally the PERSEUS dataset (Report, 2015) for the remaining 32 rivers: Piave, Tagliamento, Soca/Isonzo, Livenza, Brenta-Bacchiglione, Adige, Lika, Reno, Krka, Arno, Nerveta, Aude, Trebisjnica, Tevere/Tiber, Mati, Volturno, Shkumbini, Struma/Strymonas, Meric/Evros/Maritsa, Axi-os/Vadar, Arachtos, Pinios, Acheloos, Gediz, Buyuk Menderes, Kopru, Manavgat, Seyhan, Ceyhan, Gosku, Medjerda, Asi/Orontes. The river runoff has a non-zero salinity to avoid a salinity drift. This value is set at 15 PSU for most rivers except for the Po (18 PSU), the Rhône (25 PSU), the Ebro (30 PSU) and the Nile (8 PSU). More details about the runoff can be found in Delrosso (2020).

Sea Surface Temperature (SST) fields, described in the next section, are used for the correction of surface heat fluxes with a Gaussian relaxation coefficient *dQ/dSST* applied around midnight since the observed dataset corresponds to the foundation SST (which is equivalent to the SST at midnight). The maximum of this coefficient is 110 W $m^{-2}K^{-1}$. **Table 1** summarizes the MEDREA24 configuration and the corresponding setup for MEDREA16.

2.2 Observations

The SST data used to correct the heat fluxes in the numerical model are L4 interpolated fields from CMEMS (CMEMS product name is SST_MED_SST_L4_REP_OBSERVATIONS_010_021). This is an optimally interpolated satellite-based estimate of the foundation SST in the Mediterranean Sea and adjacent North Atlantic box over a 1/24° resolution grid. This product is built from a consistent

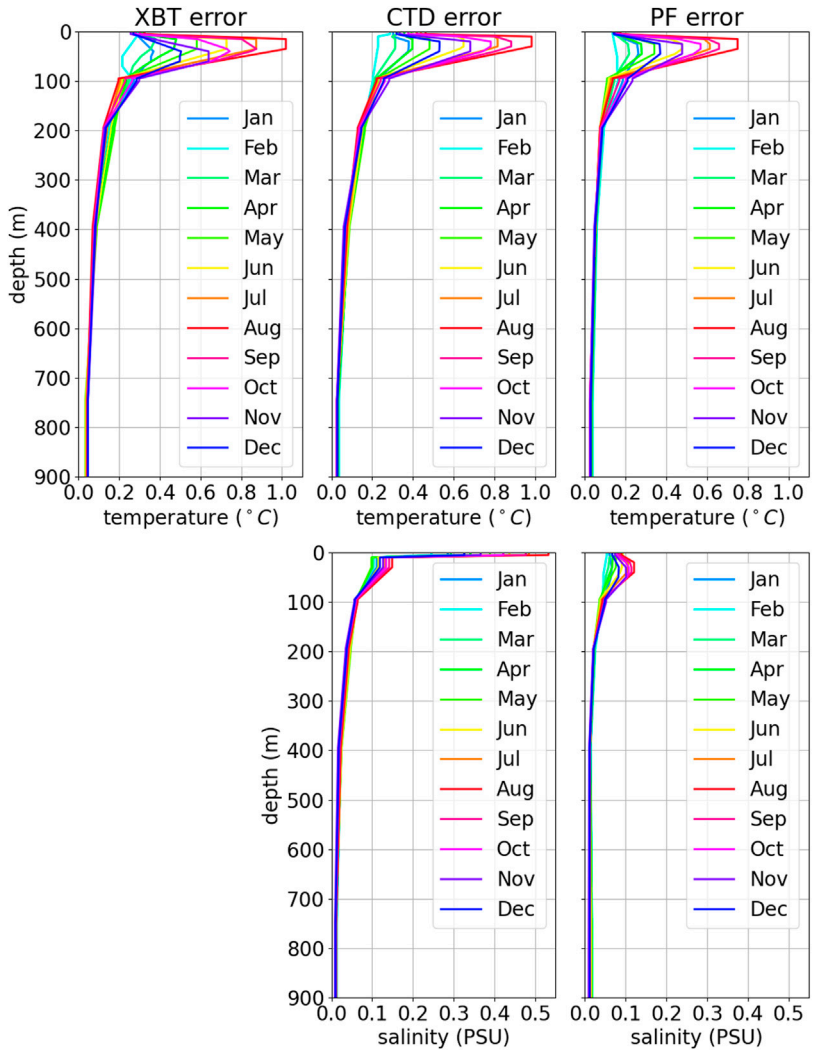

FIGURE 3 | Insitu error profiles used in the data assimilation. Top panels are temperature errors while bottom panels are salinity. Errors for XBT, CTD and ARGO floats are respectively plotted on the left, center and right columns.

reprocessing of the level-3 (merged multi-sensor, L3) climate data record provided by the ESA Climate Change Initiative (CCI) and Copernicus Climate Change Service (C3S) initiatives, but also includes an adjusted version of the AVHRR Pathfinder dataset version 5.3 to increase the input observation coverage (Buongiorno Nardelli et al., 2013; Pisano et al., 2016). This product is the result of a merge of several sensors documented extensively in its documentation (see on CMEMS website).

The 3DVar system described below assimilates the along-track sea level anomalies (SLA) from satellite altimetry. This reprocessed data over the European region, using all available satellites, is also provided through CMEMS project by the DUACS multimission altimeter data processing system (CMEMS product name is SEALEVEL_EUR_PHY_L3_REP_OBSERVATIONS_008_061). The product provides the different corrections applied to the data as separate variables which allows us to choose not to apply the Dynamic Atmospheric Correction (DAC) since the NEMO configuration uses a free surface equation that accounts for the atmospheric pressure effect (Dobricic et al., 2012; Oddo et al., 2014). It was also chosen to use unfiltered SLA to avoid the filtering of physical signal and let the assimilation system handle the resulting noise. For each track and each pass of the satellite the mean bias over the whole uninterrupted track between the observation and the model value is removed from the innovation. This enables to avoid lingering large scale atmospheric effects and other uncorrected signal.

The system also assimilates *in-situ* temperature and salinity profiles for the whole period. These profiles come from CTD ("Conductivity Temperature and Depth", ship measurements), XBT (Expendable bathythermograph) and ARGO floats (profiling floats). They are obtained by merging the data from CMEMS historical NRT *in-situ* observations (CMEMS product name is INSITU_GLO_NRT_OBSERVATIONS_013_030) into the

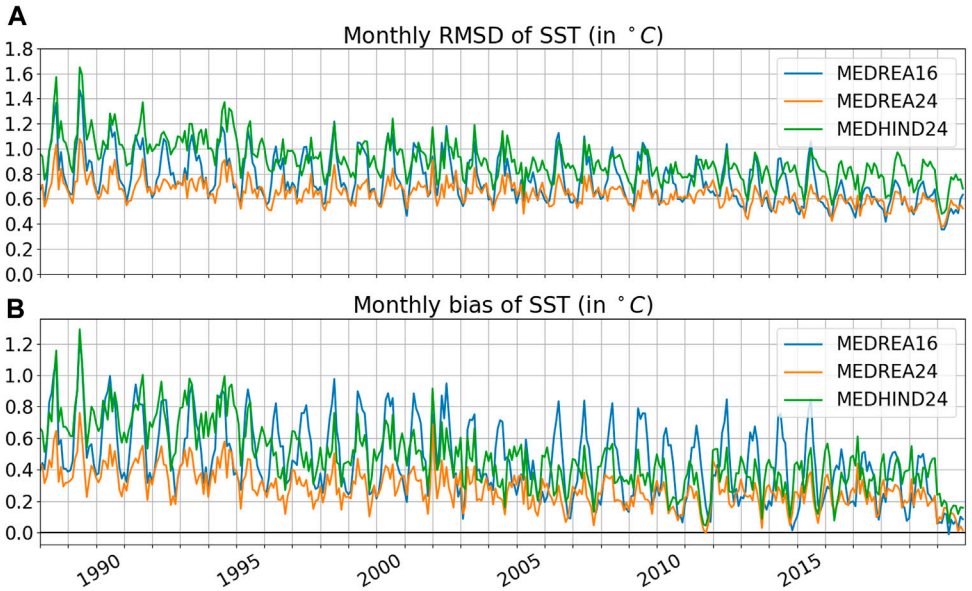

FIGURE 4 | Monthly RMSD **(A)** and bias **(B)** of SST (in ˚C) for the two reanalyses and the hindcast when compared to satellite SST. The first model layer is used for the model SST.

database of *in-situ* observations from SeaDataNet (https://www.seadatanet.org/). We found out that both datasets were missing some good observations and by merging the two we obtain a larger database (around 30% more data after preprocessing). The merging procedure removes profiles from CMEMS that were already in SeaDataNet. The resulting database is then pre-processed before the observations are introduced into the system. First, only the physical profiles for ARGO (first profile of the day in the CMEMS database) are kept. From this sensor, profiles with gap in thermocline (more than 40 m in the first 300 m) are removed. Only data with quality check value of 1 (good data) are retained and temperature values must be within (0–35)˚C and salinity within (0–45) PSU. If the data has no recognized type, it is considered a CTD if there are salinity values in the profile, XBT otherwise. For CTD data, only ascending profiles are selected. All measurements above 2 m are discarded (for ARGO and XBT). 17% of data is rejected with the above pre-processing. Finally, a vertical subsampling is performed to keep no more than 3 observations per model level.

For the evaluation of the performance of the reanalysis, assimilated observations were compared to the model outputs as quasi-independent observations. Fully independent observations take the form of fixed mooring time series of temperature and salinity as well as tide gauges measurements. This data comes from the European Marine Observation and Data Network (EMODnet, https://emodnet.ec.europa.eu/). Interpolated 2D daily maps of satellite altimetry are also used in the validation to generate the Eddy Kinetic Energy (EKE) maps and compare them to the reanalysis outputs. These maps are obtained from the CMEMS database (CMEMS product name is SEALEVEL_MED_PHY_L4_REP_OBSERVATIONS_008_051) and are estimated by an optimal interpolation method, merging the measurements from the different available altimeter missions.

2.3 Data Assimilation

The OceanVar data assimilation scheme (Dobricic and Pinardi, 2008) is a variational scheme in which the slowly evolving vertical part of temperature and salinity background error covariances is represented by monthly climatological spatially varying empirical orthogonal functions (EOFs), whilst their horizontal part is assumed to be Gaussian isotropic depending only on distance. In the horizontal direction, we apply the isotropic covariances, because we assume that, due to the large variability of parameters at the high horizontal resolution of the model, it could become very difficult to correctly estimate the complex structures of the horizontal background error covariances by a set of climatological EOFs.

2.3.1 Principles

In the 3DVar formulation of the data assimilation, we need to minimize a cost function J that represents the distance between the analysis and both the background state (the physical model outputs) and the observations. The incremental formulation of J is:

$$J(\delta\mathbf{x}) = \frac{1}{2}\delta\mathbf{x}^{\mathrm{T}}\mathbf{B}^{-1}\delta\mathbf{x} + \frac{1}{2}[\mathbf{H}(\delta\mathbf{x}) - \mathbf{d}]^{\mathrm{T}}\mathbf{R}^{-1}[\mathbf{H}(\delta\mathbf{x}) - \mathbf{d}] \quad (1)$$

where $\mathbf{B}$ and $\mathbf{R}$ are the background- and observation-error covariance matrices. $\delta\mathbf{x} = \mathbf{x} - \mathbf{x}^b$ with $\mathbf{x}$ the ocean state, i.e., the analysis at the minimum of J, and $\mathbf{x}^b$ the background state. In our formulation, we want to correct temperature, salinity and sea surface height so the ocean state is $\mathbf{x} = (T, S, \eta)$. $\mathbf{H}$ is the

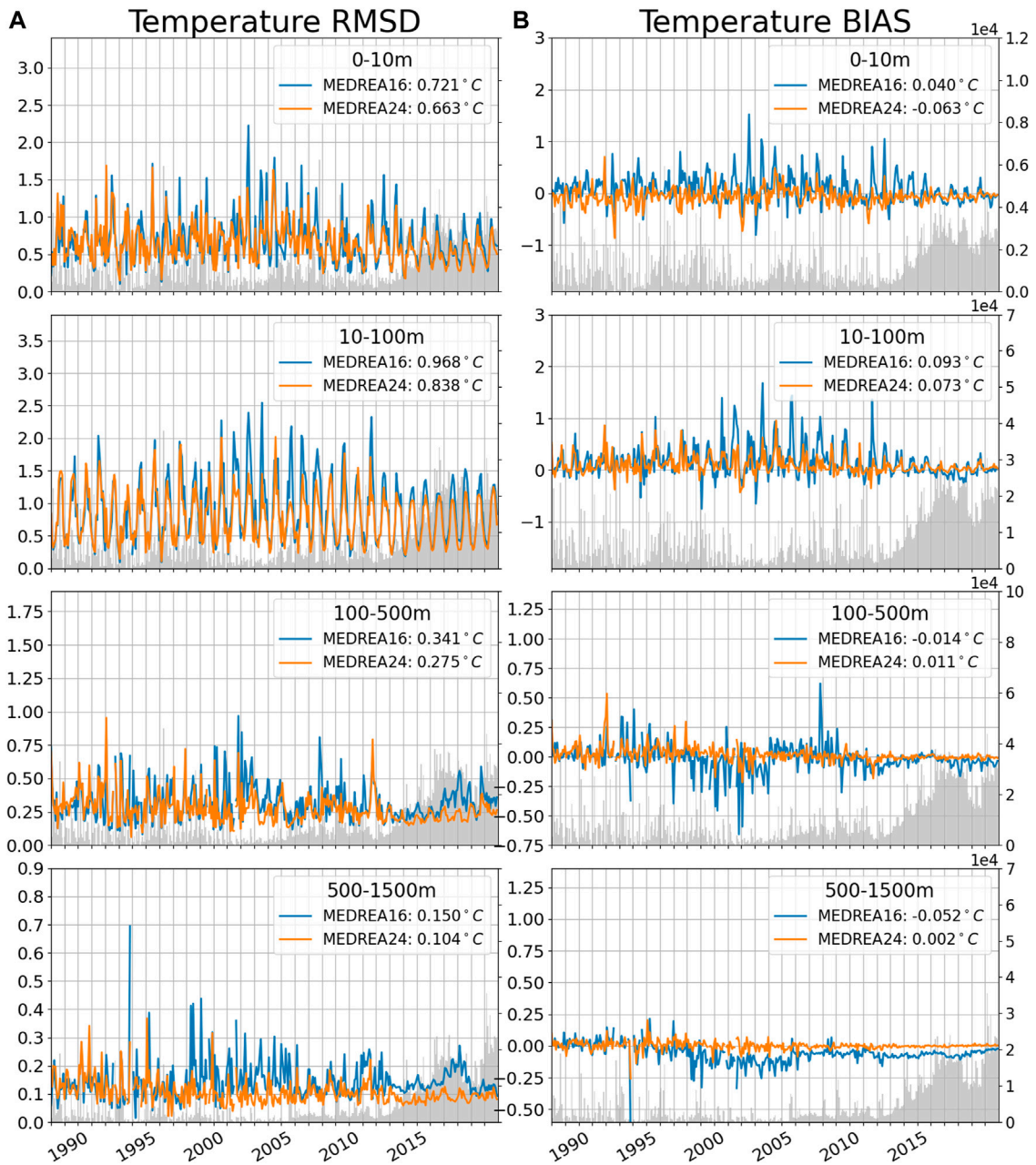

FIGURE 5 | Monthly temperature RMSD **(A)** and bias **(B)** (in °*C*) for the two reanalyses and the hindcast when compared to observed profiles for different layers. The values of RMSD/bias for the whole period are indicated in the legend. The shaded area represents the number of observations for each month **(axis is on the right).** Note the different *y*-axis in the different layers.

observation operator and $\mathbf{d}$ is the innovation vector (background minus observations in the observation space).

We assume that $\mathbf{B}$ can be written in the form $\mathbf{B} = \mathbf{V}\mathbf{V}^{\mathrm{T}}$. Then using the change of variable $\delta\mathbf{x} = \mathbf{V}\mathbf{v}$, the cost function can be written (Control Variable Transformation or CVT):

$$J(\mathbf{v}) = \frac{1}{2}\mathbf{v}\mathbf{v}^{\mathrm{T}} + \frac{1}{2}(\mathbf{H}\mathbf{V}\mathbf{v} - \mathbf{d})^{\mathrm{T}}\mathbf{R}^{-1}(\mathbf{H}\mathbf{V}\mathbf{v} - \mathbf{d}) \quad (2)$$

The CVT provides a way to represent error covariances without explicitly constructing the background-error covariance matrix $\mathbf{B}$. The gradient of the cost function becomes:

$$J' = \mathbf{v} - \mathbf{V}^{\mathrm{T}}\mathbf{H}^{\mathrm{T}}\mathbf{R}^{-1}(\mathbf{H}\mathbf{V}\mathbf{v} - \mathbf{d}) \quad (3)$$

The matrix $\mathbf{V}$ is decomposed into a series of linear operators as follows:

$$\mathbf{V} = \mathbf{V}_{\eta}\mathbf{V}_{H}\mathbf{V}_{V} \quad (4)$$

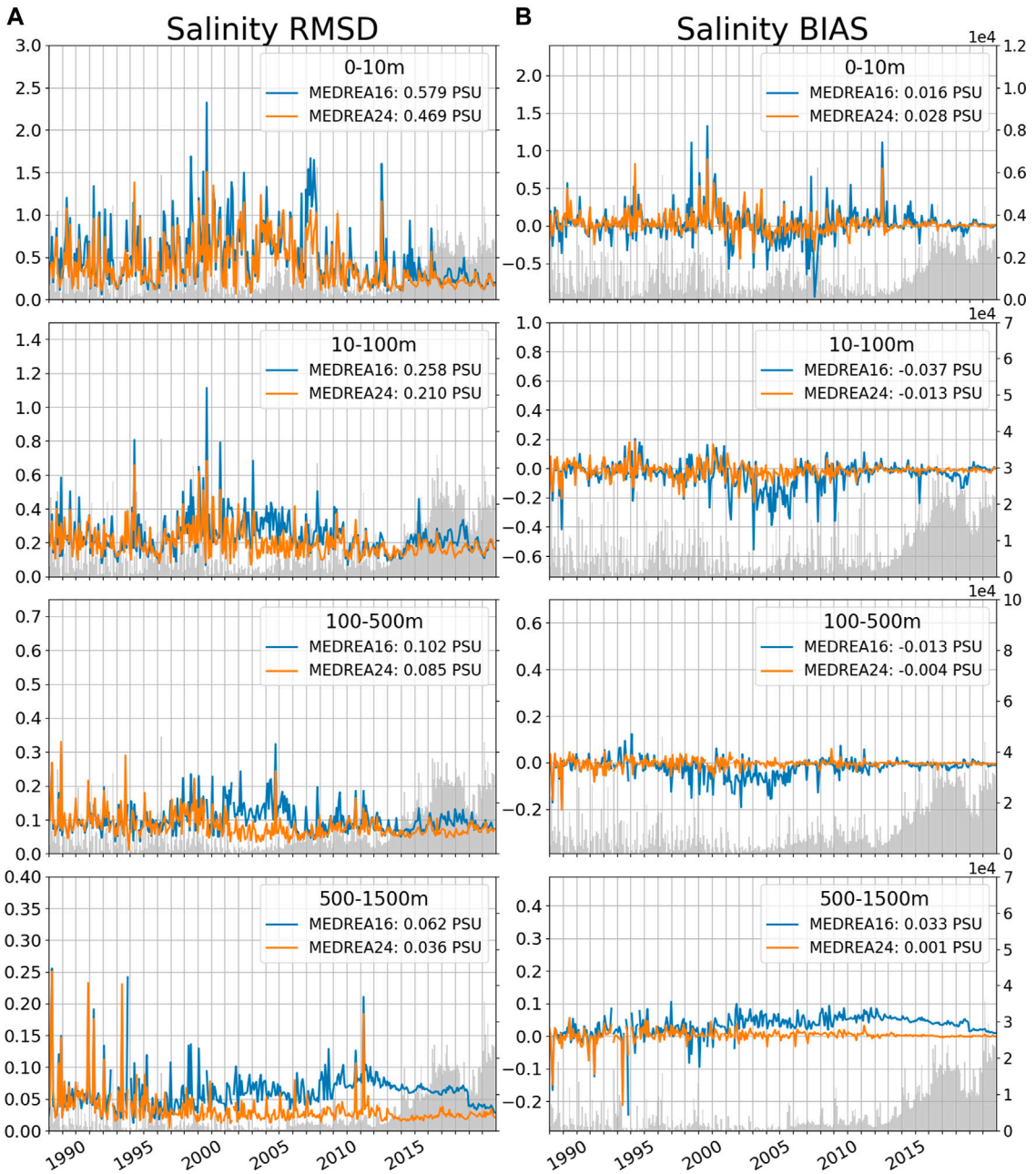

FIGURE 6 | Monthly salinity RMSD **(A)** and bias **(B)** (in PSU) for the two reanalyses and the hindcast when compared to observed profiles for different layers. The values of RMSD/bias for the whole period are indicated in the legend. The shaded area represents the number of observations for each month **(axis is on the right).** Note the different *y*-axis in the different layers.

In **Equation 4** the linear operator $\mathbf{V}_V$ transforms coefficients which multiply vertical EOFs into vertical profiles of temperature and salinity defined at the model vertical levels, $\mathbf{V}_H$ applies horizontal covariances on fields of temperature and salinity, $\mathbf{V}_\eta$ covaries the SSH increments with three-dimensional salinity and temperature increments using dynamic height formulation (Cooper and Haines, 1996; Storto et al., 2011).

In the formulation of **Equation 1**, the fully nonlinear observation operator is used only once for computing the initial departures employing the background fields closer to the observation time (FGAT). The tangent-linear model is used for updating the cost function at each iteration according to the new model state, while the adjoint model is used for mapping the new observation departures back onto the control space for the gradient computation. Their linearization is

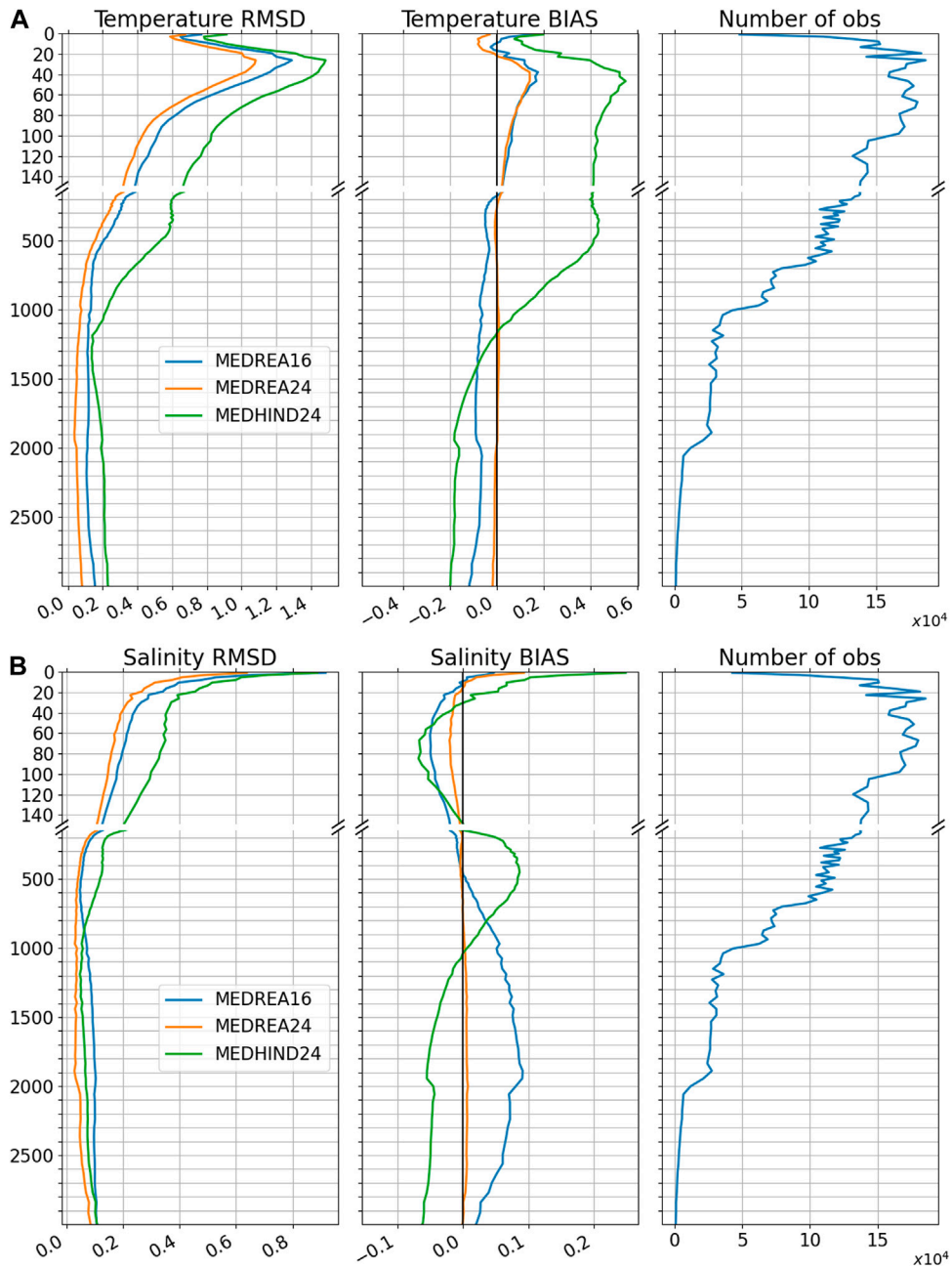

FIGURE 7 | Vertical temperature [**(A)**, in °C] and salinity [**(B)**, in PSU] diagnostics for the two reanalyses and the hindcast when compared to observed profiles for the whole period (1987–2019). The diagnostics were computed on the model layers and the right panel present the number of observations used. The vertical scale is increased on the plot for the first 150 m to better see the upper layers values.

performed around the background fields closer to the observation time. A hybrid-parallel version of OceanVar (similarly to Cipollone et al., 2020) with a standard formulation of the cost function (**Eq. 1** and **Eq. 2**) without other penalty terms is used.

2.3.2 B Matrix

The vertical covariance operator $\mathbf{V}_V$ is composed of 50 monthly climatological trivariate EOFs that were computed from the daily anomalies of a previous 32 years run with data assimilation. These EOF are computed at each model grid point and we apply a vertical localization (Gaussian with length scale of 800 m) to avoid spurious covariances between upper and lower layers. In order to have more independent profiles, we selected only profiles every 5 days. This means that, for example, we use 192 profiles at each location to compute the EOF of the month of January (6 days in each of the 32 years). 50 EOF are enough to reproduce the variability at more

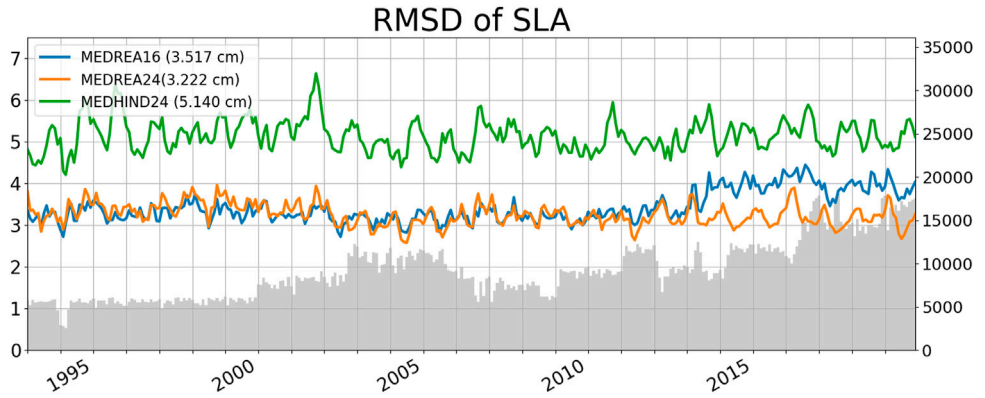

FIGURE 8 | Time evolution of the monthly RMSD of SLA (in cm) for the two reanalyses and the hindcast. The SLA is taken where the ocean is deeper than 1,000 m as it is done for the assimilation. In grey is the number of observations used for this diagnostic.

TABLE 2 | Summary of estimated RMSD compared to observations for the whole Mediterranean Sea. The value is for MEDREA24 and the percentage in parenthesis is the change from MEDREA16.

		Temperature (°C)	Salinity (PSU)
Profiles	Whole column	0.54 (–14%)	0.17 (–18%)
	0–10 m	0.66 (–9%)	0.47 (–19%)
	10–100 m	0.84 (–13%)	0.21 (-19%)
	100–500 m	0.28 (–18%)	0.08 (-20%)
	500–1,500 m	0.11 (–36%)	0.04 (-33%)
Moorings		0.98 (–3%)	0.74 (0%)
	SSH (cm)		
Altimetry		3.2 (–8%)	
Tide gauges		6.7 (–21%)	

than 99.9% (not shown). As an illustration, **Figure 2** presents the correlation between different levels of the model and different variables that come from the 50 EOF computed for two different months at two different points of the Mediterranean Sea. The effect of the vertical localization is visible as the correlations tend towards zero between two levels that are far apart. In the first location and month, temperature and salinity have negative correlation in the first 40 model levels while the second location has a positive correlation for the first 20 model levels. The same procedure adopted for covarying T and S can be extended to include SSH. The correlation obtained in this case is also here plotted (right panels) as information. It is worth stressing that this correlation is purely empirical and can therefore potentially destroy the hydrostatic equilibrium of the water column. In the current version of the reanalysis, we covaried SSH with T and S through a balance operator that will be discussed later. Developments are in place to include also the unbalanced part (from the EOF) in the next version of the system.

The second component of the **V** operator is the recursive filter ($\mathbf{V}_H$). This filter follows the design of Dobricic and Pinardi (2008) to propagate the information of the increment in the horizontal direction. We use a correlation length scale of 15 km which represents the typical Rossby radius of the basin and perform 4 iterations of the first-order filter that are sufficient to reproduce the Gaussian shape with a good degree of accuracy (Dobricic and Pinardi, 2008; Farina et al., 2015).

Finally, the last operator is the dynamic height operator $\mathbf{V}_\eta$. This operator is used to get the SLA anomaly from the temperature and salinity profiles and vice-versa. The method, described in Storto et al. (2011), uses the local hydrostatic adjustment that relies on the vertical integration of density from a "no motion" level where it is assumed that the horizontal pressure gradient is almost zero. This level is fixed at 1,000 m in our configuration and consequently SLA observations in regions where the maximum depth is less than 1,000 m are discarded.

2.3.3 R Matrix

For the covariance error matrix of observations, we assume that the observations are uncorrelated and thus the matrix is diagonal. The information needed is then the variance of the observation error. This error e^o is the sum of the measurement or instrument error e^μ and the representativity error e^r that is made when we put the continuous ocean into a gridded field: $e^o = e^\mu + e^r$. While the former is relatively easy to get from sensor manufacturers, the second is more difficult as it depends on the model grid and local dynamics. To estimate the full observation error, we then used the method prescribed in Desroziers et al. (2005). This iterative method estimates the observation errors by using the innovations and residuals from repeated runs of the system. We first prescribed the errors used in the previous system and then iterated using errors estimated from the formulae in Desroziers et al. (2005). When the errors are no longer changing (3 iterations in our case), we have obtained an estimation of e^o.

Figure 3 presents the final vertical profile of the observation error standard deviation that we obtained for the different platforms that we assimilate (XBT, CTD, and ARGO floats). We apply these profiles of error in the whole domain, meaning that there is no space dependency and only seasonal and vertical dependency. For the temperature, the

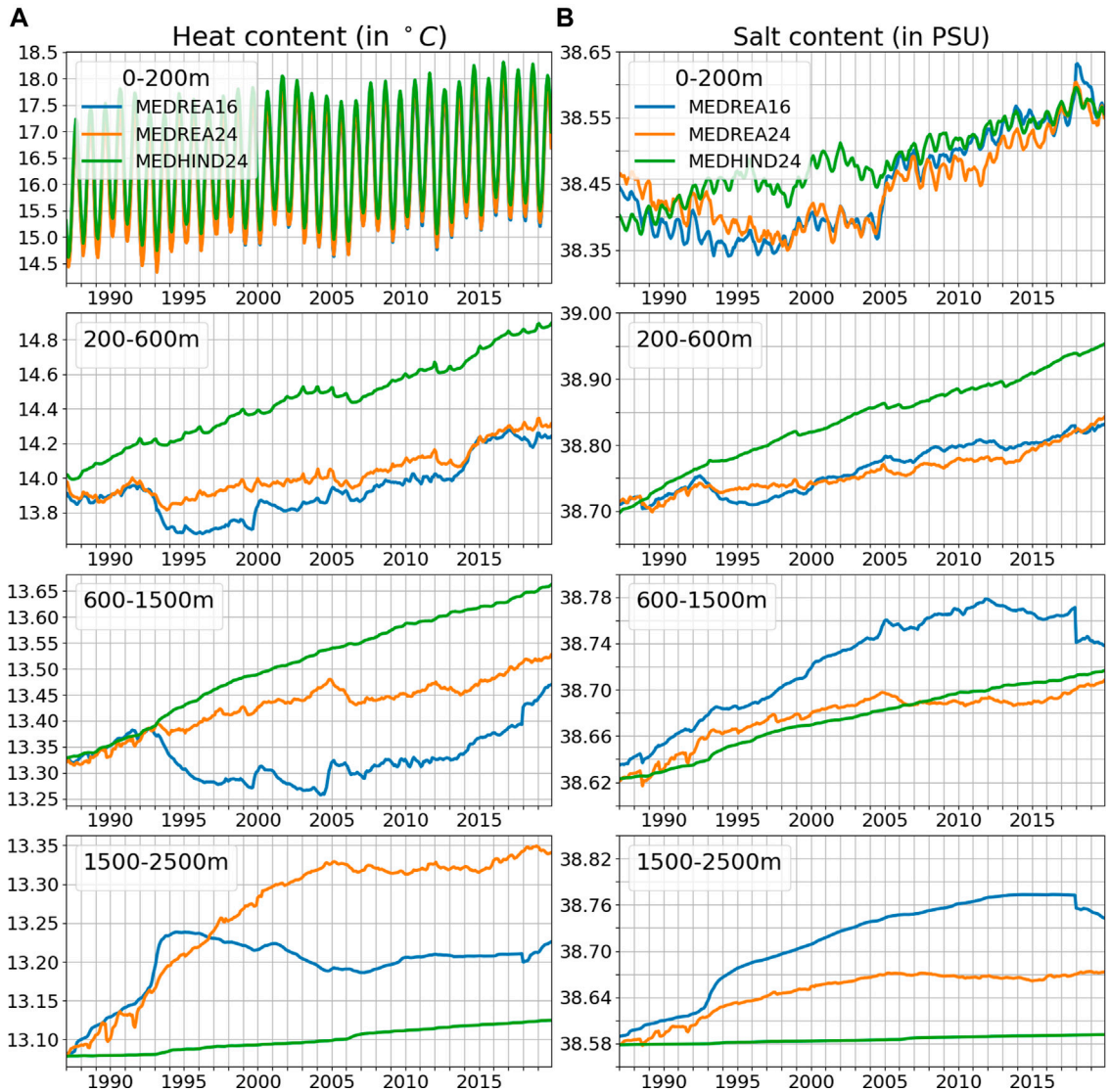

FIGURE 9 | Time evolution of heat content [**(A)**, in °C] and salt content [**(B)**, in PSU] in different layers for both reanalyses and the hindcast. These are averaged over the whole Mediterranean Sea.

error profiles are similar with a strong seasonal variability in the thermocline region. We can note that the salinity error for the CTD is much higher in the surface than ARGO error. This is because CTD observations are much more coastal and model salinity in these locations can diverge strongly from observations due to rivers outflow. The observations error then reflects this discrepancy.

For the SLA assimilation, the observation error is fixed to be constant in time and space. The satellites have different instrument error but the differences are assumed to be small and therefore we can use the same error as a first approximation. The value of this observation error is set to 3 cm and was estimated using sensitivity experiments. These experiments were performed for 2 years (2004–2005) and the analysis global statistics as well as the study of well documented mesoscale events resulted in the value of 3 cm and the use of unfiltered SLA variable in the dataset proving to better represent the regional features with lower error. The estimation from the formula in Desroziers et al. (2005) confirms that 3 cm is a good guess for the total error.

The system implements a background quality check procedure that rejects observations whose square departure exceeds a certain number of times the sum of the observational and background-error variances. For the *ith* observation, the observation retention criterion reads

$$\left(y_i - H_i\left(x^b\right)\right)^2 \leq \gamma\left[\sigma_{o,i}^2 + \sigma_{b,i}^2\right] \tag{5}$$

with $\sigma_{o,i}^2$ and $\sigma_{b,i}^2$ the observation and background-error variances, in observation space, and γ the quality check threshold. In order to be conservative and remove very few observations while still rejecting observations that really diverge from the model

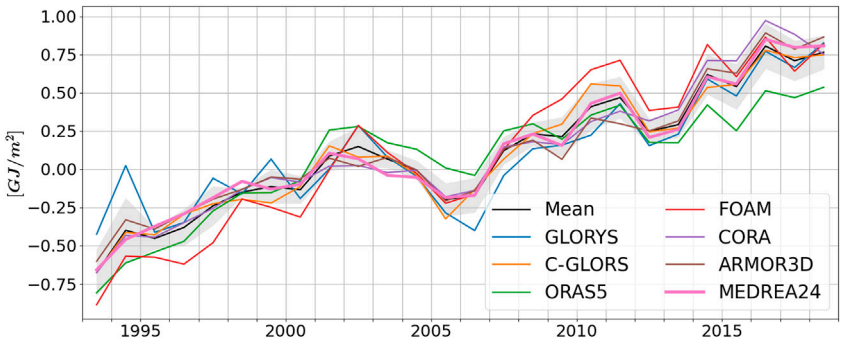

FIGURE 10 | Time series of area averaged ocean heat content anomaly in the Mediterranean Sea, and integrated over the 0–700 m depth layer. Time series are based on different data products. The mean profile is in black and the grey shaded area corresponds to the ensemble spread.

trajectory, we decided to use $\gamma = 64$ for SLA observations and $\gamma = 100$ for *in-situ* profiles after performing a sensitivity study.

3 ASSESSMENT

To evaluate the quality of the reanalyses, the daily model outputs have been bi-linearly horizontally interpolated at each observational position considering the four closest model grid points and then linearly vertically interpolated. These interpolated outputs (Y_{model}) are then compared to the observations measurements (Y_{obs}) and we compute the Root Mean Square Difference (RMSD) and bias as:

$$RMSD = \sqrt{\frac{\sum^{N_{obs}} (Y_{model} - Y_{obs})^2}{N_{obs}}} \quad , \qquad bias = \frac{\sum^{N_{obs}} (Y_{model} - Y_{obs})}{N_{obs}} \tag{6}$$

The observations used in the validation assessment are mostly from the same datasets used for the data assimilation. However, since the assimilation is performed at the end of the day, the evaluation is done before each observation is assimilated (the increment is applied on the following day) and thus it can be considered as quasi-independent.

To provide another reference, a hindcast, run of the numerical model without data assimilation or SST relaxation, is also presented (hereafter called MEDHIND24).

3.1 Sea Surface Temperature

The time evolution of the RMSD and bias of the comparison with SST observations from satellites is shown in **Figure 4**. For the SST diagnostics, the observations are not fully independent as the SST observations are used to correct the heat fluxes in NEMO (see *Numerical Model*).

Both MEDREA16 and MEDREA24 present a positive bias, meaning that the first layer of the model is warmer than the SST observations. This bias is positive in the whole basin (not shown). However, it is decreasing with time as the model gets closer to the observed SST values. The RMSD also decreases with time as a consequence of the diminishing bias. The new reanalysis has consistently a smaller bias and RMSD than MEDREA16 in summer when the difference is the largest. The RMSD value over the whole period is $0.78^{\circ}C$ for the previous reanalysis and $0.65^{\circ}C$ for the new one. This improvement is attributed to the atmospheric forcing fields (ERA5) that perform better in the region compared to the previous version (ERA-INTERIM). The hindcast SST RMSD and bias is higher than the reanalysis showing that the relaxation to the SST observations is having the intended effect.

3.2 Temperature

In this section, we compare the model outputs with temperature profile measurements from CTD, XBT, and ARGO floats. These observations are assimilated but, as mentioned before, their values are compared to the model daily outputs before the observation is assimilated.

The time evolution of the monthly RMSD for different layers of the whole Mediterranean domain is reported in the of **Figure 5A**. The RMSD is highest in the 10–100 m depth layer with highly seasonal variability and largest values in summer. The shallow layer (0–10 m) also presents a seasonal signal with high values in summer. This is clearer in the most recent years (after 2010) when there is a more constant time coverage of the observations due to the ARGO floats. Deeper layers have very little seasonality and also present a very low variability after 2010. MEDREA24 performs consistently better than MEDREA16, especially at depth and in the most recent years. A possible reason for this improvement is that, in MEDREA16, there were less assimilated profiles and virtually no assimilated observation below 1,000 m.

Looking at the bias in **Figure 5B** , this improvement at depth is associated to a reduction of a negative bias. This figure also shows less temporal variability of the bias in MEDREA24 in all the layers confirming the better skill of this version. In this reanalysis there is no persistent bias that we can detect at any layer. We note that in January 2000, there is a spike in the RMSD with a corresponding negative bias. This comes from "bad observations" where a whole campaign of observations in the Western Mediterranean is present in the observation dataset but

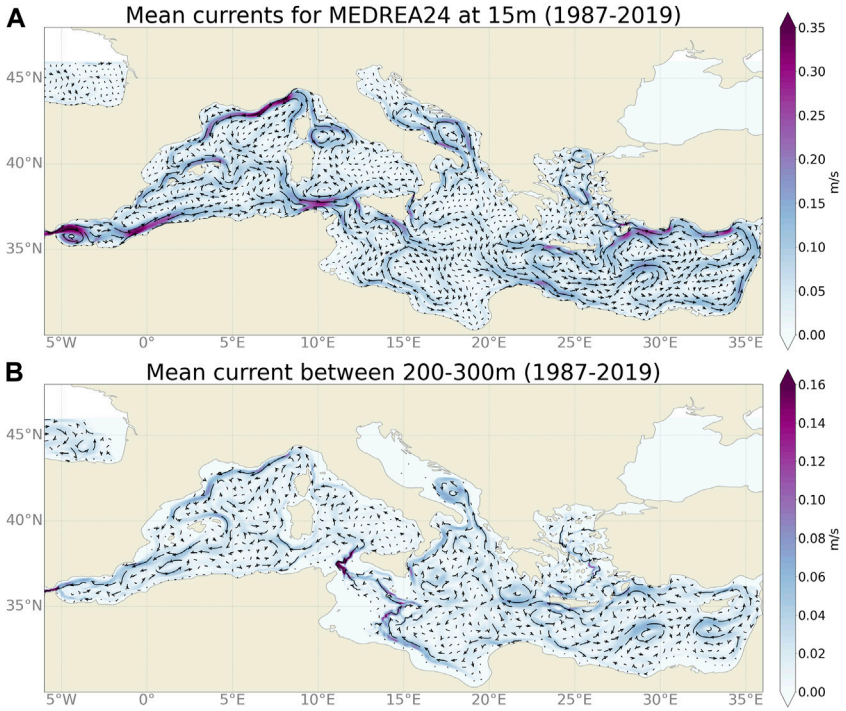

FIGURE 11 | Average currents from MEDREA24 at 15 m **(A)** and between 200–300 m depth **(B)** for the period 1987–2019.

the values of temperature (around 28°*C* at the surface) suggest that these observations were made in summer.

A more detailed view of the vertical comparison and the comparison with the hindcast outputs is offered in the top panels of **Figure 7**. It clearly shows the improvement of the new reanalysis compared to MEDREA16 in temperature at all depths, especially in the deep ocean. Below 200 m, the remaining bias is largely reduced in MEDREA24. The hindcast results show that the reduction of the bias can be largely attributed to data assimilation. The maximum error is found in the thermocline, at around 30 m, in both reanalyses and corresponds to the peak in summer in the time evolution. It is hypothesized that this error is due to an imperfect vertical mixing scheme that results in errors in the position of the thermocline during this season. The bias maximum is slightly below the depth of the maximum error, at around 50 m, and positive, indicating a possible overestimation of the mixed layer thickness as the temperature is stratified during summer period and the water column is well mixed during winter season. As seen in **Figure 5**, this bias is however greatly reduced in the more recent years. Between 20 and 200 m, both reanalyses present a resulting positive bias due to the summer overestimation of the temperature shown in the previous picture. In the upper layers, the error is very similar between the two experiments but the bias has an opposite sign. This discrepancy should come from data assimilation or more likely the heat flux correction by the observed SST since the hindcast shows a similar bias as MEDREA16. Indeed, in the previous section, the SST from satellite was consistently lower than the model SST resulting in relaxation toward cooler SST. The atmospheric forcing could have also an impact as the atmospheric fields are different with MEDREA24 using the more recent hourly fields from ERA5 whereas MEDREA16 uses 6-hourly fields from ERA-INTERIM. An internal evaluation of the ERA5 fields showed lower values of 2 m temperature in summer and an increase of the averaged cloud cover all year over the Mediterranean in comparison with ERA-Interim. This can explain part of the reduction of the positive bias in the surface layers as, which is highest in summer (see **Figure 5**).

3.3 Salinity

The daily model estimates are here compared to the salinity profiles from CTD surveys and ARGO floats. The monthly time evolution of the RMSD for different layers is shown in **Figure 6A**. The highest error is found in the upper layers as 0.47 PSU and 0.58 PSU for the new and the old reanalysis, respectively. At all the layers, there is a strong variability in the early years that is reduced significantly in the ARGO era when there is a much better coverage of the region. The error is consistently decreased with the new reanalysis with the largest improvement in the deep layers.

Bias evolution (**Figure 6B**) confirms the decrease of variability in the later years. Below 50 m, the increase of the error of the MEDREA16 is shown to be related to a positive salinity bias. On average, the bias is improved in MEDREA24 except in the near surface where the average value is higher. However, at the surface, the bias of the new reanalysis does not appear to be consistent and

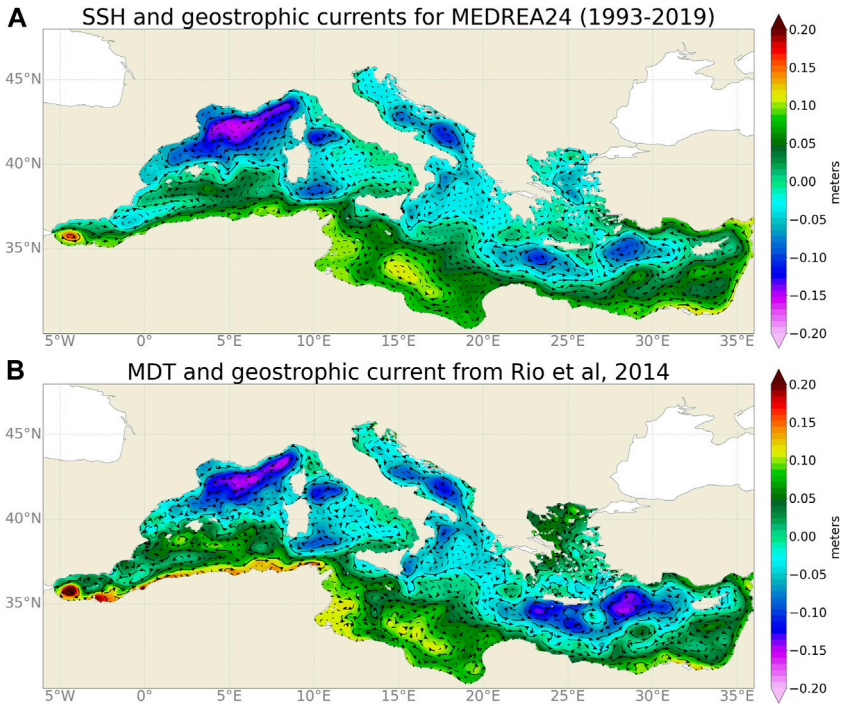

FIGURE 12 | Mean SSH and associated geostrophic currents for MEDREA24 during the period 1993–2019 **(A)** and Mean Dynamic Topography **(B)** used for the SLA assimilation. A global constant has been removed in the basin in both plots.

fluctuates in time pointing that this average value may not be significant.

The vertical distribution of these diagnostics is specified in the bottom panels of **Figure 7**, with the hindcast values added for comparison. They confirm that the error is consistently reduced at all depth. The bias is largely reduced at depth too, especially below 1,000 m where the previous reanalysis had a bias. Increased vertical resolution and a more realistic representation of the freshwater inputs, achieved thanks to the increased number of rivers (from 7 to 39, Delrosso 2020) implemented in the new reanalysis, the use of higher spatial and temporal precipitation data, and the improved nesting in the Atlantic Ocean by means of daily open boundary conditions from a global model (instead of monthly climatological fields), could have concurred in the improved representation of the salt budget of the basin. The hindcast salt content (**Figure 7**) still presents some bias at depth and these are corrected by the assimilation of profiles. In the case of MEDREA16, very few observations were assimilated below 1,000 m. We notice that in the first 10 m, the previously mentioned (see **Figure 6**) larger positive bias in the new reanalysis. Horizontal maps of the bias (not shown) seem to indicate that it is related to an underestimation of the low salinity near the rivers and may be related to the non-zero salinity imposed for the river inflow.

3.4 Sea Level Anomalies

The monthly RMSD with SLA observations is reported in **Figure 8**. Again, this is a quasi-independent evaluation as these observations are ingested by the system to correct itself after the evaluation is done.

Both reanalyses boast similar skill with respect to this observational dataset with an error value of 3.2 cm until 2013. Then they start to diverge and the new reanalysis MEDREA24 continues with this behavior whereas MEDREA16 shows a decrease of skill. This is due to the fact that the older reanalysis did not assimilate all the satellites present in this period. Over the whole period, the new reanalysis presents a 8% decrease of the error (from 3.5 to 3.2 cm).

Table 2 presents a summary of the RMSD of the new reanalysis with respect to observations along with the percentage difference compared to the previous reanalysis skill. It highlights the improvement brought by the new reanalysis at least on this particular skill assessment. On the table the RMSD evaluated comparing with fixed moorings surface temperature and salinity and with tide gauges SSH. Considering the moorings temperature and salinity, the new reanalysis does not show significant skill improvements when compared with the previous one. It is to be noted that this comparison is very coastal and near the surface and thus quite limited. Considering the comparison with tide gauges, the reanalysis sea level shows an error of 6.7 cm which is larger than the sea level anomaly error (3.8 cm) computed using altimeter data since tide gauges are located close to the coast but there is an improvement relative to the previous reanalysis (21% decrease of RMSD). In general, the improved skill of the new reanalysis when comparing to fixed and not assimilated data, is mostly due

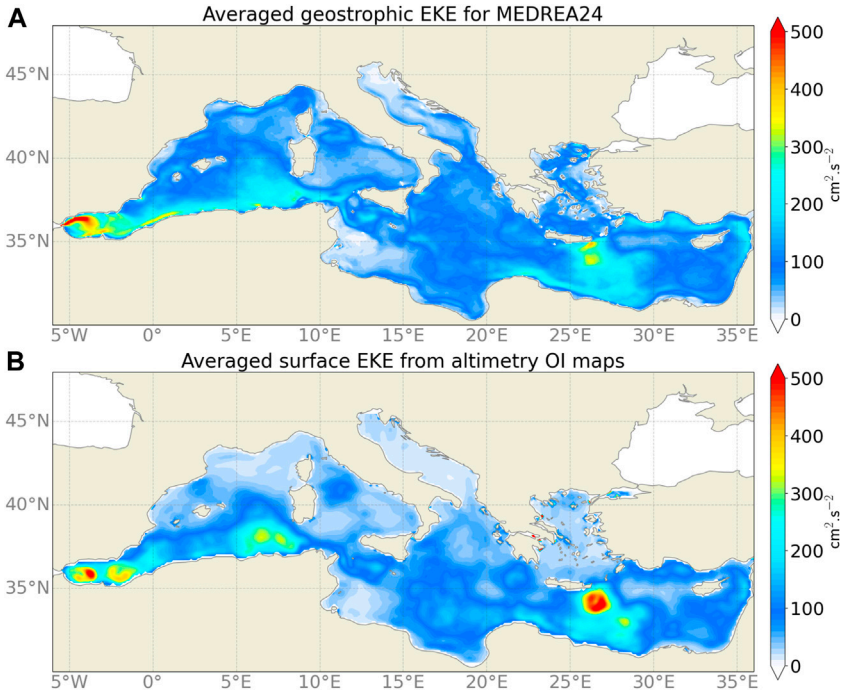

FIGURE 13 | Average geostrophic EKE (in $cm^2.\ s^{-2}$) computed from MEDREA24 SSH **(A)** and altimetry interpolated maps **(B)** for the period 1987–2019.

to improvement of the numerical model as the hindcast skill (not shown) is quite similar.

4 CLIMATE SIGNAL

4.1 Heat Content

The ability of the system to represent climate signals is evaluated looking at the heat content in different layers of the ocean. This heat content, computed as the volume-averaged temperature in different layers from both reanalyses and the hindcast, is presented in **Figure 9A** showing an overall increase of temperature during the considered period in the whole water column.

In the upper 20 m, this signal is mostly dominated by a strong seasonal cycle. The new reanalysis presents a marginally stronger seasonal amplitude (1.30°*C* vs 1.25°*C*) with warmer summers. The hindcast has an intermediate seasonal amplitude (1.28°*C*) with warmer winters, meaning that the assimilation contributes to the cooling of winters. This signal is also modulated by large interannual variability and a positive trend. The interannual variability is similar for all experiments and not negligible and for example, between 1990 and 1992 there is a decrease of 2°*C*. The standard deviation for the interannual signal is 0.16°*C* for all the curves. Concerning the trend, we get 0.026°*C*/year (0.023°*C*/year) increase of temperature for MEDREA24 (MEDREA16). The hindcast trend at the surface is slightly weaker (0.022°*C*/year).

In the layer below (200–600 m), the seasonal signal drops completely with an amplitude below 0.01°*C* for both reanalyses. The new reanalysis presents a steady increase of temperature modulated by some interannual variability. The other reanalysis however saw a larger drop of temperature from 1992 to 1994 followed by a stronger positive trend later. The drop around 1993 is not reproduced in the hindcast. In the end, the computed trend for both is equal to 0.013°*C*/year over the period while the hindcast presents a trend twice as large.

The decreased temperature in the early 90s is also noticeable in the deeper layer (600–1,500 m) for MEDREA16 although it occurs at a later date (after 1993) and more gradually. In MEDREA24, there is no drop of temperature but the trend is reduced after this period while the hindcast heat content keeps increasing at the same pace. Around the end of the simulation, MEDREA16 catches up with the estimation from the new reanalysis, probably thanks to the assimilated observations. As shown in **Figure 5**, the new reanalysis estimate is closer to the observations and the previous one had a cold bias. The trends are respectively 0.002°*C*/year and 0.005°*C*/year for MEDREA16 and MEDREA24 (the hindcast trend is 0.01°*C*/year).

In the bottom layer, both reanalyses have first a phase of warming followed by a period of relative stability. However, the new reanalysis warming phase is longer, lasting until around 2005 and there is still some lighter warming afterwards. The hindcast presents a weaker and constant warming in the deep ocean.

The accuracy of the heat content variations in the new reanalysis can be assessed by comparing it to other products. This is done in the CMEMS OMI (ocean monitoring inticators https://marine.copernicus.eu/access-data/ocean-monitoring-indicators) where the heat content deviation from a reference

period (1993–2014) integrated over the 0–700 m depth layer is computed for global reanalyses and observation-only based products. This is reproduced in **Figure 10** where the estimates from global reanalyses (GLORYS, C-GLORS, ORAS5 and FOAM, from the CMEMS product GLOBAL_REANALYSIS_PHY_001_031) and MEDREA24 are plotted alongside estimates from observation based products (CORA and ARMOR3D). The ensemble mean ocean heat content anomaly time series over the Mediterranean Sea shows a continuous increase in the period 1993–2018 at rate of $1.5 \pm 0.2 W/m^2$ in the upper 700 m. After 2005 the rate has clearly increased with respect to the previous decade, in agreement with Iona et al. (2018). The picture confirms that MEDREA24 is well within the ensemble of estimates and is actually the one that is closest to the mean of all products (lowest RMSD).

4.2 Salt Content

The salt content time evolution in different layers for both reanalyses and the hindcast is reported on **Figure 9B**.

On the first layer, from the surface to 200 m, as with temperature, we observe a seasonal cycle with saltier waters in winter and fresher in summer. However, it accounts for less of the total variability in salt content (58%) than in heat content (97%) in both reanalyses. The salt content is slowly decreasing from 1987 to 2005 when there is a sharp increase followed by a slow increase of salt in the basin. Despite some small differences, the interannual variations are similar in both reanalyses. The hindcast, however, shows a quite different behavior before 2005. This hints that the assimilation of *in-situ* observations has a large effect in the salt content interannual variability for the upper layers. The trend is respectively 0.007 PSU and 0.005 PSU for MEDREA16 and MEDREA24 reflecting that the older reanalysis had a more pronounced decrease at the start and then increase at the end of the period.

On the layer below, there is no more perceivable seasonal cycle and the signal is dominated by interannual variability. Both timeseries present similar characteristics with a trend of 0.0038 PSU/year (MEDREA16) and 0.0032 PSU/year (MEDREA24). As in the heat content, there is a drop of salinity in 1992 in MEDREA16. This dip is no longer present in the new dataset. It is unclear what was the source of this behavior and therefore why it is not seen in the new reanalysis. As seen in the heat content, the trend for the hindcast is twice as large and the assimilation helps avoiding the non-realistic drifts.

In the deeper layer, the drift in the old reanalysis that we already discussed is evidenced with a trend twice higher (0.004 PSU/year) than in the new reanalysis. This trend was not realistic and is here corrected as shown in the previous section (**Figure 7** for example). In 2018, a new initial condition for the extension of the timeseries corrected this bias partially but was not sufficient. For this layer, the hindcast trend is similar to the assimilated run, meaning that the correction of the trend is related to the change in the physical model.

At the bottom of the basin, a similar analysis can be made with the new reanalysis correcting the bottom drift in salinity and the new trend is now 0.0026 instead of 0.0057 PSU/year. Now, the trend of the hindcast is too low compared to the other experiments and this explains the negative bias in the deeper layers found in **Figure 7**.

The changes in temperature and salinity content also have an impact on the mixed layer depth (MLD) in the basin. MEDREA24 MLD climatology is quite consistent with estimations from observations (see the QUID documentation on the CMEMS website for more details, Escudier et al., 2016). Looking at the mean mixed layer depth in convection areas reveals that the new reanalysis has stronger deep convection than MEDREA16 but also the hindcast (not shown), showing that the corrections of temperature and salinity have a strong impact on this variable. This will be analyzed and described more in depth in a further study.

4.3 Currents

The average circulation of MEDREA24 is presented in **Figure 11** on the surface and on the sub-surface (200–300 m). It shows that the new reanalysis is able to correctly reproduce the main currents and circulation. A full description of the circulation can be found in Pinardi et al. (2015) but here we will point out the main features.

At the surface, the water coming from the Atlantic flows through the Gibraltar Strait and forms the two Alboran gyres in the Alboran Sea. The Eastern gyre is smaller in amplitude as it is only semi-permanent. Then the Algerian current that transports this water along the African coast is strong and narrow in the western part and less intense and defined in the eastern part due to the high mesoscale activity and the large anticyclonic eddies that modulate the mean current. South of Sardinia, the current is joined by a current coming from the North along the Sardinia western coast and flows eastward along the Tunisia coast toward the Tyrrhenian Sea. A part of this current then continues eastward along the Northern Sicilian coast, another loops around the South-Western Tyrrhenian Gyre and the rest crosses the Sicily Strait. From the first part, a relatively strong current flows on the surface through the Messina Strait between Sicilia and Italy's mainland while there is a weak circulation northeastward along the Italian coast. In this Tyrrhennian Sea, the other known gyre is the Northern Tyrrhenian Gyre (Artale et al., 1994) which is strongly reproduced in the model. From this gyre, the waters passing through the Corsica channel join the Gulf of Lion gyre and more specifically the northern part of it, the Northern current. This is a relatively strong current that follows the Southern coast of France and even extends along the Spanish Catalan coast, which is better reproduced in this version of the reanalysis. The Balearic current forms the beginning of the return part of the gyre flowing along the Northern coast of the Balearic Islands. In the Ibiza channel, there should be two current, one northward and the other southward (Heslop et al., 2012) and the reanalysis only has a northward current joining the Balearic current. Back at the Sicily Strait, the Algerian current branches into two currents, one southward (Sicily Strait Tunisian Current) and the other eastward along the Southern Sicily coast (Atlantic Ionian Stream, AIS). Both currents then meet a large anticyclonic gyre in the Southern part of the Ionian Sea (Sirte gyre in Pinardi et al., 2015). A part of the AIS meanders northward

until both branches join into the Cretan Passage Southern Current (CPSC). North of this current, the Pelops Eddy (or Pelops Gyre) and the Western Cretan Eddy (Mkhinini et al., 2014) are represented. The CPSC then goes northward to become the Mid-Mediterranean Jet (MMJ, Golnaraghi and Robinson 1994) to form the Mersa Matruh gyre. The Southern Levantine current (SLC) follows the African coastline, bordering the Shikmona gyre in the eastern part of the basin and going northward around Cyprus to become the Asia Minor Current. This current turns southward when arriving at Crete forming the Rhodes gyre on the east and the IeraPetra gyre on the west. In the Aegean Sea, the main currents form a cyclonic circulation around the sea.

The subsurface circulation (bottom of **Figure 11**) corresponds to the circulation of the Levantine Intermediate Water. Starting from the Levantine Sea where the LIW is formed, the Shikmona and Mersa-Matruh gyres are also well defined. The flow follows the surface currents northward along the middle eastern coast and then westward like the Asia Minor current. Then both the Pelops Eddy and the Western Cretan Eddy will modulate the western propagation of the LIW. Some of the current goes northward to the Adriatic Sea and then south-westward along the Italian coast to the Sicily coast. The rest is flowing southward then westward on a coastal current that follows the Sirte gyre southern part. Both branches then join in the Sicily Strait where the highest velocities (0.2 m/s) are reached. The LIW is then advected towards the southern coast of France either in the Tyrrhenian Sea or along the western coast of Sardinia and Corsica. The Northern Current then propagates these waters south-westward to the Balearic Sea where they either turn east along the Balearic Current to circle around the Balearic Islands or they flow through the Ibiza Channel. Then they continue westward along the Spanish coast to reach the Gibraltar Strait.

It is difficult to evaluate quantitatively the differences in the mean circulation with respect to the previous reanalysis and an in-depth analysis is outside of the scope of this section. However, we can highlight some improvements in the surface (see **Figure 3** of Pinardi et al., 2015) such as the Algerian current that is stronger and closer to the coast, the Northern current that reaches further in the Balearic Sea, the clearer separation in three branches south of Sicily (with current coming from the now open Messina Strait), a better representation of the Western Cretan Eddy or the Mersa Matruh gyre that has a better defined structure. As for the subsurface circulation, less is known about it but we can note that the gyres in the Eastern basin are more clearly defined and, in the Western basin, the Northern current goes further west also at depth.

Another view of the surface currents is presented in **Figure 12**. Here the averaged Sea Surface Height (SSH) over the altimetry time period is shown with the resulting geostrophic currents computed from the geostrophic equilibrium. In the figure, the Mean Dynamic Topography (MDT) from Rio et al. (2014) is plotted below as "reference". This MDT is computed using a numerical model as a first guess and then combining it with all the available observations of the currents. This plot allows to clearly see the circulation and especially the various gyres that were discussed above. The modelized mean SSH is smoother than the MDT but displays very similar structures. Some differences can be found in both circulations such as the situation in the Aegean Sea where the model has a more accurate representation of the circulation (see Olson et al., 2007 for an independent estimation).

To characterize the mesoscale activity in the new reanalysis, the average Eddy Kinetic Energy (EKE) over the whole period is represented in **Figure 13**. This EKE was computed from the SSH of the model as well as the SSH from altimetry maps. It allows to estimate the skill of the model keeping in mind the flaws and shortcomings of the altimetry interpolated maps. Indeed, these maps come from an optimal interpolation and therefore the fields are smoothed. In the Alboran Sea, the reanalysis has an eddy activity at the entrance from the Gibraltar Strait and along the entering current. This higher mesoscale activity close to the coast was also found in a high resolution regional model of the Alboran Sea (Peliz et al., 2013). Altimetry maps do not have the capability to resolve these small coastal eddies. In the Algerian current, similar levels of EKE is found in both datasets with the reanalysis having more coastal mesoscale activity. The Northern part of this sub-basin highlights stronger differences with almost no activity in the altimetry maps whereas the reanalysis shows mesoscale variability along the Northern current and in the Balearic Sea. The explanation for this is that the Rossby radius is smaller there than in the Southern part and thus the eddies are smaller (Escudier et al., 2013, 2016). Filtered and interpolated altimetry maps are thus not able to reproduce these structures. In the Tyrrhenian Sea, the EKE is highest around the Northern Tyrrhenian Gyre in both maps but, in the model, the current flowing north of Sicily also presents a stronger EKE. The model EKE in the Adriatic Sea contours the surface currents while the altimetry maps show no mesoscale activity. Here again, the smaller eddies due to a smaller Rossby radius can be the reason behind this discrepancy. In the Eastern part of the basin, the model differs from the remote sensing data with higher EKE along the coast and the coastal surface currents that compose the main cyclonic circulation. The strongest mesoscale activity is found around the Iera-Petra eddy location for both. However, in the altimetry product, variations in the eddy intensity are stronger and there is a clear trace in the EKE. This means that the reanalysis is not capable of fully reproducing the variability of this eddy. The Aegean Sea is a region that is difficult to observe with altimetry due to the high density of islands, therefore the higher EKE in the model is expected. Overall, the model and the observation datasets present similar patterns and most differences can be explained by the fact that the model can resolve smaller scales than the interpolated maps of altimetry.

5 DISCUSSION

This paper describes a new reanalysis of the Mediterranean Sea that was produced in the framework of CMEMS. The new, higher resolution reanalysis shows good skill in the diagnostics performed and represents a significant improvement with respect to the previous version. The positive surface bias in SST is reduced, as well as the negative bias of temperature in the deeper layers.

Concerning salinity, the biases below 500 m are now largely removed. The RMSD when compared to observations is reduced for all variables. The heat content evolution is consistent with observations and other estimates from global models. The surface and sub-surface currents correspond to previous knowledge and the surface EKE is comparable to what is observed with satellite altimetry.

There is still some bias observed in the comparison with satellite SST, even though it is reduced in the new version. This positive bias however is not present in the upper layers when compared to *in-situ* temperature profiles where it is instead negative. This discrepancy hints that the observed profiles are underestimated in the assimilation and that they do not agree with satellite SST. This issue with SST could come from a difference between the model SST we use, the model first layer temperature value, and the SST from satellite observations which is the night SST, so-called foundation SST. These may not be exactly the same and then introduce some biases in temperature at the surface.

The evaluation of the system is mainly done with the same *in-situ* observation dataset that was prepared for the assimilation. However, as mentioned, the model is evaluated before the observation is ingested. We can mention that all the diagnostics were also performed with a different database (EN4, Good et al., 2013) and the results are the same, confirming that the assessment does not depend on the specific dataset used. Completely independent observations are difficult to find as we want to assimilate all the good quality available observations. The comparison with fixed moorings shows relatively high errors for these coastal and sparse measurement and no difference between the two reanalyses. Comparisons with drifters can be made but these have to be treated carefully and some high order diagnostics such as presented in Bouffard et al. (2014) are outside of the scope of this paper.

Concerning the increased error in temperature around 30 m depth, an issue which was also present in the previous version, it is believed to be related to the vertical mixing in the model. Part of this error has been corrected but is still the highest error in temperature. The step forward to improve the model will then be to use a better parametrization of the vertical mixing and the introduction of tides (barotropic and internal) that may affect this process.

This new reanalysis offers a new estimate, more accurate, of the Mediterranean Sea circulation and characteristics. We have shown that its heat content is consistent with other analysis and that the higher resolution allowed to better reproduce the eddy kinetic energy of the geostrophic velocity field with respect to altimetry. The salinity in the deep layers has been corrected and corresponds more closely the observed values. In the future, this reanalysis could be used to study processes such as the overturning circulation or the deep convection in the different basins (i.e. Pinardi et al., 2019; Somot et al., 2016) as well as initial and boundary conditions for nested modeling studies at sub-regional scales.

DATA AVAILABILITY STATEMENT

The original contributions presented in the study are included in the article/Supplementary Materials, further inquiries can be directed to the corresponding author.

AUTHOR CONTRIBUTIONS

RE performed the computation of the reanalysis and its assessment. The other authors contributed to the design of the system. RE wrote the first draft of the manuscript. All authors contributed to manuscript revision, read, and approved the submitted version.

FUNDING

This work was supported by CMEMS Med-MFC (Copernicus Marine Environment Monitoring Service–Mediterranean Marine Forecasting Centre), Mercator Ocean International Service.

REFERENCES

Adani, M., Dobricic, S., and Pinardi, N. (2011). Quality Assessment of a 1985–2007 Mediterranean Sea Reanalysis. *J. Atmos. Oceanic Technol.* 28, 569–589. doi:10.1175/2010JTECHO798.1

Artale, V., Astraldi, M., Buffoni, G., and Gasparini, G. (1994). Seasonal Variability of Gyre-Scale Circulation in the Northern Tyrrhenian Sea. *J. Geophys. Res. Oceans* 99, 14127–14137. doi:10.1029/94JC00284

Bethoux, J., Gentili, B., Morin, P., Nicolas, E., Pierre, C., and Ruiz-Pino, D. (1999). The Mediterranean Sea: a Miniature Ocean for Climatic and Environmental Studies and a Key for the Climatic Functioning of the north atlantic. *Prog. Oceanography* 44, 131–146. doi:10.1016/S0079-6611(99)00023-3

Bouffard, J., Nencioli, F., Escudier, R., Doglioli, A. M., Petrenko, A. A., Pascual, A., et al. (2014). Lagrangian Analysis of Satellite-Derived Currents: Application to the north Western Mediterranean Coastal Dynamics. *Adv. Space Res.* 53, 788–801. doi:10.1016/j.asr.2013.12.020

Buongiorno Nardelli, B., Tronconi, C., Pisano, A., and Santoleri, R. (2013). High and Ultra-high Resolution Processing of Satellite Sea Surface Temperature Data over Southern European Seas in the Framework of Myocean Project. *Remote Sensing Environ.* 129, 1–16. doi:10.1016/j.rse.2012.10.012

Carton, J. A., and Santorelli, A. (2008). Global Decadal Upper-Ocean Heat Content as Viewed in Nine Analyses. *J. Clim.* 21, 6015–6035. doi:10.1175/2008JCLI2489.1

Cipollone, A., Storto, A., and Masina, S. (2020). Implementing a Parallel Version of a Variational Scheme in a Global Assimilation System at Eddy-Resolving Resolution. *J. Atmos. Oceanic Technol.* 37, 1865–1876. doi:10.1175/JTECH-D-19-0099.1

Clementi, E., Pistoia, J., Delrosso, D., Mattia, G., Fratianni, C., Storto, A., et al. (2017). "A 1/24 Degree Resolution Mediterranean Analysis and Forecast Modeling System for the Copernicus marine Environment Monitoring Service," in Eight EuroGOOS International Conference, Bergen, Norway, October 3–5, 2017.

Cooper, M., and Haines, K. (1996). Altimetric Assimilation with Water Property Conservation. *J. Geophys. Res. Oceans* 101, 1059–1077. doi:10.1029/95JC02902

Delrosso, D. (2020). *Numerical modelling and analysis of riverine influences in the Mediterranean Sea. Ph.D. thesis, Alma Mater Studiorum Università di Bologna*. Bologna, Italy: Dottorato di ricerca in Geofisica. doi:10.6092/unibo/amsdottorato/9392

Demiraj, E., Bicja, M., Gjika, E., Gjiknuri, L., Gjoka Mucaj, L., Hoxha, F., et al. (1996). *Implications Of Climate Change for the Albanian Coast. Tech. Rep*. Athens, Greece: United Nations Environment Programme.

Desroziers, G., Berre, L., Chapnik, B., and Poli, P. (2005). Diagnosis of Observation, Background and Analysis-Error Statistics in Observation Space. *Q. J. R. Meteorol. Soc.* 131, 3385–3396. doi:10.1256/qj.05.108

Dobricic, S., Dufau, C., Oddo, P., Pinardi, N., Pujol, I., and Rio, M.-H. (2012). Assimilation of Sla along Track Observations in the Mediterranean with an Oceanographic Model Forced by Atmospheric Pressure. *Ocean Sci.* 8, 787–795. doi:10.5194/os-8-787-2012

Dobricic, S., and Pinardi, N. (2008). An Oceanographic Three-Dimensional Variational Data Assimilation Scheme. *Ocean Model* 22, 89–105. doi:10.1016/j.ocemod.2008.01.004

Dufau-Julliand, C., Marsaleix, P., Petrenko, A., and Dekeyser, I. (2004). Three-dimensional Modeling of the Gulf of Lion's Hydrodynamics (Northwest Mediterranean) during January 1999 (Moogli3 experiment) and Late winter 1999: Western Mediterranean Intermediate Water's (Wiw's) Formation and its Cascading over the Shelf Break. *J. Geophys. Res. Oceans* 109. doi:10.1029/2003JC002019

Escudier, R., Bouffard, J., Pascual, A., Poulain, P. M., and Pujol, M. I. (2013). Improvement of Coastal and Mesoscale Observation from Space: Application to the Northwestern Mediterranean Sea. *Geophys. Res. Lett.* 40 (10), 2148–2153. doi:10.1002/grl.50324

Escudier, R., Clementi, E., Omar, M., Cipollone, A., Pistoia, J., Aydogdu, A., et al. (2020). Mediterranean Sea Physical Reanalysis (CMEMS MED-Currents) (Version 1) [Data set]. Copernicus Monitoring Environment Marine Service (CMEMS). doi:10.25423/CMCC/MEDSEA_MULTIYEAR_PHY_006_004_E3R1

Escudier, R., Renault, L., Pascual, A., Brasseur, P., Chelton, D., and Beuvier, J. (2016). Eddy Properties in the Western Mediterranean Sea from Satellite Altimetry and a Numerical Simulation. *J. Geophys. Res. Oceans* 121, 3990–4006. doi:10.1002/2015JC011371

Estubier, A., and Lévy, M. (2000). *Quel schéma numérique pour le transport d'organismes biologiques par la circulation océanique*. Note Techniques du Pole de modelisation, Institut Pierre-Simon Laplace, 81.

Farina, R., Dobricic, S., Storto, A., Masina, S., and Cuomo, S. (2015). A Revised Scheme to Compute Horizontal Covariances in an Oceanographic 3d-Var Assimilation System. *J. Comput. Phys.* 284, 631–647. doi:10.1016/j.jcp.2015.01.003

Fekete, B. M., Vörösmarty, C. J., and Grabs, W. (1999). *Global, Composite Runoff fields Based on Observed River Discharge and Simulated Water Balances*.

Giorgi, F. (2006). Climate Change Hot-Spots. *Geophys. Res. Lett.* 33. doi:10.1029/2006GL025734

Golnaraghi, M., and Robinson, A. R. (1994). "Dynamical Studies of the Eastern Mediterranean Circulation," in *Ocean Processes in Climate Dynamics: Global and Mediterranean Examples* (Springer), 395–406. doi:10.1007/978-94-011-0870-6_17

Good, S. A., Martin, M. J., and Rayner, N. A. (2013). En4: Quality Controlled Ocean Temperature and Salinity Profiles and Monthly Objective Analyses with Uncertainty Estimates. *J. Geophys. Res. Oceans* 118, 6704–6716. doi:10.1002/2013JC009067

Hamon, M., Beuvier, J., Somot, S., Lellouche, J.-M., Greiner, E., Jordà, G., et al. (2016). Design and Validation of Medrys, a Mediterranean Sea Reanalysis over the Period 1992–2013. *Ocean Sci.* 12, 577–599. doi:10.5194/os-12-577-2016

Hersbach, H., Bell, B., Berrisford, P., Hirahara, S., Horányi, A., Muñoz-Sabater, J., et al. (2020). The Era5 Global Reanalysis. *Q. J. R. Meteorol. Soc.* 146, 1999–2049. doi:10.1002/qj.3803

Heslop, E. E., Ruiz, S., Allen, J., López-Jurado, J. L., Renault, L., and Tintoré, J. (2012). Autonomous Underwater Gliders Monitoring Variability at "Choke Points" in Our Ocean System: A Case Study in the Western Mediterranean Sea. *Geophys. Res. Lett.* 39. doi:10.1029/2012GL053717

Houpert, L., Durrieu de Madron, X., Testor, P., Bosse, A., d'Ortenzio, F., Bouin, M.-N., et al. (2016). Observations of Open-Ocean Deep Convection in the Northwestern M Editerranean S Ea: Seasonal and Interannual Variability of Mixing and Deep Water Masses for the 2007-2013 Period. *J. Geophys. Res. Oceans* 121, 8139–8171. doi:10.1002/2016JC011857

Hulme, M., Barrow, E. M., Arnell, N. W., Harrison, P. A., Johns, T. C., and Downing, T. E. (1999). Relative Impacts of Human-Induced Climate Change and Natural Climate Variability. *Nature* 397, 688–691. doi:10.1038/17789

Iona, A., Theodorou, A., Sofianos, S., Watelet, S., Troupin, C., and Beckers, J.-M. (2018). Mediterranean Sea Climatic Indices: Monitoring Long-Term Variability and Climate Changes. *Earth Syst. Sci. Data* 10, 1829–1842. doi:10.5194/essd-10-1829-2018

Juza, M., Mourre, B., Lellouche, J.-M., Tonani, M., and Tintoré, J. (2015). From basin to Sub-basin Scale Assessment and Intercomparison of Numerical Simulations in the Western Mediterranean Sea. *J. Mar. Syst.* 149, 36–49. doi:10.1016/j.jmarsys.2015.04.010

Juza, M., Mourre, B., Renault, L., Gómara, S., Sebastián, K., Lora, S., et al. (2016). Socib Operational Ocean Forecasting System and Multi-Platform Validation in the Western Mediterranean Sea. *J. Oper. Oceanography* 9, s155–s166. doi:10.1080/1755876X.2015.1117764

Kourafalou, V., and Barbopoulos, K. (2003). *High Resolution Simulations on the north Aegean Sea Seasonal Circulation*. doi:10.5194/angeo-21-251-2003

Le Traon, P. Y., Reppucci, A., Alvarez Fanjul, E., Aouf, L., Behrens, A., Belmonte, M., et al. (2019). From Observation to Information and Users: The Copernicus marine Service Perspective. *Front. Mar. Sci.* 6, 234. doi:10.3389/fmars.2019.00234

Madec, G., Bourdallé-Badie, R., Bouttier, P.-A., Bricaud, C., Bruciaferri, D., Calvert, D., et al. (2017). *NEMO Ocean Engine*. Paris, France: Notes du Pôle de modélisation de l\'Institut Pierre-Simon Laplace (IPSL). doi:10.5281/zenodo.1472492

Madec, G., Delecluse, P., Imbard, M., and Levy, C. (1997). *OPA, Release 8, Ocean General Circulation Reference Manual Tech. Rep*. Technical report 96/xx. LODYC/IPSL, Paris, France.

Malanotte-Rizzoli, P., Manca, B. B., d'Alcala, M. R., Theocharis, A., Brenner, S., Budillon, G., et al. (1999). The Eastern Mediterranean in the 80s and in the 90s: the Big Transition in the Intermediate and Deep Circulations. *Dyn. Atmospheres Oceans* 29, 365–395. doi:10.1016/S0377-0265(99)00011-1

Maraldi, C., Chanut, J., Levier, B., Ayoub, N., De Mey, P., Reffray, G., et al. (2013). NEMO on the Shelf: Assessment of the Iberia–Biscay–Ireland Configuration. *Ocean Sci.* 9 (4), 745–771. doi:10.5194/os-9-745-2013

Medoc Group, T., et al. (1970). Observation of Formation of Deep Water in the Mediterranean Sea, 1969. *Nature* 227, 1037–1040. doi:10.1038/2271037a0

Mkhinini, N., Coimbra, A. L. S., Stegner, A., Arsouze, T., Taupier-Letage, I., and Béranger, K. (2014). Long-lived Mesoscale Eddies in the Eastern Mediterranean Sea: Analysis of 20 Years of Aviso Geostrophic Velocities. *J. Geophys. Res. Oceans* 119, 8603–8626. doi:10.1002/2014JC010176

Oddo, P., Adani, M., Pinardi, N., Fratianni, C., Tonani, M., and Pettenuzzo, D. (2009). A Nested Atlantic-Mediterranean Sea General Circulation Model for Operational Forecasting. *Ocean Sci.* 5 (4), 461–473. doi:10.5194/os-5-461-2009

Oddo, P., Bonaduce, A., Pinardi, N., and Guarnieri, A. (2014). Sensitivity of the Mediterranean Sea Level to Atmospheric Pressure and Free Surface Elevation Numerical Formulation in Nemo. *Geosci. Model. Dev.* 7, 3001–3015. doi:10.5194/gmd-7-3001-2014

Oddo, P., Pinardi, N., and Zavatarelli, M. (2005). A Numerical Study of the Interannual Variability of the Adriatic Sea (2000–2002). *Sci. Total Environ.* 353, 39–56. Mucilages in the Adriatic and Tyrrhenian Seas. doi:10.1016/j.scitotenv.2005.09.061

Olita, A., Dobricic, S., Ribotti, A., Fazioli, L., Cucco, A., Dufau, C., et al. (2012). Impact of Sla Assimilation in the Sicily Channel Regional Model: Model Skills and Mesoscale Features. *Ocean Sci.* 8, 485–496. doi:10.5194/os-8-485-2012

Olson, D. B., Kourafalou, V. H., Johns, W. E., Samuels, G., and Veneziani, M. (2007). Aegean Surface Circulation from a Satellite-Tracked Drifter Array. *J. Phys. Oceanography* 37, 1898–1917. doi:10.1175/JPO3028.1

Pacanowski, R., and Philander, S. (1981). Parameterization of Vertical Mixing in Numerical Models of Tropical Oceans. *J. Phys. Oceanography* 11, 1443–1451. doi:10.1175/1520-0485

Peliz, A., Boutov, D., and Teles-Machado, A. (2013). The Alboran Sea Mesoscale in a Long Term High Resolution Simulation: Statistical Analysis. *Ocean Model.* 72, 32–52. doi:10.1016/j.ocemod.2013.07.002

Pettenuzzo, D., Large, W., and Pinardi, N. (2010). On the Corrections of Era-40 Surface Flux Products Consistent with the Mediterranean Heat and Water Budgets and the Connection between basin Surface Total Heat Flux and Nao. *J. Geophys. Res. Oceans* 115. doi:10.1029/2009JC005631

Pinardi, N., Cessi, P., Borile, F., and Wolfe, C. L. P. (2019). The Mediterranean Sea Overturning Circulation. *J. Phys. Oceanography* 49, 1699–1721. doi:10.1175/jpo-d-18-0254.1

Pinardi, N., Zavatarelli, M., Adani, M., Coppini, G., Fratianni, C., Oddo, P., et al. (2015). Mediterranean Sea Large-Scale Low-Frequency Ocean Variability and

Water Mass Formation Rates from 1987 to 2007: A Retrospective Analysis. *Prog. Oceanography* 132, 318–332. doi:10.1016/j.pocean.2013.11.003

Pisano, A., Buongiorno Nardelli, B., Tronconi, C., and Santoleri, R. (2016). The New Mediterranean Optimally Interpolated Pathfinder Avhrr Sst Dataset (1982–2012). *Remote Sensing Environ.* 176, 107–116. doi:10.1016/j.rse.2016.01.019

Raicich, F. (1996). On the Fresh Balance of the Adriatic Sea. *J. Mar. Syst.* 9, 305–319. doi:10.1016/S0924-7963(96)00042-5

Report, P. U. (2015). Atlas of Riverine Inputs to the Mediterranean Sea. *Tech. Rep.*.

Reynolds, R. W., Smith, T. M., Liu, C., Chelton, D. B., Casey, K. S., and Schlax, M. G. (2007). Daily High-Resolution-Blended Analyses for Sea Surface Temperature. *J. Clim.* 20, 5473–5496. doi:10.1175/2007JCLI1824.1

Rio, M.-H., Pascual, A., Poulain, P.-M., Menna, M., Barceló, B., and Tintoré, J. (2014). Computation of a New Mean Dynamic Topography for the Mediterranean Sea from Model Outputs, Altimeter Measurements and Oceanographic *In Situ* Data. *Ocean Sci.* 10, 731–744. doi:10.5194/os-10-731-2014

Robinson, A., Leslie, W., Theocharis, A., and Lascaratos, A. (2001). "Mediterranean Sea Circulation," in *Encyclopedia of Ocean Sciences*. Editor J. H. Steele (Oxford: Academic Press), 1689–1705. doi:10.1006/rwos.2001.0376

Simoncelli, S., Coatanoan, C., Myroshnychenko, V., Sagen, H., Bäck, Örjan., Scory, S., et al. (2015). First Release of Regional Climatologies. WP10 Third Year Report - DELIVERABLE D10.3. *Tech. Rep., Seadatanet*. doi:10.13155/50381

Simoncelli, S., Fratianni, C., Pinardi, N., Grandi, A., Drudi, M., Oddo, P., et al. (2019). Mediterranean Sea Physical Reanalysis (CMEMS MED-Physics) (Version 1) [Data set]. Copernicus Monitoring Environment Marine Service (CMEMS). doi:10.25423/MEDSEA_REANALYSIS_PHYS_006_004

Simoncelli, S., Masina, S., Axell, L., Liu, Y., Salon, S., Cossarini, G., et al. (2016). MyOcean Regional Reanalyses: Overview of Reanalyses Systems and Main Results. *Mercator Ocean J.* 54.

Somot, S., Houpert, L., Sevault, F., Testor, P., Bosse, A., Taupier-Letage, I., et al. (2016). Characterizing, Modelling and Understanding the Climate Variability of the Deep Water Formation in the north-western Mediterranean Sea. *Clim. Dyn.* 51, 1179–1210. doi:10.1007/s00382-016-3295-0

Storto, A., Alvera-Azcárate, A., Balmaseda, M. A., Barth, A., Chevallier, M., Counillon, F., et al. (2019). Ocean Reanalyses: Recent Advances and Unsolved Challenges. *Front. Mar. Sci.* 6, 418. doi:10.3389/fmars.2019.00418

Storto, A., Dobricic, S., Masina, S., and Di Pietro, P. (2011). Assimilating Along-Track Altimetric Observations through Local Hydrostatic Adjustment in a Global Ocean Variational Assimilation System. *Monthly Weather Rev.* 139, 738–754. doi:10.1175/2010MWR3350.1

Storto, A., and Masina, S. (2016). C-glorsv5: An Improved Multipurpose Global Ocean Eddy-Permitting Physical Reanalysis. *Earth Syst. Sci. Data* 8, 679. doi:10.5194/essd-8-679-2016

Storto, A., Masina, S., and Navarra, A. (2016). Evaluation of the[Cmcc Eddy-Permitting Global Ocean Physical Reanalysis System (C-glors, 1982–2012) and its Assimilation Components. *Q. J. R. Meteorol. Soc.* 142, 738–758. doi:10.1002/qj.2673

Tintoré, J., Pinardi, N., Álvarez-Fanjul, E., Aguiar, E., Álvarez-Berastegui, D., Bajo, M., et al. (2019). Challenges for Sustained Observing and Forecasting Systems in the Mediterranean Sea. *Front. Mar. Sci.* 6, 568. doi:10.3389/fmars.2019.00568

Tonani, M., Balmaseda, M., Bertino, L., Blockley, E., Brassington, G., Davidson, F., et al. (2015). Status and Future of Global and Regional Ocean Prediction Systems. *J. Oper. Oceanography* 8, s201–s220. doi:10.1080/1755876X.2015.1049892

Tonani, M., Nadia, P., S, D., Pujol, I., and Fratianni, C. (2008). A High-Resolution Free-Surface Model of the Mediterranean Sea. *Ocean Sci. (Os)* 4. doi:10.5194/osd-4-213-2007

Tsimplis, M. N., Zervakis, V., Josey, S. A., Peneva, E. L., Struglia, M. V., Stanev, E. V., et al. (2006). "Chapter 4 Changes in the Oceanography of the Mediterranean Sea and Their Link to Climate Variability," in *Of Developments In Earth And Environmental Sciences*. Editors P. Lionello, P. Malanotte-Rizzoli, and R. Boscolo (Elsevier), Vol. 4. doi:10.1016/S1571-9197(06)80007-8

Van Leer, B. (1979). Towards the Ultimate Conservative Difference Scheme. V. A Second-Order Sequel to Godunov's Method. *J. Comput. Phys.* 32, 101–136. doi:10.1016/0021-9991(79)90145-1

Vetrano, A., Napolitano, E., Iacono, R., Schroeder, K., and Gasparini, G. (2010). Tyrrhenian Sea Circulation and Water Mass Fluxes in spring 2004: Observations and Model Results. *J. Geophys. Res. Oceans* 115. doi:10.1029/2009JC005680

Weatherall, P., Marks, K. M., Jakobsson, M., Schmitt, T., Tani, S., Arndt, J. E., et al. (2015). A New Digital Bathymetric Model of the World's Oceans. *Earth Space Sci.* 2, 331–345. doi:10.1002/2015EA000107

Conflict of Interest: The authors declare that the research was conducted in the absence of any commercial or financial relationships that could be construed as a potential conflict of interest.

The reviewer CY declared a past co-authorship with one of the authors SM to the handling Editor.

Publisher's Note: All claims expressed in this article are solely those of the authors and do not necessarily represent those of their affiliated organizations, or those of the publisher, the editors and the reviewers. Any product that may be evaluated in this article, or claim that may be made by its manufacturer, is not guaranteed or endorsed by the publisher.

frontiers in Marine Science

ORIGINAL RESEARCH
published: 29 November 2021
doi: 10.3389/fmars.2021.741486

High-Resolution Reanalysis of the Mediterranean Sea Biogeochemistry (1999–2019)

Gianpiero Cossarini, Laura Feudale, Anna Teruzzi, Giorgio Bolzon, Gianluca Coidessa, Cosimo Solidoro, Valeria Di Biagio, Carolina Amadio, Paolo Lazzari, Alberto Brosich and Stefano Salon*

National Institute of Oceanography and Applied Geophysics - OGS, Trieste, Italy

Ocean reanalyses integrate models and observations to provide a continuous and consistent reconstruction of the past physical and biogeochemical ocean states and variability. We present a reanalysis of the Mediterranean Sea biogeochemistry at a 1/24° resolution developed within the Copernicus Marine Environment Monitoring Service (CMEMS) framework. The reanalysis is based on the Biogeochemical Flux Model (BFM) coupled with a variational data assimilation scheme (3DVarBio) and forced by the Nucleus for European Modeling of the Ocean (NEMO)–OceanVar physical reanalysis and European Centre for medium-range weather forecasts (ECMWF) reanalysis ERA5 atmospheric fields. Covering the 1999–2019 period with daily means of 12 published and validated biogeochemical state variables, the reanalysis assimilates surface chlorophyll data and integrates EMODnet data as initial conditions, in addition to considering World Ocean Atlas data at the Atlantic boundary, CO_2 atmospheric observations, and yearly estimates of riverine nutrient inputs. With the use of multiple observation sources (remote, *in situ*, and BGC-Argo), the quality of the biogeochemical reanalysis is qualitatively and quantitatively assessed at three validation levels including the evaluation of 12 state variables and fluxes and several process-oriented metrics. The results indicate an overall good reanalysis skill in simulating basin-wide values and variability in the biogeochemical variables. The uncertainty in reproducing observations at the mesoscale and weekly temporal scale is satisfactory for chlorophyll, nutrient, oxygen, and carbonate system variables in the epipelagic layers, whereas the uncertainty increases for a few variables (i.e., oxygen and ammonium) in the mesopelagic layers. The vertical dynamics of phytoplankton and nitrate are positively evaluated with specific metrics using BGC-Argo data. As a consequence of the continuous increases in temperature and salinity documented in the Mediterranean Sea over the last 20 years and atmospheric CO_2 invasion, we observe basin-wide biogeochemical signals indicating surface deoxygenation, increases in alkalinity, and dissolved inorganic carbon concentrations, and decreases in pH at the surface. The new, high-resolution reanalysis, open and freely available from the Copernicus Marine Service, allows users from different communities to investigate the spatial and temporal variability in 12 biogeochemical variables and fluxes at different scales (from

OPEN ACCESS

Edited by:
Marilaure Gregoire, University of Liège, Belgium

Reviewed by:
John Patrick Dunne, Geophysical Fluid Dynamics Laboratory (GFDL), United States
Cristina Sobrino, University of Vigo, Spain

***Correspondence:**
Gianpiero Cossarini
gcossarini@inogs.it

Specialty section:
This article was submitted to Marine Biogeochemistry, a section of the journal Frontiers in Marine Science

Received: *14 July 2021*
Accepted: *28 September 2021*
Published: *29 November 2021*

Citation:
Cossarini G, Feudale L, Teruzzi A, Bolzon G, Coidessa G, Solidoro C, Di Biagio V, Amadio C, Lazzari P, Brosich A and Salon S (2021) High-Resolution Reanalysis of the Mediterranean Sea Biogeochemistry (1999–2019). Front. Mar. Sci. 8:741486. doi: 10.3389/fmars.2021.741486

the mesoscale to the basin-wide scale and from daily to multiyear scales) and the interaction between physical and biogeochemical processes shaping Mediterranean marine ecosystem functioning.

Keywords: Mediterranean Sea, biogeochemistry, reanalysis, data assimilation, multi-level validation, multi-scale variability

INTRODUCTION

Optimal integration of physical-biogeochemical observations and models is becoming increasingly urgent to support both scientific and broader environmental communities. This urgency has emerged from the necessity of quantifying the current characteristics and trends of physical and biogeochemical states at global or regional scales (Fennel et al., 2019), including estimates of the carbon cycle, acidification, primary production, and oxygen and nutrient availability. Given their basin-wide, regular, and seamless spatial and temporal coverage, multidecadal reanalyses can constitute a robust basis to compute meaningful and specific environmental indicators that describe the states and trends of key biogeochemical features (e.g., essential climate and ecological variables; Bojinski et al., 2014; Miloslavich et al., 2018), fluxes, and processes that cannot be completely and extensively observed (e.g., the flux of CO_2, primary production, and carbon sequestration). These indicators may support environmental state assessment and monitoring of climate change, and its impact on marine ecosystems, following national or international directives [e.g., European Marine Strategy Framework Directive (MSFD), UNEP/MAP]. From this perspective, the EU Copernicus Marine Environment Monitoring Service (CMEMS) has developed ocean monitoring indicators (OMIs), defined as trends and variability indexes of key marine variables computed for the global ocean and European seas (von Schuckmann et al., 2016, 2018, 2020). At the global scale, OMIs for the ocean biogeochemistry presently account for pH, chlorophyll, CO_2, nitrate, and oxygen minimum zones, whereas in most regional seas, only the surface chlorophyll OMI extracted from reprocessed satellite ocean color data is available.

As a semienclosed sea with a complex orography, the Mediterranean Sea exhibits high variability in physical (Pinardi and Masetti, 2000; Pinardi et al., 2015), biogeochemical, and biological characteristics (Siokou-Frangou et al., 2010). Additionally, intense anthropogenic pressure (Hulme et al., 1999; Micheli et al., 2013) and effects of climate change (Giorgi, 2006) make the Mediterranean Sea a challenging research area, as multiple signals at different scales interact. While basin-wide physical tendencies have been presented (Escudier et al., 2021 and references therein), biogeochemical tendencies are absent and mostly related to single variables (e.g., chlorophyll). Few long-term basin-scale signals of ecosystem changes have been reported for the Mediterranean Sea considering ocean color and *in situ* data. For example, using surface chlorophyll concentrations retrieved from satellite data, Colella et al. (2016) analyzed the 1998–2009 period and reported significant positive trends in most of the western Mediterranean and Rhodes gyre areas and negative trends in the northern Adriatic Sea. A slightly contrasting result was reported by Salgado-Hernanz et al. (2019) and by the CMEMS ocean monitoring product (Sathyendranath et al., 2018) that showed a positive (negative) trend in the western (eastern) Mediterranean subbasin based on an extended period of the reprocessed satellite dataset. Interannual variability in the dissolved oxygen concentration and a link between ventilation change signals in eastern and western Mediterranean deep waters and two major subbasin climatic shifts, i.e., the Eastern and Western Mediterranean Transients (EMT between 1995 and 2001, and WMT between 2004 and 2006, respectively), were recently highlighted (Li and Tanhua, 2020; Mavropoulou et al., 2020). Focusing on limited areas and periods (given the length of *in situ* time series), changes in the deep oxygen concentration have been reported for the Levantine basin (Sisma-Ventura et al., 2021), Gulf of Lions (Coppola et al., 2018), southern Adriatic Sea (Lipizer et al., 2014), and southern Aegean Sea (Velaoras et al., 2019). Additionally, acidification tendency signals have been observed in the western (Gibraltar Strait; Flecha et al., 2015) and eastern Mediterranean Sea (Cretan basin; Wimart-Rousseau et al., 2021), whereas changes in carbonate system variables [e.g., an increase in alkalinity and dissolved inorganic carbon (DIC) concentrations] have been indirectly estimated in relation to climate change and anthropogenic pressure (Schneider et al., 2010; Touratier and Goyet, 2011; Álvarez et al., 2014; Wimart-Rousseau et al., 2021).

Reanalyses can fill observational gaps, providing a three-dimensional, basin-wide, and seamless dataset to investigate temporal and spatial variability on a variety of scales. However, producing a physical–biogeochemical reanalysis is not a trivial task (Park et al., 2018), given the uncertain representativeness of the coupling between physical and biogeochemical processes (particularly vertical transport and consequent effects on the nutricline shape), the limited amount of biogeochemical data (both for assimilation and validation), and the multivariate nature of the biogeochemical state, which includes the complex links between observed (sparse) and simulated (many, in principle) variables. Thus, assessment of the quality of reanalysis products is of paramount importance considering their potential multiple uses (Hernandez et al., 2018). Model validation can be accomplished at different levels (Hipsey et al., 2020), providing uncertainty estimation for modeled variables at different spatial and temporal scales (Stow et al., 2009) and quantifying the modeling capability in terms of the reproduction of ecosystem processes (e.g., Salon et al., 2019; Mignot et al., 2021).

At the Mediterranean basin scale, while long-term simulations with a good performance in reproducing certain specific aspects are available (Lazzari et al., 2012; Macias et al., 2014; Guyennon et al., 2015; Richon et al., 2018; Di Biagio et al., 2019), biogeochemical reanalyses are quite rare. Through the

assimilation of ocean color data in a POLCOMS-ERSEM reanalysis at a 1/10° resolution, Ciavatta et al. (2019) derived a specific eco-regionalization based on phytoplankton functional types. Within the CMEMS framework, a reanalysis at a 1/16° horizontal resolution covering the period from 1999 to 2014 and assimilating ocean color chlorophyll data was made available in 2016 (Teruzzi et al., 2016), and annually extended until 2018 (Teruzzi et al., 2019a). This low-resolution reanalysis has been adopted to investigate the surface nutrient trend (von Schuckmann et al., 2018), the positive trend of the CO_2 air-sea flux (von Schuckmann et al., 2018), and the multidecadal variation in primary production and its relationship with mixing events in the North–Western Mediterranean Sea (Cossarini et al., 2020).

In the present study, we describe a novel version of the CMEMS biogeochemical reanalysis product covering the 1999–2019 period, with a spatial resolution as high as 1/24° horizontally and 125 vertical levels, based on the most advanced version of the Mediterranean Sea Biogeochemical Flux Model system (MedBFM) operationally employed in CMEMS for short-term prediction purposes (Salon et al., 2019). Additionally, the biogeochemical reanalysis includes the latest update of the assimilation scheme (Teruzzi et al., 2018) of ocean color data (Colella et al., 2021) and off-line coupling with the latest release of a physical reanalysis (Escudier et al., 2021). The reanalysis results are available as daily and monthly 3D fields of 12 biogeochemical variables and fluxes through the CMEMS service.

This study is organized as follows: section "Materials and Methods" describes the MedBFM model setup, the upstream data considered to perform the reanalysis, and the validation framework. Section "Reanalysis Validation" presents the main results in terms of multilevel validation. The temporal tendencies and variability emerging from the reanalysis data are provided in section "Reanalysis Variabilities and Trends." A discussion on the reanalysis quality and long-term tendency and conclusions are outlined in sections "Discussion" and "Conclusion," respectively.

MATERIALS AND METHODS

Modeling Framework

The reanalysis of the Mediterranean Sea biogeochemistry at a horizontal resolution of 1/24° (approximately 4 km; the model domain is shown in **Figure 1**), covering the period 1999–2019, was produced with an upgraded version of the MedBFM model system, as detailed and assessed with regard to quality in Salon et al. (2019). In summary, MedBFM was built over the coupling between the OGS transport model (OGSTM), the BFM (Lazzari et al., 2010, 2012, 2016; Cossarini et al., 2015a; Vichi et al., 2020, and references therein), and the 3DVarBio variational scheme that assimilates surface chlorophyll concentrations (Teruzzi et al., 2014, 2018, 2019b). The BFM describes the biogeochemical cycles of carbon and macronutrients (nitrogen, phosphorus, and silicon) in terms of dynamic interactions among the dissolved inorganic, living organic, and non-living organic compartments. Recent MedBFM upgrades, including the assimilation of BGC-Argo float data and biooptical components, have been described in Cossarini et al. (2019) and Terzić et al. (2019, 2021), respectively. MedBFM is coupled off-line with the CMEMS Mediterranean Sea physical reanalysis system (Escudier et al., 2021), which has provided the necessary fields at a daily frequency for 21-year integration (currents, temperature, salinity, diffusivity, wind, and solar radiation) to force tracer transport, dependency of biochemical kinetics on the temperature, and air-sea interactions.

The setup of the biogeochemical component, in addition to that of the physical component, is reported in **Table 1**. Among the listed elements, a relevant dependency is the atmospheric CO_2 partial pressure, which increased almost linearly from 370 ppm in 1999 to 410 ppm in 2019 (data obtained from the ENEA Lampedusa station; Artuso et al., 2009). The nutrient inputs are imbalanced between the two main basins (i.e., the eastern basin receives almost 70% of the loads) and with atmospheric inputs higher than the nutrient discharges originating from rivers. Indeed, the nitrogen inputs into the western and eastern basins reach 41.4 and 39.8 $\times$ 10^9 mol yr^{-1}, respectively stemming from air deposition, and 10.1 and 34.7 $\times$ 10^9 mol yr^{-1} stemming from rivers, respectively. The western and eastern basin phosphorus inputs are 0.53 and 0.67 $\times$ 10^9 mol yr^{-1} originating from the atmosphere and 0.16 and 0.69 $\times$ 10^9 mol yr^{-1} originating from rivers, respectively (Ribera d'Alcalà et al., 2003; van Apeldoorn and Bouwman, 2012).

Although the boundary conditions data [i.e., Atlantic boundaries retrieved from the World Ocean Atlas and GLobal Ocean Data Analysis Project (GLODAP), and nutrient inputs obtained from Perseus] are climatological, the atmospheric (ERA5 data) and ocean dynamics forcing data (Escudier et al., 2021) are daily data, and the assimilated biogeochemical data (surface chlorophyll; Teruzzi et al., 2018) are weekly data, thus driving the high-frequency dynamics of the 21-year long reanalysis model simulation.

Validation Framework

To assess the reanalysis quality, we extended the CMEMS validation metrics framework (Hernandez et al., 2009, 2015, 2018), which was inspired by the GODAE Ocean View initiative (now OceanPredict), by including a set of ecosystem process-based metrics (Salon et al., 2019). Drawing from the multilevel validation framework proposed by Hipsey et al. (2020), we proposed three levels of skill performance metrics applicable to 12 state variables and model fluxes depending on the availability of observations:

- Level 1: Model outputs are compared with climatological references (observational datasets or literature reviews) to quantify the model capability to reproduce basin-wide spatial gradients and mean annual values and average vertical profiles on a subbasin scale (i.e., based on GODAE Class 1 metrics);
- Level 2: Model outputs are compared with observations at the same time and locations (match-ups) to quantify the model capability to reproduce the observed

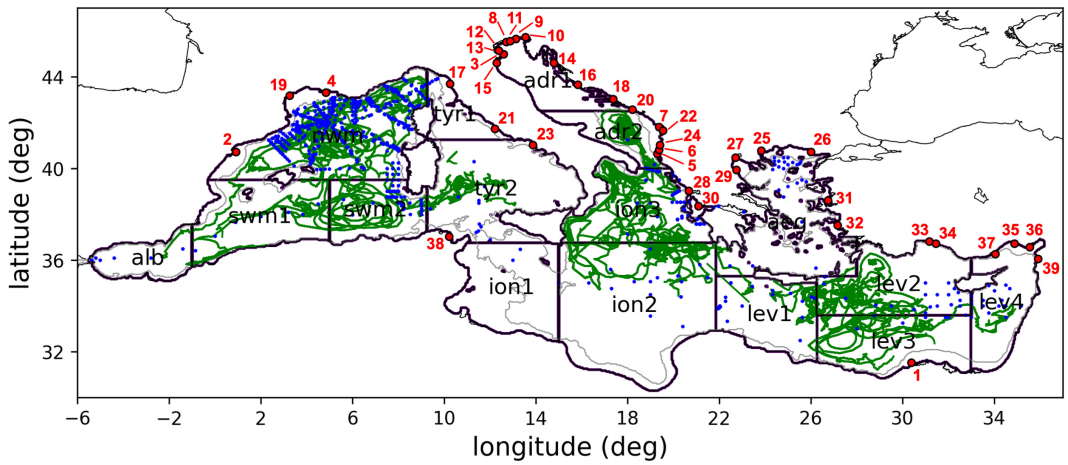

FIGURE 1 | Subdivision of the model domain in sub-basins used for the validation of the reanalysis. According to data availability and to ensure consistency and robustness of the metrics, different subsets of the sub-basins or some combinations among them can be used for the different metrics: lev = lev1 + lev2 + lev3 + lev4; ion = ion1 + ion2 + ion3; tyr = tyr1 + tyr2; adr = adr1 + adr2; swm = swm1 + swm2. The gray line defines the bathymetric contour at 200 m. Blue dots represent open sea observations of nitrate from EMODnet_int data collection (period 1999–2016). Green lines correspond to trajectories of BGC-Argo floats with chlorophyll observations (period 2013–2018). Red dots with numbers correspond to main river mouth positions: Nile (1), Ebro (2), Po (3), Rhone (4), Vjosë (5), Seman (6), Buna/Bojana (7), Piave (8), Tagliamento (9), Soča/Isonzo (10), Livenza (11), Brenta-Bacchiglione (12), Adige (13), Lika (14), Reno (15), Krka (16), Arno (17), Nerveta (18), Aude (19), Trebisjnica (20), Tevere (21), Mati (22), Volturno (23), Shkumbini (24), Struma/Strymonas (25), Meric/Evros/Maritsa (26), Axios/Vadar (27), Arachtos (28), Pinios (29), Acheloos (30), Gediz (31), Buyuk Menderes (32), Kopru (33), Manavgat (34), Seyhan (35), Ceyhan (36), Gosku (37), Medjerda (38), Asi/Orontes (39).

TABLE 1 | Setup of the biogeochemical reanalysis and its off-line coupling with the physical component reanalysis.

	Physical component Escudier et al. (2021)	**Biogeochemical component** Teruzzi et al. (2021)
Bathymetry	Modified GEBCO 30 arc-sec	Modified GEBCO 30 arc-sec
Spatial coverage and resolution	17.3°W, 36.3°E; 30.187°N, 45.98°N	9.0°W, 36.3°E; 30.187°N, 45.98°N
	1/24° horizontal	1/24° horizontal
	141 uneven distributed vertical levels	141 uneven distributed vertical levels (first 125 levels till the 4500 m depth used in the biogeochemical component)
Time coverage	1993–2019 + spin-up	1999–2019 + spin-up
Model	NEMOv3.6 non-linear free-surface; rescaled vertical coordinates (z*)	OGSTM-BFMv5 with non-linear free-surface and rescaled vertical coordinates (z*)
Data assimilation	OceanVar (Dobricic and Pinardi, 2008)	3DVarBio (Teruzzi et al., 2019b)
Assimilated observations	T/S Vertical profiles, SLA along track altimeter (Storto et al., 2016)	Weekly maps of surface chlorophyll from satellite (Colella et al., 2021)
SST nudging	Gaussian around midnight (max = –110 W/m^2/K)	
Kd (light absorption factor)		Weekly from CMEMS OC data (Terzić et al., 2021)
Initial conditions	SeaDataNet Climatological T and S	EMODnet climatological profiles of nitrate, phosphate, silicate, alkalinity, dissolved inorganic carbon and oxygen for 16 sub-basins; reference values for the other state variables (Salon et al., 2019)
Atm. forcing	ECMWF ERA5 (0.25°, 1 h)	Solar radiation (1 h); wind (daily)
		Nitrogen and phosphorus air deposition (Ribera d'Alcalà et al., 2003); air pCO_2 from ENEA Lampedusa station (Artuso et al., 2009)
River input	39 rivers with runoff > 50m^3/s including input from the Dardanelles Strait (treated as a river)	39 rivers with runoff > 50m^3/s including input from the Dardanelles Strait (treated as a river)
	Climatological monthly runoff from Perseus FP7-287600 dataset D4.6	Nitrogen and phosphorus loads from Perseus FP7-287600 dataset D4.6 (van Apeldoorn and Bouwman, 2012); alkalinity and DIC loads from runoff multiplied by reference freshwater concentration (Kempe et al., 1991; Copin-Montégut, 1993; Meybeck and Ragu, 1997)
Atlantic boundary	Boundary at 20°W; data from CGLORS REA 1/4° daily fields	Boundary at 9°W; climatological profiles of nitrate, phosphate, silicate, alkalinity, dissolved inorganic carbon and oxygen from WOA2018 (Garcia et al., 2019) and GLODAP (Olsen et al., 2016, 2019)

Further details can be found in Escudier et al. (2020) and Teruzzi et al. (2021). The symbol "" in the "z*" expression commonly refers to rescaled vertical coordinates.*

spatial-temporal variability due to mesoscale and high-temporal dynamics (i.e., based on GODAE Class4 metrics; Hernandez et al., 2018);

- Level 3: The model capability is evaluated to reproduce key biogeochemical emergent properties using specific process-based metrics and BGC-Argo data (Salon et al., 2019; Feudale et al., 2021). The metrics for nutrient vertical dynamics include the nitracline depth computed as the depth at which the nitrate concentration reaches 2 mmol/m^3 (NITRCL). The metrics for the system productivity include the chlorophyll concentration and depth of the winter bloom layer (WBL), the maximum chlorophyll concentration, and depth of the deep chlorophyll maximum (DCM), and the depth of the subsurface oxygen maximum (OXYMAX).

Most Level 1 and 2 metrics are spatially evaluated for 16 Mediterranean sea subbasins (**Figure 1**), in the open sea region (defined as the area with a depth greater than 200 m), and for the full water column in selected layers, i.e., 0–10, 10–30 m (for certain metrics these layers are merged into a single layer, namely, 0–30 m), 30–60, 60–100, 100–150, 150–300, 300–600, and 600–1,000 m. In the coastal areas, the reanalysis accuracy can be assessed only for surface chlorophyll using the CMEMS satellite product and for other variables and a few subbasins according to *in situ* data availability. The 16 subbasins synthesize the heterogeneity in the Mediterranean Sea into homogeneous areas, considering previous bioregionalization analyses (D'Ortenzio and Ribera d'Alcalà, 2009; Ayata et al., 2018; Di Biagio et al., 2020; El Hourany et al., 2021; Novi et al., 2021).

The skill performance metrics include the bias, root mean square of the differences between the model output and observations (RMSD). Even if other more robust and non-parametric skill metrics and diagrams (Jolliff et al., 2009; Stow et al., 2009) could be preferable for certain variables (e.g., variables not normally distributed), we preferred to adopt the same skill metrics (i.e., applying the CMEMS validation standard; Hernandez et al., 2018) for all variables and validation levels to enhance the comparability and communicability of the results.

The variables and their validation levels are listed in **Table 2** along with a list of the reference data used. In particular, the EMODnet data collections (Buga et al., 2018) integrated with additional oceanographic cruises (references in Cossarini et al., 2015a; Lazzari et al., 2016), hereinafter referred to as EMODnet_int, include 12,257 observations for nitrate, 17,323 observations for phosphate, 104,910 observations for dissolved oxygen, and approximately 4,000 observations for the DIC and alkalinity covering the 1999–2016 period. The CMEMS ocean color product (Colella et al., 2021) comprises daily L3 chlorophyll maps from 1999 to 2019, whereas the surface ocean CO_2 Atlas Database (SOCAT) dataset (Bakker et al., 2016) includes 6,500 surface pCO_2 observations over the 1998–2018 period.

Regarding the ocean color dataset, since assimilation was performed once a week, the above skill performance computation was performed before the surface chlorophyll maps were assimilated. Hence, this dataset could be considered a quasi-independent dataset.

Finally, a quality-checked dataset of BGC-Argo float profiles obtained from Coriolis/Ifremer (Thierry et al., 2018; Argo, 2021) was provided stemming from a number of chlorophyll (53), bbp700 (54), oxygen (53), and nitrate (23) float sensors for the 2014–2019 period. The bbp700 data were converted into carbon biomass data with the relationship proposed by Bellacicco et al. (2019).

Net primary production (NPP) and flux of CO_2 across the air-sea interface validation were based on estimates published in Bosc et al. (2004); Colella (2006), Siokou-Frangou et al. (2010), and Lazzari et al. (2012) in regard to the former process and D'Ortenzio et al. (2008); Melaku Canu et al. (2015), and von Schuckmann et al. (2018) regarding the latter process. In the "Results" section, we present the different validation levels for the selected variables and provide a synthesis of representative normalized skill indicators for all variables, layers, and subbasins. However, to refine uncertainty error estimates at the local scale (e.g., error maps, where available), complementary information is provided in the Quality Information Document contained in the CMEMS catalog (Teruzzi et al., 2021).

Statistical Methods

The reanalysis results were analyzed to estimate different scales of temporal variability, including the overall average, range of the seasonal cycle (difference between the minimum and maximum monthly average values), overall temporal variability (standard deviation of the time series), interannual variability (standard deviation of the annual averages), and trend slope (C-1 method by removing fixed seasonal cycles; Vantrepotte and Mélin, 2009). The significance of the trend slope was assessed with the *t*-test at a *p*-level of 0.025.

RESULTS

Reanalysis Validation

The next three sections (Level 1 Validation to Level 3 Validation) illustrate the application of the three validation levels, thereby providing examples of the comparison between the observations and model results. Although these three sections illustrate the accuracy of the model in terms of RMSD and bias, thus revealing the different spatial and temporal comparison scales, section "Synthesis of the Reanalysis Validation" presents an overall synthesis of the accuracy of all variables and levels using normalized metrics, which allows us to assess the reanalysis quality against a common reference (i.e., the observed variability in each variable at the different levels).

Among the 12 variables of the published reanalysis dataset, chlorophyll, nitrate, and oxygen were the only variables covering all three validation levels, basically due to the large amount of data recently made available in BGC-Argo float profiles. BGC-Argo data were also considered to validate the phytoplankton biomass, but only at Level 2. Phosphate, ammonium, and carbonate system variables (pH, alkalinity, DIC, and pCO_2) satisfied Levels 1 and 2, basically considering data retrieved from the EMODnet_int and SOCAT repositories,

TABLE 2 | Reference datasets used for the 3-level validation.

Variable	Level 1	Level 2	Level 3
Chlorophyll	CMEMS-OC climatology	CMEMS-OC daily maps BGC-Argo profiles	BGC-Argo profiles
Phytoplankton biomass		BGC-Argo profiles	
Net primary production	Literature estimates		
Phosphate	*In situ* climatology	EMODnet *in situ*	
Nitrate	*In situ* climatology	EMODnet *in situ* BGC-Argo profiles	BGC-Argo profiles
Oxygen	*In situ* climatology	EMODnet *in situ* BGC-Argo profiles	BGC-Argo profiles
Ammonium	*In situ* climatology	EMODnet *in situ*	
pH on total scale	*In situ* climatology	EMODnet *in situ*	
Alkalinity	*In situ* climatology	EMODnet *in situ*	
DIC	*In situ* climatology	EMODnet *in situ*	
pCO_2 at sea surface	*In situ* climatology	EMODnet *in situ* SOCAT	
CO_2 flux at air-sea interface	Literature estimates		

Note that both "in situ climatology" and "EMODnet in situ" refer to EMODnet_int data set. Up to three quarters of pH and in situ pCO_2 observations were reconstructed using CO_2sys software (Sharp et al., 2020) with available DIC, ALK and other regulatory information (i.e., temperature, salinity and concentration of phosphate and silicate).

whereas NPP and air-sea CO_2 flux were validated at Level 1 only (**Table 2**).

Level 1 Validation

To illustrate the applicability of Level 1 validation, in this section we provide a quality assessment of surface chlorophyll, NPP, and alkalinity, whereas a global overview of the normalized skill indicators based on the mean annual spatial distribution is provided in section "Synthesis of the Reanalysis Validation" for 10 state variables (thus, excluding NPP and CO_2 flux).

In terms of surface chlorophyll, **Figure 2** shows a good agreement between the climatological maps extracted from the reanalysis and satellite datasets. The model can correctly reproduce the basin-wide zonal gradient, spatial heterogeneity at the subbasin scale, and coastal-off shore patterns in the areas most affected by terrestrial inputs (Po, Rhone, Ebro, and the Nile), external inflow into straits (Gibraltar and Dardanelles), and shallow eutrophic areas (Gulf of Gabes). The subbasin mean values, annual cycles, and interannual variability are consistent with those provided by satellite observations (not shown; please refer to Teruzzi et al., 2021).

Net primary production is a measure of the net uptake of carbon by phytoplankton groups (the gross primary production minus fast-release processes, e.g., respiration). The lack of extensive datasets of NPP observations constrains its quality assessment to a qualitative evaluation of the reanalysis consistency against previous estimations published in the scientific literature (**Supplementary Table 1**). We observe that the average NPP estimates (i.e., ranging from 100 to 170 $gC/m^2/y$ across the different subbasins, as shown in **Figure 3**) agree with basin-wide estimations (the maps in Figure 8 in Lazzari et al., 2012 and Figure 13 in Bosc et al., 2004) and with published values for the reference subbasins (**Supplementary Table 1**). The reanalysis outcomes for the Ionian and Levantine subbasins appear slightly higher than previous estimates (**Supplementary Table 1**).

Given the sparse and uneven distribution in time and space of the reference *in situ* EMODnet_int data, the mean surface variables obtained in the reanalysis can be compared with climatological maps, reconstructed following the approach described in Cossarini et al. (2015a). In the case of alkalinity (**Figure 4**), the surface basin-wide gradient and subbasin-scale spatial variability are consistently reproduced in the reanalysis with a correlation of 0.95. Comparing the reanalysis to the EMODnet_int climatology at the basin scale, an overestimation occurs in the 0–150 m layers (between 20 and 30 μmol/kg), decreasing to less than 10 μmol/kg below 150 m, and an RMSD value of 40 μmol/kg is observed in the surface layer, decreasing to 20–30 μmol/kg below 300 m and maintaining a constant value of approximately 12 μmol/kg in the deeper layers (**Supplementary Figure 1**; the normalized skill indexes at all levels and subbasins are shown in **Supplementary Figure 2**, respectively).

Level 2 Validation

To illustrate the applicability of Level 2 validation, we provide a quality assessment of selected variables (i.e., phosphate, nitrate, oxygen, and pH) in this section, whereas a summary of Level 2 validation of all variables is provided in section "Synthesis of the Reanalysis Validation." All these variables were validated by matching model results with collected EMODnet_int data and in terms of nitrate and oxygen, with BGC-Argo float

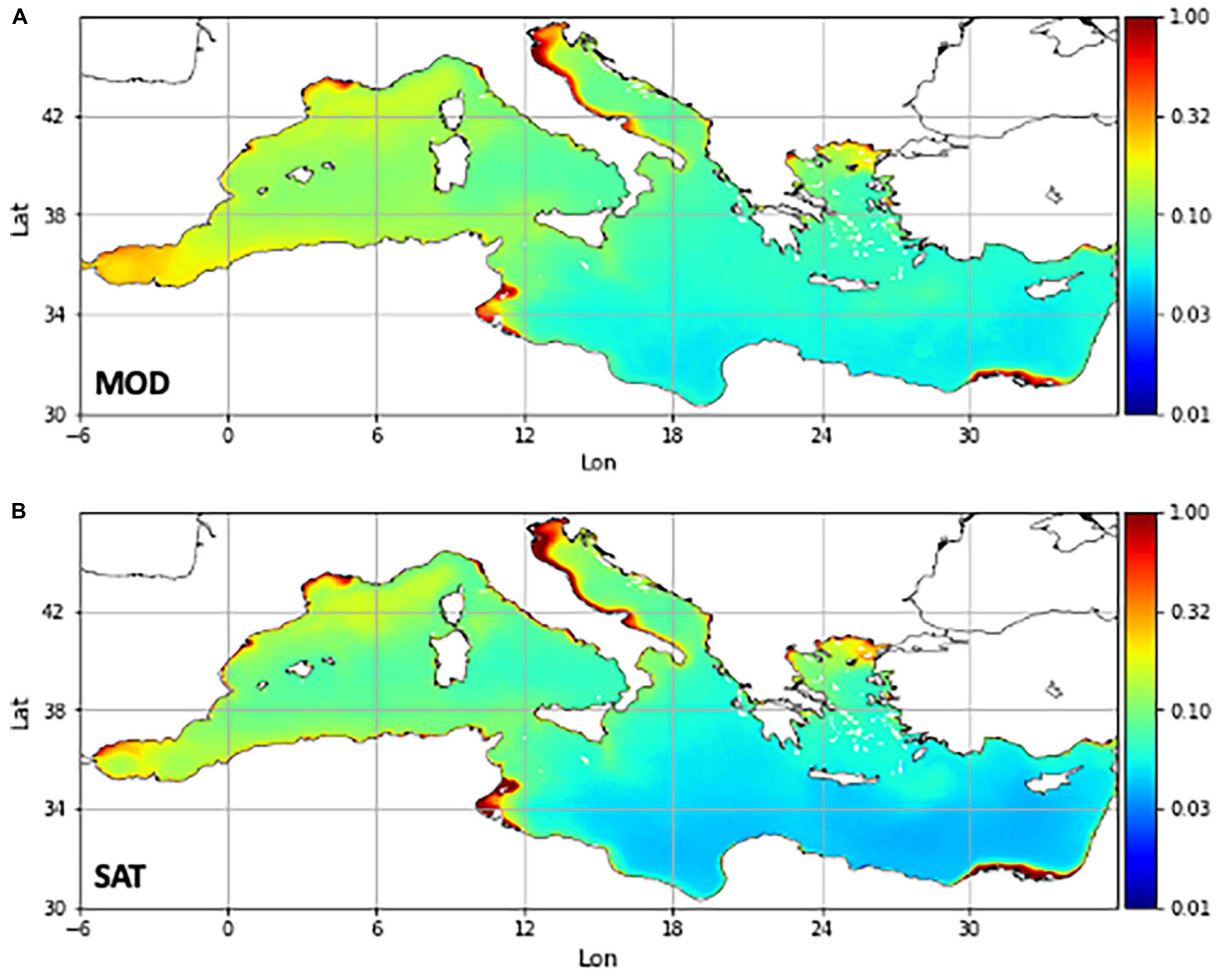

FIGURE 2 | Averaged annual maps of surface chlorophyll (in log-scale) from reanalysis **(A)** and from the CMEMS-OC multi-sensor satellite data **(B)**. The average is computed considering the period 1999–2019 over the layer 0–10 m for the reanalysis results.

vertical profiles, and the skill scores are comprehensively reported in terms of RMSD at the different layers and subbasins (**Figures 5G**, **6**).

Good agreement is found both in terms of mean phosphate values and the spread (**Figures 5A–C**), and variability in the upper layer, whereas the reanalysis tends to underestimate phosphate over EMODnet_int in deep layers (below 500 m), especially in the western subbasins (**Figures 5D–F**). Quantitatively, the uncertainty, expressed as RMSD computed at the subbasin scale for the different vertical layers, varies, on an average, between 0.03 and 0.06 mmol/m^3 in the 0–300 m layer, increasing to 0.08 mmol/m^3 below 300 m, and the RMSD is greater in the western subbasins (**Figure 5G**). Generally, Level 2 uncertainty is higher than that related to the mean annual value (i.e., level 1), which ranges from 0.02 to 0.04 mmol/m^3 in the 0–300 m layer and reaches 0.07 mmol/m^3 below 300 m.

The nitrate skill in regard to Level 2 validation (**Figure 6A**) is similar to that of phosphate, namely, a very good performance in the upper layer that decreases with depth, with underestimation in the western subbasins and lower variability than the reference value. The average uncertainty, based on EMODnet_int, varies between 0.7 and 1.5 mmol/m^3 in the 0–300 m layer, increasing to 1.7 mmol/m^3 below 300 m. While the surface errors are similar among the subbasins, the western subbasins exhibit a higher uncertainty than do the eastern subbasins in the deep layers. Level 2 validation of nitrate was also conducted by matching the reanalysis results with BGC-Argo data, providing a similar picture but with slightly different values, namely the average RMSD value varies between 0.41 and 0.62 mmol/m^3 in the upper 60-m layer, increases to 0.73 mmol/m^3 in the 60–100 m layer, remains smaller than 2 mmol/m^3 in the 100–600 m layer, and increases to 2 mmol/m^3 in the 600–1000 m layer (**Figure 6D**).

The two datasets are self-consistent and robust [the EMODnet_int quality was reported by Buga et al., 2018, and the BGC-Argo quality control (QC) protocol was provided by Bittig et al., 2019] and capture different levels of variability, namely a broader range of values encompassing sparse observations in time and space over two decades in terms of EMODnet_int and a series of profiles closely located in time and space capturing mesoscale and short-term dynamics, but covering only the last

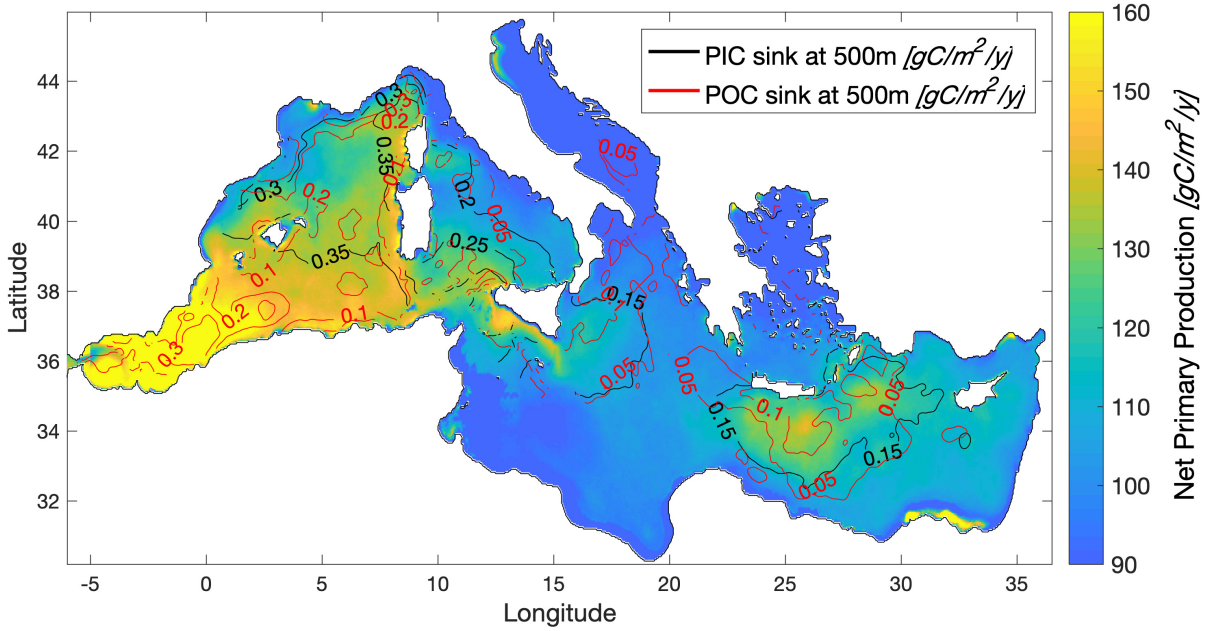

FIGURE 3 | Map of the net primary production vertically integrated and contour of the sink fluxes at 500 m depth of POC (red contour) and PIC (black contour).

5 years in terms of BGC-Argo. Thus, by separately employing these two validation datasets, we reveal a slightly lower reanalysis uncertainty when matched with the more localized (i.e., capturing mesoscale weekly dynamics within limited areas) BGC-Argo float data than that when matched with the broader-ranging (in value terms) and more dispersed (in terms of its spatial and temporal coverage) EMODnet_int dataset.

The amount of EMODnet_int oxygen data is one order of magnitude larger than that of nutrient data, which supports a more reliable uncertainty estimation. While the surface layer is very well simulated (**Figures 6B,E**), the reanalysis tends to overestimate the oxygen observations, with a positive bias of approximately 20 mmol/m^3 below 300–400 m (**Supplementary Figure 1**). Small errors in oxygen at the surface (e.g., RMSD values between 5 and 13 mmol/m^3; **Figure 6E**) confirm that the high-temporal resolution temperature dynamics at the mesoscale (Escudier et al., 2021), which drive saturation and biological production, are generally suitably reproduced. In the deep layers, the reanalysis does not fully capture the oxygen dynamics due to the observed bias, and the uncertainty increases in the mesopelagic zone of the water column, specifically in the western subbasins, where it overcomes 30 mmol/m^3. The oxygen from BGC-Argo floats indicates a reanalysis skill assessment similar to the EMODnet_int-based metrics (**Figure 6B**), with the RMSD values generally increasing with depth, particularly in the western subbasins.

Qualitatively, the reanalysis correctly reproduces the observed pH values and the spatial (both horizontal and vertical) variability (**Supplementary Figure 1**). Quantitatively, the uncertainty in reproducing high-temporal frequency observations, expressed as RMSD, remains relatively constant along the water column, varying between 0.01 and 0.04 pH units, with high RMSD values in the Alboran Sea and marginal seas (Adriatic and Aegean, as shown in **Figure 6C**). In addition to the model inaccuracy linked to specific and local conditions in marginal seas, the model-observation mismatches are possibly related to the inaccuracy of the reconstruction method of *in situ* pH observations based on other carbonate system variables, which can reach as high as 0.005 pH units (Álvarez et al., 2014).

Level 3 Validation

The increasing availability of BGC-Argo data has allowed us to design fit-for-purpose metrics that quantify the model skill in reproducing specific emergent properties of biogeochemical dynamics and their seasonal variability (please refer to Salon et al., 2019; Feudale et al., 2021; Mignot et al., 2021).

Given the general quasi-stationary trajectory of BGC-Argo floats in the Mediterranean Sea (e.g., the red points in the upper panel of **Figure 7**), qualitative comparison of the temporal evolution of model-float vertical profiles of nitrate and oxygen (**Figure 7**, second and third rows; for chlorophyll, please refer to the example in Salon et al., 2019) provides an outlook capturing seasonal and monthly variations due to local physical (e.g., vertical mixing) and biological (e.g., phytoplankton bloom) dynamics.

In addition to the quantification of model-observation mismatches with classical metrics, we computed different quality assessment metrics to assess the model capability to reproduce emergent characteristics of the vertical structure, as defined in section "Validation Framework." Examples of emergent vertical characteristic metrics for nitrate (the nitracline depth; NITRCL) and oxygen (the depth of the oxygen maximum; OXYMAX) are reported in the lower panels of **Figures 7A,B**. With regard to the specific nitrate float (**Figure 7A**), we observed that the model

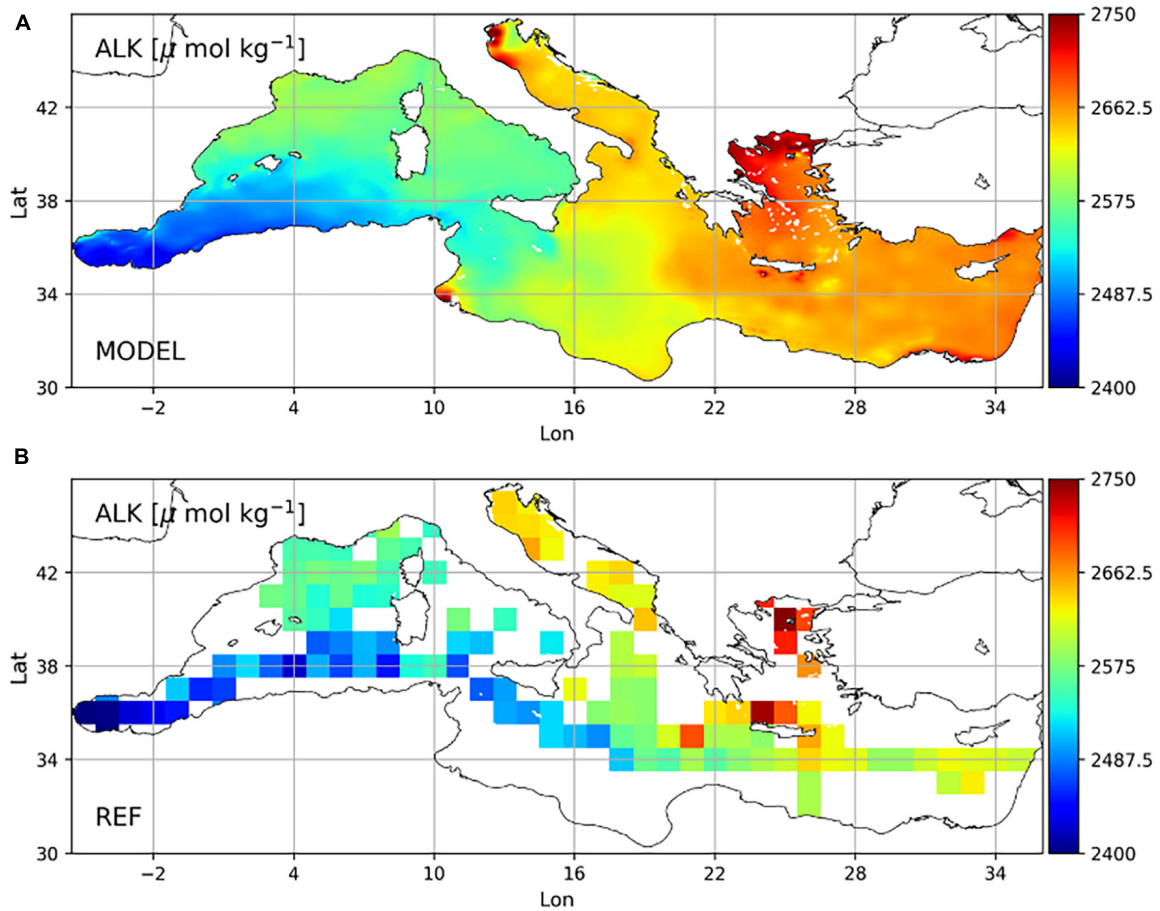

FIGURE 4 | Mean alkalinity maps at surface (layer 0–30 m) in the period 1999–2019 produced by the reanalysis **(A)** and the climatology from EMODnet dataset at 1° resolution **(B)**.

tends to generate a lower nitrate vertical gradient (the model surface values are overestimated and the values below 200 m are underestimated; upper panels), whereas the model skill increases after March 2014, as further verified by the improvement in the integrated value and correlation (**Figure 7A**, middle panels). Despite the surface bias, the model attains a good skill in reproducing the nitracline depth (NITRCL in **Figure 7A**) during the whole period, indicating how the interaction between vertical physical and biological dynamics, which determines the profile shape separating nutrient-rich deep waters from depleted surface waters, is suitably simulated by the model.

The epipelagic seasonal dynamics of the oxygen profile measured by floats (**Figure 7B**) are characterized by a spring surface maximum, summer surface deoxygenation and penetration into the euphotic layer, and winter mixing. These dynamics are qualitatively well represented by the model, with a simulated oxygen maximum depth during the penetration period but with systematically overestimated values below the euphotic layer. The model performs very well in reproducing surface values, mostly driven by saturation (the red dots in the third row of **Figure 7B**), while integrated values are overestimated by approximately 10 mmol/m^3 (INTG 0_200m; the fourth row of **Figure 7B**). Interestingly, the divergent evolution of the 0–200 m integrated oxygen values after January 2014 suggests either a possible model flaw or a drift in BGC-Argo float data considering that quality assessment of BGC-Argo variables is continuously progressing (Bittig et al., 2019).

Once computed for all available BGC-Argo float data and comprehensively captured with RMSD in the selected subbasins, the metrics quantify the model skill in the reproduction of the seasonal dynamics of the emergent properties of biogeochemical processes. The reanalysis reproduces the depth of the DCM (i.e., with an uncertainty of approximately 15–20 m, **Table 3**), which varies between 60 m (western basins) and 120 m (eastern basins, Lavigne et al., 2015). Slightly higher uncertainty is computed for the modeled depth of the WBL, at approximately 30 m, while the intensity of chlorophyll peak values (CHLMAX and winter maximum values) is reproduced with an uncertainty lower than 0.2 mg/m^3. The uncertainty increases to 0.3 and 0.5 mg/m^3 in the south-western Mediterranean (swm) and north-western Mediterranean (nwm), respectively, with the latter subbasin already addressed by Salon et al. (2019), which is basically related to the MedBFM limits in reproducing local dynamics under stratified conditions. Then, **Table 3** reports that the RMSD value

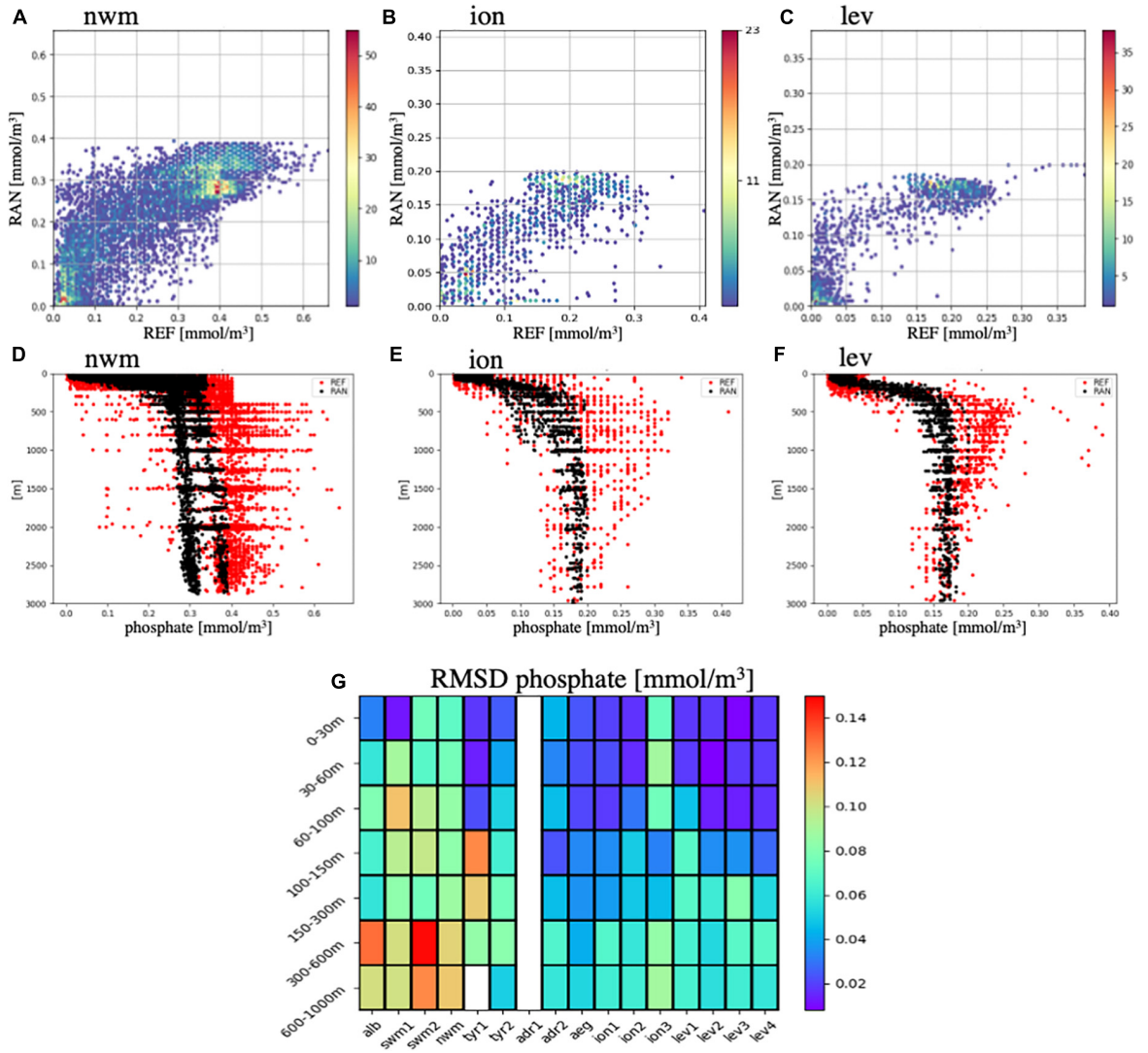

FIGURE 5 | Level 2 validation for phosphate based on the match-ups between model results and reference EMODnet_int dataset for three sub-basins (nwm, ion and lev) in the open sea. **(A–C)** Density plots of model (RAN) and EMODnet_int (REF) match-ups; **(D–F)** vertical profiles for reanalysis (RAN, black) and reference dataset (REF, red); n. of match ups are 10,774 (nwm), 1,410 (ion) and 1623 (lev); **(G)** RMSD (mmol/m^3) computed for selected vertical layers and for each sub-basin (white boxes correspond to data unavailability).

for the nitracline depth (NITRCL) varies between 30 and 40 m, whereas the accuracy of the depth of the oxygen maximum is on average 25 m, which is a reasonably good result considering the dispersion in these ecosystem features (refer to **Figure 7** and **Supplementary Figure 1**) resulting from the interaction between vertical transport and mixing and biological processes.

Synthesis of the Reanalysis Validation

To provide an overall view of the reanalysis uncertainty at the different levels of validation, we derived two normalized indicators for the model variables from the metrics presented in the previous sections, including a cost function, defined as the ratio between the absolute bias and the standard deviation of the observations σ_O (qualified as very good if lower than 1, good if ranging from 1 to 2, reasonable if ranging from 2 to 5, and poor if higher than 5; Moll, 2000), and RMSD normalized with σ_O, which should ideally be lower than 1 when the model predictions of individual observations are better than the average observation values (i.e., conceptually the model efficiency index defined in Stow et al., 2009).

Figure 8 shows a synthesis of validation Levels 1 and 2, mainly considering the surface layer of the Mediterranean Sea. The indicators extended to all subbasins and vertical layers are shown in **Supplementary Figures 2–4**. The cost function at Levels 1 and 2 is lower than 1 for all the variables in the upper layer (**Figures 8A–C**), thus demonstrating an overall very good quality of the reanalysis in reproducing values and variability linked to basin-wide dynamics. The cost function values remain well below 1 in all layers and deteriorate only in the two deepest layers (**Supplementary Figure 2**, top).

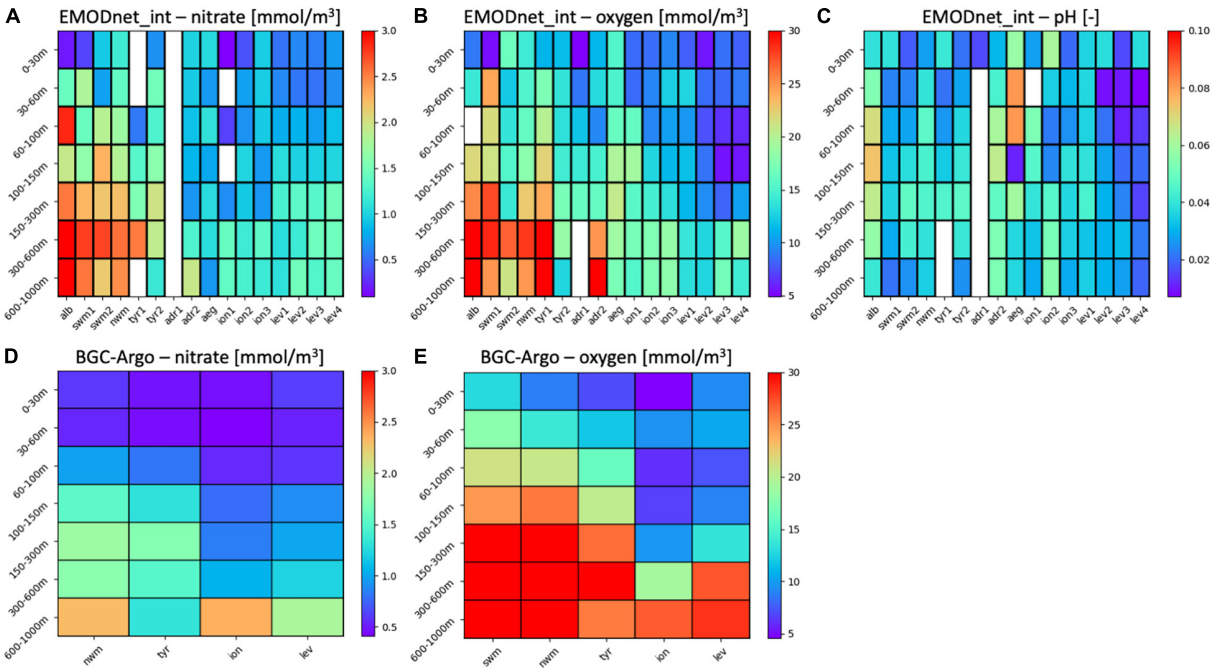

FIGURE 6 | Validation (RMSD metric) for nitrate **(A,D)**, oxygen **(B,E),** and pH **(C)** based on the match-ups between model results and reference data sets EMODnet_int (upper panel) and BGC-Argo (lower panel). White boxes correspond to data unavailability.

Among the subbasins, the Alboran Sea (alb), southwestern Mediterranean Sea (swm1), northern Tyrrhenian Sea (tyr1), and eastern Levantine (lev4) exhibit at least four variables for which the cost function value exceeds 1 in certain layers (**Supplementary Figure 3**), e.g., the carbonate system variables in the far eastern subbasins and nutrients in the subbasins close to the Atlantic boundary, which are affected by possible systematic biases.

The model also achieves an overall good skill when quantified with the normalized RMSD at both Levels 1 and 2 in the surface layer, with the exception of ammonium at Levels 1 and 2 and the average values of chlorophyll, phytoplankton biomass, and oxygen in the euphotic layer at Level 2 computed based on BGC-Argo data (**Figure 8C**). Considering all layers, ammonium and oxygen below 100 m exhibit values higher than 1 in more than three layers (**Supplementary Figure 2**, bottom). Phosphate in the upper layers and DIC and alkalinity below 150 m attain very low values of the standard deviation of the observations driving normalized RMSD values that are higher than 1 in at least two layers for each variable.

Even if less robust because of the fewer number of available observations, the normalized RMSD computed for the subbasins and layers provide useful indications of possible model flaws (**Supplementary Figure 4**). Nutrients in the western subbasins in the deepest layers and carbonate system variables in the most eastern subbasins are the most frequent cases with normalized RMSD values above 1. As already mentioned, ammonium is by far the least accurately modeled variable, while oxygen below 300 m attains values higher than 1 in at least 12 subbasins (**Supplementary Figure 4**).

Among the subbasins, the northern Tyrrhenian Sea (tyr1), which exhibits a high variability and is a transitional area (as reported in several regionalization analyses, e.g., Ayata et al., 2018; Di Biagio et al., 2020), reveals a normalized RMSD value higher than 1 for at least four variables in several layers.

Reanalysis Variabilities and Trends

Mean Spatial and Temporal Variabilities

The reanalysis provides an overall view of the average spatial and temporal variabilities in the biogeochemical state of the Mediterranean Sea over the past two decades. The spatial variability at the basin scale is computed as the range of the average annual subbasin values, whereas the average temporal variability is computed as the mean range (i.e., throughout the 21-year simulated period) between the minimum and maximum subbasin monthly average values (**Figure 9** and **Supplementary Table 2**). The selected subbasins reveal a typical zonal Mediterranean gradient, while the marginal seas (Adriatic and Aegean Seas), which are characterized by important anomalies (Teruzzi et al., 2021), are not shown in **Figure 9**.

Certain variables (e.g., alkalinity and DIC) are characterized by a higher spatial than temporal variability. In terms of nutrients such as nitrate and phosphate, even when the spatial variability is notable, the variability in the seasonal cycle at the surface in several western subbasins can reach as high as the spatial variability. The spatial variability in nutrients remains a peculiar signature of the subsurface layers (i.e., below 100 m), where the seasonal cycle is narrow and the

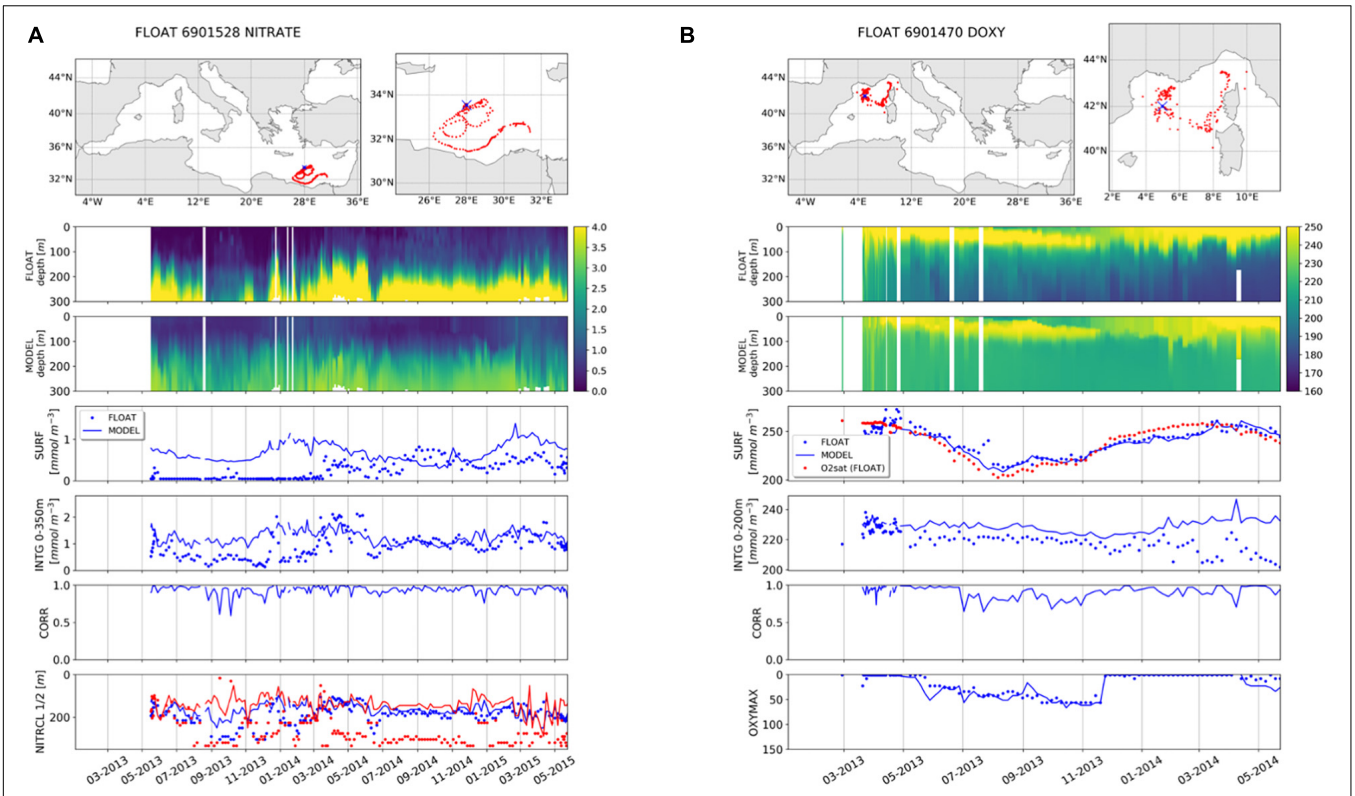

FIGURE 7 | Examples of level-3 validation for nitrate **(A)** and oxygen **(B)** based on the comparison between BGC-Argo floats and model. From top to bottom, panels are: trajectory of the BGC-Argo float (red dots) with deployment position (blue cross); Hovmöller diagrams of nitrate (mmol/m^3) and oxygen (mmol/m^3) concentration from float data (2nd row) and model outputs (3rd row) matched-up with float position for the period of float life; selected skill indexes for model (solid line) and float data (dots): surface nitrate and oxygen (SURF, 4th row; with oxygen saturation, red dots), vertical average of nitrate in the 0–350 m layer and of oxygen in the 0–200 m layer (INTG, 5th row), correlation between vertical profiles (CORR, 6th row), and depth of the nitracline and of the oxygen maximum (NITRCL, blue; OXYMAX, 7th row).

TABLE 3 | Metrics computed for the level-3 validation.

	RMSD of metrics						Avg. n. of available profiles per month		
	NITRCL1 (m)	WBL (m)	DCM (m)	CHLMAX (mg/m^3)	CHL0-200 (mg/m^3)	OXYMAX (m)	NIT	CHL	OXY
swm	–	32	20	0.29	0.05	28	–	8	7
nwm	32	38	14	0.50	0.12	14	7	23	31
tyr	31	24	17	0.18	0.06	16	6	7	7
adr	–	24	15	0.18	0.05	80	–	5	2
ion	45	28	17	0.13	0.06	24	9	22	11
lev	32	30	21	0.15	0.05	35	15	22	11

Details of the metrics are in the text. Aggregated sub-basins are considered, and statistics computed when at least two profiles per month are available.

Mediterranean reveals two distinctive conditions separated by the Sicily channel (**Figure 9**). In marine ecosystems, ammonium is generally produced by remineralization processes of organic matter and rapidly assimilated by plankton or oxidized into nitrate. Reanalysis ammonium, which exhibits a relatively high level of uncertainty (**Figure 8**), tends to reach zero below the euphotic layer and indicates a seasonal variability that exceeds the spatial variability.

Chlorophyll simulation achieves a good skill (**Figure 8**) and captures important spatial and temporal signals, which have already been reported in the literature (Lavigne et al., 2015; Barbieux et al., 2019), the enhanced seasonal cycle in both the surface (i.e., winter/spring blooms, especially in the western regions) and subsurface (50–150 m, with DCM onset from April to October) layers and significant spatial variability both in terms of the zonal gradient and vertical displacement

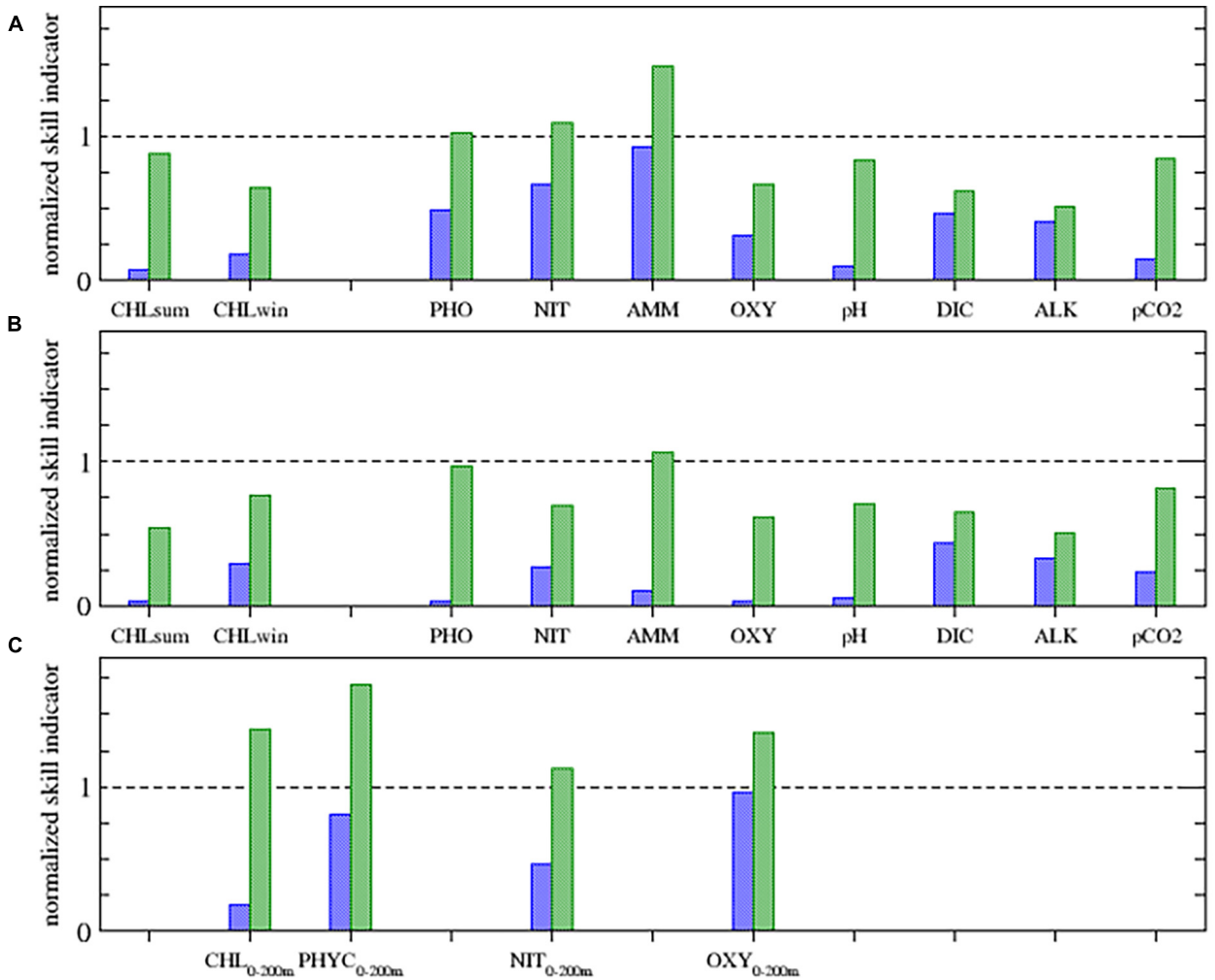

FIGURE 8 | Synthesis of validation Level 1 and 2 for 10 reanalysis variables with related emergent properties metrics in terms of the cost function (blue) and normalized RMSD (green): **(A)** Level 1 computed for the whole Mediterranean Sea 10–30 m layer (surface for chlorophyll summer and winter values, and for pCO_2). Level 2 computed comparing reanalysis with **(B)** satellite (for surface chlorophyll summer and winter values) and EMODnet_int for the whole Mediterranean Sea 0–30 m layer and with **(C)** BGC-Argo for chlorophyll, phytoplankton biomass, nitrate and oxygen 0–200 m averaged values.

of the subsurface chlorophyll maximum (**Figure 9**). At the surface, the oxygen temporal variability reaches as high as approximately 50–60 mmol/m^3 following the seasonal saturation cycle, with important spatial differences among the subbasins attributed to the spatial gradient of the surface temperature (Escudier et al., 2021). In the subsurface layer, biological activity drives the variability associated with a maximum at a depth from approximately 50–100 m (i.e., just above the DCM), and important spatial differences are associated with the different levels of productivity in the various subbasins, with the western subbasins being more productive and shallower than are the eastern subbasins.

Trends During the 1999–2019 Period

Trends were evaluated considering the simple, fixed-seasonal cycle (as shown in **Figure 9**) C-1 method (Vantrepotte and Mélin, 2009) based on the monthly time series for the 16 subbasins. Trends were computed for certain important layers (e.g., surface, subsurface, or vertically integrated) and variables to provide a general view of the different scales of variability in the euphotic layer. **Figure 10** shows values of the trend slope considering an arbitrary range based on either the seasonal or interannual variability (**Supplementary Table 2**), and highlights when trends are inferred in addition to the statistical significance.

Chlorophyll generally attained very low trends, either positive or negative, mostly not significant. Indeed, considering the surface (CHL_{surf}), only the Adriatic Sea (adr1) and southern Ionian (ion2) exhibit positive and negative significant trends, respectively. However, when the trends were computed based on vertically integrated values ($CHL_{0-200\ m}$), a generally positive (negative) trend characterizes the western (eastern) subbasins. Consistent with the negative trend of chlorophyll in the eastern Mediterranean Sea, the annual vertically integrated primary production reveals very small negative values in the eastern

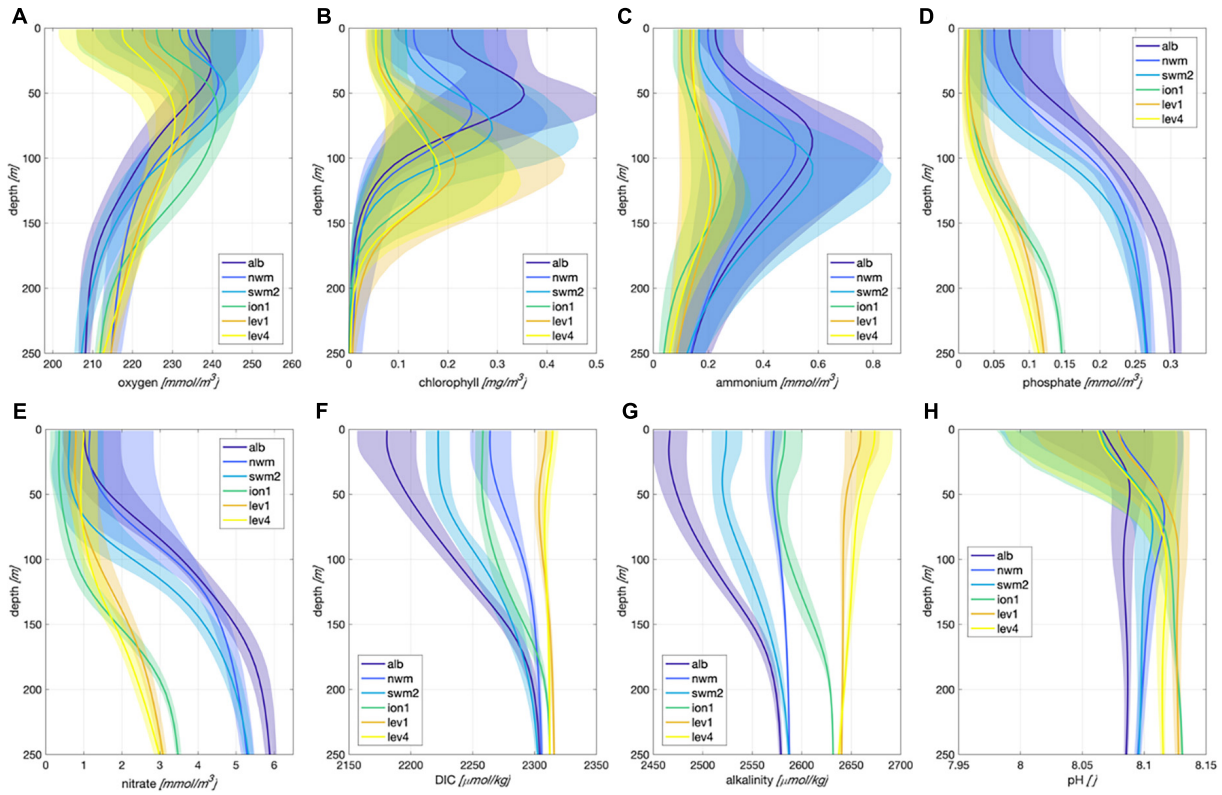

FIGURE 9 | Spatial and temporal variability for selected variables: oxygen **(A)**, chlorophyll **(B)**, ammonium **(C)**, phosphate **(D)**, nitrate **(E)**, DIC **(F)**, alkalinity **(G)**, pH **(H)**. For each variable, mean annual average profiles for sub-basins along the zonal direction (colored solid lines) and mean seasonal cycle within each sub-basin (colored shaded areas) are plotted.

subbasins and an absence of long-term signals in the western subbasins, except the north-western Mediterranean (nwm). The negative trend values seem mostly associated with a decrease in the summer productivity, whereas the productivity of the winter bloom (NPP_{winter}) increases in the western subbasins due to the presence of a larger number of intense winter blooms with enhanced vertical mixing in the second part of the reanalysis with respect to the initial period, as reported in Cossarini et al. (2020). However, the limited length of the reanalysis (i.e., 21 years) might influence the robustness of the above trend analysis when the interannual variability is high (i.e., the trend slope values are generally lower than 10% of the interannual variability, as indicated in **Supplementary Table 2**). While a negative trend in the surface layer nitrate occurs in most of the subbasins, in the case of phosphate the trend is practically null and not significant. Most of the eastern subbasins and several western subbasins indicate a very small but significant tendency for oxygen [(−0.05, −0.10) mmol/m^3/y], which corresponds to a decrease in the oxygen content of approximately 1.0–2.0 mmol/m^3 during the simulated period.

Significant trends for all carbonate variables were obtained for the whole Mediterranean Sea. In particular, the two prognostic model variables (alkalinity and DIC) exhibit positive trends in the eastern subbasins that are higher than those in the western subbasins: at 1.5 and 0.7 µmol/kg/y, respectively, for the alkalinity and 2 and 0.6 µmol/kg/y, respectively, for DIC. While the DIC and alkalinity variations impose opposite effects on pH, which is a diagnostic variable of the carbonate system, the overall effect revealed by the reanalysis is a pH decrease at a rate of approximately 0.0006–0.0012 y^{-1} (higher in the eastern subbasins). Finally, a significant trend of the CO_2 air-sea flux is detected, with values ranging from 0.05 to 0.15 (mmol/m^2/d)/y, with the highest values in the western subbasins.

Temporal Evolution and Trend of the Carbonate System Variables

One of the most relevant signals in the present reanalysis dataset is the impact of the increase in the atmospheric CO_2 partial pressure, which affects the carbon sink in the marine system. Despite the very high seasonal cycle, the Mediterranean Sea exhibits nearly neutral conditions, with a mean annual value of 0.35 (0.24 in open sea areas only) mmol/m^2/d in the 2010–2019 period (**Figure 11**). However, we observe a possible shift in CO_2 behavior between a net source and a net sink over the last two decades, at least in the open sea areas, as a consequence of the increase in atmospheric CO_2. It should be noted that the dynamics in coastal areas that are simulated as net sinks of atmospheric CO_2 are highly uncertain due to the uncertainty in terrestrial inputs and the impact of benthic and coastal biogeochemical dynamics (Borges et al., 2006; Cossarini et al.,

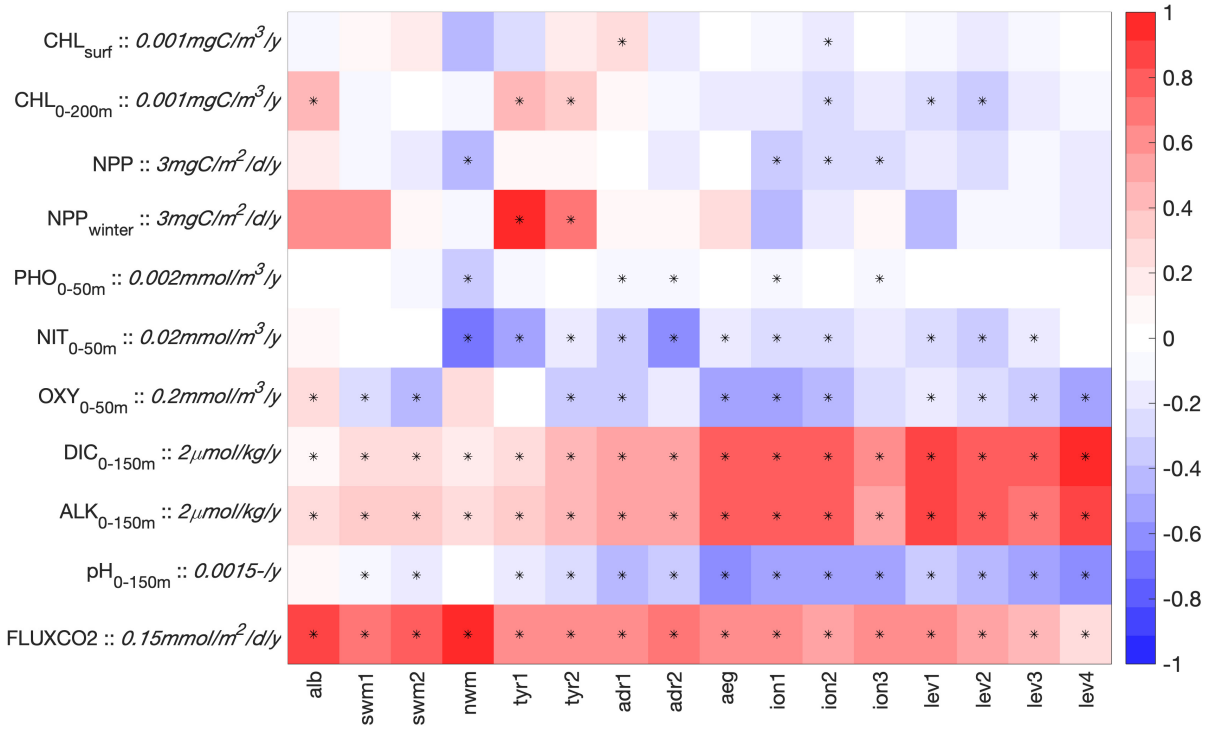

FIGURE 10 | Trend slope values for selected variables in the 16 sub-basins. Color scale range is adapted considering the range of variability or mean values of each variable (scale factor is provided together with the variable unit). The symbol * marks significant trend (*t*-test at *p*-level of 0.05).

2015b). Regarding the spatial variability, the model exhibits strong CO_2 uptake (ingassing) in the nwm subbasin, Adriatic, and Aegean Seas and CO_2 outgassing in the south-eastern Mediterranean (**Figure 11B**). Hotspots of CO_2 atmospheric uptake occur in areas of dense water formation (Pinardi et al., 2015), fostering the carbon pump mechanism in marginal areas (Cossarini et al., 2017). Considering the marine carbon cycle functioning in the open sea areas, primary production is a key component that, in addition to constituting the base of oceanic food webs, contributes to atmospheric CO_2 sequestration through CO_2 fixation and subsequent organic carbon sinks (Siegel et al., 2014; Morrow et al., 2018). We provide the mean annual value of the integrated NPP, together with an estimation of the sink of particulate organic carbon (POC) and particulate inorganic carbon (PIC) at a depth of 500 m (**Figure 3**). According to the BFM formulation (Lazzari et al., 2016; Vichi et al., 2020), NPP is determined as photosynthesized carbon minus respiration and fast-release carbon due to a lack of nutrients for biomass synthesis. While organic carbon is produced through mortality and grazing of all plankton groups, the dynamics of PIC (i.e., calcite) comprise calcite precipitation by coccolithophores (parameterized as the mortality of nano-flagellate functional types multiplied by a PIC:POC ratio factor of 1; Krumhardt et al., 2017) and the dissolution process (Morse and Berner, 1972).

The zonal trophic gradient of primary production reflects a sink of particulate carbon, where the carbon export of the western subbasins was double that of the eastern subbasins. The particulate organic and inorganic carbon exports are similar across the western subbasins, with values of approximately 0.1–0.3 g/m^2/y, whereas the PIC sink seems to be the dominant carbon export process in the eastern subbasins, where coccolithophores are recognized to increase eastward in the Mediterranean basin and could be the relevant phytoplankton group (Siokou-Frangou et al., 2010; Oviedo et al., 2015). Carbon sequestration in the deep layers is approximately 10–20% of atmospheric CO_2 absorption. No significant temporal tendency was detected in the sinks of POC and PIC, suggesting that the increase in carbon accumulation in the deepest layers (not shown) was mostly related to the downward diffusion/transport of DIC from the surface rather than an alteration in the model internal biogeochemistry.

DISCUSSION

This study describes a 1999–2019 reanalysis of the Mediterranean Sea biogeochemistry produced within the CMEMS framework. Combined with related physical reanalysis (Escudier et al., 2021), biogeochemical 3D daily and monthly fields are open and freely available through the CMEMS web portal.[1] A robust and rigorous validation is a critical point to inspire user confidence toward model products (Hernandez et al., 2018; Hipsey et al., 2020). Through the three-level validation framework (section "Reanalysis Validation"), the Mediterranean biogeochemical

[1] marine.copernicus.eu

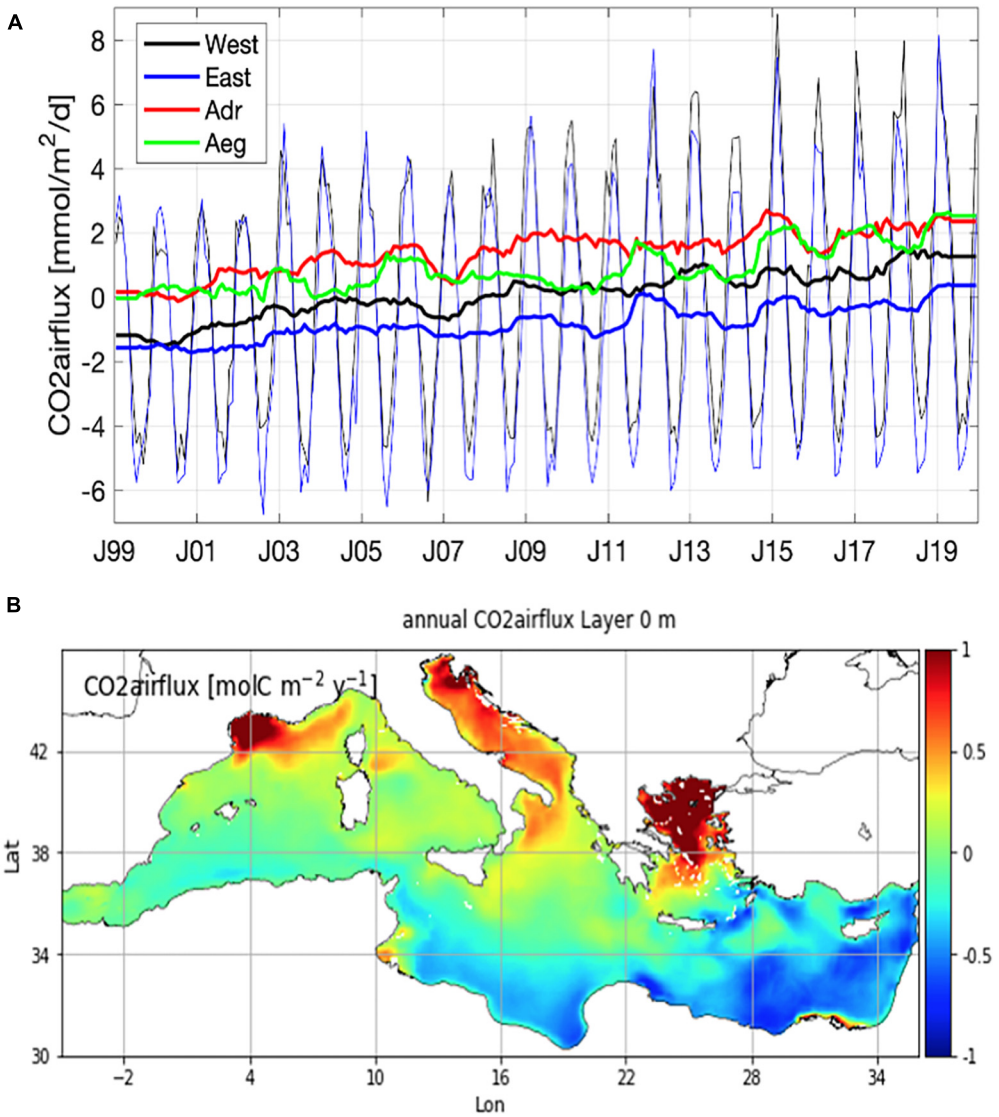

FIGURE 11 | Monthly time evolution (thin lines) and its moving average (thick lines) of CO_2 air-sea flux **(A)** in the western and eastern Mediterranean Sea, Adriatic and Aegean Seas. Map of the mean annual CO_2 air-sea flux **(B)**. Positive values indicate sink of atmospheric CO_2.

reanalysis was demonstrated to constitute a valid multiscale product that can be applied to investigate variability at different temporal and spatial scales (refer to the examples in the Ocean State Report, von Schuckmann et al., 2016) and can serve as qualified boundary conditions for subregional high-resolution model systems (refer to the example in Bruschi et al., 2021). To our knowledge, this is the first time that different levels of validation have been achieved in a reanalysis of the Mediterranean Sea biogeochemistry, quantifying the uncertainty in as many as 12 variables: chlorophyll, phytoplankton biomass, NPP, phosphate, nitrate, oxygen, ammonium, pH, alkalinity, DIC, sea surface pCO_2, and air-sea CO_2 flux.

As thoroughly outlined by Hipsey et al. (2020) and demonstrated in specific cases within the CMEMS regional forecasting system (as an example, Gutknecht et al., 2019; Salon et al., 2019), biogeochemical data availability is an important constraint for model validation since different variables exhibit varying uncertainty levels on the basis of the availability of reference data. Therefore, our proposed framework offers a degree of confirmation (Oreskes et al., 1994) concerning the different spatial-temporal variability scales determined by the availability of observations specific to various datasets.

One caveat regarding the robustness of the present analysis is that surface chlorophyll comparison at Levels 1 and 2 was performed with the same satellite observations previously assimilated, which is a common procedure in skill assessment of assimilative systems (Gregg et al., 2009). Nevertheless, as mentioned, the model is evaluated before the observations are assimilated. Hence, the metrics provide an assessment of the skill performance in regard to short-term temporal dynamics. Among

the 10 model variables compared to the EMODnet dataset, three variables were further compared with the BGC-Argo dataset. These two validations were kept separate to ensure consistent accuracy in the calculations, given the relatively different spatial and temporal coverage levels and QC procedures between the EMODnet and BGC-Argo data. Furthermore, the BGC-Argo floats provide observations at high vertical and temporal resolutions, allowing us to compute time series of the vertical properties of oxygen, chlorophyll, and nitrate (in the three-level validation framework).

Generally, our validation results revealed the good model performance and certain flaws in the reanalysis. The impact of the accuracy of the climatological Atlantic boundary, the low spatial variability in the initial conditions (i.e., a single profile for each subbasin), and the possible imbalance between deep ventilation and mesopelagic mineralization processes could be the reason for the model errors in the western subbasins and the deep-layer values for nutrients and oxygen (i.e., nitrate and phosphate underestimation and oxygen overestimation in the mesopelagic layer, with a larger error in ammonia, as shown in **Figures 6–8**, and **Supplementary Figures 2–4**). Additionally, a possible excess evaporation effect could be the cause of the alkalinity overestimation in the eastern subbasins, causing a slight overestimation of the pH (**Figure 6**). However, it should be noted that the alkalinity trend is fairly well aligned with the salinity trend, as described in Escudier et al. (2021), highlighting that the slight alkalinity overestimation could be attributable to a possible error in the initial conditions (stemming from the 1999 to 2016 EMODnet_int climatology, which might already include part of the trends).

Focusing on the epipelagic layer, where the accuracy is higher than that in the mesopelagic layer, the reanalysis reproduces certain long-term tendencies that occur in the Mediterranean Sea as a response to changes in atmospheric forcing. The increase in heat content (Escudier et al., 2021) and the increase in atmospheric CO_2 (Artuso et al., 2009) are the main drivers of the detected significant changes in oxygen at the surface and carbonate system variables.

Indeed, the trend of oxygen is compatible with the decrease in oxygen solubility due to the estimated increase of 0.7°C in the sea surface temperature over the last two decades (Escudier et al., 2021). However, it should be noted that the mesopelagic layer (i.e., 300–700 m) instead indicates a positive significant trend of approximately 0.5 mmol/m^3/y (not reported), which we hypothesize is caused by a possible missing respiration term in the BFM model formulation, as also reported in Reale et al. (2021). Thus, the reanalysis yields an accumulation of 10 mmol/m^3 that affects its quality in the deeper layers (**Figure 6** and **Supplementary Figure 4**).

The positive alkalinity trend could be linked to the long-term change in the water balance (refer to Skliris et al., 2018), which has also caused an increase in the 0–200 m layer salt content of approximately 0.15 PSU over the last 20 years (Escudier et al., 2021).

A constant and spatially homogeneous increase in the atmospheric pCO_2 value from 370 to 410 ppm during the 1999–2019 period caused a positive increase in the sink of atmospheric CO_2. The simulated values are in line with those already published for the Mediterranean Sea (von Schuckmann et al., 2018) and reveal how the Mediterranean has become a net sink of atmospheric CO_2 over the last 20 years. Excess of evaporation over runoff and precipitation combined with the increase in atmospheric CO_2 absorption determined the trend of DIC in the upper layer, with values ranging from 0.6 to 2 μmol/kg/y. The use of climatological boundary conditions throughout the entire duration of the simulation might have partially hampered the positive tendency of the long-term evolution of alkalinity and DIC in the southern areas of the western Mediterranean Sea, mostly influenced by Atlantic inflow. Consequently, lower pH trends were simulated in the western subbasins, where conversely, the increase in the CO_2 sink is 50% larger, suggesting an increase in the net export of carbon through the Gibraltar Strait.

The simulated trend of acidification (0.0006–0.0012 pH units y^{-1}; higher in the eastern subbasins) agrees with previously estimated global acidification trends (e.g., 0.0016 pH units y^{-1}; Gehlen et al., 2020; Kwiatkowski et al., 2020), and is confirmed by the regional observations reported in Flecha et al. (2015) for the Gibraltar Strait over the 2012–2015 period (i.e., an annual pH variation of -0.0044 ± 0.00006) and in Wimart-Rousseau et al. (2021) for the north-western Levantine basin (i.e., an annual pH variation of -0.0024 ± 0.0004).

We also confirmed specific long-term tendencies already unveiled by satellite and model results for chlorophyll (Salgado-Hernanz et al., 2019) and winter primary production (Cossarini et al., 2020). The consistency in surface chlorophyll tendency should not be surprising since this is an assimilated variable. Even though there is no consensus on significant trends or regime shifts in ventilation (Li and Tanhua, 2020; Mavropoulou et al., 2020), the negative trend in nitrate appears to be linked to the impact of chlorophyll satellite assimilation on non-limiting nutrients (Teruzzi et al., 2014). Indeed, in late winter and early spring, the assimilation of satellite chlorophyll observations mainly acts to correct bloom overestimation, thereby nearly uniformly reducing the phytoplankton concentration in the euphotic layer. The negative trend of nitrate occurs due to the consequent reduction in phytoplankton nitrogen remineralization. Even if this phenomenon might be a spurious tendency, the reduction is much lower than the mean value (i.e., approximately 1% over the two simulated decades) and far below that of the variable error (refer to the previous section).

As a general remark, it should be noted that some of the values of these trends, even if significant in several cases (i.e., in specific subbasins), are very low and affected by the length of the time series of the reanalysis, which cannot be extended toward the past beyond the start of the European Space Agency (ESA)–Climate Change Initiative (CCI) satellite time series.

The reanalysis was produced with the primary focus of providing the best 3D estimate of the biogeochemical state of the Mediterranean Sea, integrating the most recent upstream data made available within CMEMS and other communities, including the assimilation of surface chlorophyll data, the atmospheric and hydrodynamic physical forcing, and the

biogeochemical boundary conditions. Robust validation of the 12 variables constituting the reanalysis dataset offers users a measure of the accuracy at different spatial and temporal scales. Our approach highlighted large-scale changes, whereas unveiling specific impacts on the biogeochemical features of changes in water circulation and water mass movements (Malanotte-Rizzoli et al., 2014; Schneider et al., 2014) is left to subsequent papers. In particular, changes and accuracy of the circulation fields are examined in Escudier et al. (2021), and specific analyses can be addressed in the future given the availability of physical and biogeochemical reanalysis data in CMEMS.

Furthermore, our comprehensive validation approach highlighted possible model errors, such as nutrients and oxygen in the mesopelagic-bathypelagic layers, that should be considered before drawing conclusions concerning the analysis of intermediate and deep Mediterranean waters. Thus, important multidecadal signals, such as the presence of a deep dissolved oxygen variability linked to shifts with a multidecadal signal (Mavropoulou et al., 2020) or bathypelagic negative oxygen trends (Sisma-Ventura et al., 2021), when compared with the reanalysis, could help to improve the next generation of reanalysis products, shifting the focus of biogeochemical analysis from the epipelagic layer to the meso and bathypelagic layers.

CONCLUSION

A new and high-resolution biogeochemical reanalysis of the Mediterranean Sea is presented, and the resultant dataset of daily and monthly 3D fields of 12 variables and ecosystem fluxes is freely available from the CMEMS web portal. In summary:

- The new reanalysis integrates several novel elements: ERA5 atmospheric forcing, coupling with the new 1/24° physical reanalysis, updated versions of the BFM model and biogeochemical variational assimilation scheme, and several updated observational datasets for assimilation and validation purposes.
- As a result of the developed three-level validation framework, robust skill assessment of the 12 considered variables offers CMEMS users a measure of accuracy at different spatial and temporal scales. The estimated accuracy of the reanalysis is high for all variables, except ammonium, and the validation is successfully extended to certain emerging properties describing ecosystem processes (e.g., DCM and the depth of the nitracline and subsurface oxygen maximum) using the BGC-Argo dataset. A certain degradation in the quality of oxygen and nutrient estimates is reported in the deep layers.
- The reanalysis represents a consistent reconstruction of the Mediterranean Sea biogeochemical state and its multiscale variability over the last two decades, quantifying the impact of external and atmospheric forcing on basin-scale tendencies toward surface deoxygenation and acidification, in agreement with previous works.

DATA AVAILABILITY STATEMENT

Publicly available datasets were analyzed in this study. This data can be found here: https://resources.marine.copernicus.eu/?option=com_csw&view=details&product_id=MEDSEA_MULTIYEAR_BGC_006_008.

AUTHOR CONTRIBUTIONS

GCos, SS, AT, GB, and LF contributed to the design of the system. GCos and SS wrote the first draft of the manuscript. All authors contributed to the computation of the reanalysis and its assessment and contributed to manuscript revision, read, and approved the submitted version.

FUNDING

This study was supported by CMEMS Med-MFC (Copernicus Marine Environment Monitoring Service Mediterranean Marine Forecasting Centre), Mercator Ocean International Service.

ACKNOWLEDGMENTS

We thank Alessandro Marani (Cineca, Bologna, Italy) for his support in HPC management of the reanalysis. The simulation was carried out on the Galileo facility at Cineca. This study has been conducted using E.U. Copernicus Marine Service Information.

SUPPLEMENTARY MATERIAL

The Supplementary Material for this article can be found online at: https://www.frontiersin.org/articles/10.3389/fmars.2021.741486/full#supplementary-material

REFERENCES

Álvarez, M., Sanleón-Bartolomé, H., Tanhua, T., Mintrop, L., Luchetta, A., Cantoni, C., et al. (2014). The CO_2 system in the Mediterranean Sea: a basin wide perspective. *Ocean Sci.* 10, 69–92. doi: 10.5194/os-10-69-2014

Argo. (2021). Argo Float Data and Metadata from Global Data Assembly Centre (Argo GDAC). Brest: Ifremer. doi: 10.17882/42182

Artuso, F., Chamard, P., Piacentino, S., Sferlazzo, D. M., De Silvestri, L., di Sarra, A., et al. (2009). Influence of transport and trends in atmospheric CO2 at Lampedusa. *Atmos. Environ.* 43, 3044–3051. doi: 10.1016/j.atmosenv.2009.03.027

Ayata, S. D., Irisson, J. O., Aubert, A., Berline, L., Dutay, J. C., Mayot, N., et al. (2018). Regionalisation of the Mediterranean basin, a MERMEX synthesis. *Progr. Oceanogr.* 163, 7–20.

Bakker, D. C. E., Pfeil, B., Landa, C. S., Metzl, N., O'Brien, K. M., Olsen, A., et al. (2016). A multi-decade record of high-quality fCO2 data in version 3 of the Surface Ocean CO2 Atlas (SOCAT). *Earth Syst. Sci. Data* 8, 383–413. doi: 10.5194/essd-8-383-2016

Barbieux, M., Uitz, J., Gentili, B., Pasqueron de Fommervault, O., Mignot, A., Poteau, A., et al. (2019). Bio -optical characterization of subsurface chlorophyll maxima in the Mediterranean Sea from a Biogeochemical-Argo float database. *Biogeosciences* 16, 1321–1342. doi: 10.5194/bg-16-1321-2019

Bellacicco, M., Vellucci, V., Scardi, M., Barbieux, M., Marullo, S., and D'Ortenzio, F. (2019). Quantifying the Impact of Linear Regression Model in Deriving Bio-Optical Relationships: the Implications on Ocean Carbon Estimations. *Sensors* 19:3032. doi: 10.3390/s19133032

Bittig, H. C., Maurer, T. L., Plant, J. N., Schmechtig, C., Wong, A. P., Claustre, H., et al. (2019). A BGC-Argo guide: planning, deployment, data handling and usage. *Front. Mar. Sci.* 6:23. doi: 10.3389/fmars.2019.00502

Bojinski, S., Verstraete, M., Peterson, T. C., Richter, C., Simmons, A., and Zemp, M. (2014). The concept of essential climate variables in support of climate research, applications, and policy. *Bull. Am. Meteorol. Soc.* 95, 1431–1443. doi: 10.1175/BAMS-D-13-00047.1

Borges, A. V., Schiettecatte, L. S., Abril, G., Delille, B., and Gazeau, F. (2006). Carbon dioxide in European coastal waters. *Estuar. Coasta. Shelf Sci.* 70, 375–387.

Bosc, E., Bricaud, A., and Antoine, D. (2004). Seasonal and inter-annual variability in algal biomass and primary productionin the Mediterranean Sea, as derived from 4 years of Sea-WiFS observations. *Glob. Biogeochem.* 18:2004. doi: 10.1029/2003GB002034

van Apeldoorn, D., and Bouwman, L. (2012). SES land-based runoff and nutrient load data (1980–2000). *PERSEUS Deliv. Nr.* 4:6.

Bruschi, A., Lisi, I., De Angelis, R., Querin, S., Cossarini, G., Di Biagio, V., et al. (2021). Indexes for the assessment of bacterial pollution in bathing waters from point sources: the northern Adriatic Sea CADEAU service. *J. Environ. Manag.* 293:112878. doi: 10.1016/j.jenvman.2021.112878

Buga, L., Sarbu, G., Fryberg, L., Magnus, W., Wesslander, K., Gatti, J., et al. (2018). *EMODnet Thematic Lot n? 4/SI2.749773 EMODnet Chemistry Eutrophication and Acidity Aggregated Datasets*. doi: 10.6092/EC8207EF-ED81-4EE5-BF48-E26FF16BF02E

Ciavatta, S., Kay, S., Brewin, R. J. W., Cox, R., Di Cicco, A., Nencioli, F., et al. (2019). Ecoregions in the Mediterranean Sea through the reanalysis of phytoplankton functional types and carbon fluxes. *J. Geophys. Res. Oceans* 124, 6737–6759. doi: 10.1029/2019JC015128

Colella, S. (2006). *La produzione primaria nel Mar Mediterraneo da satellite: sviluppo di un modello regionale e sua applicazione ai dati SeaWiFS, MODIS e MERIS*. Italy: Università Federico II Napoli. 162.

Colella, S., Brando, V. E., Di Cicco, A., D'Alimonte, D., Forneris, V., and Bracaglia, M. (2021). *Quality Information Document for the OCEAN COLOUR PRODUCTION CENTRE - Ocean Colour Mediterranean and Black Sea Observation Product [Data Set]*. Copernicus Monitoring Environment Marine Service (CMEMS). Available online at: https://resources.marine.copernicus.eu/?option=com_csw&view=details&product_id=OCEANCOLOUR_MED_CHL_L3_REP_OBSERVATIONS_009_073 (accessed January 15, 2021).

Colella, S., Falcini, F., Rinaldi, E., Sammartino, M., and Santoleri, R. (2016). Mediterranean ocean colour chlorophyll trends. *PLoS One* 11:e0155756. doi: 10.1371/journal.pone.0155756

Copin-Montégut, C. (1993). Alkalinity and carbon budgets in the Mediterranean Sea. *Glob. Biogeochem. Cycles* 7, 915–925. doi: 10.1029/93GB01826

Coppola, L., Legendre, L., Lefevre, D., Prieur, L., Taillandier, V., and Riquier, E. D. (2018). Seasonal and inter-annual variations of dissolved oxygen in the northwestern Mediterranean Sea (DYFAMED site). *Progr. Oceanogr.* 162, 187–201. doi: 10.1016/j.pocean.2018.03.001

Cossarini, G., Bretagnon, M., Di Biagio, V., d'Andon, O., Garnesson, P., Mangin, A., et al. (2020). "Primary Production" in *Copernicus Marine Service Ocean State Report*. ed. von Schuckmann K., LeTraon P.-Y., Smith N., Pascual A., Djavidnia S., Gattuso J.-P., Grégoire M., Nolan G. Italy: National Institute of Oceanography and Applied Geophysics. 13, S1–S172. doi: 10.1080/1755876X.2020.1785097

Cossarini, G., Lazzari, P., and Solidoro, C. (2015a). Spatiotemporal variability of alkalinity in the Mediterranean Sea. *Biogeosciences* 12, 1647–1658.

Cossarini, G., Mariotti, L., Feudale, L., Mignot, A., Salon, S., Taillandier, V., et al. (2019). Towards operational 3D-Var assimilation of chlorophyll Biogeochemical-Argo float data into a biogeochemical model of the Mediterranean Sea. *Ocean Model.* 133, 112–128. doi: 10.1016/j.ocemod.2018.11.005

Cossarini, G., Querin, S., and Solidoro, C. (2015b). The continental shelf carbon pump in the northern Adriatic Sea (Mediterranean Sea): influence of wintertime variability. *Ecol. Model.* 314, 118–134.

Cossarini, G., Querin, S., Solidoro, C., Sannino, G., Lazzari, P., Biagio, V. D., et al. (2017). Development of BFMCOUPLER (v1. 0), the coupling scheme that links the MITgcm and BFM models for ocean biogeochemistry simulations. *Geosci. Model. Dev.* 10, 1423–1445.

D'Ortenzio, F., Antoine, D., and Marullo, S. (2008). Satellite-driven modeling of the upper ocean mixed layer and air–sea CO2 flux in the Mediterranean Sea. *Deep Sea Research Part I Oceanogr. Res. Papers* 55, 405–434. doi: 10.1016/j.dsr.2007.12.008

Di Biagio, V., Cossarini, G., Salon, S., and Solidoro, C. (2020). Extreme event waves in marine ecosystems: an application to Mediterranean Sea surface chlorophyll. *Biogeosciences* 17, 5967–5988.

Di Biagio, V., Cossarini, G., Salon, S., Lazzari, P., Querin, S., Sannino, G., et al. (2019). Temporal scales of variability in the Mediterranean Sea ecosystem: insight from a coupled model. *J. Mar. Syst.* 197:103176. doi: 10.1016/j.jmarsys.2019.05.002

Dobricic, S., and Pinardi, N. (2008). An oceanographic three-dimensional variational data assimilation scheme. *Ocean Model.* 22, 89–105. doi: 10.1016/j.ocemod.2008.01.004

D'Ortenzio, F., and Ribera d'Alcalà, M. (2009). On the trophic regimes of the Mediterranean Sea: a satellite analysis. *Biogeosciences* 6, 139–148.

El Hourany, R., Mejia, C., Faour, G., Crépon, M., and Thiria, S. (2021). Evidencing the impact of climate change on the phytoplankton community of the Mediterranean Sea through a bioregionalization approach. *J. Geophys. Res. Oceans* 126:e2020JC016808.

Escudier, R., Clementi, E., Cipollone, A., Pistoia, J., Drudi, M., Grandi, A., et al. (2021). A high resolution reanalysis for the Mediterranean Sea. *Front. Earth Sci.* 9:702285. doi: 10.3389/feart.2021.702285

Escudier, R., Clementi, E., Omar, M., Cipollone, A., Pistoia, J., Aydogdu, A., et al. (2020). *Mediterranean Sea Physical Reanalysis (CMEMS MED-Currents) (Version 1) set. Copernicus Monitoring Environment Marine Service (CMEMS)*. doi: 10.25423/CMCC/MEDSEA_MULTIYEAR_PHY_006_004_E3R1

Fennel, K., Gehlen, M., Brasseur, P., Brown, C. W., Ciavatta, S., Cossarini, G., et al. (2019). Advancing marine biogeochemical and ecosystem reanalyses and forecasts as tools for monitoring and managing ecosystem health. *Front. Mar. Sci.* 6:89. doi: 10.3389/fmars.2019.00089

Feudale, L., Cossarini, G., Bolzon, G., Lazzari, P., Solidoro, C., Teruzzi, A., et al. (2021). "Entering in the BGC-Argo era: improvements of the Mediterranean Sea biogeochemical operational system," in *Proceedings of the 9th EuroGOOS conference*. (France: EuroGOOS AISBL).

Flecha, S., Pérez, F. F., García-Lafuente, J., Sammartino, S., Ríos, A. F., and Huertas, I. E. (2015). Trends of pH decrease in the Mediterranean Sea through high frequency observational data: indication of ocean acidification in the basin. *Sci. Rep.* 5, 1–8. doi: 10.1038/srep16770

Garcia, H., Weathers, K., Paver, C., Smolyar, I., Boyer, T., Locarnini, M., et al. (2019). *World Ocean Atlas 2018. Volume 4 Dissolved Inorganic Nutrients (phosphate, nitrate and nitrate+nitrite, silicate)*. United States: National Oceanic and Atmospheric Administration.

Gehlen, G., Trang Chau, T. T., Conchon, A., Denvil-Sommer, A., Chevallier, F., Vrac, M., et al. (2020). "Section 2.10: Ocean acidification," in *Copernicus Marine Service Ocean State Report, Issue 4. Journal of Operational Oceanography*, Vol. 13 (Suppl. 1) (Abingdon: Taylor & Francis), S1–S172. doi: 10.1080/1755876X.2020.1785097

Giorgi, F. (2006). Climate change hot-spots. *Geophys. Res. Lett.* 33:2006. doi: 10.1029/2006GL025734

Gregg, W. W., Friedrichs, M. A., Robinson, A. R., Rose, K. A., Schlitzer, R., Thompson, K. R., et al. (2009). Skill assessment in ocean biological data assimilation. *J. Mar. Syst.* 76, 16–33.

Gutknecht, E., Reffray, G., Mignot, A., Dabrowski, T., and Sotillo, M. G. (2019). Modelling the marine ecosystem of Iberia–Biscay–Ireland (IBI) European waters for CMEMS operational applications. *Ocean Sci.* 15, 1489–1516. doi: 10.5194/os-15-1489-2019

Guyennon, A., Baklouti, M., Diaz, F., Palmieri, J., Beuvier, J., Lebaupin-Brossier, C., et al. (2015). New insights into the organic carbon export

in the Mediterranean Sea from 3-D modeling. *Biogeosciences* 12, 7025–7046.

Hernandez, F., Bertino, L., Brassington, G. B., Chassignet, E. P., Cummings, J. A., Davidson, F., et al. (2009). Validation and intercomparison studies within GODAE. *Oceanogr. Magaz.* 22, 128–143. doi: 10.5670/oceanog.2009.71

Hernandez, F., Blockley, E., Brassington, G. B., Davidson, F., Divakaran, P., Drévillon, M., et al. (2015). Recent progress in performance evaluations and near real-time assessment of operational ocean products. *J. Operat. Oceanogr.* 8, s221–s238. doi: 10.1080/1755876X.2015.1050282

Hernandez, F., Smith, G., Baetens, K., Cossarini, G., Garcia-Hermosa, I., Drévillon, M., et al. (2018). "Measuring performances, skill and accuracy in operational oceanography: new challenges and Approaches" in *New Frontiers in Operational Oceanography*. eds E. Chassignet, A. Pascual, J. Tintoré, and J. Verron (Tallahassee, FL: GODAE OceanView). 759–796. doi: 10.17125/gov2018

Hipsey, M. R., Gal, G., Arhonditsis, G. B., Carey, C. C., Elliott, J. A., Frassl, M. A., et al. (2020). A system of metrics for the assessment and improvement of aquatic ecosystem models. *Environ. Model. Softw.* 128:104697. doi: 10.1016/j.envsoft.2020.104697

Hulme, M., Mitchell, J., Ingram, W., Lowe, J., Johns, T., New, M., et al. (1999). Climate change scenarios for global impacts studies. *Glob. Environ. Change* 9, S3–S19. doi: 10.1016/S0959-3780(99)00015-1

Jolliff, J. K., Kindle, J. C., Shulman, I., Penta, B., Friedrichs, M. A., Helber, R., et al. (2009). Summary diagrams for coupled hydrodynamic-ecosystem model skill assessment. *J. Mar. Syst.* 76, 64–82.

Kempe, S., Pettine, M., and Cauwet, G. (1991). "). Biogeochemistry of European rivers" in *Biogeochemistry of Major World Rivers, Scope 42*. (eds) E. T. Degens, S. Kempe, and J. E. Richey (Chichester: John Wiley). 169–211.

Krumhardt, K. M., Lovenduski, N. S., Iglesias-Rodriguez, M. D., and Kleypas, J. A. (2017). Coccolithophore growth and calcification in a changing ocean. *Progr. Oceanogr.* 159, 276–295.

Kwiatkowski, L., Torres, O., Bopp, L., Aumont, O., Chamberlain, M., Christian, J. R., et al. (2020). Twenty-first century ocean warming, acidification, deoxygenation, and upper-ocean nutrient and primary production decline from CMIP6 model projections. *Biogeosciences* 17, 3439–3470. doi: 10.5194/bg-17-3439-2020

Lavigne, H., D'Ortenzio, F., d'Alcalà, M. R., Claustre, H., Sauzède, R., and Gacic, M. (2015). On the vertical distribution of the chlorophyll a concentration in the Mediterranean Sea: a basin-scale and seasonal approach. *Biogeosciences* 12, 5021–5039. doi: 10.5194/bg-12-5021-2015

Lazzari, P., Solidoro, C., Ibello, V., Salon, S., Teruzzi, A., Béranger, K., et al. (2012). Seasonal and interannual variability of plankton chlorophyll and primary production in the Mediterranean Sea: a modelling approach. *Biogeosciences* 9, 217–233. doi: 10.5194/bg-9-217-2012

Lazzari, P., Solidoro, C., Salon, S., and Bolzon, G. (2016). Spatial variability of phosphate and nitrate in the Mediterranean Sea: a modelling approach. *Deep Sea Res.* 108, 39–52. doi: 10.1016/j.dsr.2015.12.006

Lazzari, P., Teruzzi, A., Salon, S., Campagna, S., Calonaci, C., Colella, S., et al. (2010). Pre-operational short-term forecasts for the Mediterranean Sea biogeochemistry. *Ocean Sci.* 6, 25–39. doi: 10.5194/os-6-25-2010

Li, P., and Tanhua, T. (2020). Recent changes in deep ventilation of the Mediterranean Sea; evidence from long-term transient tracer observations. *Front. Mar. Sci.* 7:594. doi: 10.3389/fmars.2020.00594

Lipizer, M., Partescano, E., Rabitti, A., Giorgetti, A., and Crise, A. (2014). Qualified temperature, salinity and dissolved oxygen climatologies in a changing Adriatic Sea. *Ocean Sci.* 10, 771–797. doi: 10.5194/os-10-771-2014

Macias, D., Stips, A., and Garcia-Gorriz, E. (2014). The relevance of deep chlorophyll maximum in the open Mediterranean Sea evaluated through 3d hydrodynamic-biogeochemical coupled simulations. *Ecol. Model.* 281, 26–37.

Malanotte-Rizzoli, P., Artale, V., Borzelli-Eusebi, G. L., Brenner, S., Crise, A., Gacic, M., et al. (2014). Physical forcing and physical/biochemical variability of the Mediterranean Sea: a review of unresolved issues and directions for future research. *Ocean Sci.* 10, 281–322.

Mavropoulou, A. M., Vervatis, V., and Sofianos, S. (2020). Dissolved oxygen variability in the Mediterranean Sea. *J. Mar. Syst.* 208:103348. doi: 10.1016/j.jmarsys.2020.103348

Melaku Canu, D., Ghermandi, A., Nunes, P. A. L. D., Lazzari, P., Cossarini, G., and Solidoro, C. (2015). Estimating the value of carbon sequestration ecosystem services in the Mediterranean Sea: an ecological economics approach. *Glob. Environ. Change* 32, 87–95. doi: 10.1016/j.gloenvcha.2015.02.008

Meybeck, M., and Ragu, A. (1997). *River Discharges to the Oceans: an Assessment of Suspended Solids, Major Ions and Nutrients*. Kenya: UNEP.

Micheli, F., Halpern, B. S., Walbridge, S., Ciriaco, S., Ferretti, F., Fraschetti, S., et al. (2013). Cumulative human impacts on Mediterranean and Black Sea marine ecosystems: assessing current pressures and opportunities. *PLoS One* 8:e79889. doi: 10.1371/journal.pone.0079889

Mignot, A., Claustre, H., Cossarini, G., D'Ortenzio, F., Gutknecht, E., Lamouroux, J., et al. (2021). *Defining BGC-Argo-based Metrics of Ocean Health and Biogeochemical Functioning for the Evaluation of Global Ocean Models*. Germany: European Geosciences Union. doi: 10.5194/bg-2021-2

Miloslavich, P., Bax, N. J., Simmons, S. E., Klein, E., Appeltans, W., Aburto-Oropeza, O., et al. (2018). Essential ocean variables for global sustained observations of biodiversity and ecosystem changes. *Glob. Change Biol.* 24, 2416–2433. doi: 10.1111/gcb.14108

Moll, A. (2000). Assessment of three-dimensional physical-biological ECOHAM1 simulations by quantified validation for the North Sea with ICES and ERSEM data. *ICES J. Mar. Sci.* 57, 1060–1068.

Morrow, R. M., Ohman, M. D., Goericke, R., Kelly, T. B., Stephens, B. M., and Stukel, M. R. (2018). Primary productivity, mesozooplankton grazing, and the biological pump in the california current ecosystem: variability and response to El niño. *Deep Sea Res.* 140, 52–62. doi: 10.1016/j.dsr.2018.07.012

Morse, J. W., and Berner, R. A. (1972). Dissolution kinetics of calcium carbonate in sea water; I, A kinetic origin for the lysocline. *Am. J. Sci.* 272, 840–851.

Novi, L., Bracco, A., and Falasca, F. (2021). Uncovering marine connectivity through sea surface temperature. *Sci. Rep.* 11, 1–9.

Olsen, A., Key, R. M., van Heuven, S., Lauvset, S. K., Velo, A., Lin, X., et al. (2016). The Global Ocean Data Analysis Project version 2 (GLODAPv2) – an internally consistent data product for the world ocean. *Earth Syst. Sci. Data* 8, 297–323. doi: 10.5194/essd-8-297-2016

Olsen, A., Lange, N., Key, R. M., Tanhua, T., Álvarez, M., Becker, S., et al. (2019). GLODAPv2.2019 – an update of GLODAPv2. *Earth Syst. Sci. Data* 11, 1437–1461. doi: 10.5194/essd-11-1437-2019

Oreskes, N., Shrader-Frechette, K., and Belitz, K. (1994). Verification, validation, and confirmation of numerical models in the earth sciences. *Science* 263, 641–645. doi: 10.1126/science.263.5147.641

Oviedo, A., Ziveri, P., Álvarez, M., and Tanhua, T. (2015). Is coccolithophore distribution in the Mediterranean Sea related to seawater carbonate chemistry? *Ocean Sci.* 11, 13–32.

Park, J. Y., Stock, C. A., Yang, X., Dunne, J. P., Rosati, A., John, J., et al. (2018). Modeling global ocean biogeochemistry with physical data assimilation: a pragmatic solution to the equatorial instability. *J. Adv. Model. Earth Syst.* 10, 891–906. doi: 10.1002/2017MS001223

Pinardi, N., and Masetti, E. (2000). Variability of the large scale general circulation of the Mediterranean Sea from observations and modelling: a review. *Palaeogeogr. Palaeoclimatol. Palaeoecol.* 158, 153–173.

Pinardi, N., Zavatarelli, M., Adani, M., Coppini, G., Fratianni, C., Oddo, P., et al. (2015). Mediterranean Sea large-scale low-frequency ocean variability and water mass formation rates from 1987 to 2007: a retrospective analysis. *Progr. Oceanogr.* 132, 318–332.

Reale, M., Cossarini, G., Lazzari, P., Lovato, T., Bolzon, G., Masina, S., et al. (2021). *Acidification, Deoxygenation, and Nutrient Decline in a Warming Mediterranean Sea*. (Submitted in Biogeosciences discussion).

Ribera d'Alcalà, M., Civitarese, G., Conversano, F., and Lavezza, R. (2003). Nutrient ratios and fluxes hint at overlooked processes in the Mediterranean Sea. *J. Geophys. Res.* 108:8106. doi: 10.1029/2002JC001650

Richon, C., Dutay, J. C., Dulac, F., Wang, R., Balkanski, Y., Nabat, P., et al. (2018). Modeling the impacts of atmospheric deposition of nitrogen and desert dust derived phosphorus on nutrients and biological budgets of the Mediterranean Sea. *Prog. Oceanogr.* 163, 21–39.

Salgado-Hernanz, P. M., Racault, M. F., Font-Muñoz, J. S., and Basterretxea, G. (2019). Trends in phytoplankton phenology in the Mediterranean Sea based on ocean-colour remote sensing. *Remote Sens. Environ.* 221, 50–64. doi: 10.1016/j.rse.2018.10.036

Salon, S., Cossarini, G., Bolzon, G., Feudale, L., Lazzari, P., Teruzzi, A., et al. (2019). Novel metrics based on Biogeochemical Argo data to improve the

model uncertainty evaluation of the CMEMS Mediterranean marine ecosystem forecasts. *Ocean Sci.* 15, 997–1022. doi: 10.5194/os-15-997-2019

Sathyendranath, S., Pardo, S., Benincasa, M., Brando, V. E., Brewin, R. J. W., Mélin, F., et al. (2018). 1.5. Essential Variables: ocean Colour in Copernicus Marine Service Ocean State Report - Issue 2. *J. Operat. Oceanogr.* 11, 1–142. doi: 10.1080/1755876X.2018.1489208

Schneider, A., Tanhua, T., Körtzinger, A., and Wallace, D. W. R. (2010). High anthropogenic carbon content in the eastern Mediterranean. *J. Geophys. Res.* 115:C12050. doi: 10.1029/2010JC006171

Schneider, A., Tanhua, T., Roether, W., and Steinfeldt, R. (2014). Changes in ventilation of the Mediterranean Sea during the past 25 year. *Ocean Sci.* 10, 1–16. doi: 10.5194/os-10-1-2014

Sharp, J. D., Pierrot, D., Humphreys, M. P., Epitalon, J.-M., Orr, J. C., Lewis, E. R., et al. (2020). *CO2SYSv3 for MATLAB (Version v3.2.0)*. Zenodo. Available online at: (https://zenodo.org/record/4774718#.YWRThxBBw7w

Siegel, D. A., Buesseler, K. O., Doney, S. C., Sailley, S. F., Behrenfeld, M. J., and Boyd, P. W. (2014). Global assessment of ocean carbon export by combining satellite observations and food-web models. *Glob. Biogeochem. Cycles* 28, 181–196.

Siokou-Frangou, I., Christaki, U., Mazzocchi, M. G., Montresor, M., Ribera d'Alcalá, M., Vaqué, D., et al. (2010). Plankton in the open Mediterranean Sea: a review. *Biogeosciences* 7, 1543–1586. doi: 10.5194/bg-7-1543-2010

Sisma-Ventura, G., Kress, N., Silverman, J., Gertner, Y., Ozer, T., Biton, E., et al. (2021). Post-eastern Mediterranean transient oxygen decline in the deep waters of the southeast Mediterranean Sea supports weakening of ventilation rate. *Front. Mar. Sci.* 7:598686. doi: 10.3389/fmars.2020.598686

Skliris, N., Zika, J. D., Herold, L., Josey, S. A., and Marsh, R. (2018). Mediterranean sea water budget long-term trend inferred from salinity observations. *Clim. Dyn.* 51, 2857–2876. doi: 10.1007/s00382-017-4053-7

Storto, A., Masina, S., and Navarra, A. (2016). Evaluation of the CMCC eddy-permitting global ocean physical reanalysis system (C-GLORS, 1982–2012) and its assimilation components. *Q. J. R. Meteorol. Soc.* 142, 738–758.

Stow, C. A., Jolliff, J., McGillicuddy, D. J. Jr., Doney, S. C., Allen, J. I., Friedrichs, M. A., et al. (2009). Skill assessment for coupled biological/physical models of marine systems. *J. Mar. Syst.* 76, 4–15.

Teruzzi, A., Bolzon, G., Cossarini, G., Lazzari, P., Salon, S., Crise, A., et al. (2019a). *Mediterranean Sea Biogeochemical Reanalysis (CMEMS MED-Biogeochemistry) Data set*. Copernicus Monitoring Environment Marine Service (CMEMS). doi: 10.25423/MEDSEA_REANALYSIS_BIO_006_008

Teruzzi, A., Bolzon, G., Salon, S., Lazzari, P., Solidoro, C., and Cossarini, G. (2018). Assimilation of coastal and open sea biogeochemical data to improve phytoplankton modelling in the Mediterranean Sea. *Ocean Model.* 132, 46–60. doi: 10.1016/j.ocemod.2018.09.007

Teruzzi, A., Cossarini, G., Lazzari, P., Salon, S., Bolzon, G., Crise, A., et al. (2016). *Mediterranean Sea Biogeochemical Reanalysis (CMEMS MED REABiogeochemistry 1999–2015). Copernicus Monitoring Environment Marine Service*. Lecce: Centro Euro-Mediterraneo sui Cambiamenti Climatici.

Teruzzi, A., Di Biagio, V., Feudale, L., Bolzon, G., Lazzari, P., Salon, S., et al. (2021). *Data from: mediterranean Sea Biogeochemical Reanalysis (CMEMS MED-Biogeochemistry, MedBFM3 system) (Version 1) [Data set]*. Copernicus Monitoring Environment Marine Service (CMEMS), doi: 10.25423/CMCC/MEDSEA_MULTIYEAR_BGC_006_008_MEDBFM3

Teruzzi, A., Di Cerbo, P., Cossarini, G., Pascolo, E., and Salon, S. (2019b). Parallel implementation of a data assimilation scheme for operational oceanography: the case of the OGSTM-BFM model system. *Comput. Geosci.* 124, 103–114. doi: 10.1016/j.cageo.2019.01.003

Teruzzi, A., Dobricic, S., Solidoro, C., and Cossarini, G. (2014). A 3-D variational assimilation scheme in coupled transport biogeochemical models: forecast of Mediterranean biogeochemical properties. *J. Geophys. Res. Oceans* 119, 200–217. doi: 10.1002/2013JC009277

Terzić, E., Lazzari, P., Organelli, E., Solidoro, C., Salon, S., D'Ortenzio, F., et al. (2019). Merging bio-optical data from Biogeochemical-Argo floats and models in marine biogeochemistry. *Biogeosciences* 16, 2527–2542. doi: 10.5194/bg-16-2527-2019

Terzić, E., Salon, S., Cossarini, G., Solidoro, C., Teruzzi, A., Miró, A., et al. (2021). Impact of interannually variable diffuse attenuation coefficients for downwelling irradiance on biogeochemical modelling. *Ocean Model.* 161:101793. doi: 10.1016/j.ocemod.2021.101793

Thierry, V., Bittig, H., and The Argo BGC Team. (2018). *Argo Quality Control Manual for Dissolved Oxygen Concentration, Version 2.0*. France: October 2018, IFREMER for Argo BGC Group, Villefranche-sur-Mer, France, p. 33. . doi: 10.13155/46542

Touratier, F., and Goyet, C. (2011). Impact of the Eastern Mediterranean Transient on the distribution of anthropogenic CO2 and first estimate of acidification for the Mediterranean Sea. *Deep Sea Res.* 58, 1–15. doi: 10.1016/j.dsr.2010.10.002

Uitz, J., Stramski, D., Gentili, B., D'Ortenzio, F., and Claustre, H. (2012). Estimates of phytoplankton class-specific and total primary production in the Mediterranean Sea from satellite ocean color observations. *Glob. Biogeochem. Cycles* 26:GB2024. doi: 10.1029/2011GB004055

Vantrepotte, V., and Mélin, F. (2009). Temporal variability of 10-year global SeaWiFS time-series of phytoplankton chlorophyll a concentration. *ICES J. Mar. Sci.* 66, 1547–1556.

Velaoras, D., Papadopoulos, V. P., Kontoyiannis, H., Cardin, V., and Civitarese, G. (2019). Water masses and hydrography during april and june 2016 in the cretan sea and cretan passage (Eastern Mediterranean Sea). *Deep Sea Res. Part II Top. Stud. Oceanogr.* 164, 25–40. doi: 10.1016/j.dsr2.2018.09.005

Vichi, M., Lovato, T., Butenschön, M., Tedesco, L., Lazzari, P., Lazzari, P., et al. (2020). *The Biogeochemical Flux Model (BFM): equation Description and User Manual in BFM Version 5.2 BFM Report Series N. 1. Release 1.2, BFM Report Series N. 1*. Bologna, 87. Available online at: http://bfm-community.eu (accessed November 15, 2020).

von Schuckmann, K., Le Traon, P. Y., Alvarez-Fanjul, E., Axell, L., Balmaseda, M., Breivik, L. A., et al. (2016). The Copernicus Marine Environment Monitoring Service Ocean State Report. *J. Operat. Oceanogr.* 9, s235–s320. doi: 10.1080/1755876X.2016.1273446

von Schuckmann, K., Le Traon, P. Y., Smith, N., Pascual, A., Brasseur, P., Fennel, K., et al. (2018). Copernicus marine service ocean state report. *J. Operat. Oceanogr.* 11, S1–S142.

von Schuckmann, K., Le Traon, P.-Y., Smith, N., Pascual, A., Djavidnia, S., Gattuso, J. P., et al. (2020). Copernicus Marine Service Ocean State Report, Issue 4. *J. Operat. Oceanogr.* 13, S1–S172.

Wimart-Rousseau, C., Wagener, T., Alvarez, M., Moutin, T., Fourrier, M., Coppola, L., et al. (2021). Seasonal and Interannual Variability of the CO2 System in the Eastern Mediterranean Sea: a Case Study in the North Western Levantine Basin. *Front. Mar. Sci.* 8:649246. doi: 10.3389/fmars.2021.649246

Conflict of Interest: The authors declare that the research was conducted in the absence of any commercial or financial relationships that could be construed as a potential conflict of interest.

frontiers in Marine Science

ORIGINAL RESEARCH
published: 08 February 2022
doi: 10.3389/fmars.2022.781788

The Role of Eddies in the North Atlantic Decadal Variability

Chunxue Yang[1], Clément Bricaud[2], Marie Drévillon[2], Andrea Storto[1], Alessio Bellucci[3] and Rosalia Santoleri[1]*

[1] Institute of Marine Sciences, National Research Council of Italy, Rome, Italy, [2] Mercator Ocean International, Ramonville-Saint-Agne, France, [3] Institute of Atmospheric Sciences and Climate, National Research Council of Italy, Bologna, Italy

The role of eddies in the North Atlantic decadal variability is investigated in this study by using two ocean reanalyses, including an eddy permitting (or eddy poor) reanalysis with horizontal resolution of 0.25 degree and 75 vertical levels and an eddy resolving (or eddy rich) reanalysis with horizontal resolution of 1/12 degree and 50 vertical levels. The prominent mid-1990s warming and post-2005 cooling trend as part of the North Atlantic decadal variability is well displayed in both reanalyses with no significant difference between them. The main driver of the mid-1990s warming and post-2005 cooling trend is the increase and reduction of the meridional ocean heat transport showing similar patterns in both reanalyses. The relative contribution of the heat transport anomalies from eddies to the total heat transport anomalies is slightly larger in eddy resolving than in eddy permitting ocean reanalysis. However, the total mean ocean meridional heat transport increases by 10% in eddy resolving reanalysis with respect to eddy permitting reanalysis and is mainly due to the associated increase of the mean states (temperature and velocity). Therefore, the increase of eddy population due to the increase of horizontal resolution, found by comparing the two datasets, does not affect the MHT anomalies significantly and, consequently, the North Atlantic decadal variability. It is found that the importance of the model horizontal resolution for the North Atlantic decadal variability depends on the interaction between the eddies (small scale) and the mean state (large scale) at decadal time scales. Although the fast increase of computational power will allow soon for eddy-resolving predictions, the need to use high resolution modeling tools for decadal predictions depends on the importance of initialization methods and the interaction between small scale and large-scale variabilities. This study has pivotal implications for the development of North Atlantic decadal prediction systems.

Keywords: eddies, North Atlantic, decadal variability, reanalyses, meridional heat transport, eddy-large scale interaction

OPEN ACCESS

Edited by:
Sergio M. Vallina, Spanish Institute of Oceanography (IEO), Spain

Reviewed by:
Emilio Hernandez-Garcia, Institute of Interdisciplinary Physics and Complex Systems, Spanish National Research Council (CSIC), Spain
Antonio Bonaduce, Nansen Environmental and Remote Sensing Center (NERSC), Norway

****Correspondence:***
Chunxue Yang
chunxue.yang@cnr.it

Specialty section:
This article was submitted to Global Change and the Future Ocean, a section of the journal Frontiers in Marine Science

Received: *23 September 2021*
Accepted: *03 January 2022*
Published: *08 February 2022*

Citation:
Yang C, Bricaud C, Drévillon M, Storto A, Bellucci A and Santoleri R (2022) The Role of Eddies in the North Atlantic Decadal Variability. Front. Mar. Sci. 9:781788. doi: 10.3389/fmars.2022.781788

INTRODUCTION

The North Atlantic is an important region displayed with prominent decadal variability phenomena. Robson et al. (2016) show that the rapid warming in the mid-1990s and cooling from 2005 to 2016 in the eastern subpolar gyre region (SPG) are part of the decadal variability in the North Atlantic. In terms of the mid-1990s rapid warming, several studies have been devoted to study the oceanic and atmospheric processes that are responsible for this abrupt climate change

by using observations, climate model simulations and decadal prediction experiments (Robson et al., 2012, 2016; Yeager et al., 2012; Delworth et al., 2016). Ocean reanalyses for the first time are used to study the mid-1990s rapid warming by Yang et al. (2016). The role of data assimilation is investigated therein, showing that the ingestion of observations through data assimilation improves the mean state of the North Atlantic, while the mid-1990s rapid warming event is well represented in both control run (without data assimilation) and ocean reanalysis.

The mechanisms that are responsible for the mid-1990s warming have been proposed in an extensive body of studies (Haìtuìn et al., 2005; Bersch et al., 2007; Sarafanov et al., 2008; Herbaut and Houssais, 2009; Häkkinen et al., 2011; Robson et al., 2012, 2016; Yeager et al., 2012; Delworth et al., 2016; Yang et al., 2016). One of the main drivers of Atlantic variability is the North Atlantic Oscillation (NAO) showing an abrupt change between winters of 1994/1995 and 1995/1996 from a positive to a negative phase. The advection of warm water due to the gyre circulation and the strengthening of the Atlantic Meridional Overturning Circulation (AMOC) accompanied by increasing Meridional Heat Transport (MHT) that results from the change of the NAO are responsible for the mid-1990s rapid warming in the SPG region (Haìtuìn et al., 2005; Bersch et al., 2007; Sarafanov et al., 2008; Robson et al., 2012, 2016; Yeager et al., 2012; Delworth et al., 2016; Yang et al., 2016). A recent study by Robson et al. (2016) shows a reversal in the North Atlantic temperatures trend, turning from warming to cooling around 2005, and the concomitant weakening of the ocean circulation associated with a reduction of MHT due to the occurrence of low-density surface waters in the Labrador Sea. The mid-1990s warming and post 2005 cooling in the North Atlantic are prominent manifestations of decadal variability in the North Atlantic Ocean, where changes in the MHT play a significant role. This prominent decadal variability is also demonstrated in the sea level change in the North Atlantic (Chafik et al., 2019). There is indeed evidence of significant predictability in the North Atlantic sector displayed by decadal prediction experiments, associated with the use of ocean analyses as initialization products (Matei et al., 2012; Bellucci et al., 2013, 2015; Polkova et al., 2019a,b).

Along with numerical and technological developments, the spatial and temporal resolution of climate models has been increasing (Haarsma et al., 2016), allowing the delivery of eddy-resolving (e.g., 1/12 degree resolution) global datasets for large scale climate studies. The primary question we would like to address in this study is the relative role of eddies in the North Atlantic decadal climate variability. More specifically we investigate the contribution of mesoscale ocean eddies to the MHT variability, which in turn drives the decadal climate changes recently observed in the North Atlantic.

The contribution of eddies to the ocean MHT has been investigated in several studies (Roemmich and Gilson, 2001; Jayne and Marotzke, 2002; Qiu and Chen, 2005; Aoki et al., 2013; Treguier et al., 2017; Zhao et al., 2018; Docquier et al., 2019; Sun et al., 2019; Delman and Lee, 2020). For example, a latest estimation using Argo and altimetry observations shows that the eddy heat transport is mainly located within the top 1,000 m and accounts for half of the total heat transport at 45°S and one third at 35°N (Sun et al., 2019). Model studies show that with the increase of model resolution the total MHT increases (Treguier et al., 2012; Grist et al., 2018; Docquier et al., 2019), mainly due to the change of time-mean circulation rather than the eddy component (Treguier et al., 2012). However, previous studies have mainly focused on the role of eddies in the climatology of the total MHT at a certain time period. The impact of model resolution on the MHT variability that is responsible to the North Atlantic decadal variability has been overlooked to the best of the authors' knowledge. Additionally, the eddy MHT has been explored by using either observations or numerical model simulations. In this study our goal is to investigate the role of eddies in the Atlantic MHT variability by using ocean reanalyses at different model resolutions (1/4 and 1/12 degree).

Ocean reanalyses have been used in several climate studies (Storto et al., 2016; Yang et al., 2016) and climate change monitoring owing to their temporal and spatial consistency of data coverage and dynamically consistent estimates of the ocean states compared to either observations or climate models. Complementing ocean general circulation models with data assimilation has indeed shown to greatly improve the representation of eddies (population, life and extension) with respect to free-run models even in eddy-permitting comparisons in the North Atlantic (Cipollone et al., 2017). Likewise, transports representation has been demonstrated to be better reproduced than in ocean simulations (Jackson et al., 2016, 2018). This study will shed light on the importance of eddy-induced MHT in the large-scale climate variability.

DATA AND METHODS

In this study we use two sets of global ocean reanalyses produced by Mercator Ocean International including the Global Ocean Reanalysis 2 version 4 (GLORYS2V4, hereafter G4, Storto et al., 2019) at 1/4 degree (eddy permitting), and the Global Ocean Reanalysis 12 version 1 (GLORYS12V1, hereafter G12, Lellouche et al., 2021) at 1/12 degree horizontal resolution (eddy resolving), both covering the period from 1993 to 2016. A robust validation of these products can be found in quality information documents (Garric and Parent, 2017; Drèvillon et al., 2021a).

The details of the production of G4 are given in Garric and Parent (2018). Here we provide a brief introduction of G4. The ocean dynamic model of the G4 is the Nucleus for European Models of the Ocean version 3.1 (NEMO 3.1, Madec, 2008) coupled with the thermodynamic-dynamic Louvain-la Neuve Sea Ice Model version 2 (LIM2, Fichefet and Morales Maqueda, 1997). The horizontal grid of NEMO is based on a tripolar grid with 1/4 degree of horizontal resolution and 75 depth levels. The momentum, heat and freshwater fluxes driving the ocean are calculated based on Large and Yeager (2004) bulk formulas by using atmospheric variables from the ECMWF ERA-Interim atmospheric reanalysis (Dee et al., 2011). The initial conditions are from the United Kingdom Met office EN4 objective analyses (Good et al., 2013) version 4.0.2 for temperature and salinity

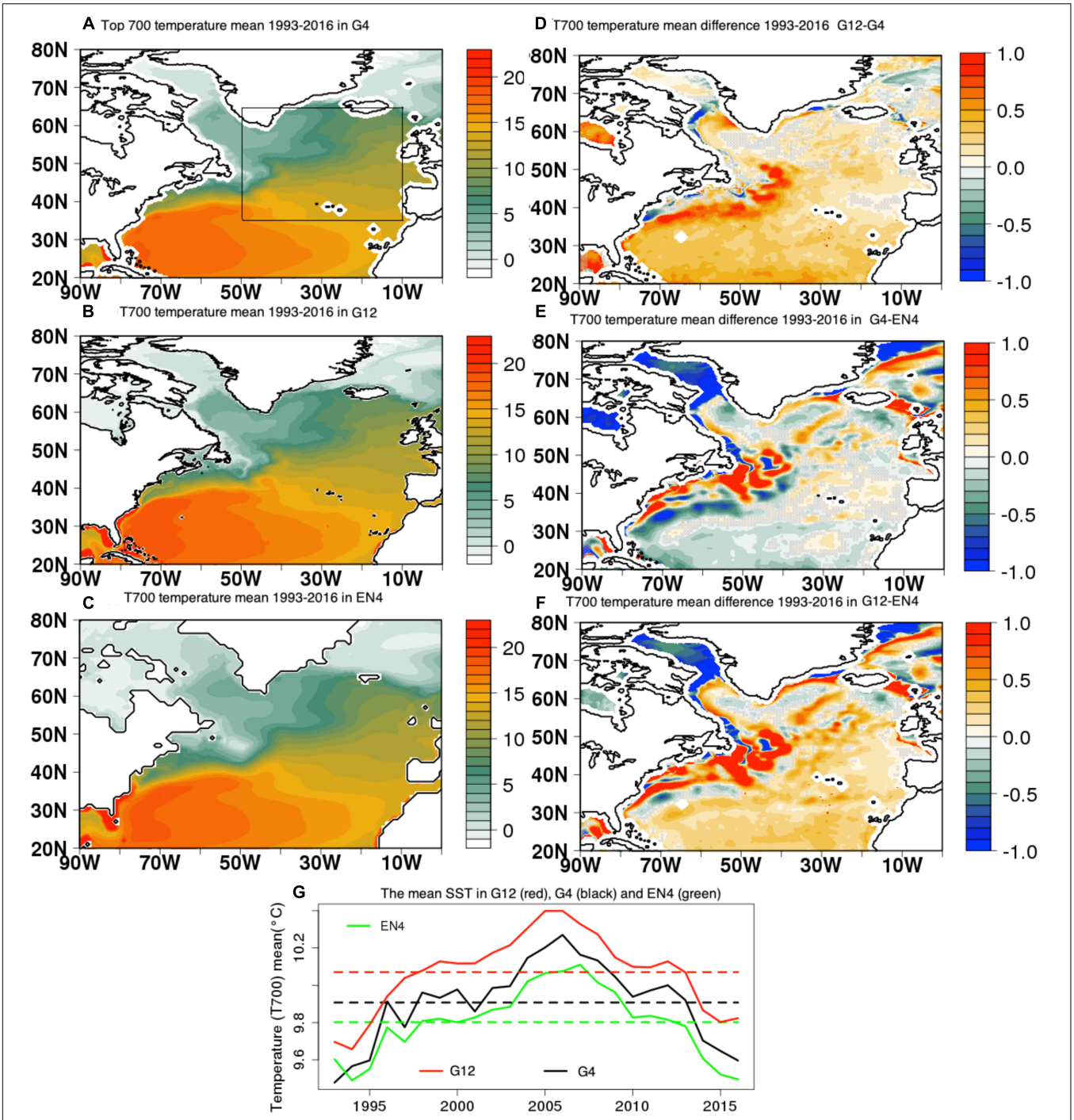

FIGURE 1 | The mean climatology of top 700 m (T700) temperature computed for the 1993–2016 period **(A)** in G4, **(B)** in G12, **(C)** in EN4, **(D)** the difference between G12 and G4, **(E)** the difference between G4 and EN4, **(F)** the difference between G12 and EN4, **(G)** The T700 averaged in the box area shown in panel **(A)**. Areas with differences that do not pass *t*-test 95% confidence interval are marked with light gray crosses.

and the sea ice initial conditions come from National Snow and Ice Data Center (NSDIC) bootstrap products (Comiso, 2000). The data assimilation scheme is the reduced order Kalman filter based on the SEEK formulation (Pham et al., 1998), named as Système d'Assimilation Mercator version 2 (SAM2) and a three-dimensional variational (3D-Var) bias correction scheme is used to correct large-scale temperature and salinity biases (Lellouche et al., 2018). The surface observations assimilated into G4 include satellite-based sea level anomaly and SST and temperature and salinity profiles from CORA 4.1 *in situ* database

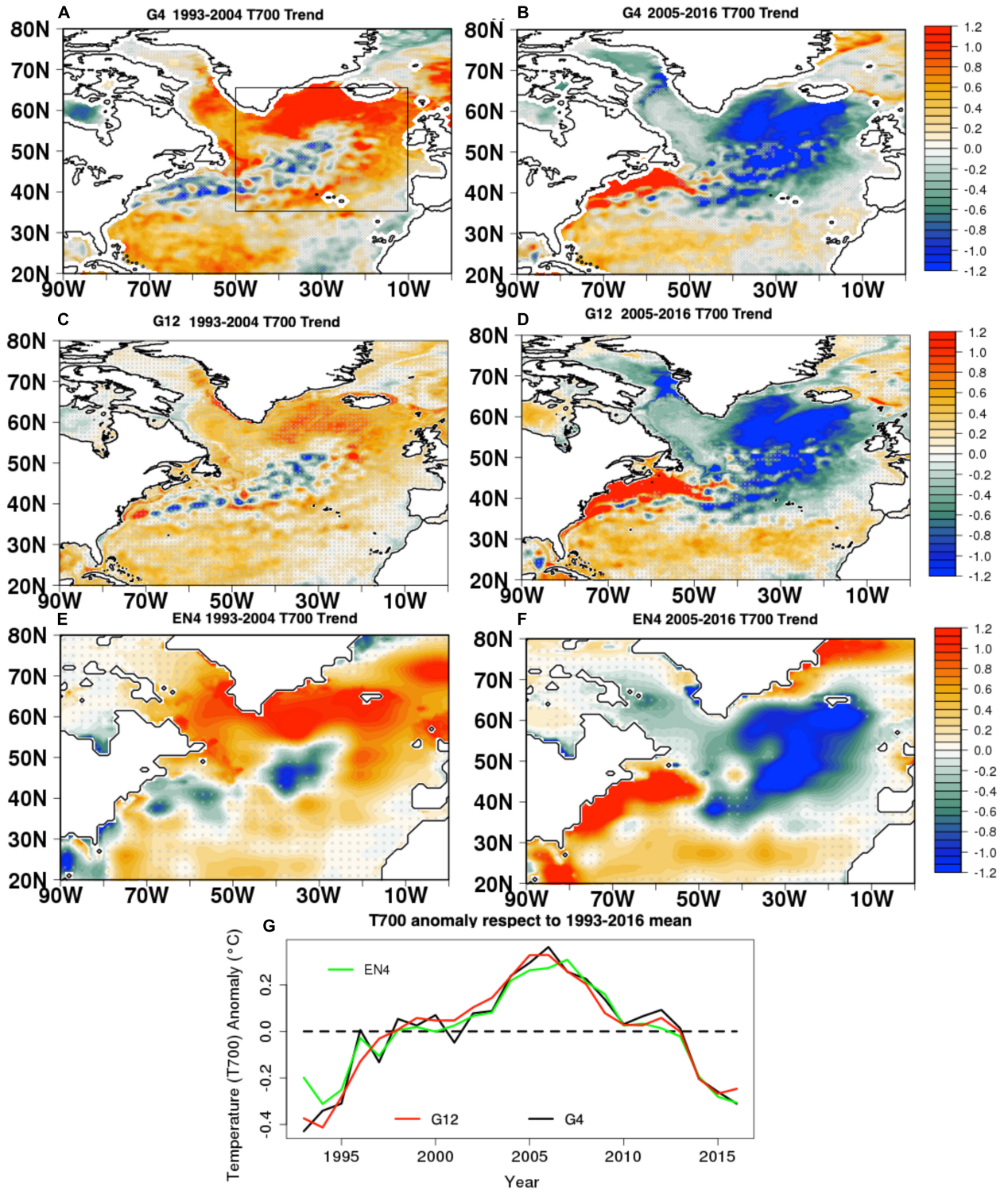

FIGURE 2 | Top 700 temperature (T700) linear trend (unit: °C per decade) **(A)** from 1993–2004 in G4, **(B)** from 2005 to 2016 in G4, **(C)** from 1993–2004 in G12, **(D)** from 2005 to 2016 in G12, **(E)** from 1995–2016 in EN4, **(F)** from 2005–2016 in EN4 and **(G)** T700 anomaly respect to 1993–2016 mean averaged in the boxed regions (35 N–65 N. 10 W–50 W) shown in panel **(A)** for G4 (black), G12 (red) and EN4 (green). In panels **(A–F)** regions that do not pass *t*-test 95% confidence interval are marked with light gray cross.

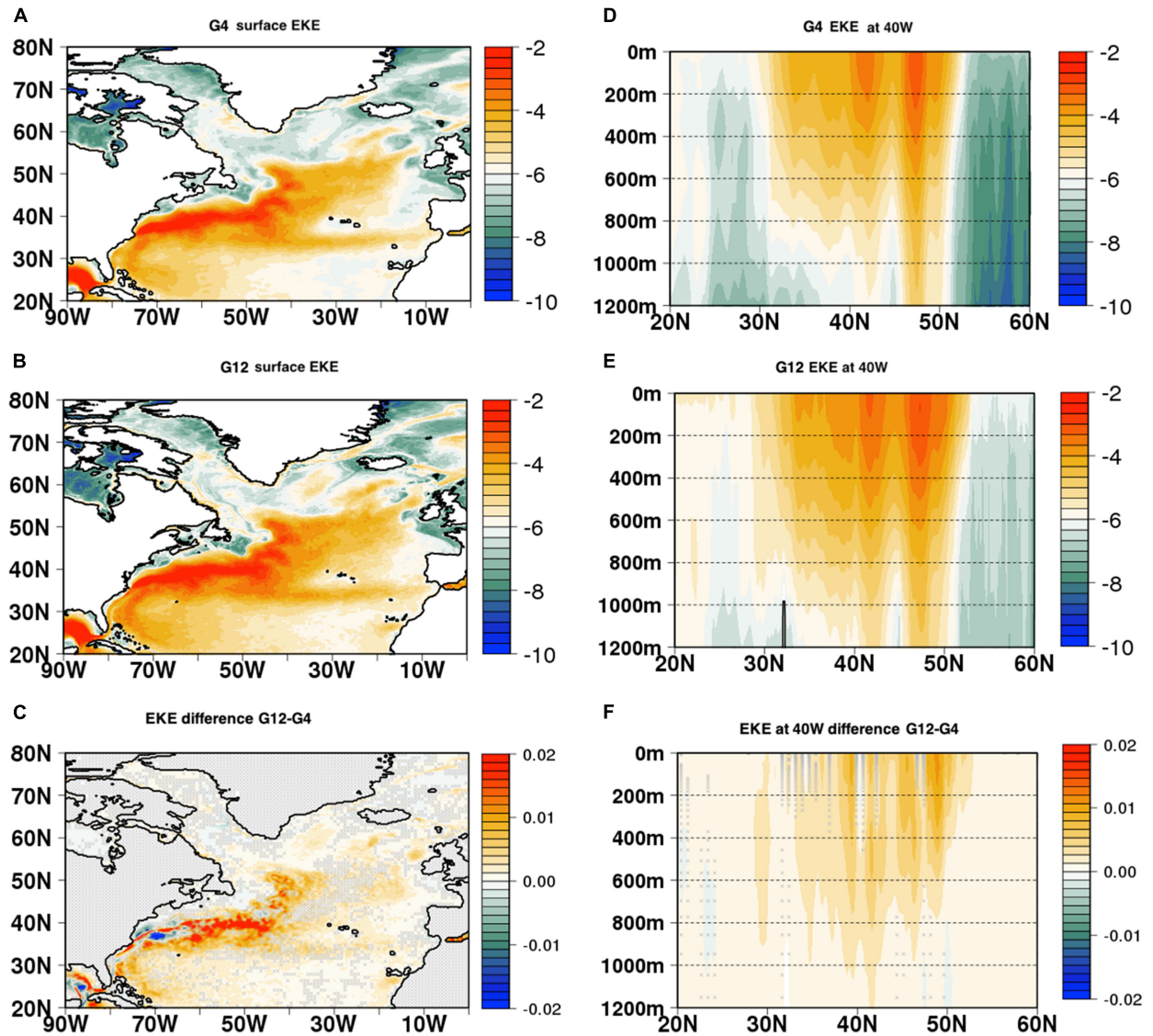

FIGURE 3 | Eddy kinetic energy (EKE) climatology (1993–2016) in **(A)** G4 and **(B)** G12 at the surface, **(C)** the surface EKE difference between G12 and G4, **(D)** EKE at 40°W in G4, **(E)** EKE at 40°W in G12 **(F)** the difference between G12 and G4 from surface to 1,200 m at 40°W. The analysis is based on monthly data. In panels **(E,F)** areas with values that do not pass *t*-test 95% confidence interval are indicated with light gray crosses (Unit: log m2/s2 for EKE and m2/s2 for EKE differences).

provided by the Copernicus Marine Environment Monitoring Service (CMEMS) (Szekely et al., 2015). Sea ice concentrations from IFREMER/CERSAT products (Ezraty et al., 2007) are also assimilated.

The main difference between G12 and G4 is the resolution of the ocean model. As G4, the ocean model of G12 is based on NEMO 3.1 but with the horizontal resolution of 1/12 degree and 50 vertical levels. Further to the resolution, the two reanalyses differ for the precipitation dataset toward which the atmospheric fluxes are corrected (PMWC and GPCPV2.2 for G4 and G12, respectively). The initial conditions and restoring climatology for Gibraltar and Bab-El-Mandeb straits come from EN4.2.0 for G12 and EN4.0.2 for G4 respectively. Details of the G12 configuration are described in Drèvillon et al. (2021a) and the detailed differences between G4 and G12 are described in Drèvillon et al. (2021b).

The method to calculate the eddy component of MHT follows the traditional scale separation approach, as schematized below:

$$v = \overline{v} + v' \tag{1}$$

$$T = \overline{T} + T' \tag{2}$$

in which T represents ocean temperature and v represents ocean meridional velocity. The $\overline{v}$ and $\overline{T}$ are time mean of v and T for the whole time period (1993–2016); and v' and T' are the deviation from the time mean. We follow Crosnier et al. (2001), and use 5-day fields, in order to secure an accurate estimate of MHT. The

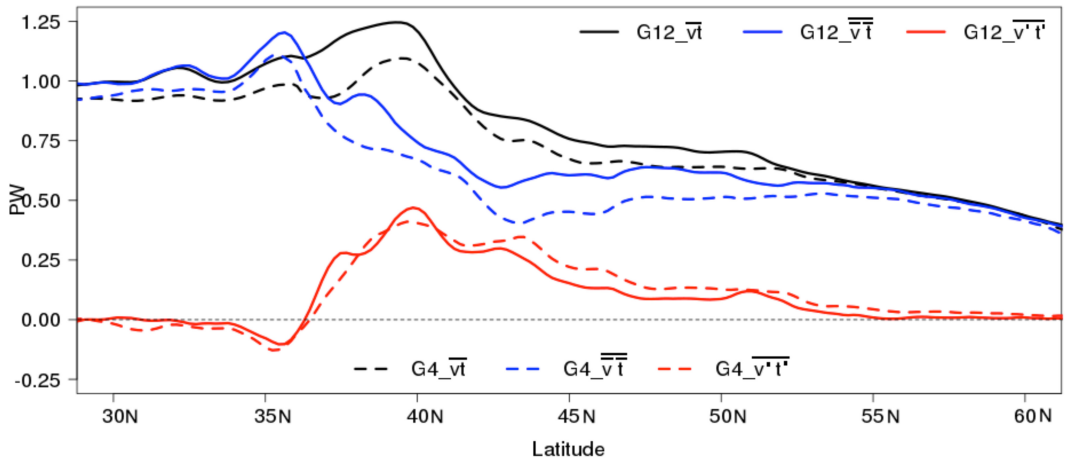

FIGURE 4 | Total mean meridional heat transport ($\overline{vT}$, black lines) and decomposition ($\overline{\overline{v}\,\overline{T}}$ blue lines and $\overline{v'T'}$ red lines) in G4 (dashed lines) and G12 calculated with 5-day data.

decomposition of vT for calculating MHT is as follows:

$$vT = \overline{v}\,\overline{T} + v'\overline{T} + \overline{v}T' + v'T' \tag{3}$$

Therefore, the total MHT and decomposition of MHT are calculated according to Equation 4:

$$\rho_0 C_P \int_{-H}^{0}\int_{\lambda_W}^{\lambda_E} vT\,dxdz = \rho_0 C_P \int_{-H}^{0}\int_{\lambda_W}^{\lambda_E} \overline{v}\,\overline{T}\,dxdz$$

$$+\rho_0 C_P \int_{-H}^{0}\int_{\lambda_W}^{\lambda_E} \overline{v}T'\,dxdz + \rho_0 C_P \int_{-H}^{0}\int_{\lambda_W}^{\lambda_E} v'\overline{T}\,dxdz$$

$$+\rho_0 C_P \int_{-H}^{0}\int_{\lambda_W}^{\lambda_E} v'T'\,dxdz \tag{4}$$

The quantities ρ_0 and C_p are seawater density ($1,020\ kgm^{-3}$) and heat capacity ($4{,}000\ Jkg^{-1}C^{-1}$), respectively.v and T are the meridional velocity and ocean temperature as stated in Equation 1. H is the ocean depth, and λ_E and λ_W are the longitude of the eastern and western boundaries of the ocean basin. On the right-hand side of Equation 1, the first term ($\overline{v}\,\overline{T}$) represents the contribution of the mean advection of mean temperature, the second term ($v'\overline{T}$) represents the anomalous advection of mean temperature, the third term ($\overline{v}T'$)is the mean advection of temperature anomalies and the last term ($v'T'$) is the contribution of co-variation of anomalous current and anomalous temperature (eddy covariance) to the total ocean MHT.

For simplicity, we omit the integration symbols in the heat transport equation (Equations 5–7). The mean meridional heat transport for the whole time period (1993–2016) $\overline{vT}$ is composed of $\overline{v}\,\overline{T}$ and $\overline{v'T'}$, described as below:

$$\overline{vT} = \overline{v}\,\overline{T} + \overline{v'T'} \tag{5}$$

The anomaly MHT respect to the mean for the period of 1993–2016 and the decomposition becomes:

$$vT - \overline{vT} = \overline{vT} + \overline{v}T' + v'\overline{T} + v'T' - \overline{(\overline{vT} + \overline{v}T' + v'\overline{T} + v'T')} \tag{6}$$

in which the first term on the right side is canceled by the fifth term, and the sixth and seventh terms are 0. Then for the anomalies we have

$$vT - \overline{vT} = \overline{v}T' + v'\overline{T} + (v'T' - \overline{v'T'}) \tag{7}$$

The eddy explained variances (EEV) are calculated as

$$EEV = \frac{var(MHT_T) - var(MHT_L)}{var(MHT_T)} \tag{8}$$

in which MHT_T indicates the total Meridional Heat Transport (MHT), MHT_L

means the MHT contributed by large scale processes and var is the variance function.

RESULTS

The North Atlantic Decadal Variability

First, we calculated the climatology (**Figure 1**) of the upper 700 m averaged temperature (T700) in the North Atlantic Ocean in two ocean reanalyses G4 (1/4 degree horizontal resolution), G12 (1/12 degree horizontal resolution) and EN4 objective analysis (EN4.2.1, 1 degree resolution). EN4 objective analysis is from United Kingdom Met Office (Good et al., 2013). Climatological maps of T700 show that in the North Atlantic Ocean, the upper ocean is generally warmer in G12 than in G4 (**Figure 1D**). Meanwhile, the mean climatology of T700 in G4 and G12 (**Figures 1E,F**) is warmer than EN4. Due to the prominent decadal signal in the eastern SPG region, we have calculated the time series of T700 in all three datasets over the box (35°N–65°N, 10°W–50°W) following Robson et al. (2016) for

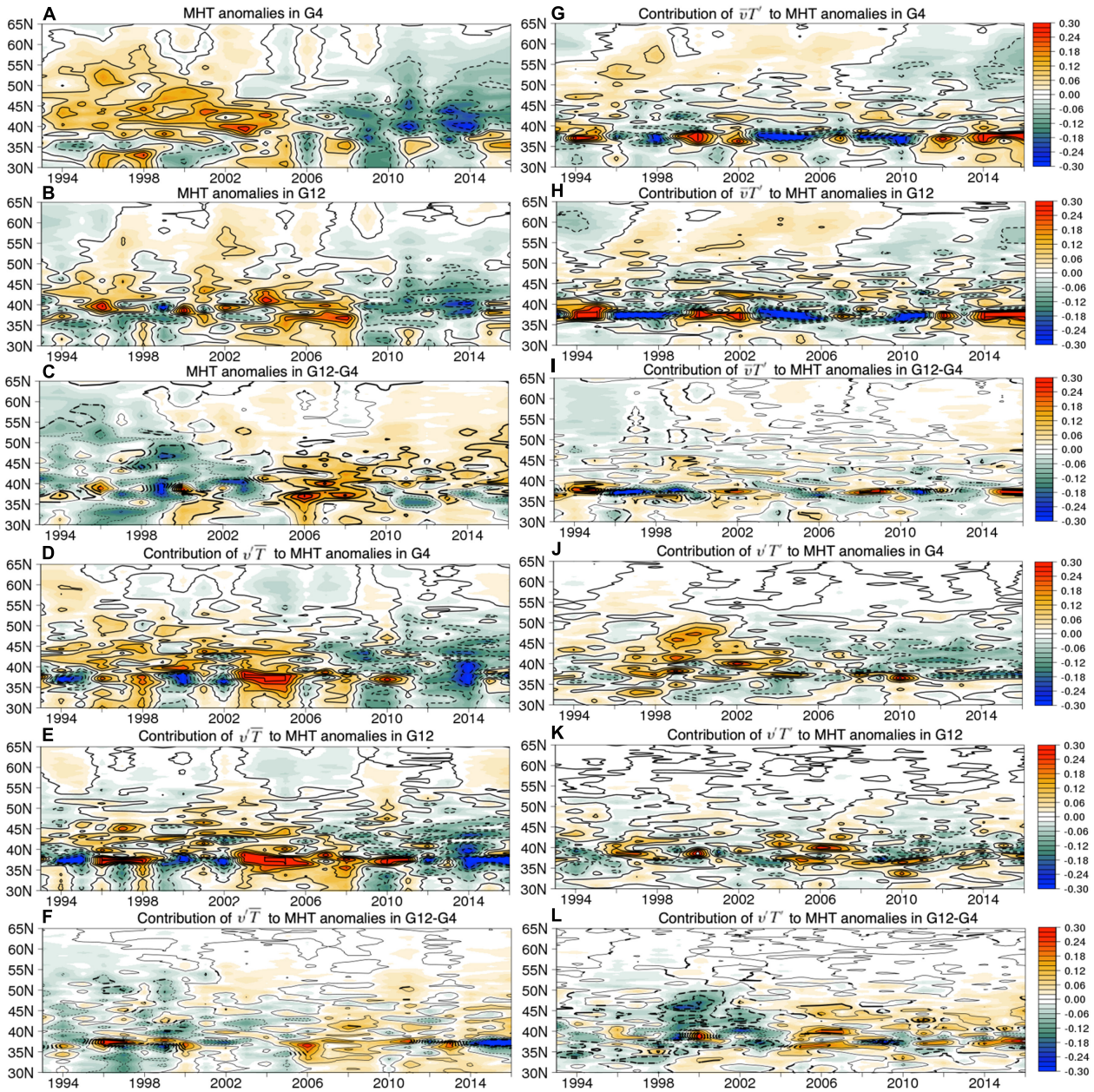

FIGURE 5 | Meridional heat transport anomaly $vT - \overline{vT}$ and decomposition $v'\overline{T}$, $\overline{v}\,T'$, $(v'T' - \overline{v'T'})$ in G4 **(A,D,G,J)** and in G12 **(B,E,H,K)** calculated with 5-day data. (unit: PW) The differences between G12-G4 are shown in panels **(C,F,I,L)**, and areas with values that pass *t*-test 95% confidence interval are indicated in thick contours.

the period 1993–2016. It shows that in the eastern SPG region T700 is warmer in G12 than G4 by 0.16°C and EN4 by 0.27°, respectively (**Figure 1G**).

The linear trend associated with the T700, calculated over for the (1993–2004) and (2005–2016) periods from G4, G12 and EN4, are shown in **Figures 2A–F**. A prominent warming trend during the period of 1993–2004 and a cooling trend during the period of 2005–2016 in the eastern North Atlantic subpolar gyre region is evident in both G4 and G12 reanalyses, and as well as in EN4. Here the linear trend of T700 is based on yearly data. The time series of the annual mean T700 anomaly (**Figure 2G**), computed with respect to the 1993–2016 baseline and basin averaged over the (35°N–65°N, 50°W–10°W) box in the subpolar gyre (as indicated in **Figures 2A–F**), shows a consistent linear warming before 2005 and cooling trend after 2005. G4 and G12 show consistent results with EN4, an observation-only estimates, which has been used in previous studies (see Robson et al., 2016) in terms of temperature variability in the North Atlantic Ocean. The distribution of warming and cooling signals is slightly different in G12, G4,

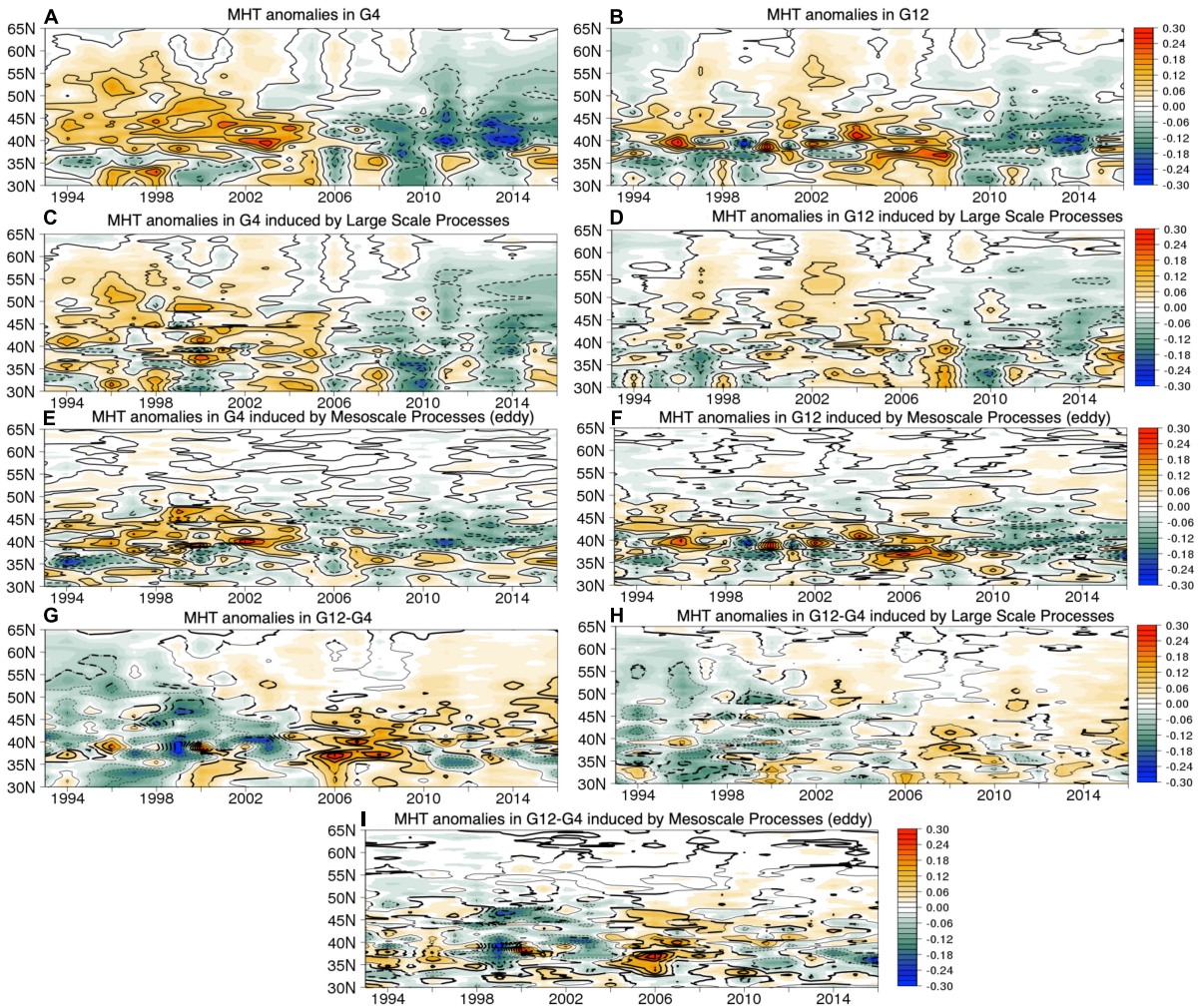

FIGURE 6 | Meridional heat transport anomaly and the anomalies induced by large scale process and mesoscale processes in G4 **(A,C,E)** and G12 **(B,D,F)**, differences between G4 and G12 **(G,H,I)** calculated with 5-day data. In panels **(G,H,I)**, areas with values that pass *t*-test 95% confidence interval are indicated in thick contours (unit: PW).

and EN4 mainly due to the representation of eddy features of the ocean state. However, the temporal variability is very similar in G12, G4 and EN4 (**Figures 1G**, **2G**). The increase of horizontal resolution alters the mean state of the ocean in terms of temperature (**Figure 1**) most likely due to better representation of the eddy features in high resolution reanalyses.

In order to have a more in-depth view on the impact of the resolution, we analyzed the eddy kinetic energy (EKE) in G4 and G12 (**Figure 3**). At the surface, the mean EKE displays a larger amplitude in G12 than in G4. The eddy active areas in G12 extend further north and east compared to G4 and the amplitude of EKE is stronger in the North Atlantic current pathway in G12 than in G4 (**Figure 3C**). In order to inspect the subsurface structure of EKE in the two reanalyses (**Figure 3**) we select a meridional section at 40°W, a region where the surface signature of the EKE shows a wide latitudinal extent in both G4 and G12. The subsurface EKE in G12 is stronger and its signature penetrates deeper than in G4 (**Figure 3F**). As for the temperature, the average EKE in the box shown in **Figure 2** (35°N–65°N, 10°W–50°W) for the top 700 m shows that EKE increases by 30% in G12 compared to G4 (not shown here). The EKE difference in G12 and G4 implies that the model resolution has an impact on the eddy activity (increasing of EKE) in contrast to the minor impact on the T700 variability.

The North Atlantic Meridional Ocean Heat Transport

As previous studies have shown, decadal variability in the North Atlantic Ocean (including episodes such as the mid-1990s warming and the post-2005 cooling in the subpolar gyre region) is largely associated with changes in the meridional ocean heat transport (Robson et al., 2016; Yang et al., 2016).

First, we have investigated the total mean MHT in G12 and G4 for the whole time period (1993–2016). The total mean MHT ($\overline{vT}$) (**Figure 4**) in G12 is larger than in G4 especially

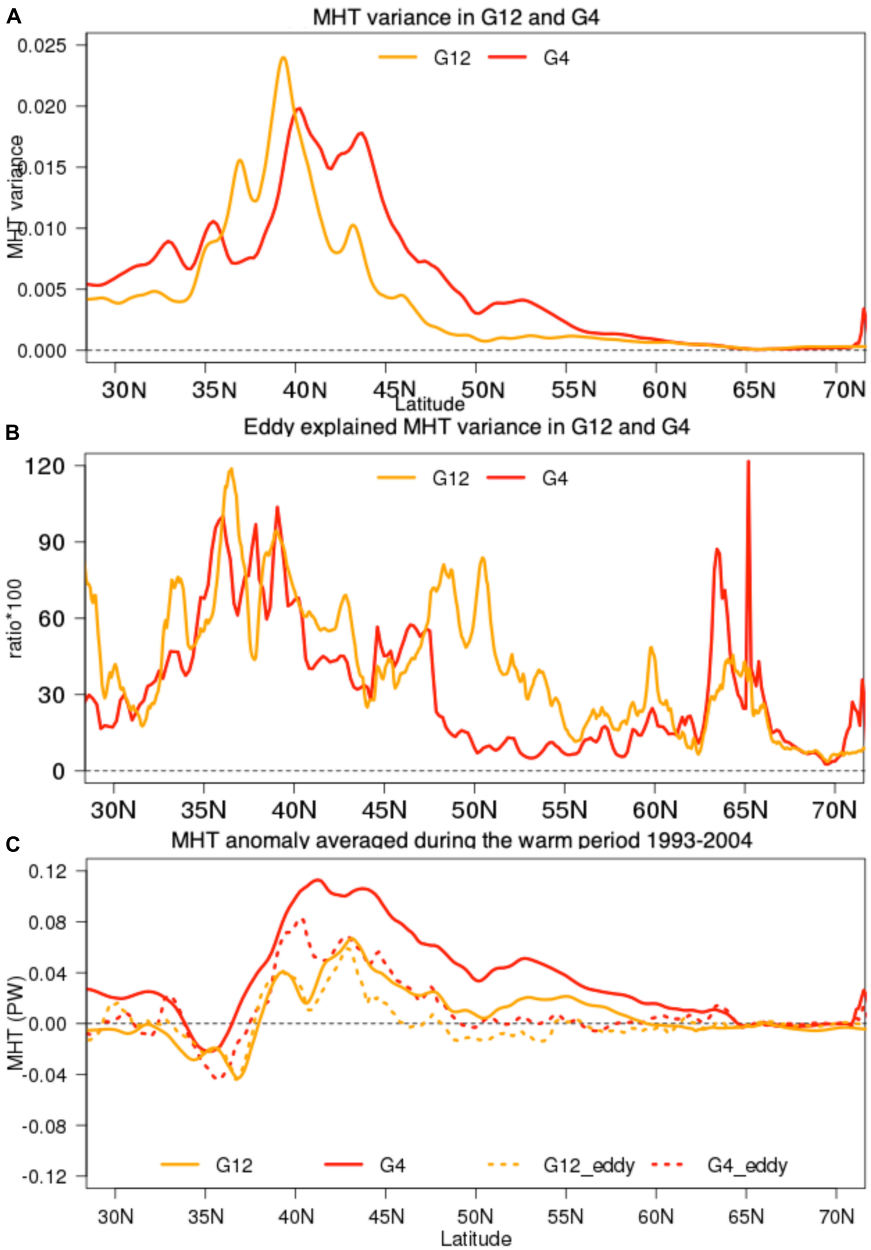

FIGURE 7 | (A) The temporal variance of MHT anomalies in G4 and G12 **(B)** Eddy explained MHT variance in G4 and G12 calculated as shown in Equation 8. The values have been multiplied by 100. **(C)** MHT anomalies averaged for the warm period (1993–2004) and the contribution from meso-scale eddies.

at eddy active latitudinal bands (35°N–40°N), where the eddy heat transport is the largest (Treguier et al., 2017), implying that with the increase of spatial horizontal resolution, the total mean MHT $\overline{vT}$ increases (**Figure 4**, black lines). The increase of total mean MHT is not only located at the eddy active regions but over the whole North Atlantic basin (here 30°N–60°N). The decomposition of the total mean MHT shows that the main contributor to the increase in G12 comes from the time mean field ($\overline{v}\,\overline{T}$) for all latitude bands. The mean contribution of the mean field for the time period 1993–2016 (calculated as $\overline{\overline{v}}\,\overline{\overline{T}}$) to the total MHT ($\overline{vT}$) shows a 10% increase from 669 TW in G4 to 738 TW in G12 at 40°N. The differences between G12 and G4 in terms of the attribution to the eddy covariance contribution to the total MHT plays a minor role (red lines), and the mean eddy covariance contribution (calculated as $\overline{v'T'}$) to the total MHT at 40°N for the whole time period (1993–2016) increases from 43 ± 6 TW in G4 to 46 ± 10 TW in G12. This finding is consistent with previous studies (Hecht and Smith, 2008; Treguier et al., 2012) showing that the total mean MHT increases with enhanced horizontal resolution due to the change

of the time mean field instead of the change of eddy component and the change of representation of bathymetry, air-sea flux with resolution contribute to the change of the mean state. As shown in **Figure 1**, the mean T700 in G12 is warmer than in G4, supporting that the time-mean field ($\overline{T}$) difference is one of the main factors that is responsible for the total increase of MHT.

The impact of the resolution on the mean state of the meridional mass transport in terms of meridional velocity ($\overline{v}$) is assessed through first Atlantic Meridional Overturning Circulation (AMOC) stream function. **Supplementary Figures 1**, **2** shows that the mean AMOC in G12 is stronger than in G4. Observations from the 26°N RAPID array (Srokosz and Bryden, 2015) for the 2005–2016 period yield a 16.8 Sv estimate, while G4 and G12 display a 16.3 Sv and 17.4 Sv amplitude, respectively. The mean gyre circulation (diagnosed *via* the barotropic stream function) slightly strengthens (**Supplementary Figure 3**) with the increase of horizontal resolution, meaning that the mean meridional velocity field ($\overline{v}$) increases with horizontal resolution along with mean temperature field ($\overline{T}$) increases corroborating the evidence that the time mean ocean states ($\overline{v}\overline{T}$) increase is the main factor for the total MHT increases.

The MHT anomalies that drive the mid-1990s warming and post-2005 cooling trend in the North Atlantic Ocean in G4 and G12 are calculated by subtracting the mean climatology from 1993–2016 and the decomposition of the MHT anomalies is shown in **Figure 5**. A prominent increase and reduction of MHT in G4 and G12, consistent with the mid-1990s warming and post-2005 cooling trend of T700 in the North Atlantic Ocean, is evident. The decline of the MHT in G4 begins around year 2005, in the 45°N–50°N latitude range and extends to the subtropical regions with time. In G12, instead, the reduction of MHT starts around year 2007 in the mid-latitudes and has a sharper decrease around 2008/2009, extending to the subtropical region. The difference between MHT anomalies in G12 and G4 shows that MHT anomalies have a stronger variability in G12 compared to G4. The decomposition (**Figure 5**) of the MHT evolution reveals that the anomalous advection of mean temperature ($v'\overline{T}$) is the main contributor to the MHT anomalies in both G4 and G12. The advection of temperature anomalies due to the mean flow ($\overline{v}T'$) plays a minor role in the MHT variability in both reanalyses. Despite the smaller contribution to the total MHT variability compared with the change of ocean circulation, the eddy-eddy correlation term ($v'T'$) shows similar variability to the total MHT change, and contributes to the mid-1990's warming and the post-2005 cooling.

In order to further investigate the role of eddies in the MHT, we separate the whole field (T and v) into large scale and eddy scale processes (calculated by subtracting the large scale from the full field) by applying a Shapiro spatial filter with a 10 degree frame window following Zhao et al. (2018). The MHT anomalies, MHT anomalies induced by large scale and MHT anomalies induced by mesoscale processes are shown in **Figure 6**. The major contribution of the MHT anomalies are induced by large scale processes in both G4 and G12. However, eddies contribute to both MHT warming and cooling anomalies that are related to the decadal variability. The variance of MHT (**Figure 7A**) shows that the eddy activity is mainly located in the 35°N to 45°N latitudes band for both G12 and G4. However, in G12 the largest variance is localized at around 38°N, while in G4 the variance is overall weaker than in G12 but spread across a wider latitude band. The eddy-explained variance (see section "Data and Methods") in MHT anomalies in both G4 and G12 (**Figure 7B**), confirms that over the 35°N–45°N latitudes band the eddies are very active in both G4 and G12, consistent with **Figure 4A**. The most prominent difference between G4 and G12 is at higher latitudes (45°N–55°N) where eddies explained more variances in G12 than G4 (**Figure 7B**). Further analysis (**Figure 7C**) focusing on the warming period, 1993–2004 (cold period from 2005–2016 is not shown because they are out of phase to have zero sum for anomalies), shows that large scale processes contribute more to the mean heat transfer anomalies for the warming and cooling period in G4 than in G12. On the other hand, eddies contribute relatively more to the mean heat transfer anomalies in G12 than in G4.

In general, the MHT variability in G12 and G4 show similar evolutions, especially during warming and the post-2005 cooling phase, with slightly larger amplitudes in G4. The contribution associated with different components ($v'\overline{T}$, $\overline{v}T'$ and $v'T'$) of the total MHT anomalies in both G4 and G12 is very similar, with the anomalous advection of mean temperature as the lead contributor, followed by the eddy-eddy correlation term, and finally the mean advection of temperature anomalies as the smallest contributor. This indicates that the North Atlantic decadal variability, here mid-1990s warming and post-2005 cooling period, is reproduced in both eddy-permitting (G4) and the eddy-resolving (G12) reanalyses, associated with the increase and decrease of the poleward heat transport. The relative role of eddies in terms of the contribution to the MHT anomalies is slightly more prominent in the eddy-resolving reanalysis (G12) compared with the eddy-permitting reanalysis (G4), especially at higher latitude (45°N–55°N).

CONCLUSION AND DISCUSSION

In this study we investigate the role of eddies in the North Atlantic decadal variability by using two ocean reanalysis products with different spatial resolutions. One reanalysis (G4) features a 1/4 degree horizontal resolution (eddy-permitting) and 75 vertical levels while the other one (G12) features a 1/12 degree horizontal resolution (eddy-resolving) and 50 vertical levels. Here we focus on the mid-1990s warming and post-2005 cooling in the North Atlantic Ocean as part of the North Atlantic decadal variability (Robson et al., 2016). The results show that both ocean reanalyses represent the prominent mid-1990s warming and post-2005 cooling trend (Top 700 m temperature, **Figure 1**) in the North Atlantic with minor differences between the two reanalyses. A linear warming trend of 0.48°C in G4, 0.53°C in G12 for the mid-1990s period, and a cooling trend of −0.54°C in G4 and −0.53°C for G12 per decade for the post-2005 period suggests a minor role of spatial resolution on the inter-annual variability. However, the mean state of the North Atlantic Ocean does change after increasing the horizontal resolution, as revealed by

comparing climatological patterns of T700, ocean circulation and EKE (the latter, both at surface and sub-surface) in G4 and G12.

The analysis of the poleward ocean heat transport shows a similar variability of the total MHT signal in both G4 and G12. The main contributor to the total MHT change in both reanalyses is the anomalous advection of mean temperature ($v'\overline{T}$) associated with the weakening of the AMOC strength (**Supplementary Figures 1**, **2**) and North Atlantic gyre circulation (**Supplementary Figure 3**) consistent with previous studies (Msadek et al., 2014). The quantitative analysis of the eddy contribution to the total MHT variability, which is the focus of this study, shows that the contribution of eddy MHT to the total MHT variability is slightly larger in the eddy-resolving than in the eddy-permitting reanalysis. Additionally, G12 shows a 10% increase in the total mean MHT compared to G4 and the decomposition of the total MHT suggests that the main factor is the increase of mean circulation and mean temperature, as also discussed in other studies (Hecht and Smith, 2008; Treguier et al., 2012).

Overall, our intercomparison of G12 and G4 shows that the change in the resolution mostly affects the climatological features, while the decadal variability signal is relatively less affected with eddies playing slightly larger role in G12. However, the increases of resolution has a larger impact on the poleward heat transport at the higher latitude. One point in this study we have to bear in mind is that G12 has higher horizontal resolution but lower vertical resolution compared with G4. Thus, with the future new 1/12 degree ocean reanalyses (G12) the results could be slightly different.

The implications of this study go beyond the North Atlantic mid-1990s and post-2005 cooling event. The North Atlantic displays prominent decadal fluctuations. Understanding the underlying mechanisms and improving the skill of decadal predictions in the North Atlantic sector is a very active and promising area of research for the climate prediction community. Previous studies have shown that an accurate initialization of the ocean state is key for making skillful predictions of the North Atlantic variability (Msadek et al., 2014) and ocean reanalyses have been used as initial conditions for decadal prediction experiments (Bellucci et al., 2013, 2015). This study confirms the reliability of ocean reanalyses as initial conditions for decadal predictions even with eddy-permitting (and eddy rich) resolution.

The fast development of computational power will pave the way to high-resolution decadal prediction systems. However, the importance of model resolution needs to be evaluated in order to optimize the usage of the resources. This study focusing on the North Atlantic Ocean shows that the increase of resolution affects the mean state of the ocean but has no significant impacts on the decadal scale variability. However, the interaction between eddies (small scale) and the mean state (large scale) needs to be explored further in order to understand the importance and usefulness of high resolution for decadal predictions and initialization strategies, which will be a vital research area that the climate community needs to pursue in the coming years or decades in order to improve decadal prediction skill.

DATA AVAILABILITY STATEMENT

Publicly available datasets were analyzed in this study. This data can be found here: https://resources.marine.copernicus.eu/product-detail/GLOBAL_MULTIYEAR_PHY_001_030/INFORMATION; https://resources.marine.copernicus.eu/product-detail/GLOBAL_REANALYSIS_PHY_001_031/INFORMATION.

AUTHOR CONTRIBUTIONS

CY designed the study and wrote the initial manuscript. CY and CB conducted the analyses. All authors contributed to the interpretation of the results and to the improvement of the manuscript.

FUNDING

This study was funded by EU cost action (Earth System Science and Environmental Management ES1402, Evaluation of Ocean Syntheses), and Copernicus Marine Environment Monitoring Service (CMEMS) Contract (GLO-RAN-Lot 6). The computing resource is funded by CINECA ISCRA project (PRORP_HP10C2FG9V).

ACKNOWLEDGMENTS

We would like to thank Daniele Ciani and two reviewers for their useful comments to improve the manuscript. Reanalyses data are available in CMEMS data portal and EN4 is public available in United Kingdom Met office data portal (https://www.metoffice.gov.uk/hadobs/en4/).

SUPPLEMENTARY MATERIAL

The Supplementary Material for this article can be found online at: https://www.frontiersin.org/articles/10.3389/fmars.2022.781788/full#supplementary-material

REFERENCES

Aoki, K., Minobe, S., Tanimoto, Y., and Sasai, Y. (2013). Southward eddy heat transport occurring along southern flanks of the kuroshio extension and the gulf stream in a 1/108 global ocean general circulation model. *J. Phys. Oceanogr.* 43, 1899–1910. doi: 10.1175/JPO-D-12-0223.1

Bellucci, A., Gualdi, S., Masina, S., Storto, A., Scoccimarro, E., Cagnazzo, C., et al. (2013). Decadal climate predictions with a coupled OAGCM initialized with oceanic reanalyses. *Clim. Dyn.* 40:1483. doi: 10.1007/s00382-012-1468-z

Bellucci, A., Haarsma, R., Gualdi, S., Athanasiadis, P. J., Caian, M., Cassou, C., et al. (2015). An assessment of a multi-model ensemble of decadal climate predications. *Clim. Dyn.* 44:2787. doi: 10.1007/s00382-014-2164-y

Bersch, M., Yashayaev, I., and Koltermann, K. P. (2007). Recent changes of the thermohaline circulation in the subpolar North Atlantic. *Ocean Dyn.* 57, 223–235. doi: 10.1007/s10236-007-0104-7

Chafik, L., Nilsen, J. E. Ø, Dangendorf, S., Reverdin, G., and Frederikse, T. (2019). North atlantic ocean circulation and decadal sea level change during the altimetry era. *Sci. Rep.* 9:1041. doi: 10.1038/s41598-018-37603-6

Cipollone, A., Masina, S., Storto, A., and Iovino, D. (2017). Benchmarking the mesoscale variability in global eddy-permitting numberical systems. *Ocean Dyn.* 67:1313. doi: 10.1007/s10236-017-1089-5

Comiso, J. C. (2000). *Updated 2015. Bootstrap Sea Ice Concentrations from Nimbus-7 SMMR and DMSP SSM/I-SSMIS, Version 2*. Boulder, CO: NASA National Snow and Ice Data Center Distributed Active Archive Center, doi: 10.5067/J6JQLS9EJ5HU

Crosnier, L., Barnier, B., and Treguier, A. M. (2001). Aliasing inertial oscillations in a 1/6° Atlantic circulation model: impact on the mean meridional heat transport. *Ocean Model.* 3, 21–31.

Dee, D. P., Uppala, S. M., Simmons, A. J., Berrisford, P., Poli, P., Kobayashi, S., et al. (2011). The ERA-Interim reanalysis: configuration and performance of the dataassimilation system.Q. *J. R. Meteorol. Soc.* 137, 553–597. doi: 10.1002/qj.828

Delman, A., and Lee, T. (2020). A new method to assess mesoscale contributions to meridional heat transport in the North Atlantic Ocean. *Ocean Sci.* 16, 979–995. doi: 10.5194/os-16-979-2020

Delworth, T. L., Zeng, F., Vecchi, G. A., Yang, X., Zhang, L., and Zhang, R. (2016). The North Atlantic Oscillation as a driver of rapid climate change in the Northern Hemisphere. *Nat. Geosci.* 9, 509–513. doi: 10.1038/NGEO2738

Docquier, D., Grist, J. P., Roberts, M. J., Roberts, C. D., Semmler, T., Ponsoni, L., et al. (2019). Impact of model resolution on Arctic sea ice and North Atlantic Ocean heat transport. *Clim. Dyn.* 53, 4989–5017. doi: 10.1007/s00382-019-04840-y

Drévillon, M., Fernandez, E., and Lellouche, J.-M. (2021a). *Product User Manual for the Global Ocean Physical Multi Year Product Global_Multiyear_Phy_001_030*. Available online at: https://catalogue.marine.copernicus.eu/documents/PUM/CMEMS-GLO-PUM-001-030.pdf (accessed January 20, 2020).

Drévillon, M., Lellouche, J.-M., Reìgnier, C., Garric, G., Bricaud, C., Hernandez, O., et al. (2021b). *Quality Information Document for Global Ocean Reanalysis Products Global_Reanalysis_Phy_001_030*. Available online at: https://catalogue.marine.copernicus.eu/documents/QUID/CMEMS-GLO-QUID-001-030.pdf (accessed January 20, 2020).

Ezraty, R., Girard-Ardhuin, F., Piollé, J. F., Kaleschke, L., and Heygster, G. (2007). *Arctic and Antarctic Sea Ice Concentration and Arctic Sea Ice Drift Estimated from Special Sensor Microwave Data, User's Manuel Version 2.1. IFREMER CERSAT Document. 22*, 2.1 Edn. Brest: Département d Océanographie Physique et Spatiale, IFREMER.

Fichefet, T., and Morales Maqueda, M. A. (1997). Sensitivity of a global sea ice model to the treatment of ice thermodynamics and dynamics. *J. Geophys. Res.* 102, 12609–12646. doi: 10.1029/97jc00480

Garric, G., and Parent, L. (2017). *Quality Information Document for Global 1330 Ocean Reanalysis Products Global-Reanalysis-Phy-001-025*. Available online at: https://catalogue.marine.copernicus.eu/documents/QUID/CMEMS-GLO-QUID-001-025.pdf (accessed January 20, 2020).

Garric, G., and Parent, L. (2018). *Product User Manual for Global Ocean Reanalysis Products Global-Reanalysis-Phy-001-025*. Available online at: https://catalogue.marine.copernicus.eu/documents/PUM/CMEMS-GLO-PUM-001-025.pdf (accessed January 20, 2020).

Good, S. A., Martin, M. J., and Rayner, N. A. (2013). EN4: quality controlled ocean temperature and salinity profiles and monthly objective analyses with uncertainty estimates. *J. Geophys. Res. Oceans* 118, 6704–6716. doi: 10.1002/2013JC009067

Grist, J. P., Josey, S. A., New, A. L., Roberts, M., Koenigk, T., and Iovino, D. (2018). Increasing atlantic ocean heat transport in the latest generation coupled ocean-atmosphere models: the role of air-sea interaction. *J. Geophys. Res. Oceans* 23, 8624–8637. doi: 10.1029/2018jc014387

Haarsma, R. J., Roberts, M. J., Vidale, P. L., Senior, C. A., Bellucci, A., Bao, Q., et al. (2016). High resolution model intercomparison project (HighResMIPv1.0) for CMIP6. *Geosci. Model Dev.* 9, 4185–4208. doi: 10.5194/gmd-9-4185-2016

Häkkinen, S., Rhines, P. B., and Worthen, D. L. (2011). Warm and saline events embedded in the meridional circulation of the northern North Atlantic. *J. Geophys. Res.* 116:C03006.

Haìtuìn, H., Sando, A. B., Drange, H., Hansen, B., and Valdimarsson, H. (2005). Influence of the Atlantic subpolar gyre on the thermohaline circulation. *Science* 309, 1841–1844. doi: 10.1126/science.1114777

Hecht, M. W., and Smith, R. D. (2008). "Toward a physical understanding of the North Atlantic: a review of model studies in an eddying regime," in *Oceano Modeling in an Eddying Regime, Geophysical Monograph Series*, Vol. 177, eds M. W. Hecth and H. Hasumi (Washington, DC: American Geophysical Union), 213–239. doi: 10.1029/177GM15

Herbaut, C., and Houssais, M. N. (2009). Response of the eastern North Atlantic subpolar gyre to the North Atlantic Oscillation. *Geophys. Res. Lett.* 36:L17607. doi: 10.1029/2009GL039090

Jackson, L. C., Peterson, K. A., Roberts, C. D., and Wood, R. A. (2016). Recent slowing of Atlantic overturning circulation as a recovery from earlier strengthening. *Nat. Geosci.* 9, 518–522. doi: 10.1038/ngeo2715

Jackson, L., Dubois, C., Masina, S., Storto, A., and Zuo, H. (2018). Atlantic meridional overturning circulation. in copernicus marine service ocean state report, issue 2. *J. Operat. Oceanogr.* 11(Suppl.1), S65–S66. doi: 10.1080/1755876X.2018.1489208

Jayne, S. R., and Marotzke, J. (2002). The oceanic eddy heat transport. *J. Phys. Oceanogr.* 32, 3328–3345.

Large, W., and Yeager, S. (2004). *Diurnal To Decadal Global Forcing For Ocean And Seaice Models: The Data Sets And Climatologies*. Technical Report TN-460 + STR. Boulder, CO: National Center for Atmospheric Research.

Lellouche, J. M., Greiner, E., Bourdallé-Badie, R., Garric, G., Melet, A., Drevillon, M., et al. (2021). The copernicus global 1/12° oceanic and sea ice glorys12 reanalysis. *Front. Earth Sci.* 9:698876. doi: 10.3389/feart.2021.698876

Lellouche, J. M., Greiner, E., Le Galloudec, O., Garric, G., Regnier, C., Drevillon, M., et al. (2018). Recent updates on the Copernicus Marine Service global ocean 1323 monitoring and forecasting real-time 1/12 high resolution system. *Ocean Sci.* 14, 1093–1126. doi: 10.5194/os-14-1093-2018

Madec, G. (2008). *NEMO Ocean Engine: Note Du Pôle De Modélisation*. Guyancourt: Institut Pierre-Simon Laplace(IPSL).

Matei, D., Pohlmann, H., Jungclaus, J., Muller, W., Haak, H., and Marotzket, J. (2012). Two tales of initializing decadal climate prediction experiments with the ECHAM5/MPI-OM model. *J. Clim.* 25, 8502–8523. doi: 10.1175/jcli-d-11-00633.1

Msadek, R., Delworth, T. L., Rosati, A., Anderson, W., Vecchi, G., Chang, Y.-S., et al. (2014). Predicting a decadal shift in North Atlantic climate variability using the GFDL forecast system. *J. Clim.* 27, 6472–6496.

Pham, D., Verron, J., and Roubaud, M. (1998). A singular evolutive extended Kalman filter for data assimilation in oceanography. *J. Mar. Syst.* 16, 323–340. doi: 10.1016/s0924-7963(97)00109-7

Polkova, I., Brune, S., Kadow, C., Romanova, V., Gollan, G., Baehr, J., et al. (2019a). Initialization and ensemble generation for decadal climate predictions: a comparison of different methods. *J. Adv. Modeling Earth Syst.* 11, 149–172. doi: 10.1029/2018ms001439

Polkova, I., Kohl, A., and Stammer, D. (2019b). Climate-mode initialization for decadal climate predictions. *Clim. Dyn.* 53, 7097–7111. doi: 10.1007/s00382-019-04975-y

Qiu, B., and Chen, S. (2005). Eddy-induced heat transport in the subtropical north pacific from argo, tmi, and altimetry measurements . *J. Phys. Oceanogr.* 35, 458–473. doi: 10.1175/jpo2696.1

Robson, J. I., Sutton, R., Lohmann, K., Smith, D., and Palmer, M. D. (2012). Causes of the rapid warming of the North Atlantic Ocean in the mid-1990s. *J. Clim.* 25, 4116–4134.

Robson, J., Ortega, P., and Sutton, R. (2016). A reversal of climatic trends in the North Atlantic since 2005. *Nat. Geosci.* 9, 513–517. doi: 10.1038/ngeo2727

Roemmich, D., and Gilson, J. (2001). Eddy transport of heat and thermocline waters in the north pacific: a key to interannual/decadal climate variability? *J. Phys. Oceanogr.* 31, 675–687.

Sarafanov, A., Falina, A., Solov, A., and Demidov, A. (2008). In- tense warming and salinification of intermediate waters of southern origin in the eastern subpolar North Atlantic in the 1990s to mid-2000s. *J. Geophys. Res.* 113:C12022.

Srokosz, M. A., and Bryden, H. L. (2015). Observing the Atlantic meridional overturning circulation yields a decade of inevitable surprises. *Science* 348:1255575. doi: 10.1126/science.1255575

Storto, A., Masina, S., Simoncelli, S., Iovino, D., Cipollone, A., Drevillo, M., et al. (2019). The added value of the multi-system spread information for ocean heat content and steric sea level investigations in the CMEMS GREP ensemble reanalysis product. *Clim. Dyn.* 53, 287–312. doi: 10.1007/s00382-018-4585-5

Storto, A., Yang, C., and Masina, S. (2016). Sensitivity of global ocean heat content from reanalyses to the atmospheric reanalysis forcing: a comparative study. *Geophys. Res. Lett.* 43, 5261–5270. doi: 10.1002/2016GL068605

Sun, B., Liu, C., and Wang, F. (2019). Global meridional eddy heat transport inferred from Argo andaltimetry observations. *Sci. Rep.* 9:1345.

Szekely, T., Gourrion, J., Brion, E., Von Schuckmann, K., Reverdin, G., Grouazel, A., et al. (2015). "CORA4.1: a delayed-time validated temperature and salinity profiles and timeseries product," in *Proceeding of the 7th EuroGOOS International Conference, 28-20 October, 2014*, Lisbon.

Treguier, A. M., Deshayes, J., Lique, C., Dussin, R., and Molines, J. M. (2012). Eddy contributions to the meridional transport of salt in the North Atlantic. *J. Geophys. Res.* 117:C05010. doi: 10.1029/2012JC007927

Treguier, A. M., Lique, C., Deshayes, J., and Molines, J. M. (2017). The North Atlantic eddy heat transport and its relation with the vertical tilting of the gulf stream axis. *J. Phys. Oceanogr.* 47, 1281–1289. doi: 10.1175/JPO-D-16-0172.1

Yang, C., Masina, S., Bellucci, A., and Storto, A. (2016). The rapid warming of the north atlantic ocean in the mid-1990s in an eddy-permitting ocean reanalysis (1982–2013). *J. Clim.* 29, 5417–5430. doi: 10.1175/JCLI-D-15-0438.1

Yeager, S., Karspeck, A., Danabasoglu, G., Tribbia, J., and Teng, H. (2012). A decadal prediction case study: late twentieth-century North Atlantic Ocean heat content. *J. Clim.* 25, 5173–5189. doi: 10.1175/JCLI-D-11-00595.1

Zhao, J., Bower, A., Yang, J., Lin, X., and Holliday, N. P. (2018). Meridional heat transport variability induced by mesoscale processes in the subpolar North Atlantic. *Nat. Commun.* 9:1124. doi: 10.1038/s41467-018-03134-x

Conflict of Interest: The authors declare that the research was conducted in the absence of any commercial or financial relationships that could be construed as a potential conflict of interest.

frontiers in Earth Science

ORIGINAL RESEARCH
published: 10 February 2022
doi: 10.3389/feart.2022.745274

The Antarctic Marginal Ice Zone and Pack Ice Area in CMEMS GREP Ensemble Reanalysis Product

Doroteaciro Iovino[1*†], *Julia Selivanova*[1,2*†], *Simona Masina*[1] *and Andrea Cipollone*[1]

[1]*Ocean Modeling and Data Assimilation Division, Centro Euro-Mediterraneo Sui Cambiamenti Climatici, Bologna, Italy,*
[2]*Department of Physics and Astronomy, University of Bologna, Bologna, Italy*

Global ocean reanalyses provide consistent and comprehensive records of ocean and sea ice variables and are therefore of pivotal significance for climate studies, particularly in data-sparse regions such as Antarctica. Here, for the first time, we present the temporal and spatial variability of sea ice area in the ensemble of global ocean reanalyses produced by the Copernicus Marine Environment Monitoring Service (CMEMS) for the period 1993–2019. The reanalysis ensemble robustly reproduces observed interannual and seasonal variability, linear trend, as well as record highs and lows. While no consensus has been reached yet on the physical source of Antarctic-wide ice changes, our study also emphasizes the importance of understanding the different responses of ice classes, marginal ice zone (MIZ) and pack ice, to climate changes. Modifications of the distribution of MIZ and pack ice have implications for the level of air/sea exchanges and for the marine ecosystem. Analysis of the spatial and temporal variability of ice classes can provide further insights on long-term trends and help to improve predictions of future changes in Antarctic sea ice. We assess the ability of the reanalysis ensemble to adequately capture variability in space and time of the MIZ and pack ice area, and conclude that it can provide consistent estimates of recent changes in the Antarctic sea ice area. Our results show that the Antarctic sea ice area agrees well with satellite estimates, and the hemispheric and regional sea ice area variability are properly reproduced on seasonal and interannual time scales. Although the ensemble reanalysis product tends to slightly overestimate MIZ in summer, results show that it properly represents the variability of MIZ minima and maxima as well as its interannual variability during the growing and melting seasons. Our results confirm that Global Reanalysis Ensemble Product is able to reproduce the observed substantial regional variability, in regions covered by marginal ice.

Keywords: Antarctic sea ice, marginal ice zone, pack ice, ocean reanalyses, GREP

OPEN ACCESS

Edited by:
Stefanie Arndt,
Alfred Wegener Institute Helmholtz Centre for Polar and Marine Research (AWI), Germany

Reviewed by:
Alexander Fraser,
University of Tasmania, Australia
Lu Zhou,
University of Gothenburg, Sweden

****Correspondence:***
Doroteaciro Iovino
dorotea.iovino@cmcc.it
Julia Selivanova
iuliia.selivanova@unibo.it

†These authors share first authorship

Specialty section:
This article was submitted to Cryospheric Sciences, a section of the journal Frontiers in Earth Science

Received: *21 July 2021*
Accepted: *17 January 2022*
Published: *10 February 2022*

Citation:
Iovino D, Selivanova J, Masina S and Cipollone A (2022) The Antarctic Marginal Ice Zone and Pack Ice Area in CMEMS GREP Ensemble Reanalysis Product. Front. Earth Sci. 10:745274. doi: 10.3389/feart.2022.745274

INTRODUCTION

Antarctic sea ice plays a critical role in the polar and global climate and ecosystems, modulating the exchanges of momentum, gases and heat between the ocean and the atmosphere. A deep knowledge of sea ice variability is necessary for adequately simulating these fluxes and thus for climate modelling. In stark contrast to the Arctic, where sea ice has declined significantly in all areas and seasons (e.g., Parkinson and Cavalieri, 2012; Serreze and Stroeve 2015; Onarheim et al., 2018), Antarctic sea ice has not experienced a drastic and continuous decline during recent decades. Satellite

records show a slight increasing trend in total annual-mean Antarctic sea ice extent (SIE) at a rate of ~1.5% per decade for the 1979–2015 period, with modest increases in the maxima and minima (Turner et al., 2015; Comiso et al., 2017), albeit individual regions experienced much larger gains and losses that almost offset each other overall (Parkinson, 2019). After record maxima successively occurred in 2012, 2013, and 2014, Antarctic sea ice decreased below the long-term average in 2015, with unprecedented record low minima in 2016, 2017 and 2018 (Parkinson, 2019). However, the recent decrease does not signify a change in the sign of the long-term trend, which remains positive over the period 1979–2019, though with lower magnitude compared to the 1979–2015 trend (Wachter et al., 2021).

Understanding this quasi-stable situation in Antarctic sea ice and its link to climate change is still a significant scientific challenge (Kennicutt et al., 2015). Rather than by a single mechanism, the long-term sea ice variability is driven by a combination of processes, such as local changes in the atmospheric dynamics and wind patterns (e.g., Holland and Kwok, 2012; Meehl et al., 2016; Vichi et al., 2019; Blanchard-Wrigglesworth et al., 2021), shifts in the dominant modes of large-scale atmospheric circulation in the southern hemisphere (Stammerjohn et al., 2008), changes in the vertical structure of the near-surface water column (Goosse and Zunz, 2014; Venables and Meredith, 2014), changes in ice albedo feedback (Riihelä et al., 2021), ice-ocean feedbacks (Goosse and Zunz, 2014; Frew et al., 2019), and variability of the ice sheet water discharge (Bintanja et al., 2013; Haid et al., 2017; Pauling et al., 2017). These processes combine in different ways at regional scales. Significant regional contrasts and variability are nested within the Antarctic-wide changes: while the Ross and Weddell Seas dominate the overall upward trend, the Amundsen-Bellingshausen Seas have undergone a considerable decrease (Massom and Stammerjohn, 2010; Parkinson, 2019). High-magnitude seasonal variability is also disguised in long-term expansion of total sea ice cover: a complex seasonal pattern of trends emerges across the regions, with positive expansion trend in one season and negative in another (Holland, 2014; Hobbs et al., 2016; Parkinson, 2019). Considering the spatial and seasonal heterogeneity of trends, the Antarctic-wide changes could not aid in the attribution of those trends. The focus instead should be on the regional and seasonal variability which may give a better understanding of the long-term changes in Antarctic sea ice area.

While changes in total sea ice at different spatial/temporal scales remain puzzling, it is likely that these changes also affect the distribution and variability of ice classes in different ways (Stroeve et al., 2016; Iovino et al., 2022). Here, we define ice classes to distinguish between consolidated pack ice and the marginal ice zone (MIZ). Understanding how the spatial patterns of different ice classes change may help to elucidate the mechanisms contributing to the expansion of Antarctic ice in some regions and contraction in others (Maksym et al., 2012). In spite of the large winter cover, sea ice around Antarctica forms a vast field of small broken ice floes, with compact and consolidated ice remaining all year around only in a few coastal regions (e.g., Holland et al., 2014). The MIZ is highly dynamic and its response to climate variability differs from the inner pack ice: it undergoes faster melting due to a larger lateral melt rate (Tsamados et al., 2015), responds more easily to winds and current forcing (Manucharyan and Thompson, 2017; Alberello et al., 2020), and is highly vulnerable to waves and swell (Kohout et al., 2014). The MIZ is fundamental for climate dynamics and polar ecosystems, given its roles as a region of intense atmosphere-sea ice interactions and as a physical buffer between the consolidated pack ice zone and the effects of open ocean dynamics (e.g., Squire 2007). Monitoring changes of the MIZ environment can help us understand the associated changes in the climate system. An accurate assessment of Antarctic MIZ variability is still missing, as well as a deep insight into how ice conditions correlate with atmospheric fields and surface oceanic waves (Meylan et al., 2014, Sutherland and Balmforth 2019). The MIZ can be operationally defined through sea ice concentration (SIC) thresholds as the transitional region between open water and consolidated pack ice, where the ocean is covered by SIC between 15 and 80% (e.g., Pauling et al., 2017).

There is growing demand for comprehensive records of the historical ocean state. Ocean Reanalyses (ORAs) represent an essential tool to monitor long-term variability of various climate indices, especially in areas with sparse data such as the Antarctic Ocean. Observations alone can not reasonably reproduce consistent and homogeneous time series of three-dimensional gridded fields of ocean and ice parameters. Model simulations, on other hand, can provide somewhat accurate information regarding the ocean and ice mean states and variability, despite being prone to errors related to model formulation, initialization and forcing. A number of experiments with global ocean-sea ice models were carried out in the framework of the Coordinated Ocean-ice Reference Experiments (CORE-II) and the Ocean Model Intercomparison Project (OMIP), albeit with little focus on sea ice performance in polar regions (e.g., Downes et al., 2015; Farneti et al., 2015; Tsujino et al., 2020). Most CORE-II models are found to underestimate Antarctic SIC in summer and reproduce the sea ice edge further south compared to observations (Downes et al., 2015). The OMIP simulations reproduce a very wide range of models spread in sea ice concentration and volume, with ratios of the maximum to the minimum reaching a factor of two to three (Tsujino et al., 2020). Inaccurate representation of sea ice and a large spread across model output is due to the fact that these model systems are not constrained by observations through data assimilation schemes. The advantage of ORAs with respect to observation-only products and ocean models, is the combination of ocean/sea ice models and observational data sets driven by atmospheric forcing. The errors from models and forcing datasets are reduced through assimilation of observations. Ocean reanalyses are a fundamental tool for climate investigation, as indicated by the large number of studies that make use of them. Within the Ocean Reanalyses Intercomparison Project (Balmaseda et al., 2015), several exercises were undertaken to study the variability of many well-constrained ocean fields, such as steric sea level (Storto et al., 2017), air-sea heat fluxes (Valdivieso et al., 2017), ocean heat content (Palmer et al., 2017). ORAs are also a key tool for evaluating key climate diagnostics that are not

directly observed, such as deep ocean warming (Balmaseda et al., 2013), the reconstruction of the overturning circulation (Jackson et al., 2016). Few ORAs studies so far have focused on their performance in polar regions. Chevallier et al. (2017) used 14 global ORAs to analyze the seasonal variability of the sea ice area and sea ice edge position in the Arctic region. They showed that the ensemble-mean SIC agrees quite well with the observations but there is significant disagreement among systems in simulated sea ice thickness (which is not directly assimilated in any of the ORAs). However, they also revealed a large spread in the representation of pack ice and the MIZ extent. Using a set of 10 ORAs, Uotila et al. (2019) found an overall agreement with observations in the location of both Arctic and Antarctic sea ice edges, and showed that ORAs are able to capture seasonal variability of sea ice area (SIA). The large differences in the 10 reanalysis systems resulted in a poor representation of the seasonal variability of the MIZ and pack ice area. Nevertheless, Uotila et al. (2019) discussed the fidelity of ensemble mean estimates and proved that the multi-system concept provides the most robust results owing to the cancellation of the individual errors.

In this study, we investigate the interannual and seasonal changes of Antarctic SIA on hemispheric and regional scales with the purpose of identifying the differences between MIZ and total/consolidated pack ice. We use an ensemble-mean of four global ocean-sea ice reanalyses (ORAs) together with long-term passive microwave sea ice estimates. We examine the quality of the Global ocean Reanalysis Ensemble Product (version 2, hereafter called GREP) provided by the Copernicus Marine Environment Monitoring Service (CMEMS) of the European Union. GREP is an ensemble of four global ocean-sea ice reanalyses produced at eddy-permitting resolution for the period from 1993 to present. GREP has already been successfully validated with respect to a range of ocean variables (Masina et al., 2015; Storto et al., 2019) and have been largely adopted for evaluating key climate diagnostics that are not easily observed. In this study, we evaluate the capability of GREP in reproducing the Antarctic sea ice area in the marginal ice and pack ice regions, in the 1993–2019 period. We analyse the interannual and seasonal variability in five sectors of the Antarctic Ocean. The main objectives of this work are to validate GREP Antarctic SIA against satellite estimates and to investigate the benefits of a multi-system ensemble approach. Since the multi-model mean can offset systematic errors of individual systems, we expect GREP to perform generally better than single reanalysis and provide the most consistent estimates of sea ice state and variability. We also intend to encourage the use of GREP in a wide range of applications.

DATA AND METHODS

The Global Reanalysis Ensemble Product (GREP version 2) consists of four global ocean-sea ice reanalyses (C-GLORSv7, Storto et al., 2016; FOAM-GloSea5, MacLachlan et al., 2015; GLORYS2v4, Lellouche et al., 2013; ORAS5, Zuo et al., 2019), all constrained by satellite and *in-situ* observations, and driven by the ECMWF ERA-Interim atmospheric reanalysis (Dee et al., 2011). Monthly means of ocean and sea ice variables, for individual reanalysis as well as the ensemble mean and spread, are produced and freely disseminated by CMEMS through the CMEMS catalogue (product reference GLOBAL_REANALYSIS_PHY_001_031).

The four reanalyses share the ocean components of the state-of-the-art NEMO model, and are produced on the same tripolar ORCA025 grid at an eddy-permitting resolution (approximately ¼ degree of horizontal resolution and 75 depth levels). Three reanalyses use the LIM2 thermodynamic-dynamic sea-ice model, while the other (FOAM-GloSea5) employs CICE4.1 which includes more complex physics parameterizations compared to LIM2. Although many physical and numerical schemes are similar in the four reanalyses, there are a number of significant changes including the ocean model version and some parameterizations, thus introducing differences in the four ocean model configurations. There are also differences in the data assimilation methods used by the single products, in terms of data assimilation scheme, code, frequency of analysis and assimilation time-windows, input observational data-sets, error definitions and bias correction schemes, which introduce a large number of uncertainties as ensemble spread. The main characteristics of the GREP members are summarized in **Table 1** – a detailed description of model setup and data assimilation methods is outside of the scope of this study. GREP and its constituent reanalyses cover the altimetric period from 1993. Our analysis extends to 2019.

We consider a set of sea ice satellite products in order to evaluate the GREP performance. We use SIC fields from NOAA/NSIDC Climate Data Record (version 3, Meier et al., 2017, hereafter CDR), EUMETSAT OSISAF Climate Data Record and Interim Climate Data Record (release 2, products OSI-450 and OSI-430-b, Lavergne et al., 2019), and IFREMER/CERSAT (Ezraty et al., 2007). Firstly, the CDR algorithm output is a combination of SIC estimates from two well-established algorithms: the NASA Team (NT) algorithm (Cavalieri et al., 1984) and the Bootstrap (BT) algorithm (Comiso 1986). CDR SIC is based on gridded brightness temperatures (TBs) from the Nimbus-7 SMMR and the DMSP series of SSM/I and SSMIS passive microwave radiometers; the final product is provided at daily and monthly frequency on a 25 km × 25 km grid.

Secondly, the EUMETSAT OSI-450 is a level 4 product that covers the period from 1979 to 2015. The sea ice concentration is computed from the SMMR (1979–1987), SSM/I (1987–2008), and SSMIS (2006–2015) instruments, as well as ECMWF ERA-Interim data. The Interim OSI-430-b extends OSI-450 from 2016 onwards; it is an off-line product based on the same algorithms as OSI-450, and uses SSMIS data available through the NOAA CLASS, as well as operational analysis and forecast from ECMWF. The data processing introduced an open-water filter aimed at removing weather-induced false ice over open water, which unfortunately may remove some true low-concentration ice in the MIZ (Lavergne et al., 2019). OSISAF products are delivered at daily frequency on a 25 × 25 km grid. Lastly, the IFREMER/CERSAT product used here is derived from high

TABLE 1 | The central characteristics of ocean reanalyses.

Name	CGLORSv7	GLORYS2v4 (hereafter GLORYS2)	ORAS5	FOAM-GLOSEA5v13
Institution	CMCC	Mercator Ocean	ECMWF	United Kingdom Met Office
Ocean-ice model	NEMO3.6-LIM2 (EVP rheology)	NEMO3.1-LIM2 (EVP rheology)	NEMO3.4-LIM2 (VP rheology)	NEMO3.2-CICE4.1 (EVP rheology)
Time period	1986–2019	1993–2019	1979–2019	1993–2019
Sea ice data assimilation method	Linear nudging	Reduced order KF (SEEK)	3DVAR-FGAT	3DVAR
Ocean data assimilation method	3DVAR (7 days)	SAM2 (SEEK) (7 days)	3DVAR-FGAT (5 days)	3DVAR (1 day)
DA sea ice data	OSI-SAF	IFREMER/CERSAT	OSTIA (reprocessed before 2008, analysis from 2008)	OSI-SAF
Thickness categories	1	1	1	5

frequency channels of SSM/I that yield a spatial resolution of 12.5 × 12.5 km. SIC is provided at daily and monthly frequency.

It is worth mentioning that OSISAF and IFREMER/CERSAT sea ice concentration are ingested by the data assimilation systems employed in the ORAs constituting GREP, while CDR is not assimilated in any ORA. The use of CDR is, hence, considered an advantage for the robustness of the GREP validation; OSISAF and IFREMER/CERSAT datasets are anyway used in our analysis. It has been shown that NT generally underestimates SIC (Andersen et al., 2007; Meier et al., 2014), and overestimates MIZ and underestimates pack ice by a factor of two compared to BT (Stroeve et al., 2016). On the other hand, BT produces too low SIC under extremely cold conditions (Comiso et al., 1997). The CDR algorithm blends NT and BT output concentration by selecting, for each grid cell, the higher concentration value, taking advantage of the strengths of each algorithm to produce concentration fields more accurate than those from either algorithm alone. Since passive microwave instruments tend to underestimate SIC, the aforementioned approach is considered to be more accurate (Meier et al., 2014). Given that observational datasets and ORAs use different horizontal grids, we interpolated the former onto the ORCA025 grid for the grid-point diagnostics.

In this paper, sea ice variability is described in terms of sea ice area (SIA) rather than sea ice extent (SIE). Sea ice extent is defined as the integral sum of the areas of all grid cells with at least 15% ice concentration, whereas sea ice area is the sum of the product of each grid cell area with at least 15% ice concentration and the respective ice concentration. Hence, sea ice area excludes open water areas between ice floes. Although these two metrics are highly correlated, uncertainties in SIC retrievals from passive microwave sensors have a larger impact on SIA that results in a weaker agreement across data records.

In addition to the total sea ice area, we consider two sea ice classes defined through SIC thresholds. The MIZ is here identified as the region extending from the outer sea ice–open-ocean boundary (defined by SIC equal to or higher than 15%) to the boundary of the consolidated pack ice (defined by 80% SIC). This definition has been previously used by Stroeve et al. (2016) to assess observed MIZ changes in Antarctica. The consolidated pack ice is then defined as the area with ice concentrations higher than 80%.

The seasonal variability of SIA is analysed for total, pack and MIZ sea ice on the hemispheric domain and in selected regions where satellite records have highlighted large differences in the ice response to climate. As in previous studies (e.g., Parkison and Cavalieri, 2012), the Antarctic domain is divided in the following five sectors (**Figure 1**): Weddell Sea (60° W–20° E, plus the small ocean area between the east coast of the Antarctic Peninsula and 60° W), Indian Ocean (20–90° E), western Pacific Ocean (90–160° E), Ross Sea (160° E–130° W), and the combined Amundsen-Bellingshausen Seas (130–60° W).

RESULTS

We begin with the assessment of the interannual variability of total SIA reproduced by GREP and derived from satellite data sets. The GREP and observational products monthly-mean SIA is presented for the Southern Ocean as a whole, from January 1993 to December 2019, in **Figure 2A**. GREP SIA ranges from the summer minima occurring in February to winter maxima occurring generally in September, with a huge amount of sea ice growing and melting each year in very good agreement with observations. While the reanalysis ensemble slightly underestimates minima and maxima SIA, it correctly reproduces the large interannual variability, and properly depicts the record high in September 2014 (16.73×10^6 km^2 in GREP and 17.42×10^6 km^2 in CDR) and the marked decreases in the subsequent 3 years, with the record low in February 2017 (1.16×10^6 km^2 in GREP and 1.57×10^6 km^2 in CDR). GREP and CDR monthly anomalies of SIA show similar patterns and trends are basically consistent (**Figure 2B**), with an upward trend in yearly average SIA of 0.32×10^6 km^2/decade in GREP and 0.31×10^6 km^2/decade in CDR for 1993–2014, and trend close to zero (-0.04×10^6 km^2/decade in GREP and -0.036×10^6 km^2/decade in CDR) for the entire period 1993–2019. The good agreement between the three observational products (gray shading) and the four ORAs (pink shading) is notable; differences are greatest at the winter maxima.

To quantify the inconsistency between GREP and satellite estimates, we use the integrated ice area error (IIAE) approach of Roach et al. (2018, 2020). The IIAE identifies the area of sea ice on which ORAs and observations disagree; it is computed as the sum

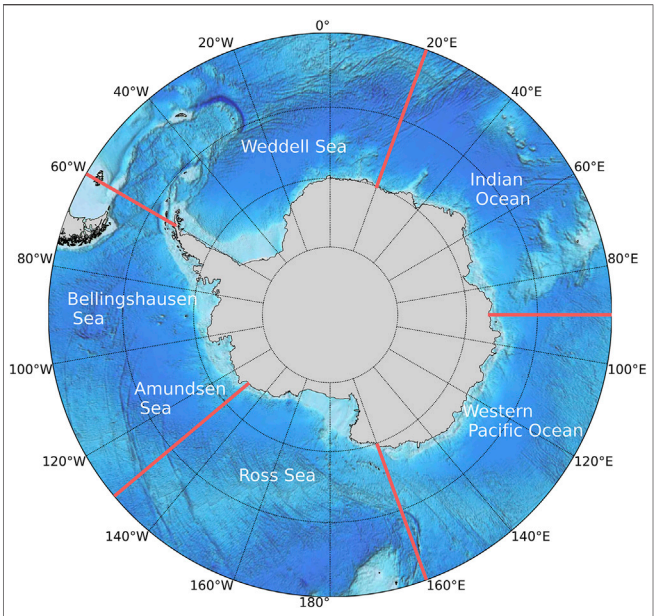

FIGURE 1 | Map of the five Antarctic sectors used in the regional analysis.

of overestimated (O) and underestimated (U) sea ice area. These two O and U components are calculated as the sum of the product of the area and the SIC of each grid cell where GREP has a higher or lower concentration compared to observations. We apply the same metric also to pack ice and MIZ to determine how each sea ice class contributes to the overall error. The location of sea ice classes in CDR estimates is taken as the "true state". The time series of IIAE O and U components for total ice, pack ice and the MIZ area computed relative to CDR are shown for the period 1993–2019 (**Figure 3**).

For every month, errors are very low relative to the mean SIA values, even for February and September. In general, GREP tends to underestimate total SIA area with the error ranging from 0.1 × 10^6 km^2 in March-April to 0.7 × 10^6 km^2 in October-December. Reanalyses generally tend to reproduce lower SIC than CDR, within the pack ice region: while IIAE O component in pack ice is relatively small (~0.05 × 10^6 km^2 all year round) and similar among the individual ORAs, IIAE U component grows up to 0.6 × 10^6 km in August-November and doubles for two reanalysis products. The MIZ also contributes to the total overestimated and underestimated area, but the error does not generally exceed 0.2 × 10^6 km^2. There is one ORA outlier (GLORYS2) that generally contributes to overestimating SIA, and one (CGLORS) to underestimating it. The former (the latter) reproduces too high (low) SIC in the MIZ. Overall, GREP performs well owing to minimization of systematic errors in individual products. Additionally, the error in the ensemble mean is consistent throughout the years, which is not the case for single ensemble members.

The accuracy of GREP and individual ORAs in reproducing the spatial distribution of SIC is shown in **Figure 4**, where maps of the SIC root mean square errors (RMSE) for GREP and individual ORAs against CDR are presented for September

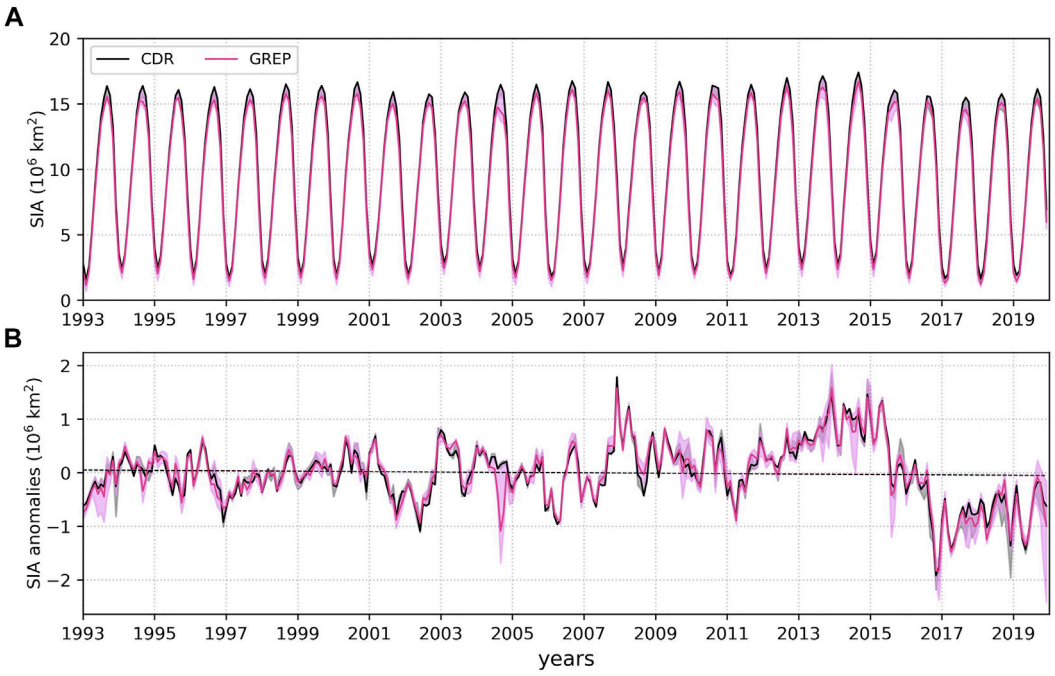

FIGURE 2 | Time series of **(A)** monthly averages and **(B)** monthly anomalies of Antarctic sea ice area in GREP (magenta) and CDR (black) from January 1993 to December 2019, for GREP (magenta) and CDR (black). Pink (gray) shading denotes the envelope of GREP members (CDR, OSISAF, Ifremer CERSAT satellite records).

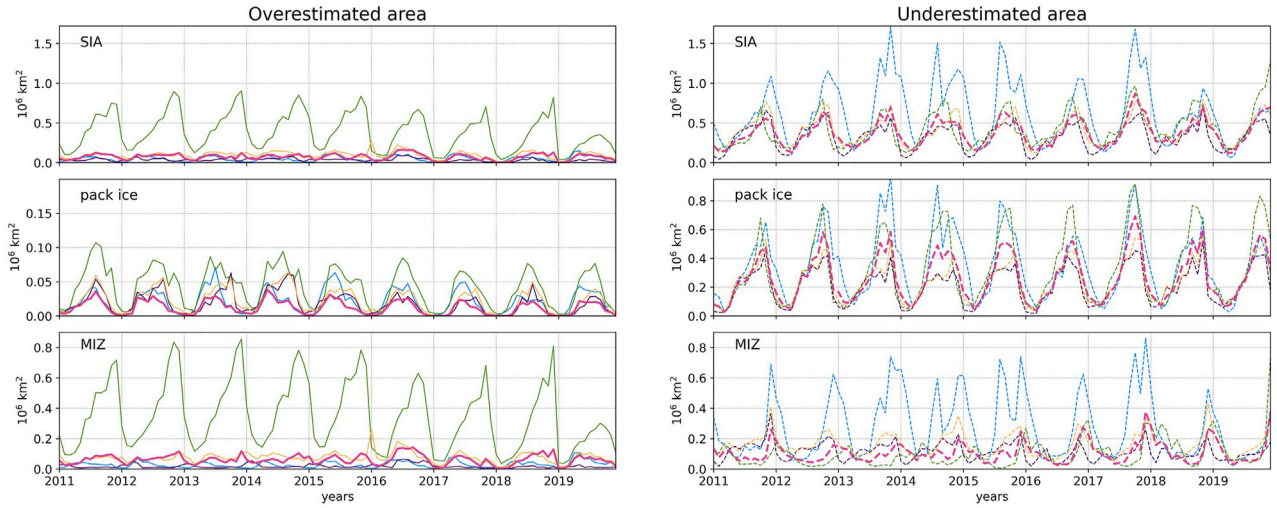

FIGURE 3 | Time series of the GREP integrated ice area error components (in magenta) calculated with respect to CDR for total SIA (top panel), pack ice (middle panel) and the MIZ (bottom panel). Area of sea ice where GREP simulates higher (lower) SIC is on the left (right) column. The *y*-axis scales for pack ice are different. Thin lines represent the individual ORAs: CGLORS in light blue, FOAM-GloSea5 in violet, GLORYS2 in green, and ORAS5 in yellow–the same colors will be used in the following figures for single ORAs.

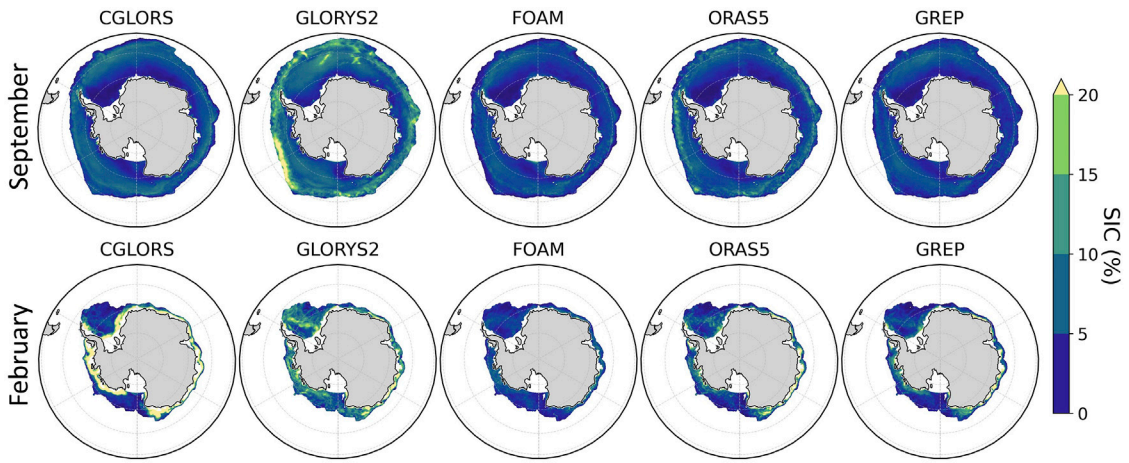

FIGURE 4 | Mean root mean square error for SIC at every grid cell for the single ORAs and GREP against CDR in September (upper row) and February (lower row).

and February, which are typically the months of maximum and minimum ice coverage respectively. The monthly climatologies are computed over the years 1993–2019. The sign of the errors has also been analyzed through the spatial distribution of the average bias (not shown). In September, RMSEs are lower than 5% along the Antarctic coast for all ORAs and tend to grow towards the ice edge, with the highest values generally smaller than 15% except for one single product, GLORYS2, which overestimates SIC by up to 20% in the Ross Sea and the Bellingshausen and Amundsen Seas. In February, the largest disagreement with CDR is located near the Antarctic coast, in particular in the Indian Ocean and the Western Pacific Ocean sectors, where three of the four ORAs underestimate the observed concentration. This error may be primarily linked to the reanalyses representation of sea ice drift and the Antarctic coastal current in the eastern Antarctica (not shown). One product (CGLORS) exhibits an unique behavior with the RMSE for SIC exceeding 30% along the entire Antarctic coastline - this indicates a lower concentration compared to CDR that may be related to a large warm bias in sea surface temperature along the coast, in particular in the Indian and the Western Pacific Oceans (not shown). GREP compares well with satellite estimates considering that the RMSEs are of the same order as the uncertainties from SIC retrievals using passive microwave radiometry (Ivanova et al., 2015). Time evolution of the mean over area RMSE (not shown) indicates that the

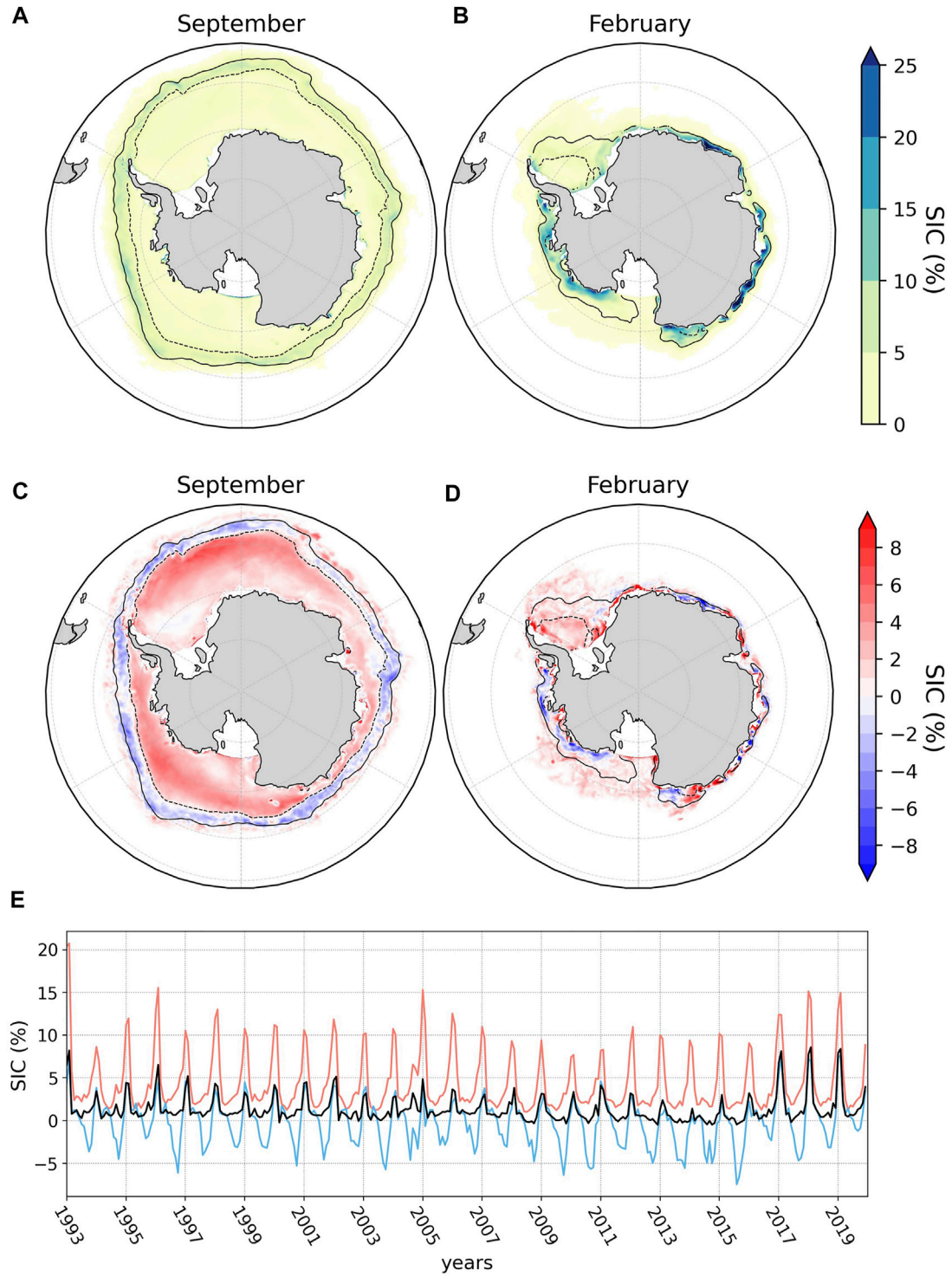

FIGURE 5 | Spatial distribution of **(A,B)** ensemble spread (ES) and **(C,D)** difference (in %) between GREP RMSE and ES for SIC in September and February. Contours indicate the mean position of 15% (solid) and 80% (dashed) ice concentration over the period 1993–2019 from CDR. **(E)** Time series of the difference (in %) between GREP RMSE and ES spread of SIC for total area (black), pack ice (red), the MIZ (blue).

RMSE for GREP concentration is up to ~10% in summer months (January-February) and does not exceed 7% in other months.

We also analyze the ensemble spread (ES) in order to assess the overall consistency across ORAs (**Figures 5A,B**). The largest ES in SIC (~35% in February) is found during the melting season

everywhere along the Antarctic coast, except in the Weddell and the Ross Seas. Increased ES is consistent with uncertainties coming from the assimilated satellite data - SIC retrievals present larger uncertainties within the melting season due to surface wetness and a broad variety of sea ice forms that affect sea ice emissivity (Ivanova et al., 2015; Meier and Stewart, 2019). In September, there is high consistency among ORAs due to the larger portion of stable and compact pack ice. Larger ES is located in the MIZ and does not exceed 10%. Finally, we compare RMSE of GREP SIC calculated against CDR, with the SIC ES to evaluate whether the ensemble is over-dispersive or under-dispersive. The spatial distribution of the metric (GREP RMSE minus ES) is shown for September and February in **Figures 5C,D**. GREP is over-dispersive when RMSE < ES (blue/negative) and under-dispersive when RMSE > ES (red/positive). In September, it appears that ensemble dispersion depends on sea ice class: GREP is over-dispersive in the MIZ (represented by the region between contour lines), whereas GREP is under-dispersive within the pack ice. This means that ORAs agree better on the representation of high concentration in the region of stable pack ice, where the ORAs performances are less challenging compared to the MIZ. In February, there does not seem to be a direct relationship between ensemble dispersion and sea ice class. The pattern of the difference is heterogeneous, particularly along the coast of the eastern Antarctic. In the Weddell and Ross Seas, the GREP remains over-dispersive. Time series of the difference between GREP RMSE and ES better presents the opposite behavior of sea ice classes and the contribution to total sea ice changes (**Figure 5E**). The compensation between sea ice classes in all seasons, except in summer, translates into close-to-zero values for the total ice concentration. From December to February, GREP RMSE exceeds ES in both pack ice and the MIZ, leading to an increased difference for the total ice area.

Seasonal Variability

We proceed with an assessment of the consistency of the seasonal sea ice variability between the reanalysis ensemble and satellite estimates. The climatological mean seasonal cycle of the circumpolar SIA as represented by GREP, single ORAs and observational estimates, is shown for total sea ice, pack ice, and MIZ, in **Figure 6A**. The seasonal cycle of Antarctic sea ice is consistent among ORAs and in phase with observations. All systems have a maximum in total SIA in September, and a minimum in February; it takes about 7 months to expand sixfold from summer minimum of ~2.5 $\times$ 10^6 km^2 to winter maximum of ~15 $\times$ 10^6 km^2, and about 5 months to melt again. It is worth noting that the ensemble spread of ORA SIA is limited throughout the year, and is comparable to the estimated observational uncertainty. The seasonal cycle of Antarctic-wide total SIA is dominated by the variability of pack ice, whose area evolves at the same rate as total ice. GREP slightly underestimates the area of pack ice from August for the melting season (only one reanalysis, GLORYS2, is larger than observational products), but all ORAs align well with observations during refreezing in autumn.

The seasonal changes in the MIZ are quite different from those in total ice and pack ice. On average, the MIZ advance needs about 10 months to progress from near the coast (in February) to its most equatorward maximum (in November or December) and about only 2 months to revert to a minimum. After summer, the MIZ area grows simultaneously with pack ice, in part transforming into it, and continues to expand in spring after the total (and pack) SIA peaks. The further increase in the MIZ area after the consolidated ice pack begins to melt implies that, as it starts to retreat, the pack ice converts in part to MIZ over a wider area. We note the Antarctic MIZ/pack-ice ratio is close to 1 from December to March. GREP is always in the observed envelope; the ensemble spread of ORA SIA is generally smaller or comparable to the estimated observational uncertainty. Here, the larger spread among the observed MIZ area (found also between NT and BT algorithms by Stroeve et al., 2016) reflects the different ability of high and low frequency channels used in the different data algorithms to retrieve low fraction sea ice. However, GLORYS2 underestimates the MIZ area from July to December, and this can be attributed to faster sea ice consolidation in the growing season. This is consistent with the IIAE analysis (**Figure 3**), which indicates that this system simulates higher SIC in those grid cells that are considered to belong to the MIZ in observations, and with the RMSE of SIC (**Figure 4**) with larger errors in the outer ice region where MIZ is located. CGLORS underestimates the MIZ area in summer from December to February, causing a large impact on the minimum of total SIA (as seen in **Figures 3**, **4**).

For all sea ice classes, the highest consistency among datasets is observed throughout autumn freezing, from March to June. Overall, due to the realistic performance of all single members and the cancellation of systematic errors, GREP reproduces robust estimates of the seasonal cycle of Antarctic total ice area and the two sea ice classes.

The different seasonality of sea ice classes is a notable result that confirms a different interplay of ice classes with the ocean and the atmosphere. Seasonal variability of Antarctic sea ice is governed by the position of the circumpolar trough relative to the ice edge and associated wind field and Ekman transport (Enomoto and Ohmura, 1990; Eayrs et al., 2019). In spring, when the circumpolar trough is north of the ice edge, hastened conversion of pack ice to the MIZ is supported by divergence which results in opening of pack ice. This consequently facilitates solar absorption in the upper ocean and accelerates lateral melting of ice floes (e.g., Perovich and Jones, 2014) which contributes to the MIZ growth. From December to February, the MIZ area rapidly retreats together with pack ice, driven by southward Ekman forcing and sea ice convergence. However, the MIZ represents a significant part of the overall ice cover from December to March (the proportion between the MIZ and pack ice area is in the range between 0.8 and 1.2).

Analysis in the Sub-regions

Since Antarctic sea ice variability and trends are spatially heterogeneous (e.g., Parkinson and Cavalieri, 2012; Parkinson 2019), the analysis of the Antarctic circumpolar sea ice is rather limited. In this section, we investigate the accuracy of GREP

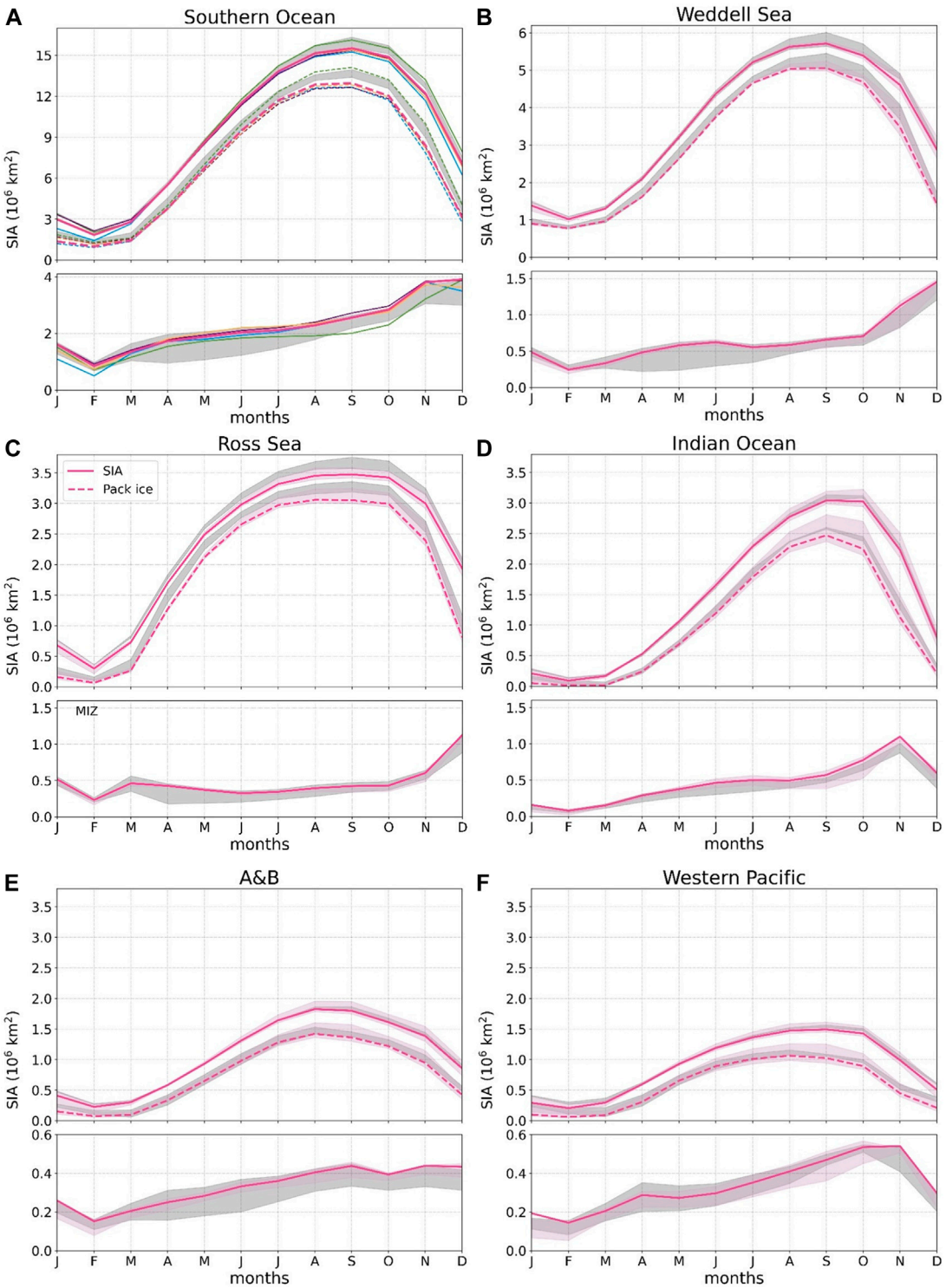

FIGURE 6 | Mean seasonal cycle (1993–2019) in the total SIA (solid), pack ice (dashed) (upper subplots), and the area covered by Marginal Ice Zone (MIZ) (lower subplots) computed for GREP (in magenta) and the individual ORA (thin colored lines) in the Antarctic-wide region **(A)**, for GREP in the five sub-sectors **(B-F)**. Pink shading denotes the envelope of GREP members. Gray shading denotes the envelope of observational estimates (CDR, OSISAF, Ifremer CERSAT). Please note the different y-axis scales for the Southern Ocean and Weddell Sea.

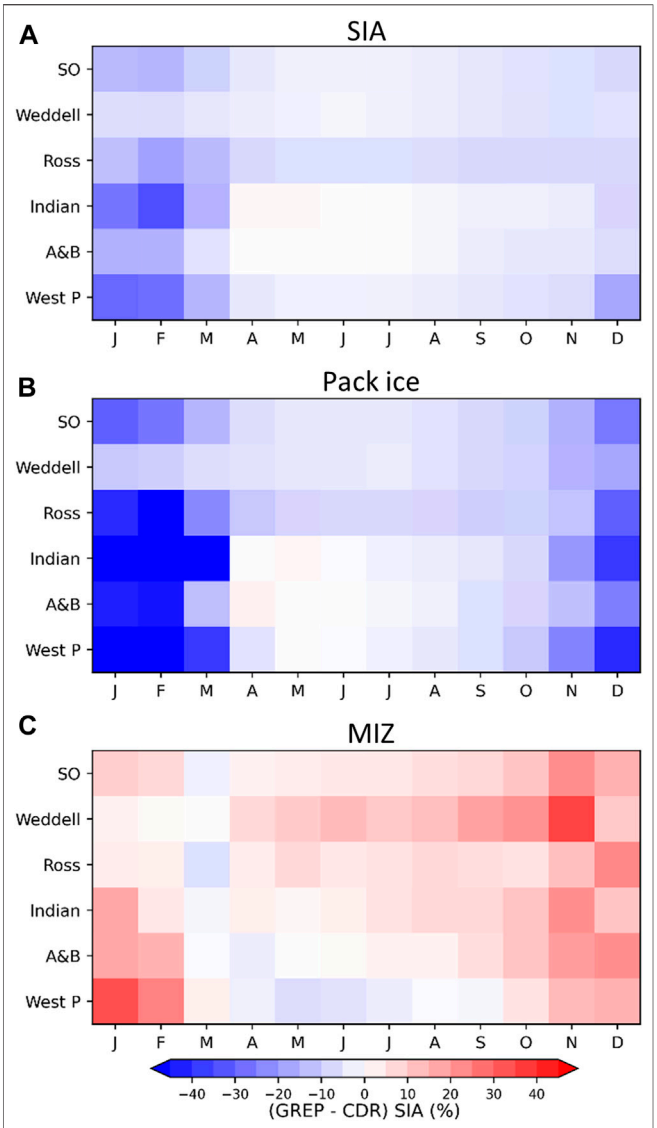

FIGURE 7 | Seasonal cycle of (GREP minus CDR, in %) monthly climatology of **(A)** total ice (upper panel), **(B)** pack ice (middle) and **(C)** MIZ area in the Southern Ocean and its five sectors. Differences are shown as a percentage of CDR values computed for the years 1993–2019. Red (blue) indicates that GREP reproduces higher (lower) SIA compared to CDR.

performance on regional scales by analysing the seasonal variability of total ice, pack ice and MIZ area for each of the five Antarctic sectors (shown in **Figure 1**), and by comparing GREP output with the CDR product.

As expected, there are significant differences among the five sectors in the amount of ice classes, the timing of maxima and minima, the rate of sea ice expansion and the retreat phase (**Figures 6B–F**). This contrast in the regional patterns of sea ice growth and melt is associated with geographic differences and interplay of leading climate processes (Maksym et al., 2012).

There is a very good agreement between GREP and CDR variability in all regions (**Figures 6B–F**, **Figure 7**). It is worth noting that the spread in observational products (and in the reanalyses) varies not only among sea ice classes, but also among regions. The spread of observational estimates of MIZ area is generally larger than the spread of the reanalysis ensemble, in particular in the Weddell Sea and Ross Sea in autumn months and in the Amundsen-Bellingshausen (A-B) Seas from March to December.

As in the Southern Ocean as a whole, all sectors exhibit a large annual cycle of monthly total SIA (**Figure 6**), with asymmetric growth and melt seasons. However, there are large differences in the timing and magnitude of the sub-region seasonality, given that the rate of waxing and waning of sea ice and the interplay with air-sea components vary across the sectors. Minima of total SIA always occur in February and maxima occur frequently in September (**Figure 6**), although with much greater interannual variability than in the Southern Ocean as a whole (not shown). The pattern and ratio of pack and marginal ice widely varies among the regions.

The regional variability as reproduced by the GREP ensemble-mean is described for individual sectors. In the Weddell Sea (**Figure 6B**), the SIA is much higher than other regions and has the largest distribution of pack ice. Its seasonality is consistent with the Southern Ocean as a whole. From the February minima ($\sim 1 \times 10^6$ km^2), total and pack ice areas begin to expand in March and peak (at $\sim 5.7 \times 10^6$ km^2 and $\sim 5 \times 10^6$ km^2 respectively) on average in September, but maximum timing varies frequently from August to October (not shown). The Weddell Sea provides the greatest contribution (~55%) to the summer sea ice area in the Southern Ocean, due to the presence of consolidated pack ice all year around. In agreement with CDR, the ensemble-mean shows that the Weddell Sea holds the largest percentage (~75%) of February pack ice. The MIZ area also starts to advance in March and continues to increase until December ($\sim 1.45 \times 10^6$ km^2), as the pack ice quickly retreats. In this region, the sea ice cover expands northwards until it reaches a region with strong air-sea dynamics. North of the consolidated pack ice region, ice continues to advance, thanks to further freezing or breaking by the winds and currents.

The second largest contribution to the Antarctic-wide ice area comes from the Ross Sea (**Figure 6C**). In this sector, the total ice and pack ice areas present a large asymmetric seasonal cycle, with, approximately, a 9-months growth period and a 3-months melting period. With almost no pack ice, the total sea ice and MIZ areas have a marked minimum always occurring in February. There is a large variability in the timing of total and consolidated pack ice maxima occurring generally from August to October and reaching $\sim 3.5 \times 10^6$ km^2 and $\sim 3 \times 10^6$ km^2 respectively. In February, the minimum SIA mainly consists of MIZ that covers ~0.25 10^6 km^2; the MIZ fraction is then nearly constant throughout the expansion and retreat of the pack ice, with a maximum in December (1.13×10^6 km^2) as the pack ice rapidly decays. The Ross Sea, like the Western Pacific (**Figure 6F**), exhibits a second peak in the MIZ area in March, in the freezing season, when the area of MIZ and pack ice starts to expand and the increasing sea ice consolidation is accompanied by MIZ-to-pack ice transformation.

In the Indian Ocean, the total SIA maximum (3×10^6 km^2) is reached in October rather than September (**Figure 6D**), about

1 month later the pack ice peak (2.4×10^6 km^2) is reached. The pack ice tends to disappear completely in summer and when MIZ comprises the largest portion of the overall ice cover. The MIZ advances from March until November when its area (~1.1×10^6 km^2) is comparable to that of pack ice.

At their largest, the A-B Seas and Western Pacific Ocean together account for less than 20% of the Antarctic-wide SIA, with the lowest winter maxima (1.83 and 1.5×10^6 km^2, respectively); they can weakly affect the Antarctic sea ice seasonal cycle. In both sectors, the areas of consolidated pack ice and MIZ are generally comparable in the winter months. The A-B Seas are in major contrast with the rest of the Southern Ocean (Parkinson, 2019), and are characterized by an overall downward sea ice trend (not shown) related to the upper ocean warming at the west of the Antarctic Peninsula (e.g., Ducklow et al., 2012). Seasonality of ice expansion and retreat are almost symmetric for total ice and pack ice areas (**Figure 6D**) that both peak in August (the maximum timing varies from July to October from year to year) and are minimum between February and March. The MIZ area increases during most of the year, from February to December. There is a large interannual variability in the timing of the maximum that results in the double peaks in September and November (approximately 0.42×10^6 km^2). Here, the MIZ area does not further increase when pack ice starts to retreat, in contrast to other regions. The MIZ gives the largest contribution to total area from January to April. In this sector the spread of observational estimates of MIZ is very large compared to the ORAs spread- GREP is always located within the observed envelope. In the Western Pacific Ocean, the total SIA reaches the highest value from August to October (**Figure 6F**), with the maximum generally occurring in September (~1.5×10^6 km^2). While pack ice area exhibits very low values and stays nearly constant throughout the summer period, MIZ area presents a prominent minimum in February and then begins to quickly expand until November when it exceeds pack ice area. The MIZ area remains larger until autumn.

Figure 7 shows how GREP representation of the seasonal variability of total ice, pack ice and the MIZ area differs from CDR estimates; due to the large regional contrasts in the amount of sea ice, the differences are expressed as a percentage of the average of CDR values. For total SIA, the difference between GREP and CDR is almost everywhere within 15% from April to December (**Figure 7A**). Thus, GREP seasonal variability is consistent in time and space with the observed sea ice changes over the period 1993–2019. The largest differences are generally found in summer, in particular in the Indian Ocean and the Western Pacific where GREP area is about 25% lower than CDR. The accuracy of GREP stands out in the Weddell Sea where total sea ice area differs from CDR data by -7% at the most. The high quality of total sea ice in the reanalysis ensemble results from the contrasting behaviour of pack and MIZ area. Differences have a similar pattern for pack ice areas, but with different magnitudes. The highest values are found from December to March when GREP tends to generally underestimate the area of consolidated ice in all sectors. Due to the very low amount of pack ice area in both GREP and CDR in spring and summer, this metric typically detects small differences with respect to CDR. For example, GREP pack ice area differs by ~70% from CDR in the Indian Ocean in February, when pack ice area has almost disappeared in the region, with values lower than 0.1×10^6 km^2. As for the total ice, it is in the Weddell Sea sector that GREP better reproduces the seasonal variability of the pack sea ice area. Overall, the ensemble-mean reproduces a larger area of the MIZ almost everywhere. As for pack ice, GREP and CDR differences are the smallest in the growing season when GREP MIZ extends 10% more than CDR at most - differences stay small but reverse in the Western Pacific Ocean during autumn-winter months. The GREP MIZ area is 20–30% larger than observed estimates generally in November-December, when it approaches its maximum values. The largest departures from CDR are found in the Western Pacific sector in January and the Weddell Sea in November. It is worth noting that the MIZ area reproduced by GREP has generally the largest differences from the observational estimates when they present large spread (**Figure 6**).

DISCUSSION

Understanding the mechanisms and rates of Antarctic sea ice change is crucial from a climate-change perspective. Sea ice concentration retrieved from satellite microwave radiometers has been available on a daily basis since the late 1980s at a horizontal resolution finer than 25 km. However, these observational estimates are highly dependent on which passive microwave methods and sea ice algorithms are used (Ivanova et al., 2014; 2015). There are dozens of such algorithms available. Although these products agree quite well on area trends, absolute values of total SIC and SIA are not necessarily consistent with each other. There are also large differences among observed products in the regional ice distribution and trends, as well as in the contribution of consolidated ice or MIZ in the total ice cover (Stroeve et al., 2016). This is of particular importance for accurate assessment of processes contributing to climate change and assimilation of sea-ice in models. Reliable estimates of sea ice concentration and relative parameters are necessary to constrain also other ice parameters in modelling studies of past, present and future variability.

Simulation of Antarctic sea ice remains a fundamental challenge for state-of-the-art climate models (e.g., Holmes et al., 2019; Roach et al., 2020). Despite advances in climate modeling capabilities, the CMIP5 and CMIP6 intermodel spread in Antarctic sea ice extent is large, especially in summer, and the observed weak upward trend of the Antarctic ice extent is not captured yet (Turner et al., 2013; Roach et al., 2020; Shu et al., 2020; Shu et al., 2020). The poor accuracy of Antarctic sea ice changes in the CMIP exercises limits our understanding on what drives regional and seasonal Antarctic sea ice changes, including feedback and competing processes.

Our analysis confirms that ocean reanalyses are a fundamental tool for investigating climate variability and for evaluating key climate diagnostics that are not directly observed (e.g., Masina and Storto, 2017). Given the robustness of its mean and the implicit quantification of uncertainty by means of the spread, the multi-model ensemble provides a

robust representation of the spatial and temporal variability of Antarctic sea ice. Although sea ice concentration is the most well-constrained sea ice parameter, the ensemble spread mainly comes from differences in implemented data assimilation schemes but also from other sources of uncertainty such as differences in models, observational datasets and air-sea flux formulations.

We found strong consistency between the reanalysis ensemble and the satellite products, and GREP generally outperforms or at least equals individual reanalyses in approaching observation-based estimates of sea ice area. The advantage of the multi-model approach is highlighted by the fact that it is practically impossible to determine which one of four performs the best for all metrics and seasons. GREP smooths the strengths and weaknesses of single systems and provides the most consistent and reliable estimates of the mean state and variability of sea ice area. Nevertheless, advancement in model formulations and data assimilation schemes in single members could reduce the impact of ORAs shortcomings on the realism and accuracy of the ensemble-mean solution.

Although the main objective of the study is the evaluation of the GREP ability to reproduce the observed sea ice area on interannual and seasonal scales, our results also confirm the importance of regional variability and the distinction in sea ice classes. They should be considered when assessing how Antarctic sea ice varies in model simulations and when investigating the different processes that are likely contributing to ice interannual and seasonal.

We focus on how consolidated pack ice and the marginal ice change in relation to their different characteristics and therefore their different sensitivities to the external forcing. Differences in the seasonality of ice classes suggest that their variability is driven by changes in wind and ocean conditions in a different way. While the description of processes controlling the distribution of the MIZ and pack ice is out of scope of this study, we emphasize that a better knowledge of temporal and spatial variability in the MIZ and pack ice can provide a deeper insight of possible driving mechanisms behind these changes. We show that both GREP (and individual ORAs) and satellite products present considerable differences in the climatological mean seasonal cycle in the area of ice classes. The net circumpolar changes in sea ice area is the result of the interplay of MIZ and pack ice, and their different response to changing wind and ocean conditions. The annual waxing and waning of sea ice cover implies redistribution of ice floes between the MIZ and pack ice from month to month as well as spatial expansion and contraction of sea ice edge. When pack ice starts to melt and its area to retreat in spring, the breaking of ice floes contributes to the MIZ expansion that continues for 2–3 months. That results in a strong asymmetry in the MIZ seasonal cycle in all Antarctic regions, with approximately 9–10 months of advance and 2–3 months of retreat. Contractions and expansions of pack ice and the MIZ do not necessarily follow the changes in the location of the outer sea ice edge: ice classes can contribute to changes in sea ice coverage in different ways or even exhibit an opposite behavior (Stroeve et al., 2016). GREP reproduces regional differences in the proportion between pack and MIZ, the timing and duration of freezing and melting seasons, in close agreement with observation-based results (e.g., Stroeve et al., 2016; Parkinson, 2019; Wang et al., 2021).

The reanalysis ensemble agrees well with the CDR product on the different contributions of MIZ and pack ice to changes in the Antarctic-wide total ice. Monthly trends (computed as function of longitude and month) in the total, pack and marginal ice area (**Figure 8**) indicate a large degree of seasonal and regional variability around Antarctica. In all sectors and for all months, the spatial patterns and magnitude of statistically significant positive and negative trends in total ice area are highly consistent between GREP and CDR in all sectors. Results highlight the necessity to distinguish between sea ice classes in order to assess the quality of numerical systems. Although GREP and CDR are similar in SIA trends, there are some inconsistencies when looking at sea ice classes: GREP barely reproduces the correct magnitude of trends in the Eastern Antarctic and does not simulate the MIZ area expansion in December in the Ross Sea. Generally, in both GREP and CDR, significant trends in the MIZ are less pronounced but more heterogeneous in space, and they tend to offset the significant trends in pack ice. This is for example evident in the Ross Sea, where no trend is found in the observed total sea ice area in December, due to compensation between the opposite trends in the MIZ and pack ice. Positive trends in total SIA are generally dominated by statistically significant positive trends in the consolidated pack ice as in the western Weddell Sea from January to March. Both ice classes contribute to the statistically significant negative trends in the eastern Ross Sea and eastern A-B Seas in summer. The regional variability of the MIZ area trends during spring and autumn is consistent with a complex pattern of changes in timing of sea ice advance, retreat and duration (e.g., Eayrs et al., 2019).

Differences between GREP and CDR can be also explained by some limitations in our analysis. The first caveat concerns the methodology: we distinguish sea ice classes through sea ice concentration thresholds. Although the SIC-based definition is the one most often used (e.g., Strong and Rigor, 2013; Stroeve et al., 2016; Rolph et al., 2020), Vichi (2021) showed that it is not able to adequately capture the features of the Antarctic MIZ, in which ice dynamics is determined by oceanic and atmospheric processes. Indeed, this definition of the MIZ is not physically or dynamically explained; the lower boundary is linked to uncertainty from SIC retrievals (Comiso & Zwally, 1984) while the upper boundary corresponds to the WMO definition of "close ice" (WMO, 2009). In fact, the properties of Antarctic ice cover do not directly depend on the degree of coverage. *In-situ* measurements carried out in the Southern Ocean showed that close pack ice with SIC up to 100% do have the dynamical properties of the MIZ (Alberello et al., 2019; Vichi et al., 2019; Brouwer et al., 2021), which discredits the reliability of threshold-based definition. Vichi (2021) proposed an alternative MIZ definition that is based on statistical properties of the SIC and its spatial and temporal variability. The new method indicates the measure of variability, which is a key feature of the marginal ice. It also overcomes the disparity among the algorithms that could considerably differ in their representations of sea ice concentration, area and extent.

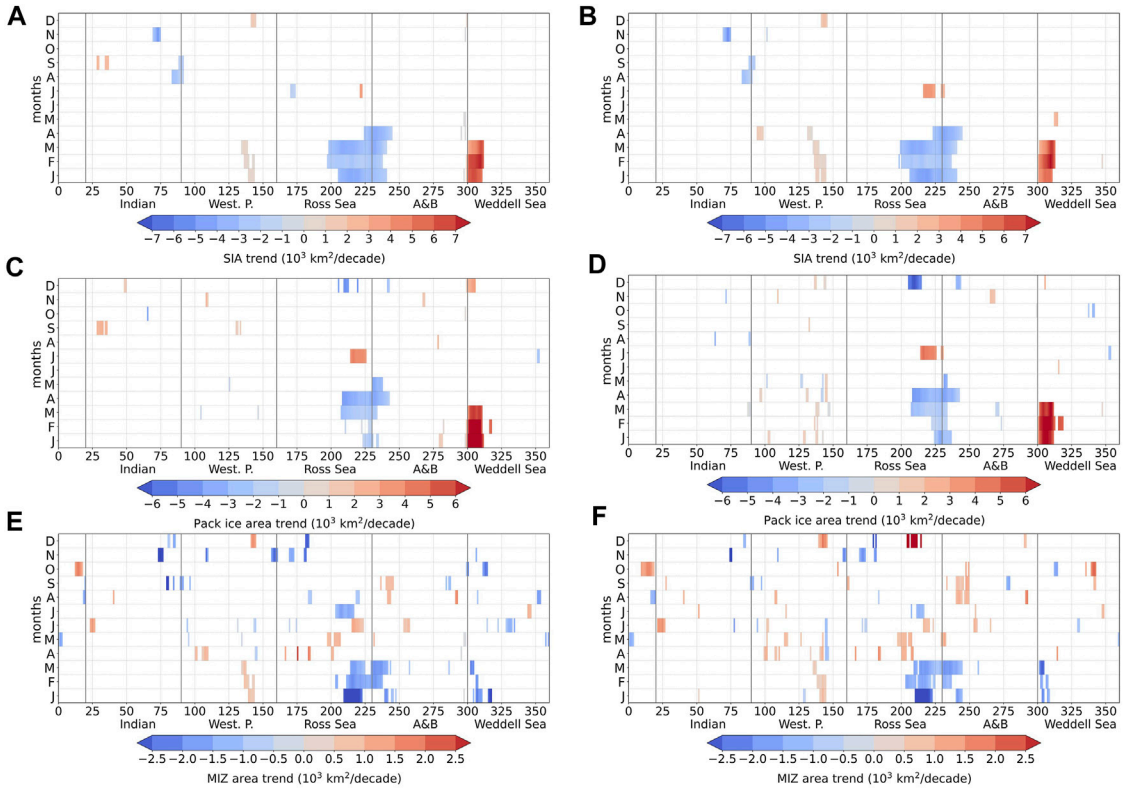

FIGURE 8 | Monthly trends (1993–2019) in regional areas of total ice **(A,B)**, pack ice **(C,D)**, and MIZ **(E,F)**, as a function of longitude. Left (right) columns correspond to GREP (CDR). Only significance higher than 95% are shown. Note that colorbar scales are different for ice classes.

Given the highly dynamic nature of the MIZ, another limitation of this study is the temporal resolution of GREP and ORAs output provided by CMEMS. Our analysis is constrained by monthly means of SIC from reanalyses. The use of daily fields might be more appropriate to investigate the MIZ variability and its linkage to regional interactions with ocean and atmosphere.

CONCLUSION

We assessed the accuracy of the CMEMS Global Reanalysis Ensemble Product (GREP) in reproducing the evolution in time and space of Antarctic total sea ice and discriminating the consolidated pack ice from the MIZ. Antarctic sea ice area from GREP is compared to a set of sea ice satellite products. GREP properly reproduces interannual and seasonal variability of total sea ice area both on hemispheric and regional scales. GREP is shown to properly represent the interannual and seasonal variability of pack and MIZ areas during the growing and melting seasons, as well as their minima and maxima. More evident discrepancies between GREP and satellite products occur during summer, when the spread among individual ORA increases; one product tends to underestimate MIZ area and another to overestimate pack ice area. Nonetheless, due to minimization of the single errors, the ensemble mean provides the most consistent and reliable estimates. The spatial distribution of RMSE in SIC also indicates that GREP smooths out strengths and weaknesses of individual systems.

For all ice classes, the ensemble spread is comparable to the spread among the observational estimates. The quality of GREP is generally comparable to that of satellite data sets and the differences between GREP and CDR are comparable or even smaller than differences between different algorithms (Stroeve et al., 2016). The seasonal cycle of the total sea ice area is within the observational uncertainty almost all year round, while the pack ice area is generally underestimated and the MIZ area is in the upper end of the observational range. This compensation between sea ice classes partly reflects misplacement of sea ice across the basin compared to the "true state".

Dispersion of GREP in sea ice concentration also appears to depend on sea ice classes. Due to the compensation between the opposite behavior in pack ice (GREP is under-dispersive) and the MIZ (GREP is over-dispersive), the difference between GREP RMSE and GREP ES is close to zero for the total ice area.

On a regional scale, the Weddell Sea is the region where GREP provides the most accurate representation of sea ice area, while the largest and most persistent discrepancies occur in the Indian and the Western Pacific sectors. This spatial distinction in GREP performance is attributed to the proportion of pack ice and the MIZ in the regions. Given its highly dynamic nature, the MIZ is more challenging to simulate compared to pack ice.

Considering that ocean reanalyses are widely used as boundary and initial conditions in forecasting systems, sub-optimal representation of the SIC distribution and variability can affect the quality of the output. The results of the current work proved the quality of the GREP product with regard to sea ice concentration and associated metrics. GREP agrees well with satellite products, and can be used to get a robust estimate of current sea ice state and recent trends in sea ice area and extent. However, improvement in data assimilation techniques, space-time data coverage in the ice-covered Southern Ocean regions, and availability of other ice properties (such as thickness and drift) from satellite measurements will most probably enhance the quality of ORAs and GREP in polar regions.

DATA AVAILABILITY STATEMENT

ORAs data and satellite datasets analyzed in this study are all freely available online. GREP output (product identifier GLOBAL_REANALYSIS_PHY_001_031) and its full documentation are provided by the Copernicus Marine Environment Monitoring Service, and are available to download through CMEMS webpage https://resources.marine.copernicus.eu/products Sea Ice Concentration data sets can be downloaded at the following links:

- NOAA/NSIDC Climate Data Record data set: https://nsidc.org/data/g02202/versions/3/
- EUMETSAT OSISAF: https://osi-saf.eumetsat.int/products/sea-ice-products
- Ifremer/CERSAT: ftp://ftp.ifremer.fr/ifremer/cersat/products/gridded/psi-concentration/

AUTHOR CONTRIBUTIONS

DI conceived and designed this study, and wrote the manuscript. JS analyzed, simulated and observed datasets, and contributed to the interpretation of results and editing. SM and AC reviewed the manuscript.

FUNDING

DI was funded by the European Union's Horizon 2020 research and innovation program under Grant agreement No 101003826 via the project CRiceS (Climate Relevant interactions and feedbacks: the key role of sea ice and Snow in the polar and global climate system). JS was supported by the Italian National Program for Research in Antarctica (PNRA) via the project INVASI (Interannual Variability of the Antarctic Sea Ice/ocean system from ocean reanalyses, Reference Number PNRA18-00244). AC and SM were supported by Copernicus Marine Service "Global Ocean Reanalysis for the GLO MFC" (Reference number: 114-R&DGLO-RAN-CMEMS).

REFERENCES

Alberello, A., Bennetts, L., Heil, P., Eayrs, C., Vichi, M., MacHutchon, K., et al. (2020). Drift of Pancake Ice Floes in the winter Antarctic Marginal Ice Zone during Polar Cyclones. *J. Geophys. Res. Oceans* 125 (3), e2019JC015418. doi:10.1029/2019jc015418

Alberello, A., Onorato, M., Bennetts, L., Vichi, M., Eayrs, C., MacHutchon, K., et al. (2019). Brief Communication: Pancake Ice Floe Size Distribution during the winter Expansion of the Antarctic Marginal Ice Zone. *The Cryosphere* 13 (1), 41–48. doi:10.5194/tc-13-41-2019

Andersen, S., Tonboe, R., Kaleschke, L., Heygster, G., and Pedersen, L. T. (2007). Intercomparison of Passive Microwave Sea Ice Concentration Retrievals over the High-concentration Arctic Sea Ice. *J. Geophys. Res. Oceans* 112 (C8), 1. doi:10.1029/2006jc003543

Balmaseda, M. A., Hernandez, F., Storto, A., Palmer, M. D., Alves, O., Shi, L., et al. (2015). The Ocean Reanalyses Intercomparison Project (ORA-IP). *J. Oper. Oceanography* 8 (Suppl. 1), s80–s97. doi:10.1080/1755876x.2015.1022329

Balmaseda, M. A., Trenberth, K. E., and Källén, E. (2013). Distinctive Climate Signals in Reanalysis of Global Ocean Heat Content. *Geophys. Res. Lett.* 40 (9), 1754–1759. doi:10.1002/grl.50382

Bintanja, R., van Oldenborgh, G. J., Drijfhout, S. S., Wouters, B., and Katsman, C. A. (2013). Important Role for Ocean Warming and Increased Ice-Shelf Melt in Antarctic Sea-Ice Expansion. *Nat. Geosci* 6 (5), 376–379. doi:10.1038/ngeo1767

Blanchard-Wrigglesworth, E., Roach, L. A., Donohoe, A., and Ding, Q. (2021). Impact of Winds and Southern Ocean SSTs on Antarctic Sea Ice Trends and Variability. *J. Clim.* 34 (3), 949–965. doi:10.1175/jcli-d-20-0386.1

Brouwer, J., Fraser, A. D., Murphy, D. J., Wongpan, P., Alberello, A., Kohout, A., et al. (2021). *Altimetric Observation of Wave Attenuation through the Antarctic Marginal Ice Zone Using ICESat-2*. The Cryosphere Discuss. [preprint], in review. doi:10.5194/tc-2021-367

Cavalieri, D. J., Gloersen, P., and Campbell, W. J. (1984). Determination of Sea Ice Parameters with the Nimbus 7 SMMR. *J. Geophys. Res.* 89 (D4), 5355–5369. doi:10.1029/jd089id04p05355

Chevallier, M., Smith, G. C., Dupont, F., Lemieux, J.-F., Forget, G., Fujii, Y., et al. (2017). Intercomparison of the Arctic Sea Ice Cover in Global Ocean-Sea Ice Reanalyses from the ORA-IP Project. *Clim. Dyn.* 49 (3), 1107–1136. doi:10.1007/s00382-016-2985-y

Comiso, J. C., Cavalieri, D. J., Parkinson, C. L., and Gloersen, P. (1997). Passive Microwave Algorithms for Sea Ice Concentration: A Comparison of Two Techniques. *Remote sensing Environ.* 60 (3), 357–384. doi:10.1016/s0034-4257(96)00220-9

Comiso, J. C. (1986). Characteristics of Arctic winter Sea Ice from Satellite Multispectral Microwave Observations. *J. Geophys. Res.* 91 (C1), 975–994. doi:10.1029/jc091ic01p00975

Comiso, J. C., Gersten, R. A., Stock, L. V., Turner, J., Perez, G. J., and Cho, K. (2017). Positive Trend in the Antarctic Sea Ice Cover and Associated Changes in Surface Temperature. *J. Clim.* 30 (6), 2251–2267. doi:10.1175/jcli-d-16-0408.1

Comiso, J. C., and Zwally, H. J. (1984). Concentration Gradients and Growth/decay Characteristics of the Seasonal Sea Ice Cover. *J. Geophys. Res.* 89 (C5), 8081–8103. doi:10.1029/jc089ic05p08081

Dee, D. P., Uppala, S. M., Simmons, A. J., Berrisford, P., Poli, P., Kobayashi, S., et al. (2011). The ERA-Interim Reanalysis: Configuration and Performance of the Data Assimilation System. *Q.J.R. Meteorol. Soc.* 137 (656), 553–597. doi:10.1002/qj.828

Downes, S. M., Farneti, R., Uotila, P., Griffies, S. M., Marsland, S. J., Bailey, D., et al. (2015). An Assessment of Southern Ocean Water Masses and Sea Ice during 1988-2007 in a Suite of Interannual CORE-II Simulations. *Ocean Model.* 94, 67–94. doi:10.1016/j.ocemod.2015.07.022

Ducklow, H., Clarke, A., Dickhut, R., Doney, S. C., Geisz, H., Huang, K., et al. (2012). "The marine Ecosystem of the Western Antarctic Peninsula," in *Antarctica: An Extreme Environment in a Changing World*. Editors

A. Rogers, N. Johnston, A. Clarke, and E. Murphy. First Edn. (Oxford: Blackwell Publishing Ltd).

Eayrs, C., Holland, D., Francis, D., Wagner, T., Kumar, R., and Li, X. (2019). Understanding the Seasonal Cycle of Antarctic Sea Ice Extent in the Context of Longer-Term Variability. *Rev. Geophys.* 57 (3), 1037–1064. doi:10.1029/2018rg000631

Enomoto, H., and Ohmura, A. (1990). The Influences of Atmospheric Half-Yearly Cycle on the Sea Ice Extent in the Antarctic. *J. Geophys. Res.* 95 (C6), 9497–9511. doi:10.1029/JC095iC06p09497

Ezraty, R., Girard-Ardhuin, F., Piollé, J. F., Kaleschke, L., and Heygster, G. (2007). "Arctic and Antarctic Sea Ice Concentration and Arctic Sea Ice Drift Estimated from Special Sensor Microwave Data," in *Département d'Océanographie Physique et Spatiale, IFREMER, Brest, France and University of Bremen Germany* (IFREMER), 2.

Farneti, R., Downes, S. M., Griffies, S. M., Marsland, S. J., Behrens, E., Bentsen, M., et al. (2015). An Assessment of Antarctic Circumpolar Current and Southern Ocean Meridional Overturning Circulation during 1958-2007 in a Suite of Interannual CORE-II Simulations. *Ocean Model.* 93, 84–120. doi:10.1016/j.ocemod.2015.07.009

Frew, R. C., Feltham, D. L., Holland, P. R., and Petty, A. A. (2019). Sea Ice-Ocean Feedbacks in the Antarctic Shelf Seas. *J. Phys. Oceanography* 49 (9), 2423–2446. doi:10.1175/jpo-d-18-0229.1

Goosse, H., and Zunz, V. (2014). Decadal Trends in the Antarctic Sea Ice Extent Ultimately Controlled by Ice-Ocean Feedback. *The Cryosphere* 8 (2), 453–470. doi:10.5194/tc-8-453-2014

Haid, V., Iovino, D., and Masina, S. (2017). Impacts of Freshwater Changes on Antarctic Sea Ice in an Eddy-Permitting Sea-Ice-Ocean Model. *The Cryosphere* 11 (3), 1387–1402. doi:10.5194/tc-11-1387-2017

Hobbs, W. R., Massom, R., Stammerjohn, S., Reid, P., Williams, G., and Meier, W. (2016). A Review of Recent Changes in Southern Ocean Sea Ice, Their Drivers and Forcings. *Glob. Planet. Change* 143, 228–250. doi:10.1016/j.gloplacha.2016.06.008

Holland, P. R., Bruneau, N., Enright, C., Losch, M., Kurtz, N. T., and Kwok, R. (2014). Modeled Trends in Antarctic Sea Ice Thickness. *J. Clim.* 27 (10), 378. doi:10.1175/jcli-d-13-00301.1

Holland, P. R., and Kwok, R. (2012). Wind-driven Trends in Antarctic Sea-Ice Drift. *Nat. Geosci* 5 (12), 872–875. doi:10.1038/ngeo1627

Holland, P. R. (2014). The Seasonality of Antarctic Sea Ice Trends. *Geophys. Res. Lett.* 41 (12), 4230–4237. doi:10.1002/2014gl060172

Holmes, C. R., Holland, P. R., and Bracegirdle, T. J. (2019). Compensating Biases and a Noteworthy Success in the CMIP5 Representation of Antarctic Sea Ice Processes. *Geophys. Res. Lett.* 46 (8), 4299–4307.

Iovino, D., Selivanova, J., Lavergne, T., Cipollone, A., Masina, S., and Garric, G. (2022). Changes in the Antarctic Marginal Ice Zone, in Copernicus Marine Service Ocean State Report, Issue 6. *J. Oper. Oceanography* 1, 1. accepted.

Ivanova, N., Johannessen, O. M., Pedersen, L. T., and Tonboe, R. T. (2014). Retrieval of Arctic Sea Ice Parameters by Satellite Passive Microwave Sensors: A Comparison of Eleven Sea Ice Concentration Algorithms. *IEEE Trans. Geosci. Remote Sensing* 52 (11), 7233–7246. doi:10.1109/tgrs.2014.2310136

Ivanova, N., Pedersen, L. T., Tonboe, R. T., Kern, S., Heygster, G., Lavergne, T., et al. (2015). Inter-comparison and Evaluation of Sea Ice Algorithms: towards Further Identification of Challenges and Optimal Approach Using Passive Microwave Observations. *The Cryosphere* 9 (5), 1797–1817. doi:10.5194/tc-9-1797-2015

Jackson, L. C., Peterson, K. A., Roberts, C. D., and Wood, R. A. (2016). Recent Slowing of Atlantic Overturning Circulation as a Recovery from Earlier Strengthening. *Nat. Geosci* 9 (7), 518–522. doi:10.1038/ngeo2715

Kennicutt, M. C., Chown, S. L., Cassano, J. J., Liggett, D., Peck, L. S., Massom, R., et al. (2015). A Roadmap for Antarctic and Southern Ocean Science for the Next Two Decades and beyond. *Antartic Sci.* 27 (1), 3–18. doi:10.1017/s0954102014000674

Kohout, A. L., Williams, M. J. M., Dean, S. M., and Meylan, M. H. (2014). Storm-induced Sea-Ice Breakup and the Implications for Ice Extent. *Nature* 509 (7502), 604–607. doi:10.1038/nature13262

Lavergne, T., Sørensen, A. M., Kern, S., Tonboe, R., Notz, D., Aaboe, S., et al. (2019). Version 2 of the EUMETSAT OSI SAF and ESA CCI Sea-Ice Concentration Climate Data Records. *The Cryosphere* 13 (1), 49–78. doi:10.5194/tc-13-49-2019

Lellouche, J.-M., Le Galloudec, O., Drévillon, M., Régnier, C., Greiner, E., Garric, G., et al. (2013). Evaluation of Global Monitoring and Forecasting Systems at Mercator Océan. *Ocean Sci.* 9 (1), 57–81. doi:10.5194/os-9-57-2013

MacLachlan, C., Arribas, A., Peterson, K. A., Maidens, A., Fereday, D., Scaife, A. A., et al. (2015). Global Seasonal Forecast System Version 5 (GloSea5): a High-Resolution Seasonal Forecast System. *Q.J.R. Meteorol. Soc.* 141, 1072–1084. doi:10.1002/qj.2396

Maksym, T., Stammerjohn, S., Ackley, S., and Massom, R. (2012). Antarctic Sea Ice-A Polar Opposite? *oceanog* 25 (3), 140–151. doi:10.5670/oceanog.2012.88

Manucharyan, G. E., and Thompson, A. F. (2017). Submesoscale Sea Ice-Ocean Interactions in Marginal Ice Zones. *J. Geophys. Res. Oceans* 122, 9455–9475. doi:10.1002/2017JC012895

Masina, S., Storto, A., Ferry, N., Valdivieso, M., Haines, K., Balmaseda, M., et al. (2015). An Ensemble of Eddy-Permitting Global Ocean Reanalyses from the MyOcean Project. *Clim. Dyn.* 49, 813–841. doi:10.1007/s00382-015-2728-5

Masina, S., and Storto, A. (2017). Reconstructing the Recent Past Ocean Variability: Status and Perspective. *J Mar. Res.* 75 (6), 727–764. doi:10.1357/002224017823523973

Massom, R. A., and Stammerjohn, S. E. (2010). Antarctic Sea Ice Change and Variability - Physical and Ecological Implications. *Polar Sci.* 4 (2), 149–186. doi:10.1016/j.polar.2010.05.001

Meehl, G. A., Arblaster, J. M., Bitz, C. M., Chung, C. T. Y., and Teng, H. (2016). Antarctic Sea-Ice Expansion between 2000 and 2014 Driven by Tropical Pacific Decadal Climate Variability. *Nat. Geosci* 9 (8), 590–595. doi:10.1038/ngeo2751

Meier, W. N., Fetterer, F., Savoie, M., Mallory, S., Duerr, R., and Stroeve, J. (2017). *NOAA/NSIDC Climate Data Record of Passive Microwave Sea Ice Concentration*. version 3. Boulder, Colorado USA: NSIDC: National Snow and Ice Data Center.

Meier, W. N., Peng, G., Scott, D. J., and Savoie, M. H. (2014). Verification of a New NOAA/NSIDC Passive Microwave Sea-Ice Concentration Climate Record. *Polar Res.* 33 (1), 21004. doi:10.3402/polar.v33.21004

Meier, W. N., and Stewart, J. S. (2019). Assessing Uncertainties in Sea Ice Extent Climate Indicators. *Environ. Res. Lett.* 14 (3), 035005. doi:10.1088/1748-9326/aaf52c

Meylan, M. H., Bennetts, L. G., and Kohout, A. L. (2014). *In Situ* measurements and Analysis of Ocean Waves in the Antarctic Marginal Ice Zone. *Geophys. Res. Lett.* 41, 5046–5051. doi:10.1002/2014GL060809

Onarheim, I. H., Eldevik, T., Smedsrud, L. H., and Stroeve, J. C. (2018). Seasonal and Regional Manifestation of Arctic Sea Ice Loss. *J. Clim.* 31 (12), 4917–4932. doi:10.1175/jcli-d-17-0427.1

Palmer, M. D., Roberts, C. D., Balmaseda, M., Chang, Y.-S., Chepurin, G., Ferry, N., et al. (2017). Ocean Heat Content Variability and Change in an Ensemble of Ocean Reanalyses. *Clim. Dyn.* 49 (3), 909–930. doi:10.1007/s00382-015-2801-0

Parkinson, C. L., and Cavalieri, D. J. (2012). Arctic Sea Ice Variability and Trends, 1979–2010. *The Cryosphere* 6 (4), 881–889. doi:10.5194/tc-6-871-2012

Parkinson, C. L. (2019). A 40-y Record Reveals Gradual Antarctic Sea Ice Increases Followed by Decreases at Rates Far Exceeding the Rates Seen in the Arctic. *Proc. Natl. Acad. Sci. USA* 116 (29), 14414–14423. doi:10.1073/pnas.1906556116

Pauling, A. G., Smith, I. J., Langhorne, P. J., and Bitz, C. M. (2017). Time-dependent Freshwater Input from Ice Shelves: Impacts on Antarctic Sea Ice and the Southern Ocean in an Earth System Model. *Geophys. Res. Lett.* 44 (20), 10–454. doi:10.1002/2017gl075017

Perovich, D. K., and Jones, K. F. (2014). The Seasonal Evolution of Sea Ice Floe Size Distribution. *J. Geophys. Res. Oceans* 119, 8767–8777. doi:10.1002/2014JC010136

Riihelä, A., Bright, R. M., and Anttila, K. (2021). Recent Strengthening of Snow and Ice Albedo Feedback Driven by Antarctic Sea-Ice Loss. *Nat. Geosci.* 14, 832–836. doi:10.1038/s41561-021-00841-x

Roach, L. A., Dean, S. M., and Renwick, J. A. (2018). Consistent Biases in Antarctic Sea Ice Concentration Simulated by Climate Models. *The Cryosphere* 12 (1), 365–383. doi:10.5194/tc-12-365-2018

Roach, L. A., Dörr, J., Holmes, C. R., Massonnet, F., Blockley, E. W., Notz, D., et al. (2020). Antarctic Sea Ice Area in CMIP6. *Geophys. Res. Lett.* 47, e2019GL086729. doi:10.1029/2019GL086729

Rolph, R. J., Feltham, D. L., and Schröder, D. (2020). Changes of the Arctic Marginal Ice Zone during the Satellite Era. *The Cryosphere* 14 (6), 1971–1984. doi:10.5194/tc-14-1971-2020

Serreze, M. C., and Stroeve, J. (2015). Arctic Sea Ice Trends, Variability and Implications for Seasonal Ice Forecasting. *Phil. Trans. R. Soc. A.* 373 (2045), 20140159. doi:10.1098/rsta.2014.0159

Shu, Q., Wang, Q., Song, Z., Qiao, F., Zhao, J., Chu, M., et al. (2020). Assessment of Sea Ice Extent in CMIP6 with Comparison to Observations and CMIP5. *Geophys. Res. Lett.* 47 (9), e2020GL087965. doi:10.1029/2020gl087965

Stammerjohn, S. E., Martinson, D. G., Smith, R. C., Yuan, X., and Rind, D. (2008). Trends in Antarctic Annual Sea Ice Retreat and advance and Their Relation to El Niño–Southern Oscillation and Southern Annular Mode Variability. *J. Geophys. Res. Oceans* 113 (C3), 1. doi:10.1029/2007jc004269

Storto, A., Masina, S., Balmaseda, M., Guinehut, S., Xue, Y., Szekely, F., et al. (2017). Steric Sea Level Variability (1993-2010) in an Ensemble of Ocean Reanalyses and Objective Analyses. *Clim. Dyn.* 49 (3), 709–729. doi:10.1007/s00382-015-2554-9

Storto, A., Masina, S., and Navarra, A. (2016). Evaluation of the CMCC Eddy-permitting Global Ocean Physical Reanalysis System (C-GLORS, 1982-2012) and its Assimilation Components. *Q.J.R. Meteorol. Soc.* 142, 738–758. doi:10.1002/qj.2673

Storto, A., Masina, S., Simoncelli, S., Iovino, D., Cipollone, A., Drevillon, M., et al. (2019). The Added Value of the Multi-System Spread Information for Ocean Heat Content and Steric Sea Level Investigations in the CMEMS GREP Ensemble Reanalysis Product. *Clim. Dyn.* 53 (1), 287–312. doi:10.1007/s00382-018-4585-5

Stroeve, J. C., Jenouvrier, S., Campbell, G. G., Barbraud, C., and Delord, K. (2016). Mapping and Assessing Variability in the Antarctic Marginal Ice Zone, Pack Ice and Coastal Polynyas in Two Sea Ice Algorithms with Implications on Breeding success of Snow Petrels. *The Cryosphere* 10 (4), 1823–1843. doi:10.5194/tc-10-1823-2016

Strong, C., and Rigor, I. G. (2013). Arctic Marginal Ice Zone Trending Wider in Summer and Narrower in winter. *Geophys. Res. Lett.* 40 (18), 4864–4868. doi:10.1002/grl.50928

Sutherland, B. R., and Balmforth, N. J. (2019). Damping of surface waves by floating particles. *Physical Review Fluids* 4 (1), 014804.

Tsamados, M., Feltham, D., Petty, A., Schroeder, D., and Flocco, D. (2015). Processes Controlling Surface, Bottom and Lateral Melt of Arctic Sea Ice in a State of the Art Sea Ice Model. *Phil. Trans. R. Soc. A.* 373, 20140167. doi:10.1098/rsta.2014.0167

Tsujino, H., Urakawa, L. S., Griffies, S. M., Danabasoglu, G., Adcroft, A. J., Amaral, A. E., et al. (2020). Evaluation of Global Ocean-Sea-Ice Model Simulations Based on the Experimental Protocols of the Ocean Model Intercomparison Project Phase 2 (OMIP-2). *Geosci. Model. Dev.* 13 (8), 3643–3708. doi:10.5194/gmd-13-3643-2020

Turner, J., Bracegirdle, T. J., Phillips, T., Marshall, G. J., and Hosking, J. S. (2013). An Initial Assessment of Antarctic Sea Ice Extent in the CMIP5 Models. *J. Clim.* 26 (5), 1473–1484. doi:10.1175/jcli-d-12-00068.1

Turner, J., Hosking, J. S., Bracegirdle, T. J., Marshall, G. J., and Phillips, T. (2015). Recent Changes in Antarctic Sea Ice. *Phil. Trans. R. Soc. A.* 373, 20140163. doi:10.1098/rsta.2014.0163

Uotila, P., Goosse, H., Haines, K., Chevallier, M., Barthélemy, A., Bricaud, C., et al. (2019). An Assessment of Ten Ocean Reanalyses in the Polar Regions. *Clim. Dyn.* 52 (3), 1613–1650. doi:10.1007/s00382-018-4242-z

Valdivieso, M., Haines, K., Balmaseda, M., Chang, Y.-S., Drevillon, M., Fujii, Y., et al. (2017). An Assessment of Air-Sea Heat Fluxes from Ocean and Coupled Reanalyses. *Clim. Dyn.* 49 (3), 983–1008. doi:10.1007/s00382-015-2843-3

Venables, H. J., and Meredith, M. P. (2014). Feedbacks between Ice Cover, Ocean Stratification, and Heat Content in Ryder Bay, Western Antarctic Peninsula. *J. Geophys. Res. Oceans* 119 (8), 5323–5336. doi:10.1002/2013jc009669

Vichi, M. (2021). A Statistical Definition of the Antarctic Marginal Ice Zone. *Cryosphere Discuss.* 1, 1–23. [preprint].

Vichi, M., Eayrs, C., Alberello, A., Bekker, A., Bennetts, L., Holland, D., et al. (2019). Effects of an Explosive Polar Cyclone Crossing the Antarctic Marginal Ice Zone. *Geophys. Res. Lett.* 46 (11), 5948–5958. doi:10.1029/2019gl082457

Wachter, P., Reiser, F., Friedl, P., and Jacobeit, J. (2021). A New Approach to Classification of 40 Years of Antarctic Sea Ice Concentration Data. *Int. J. Climatology* 41, E2683–E2699. doi:10.1002/joc.6874

Wang, M. J., Liu, T. T., Yang, Z. J., Wu, B., and Zhu, X. (2021). Variation of Antarctic Marginal Ice Zone Extent (1989–2019). *Adv. Polar Sci.* 32 (4), 341–355. doi:10.13679/j.advps.2021.0042

WMO (2009). WMO Sea-Ice Nomenclature. *WMO/OMM/BMO* 259 (Suppl. 5), 23.

Zuo, H., Balmaseda, M. A., Tietsche, S., Mogensen, K., and Mayer, M. (2019). The ECMWF Operational Ensemble Reanalysis-Analysis System for Ocean and Sea Ice: a Description of the System and Assessment. *Ocean Sci.* 15 (3), 779–808. doi:10.5194/os-15-779-2019

Conflict of Interest: The authors declare that the research was conducted in the absence of any commercial or financial relationships that could be construed as a potential conflict of interest.

frontiers in Marine Science

ORIGINAL RESEARCH
published: 18 February 2022
doi: 10.3389/fmars.2022.775394

Estimation of Ocean Biogeochemical Parameters in an Earth System Model Using the Dual One Step Ahead Smoother: A Twin Experiment

Tarkeshwar Singh[1], François Counillon[1,2], Jerry Tjiputra[3], Yiguo Wang[1] and Mohamad El Gharamti[4]*

[1] Nansen Environmental and Remote Sensing Center and Bjerknes Centre for Climate Research, Bergen, Norway, [2] Geophysical Institute, University of Bergen, Bjerknes Centre for Climate Research, Bergen, Norway, [3] NORCE Norwegian Research Centre, Bjerknes Centre for Climate Research, Bergen, Norway, [4] National Center for Atmospheric Research, Boulder, CO, United States

OPEN ACCESS

Edited by:
Heiner Dietze, Helmholtz Association of German Research Centres (HZ), Germany

Reviewed by:
Anne Willem Omta, Massachusetts Institute of Technology, United States
Emlyn Jones, Commonwealth Scientific and Industrial Research Organisation (CSIRO), Australia

***Correspondence:**
Tarkeshwar Singh
Tarkeshwar.Singh@nersc.no

Specialty section:
This article was submitted to Marine Biogeochemistry, a section of the journal Frontiers in Marine Science

Received: *29 October 2021*
Accepted: *24 January 2022*
Published: *18 February 2022*

Citation:
Singh T, Counillon F, Tjiputra J, Wang Y and Gharamti ME (2022) Estimation of Ocean Biogeochemical Parameters in an Earth System Model Using the Dual One Step Ahead Smoother: A Twin Experiment. Front. Mar. Sci. 9:775394. doi: 10.3389/fmars.2022.775394

Ocean biogeochemical (BGC) models utilise a large number of poorly-constrained global parameters to mimic unresolved processes and reproduce the observed complex spatio-temporal patterns. Large model errors stem primarily from inaccuracies in these parameters whose optimal values can vary both in space and time. This study aims to demonstrate the ability of ensemble data assimilation (DA) methods to provide high-quality and improved BGC parameters within an Earth system model in an idealized perfect twin experiment framework. We use the Norwegian Climate Prediction Model (NorCPM), which combines the Norwegian Earth System Model with the Dual-One-Step ahead smoothing-based Ensemble Kalman Filter (DOSA-EnKF). We aim to estimate five spatially varying BGC parameters by assimilating salinity and temperature profiles and surface BGC (Phytoplankton, Nitrate, Phosphate, Silicate, and Oxygen) observations in a strongly coupled DA framework—i.e., jointly updating ocean and BGC state-parameters during the assimilation. We show how BGC observations can effectively constrain error in the ocean physics and *vice versa*. The method converges quickly (less than a year) and largely reduces the errors in the BGC parameters. Some parameter error remains, but the resulting state variable error using the estimated parameters for a free ensemble run and for a reanalysis performs nearly as well as with true parameter values. Optimal parameter values can also be recovered by assimilating climatological BGC observations or sparse observational networks. The findings of this study demonstrate the applicability of the DA approach for tuning the system in a real framework.

Keywords: parameter estimation, Ensemble Kalman Filter (EnKF), biogeochemical model, Earth system model (ESM), ecosystem parameters, NorCPM, NorESM, DOSA-EnKF

1. INTRODUCTION

Ocean biogeochemistry (BGC) is an important component of an Earth system model (ESM) for simulating the anthropogenic carbon sinks across the air-sea interface (e.g., Marotzke et al., 2017; Tjiputra et al., 2020). It also simulates critical biophysical feedbacks to the climate system such as phytoplankton short-wave absorption (Jochum et al., 2010) and the production of radiatively-important marine aerosol precursor (Schwinger et al., 2017). Following the emergence of seasonal-to-decadal prediction which shows that the ocean variability can be predicted by up to 10 years in advance (Smith et al., 2007; Keenlyside et al., 2008), a similar initiative has been attempted for ocean biogeochemistry (Séférian et al., 2014; Payne et al., 2017; Lovenduski et al., 2019; Park et al., 2019; Fransner et al., 2020).

The accuracy of biological and chemical process representations in ESMs is crucial for simulating the BGC state and variability as realistically as possible. In current state-of-the-art ESMs, the inorganic chemistry is governed by well defined chemical and thermodynamic formulations. However, the biological process representations such as primary production are more uncertain, which leads to a large bias and inter-model spread in their projections (Bopp et al., 2013; Kwiatkowski et al., 2020). The uncertainty becomes more evident at regional scales (Vancoppenolle et al., 2013), hindering their application for regional impact studies. These uncertainties are associated with empirical parameterisations of the biogeochemical inter-actions, which are linked to the complexities and imperfect descriptions of the ocean physical environment that drives the biological process, among others. Generally, ocean BGC models utilise numerous poorly constrained, spatially and temporally constant parameters to simplify the marine ecosystem complexity. Consequently, the large error in the projections, primarily linked to these inaccurate parameters, limits the reliability of the ecosystem model (Losa et al., 2004). One of the reasons for inaccuracy in these parameters is their static nature. Many studies have proven that resolving space and/or time varying BGC parameters is more relevant in the context of biogeochemical modeling (e.g., Losa et al., 2003; Tjiputra et al., 2007; Mattern et al., 2012; Roy et al., 2012; Doron et al., 2013).

Ocean BGC parameters are often estimated and calibrated in small-scale laboratory experiments, which do not always reflect the large-scale open ocean conditions. Once implemented in the global model, these parameters are generalized (i.e., assumed uniform across the globe for simplicity), and tuned within observational uncertainty to capture the observed large-scale BGC properties, for instance primary production, vertical nutrient gradient, deoxygenation pattern, etc. However, this parameter tuning process often becomes complicated and inefficient when the number of parameters increases so as to represent the increasing complexity of biogeochemical models. Therefore, BGC simulations are often subject to a high level of parametric uncertainty and require an efficient method for optimal tuning of their parameters, particularly those which the model is most sensitive to.

Data assimilation (DA) schemes provide an objective and efficient methodology for parameter estimation by combining observations with a numerical model simulation (Eknes and Evensen, 2002). Particularly, ensemble based sequential DA schemes like the Ensemble Kalman Filter (EnKF) offer a simple but efficient framework for automatic optimisation of model parameters alongside the state variables by simply augmenting them together using "Joint-EnKF" formulation (Anderson, 2001; Annan et al., 2005; Jazwinski, 2007). The EnKF (Evensen, 2003) is based on a Monte Carlo sampling of the state space thereby avoiding model linearization. It updates the prior statistics (mean and covariance of state variables) by assuming Gaussian distributed variables and errors. It is one of the widely used sequential DA schemes in the field of geosciences (e.g., Houtekamer and Mitchell, 2001; Reichle et al., 2002; Counillon et al., 2014). However, the application of the EnKF for parameter estimation of numerical models like BGC is both theoretically and practically challenging. Difficulties are usually related to high dimensions and non-linearity of the models as well as other physical constraints such as the positiveness of the BGC variables and parameters. To elaborate, in a high dimensional model like ocean BGC, the number of unknown model state variables and parameters are larger than the available observations. In this case, the EnKF attempts to solve an underdetermined inverse problem at each DA cycle, where it utilises a small number of observations to estimate an extremely large set of unknowns. This problem is more pronounced when the available observations are limited to the surface only, which is often the case for satellite ocean color observations. Furthermore, BGC tracers and parameters, such as nutrient concentration and phytoplankton exudation rate, are positive quantities and cannot be negative. As such, the Gaussian assumptions made in the EnKF (Losa et al., 2004) are not satisfied. To mitigate this issue, a variable-transform approach called Gaussian anamorphosis (Bertino et al., 2003), has been successfully tested and applied for such application (e.g., Simon and Bertino, 2009; Gharamti et al., 2017a). Another challenging issue is the strongly non-linear behavior that BGC models experience during the spring bloom. The rapid temporal dynamics may create large discrepancies between the observations and the ensemble estimates. For example, few ensemble members might start producing a bloom earlier than the rest of the members, which may create inaccurate state and parameter cross-correlations with a linear analysis update. Such a situation often yields unrealistic updates of parameters. On top of the aforementioned challenges, sampling errors due to limited ensemble sizes are generally unavoidable (Natvik and Evensen, 2003), and can degrade the accuracy of the state and parameters. In short, the traditional joint-EnKF scheme for parameter estimation may suffer from above mentioned limitations that could degrade the filter performance (e.g., Moradkhani et al., 2005; Chen and Zhang, 2006; Wen and Chen, 2006).

Recently, many different analysis algorithms have been developed to tackle the limitations of the traditional joint-EnKF with the aim to estimate dynamically consistent and more accurate model parameters. Wen and Chen (2006) derived a confirming-step (CS-EnKF) where the updated parameters are

used to rerun the model and obtain reliable state estimates. Another classical approach, suggested by Moradkhani et al. (2005), is a dual updating scheme (Dual-EnKF) for the state and the parameters using two parallel and inter-active EnKFs, where one acts on the state and the other on the parameters. Both the CS-EnKF and the Dual-EnKF are heuristic in nature and do not maintain the Bayesian consistency of the joint state and parameters estimation problem. A recent work by Gharamti et al. (2015) proposed a one-step-ahead smoothing ensemble scheme (OSA-EnKF), which provides a robust estimation framework while respecting the Bayesian consistency of the problem. The algorithm shares a lot of similarities with the CS- and Dual-EnKF, and further introduces a smoothing character in which future observations are used to constrain current state variables. Gharamti et al. (2017b) applied all four estimation schemes (Joint-, CS-, Dual-, and OSA-EnKF) for optimising poorly constrained ecosystem parameters using a one-dimensional configuration of the Ocean BGC model. They concluded that OSA-EnKF is accurate and reliable compared to the others schemes and it successfully recovers the observed seasonal variability of the ecosystem dynamics. Ait-El-Fquih et al. (2016) further derived a more generalized variant of the OSA scheme, namely dual one-step-ahead smoothing EnKF (DOSA-EnKF), by using a dual updating feature where the state variables undergo both smoothing and analysis steps. Motivated by the promising results of OSA scheme in optimising ecosystem parameters, we utilise the generalized variant of the scheme, i.e., DOSA-EnKF for this study.

Another key ingredient for success is the choice of variables in the state vector such that the use of available observations is maximized and the dynamical consistency is preserved. In a coupled model, observations are available in different compartments (ocean, atmosphere, sea ice, biogeochemistry). A simple approach referred to as weakly coupled data assimilation (WCDA; Penny and Hamill, 2017), assimilates the data independently in their respective components. The other model components adjust to these individual changes dynamically in between the assimilation cycles. Allowing the assimilation to update across model components is expected to outperform WCDA because it would enhance the dynamical consistency of the initial conditions and expand the influence of the observations across its own component (strongly coupled data assimilation, SCDA; Penny and Hamill, 2017; Penny et al., 2019). However, the update would still rely on a linear analysis update step, which can be problematic as coupled covariances include complex, coupled phenomena that can be strongly non-linear. Iterative methods such as the dual one step ahead smoother, can better control the growth of non-linearities. For ocean and biogeochemistry this approximation is reasonable, and it has been shown that cross compartment update were beneficial (Yu et al., 2018).

The present study explores the efficiency and the feasibility of the DOSA-EnKF scheme to optimise BGC parameters within an Earth system model in an idealized perfect (or identical) twin experiment framework (Halem and Dlouhy, 1984). In a perfect twin experiment (or identical twin Observing System Simulation Experiment), observations are constructed from the same model and in this study, the only non-perfect aspects of the model are the parameters to be estimated. It differs from fraternal twin experiments (e.g., Arnold Jr and Dey, 1986; Masutani et al., 2010; Halliwell Jr et al., 2014) where observations are constructed from a model that differs from the model used in the data assimilation experiment. Here, we use the Norwegian Climate Prediction Model (NorCPM; Counillon et al., 2014), which provides the ensemble assimilation framework for Norwegian Earth System Model (NorESM1). We aim to estimate five spatially varying BGC parameters by assimilating salinity and temperature hydrographic profiles and surface BGC (Phytoplankton, Nitrate, Phosphorous, Silicate, and Oxygen) observations in a strongly coupled DA framework—i.e., jointly updating ocean and BGC state-parameters during the assimilation. The five ecosystem parameters were also chosen because they are essential to constrain the observed annual cycle of surface BGC, which has been identified as one of the primary sources of future projection uncertainties (Kessler and Tjiputra, 2016; Goris et al., 2018).

The rest of this article is organized as follows. Section 2 summarizes details of model, assimilation algorithm, and experimental design. Section 3 present and discuss the assimilation results and assessment of parameters estimates. Summary and conclusion of the work are given in Section 4.

2. THE NORWEGIAN CLIMATE PREDICTION MODEL AND THE EXPERIMENTAL DESIGN

NorCPM (Counillon et al., 2014) is a climate prediction system that aims to provide seasonal-to-decadal prediction (Kimmritz et al., 2019; Wang et al., 2019; Bethke et al., 2021) and long term climate reanalysis (Counillon et al., 2016). It combines the Norwegian Earth System Model (e.g., NorESM1; Bentsen et al., 2013) with the Ensemble Kalman Filter (Evensen, 2003).

2.1. The Norwegian Earth System Model

The NorESM1 is a global fully coupled system, which is based on the Community Earth System Model version 1.0.3 (CESM1; Vertenstein et al., 2012). Unlike CESM1, NorESM1 uses the atmospheric component from the modified version of Community Atmosphere Model (CAM4-Oslo; Kirkevåg et al., 2013). The ocean physical component of NorESM1 is based on Miami Isopycnic Coordinate Ocean Model (MICOM; Bleck and Smith, 1990; Bleck et al., 1992) but with modified numerics and physics (Bentsen et al., 2012). The ocean BGC compartment in NorESM1 is the Hamburg Oceanic Carbon Cycle (HAMOCC; Maier-Reimer et al., 2005; Tjiputra et al., 2013), which is embedded with the isopycnic MICOM model (Assmann et al., 2010). The other components in the model are adopted in their original form from CESM1, which are the Community Land Model (CLM4; Oleson et al., 2010; Lawrence et al., 2011), the Los Alamos sea ice model (CICE4; Gent et al., 2011; Holland et al., 2012) and with the version 7 coupler (CPL7; Craig et al., 2012).

This study utilizes the medium-resolution version of NorESM1 (Tjiputra et al., 2013). The atmospheric component

CAM4 and Land component CLM4 are configured on a horizontal resolution of 1.9° at latitude and 2.5° at longitude (approximately 2° finite volume grid). In the vertical, CAM4 features 26 hybrid sigma-pressure levels with model top at approximately 3 hPa. The ocean MICOM and sea ice CICE4 models have a common horizontal resolution of approximately 1° × 1° with refined grids near the Equator in meridional direction, and in both zonal and meridional direction at high latitudes. MICOM uses 51 isopycnal layers and 2 additional layers for representing the bulk mixed layer with time-evolving thicknesses and densities. The biogeochemical component HAMOCC utilizes the same spatial and temporal resolution as the ocean model.

HAMOCC includes an NPZD-type ecosystem module which was initially implemented by Six and Maier-Reimer (1996). It includes one generic class of phytoplankton, one generic class of zooplankton, three macronutrients (phosphate, nitrate, and silicate), and one micronutrient (dissolved iron). In addition to the ecosystem module, it also prognostically simulates full inorganic carbon chemistry, which includes dissolved inorganic carbon and alkalinity. Other key state variables include oxygen, dissolved organic carbon, particulate organic and inorganic carbon, and biogenic opal. The phytoplankton growth rate in the model is formulated as a function of temperature and light availability (Smith, 1936). The primary production is represented by a prognostic function of phytoplankton growth rate, which is limited by temperature, incoming shortwave radiation, and availability of nutrients. Further details of the HAMOCC can be sought from Tjiputra et al. (2013).

NorESM1 has been shown to capture the major observed modes of climatic variability (Bentsen et al., 2013). Further, many studies have demonstrated that it simulates well ENSO variability and its teleconnection (e.g., Sperber et al., 2013; Bellenger et al., 2014). In Anav et al. (2013), it was demonstrated that observed tropical inter-annual variability in ocean primary production reproduced by NorESM1 is in the top three among 18 ESM's used in their study. Tjiputra et al. (2013) evaluated the mean state of HAMOCC with NorESM and reported that NorESM satisfactorily reproduces many of the observed large scale ocean biogeochemical features.

2.2. The Dual One Step Ahead Smoother

The dual one step ahead smoother (DOSA, Gharamti et al., 2015) is an iterative smoother scheme based on the Ensemble Kalman Filter. The DOSA scheme respects the Bayesian consistency of the problem, and proceeds as shown in **Figure 1**. Here, we use the Deterministic EnKF (DEnKF) in DOSA. The DEnKF is a square-root (deterministic) formulation of the EnKF that solves the analysis without the need to perturb the observations. It inflates the errors by construction and is intended to perform well in operational applications (Sakov et al., 2012).

In the first step, the ensemble of analysed model state $\mathbf{X}^a_{k-1}$ and its associated parameters at time $k-1$, $\mathbf{P}^a_{k-1}$, are integrated forward: $\mathbf{X}^f_k = \mathcal{M}(\mathbf{X}^a_{k-1}, \mathbf{P}^a_{k-1})$. Note that the parameters are not changed during the model integration (i.e., $\mathbf{P}^a_{k-1} = \mathbf{P}^f_k$).

The observations at time k, $\mathbf{y}_k$, are used to produce a smoothed estimate of the state and parameters at the previous analysis step $k-1$ as follows:

$$\overline{\mathbf{X}^s_{k-1}} = \overline{\mathbf{X}^a_{k-1}} + \mathbf{K}_{k-1,k}(\mathbf{y}_k - \mathbf{H}\overline{\mathbf{X}^f_k}). \tag{1}$$

$$\mathbf{A}^s_{k-1} = \mathbf{A}^a_{k-1} - \frac{1}{2}\mathbf{K}_{k-1,k}\mathbf{H}\mathbf{A}^f_k. \tag{2}$$

where,

$$\mathbf{K}_{k-1,k} = \mathbf{A}^a_{k-1}\mathbf{A}^{f\,\mathrm{T}}_k\mathbf{H}^{\mathrm{T}}\left(\mathbf{H}\mathbf{A}^f_k\mathbf{A}^{f\,\mathrm{T}}_k\mathbf{H}^{\mathrm{T}} + \mathbf{R}\right)^{-1}. \tag{3}$$

where the superscript $^{\mathrm{T}}$ denotes a matrix transpose and $\mathbf{A}$ the ensemble anomalies, i.e., $\mathbf{A} = \mathbf{X} - \bar{\mathbf{x}}1^{\mathrm{T}}$, with $1_m = [1, 1, \ldots, 1] \in \mathcal{R}^{1\times N}$. In a similar way, the parameter ensemble, $\overline{\mathbf{P}^s_{k-1}}$, at time $k-1$ is smoothed using $\mathbf{y}_k$.

In the second step, the model is integrated forward to time k again but with smoothed ensemble of state $\mathbf{X}^s_{k-1}$ and parameters $\mathbf{P}^s_{k-1}$; i.e., $\mathbf{X}^{f2}_k = \mathcal{M}(\mathbf{X}^s_{k-1}, \mathbf{P}^s_{k-1})$.

The observations at time k, $\mathbf{y}^k$, are then used again to produce an analysis of $\mathbf{X}^a_k$.

$$\overline{\mathbf{X}^a_k} = \overline{\mathbf{X}^{f2}_k} + \mathbf{K}_{k,k}(\mathbf{y}_k - \mathbf{H}\overline{\mathbf{X}^{f2}_k}). \tag{4}$$

$$\mathbf{A}^a_k = \mathbf{A}^{f2}_k - \frac{1}{2}\mathbf{K}_{k,k}\mathbf{H}\mathbf{A}^{f2}. \tag{5}$$

$\mathbf{K}_{k,k}$ is the standard Kalman gain and $\mathbf{A}^{f2}_k$ are the ensemble anomalies constructed from $\mathbf{X}^{f2}_k$. It should be emphasized that the observations are used twice, but the second time they are used with a model that is using a different set of parameters. As such, model state is updated twice in a assimilation cycle but parameter is updated only at previous time step.

The model state ($\mathbf{X}$) includes several ocean physical and biogeochemical prognostic model variables and they are updated in isopycnal coordinates as in Counillon et al. (2014), Wang et al. (2017). In the physical component, we update the full isopycnal temperature, salinity, layer thickness and velocities (53 isopycnal layers). Similarly, we update the biogeochemical variables at all isopycnal layers which include oxygen, phytoplankton, silicate, nitrate, total dissolved inorganic carbon, total alkalinity, dissolved organic carbon, particulate organic carbon, zooplankton, and biogenic silica. The list of selected BGC parameters for this study is provided in Section 2.3. For the assimilation system, the state vector is composed of the above physical and biogeochemical model variables along with the biogeochemical parameters. When one updates the ocean variable layer thickness, one effectively updates also the mass of the BGC quantities. In Bethke et al. (2021), it was shown that this approach conserves well BGC properties and does not introduce spurious upwelling at the Equator. However, with an EnKF, the linear analysis update returns unphysical values for non-Gaussian distributed variables. Some state variables

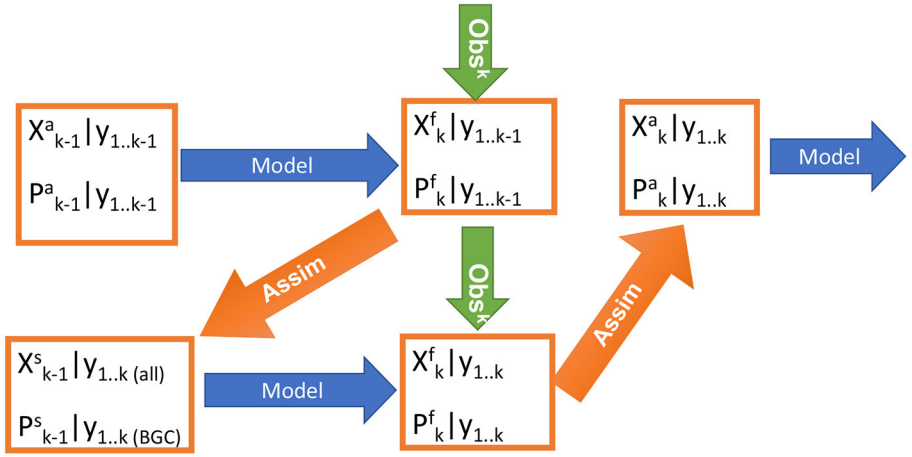

FIGURE 1 | Schematic diagram of the steps of the dual one step ahead (DOSA) scheme.

have a physical constraint and their values should be positive definite such as layer thickness and tracer concentrations. For layer thickness we use the upscaling algorithm (Wang et al., 2016) while for the BGC concentration quantity (i.e., when updating the BGC state) a post-processing step is applied so that negative values are set to zero. We have not noticed degradations caused by the post-processing. We think that it is due to the fact that 1) part of the non-Gaussianity is already handled by the super layer algorithm which updates the layer thickness, and 2) with the smoothing flavor that the DOSA scheme provides, the updated parameters rarely became non-physical (i.e., negative).

Observations are used to update both ocean and BGC components in a strongly coupled framework (Penny and Hamill, 2017). The BGC component does not feedback to the physics in this version of NorESM and thus error in the physical state cannot be caused by error in the value of the BGC parameters. Therefore, for simultaneous state-parameter estimation, we update the parameter values from only BGC observations in Equations (1) and (2) while the state variables of ocean physics and BGC are updated using all available observations (see **Figure 1**).

The rest of the configuration for the assimilation experiments in this work follows that of Counillon et al. (2014, 2016), Wang et al. (2016, 2017) and Bethke et al. (2021). The assimilation algorithm uses a local analysis framework (Evensen, 2003; Sakov et al., 2012), where a local analysis is computed for one horizontal grid point at a time by utilizing all available observation in a spatial window around the grid point. A quasi-Gaussian and distance-dependent localization function (Gaspari and Cohn, 1999) is used to smooth the impact at the boundary of the localisation radius. In this work, the localization radius varies with latitude for both hydrographic profile and BGC observations (Wang et al., 2017). We do not use vertical localization. A moderation and a pre-screening technique (Sakov et al., 2012) is used to sustain the ensemble spread during the assimilation period. We also use the moderation technique, where observation error variance is increased (here by a factor of 4) for the update of the ensemble anomalies [Equation (2)] while the original value of the observation error variance is kept to update the ensemble mean [Equation (1)]. The pre-screening method inflates the observation error such that the analysis remains within two standard deviations of the forecast error from the ensemble mean.

2.3. Experiment Design

We test the potential of the DOSA to optimise BGC parameters with NorCPM in an identical twin experiment framework. A reference model simulation performed with the prescribed parameter values is considered as the truth. We aim to retrieve the parameter values in the truth that are assumed to be unknown. We focus on optimizing five BGC parameters of NorESM1, which are among the most uncertain in the BGC model component. The parameters are: 1) the half-saturation constant for nutrient uptake during the phytoplankton growth (BKPHY), 2) Maximum zooplankton grazing rate (GRAZRA), 3) Phytoplankton exudation rate, i.e., the rate of dissolved organic carbon release by phytoplankton (GAMMAP), 4) Sinking speed for particulate organic carbon (WPOC), and 5) Half-saturation constant for silicate uptake during biogenic opal production (BKOPAL). A complete list of the ecosystem parameters used in the HAMOCC model is documented in Maier-Reimer et al. (2005).

The "true" parameters (TP) values are constant in time but they vary spatially (the first row of **Figure 6**). They have two Gaussian anomalies centered randomly: one with an isotropic distribution and another with an anisotropic distribution. The spatial pattern is purely artificial but more as a way to test the robustness of the proposed parameter estimation method in retrieving spatially varying pattern. The characteristic length scale and structure of those perturbations are unknown so that the DA system cannot be tuned specifically. The initial (first guess) perturbed parameters (PP) values (the second row of **Figure 6**) are sampled from a multi-variate Gaussian

distribution, with a spatially uniform value for each ensemble member. The ensemble mean of PP is set intentionally to be 25% lower than the global mean of TP. The standard deviation of the ensemble of PP is equal to 33% of the global mean of TP. As such the PP are chosen so that the ensemble mean differs from the truth but that it encloses the truth value.

We have first performed a NorESM simulation (one member/realisation) with TP values (the first row of **Figure 6**) from 1980 to 1999 that henceforth referred to as TRUTH. It has been initialized in January 1980 from member one of the 30-member NorCPM1 historical simulation integrated with historical forcing from 1850 to 2014 following phase 6 of the Coupled Model Inter-comparison Project (CMIP6) protocol (Bethke et al., 2021). A tiny perturbation of 10^{-6}°C was added to SST of that member in January 1980. We constructed synthetic observations from monthly averages of TRUTH with random white noise taking into account for observational error. The observation error was specified to be equal to one standard deviation of the temporal variability in TRUTH. The observation error varies with grid cell and calendar month. The monthly averaged observations of temperature, salinity, phytoplankton concentration, Oxygen, Nitrate, Silicate, and Phosphate were chosen for this study. Synthetic observations of temperature and salinity were produced at 35 vertical z-levels sampling the full water column, while in horizontal direction we kept only points at every 5th model cell. The BGC observations have been produced at surface at every 5th grid cell. Observations in ice-covered water were discarded.

Four sets of experiments have been performed in this study as follows:

- We use perfect parameters (i.e., TP;) to evaluate the impact of different observational networks for constraining error of the physical and BGC state variables. All experiments use 30 members. The initial ensemble state in January 1980 is taken from the historical ensemble NorCPM1 simulation run (Bethke et al., 2021). The initial condition is constructed from the 30-member NorCPM1 historical simulation- meaning that member 1 is nearly identical to the truth. However, two members starting with a microscopic difference in SST would be totally different at the surface within 10 months (Supplementary Figure S3 in Fransner et al., 2020), and would have produced a spread comparable to climatology in the top 1000 m. The first 10 years (i.e., 1980–1989) are considered as a spin-up period so as to let the model adjust to the perfect parameters that differ from the value used for producing the historical ensemble and so that the initial condition of member 1 differs from the truth. Assimilation of the state variables starts in February 1990 and run until July 1991 with assimilation of (1) ocean physics profiles (EnKF_PHY), (2) BGC surface observations (EnKF_BGC), and (3) combined physics and BGC observations (EnKF_ALL). All observations are time-varying and available at every 5th grid cell. We also perform a free ensemble run (without data assimilation called NorESM_TP) so it is feasible to quantify the impact of assimilation. Theses simulations are analysed in Section 3.1.
- The second set of experiments is conducted to test state-parameter estimation. A 30-member ensemble simulation is run from the initial ensemble as in the previous set of experiments but this time with PP values (the second row of **Figure 6**). Again the ensemble is integrated from January 1980 until January 1990 (NorESM_PP) to let the model state adjust to the new parameter values. From February 1990 to December 1990, three state-parameter estimation experiments are performed to test the impact of the parameter estimation. The parameters are only adjusted by assimilation and the value is kept unchanged during the model integration (persistence) until the next assimilation step. All experiments assimilate physical observations but differ in the BGC surface observation networks: (1) time-varying BGC observations at every 5th grid cell (EnKF_PE), (2) monthly climatology of BGC observations at every 5th grid cell (EnKF_PE_CO), and (3) monthly climatology of BGC observations at a sparser grid (i.e., every 10th grid cell; EnKF_PE_SCO). The monthly climatology is generated by averaging 20-years time varying observations. The results of these experiments are presented in Section 3.2.
- The parameters estimated in the previous set of experiments are now fixed and we analyse their impact on the model state for free ensemble runs (without assimilation). All simulations were initialized on the 15th of January 1980 (as in NorESM_TP) and run until December 1983. However, the state variable of member 1 is very close to the truth run in January 1980 and we have decided to consider only the other 29 members that are completely independent (member 2–30) for all experiments. Three ensemble simulations are performed with parameters obtained from EnKF_PE, EnKF_PE_CO and EnKF_PE_SCO (referred to as NorESM_PE, NorESM_PE_CO and NorESM_PE_SCO, respectively). The simulations with parameters estimated (PE) are compared to NorESM_TP and NorESM_PP. In NorESM_TP, parameters are perfect but the initial state in 1980 is imperfect and it quantifies a climatological error level expected with a perfect model (upper benchmark). In NorESM_PP, both the initial state and the parameter are inaccurate, and it represents the lower benchmark. The results of these experiments are presented in Section 3.3.
- The final set of experiments addresses the impact of the estimated parameters on the performance of reanalysis—where monthly assimilation of the state is performed. The reanalysis is started on February 1990 and run to December 1991. Prior to this, a 10 year spin up from 1980 is performed to allow the model to adjust to the new parameter values. The ensemble parameter values are from (1) parameters estimated (PE) obtained from EnKF_PE (referred as REANA_PE), (2) Perturbed parameters (REANA_PP, lower benchmark), and (3) REANA_TP with perfect parameter values. All experiments use the same observations (as in EnKF_ALL experiment), which combined physics and BGC surface time-varying observations available at every 5th grid cell. The results of these experiments are presented in Section 3.4.

A summary of all experiments is given in **Table 1**.

TABLE 1 | List of performed experiments.

Description	Experiment Name	Observations (if assimilated)	Initial ensemble from	Parameters used	Time period
Model free runs	**NorESM_PP**		Historical run	Perturbed parameters	Jan 1980–Jan 1990
	NorESM_TP		Historical run	True Parameters	Jan 1980–Jul 1991
Assimilation runs with true parameters	**EnKF_PHY**	Physics obs.	NorESM_TP	True Parameters	Feb 1990–Jul 1991
	EnKF_BGC	BGC obs.	NorESM_TP	True Parameters	Feb 1990–Jul 1991
	EnKF_ALL	Physics + BGC obs.	NorESM_TP	True Parameters	Feb 1990–Jul 1991
Online parameter estimation	**EnKF_PE**	Physics + BGC obs.	NorESM_PP	Online	Feb 1990–Dec 1990
	EnKF_PE_CO	Physics + BGC Clim. Obs.	NorESM_PP	Online	Feb 1990–Dec 1990
	EnKF_PE_SCO	Sparser grid Physics + BGC Clim. Obs.	NorESM_PP	Online	Feb 1990–Dec 1990
Free runs with fixed PE	**NorESM_PE**		Historical run	PE from EnKF_PE	Jan 1980–Jan 1990
	NorESM_PE_CO		Historical run	PE from EnKF_PE_CO	Jan 1980–Dec 1983
	NorESM_PE_SCO		Historical run	PE from EnKF_PE_SCO	Jan 1980–Dec 1983
Reanalysis runs	**REANA_PE**	Physics + BGC obs.	NorESM_PE	PE from EnKF_PE	Feb 1990–Dec 1991
	REANA_TP	Physics + BGC obs.	NorESM_TP	True parameters	Feb 1990–Dec 1991
	REANA_PP	Physics + BGC obs.	NorESM_PP	Perturbed Parameters	Feb 1990–Dec 1991

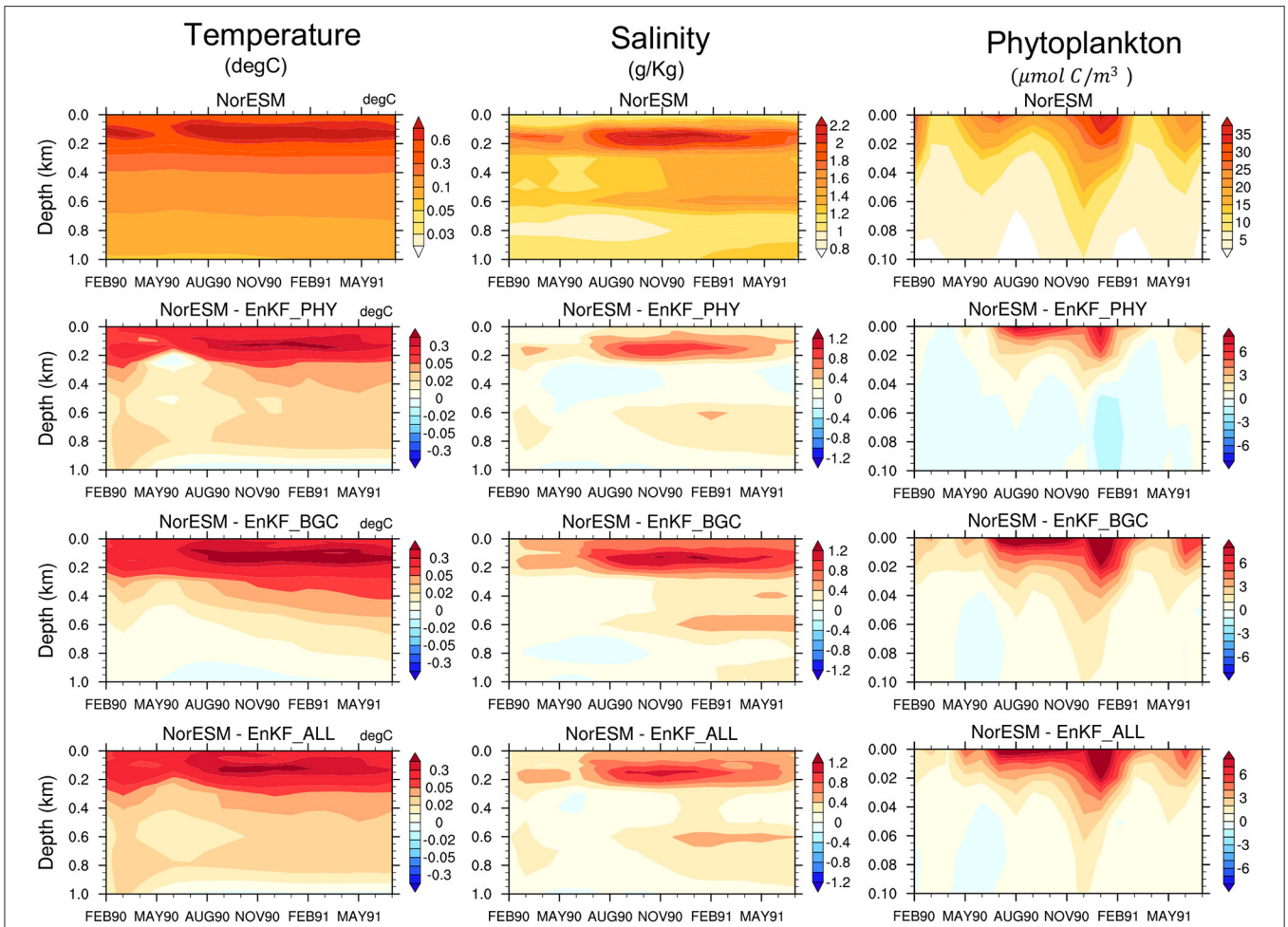

FIGURE 2 | The first row shows the time evolution of the vertical global-averaged RMSE for temperature (first column), salinity (second column), and phytoplankton concentration (third column) in the NorESM free run against TRUTH. The other rows show the RMSE difference (RMSED) for the same variables with assimilation of physics observation (EnKF_PHY), BGC surface observations (EnKF_BGC), and combined observations (EnKF_ALL), respectively. RMSED is computed by subtracting the RMSE of simulations with DA from that of free run RMSE. Warm (cold) colors represent improvement (degradation) from assimilation.

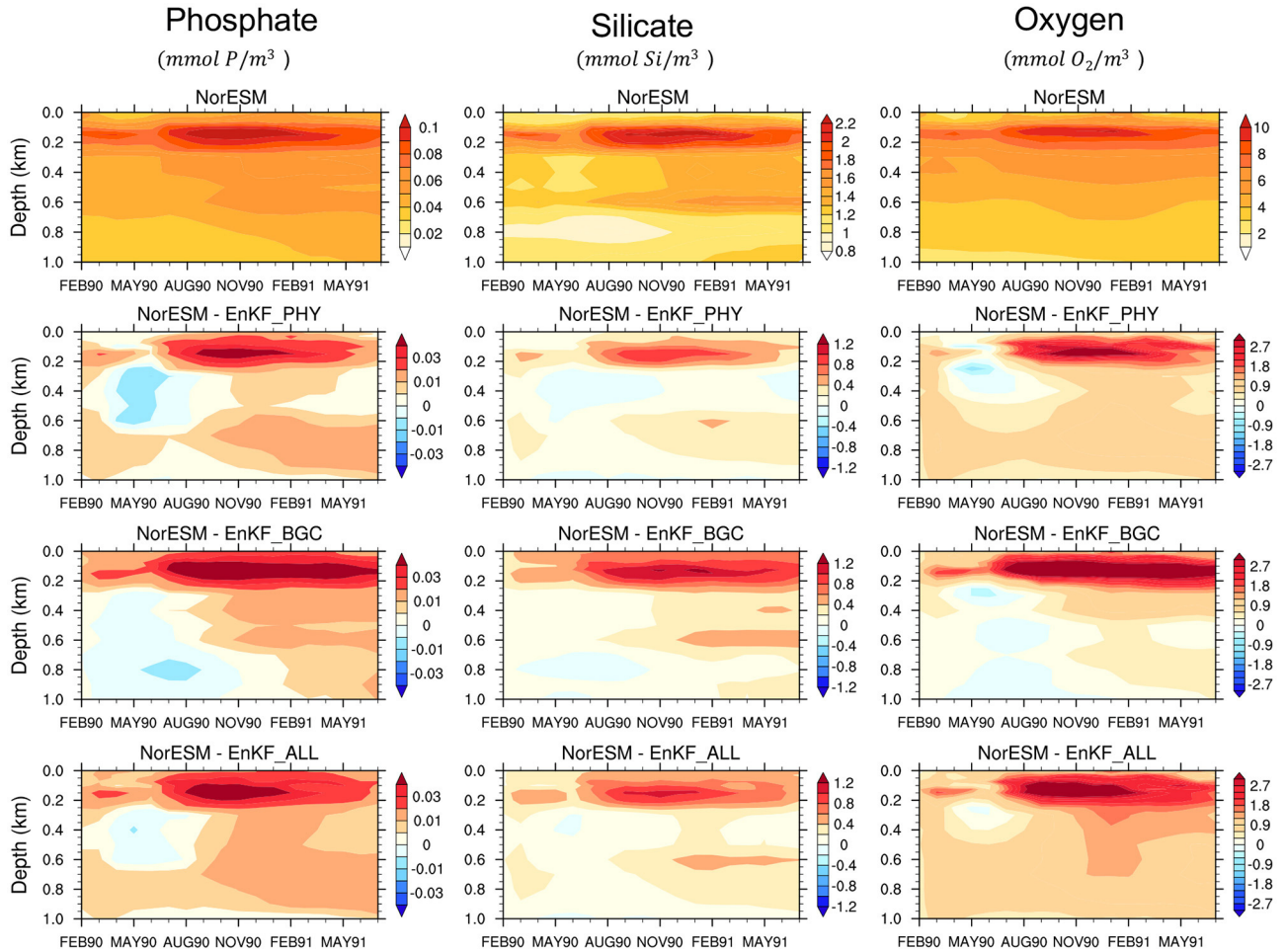

FIGURE 3 | Same as **Figure 2** but for Phosphate (first column), Silicate (second column), and Oxygen (third column).

3. RESULTS

3.1. Impact of Assimilation on the State Using True Parameters

A prerequisite for skillful parameter estimation is that assimilation constrains the error of the state variables well. Error in state variables, particularly at the surface and at inter-mediate depth can have a strong influence on near-surface biogeochemical processes. We work in a perfect model framework (i.e., all members use true parameter values) and we are interested in how well the error of the state variables is constrained by different observation networks. The monthly time evolution of the RMSE (averaged over the global domain and organized by depth level) of the NorESM free ensemble run (NorESM_TP) is shown in **Figures 2**, **3**. We also show the RMSE-difference (RMSED) of EnKF_PHY, EnKF_BGC and EnKF_ALL assimilation experiments compared to NorESM_TP.

All assimilation experiments improve the accuracy of both the ocean and the BGC state variables in the near-surface levels compared to NorESM_TP. The difference between the three DA experiments is small. Sole assimilation of BGC or physical data alone is able to constrain well the surface ocean physical and biogeochemical variables and *vice versa*. This was somewhat unexpected, and it exemplifies well the potential of strongly coupled data assimilation (Penny and Hamill, 2017). It should be reminded that we assimilate in an isopycnal coordinate that has been shown to be more effective than assimilation in geopotential depth for surface observation (Gavart and De Mey, 1997; Counillon et al., 2016). The Analysis error for phytoplankton concentration is well reduced in all experiments. Similarly, clear improvements are shown for nutrients (phosphate and silicate) and oxygen estimates. BGC data assimilation alone yields the largest reduction of errors in the top 200 m. Below 200 m depth, the combined assimilation of physical and BGC observations provides slightly better performance than the other two experiments and it mitigates the degradation seen at deeper layers for some variables, e.g., temperature, phosphate, and oxygen. Overall, the accuracy of the combined assimilation experiment is slightly better. For example, the average error in EnKF_ALL for salinity in the top 1 km is 35% lower than

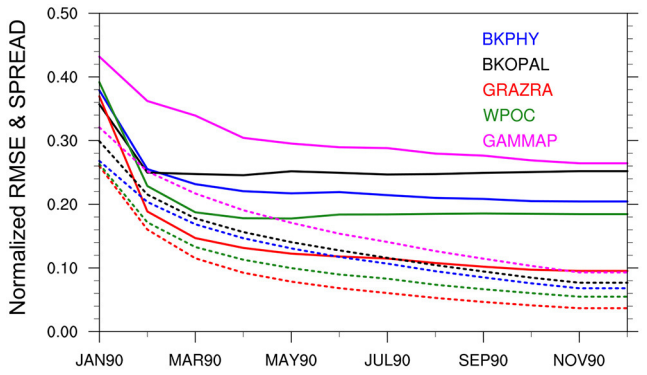

FIGURE 4 | Time evolution of global-averaged normalized RMSE (solid lines) and ensemble spread (dotted lines) of the BGC parameters from state-parameter estimation experiment using assimilation of time-varying observations (EnKF_PE). RMSE is calculated by comparing each member against the true values. Both RMSE and spread has been normalized by the global mean value of the true parameter.

that of the free run, while it is 24% for EnKF_PHY and 30% for EnKF_BGC. Similarly for Oxygen, EnKF_ALL has 28% lower error than the free run while EnKF_PHY is 19% and EnKF_BGC 24%.

3.2. Online Parameter Estimation

This section presents and assesses spatially varying ecosystem parameters estimation with the DOSA scheme (reduction of error of the estimated parameter). We analyse the EnKF_PE, EnKF_PE_CO and EnKF_PE_SCO experiments (see **Table 1**). The time evolution of the global-averaged ensemble spreads and RMSEs of the estimated parameters obtained from EnKF_PE are shown in **Figure 4**. RMSEs for all parameters reduce with time and become stable within one year of assimilation. The reduction is largest for GRAZRA that shows a 72% error reduction from its initial distribution (**Table 2**). The error reduction in the remaining parameters WPOC, BKPHY, GAMMAP, and BKOPAL is about 54, 47, 40, and 30%, respectively. Similarly, the ensemble spreads of all parameters reduce with time. However, the reduction is quicker than for RMSE, which suggests that the system may benefit from using multiplicative or additive inflation (Mitchell and Houtekamer, 2000; Anderson, 2001). Similar results have been obtained from EnKF_PE_CO and EnKF_PE_SCO experiments (not shown).

Ensemble data assimilation estimates the parameters based on their correlation with the model misfits from observations (e.g., Anderson, 2001). In order to visualise the convergence process, we have used scatter plots (see **Figure 5**) of the parameter ensemble against the model deviation from the truth at different cycles of the assimilation experiment; i.e., in the start in January 1990 (red color), after the first assimilation, the second and the last assimilation cycles (green, purple, and blue colors, respectively). Each scattered dot represents one ensemble member and the big dots represent the ensemble mean. All ecosystem variables simulated using perturbed parameters show

TABLE 2 | Spatial average of the point-wise ensemble RMSE of the parameter values obtained at the end of the estimation period (December 1990).

	NorESM_PP	EnKF_PE	EnKF_PE_CO	EnKF_PE_SCO
BKPHY	0.38	0.20	0.17	0.22
GRAZRA	0.37	0.10	0.09	0.11
BKOPAL	0.36	0.25	0.22	0.29
GAMMAP	0.43	0.26	0.30	0.32
WPOC	0.39	0.18	0.15	0.23

The RMSE has been normalized (divided) by the global mean value of the true parameter.

relatively large deviations from the TRUTH (y-axes in **Figure 5**), which underlines the sensitivity of the surface quantities to errors in the parameters. Among all parameters, GRAZRA shows the strongest linear relation with all variables and is the most important parameter for reducing model bias. For some parameters, the linear relationship is only strong with respect to some variables (e.g., WPOC with Silicate), which shows the importance of using multiple type of observations for the parameter estimation. The parameters are converging toward the true value very rapidly (already within the first 2 assimilation cycles), strongly reducing the error in ecosystem variables. After 11 assimilation cycles (corresponding to December 1990), one can notice that global means of the estimated parameters are very close to the true value and that the errors in the ecosystem variables are close to zero. This shows that the method converges quickly (within few assimilation steps) and is able to constrain the global mean of estimated parameters close to their true values by largely reducing the error in parameters. Similar results have been found for EnKF_PE_CO and EnKF_PE_SCO experiments (not shown).

We further analyse the spatial distribution of the estimated parameters obtained for December 1990 from all three experiments. **Figure 6** shows the true and ensemble mean of the experiments with perturbed and estimated parameters. First, we note that the data assimilation yields a reduction of error compared to the initial values for all parameters. We can also notice that there is some spatial coherency in the value of the pattern retrieved. Parameters show relatively good agreement with the spatial distribution of the true value with spatial RMSE reduced by 75% for GRAZRA, by 50 % for BKPHY and WPOC, 40% for GAMMAP, and only 30% for BKOPAL, see **Table 2**. However, some differences remain and there is some small-scale noise. We suspect the latter to be related to spurious correlations present in our finite size ensemble (30). The places where the estimation fails to converge to true value may relate to places where the model is insensitive to the parameters. Hence, the parameter estimation can drift towards an erroneous value—e.g., as a response to spurious correlation or because of the approximation of Gaussianity and linearity during the analysis—without having an impact on the state error. In order to assess the impact of the error reduction on the state variable, we will freeze the parameter values at the last assimilation cycle and perform simulations in a free ensemble run and in a reanalysis mode in the following sections.

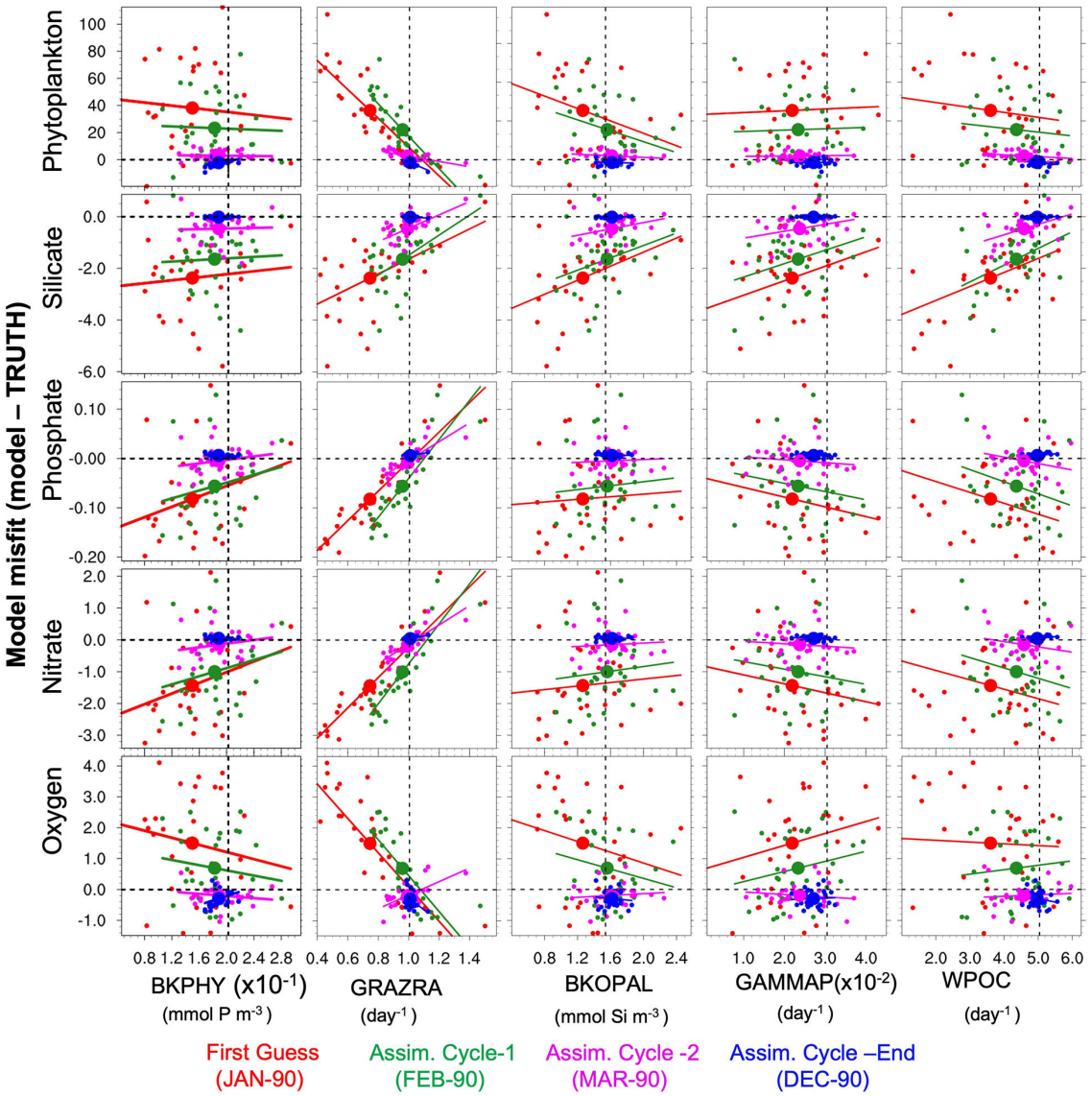

FIGURE 5 | Scatter plots for globally-averaged misfit (model-TRUTH) ensemble vs. BGC parameters ensemble. Plots are shown for surface phytoplankton (row-one), silicate (row-two), phosphate (row-three), nitrate (row-four), and oxygen (row-five) with BKPHY (column-one), GRAZRA, (column-two), BKOPAL (column-three), GAMMAP (column-four), and WPOC (column-five) parameters; obtained from first guess (red), after first assimilation cycle (green), second assimilation cycle (purple), and end of assimilation (blue) with EnKF_PE experiment. The large dots show the ensemble mean. Horizontal and vertical dashed black reference lines represent the line of zero misfit and global-averaged TP values, respectively. Solid colored lines are the linear regression lines.

3.3. Model Ensemble Free Run With Estimated Parameters

We verify the state accuracy of a free ensemble run that uses the final parameter's estimates of EnKF_PE, EnKF_PE_CO and EnKF_PE_SCO experiments, and refer to them as NorESM_PE, NorESM_PE_CO and NorESM_PE_SCO, respectively. We compare the performance against a free ensemble run using the true parameter (NorESM_TP) and one using the perturbed parameter (NorESM_PP).

In **Figure 7**, NorESM_PP poorly simulates the phytoplankton activity with a systematic overestimation of phytoplankton concentrations and generally longer spring blooms during the summer seasons compared to NorESM_TP. The runs that use the estimated parameters clearly outperform NorESM_PP, and perform closely to NorESM_TP. For instance, the global averaged RMSE of the phytoplankton concentration with NorESM_PE and NorESM_TP is roughly 51 and 54% lower than in NorESM_PP. Similarly, the biases in the parameter estimation experiments are significantly reduced to the level of that of TP. The performance of TP and PEs are also comparable in the upper 200-m as shown in **Figure 7C**. Below this depth, the model seems to

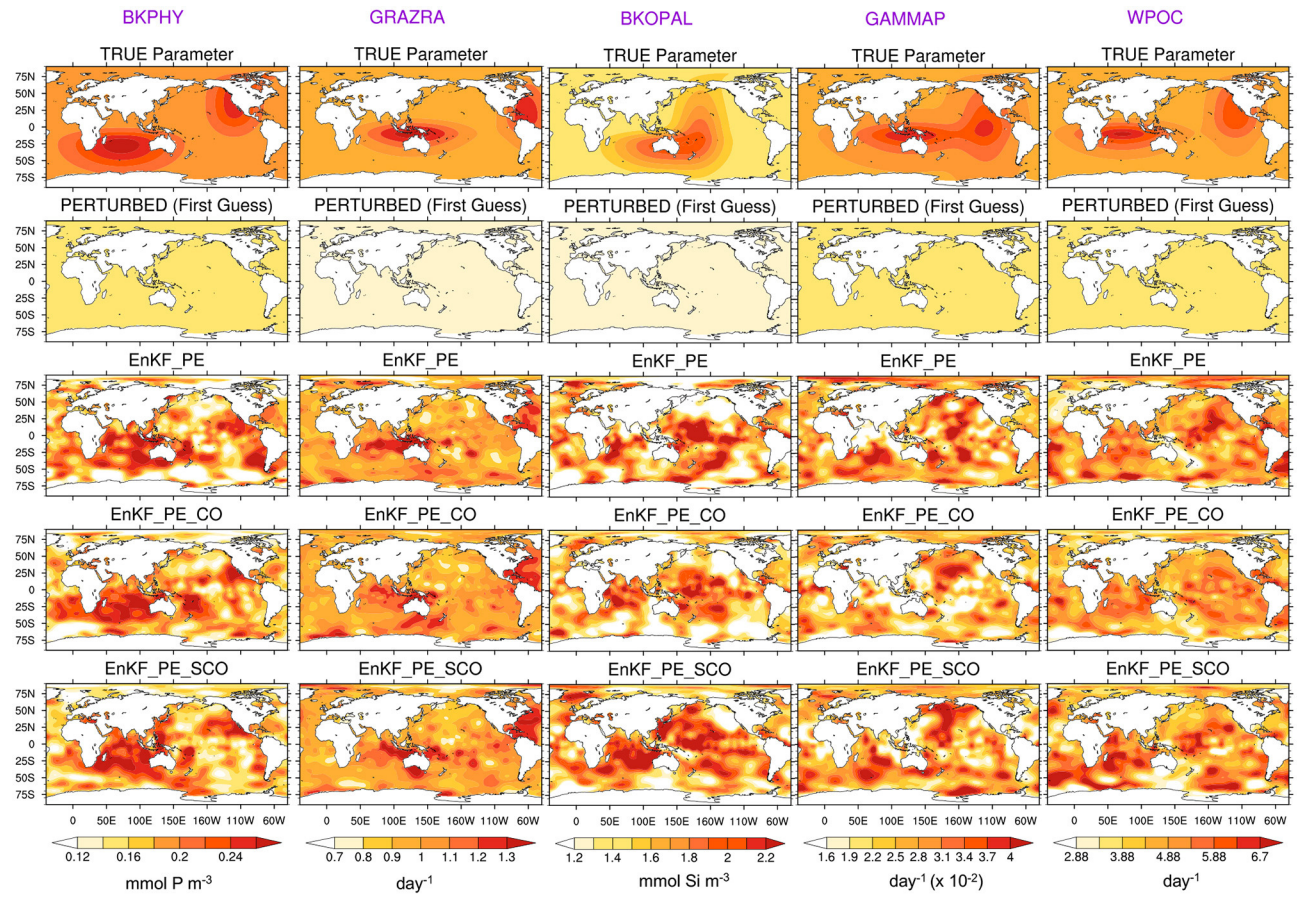

FIGURE 6 | True (row-one) and point wise ensemble mean of the perturbed (row-two) and estimated BGC parameters in December 1990 with assimilation of time-varying (row-three), climatological (row-four), and very sparse climatological (row-five) BGC surface observations in addition to time varying physics. Column-one to -five correspond to BKPHY, GRAZRA, BKOPAL, GAMMAP, and WPOC parameters.

have no sensitivity to these parameters and all experiments perform equivalently.

This conclusion is also verified for others BGC quantities such as silicate (**Figure 8**), phosphate (**Figure 9**), nitrate, and oxygen (not shown) in which PEs perform nearly as good as TP, while PP leads to a poor simulation of these variables and a large underestimate (negative bias) of the nutrient concentration, specifically during summer seasons, in the euphotic zone. This is related to the highly enhanced phytoplankton activity in PP, as seen earlier, which removes the available nutrients from the euphotic zone. RMSE and bias profile plots suggest that BGC parameters may strongly control the biogeochemical process in deeper layers up to roughly 500 m depth. Again, the simulated quality of nutrients and oxygen profiles by PEs and TP are very similar throughout entire depth.

We can also notice that NorESM_PE and NorESM_PE_SCO experiments show very comparable accuracy for ecosystem variables. Results from NorESM_PE_CO is not included to avoid overlapping lines in the Figures but we found very similar results. It suggests that BGC surface sparse climatological observations, and even very sparse climatological observations are somewhat sufficient to retrieve optimal ecosystem parameters with similar quality as time-varying observations using the DOSA-EnKF algorithm. Hence, in our model, the largest contribution to the error appears to be related to the seasonal cycle representation, which can be effectively corrected with a monthly climatology of observations.

We also analyse the impact of the parameters spatially. **Figure 10** shows the RMSE and bias averaged over 100 m depth for the phytoplankton concentration and 500 m for the silicate profile. In general, bloom intensity increases from mid to high latitudes. It is seen that PP shows a larger overestimation of phytoplankton concentration, specifically over high latitudes and over some tropical regions, e.g., the eastern tropical Pacific Ocean. In all 3 PEs, the biases and RMSEs are reduced. The RMSE and bias patterns of the PEs closely match that of TP. In the case of silicate, PP shows a severe underestimation over the region where increased phytoplankton activities are seen.

Performance of the PEs is now assessed for an observation that was not used for tuning the parameters. Hence, we investigate air-sea CO_2 flux and net primary production (NPP) (**Figure 11**) and

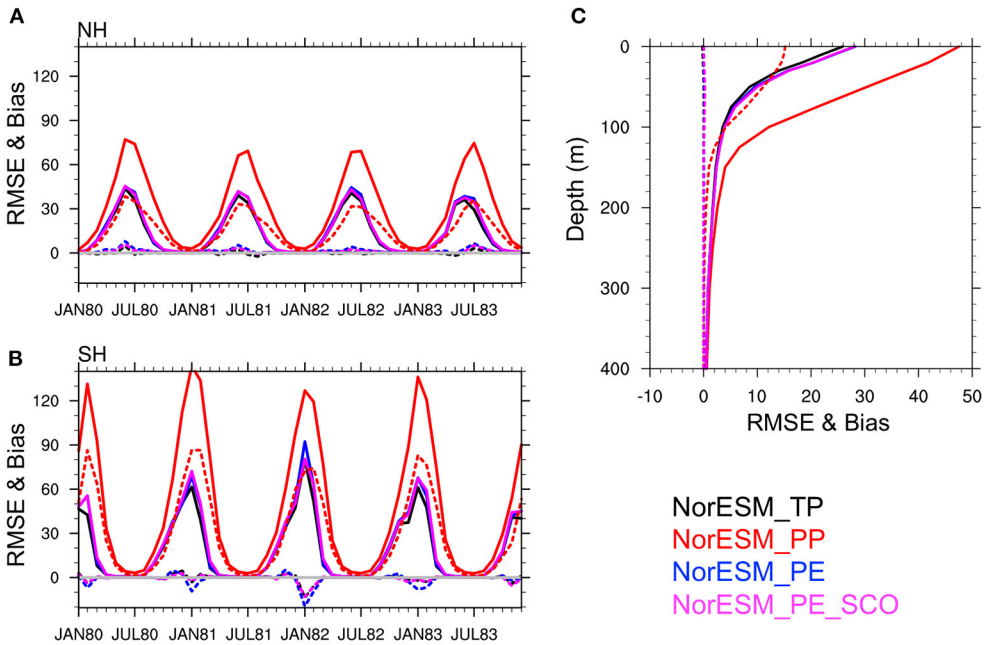

FIGURE 7 | Panels on the left show the RMSE (solid lines) and bias (dotted lines) of the ensemble mean of NorESM phytoplankton concentration compared to the TRUTH in the euphotic zone (i.e., from the surface to 100 m) in the northern hemisphere [NH, **(A)**] and in the southern hemisphere [SH, **(B)**]. **(C)** is the globally averaged vertical error profiles estimated over the 4-year period (1980–1983). The results of the free NorESM simulation using TP are shown in black, PP in red, and PE using assimilation of time-varying observations in blue and sparse climatological BGC observations in magenta.

found consistent results. Similar to previous results, PEs maintain the accuracy closer to TP.

The above results provide strong evidence that the DOSA-EnKF system can successfully recover the optimal value for chosen BGC parameters. It also suggests that the remaining parametric error does not effectively influence the behavior of the model.

3.4. Reanalysis With Estimated Parameters

This section presents the accuracy of the state variables in the reanalyses which started in February 1990 and were run until December 1991 using fixed estimated parameters (REANA_PE). We compare the performance of REANA_PE with that of a reanalysis using perturbed parameters REANA_PP (lower benchmark) and a reanalysis using true parameters REANA_TP (upper benchmark).

The time evolution of the RMSE and bias over the euphotic zone is presented in **Figure 12**. First, we notice that assimilation improves the accuracy of the ecosystem variables in all experiments. For instance, the prior distributions of phytoplankton, oxygen and net primary production (NPP) are associated with high uncertainty and biases in the months with maximum bloom activity (January in the southern hemisphere). After a few assimilation cycles, there is a lower error during the bloom seasons. This can also be verified by comparing the phytoplankton free run accuracy shown in **Figure 7** with the analysis accuracy presented here. For instance, the free run with PP shows RMSE values of roughly 70 $\mu molC\ m^{-3}$ for the spring bloom peak over the northern hemisphere (**Figure 7**), which is reduced to roughly 40 $\mu molC\ m^{-3}$ after assimilation (**Figure 12**).

Similar results are found for NPP (time evolution of free run not shown), for which observations are not being assimilated in the system (non-observed variable). Thus, the assimilation system is capable of improving the quality of not only the observed ecosystem variables (e.g., phytoplankton and Oxygen) but also of the non-observed variables. However, differences in the accuracy of reanalyses are clearly visible for the different set of parameters. REANA_PP shows larger uncertainty and stronger biases particularly during bloom seasons for phytoplankton, oxygen and net primary production reanalyses. The differences between REANA_PP and REANA_TP are more pronounced in the northern hemisphere than in the southern hemisphere. This exemplifies that assimilation cannot achieve optimum performance in the presence of model error.

The quality assessment of reanalysis has been further assessed in the deeper ocean by estimating the globally averaged RMSE and bias profiles for the top 1-km (**Figure 13**). The statistics have been computed using the July 1990 to December 1991 period. The first 6 months have been discarded for removing assimilation spinup that is longer in the deeper ocean. TP and PE show overall comparable performance for phytoplankton reanalysis whereas PP leads to degraded performance mostly in the top 150 m.

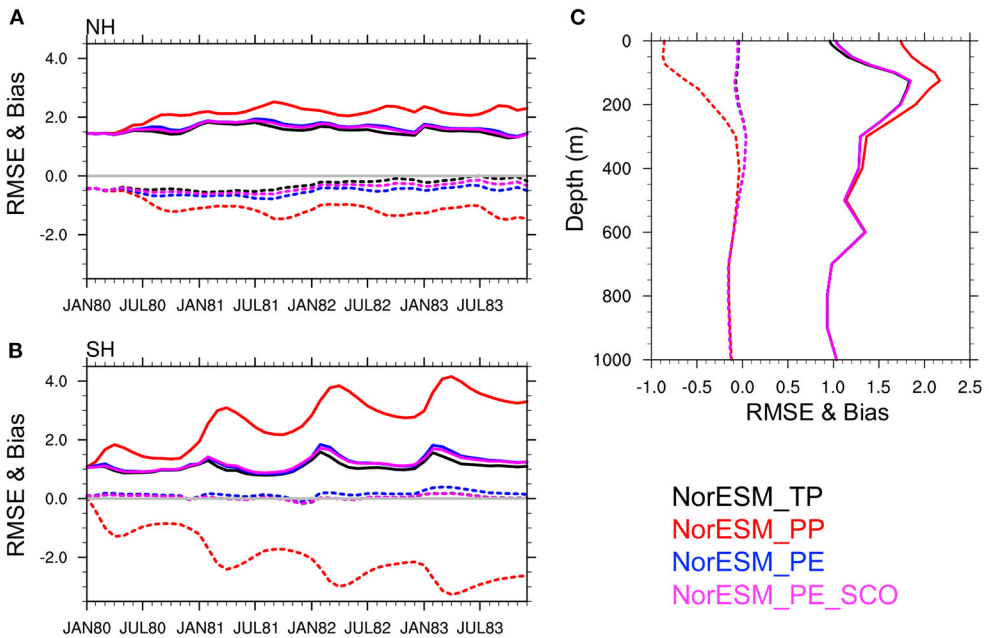

FIGURE 8 | Same as **Figure 7** but for Silicate.

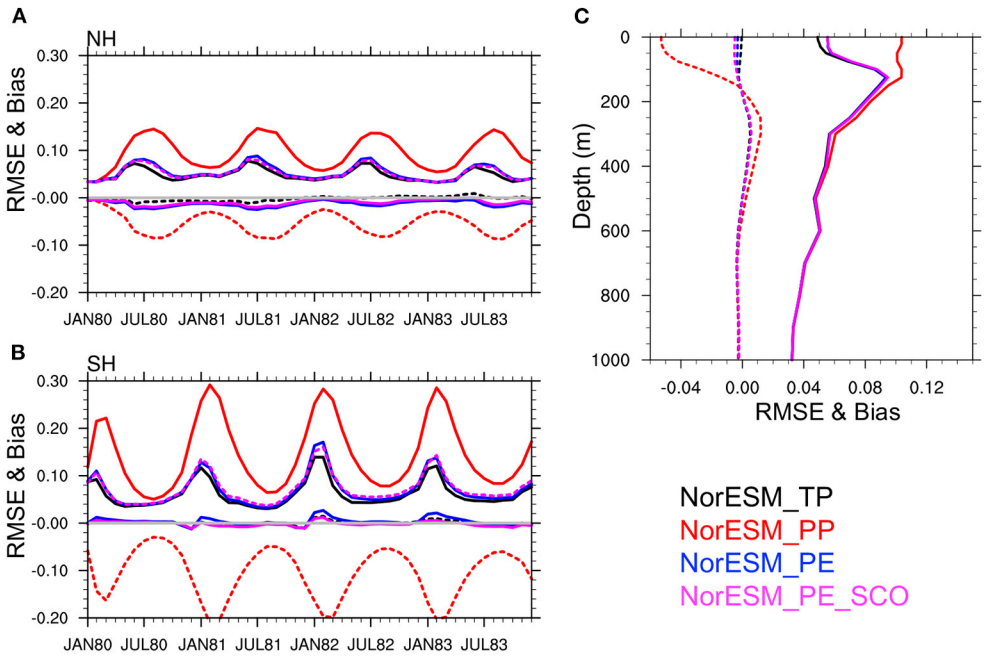

FIGURE 9 | Same as **Figure 7** but for Phosphate.

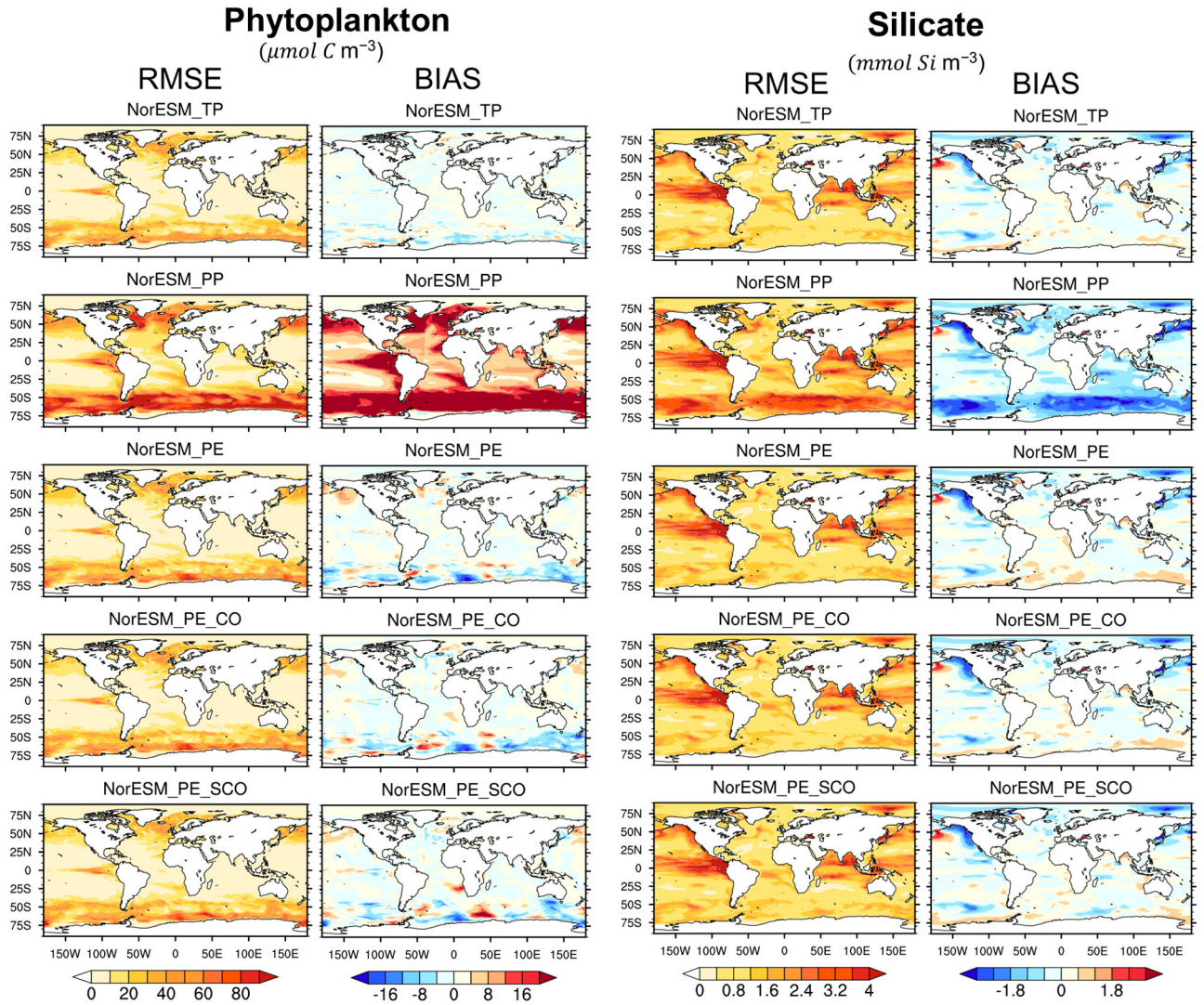

FIGURE 10 | RMSE and bias maps estimated over 1980–1983 for phytoplankton and silicate. For phytoplankton, RMSE (column-one) and bias (column-two) are averaged over euphotic zone (0–100 m), while for silicate, they are averaged over 0–500 m depth (column-three and -four, respectively). The error are computed from free NorESM simulation using TP (first row), PP (row-two), and fixed PE estimated with assimilation of time-varying observation (row-three), time varying physic and climatological BGC (row-four), and time varying physic and sparse climatological BGC (row-five).

Similar results can be seen for nutrients (e.g., phosphate and silicate) and oxygen profiles where differences of PP with TP or PE are more pronounced at inter-mediate depth levels. Still we can see that the performance of PE is not as efficient for oxygen and phosphate below 300 m. It would have been interesting to test whether training the parameters with deeper BGC observations (currently only available at the surface) would have improved performance there.

4. SUMMARY AND CONCLUSIONS

We have presented the feasibility of optimizing spatially varying ocean biogeochemical parameters in an Earth system model using an ensemble-based data assimilation method in an idealized perfect twin experiment setup. We used the NorCPM system, which combines the NorESM global model with the DOSA-EnKF assimilation method. The DOSA-EnKF applies a smoothing step to the state and parameters before propagating the model for the analysis step. We estimate five spatially varying biogeochemical parameters in addition to ocean physical and biogeochemical state variables. The parameters characterize the major surface biological processes such as phytoplankton growth, zooplankton grazing, release of dissolved organic carbon, sinking of organic matter and nutrient uptake. We assimilate synthetic monthly ocean physics profiles (temperature and salinity) and surface BGC observations (Phytoplankton, Nitrate, Phosphate, Silicate, and Oxygen) in a strongly coupled framework, where observations are

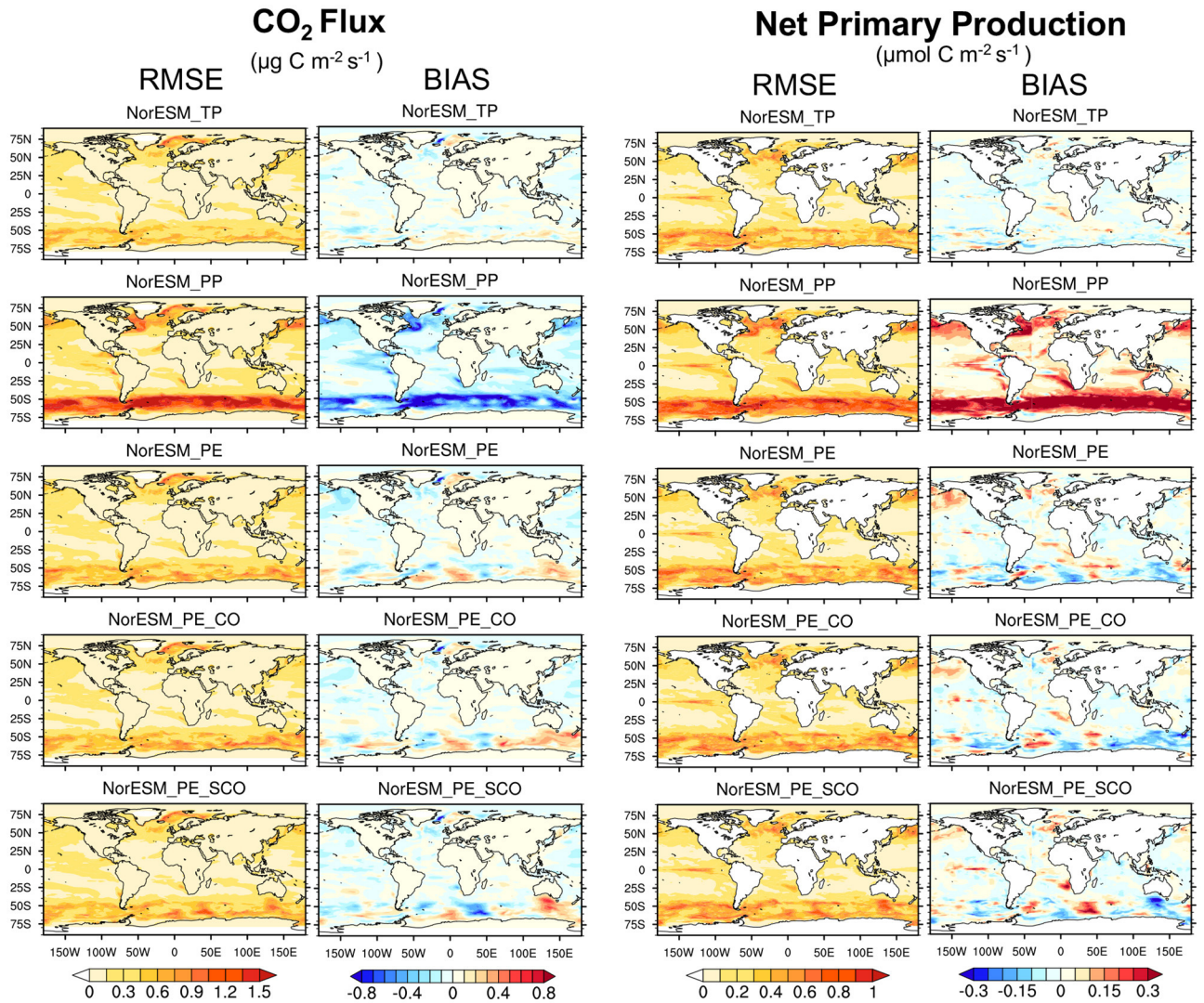

FIGURE 11 | Same as **Figure 10** but for CO_2 flux (column-one and -two) and net primary production (column-three and -four).

used to update ocean and BGC state variables jointly along with parameters.

Assimilation of different observation networks in a strongly coupled framework reveals that BGC observations can effectively constrain errors in the ocean physics and *vice versa*. It demonstrates the potential of strongly coupled data assimilation to constrain the errors in cross component state variables. It could benefit ocean BGC in real observations setup, where dense network of physical observations can be used to constrain the BGC state variables for which measured properties are under-sampled. In our setup, sole assimilation of BGC surface observations seems to yield largest error reduction in the top 200 m for both physical and ecosystem variables. Further, combined assimilation of physical and BGC observations provides more robust performance and avoid degradation in deeper layers.

The success of the parameter estimation has been tested by three state-parameter estimation experiments performed using different networks of BGC observation on top of physical observations. One of them assimilating sparse-grid (every 5th grid cell) time-varying BGC observations and the other two assimilating climatological BGC observations prepared at sparse (every 5th grid cell) and very sparse horizontal resolution (every 10th grid cell). All experiments converge quickly within a year and are able to retrieve the true global mean of estimated parameters, strongly reducing the error in the perturbed parameters. Further, the spatial pattern for nutrient uptake and zooplankton grazing parameters show relatively good agreement with that of the true values. However, some differences remain in the estimated values. The success of recovering the true parameter values in any region depends on the sensitivity of the model to those parameters. It is possible that the true values are

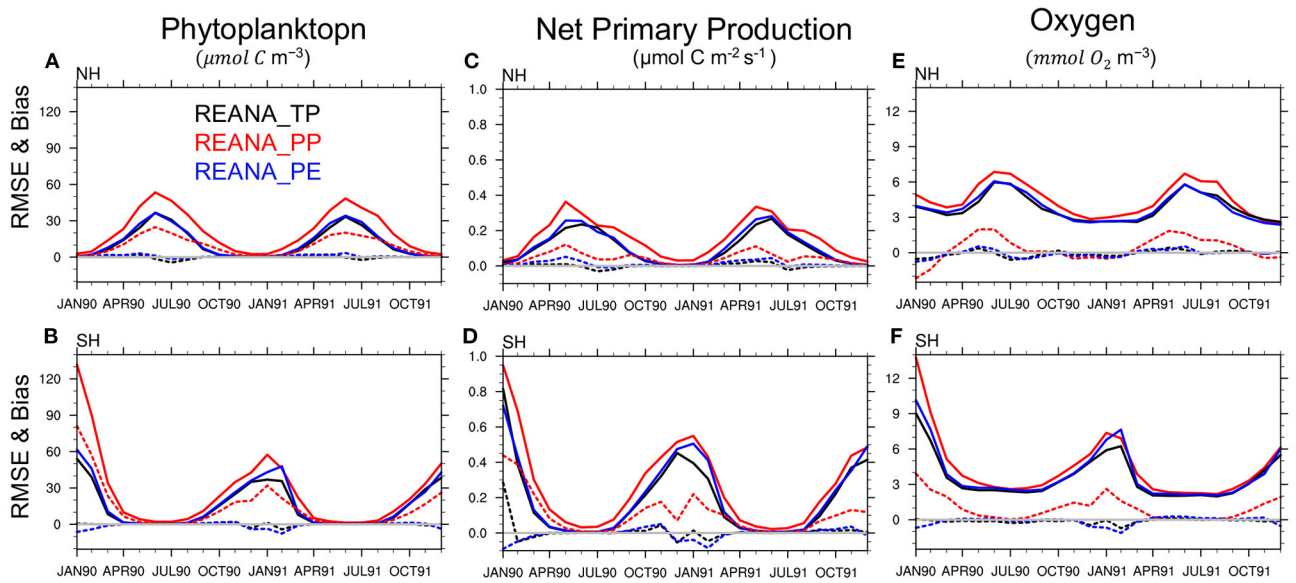

FIGURE 12 | Panels on the left show the RMSE (solid lines) and bias (dotted lines) of the ensemble mean of phytoplankton concentration reanalysis compared to the TRUTH in the euphotic zone in the northern hemisphere [NH, **(A)**] and southern hemisphere [SH, **(B)**]. The results of the reanalysis using TP are shown in black, PP in red, and PE in blue using assimilation of time-varying observations. **(C,D)** and **(E,F)** are same as **(A,B)** but for net primary production and oxygen concentration.

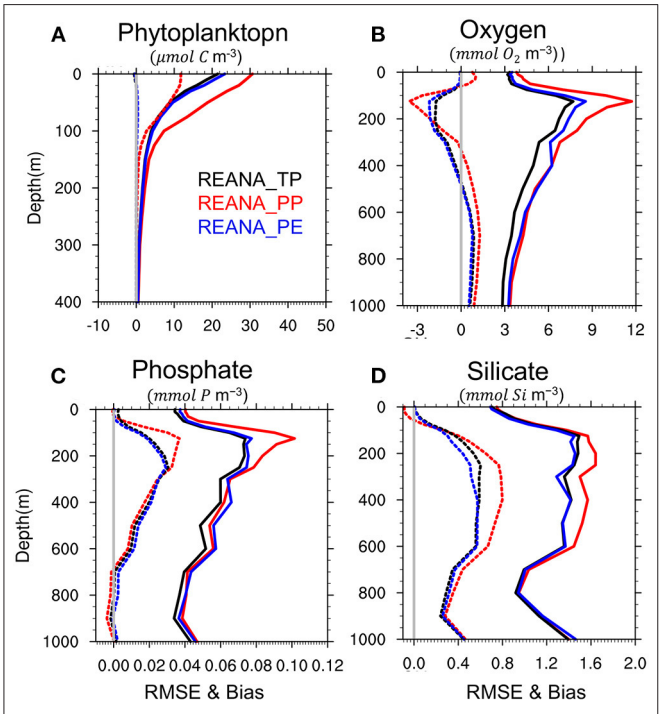

FIGURE 13 | (A) is the globally averaged RMSE (solid lines) and bias (dotted lines) profiles estimated over the 18-months reanalysis period (July 1990-December 1991) for phytoplankton concentration generated using TP (black), PP (red), fixed PE (blue), and assimilating time-varying observations. **(B–D)** are same as **(A)** but for oxygen, phosphate, and silicate, respectively.

not sensitive in many regions. Over such regions, the estimation of parameters may not work effectively and differences between estimated and true values are possible.

As a way to test the impact of the parameters on the state variables, we conducted ensemble free run using estimated parameter values obtained from three different BGC observation networks mentioned earlier. The performance of the estimated values has been compared with upper- and lower benchmark model ensemble runs conducted using true and perturbed parameter values, respectively. We found that the accuracy of simulated ecosystem variables obtained using all three sets of estimated parameters is as good as those obtained using true parameters. Perturbed parameters lead to a systematic overestimation of the phytoplankton and longer spring blooms compared to the true parameters. Similar results have been obtained for nutrient and oxygen concentrations throughout the entire water column. These results suggest that remaining differences in the estimated and true parameters do not effectively influence the behavior of the model and estimated values are optimal. As similar results have been obtained from all three sets of estimated parameters, we can conclude that very sparse BGC surface climate observations are sufficient to retrieve optimal ecosystem parameters with similar quality as time-varying observations using the DOSA-EnKF algorithm with our model system. We suspect that this is because the primary source of error is in the representation of the seasonal cycle that is well represented by the monthly climatology data.

The performance of reanalyses using fixed estimated parameters was also assessed. Again, we found that using

the estimated parameters improves the quality of ecosystem variables in the reanalyses mode. The accuracy of the reanalysis with perturbed parameters shows poorer performance than the one using true and estimated parameters with large biases and error for observed variables (e.g., phytoplankton, oxygen and phosphate) as well as for unobserved variables (e.g., net primary production which was not assimilated). This is expected because assimilation is not designed to correct model errors (Dee, 2005; Counillon et al., 2021).

The finding of this study clearly reveals that the DOSA-EnKF system in a perfect twin experiment can estimate spatially varying optimal BGC parameters for the NorESM model, even with very sparse climatological BGC surface observation. It remains to be confirmed whether the method succeeds in a real framework (assimilating real observations) as errors may originate from the other components (atmosphere, ocean physics, sea ice) or additional structural-related errors.

DATA AVAILABILITY STATEMENT

The raw data supporting the conclusions of this article will be made available by the authors, without undue reservation.

AUTHOR CONTRIBUTIONS

TS, FC, JT, and MG contributed to conception and design of the study. TS performed the numerical experiments and the statistical analysis. TS and FC wrote the first draft of the manuscript. JT, YW, and MG wrote sections of the manuscript. All authors contributed to manuscript revision, read, and approved the submitted version.

FUNDING

This study was partly funded by the Centre for climate dynamics at the Bjerknes Centre and the Research Council of Norway (INES; grant no. 270061). This work has also received funding from (EU Horizon 2020 Framework Programme) EU-TRIATLAS (grant no. 817578) and from the Trond Mohn stiftelse (grant no. BFS2018TMT01). This work has also received a grant for computer time from the Norwegian Program for supercomputing (NOTUR2, project number nn9039k) and a storage grant (NORSTORE, NS9039k). JT acknowledges funding from Research Council of Norway (COLUMBIA; grant no. 275268). YW acknowledges support from the Research Council of Norway under the CoRea project (grant no. 301396).

REFERENCES

Ait-El-Fquih, B., Gharamti, M. E., and Hoteit, I. (2016). A bayesian consistent dual ensemble kalman filter for state-parameter estimation in subsurface hydrology. *Hydrol. Earth Syst. Sci.* 20, 3289–3307. doi: 10.5194/hess-20-3289-2016

Anav, A., Friedlingstein, P., Kidston, M., Bopp, L., Ciais, P., Cox, P., et al. (2013). Evaluating the land and ocean components of the global carbon cycle in the cmip5 earth system models. *J. Clim.* 26, 6801–6843. doi: 10.1175/JCLI-D-12-00417.1

Anderson, J. L. (2001). An ensemble adjustment kalman filter for data assimilation. *Month. Weather Rev.* 129, 2884–2903. doi: 10.1175/1520-0493(2001)129<2884:AEAKFF>2.0.CO;2

Annan, J., Hargreaves, J., Edwards, N., and Marsh, R. (2005). Parameter estimation in an intermediate complexity earth system model using an ensemble kalman filter. *Ocean Model.* 8, 135–154. doi: 10.1016/j.ocemod.2003.12.004

Arnold Jr, C. P., and Dey, C. H. (1986). Observing-systems simulation experiments: past, present, and future. *Bull. Amer. Meteorol. Soc.* 67, 687–695. doi: 10.1175/1520-0477(1986)067<0687:OSSEPP>2.0.CO;2

Assmann, K., Bentsen, M., Segschneider, J., and Heinze, C. (2010). An isopycnic ocean carbon cycle model. *Geosci. Model Dev.* 3, 143–167. doi: 10.5194/gmd-3-143-2010

Bellenger, H., Guilyardi, É., Leloup, J., Lengaigne, M., and Vialard, J. (2014). Enso representation in climate models: from cmip3 to cmip5. *Clim. Dyn.* 42, 1999–2018. doi: 10.1007/s00382-013-1783-z

Bentsen, M., Bethke, I., Debernard, J., Iversen, T., Kirkevåg, A., Seland, Ø., et al. (2012). The norwegian earth system model, noresm1-m–part 1: description and basic evaluation. *Geosci. Model Dev. Discuss.* 5, 2843–2931. doi: 10.5194/gmdd-5-2843-2012

Bentsen, M., Bethke, I., Debernard, J. B., Iversen, T., Kirkevåg, A., Seland, Ø., et al. (2013). The norwegian earth system model, noresm1-m–part 1: description and basic evaluation of the physical climate. *Geosci. Model Dev.* 6, 687–720. doi: 10.5194/gmd-6-687-2013

Bertino, L., Evensen, G., and Wackernagel, H. (2003). Sequential data assimilation techniques in oceanography. *Int. Stat. Rev.* 71, 223–241. doi: 10.1111/j.1751-5823.2003.tb00194.x

Bethke, I., Wang, Y., Counillon, F., Keenlyside, N., Kimmritz, M., Fransner, F., et al. (2021). Norcpm1 and its contribution to cmip6 dcpp. *Geosci. Model Dev. Discuss.* 14, 1–84. doi: 10.5194/gmd-14-7073-2021

Bleck, R., Rooth, C., Hu, D., and Smith, L. T. (1992). Salinity-driven thermocline transients in a wind-and thermohaline-forced isopycnic coordinate model of the north atlantic. *J. Phys. Oceanograph.* 22, 1486–1505.

Bleck, R., and Smith, L. T. (1990). A wind-driven isopycnic coordinate model of the north and equatorial atlantic ocean: 1. model development and supporting experiments. *J. Geophys. Res. Oceans* 95, 3273–3285.

Bopp, L., Resplandy, L., Orr, J. C., Doney, S. C., Dunne, J. P., Gehlen, M., et al. (2013). Multiple stressors of ocean ecosystems in the 21st century: projections with cmip5 models. *Biogeosciences* 10, 6225–6245. doi: 10.5194/bg-10-6225-2013

Chen, Y., and Zhang, D. (2006). Data assimilation for transient flow in geologic formations via ensemble kalman filter. *Adv. Water Resour.* 29, 1107–1122. doi: 10.1016/j.advwatres.2005.09.007

Counillon, F., Bethke, I., Keenlyside, N., Bentsen, M., Bertino, L., and Zheng, F. (2014). Seasonal-to-decadal predictions with the ensemble kalman filter and the norwegian earth system model: a twin experiment. *Tellus Dyn. Meteorol. Oceanograph.* 66:21074. doi: 10.3402/tellusa.v66.21074

Counillon, F., Keenlyside, N., Bethke, I., Wang, Y., Billeau, S., Shen, M. L., and Bentsen, M. (2016). Flow-dependent assimilation of sea surface temperature in isopycnal coordinates with the norwegian climate prediction model. *Tellus Dyn. Meteorol. Oceanograph.* 68:32437. doi: 10.3402/tellusa.v68.32437

Counillon, F., Keenlyside, N., Toniazzo, T., Koseki, S., Demissie, T., Bethke, I., and Wang, Y. (2021). Relating model bias and prediction skill in the equatorial atlantic. *Clim. Dyn.* 56, 2617–2630. doi: 10.1007/s00382-020-05605-8

Craig, A. P., Vertenstein, M., and Jacob, R. (2012). A new flexible coupler for earth system modeling developed for ccsm4 and cesm1. *Int. J. High Perform. Comput. Appl.* 26, 31–42. doi: 10.1177/1094342011428141

Dee, D. P. (2005). Bias and data assimilation. *Quart. J. R. Meteorol. Soc. J. Atmosph. Sci. Appl. Meteorol. Phys. Oceanography* 131, 3323–3343. doi: 10.1256/qj.05.137

Doron, M., Brasseur, P., Brankart, J.-M., Losa, S. N., and Melet, A. (2013). Stochastic estimation of biogeochemical parameters from globcolour ocean colour satellite data in a north atlantic 3d ocean coupled physical–biogeochemical model. *J. Marine Syst.* 117, 81–95. doi: 10.1016/j.jmarsys.2013.02.007

Eknes, M., and Evensen, G. (2002). An ensemble kalman filter with a 1-d marine ecosystem model. *J. Marine Syst.* 36, 75–100. doi: 10.1016/S0924-7963(02)00134-3

Evensen, G. (2003). The ensemble kalman filter: theoretical formulation and practical implementation. *Ocean Dyn.* 53, 343–367. doi: 10.1007/s10236-003-0036-9

Fransner, F., Counillon, F., Bethke, I., Tjiputra, J., Samuelsen, A., Nummelin, A., et al. (2020). Ocean biogeochemical predictions–initialization and limits of predictability. *Front. Marine Sci.* 7:386. doi: 10.3389/fmars.2020.00386

Gaspari, G., and Cohn, S. E. (1999). Construction of correlation functions in two and three dimensions. *Quart. J. R. Meteorol. Soc.* 125, 723–757.

Gavart, M., and De Mey, P. (1997). Isopycnal eofs in the azores current region: a statistical tool fordynamical analysis and data assimilation. *J. Phys. Oceanography* 27, 2146–2157.

Gent, P. R., Danabasoglu, G., Donner, L. J., Holland, M. M., Hunke, E. C., Jayne, S. R., et al. (2011). The community climate system model version 4. *J. Clim.* 24, 4973–4991. doi: 10.1175/2011JCLI4083.1

Gharamti, M., Ait-El-Fquih, B., and Hoteit, I. (2015). An iterative ensemble kalman filter with one-step-ahead smoothing for state-parameters estimation of contaminant transport models. *J. Hydrol.* 527, 442–457. doi: 10.1016/j.jhydrol.2015.05.004

Gharamti, M., Samuelsen, A., Bertino, L., Simon, E., Korosov, A., and Daewel, U. (2017a). Online tuning of ocean biogeochemical model parameters using ensemble estimation techniques: application to a one-dimensional model in the north atlantic. *J. Marine Syst.* 168, 1–16. doi: 10.1016/j.jmarsys.2016.12.003

Gharamti, M., Tjiputra, J., Bethke, I., Samuelsen, A., Skjelvan, I., Bentsen, M., et al. (2017b). Ensemble data assimilation for ocean biogeochemical state and parameter estimation at different sites. *Ocean Model.* 112, 65–89. doi: 10.1016/j.ocemod.2017.02.006

Goris, N., Tjiputra, J. F., Olsen, A., Schwinger, J., Lauvset, S. K., and Jeansson, E. (2018). Constraining projection-based estimates of the future north atlantic carbon uptake. *J. Clim.* 31, 3959–3978. doi: 10.1175/JCLI-D-17-0564.1

Halem, M., and Dlouhy, R. (1984). "Observing system simulation experiments related to space-borne lidar wind profiling. part 1: forecast impacts of highly idealized observing systems," in Conference on Satellite Meteorology/Remote Sensing and Applications (Clearwater, FL: American Meteorological Society), 272–279.

Halliwell Jr, G., Srinivasan, A., Kourafalou, V., Yang, H., Willey, D., Le Hénaff, M., et al. (2014). Rigorous evaluation of a fraternal twin ocean osse system for the open gulf of mexico. *J. Atmosph. Ocean. Technol.* 31, 105–130. doi: 10.1175/JTECH-D-13-00011.1

Holland, M. M., Bailey, D. A., Briegleb, B. P., Light, B., and Hunke, E. (2012). Improved sea ice shortwave radiation physics in ccsm4: the impact of melt ponds and aerosols on arctic sea ice. *J. Clim.* 25, 1413–1430. doi: 10.1175/JCLI-D-11-00078.1

Houtekamer, P. L., and Mitchell, H. L. (2001). A sequential ensemble kalman filter for atmospheric data assimilation. *Month. Weather Rev.* 129, 123–137. doi: 10.1175/1520-0493(2001)129<0123:ASEKFF>2.0.CO;2

Jazwinski, A. H. (2007). *Stochastic Processes and Filtering Theory*. Mineola, NY: Dover Publications.

Jochum, M., Yeager, S., Lindsay, K., Moore, K., and Murtugudde, R. (2010). Quantification of the feedback between phytoplankton and enso in the community climate system model. *J. Clim.* 23, 2916–2925. doi: 10.1175/2010JCLI3254.1

Keenlyside, N., Latif, M., Jungclaus, J., Kornblueh, L., and Roeckner, E. (2008). Advancing decadal-scale climate prediction in the north atlantic sector. *Nature* 453, 84–88. doi: 10.1038/nature06921

Kessler, A., and Tjiputra, J. (2016). The southern ocean as a constraint to reduce uncertainty in future ocean carbon sinks. *Earth Syst. Dyn.* 7, 295–312. doi: 10.5194/esd-7-295-2016

Kimmritz, M., Counillon, F., Smedsrud, L. H., Bethke, I., Keenlyside, N., Ogawa, F., et al. (2019). Impact of ocean and sea ice initialisation on seasonal prediction skill in the arctic. *J. Adv. Model. Earth Syst.* 11, 4147–4166. doi: 10.1029/2019MS001825

Kirkevåg, A., Iversen, T., Seland, Ø., Hoose, C., Kristjánsson, J., Struthers, H., et al. (2013). Aerosol–climate interactions in the norwegian earth system model–noresm1-m. *Geosci. Model Dev.* 6, 207–244. doi: 10.5194/gmd-6-207-2013

Kwiatkowski, L., Torres, O., Bopp, L., Aumont, O., Chamberlain, M., Christian, J. R., et al. (2020). Twenty-first century ocean warming, acidification, deoxygenation, and upper-ocean nutrient and primary production decline from cmip6 model projections. *Biogeosciences* 17, 3439–3470. doi: 10.5194/bg-17-3439-2020

Lawrence, D. M., Oleson, K. W., Flanner, M. G., Thornton, P. E., Swenson, S. C., Lawrence, P. J., et al. (2011). Parameterization improvements and functional and structural advances in version 4 of the community land model. *J. Adv. Model. Earth Syst.* 3:M03001. doi: 10.1029/2011MS00045

Losa, S. N., Kivman, G. A., and Ryabchenko, V. A. (2004). Weak constraint parameter estimation for a simple ocean ecosystem model: what can we learn about the model and data? *J. Marine Syst.* 45, 1–20. doi: 10.1016/j.jmarsys.2003.08.005

Losa, S. N., Kivman, G. A., Schröter, J., and Wenzel, M. (2003). Sequential weak constraint parameter estimation in an ecosystem model. *J. Marine Syst.* 43, 31–49. doi: 10.1016/j.jmarsys.2003.06.001

Lovenduski, N. S., Yeager, S. G., Lindsay, K., and Long, M. C. (2019). Predicting near-term variability in ocean carbon uptake. *Earth Syst. Dyn.* 10, 45–57. doi: 10.5194/esd-10-45-2019

Maier-Reimer, E., Kriest, I., Segschneider, J., and Wetzel, P. (2005). The hamburg ocean carbon cycle model HAMOCC 5.1 (2005). Technical description release 1.1, Reports on Earth System Science. Hamburg: Max Planck Institute for Meteorology. Available online at: https://mpimet.mpg.de/fileadmin/publikationen/erdsystem_14.pdf

Marotzke, J., Jakob, C., Bony, S., Dirmeyer, P. A., O'Gorman, P. A., Hawkins, E., et al. (2017). Climate research must sharpen its view. *Nat. Clim. Change* 7, 89–91. doi: 10.1038/nclimate3206

Masutani, M., Schlatter, T. W., Errico, R. M., Stoffelen, A., Andersson, E., Lahoz, W., et al. (2010). "Observing system simulation experiments," in *Data Assimilation* Springer, 647–679.

Mattern, J. P., Fennel, K., and Dowd, M. (2012). Estimating time-dependent parameters for a biological ocean model using an emulator approach. *J. Marine Syst.* 96, 32–47. doi: 10.1016/j.jmarsys.2012.01.015

Mitchell, H. L., and Houtekamer, P. L. (2000). An adaptive ensemble kalman filter. *Month. Weather Rev.* 128, 416–433. doi: 10.1175/1520-0493(2000)128<0416:AAEKF>2.0.CO;2

Moradkhani, H., Sorooshian, S., Gupta, H. V., and Houser, P. R. (2005). Dual state–parameter estimation of hydrological models using ensemble kalman filter. *Adv. Water Resour.* 28, 135–147. doi: 10.1016/j.advwatres.2004.09.002

Natvik, L.-J., and Evensen, G. (2003). Assimilation of ocean colour data into a biochemical model of the north atlantic: part 1. data assimilation experiments. *J. Marine Syst.* 40, 127–153. doi: 10.1016/S0924-7963(03)00016-2

Oleson, K. W., Lawrence, D. M., Gordon, B., Flanner, M. G., Kluzek, E., Peter, J., et al. (2010). *Technical Description of Version 4.0 of the Community Land Model (CLM)*, Technical Report. ncar/tn-478+str. National Center for Atmospheric Research, Boulder.

Park, J.-Y., Stock, C. A., Dunne, J. P., Yang, X., and Rosati, A. (2019). Seasonal to multiannual marine ecosystem prediction with a global earth system model. *Science* 365, 284–288. doi: 10.1126/science.aav6634

Payne, M. R., Hobday, A. J., MacKenzie, B. R., Tommasi, D., Dempsey, D. P., Fässler, S. M., et al. (2017). Lessons from the first generation of marine ecological forecast products. *Front. Marine Sci.* 4:289. doi: 10.3389/fmars.2017.00289

Penny, S., Bach, E., Bhargava, K., Chang, C.-C., Da, C., Sun, L., et al. (2019). Strongly coupled data assimilation in multiscale media: experiments using a quasi-geostrophic coupled model. *J. Adv. Model. Earth Syst.* 11, 1803–1829. doi: 10.1029/2019MS001652

Penny, S. G., and Hamill, T. M. (2017). Coupled data assimilation for integrated earth system analysis and prediction. *Bull. Amer. Meteorol. Soc.* 98, ES169–ES172. doi: 10.1175/BAMS-D-17-0036.1

Reichle, R. H., McLaughlin, D. B., and Entekhabi, D. (2002). Hydrologic data assimilation with the ensemble kalman filter. *Month. Weather Rev.* 130, 103–114. doi: 10.1175/1520-0493(2002)130<0103:HDAWTE>2.0.CO;2

Roy, S., Broomhead, D. S., Platt, T., Sathyendranath, S., and Ciavatta, S. (2012). Sequential variations of phytoplankton growth and mortality in an npz model: a remote-sensing-based assessment. *J. Marine Syst.* 92, 16–29. doi: 10.1016/j.jmarsys.2011.10.001

Sakov, P., Counillon, F., Bertino, L., Lisæter, K., Oke, P., and Korablev, A. (2012). Topaz4: an ocean-sea ice data assimilation system for the north atlantic and arctic. *Ocean Sci.* 8, 633–656. doi: 10.5194/os-8-633-2012

Schwinger, J., Tjiputra, J., Goris, N., Six, K. D., Kirkevåg, A., Seland, Ø., et al. (2017). Amplification of global warming through ph dependence of dms production simulated with a fully coupled earth system model. *Biogeosciences* 14, 3633–3648. doi: 10.5194/bg-14-3633-2017

Séférian, R., Bopp, L., Gehlen, M., Swingedouw, D., Mignot, J., Guilyardi, E., et al. (2014). Multiyear predictability of tropical marine productivity. *Proc. Natl. Acad. Sci.* 111, 11646–11651. doi: 10.1073/pnas.1315855111

Simon, E., and Bertino, L. (2009). Application of the gaussian anamorphosis to assimilation in a 3-d coupled physical-ecosystem model of the north atlantic with the enkf: a twin experiment. *Ocean Sci.* 5, 495–510. doi: 10.5194/os-5-495-2009

Six, K. D., and Maier-Reimer, E. (1996). Effects of plankton dynamics on seasonal carbon fluxes in an ocean general circulation model. *Glob. Biogeochem. Cycles* 10, 559–583.

Smith, D. M., Cusack, S., Colman, A. W., Folland, C. K., Harris, G. R., and Murphy, J. M. (2007). Improved surface temperature prediction for the coming decade from a global climate model. *Science* 317, 796–799. doi: 10.1126/science.1139540

Smith, E. L. (1936). Photosynthesis in relation to light and carbon dioxide. *Proc. Natl. Acad. Sci. U.S.A.* 22:504.

Sperber, K., Annamalai, H., Kang, I.-S., Kitoh, A., Moise, A., Turner, A., et al. (2013). The asian summer monsoon: an intercomparison of cmip5 vs. cmip3 simulations of the late 20th century. *Clim. Dyn.* 41, 2711–2744. doi: 10.1007/s00382-012-1607-6

Tjiputra, J., Roelandt, C., Bentsen, M., Lawrence, D., Lorentzen, T., Schwinger, J., et al. (2013). Evaluation of the carbon cycle components in the norwegian earth system model (noresm). *Geosci. Model Dev.* 6, 301–325. doi: 10.5194/gmd-6-301-2013

Tjiputra, J. F., Polzin, D., and Winguth, A. M. (2007). Assimilation of seasonal chlorophyll and nutrient data into an adjoint three-dimensional ocean carbon cycle model: sensitivity analysis and ecosystem parameter optimization. *Glob. Biogeochem. Cycles* 21. GB1001. doi: 10.1029/2006GB002745

Tjiputra, J. F., Schwinger, J., Bentsen, M., Morée, A. L., Gao, S., Bethke, I., et al. (2020). Ocean biogeochemistry in the norwegian earth system model version 2 (noresm2). *Geosci. Model Dev.* 13, 2393–2431. doi: 10.5194/gmd-13-2393-2020

Vancoppenolle, M., Bopp, L., Madec, G., Dunne, J., Ilyina, T., Halloran, P. R., et al. (2013). Future arctic ocean primary productivity from cmip5 simulations: Uncertain outcome, but consistent mechanisms. *Glob. Biogeochem. Cycles* 27, 605–619. doi: 10.1002/gbc.20055

Vertenstein, M., Craig, T., Middleton, A., Feddema, D., and Fischer, C. (2012). *Cesm1. 0.4 User's Guide.* UCAR Doc 146.

Wang, Y., Counillon, F., and Bertino, L. (2016). Alleviating the bias induced by the linear analysis update with an isopycnal ocean model. *Quart. J. R. Meteorol. Soc.* 142, 1064–1074. doi: 10.1002/qj.2709

Wang, Y., Counillon, F., Bethke, I., Keenlyside, N., Bocquet, M., and Shen, M.-l. (2017). Optimising assimilation of hydrographic profiles into isopycnal ocean models with ensemble data assimilation. *Ocean Model.* 114, 33–44. doi: 10.1016/j.ocemod.2017.04.007

Wang, Y., Counillon, F., Keenlyside, N., Svendsen, L., Gleixner, S., Kimmritz, M., et al. (2019). Seasonal predictions initialised by assimilating sea surface temperature observations with the enkf. *Clim. Dyn.* 53, 5777–5797. doi: 10.1007/s00382-019-04897-9

Wen, X.-H., and Chen, W. H. (2006). Real-time reservoir model updating using ensemble kalman filter with confirming option. *Spe J.* 11, 431–442. doi: 10.2118/92991-PA

Yu, L., Fennel, K., Bertino, L., El Gharamti, M., and Thompson, K. R. (2018). Insights on multivariate updates of physical and biogeochemical ocean variables using an ensemble kalman filter and an idealized model of upwelling. *Ocean Model.* 126, 13–28. doi: 10.1016/j.ocemod.2018.04.005

Conflict of Interest: The authors declare that the research was conducted in the absence of any commercial or financial relationships that could be construed as a potential conflict of interest.

Publisher's Note: All claims expressed in this article are solely those of the authors and do not necessarily represent those of their affiliated organizations, or those of the publisher, the editors and the reviewers. Any product that may be evaluated in this article, or claim that may be made by its manufacturer, is not guaranteed or endorsed by the publisher.

Advantages of publishing in Frontiers

OPEN ACCESS
Articles are free to read for greatest visibility and readership

FAST PUBLICATION
Around 90 days from submission to decision

HIGH QUALITY PEER-REVIEW
Rigorous, collaborative, and constructive peer-review

TRANSPARENT PEER-REVIEW
Editors and reviewers acknowledged by name on published articles

Frontiers
Avenue du Tribunal-Fédéral 34
1005 Lausanne | Switzerland

Visit us: www.frontiersin.org
Contact us: frontiersin.org/about/contact

REPRODUCIBILITY OF RESEARCH
Support open data and methods to enhance research reproducibility

DIGITAL PUBLISHING
Articles designed for optimal readership across devices

FOLLOW US
@frontiersin

IMPACT METRICS
Advanced article metrics track visibility across digital media

EXTENSIVE PROMOTION
Marketing and promotion of impactful research

LOOP RESEARCH NETWORK
Our network increases your article's readership